RISK - COST - BENEFIT FRAMEWORK FOR THE DESIGN OF DEWATERING SYSTEMS IN OPEN PIT MINES

By

Tony Sperling

B.A.Sc., The University of British Columbia, 1983
M.A.Sc., The University of British Columbia, 1985

A THESIS SUBMITTED IN PARTIAL FULFILLMENT OF
THE REQUIREMENTS FOR THE DEGREE OF
DOCTOR OF PHILOSOPHY

in

THE FACULTY OF GRADUATE STUDIES
Department of Geological Sciences

We accept this thesis as conforming
to the required standard

THE UNIVERSITY OF BRITISH COLUMBIA

April 1991

08

Department of GEOLOGICAL SCIENCES

The University of British Columbia
Vancouver, Canada

Date APRIL 30, 1991

ABSTRACT

Control of groundwater plays an important part in operations at many open pit mines. Selection of an efficient and cost effective dewatering program that will improve slope stability of the pit walls is frequently complicated by the complex and somewhat uncertain hydrogeologic environment found at most mine sites. This dissertation describes a risk-cost-benefit (RCB) framework that can be used to identify the most effective dewatering strategy under such conditions, because the stochastic framework explicitly accounts for uncertainty in hydrogeologic and shear strength parameters in the groundwater flow, slope stability and economic analyses.

In the framework, the monetary worth of each design alternative is measured in terms of an economic objective function. This function is defined in terms of a discounted stream of benefits, costs and risks over the operational life of the mine. Benefits consist of revenue generated from the sale of mineral concentrate. Costs include normal operating and dewatering expenses. Monetary risks are defined as the economic consequences associated with slope failure of the pit wall, multiplied by the probability of such a failure occurring. Selection of the best design strategy from a specified set of alternatives is achieved by determining the economic objective function for each design and then selecting the alternative that yields the highest value of the objective function.

Estimation of the probability of slope failure requires an accurate assessment of the level of uncertainty associated with each input parameter, a forecast of how dewatering efforts are expected to affect pore pressures in the pit wall in light of the uncertain hydrogeologic environment, and an evaluation of the effect that the pore pressure reductions will have on improving stability of the pit wall. Prediction of the pore pressure response to dewatering efforts is achieved with *SG-FLOW*, a steady state, saturated-unsaturated finite element model of groundwater flow. Slope stability is evaluated with *SG-SLOPE*, a two dimensional, limit equilibrium stability model based on the versatile Sarma method of stability analysis. To account for input parameter uncertainty, both the groundwater flow stability models are invoked in a conditional Monte-Carlo simulation that is based on a geostatistical description of the level of uncertainty inherent in the available hydrogeological and geotechnical data.

Besides documenting the methodology implemented in the framework to conduct the geostatistical, groundwater flow and economic analyses of the objective function, this dissertation also presents a sensitivity analysis and a case history study that demonstrate the application of the RCB framework to design problems typically encountered in operating mines.

The sensitivity study explores how each set of input parameters, including hydrologic data, shear strength parameters, slope angles of the pit wall and dewatering system specifications impact on the profitability of the mining operation. The study utilized a base case scenario that is based on overburden conditions at Highland Valley Copper; therefore, the conclusions cannot be applied blindly at other sites. However, the framework can be used to formulate site specific conclusions for other large base-metal open pit mines. After the objective function was calculated for the base case, the aforementioned input parameters were systematically perturbed in turn to study how each parameter impacts on profitability of the mine. The sensitivity study showed that in the particular case analyzed changes in the slope angle and dewatering efforts can improve profitability by many millions of dollars. In particular, steep slope angles can be utilized in the early stages of mine development while the pit walls are relatively low, and then flattened as the pit wall height increases and the monetary consequences of slope failure become more pronounced. Furthermore, the sensitivity results indicated that pit dewatering is likely to be effective over a range of hydraulic conductivities from 1×10^{-8} m/s to 1×10^{-5} m/s and that accurate estimation of the mean hydraulic conductivity is much more important than estimating other statistics that describe the hydraulic conductivity field, including the variance and the range of correlation. Results of the sensitivity study clearly demonstrate that the RCB framework can be used effectively to identify the most effective dewatering strategy given a limited amount of geologic and hydrologic information. Also, it is shown that the framework can be used to identify the most important input parameters for each specific dewatering problem and to establish the approximate monetary worth of data collection.

The case history study documents how the RCB framework was applied at Highland Valley Copper (HVC). Groundwater control is recognized as an important component of mining operations at this mine site; dewatering measures utilized on the property involve both high capacity dewatering wells and horizontal drains. The benefits of pit dewatering include improved slope stability, drier operating conditions in the pit, and a convenient production water supply. These benefits do not come cheaply; HVC is expecting to spend in excess of six million dollars on groundwater control in the next ten years. Before investing such large sums in groundwater control, mine management should be confident that the capital investment is justified, i.e. that the resulting economic benefits will significantly exceed the costs of the dewatering effort. Using historical data provided by HVC, the case history study documented in this dissertation shows how the RCB framework is used to identify the most profitable combination of slope geometry and groundwater control in design sector R3 of HVC's Valley Pit. By considering three possible slope angle and groundwater control options it is shown that by continuing to implement an aggressive dewatering program, HVC can expect to reduce operating costs by as much as nine million dollars in this design sector.

Graduate Supervisor: R. Allan Freeze
Department of Geological Sciences

TABLE OF CONTENTS

TABLE OF CONTENTS

TABLE OF CONTENTS

TABLE OF CONTENTS

LIST OF FIGURES

LIST OF FIGURES

LIST OF FIGURES

LIST OF FIGURES

Page

LIST OF TABLES

ACKNOWLEDGEMENTS

Foremost, I would like to acknowledge the guidance and support provided by Allan Freeze in his role as thesis supervisor. His enthusiasm for widespread use of risk based engineering design in hydrogeology provided inspiration throughout all phases of this research effort.

Also, I would like to extend my appreciation to Chuck Brawner, Bill Caselton, Drummond Cavers and Les Smith for serving on the advisory committee. In particular, I wish to acknowledge the encouragement and advice in the art of geotechnique provided by Drummond Cavers, who took valuable time out from his consulting practice to review, discuss and constructively criticize at each opportunity. Also, Chuck Brawner deserves a special thank you for encouraging me to apply the research in practice, and especially for opening the doors to Highland Valley Copper's direct involvement in the case history study.

The most rewarding aspect of my research has been the application of the framework to the design of dewatering facilities at Highland Valley Copper. To this end, I would like to thank the management at Highland Valley Copper, and especially W.K. Munro and F. Amon of the Mine Engineering Department, for providing the opportunity to become directly involved in all aspects of their dewatering operations.

Financial support provided by the National Research Council of Canada Scholarships and The University Graduate Fellowships during the course of my studies has been very appreciated.

Many thanks are extended to the Department of Hydrogeology and Water Resources at the University of Arizona, and in particular Schlomo Neuman and Tom Maddock, for their hospitalities during the author's six month visit.

Among the graduate students of UBC's Groundwater Group, I wish to acknowledge Bruce James, Lorrie Cahn, and Craig Forster for their interest, insight and warm generosity.

Special gratitude is due to Dave Osmond and John Gartner of Gartner Lee Limited for providing financial support, freedom and encouragement to complete writing of the dissertation during the past year.

In closing, I would like to thank my parents, Aljeh Chambers and numerous friends for their continued interest in my progress and their encouragement to see the job completed. It is a joy to be able to say that finally, the thesis is done.

CHAPTER 1 INTRODUCTION

This thesis introduces a risk-cost-benefit framework for the design of groundwater control systems at open pit mines and demonstrates how the framework has been used successfully to identify the optimum slope configuration and dewatering design at Highland Valley Copper, one of the largest copper mines in the world.

1.1 PROBLEM DESCRIPTION

Open pit mining is a very costly endeavour. Excavation and haulage costs alone typically range from 4 to 40 million dollars per year, depending on the size of the mining operation. Steepening of the ultimate pit wall will reduce mining costs provided that stability of the pit wall can be maintained. The cost reductions are realized because less waste material has to be moved to expose and extract the ore body. A steep pit wall is also desirable during the first few pit expansions because it will lead to increased cash flow during the critical early years of mine production. For these reasons mine operators continually strive to design the pit walls as steeply as possible while maintaining stability. However, if a pit wall is over-steepened and one or more large failures develop, then the mine operator will experience severe economic consequences, especially if the failure impedes or curtails normal production.

Stability of the pit wall is controlled by geologic conditions, groundwater conditions, blasting, and slope design. Stability can often be improved by a properly engineered groundwater control program, especially if high groundwater pore pressures are anticipated. In many instances, reduction of pore pressures will improve stability sufficiently to permit steepening of the pit walls by several degrees without increasing the risk of slope failure. Unfortunately, groundwater control is also an expensive undertaking. Prior to committing to a dewatering program, mine management must ascertain whether the benefits of improved stability and a steeper slope design will be sufficient to justify the extra costs of groundwater control. Even when it appears obvious that some form of groundwater control program will be beneficial, identifying the optimum dewatering strategy is a formidable task, especially when detailed knowledge of actual subsurface conditions is not available. A satisfactory solution to the problem of selecting the most appropriate slope angle and optimum dewatering strategy under conditions of geologic and hydrologic uncertainty will benefit the mining community because a wrong design decision can result in operating cost increases of tens of millions of dollars over the life of a large open pit mine.

Providing a satisfactory solution requires an integrated, multi-disciplined analysis. The analysis must involve:

- An assessment of subsurface geologic conditions, the objective being to accurately estimate both geotechnical and hydrogeologic parameters in the pit wall. The effect of uncertainty in parameter estimates must be recognized and considered in the assessment.

- An analysis of groundwater flow, the objectives being to predict pore pressures on the failure surface and to determine the likely impact of the dewatering program being considered.

- An evaluation of slope stability. The stability evaluation must utilize the pore pressure estimates obtained above, as well as account for uncertainty in strength parameters.

- An economic evaluation of the slope design and dewatering strategy. The evaluation must consider revenues, production costs, costs of groundwater control and costs of data collection, as well as the monetary consequences of a pit wall failure, and the likelihood of such a failure developing.

1.2 RESEARCH OBJECTIVES

The primary objective of this research effort is to develop a comprehensive design tool, based on the risk-cost-benefit framework, that can address the tasks listed above in an integrated, technically sound, and economically defensible manner. A number of secondary goals were also identified at the start of the research effort. These objectives are listed below in order of importance:

- To develop a practical framework that could be applied widely in industry to any number of site specific design problems.

- To incorporate the latest engineering approaches to the analysis of each of the four design problems encountered in this framework: geostatistical interpretation, groundwater modelling, slope stability analysis, and decision analysis.

- To demonstrate that the framework can be applied successfully at an operating mine, and used to make actual dewatering design decisions that will increase profitability of the mining operation.

- To develop the framework as a flexible, user-friendly, graphically intensive software package that can be executed on low cost personal computers, yet will have sufficient power to tackle realistic design problems.

1.3 SCOPE

The research objectives were achieved in sequential fashion through literature review, algorithm development, computer programming, sensitivity analysis, geotechnical and hydrogeologic site investigation, and engineering analysis and design.

The detailed literature review, conducted in 1985-86, focused on identifying methods of estimating subsurface conditions from limited field data, of modelling groundwater flow, of evaluating slope stability, and of assessing the monetary value of various design alternatives. The goal of the literature review was to identify techniques for each of these tasks that could be successfully integrated into a unified framework. Upon completion, it was concluded that the risk-cost-benefit framework could be successfully developed if the following analytical methods were adopted: 1) geostatistical methods for the task of parameter estimation, 2) a two dimensional saturated/unsaturated finite element technique for simulation of groundwater flow, 3) the Sarma two dimensional limit equilibrium approach for slope stability, and 4) an expected value decision analysis technique for the economic impact assessment.

Development of the four principal computer modules (1. geostatistics, 2. groundwater, 3. slope stability, and 4. economic analysis) was completed in 1986-1988. All of the computer modules were developed by the author. The modules were based on solution strategies documented in the literature, and coupled with advanced, graphic intensive data entry and output display modules, also developed by the author. When developing the software modules, the intent was to prepare a user friendly software package, one that would be capable of analyzing complex design problems quickly and efficiently. Fortran-77, and Quick-Basic were selected for the programming effort so that the resulting software would be portable, and fully compatible with most IBM compatible personal computers.

Upon completion of the software development, the risk-cost-benefit framework was utilized to conduct a sensitivity study that evaluated the importance of groundwater control in open pit mines. As well, the sensitivity study examined the effect of changes to the slope angle and the dewatering budget, and the potential impact of the number and accuracy of hydraulic conductivity and shear strength measurements on mine economics.

A major part of this research effort involved the application of the risk-cost-benefit framework to evaluate the groundwater control system at Highland Valley Copper. The design effort is documented as a case history. It involved two distinct components.

First, during the spring and summer months of 1987 and 1988 the author was on site at Highland Valley Copper, where he worked closely with mine engineering personnel and drilling contractors to establish the large data base required for the analysis. The data acquisition program entailed detailed geotechnical logging, piezometer and well monitoring, pump testing, and shear strength testing. All new data, as well as previously collected information, was entered into a computer data base and analyzed to establish the best possible values for input parameters required for the risk-cost-benefit analysis.

Second, the new framework was used to conduct a detailed assessment of the current overburden dewatering strategy at Highland Valley Copper. Several alternative dewatering strategies were also evaluated with the risk-cost-benefit framework in an attempt to identify the most cost effective dewatering design for Highland Valley Copper.

1.4 THESIS OVERVIEW

This thesis is comprised of nine chapters and five appendices. This chapter and *Chapter 2* provide an introduction to the thesis research and document why the research is beneficial to Canada's mining industry. *Chapters 3* through *6* focus on the four technical components of the framework, including the decision framework in *Chapter 3*, the geostatistics methodology in *Chapter 4*, the groundwater flow model in *Chapter 5*, and the slope stability analysis in *Chapter 6*. *Chapters 7 & 8* describe how the new framework has been used to improve pit dewatering strategies in general, and at Highland Valley Copper in particular. *Chapter 9* serves as a summary of the key findings presented in this thesis, placing emphasis on research contributions to the mining, hydrogeological, and geotechnical communities. *Appendices A* through *C* provide a more detailed discussion of the theory underlying the analytical techniques utilized in this thesis, *Appendix D* presents the results of the numerous sensitivity studies, and *Appendix E* provides background information about the Highland Valley case history. The paragraphs that follow provide a brief overview of the material discussed in each chapter.

Chapter 2 describes the numerous ways groundwater can impact on the open pit mining operation. The chapter begins with a brief description of modern open pit mining methods and a discussion of how the mining operation can be affected by pit wall instability. The most common methods of improving slope stability are then reviewed, especially the techniques of groundwater control. The chapter concludes with a brief cost comparison that illustrates that groundwater control can be a very cost effective method of improving slope stability in many circumstances.

Chapter 3 presents the risk-cost-benefit framework. First, the chapter introduces decision analysis and describes how this tool can be used to evaluate the expected worth of a number of different dewatering and slope design strategies. The discussion then focuses on the objective function, explaining why *expected net income* provides a suitable measure of the monetary value of each design strategy. Each of the four terms that comprise the objective function are then examined in detail; the terms include benefits, production costs, dewatering costs, and risks. The assessment of benefits and costs is relatively straightforward; however, the calculation of monetary risk is much more complex because it is dependent on the probability of failure.

Probability of failure is a measure of slope stability. It is a function of the slope design, of the effectiveness of dewatering strategy, and of the hydrologic and the shear strength conditions in the pit wall. Both shear strength and hydrologic conditions are always uncertain to some degree. The remainder of *Chapter 3* describes the new methodology that has been developed as part of this thesis to evaluate the probability of slope failure. The methodology is different from traditional design approaches in that it explicitly accounts for uncertainty in both hydrogeologic and shear strength parameters. The probability of failure assessment involves a geostatistical analysis of subsurface conditions, followed by Monte-Carlo analyses of groundwater pore pressures and slope stability to obtain the probability of failure, and finally, an economic evaluation to determine the objective function. *Chapter 3* shows how these components come together to form the risk-cost-benefit framework; *Chapters 4* through *6* provide more detailed descriptions of the various techniques that are necessary in order to successfully apply the framework to solve actual field problems.

Chapter 4 introduces the geostatistical tools that are utilized in this framework to generate the large number of realizations of the hydraulic conductivity field required for Monte Carlo simulation. The chapter begins with a review of the basic geostatistical concepts and terminology. A number of semi-variogram models are then presented, as are several efficient techniques for fitting the semi-variogram model to the experimental semi-variogram. The discussion then focuses on *Kriging*, a parameter estimation method that results in the *Best Linear Unbiased Estimate (BLUE)*. *Kriging* is used in this framework to make an estimate of hydraulic conductivities everywhere in the flow domain based on a limited number of measurements, and to determine the estimation error associated with each hydraulic conductivity prediction. Finally, *Chapter 4* examines a number of *simulation* techniques that can be used to generate the large number of hydraulic conductivity realizations required for the Monte-Carlo analysis of groundwater flow.

Chapter 5 describes the computer modelling approach that is used to predict groundwater pore pressures in the pit wall. The discussion begins with a description of the unsaturated groundwater flow system that exists in open pit walls, and how the system can be described in terms of a boundary value problem that can be solved by numerical modelling. The finite element method is then introduced; the presentation is very brief and focuses primarily on the iterative solution strategy that is used to account for flow through the unsaturated zone and to predict the location of the water table. The theme then switches to more pragmatic issues: the important effect of stratigraphy and how it can affect the pore pressure field, the role of boundary conditions, and the importance of hydraulic conductivity measurements.

Probability of failure is the most important and complex factor in the assessment of monetary risk due to pit wall failure. *Chapter 6* describes how limit equilibrium stability analysis and Monte-Carlo simulation techniques are used to estimate this essential parameter. Beginning with a review of available limit equilibrium methods, the discussion quickly focuses on *Sarma's* method of slices, the technique utilized in this framework. The mechanics of *Sarma's* method are then explored, with special attention directed to the factor of safety convergence problem experienced by previous users. The cause of this iteration problem is identified and a new iteration strategy is introduced that overcomes the convergence problem in most circumstances. The effect of groundwater on slope stability is then explored, the objective being to illustrate why dewatering can lead to dramatic improvements in stability of the pit wall. Finally, the discussion turns to probabilistic methods of slope stability analysis that, unlike the popular factor-of-safety approach, explicitly consider the effect of uncertainty and variability of geologic and hydrologic parameters in the stability assessment of pit walls. Because the probability of failure can also be incorporated directly into the economic evaluation model, it is the preferred stability criterion in this thesis.

Chapter 7 presents the results of a detailed sensitivity study that utilized the new framework to explore how each of the many input parameters and decision variables (e.g. hydrologic data, shear strength parameters, pit angles, dewatering design, etc.) impact on the overall economics of the mining operation. Key issues that are investigated include:

- How to assess the economic impact of changes to the pit-wall angle, in particular, how the optimum slope angle can be identified.

- How to predict the influence of hydrogeologic conditions in the subsurface on the effectiveness of a dewatering program, in particular, the effect of the mean hydraulic conductivity, the variance in hydraulic conductivity, and the correlation range.

- How to determine the value of shear strength conditions, especially whether shear strength measurements are more or less important than hydraulic conductivity data.

- How to identify the optimum level of expenditure for the groundwater control effort.

- How to identify the monetary worth of hydraulic conductivity measurements, especially when to stop additional site investigation efforts.

Chapter 8 documents how the new framework was used to evaluate the current overburden dewatering strategy at Highland Valley Copper and to identify dewatering design modifications that could increase profitability of the mining operation. The case history includes a description of the input parameters that are required to conduct the analysis, including geologic conditions, hydrologic conditions, the current pit design, and the current dewatering strategy. Emphasis is placed on describing how the various types of geologic and hydrologic information were integrated into a unified geostatistical description of the hydraulic conductivity field. After evaluating the current slope design and dewatering strategy, the framework is used to evaluate several alternative dewatering designs in an attempt to identify a more efficient groundwater control plan. However, the case history presented in *Chapter 8* is not a dewatering design study. More field work (especially direct shear testing), transient flow modelling and stability analyses that consider the full spectrum of possible failure modes will be required before results of this RCB framework can be used with confidence to justify modifications to the current slope design and dewatering plan.

Chapter 9 provides a global summary of the thesis. The contents and key conclusions of each chapter are briefly reviewed. Also, the principal assumptions that have been adopted in the framework are summarized.

CHAPTER 2 GROUNDWATER CONTROL IN OPEN PIT MINES

2.1 *INTRODUCTION*

This chapter serves as an introduction to the subject of groundwater control in open pit mines. Because optimizing the design of modern open pit mines has become a complex undertaking that requires a coordinated effort amongst specialists trained in geology, geostatistics, geotechnics, mine operations, mineral processing, economics and marketing, the discussion is not limited to the narrow subject of groundwater control from a hydrogeologic perspective, rather, it examines the impacts of groundwater control on all aspects of mine operations.

The chapter begins with a brief introduction to open pit mining. Subjects that are discussed include typical pit sizes, production rates, mine design concepts and components of the mining sequence. The issue of slope stability is examined next, with emphasis on the motivation for steep slopes, the consequences of failure, and the accepted deterministic approach to slope design. The subject of groundwater is then introduced, first identifying the potential impacts of groundwater on mine operations and then presenting a review of the various control methods. The chapter concludes with a few words on the economics and suitability of various dewatering options.

2.2 *CANADIAN MINING INDUSTRY*

Over the past 30 years, Canada has consistently remained in an enviable position as one of the world's largest and lowest cost mineral producers. Mineral production in Canada has been increasing steadily, today the Canadian mining industry generates over $15 billion in revenue per year from mineral exports that include gold, coal, copper, zinc, iron ore, and a host of other mineral commodities. In 1987, Canada ranked first as a world producer of uranium and zinc, second for potash, nickel, sulphur, asbestos and gypsum, third for titanium, cadmium, aluminum, platinum and gold, and fourth for copper, molybdenum, lead and cobalt. A large percentage of these mineral commodities are produced at open pit mines.

In the late 1980's demand for many metal commodities returned to pre-recession levels, but prices remained depressed as a result of adequate supplies and strong international competition. The Mining Association of Canada predicts that the mining industry can adjust to the new, more competitive international market, but it will require careful management, cost control, and continued productivity improvements. The association believes that in the long term, increased productivity and cost control can only be achieved by technological innovation, effective marketing, and the discovery of new, high quality mineral deposits.

Based on results of risk-cost-benefit studies presented later in the sensitivity and case history chapters of this thesis, it appears that a high technology approach to dewatering design may provide the industry with one such alternative for reducing operating costs and gaining a competitive advantage in international markets.

Figure 2.1 Mine Planning and the Daily Production Cycle

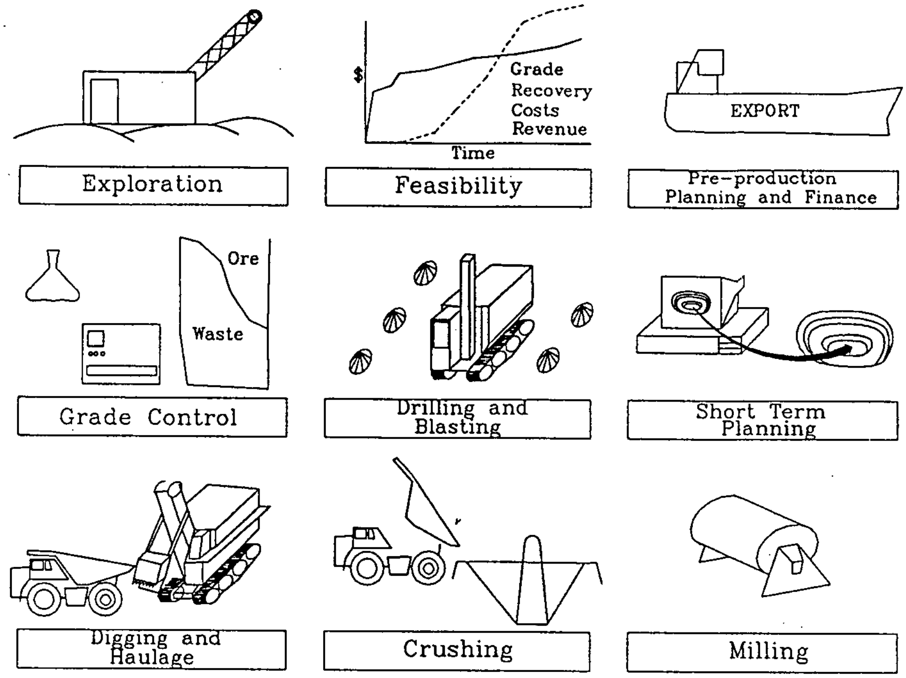

2.3 OPEN PIT MINING OPERATIONS

Open pit mining methods are used to extract ore from economic deposits situated close to surface and for large volume, low grade ore bodies, e.g. the large copper porphyry deposits found in British Columbia. The size of pits varies from small glory holes several hundred metres in diameter and less than 100 m in depth to pits over 2 km in diameter and 1 km in depth. The mill size is usually selected so that the mine will operate over a period 10 to 20 years. Production rates of 10,000 to 100,000 tons per day are typically required to provide adequate feed to the mill.

Mining operations can be broken down into three broad categories: 1) pre-production planning and infrastructure development, 2) production cycle and 3) decommissioning and reclamation. The following paragraphs provide a brief introduction to the activities conducted during each phase of operations. The normal sequence of these activities are portrayed in *Figure 2.1.*

2.3.1 Pre-production Planning

Pre-production planning begins shortly after exploration activities identify a mineral deposit of sufficient size and grade to be potentially economic. The first stage of this planning process normally involves drilling on tight spacings to prove ore reserves, detailed geologic interpretation of the drill results, and geostatistical modelling to predict grades. If the results continue to be encouraging then the planning process advances to include concentrate recovery studies, geotechnical investigations, preliminary pit design, equipment selection, environmental impact evaluations and economic studies. If these feasibility studies continue to show that the mine will be physically and economically viable then the planning process advances once more to the development stage. Markets are established, financing is arranged and construction begins on mill facilities, maintenance shops, tailing disposal facilities, and transportation corridors.

2.3.2 Production Cycle

Once the mine and mill are brought on stream, a routine daily production cycle is established. The cycle begins with short term planning to identify which benches will be worked in order to provide a balanced flow of ore and waste from the pit and to produce a mill feed with relatively constant grade and hardness properties. Blast patterns are laid out, drilled, loaded and detonated. Drill cuttings are sampled and analyzed for mineral content to differentiate between zones that should be mined as ore and those to be shipped as waste. The blasted rock is excavated with large electric shovels and loaded into haulage trucks for transport out of the pit. Ore is sent to the primary crusher where it is reduced to a coarse gravel size for feed into the mill. Waste is hauled to adjacent waste dumps. In the mill, the ore is processed through several grinding and floatation circuits to separate the economic mineralization from the tailings. The concentrate is then dried and shipped to smelters while the tailings are pumped to the tailings pond for disposal.

2.3.3 Decommissioning and Reclamation

Once all economic mineralization is removed from the pit, the mine is closed. In the past, the decommissioning process involved nothing more than salvaging any usable equipment and closing all doors. Abandoned mine sites full of interesting relics are frequently encountered in the back country. Recent amendments to the Mines Act require operators to thoroughly reclaim disturbed ground. All facilities must be removed, waste dumps and tailings facilities must be contoured and reseeded, and in the case of acid mine drainage (AMD) generating mines, adequate abatement measures must be incorporated in the reclamation plan to ensure that the environment will not be affected by AMD in perpetuity.

2.4 SLOPE STABILITY CONSIDERATIONS

There is a strong economic incentive for designing pit walls as steeply as possible, especially during the final push-back. By adopting a steep slope angle, the mine will be able to leave more waste undisturbed while fully exploiting the ore body. On account of the reduced stripping requirements, the mine will benefit from reduced operating costs, less waste rock to dispose of on dumps, and more rapid exploitation of the ore body. *Figure 2.2* provides a conceptual illustration of the relationship between slope angle, increased stripping and increased production costs. The left half of the figure shows a cross-section through a cylindrical ore body and several possible slope angles. The right half of the figure shows total waste tonnage and stripping cost as function of the slope angle. By steepening the pit from 30° to 35° for example, the mine would stand to reduce total stripping costs from $2.23 billion to $1.75 billion, based on a typical mining cost of $1.25 per tonne.

Steepening of the pit wall will usually result in decreased slope stability, and in most cases, an increase in the probability of failure. If a pit wall is over-steepened and one or more large failures develop, then the mine will experience severe economic consequences, especially if the failure impedes or curtails normal production. The consequences of slope failure may include:

- Clean up costs of removing failed material from pit. Costs may be somewhat higher than excavating material in situ if the rubble breaks into large blocks that require additional blasting.
- Lost production, especially if the slope failure affects a primary haul road or conveyor line, or if the failure buries an active mining area (e.g. bottom of pit)
- Lost ore, if the failure block contains ore that cannot be separated from waste within the failure rubble or the costs of clean-up are sufficiently high to render further mining uneconomic.
- Reduced cash-flow, especially when a primary haul road is affected.
- Damaged equipment and services, e.g. shovels, water pipe lines, conveyor systems.
- Physical risk to workers and portable equipment in pit.

Figure 2.2 Relationship Between Slope Angle and Stripping Costs

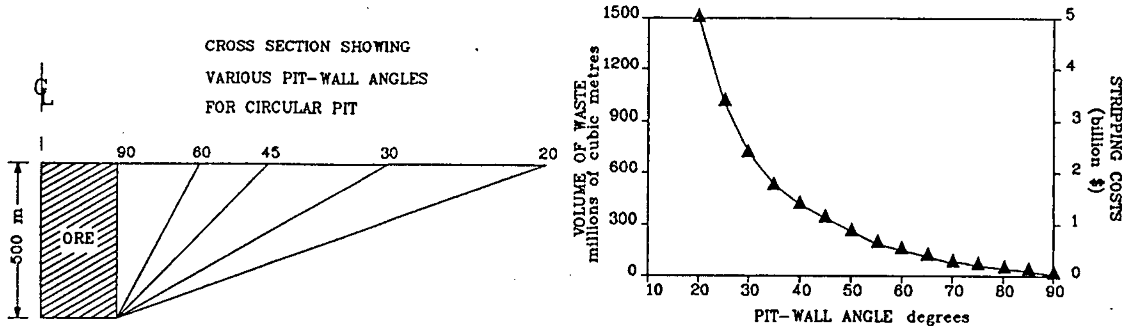

Only costs of clean-up, lost production and lost ore are considered in this risk-cost-benefit formulation because these items generally represent the most costly consequences of slope failure. It is also possible to assign a fair monetary value to these consequences directly, based on ore grade and slope geometry data. Cash-flow and equipment damage considerations have not been incorporated in the formulation as yet, because these consequences are believed to be economically less significant than consequences 1 to 3 and because estimation of these parameters would require a detailed economic study that is beyond the scope of this thesis. The potential hazard to mine workers as a result of slope failure is also not addressed explicitly in this study because it is assumed that for the large volume slides considered, modern slope monitoring methods will provide sufficient advance warning of impending slope failure to ensure that all men and equipment are removed from the pit well in advance of any life threatening slope movement.

In the process of selecting the most suitable slope geometry, mine engineering staff usually attempt to identify the steepest slope angle that will have an acceptable factor of safety against failure. The traditional deterministic approach to this problem has been to design large pit slopes to a factor of safety of 1.1 to 1.5. The higher factor of safety is adopted when there is uncertainty regarding shear strength parameters or when it is especially important to maintain stability in a particular design sector (e.g. haul road or in-pit crusher located below wall).

In the risk-based design approach proposed in this thesis economic considerations dictate the optimum probability of failure. The objective is to balance the benefits of a steeper slope against the monetary risks of failure. During the limited number of sensitivity and case history analyses conducted as part of this thesis research it was found that the optimum slope design was always associated with a low probability of failure, typically in the range of 0 to 5%. In the same studies, it was also observed that the mean factor of safety for the optimum slope design usually exceeded a factor of safety of 1.1, the minimum deterministic stability criterion.

Additional research and more case history studies of the risk-cost-benefit approach to slope design are required before suitable design guidelines can be drawn-up in terms of probability of failure and monetary risk. In the interim, it is recommended that the risk-cost-benefit framework proposed in this thesis be applied in parallel with the traditional factor of safety approach, and that all designs exceed a minimum factor of safety criterion of 1.1.

2.5 GROUNDWATER IMPACTS ON MINE PRODUCTION

Groundwater can impact on open pit mine operations in many ways. The most common impacts include:

- Slope Stability
- Slope Erosion
- Trafficability
- Blasting
- Production Water
- Environmental Impacts

Each of these impacts are discussed briefly in the following paragraphs.

Slope Stability: The effect of groundwater pore pressures on slope stability is explained by the principle of effective stress. Given that the total stress remains constant, any increase in pore pressure will result in an equal decrease in effective stress and a loss in the frictional component of shear strength. The underlying theory is reviewed more completely in *Section 6.6* of this thesis, additional references are also cited in that section. Recently, many open pit mines have introduced groundwater control programs to improve slope stability, and especially, to stabilize problem areas that have experienced some deformation.

Slope Erosion: Groundwater seepage can lead to gradual berm deterioration in areas where the pit wall is excavated in overburden or highly weathered bedrock. The deterioration can be caused by the following mechanisms. Rapid excavation or freezing at the seepage face can induce pore pressures that exceed the confining stress and result in berm scale spalling failures. Accumulation of water within the loose sluff found at the toe of overburden berms can lead to liquefaction failures. Continued seepage can wash-out fine grained soils from the berm face, resulting in progressive over-steepening and eventual collapse.

Trafficability: In overburden and highly weathered bedrock, uncontrolled seepage can turn operating surfaces into a quagmire that bogs down equipment and results in an increased frequency of mechanical breakdowns, especially the front drives on shovel undercarriages. In problem areas, mine operators place a 1 to 2 m thick layer of waste rock to establish a bearing pad capable of sustaining vehicle traffic. This double handling of waste rock can increase mining costs by 10 to 20%.

Blasting: On account of it's low cost, ANFO (Ammonium Nitrate Fuel Oil) is the explosive of choice in open pit mining applications. However, ANFO is unstable in water, so more expensive emulsion based slurry explosives must be utilized in wet blast holes. Because of the difference in the price of the two explosives ($24.90/m loaded with ANFO vs. $59.30/m loaded with slurry), blasting costs typically increase by several million dollars per year when wet conditions requiring slurry explosives are consistently encountered.

Production Water: Immense quantities of production water are required by modern high tonnage mills. For example, the mill complex at Highland Valley Copper requires 291 million litres of water per day. Although much or the production water is continuously recycled from the tailings pond, 10 to 20% of the daily demand must be replenished on a continuous basis. Although many mines in British Columbia can draw on local surface water supplies to provide all of their water requirements at nominal cost, other mines must pump water from far away sources at substantial cost. In the later situation, groundwater generated by the dewatering program provides a cost effective substitute to pumping from a remote source.

Environmental Impacts: Without proper regard for environmental issues, operating mines can have a detrimental impact on surface and groundwater hydrology, affecting both water quality and quantity. Due to growing public awareness in environmental issues, legislation is being introduced to ensure that all future mining operations will be conducted in a responsible manner. As a result of these developments, the additional costs and risks of environmental protection will have to be incorporated in future risk-cost-benefit evaluations of the groundwater control plans.

The most severe environmental problem that affects a number of producing and abandoned mines in British Columbia is Acid Mine Drainage (AMD). The problem develops when gangue sulphide minerals within the waste rock piles and tailings ponds oxidize to generate strongly acidic groundwater. Toxic metals, including copper, lead and zinc, are easily mobilized under these conditions. Environmental damage occurs when the contaminant loadings enter the biosphere, most commonly as groundwater discharge to a streams or lakes, where the toxins can gradually poison aquatic organisms for several kilometres downstream. Cyanide, a toxic chemical used in the recovery of gold, can lead to similar environmental impacts.

Open pit mines can also have negative impact on surface and groundwater supplies. The most common of these impacts, especially in the coal fields of eastern United States and Europe, is aquifer depressurization. In this situation, seepage into the pit, or pumping from high capacity dewatering wells will induce a large drop in the piezometric surface that may leave surrounding domestic water supply wells dry (Bair, 1981). Surface settlement may also be experienced as a result of the depressurization. Utilization of a large portion of surface and groundwater resources within a watershed can also impact downstream users.

2.6 DEWATERING ALTERNATIVES

A number of groundwater control methods have evolved in the mining industry to improve stability and operating conditions in the pit. This section reviews the most widely used drainage methods, including horizontal drains, wells, and drainage galleries. The review of each option includes a discussion on the advantages and disadvantages of the method, on recent developments in the technology, and a rough estimate of installation and operating costs for each system.

Horizontal Drains: This dewatering approach provides the most effective and economical technique for dewatering both bedrock and low permeability overburden slopes. The dewatering program usually involves one or more rows of horizontal drains along berms in potentially unstable areas. If movement is not occurring, individual drains are normally drilled a short distance beyond the anticipated slip surface to facilitate depressurization on both sides of the discontinuity. If deformation has occurred then it may be possible to reduce damage to the drains by completing them before they penetrate the slip surface, thus avoiding potential drilling difficulties and subsequent shearing of drains. The drains are usually inclined slightly upward (2 to 5°) to facilitate flow once water enters the drain. Horizontal spacings of 3 to 10 m are utilized, a fan like drilling pattern is often adopted to reduce the number of drill moves. Installation costs of $50 to $150 per m are typical, depending on ground conditions and site location. Water collection systems can be incorporated in the design, especially for drains situated in the upper 2/3 of the slope. This precaution prevents groundwater discharges from seeping back into the pit wall and increasing water pressures down-slope.

Temporarily placing the horizontal drains under vacuum to increase gradients and flow rates (i.e. turning drains into "horizontal wells") is a new development that has resulted in significantly improved drain performance at a number of mine sites (Brawner, 1987). The technique is useful for increasing the rate of dewatering on active slides during the critical first few weeks of stabilization efforts. Due to accessibility and maintenance difficulties, the vacuum technique is not practical for long term groundwater control.

The main advantages of horizontal drains are:

- Relatively low cost.
- No maintenance (except collection systems)
- Depressurization occurs along the failure surface, where it can provide the greatest benefit.

The disadvantages are:

- Water collection systems are susceptible to damage from ravelling rock. Continued access to the drains for repair purposes may pose a serious hazard.
- Drains may be sheared off as result of continued deformation.
- Presence of drains and collection systems in the pit may impede normal operations (e.g. scaling). Steel pipe installed during earlier pit expansions will result in production problems during subsequent push-backs.

Horizontal drains have been utilized widely in the mining industry, successful programs have been completed at Highland Valley Copper, Afton Mines and Gibraltar Mines in British Columbia, Syncrude in Alberta and Canadian Johns-Mannville in Quebec (Brawner, 1987). At present, most horizontal drains are installed as remedial stabilization measures after slope deformation is recognized. However, the findings of the risk-cost-benefit studies presented later in this thesis indicate that preventative groundwater control is also cost effective in many circumstances.

Dewatering Wells: Historically, dewatering wells have been the most widely applied method of groundwater control at open pit mines. Typical applications of dewatering wells include slope stabilization at Highland Valley Copper (Sperling, 1988), control of pit flooding and freezing problems at Pine Point Mines (Calver, 1969) and prevention of pit floor heave at Syncrude and Suncor (Fair, 1987, Purcell, 1987).

Conventional water well rigs are used to install most dewatering wells. Based on a review of the literature, there appears to be no preferred drilling technology; dewatering projects have been successfully completed with air rotary, mud rotary and cable tool equipment. Wells in competent bedrock usually remain uncased, except when poor ground is encountered. Although drilling in overburden usually progresses faster than drilling in bedrock, well casing and screens are generally required to prevent caving of the hole. As a result of the extra development time and hardware required, the costs of developing wells in overburden are approximately the same as in bedrock. Drilling and development costs of $1000 to $2000 per m are typical for large diameter dewatering wells, while annual operating, maintenance and monitoring costs range from $10,000 to $20,000 per well. *Table 2.1* provides a summary of dewatering statistics for three Canadian open pit mines that utilize wells for groundwater control.

Table 2.1 Summary Statistics for Groundwater Control Programs that Utilize Dewatering Wells.

Mine Site	Year	No. Wells	Avg. Depth (m)	Dev. Cost ($ million)	Cost per m
Pine Point	1968	21	50	2.1	$2,000
Gibraltar	1976	13	83	2.4	$2,224
Highland Valley	1988	21	100	2.6	$1,238

All costs converted to 1988 dollars, assuming an annual inflation rate of 5%.

Because in-pit wells interfere with normal operations, mine management prefers to situate dewatering wells beyond the ultimate pit perimeter. However, in large open pits where the horizontal distance between toe and crest frequently exceeds 500 m, perimeter wells will have little impact on water pressures in the lower reaches of a deep seated failure, and it is in this area that depressurization provides the greatest benefits. From a hydrologic perspective, wells located in the pit or horizontal drains will provide a more functional dewatering alternative. A co-operative design approach that involves both the mine planning team and the hydrogeologist is encouraged to ensure that the recommended dewatering design meet all geotechnical objectives while resulting in minimum impact on mine operations.

The main advantages of dewatering wells are:

- Wells can be situated outside pit limits (if pit is relatively small, i.e. less than 100 m deep).
- Depressurization can be initiated in advance of mining activity.
- Depressurization proceeds quickly.
- In arid locations the dewatering yields can be used to augment other more expensive production water supplies.

The disadvantages are:

- Development and operating costs are high.
- Wells interfere with normal operations if situated within the pit.
- Daily monitoring and periodic adjustment of wells is frequently required to maintain all wells at peak efficiency.
- Dewatering wells are not effective in geologic horizons that are either highly pervious or relatively impermeable.

Drainage Adits: This groundwater control method requires the development of one or more tunnels just beneath the slip surface of a potential failure. The smallest possible adit profile is usually selected to keep costs to a minimum. A 2x3 m opening is considered a minimum size for ease of access and machine assisted excavation. Development costs are strongly dependent on geologic and groundwater conditions, costs of $2000 to $3600 per m are considered typical (C.O. Brawner and D. Moore, personal communication).

Because development costs of drainage adits are high when compared on a per m basis, drainage adits are utilized much less frequently than horizontal drains or wells. Applications that justify the expense usually involve very large slope failures in excess of 10 million m^3. A drainage adit solution can also be very cost effective if old underground working exist below the potential failure surface, and the workings can be re-opened at nominal cost, and in third world countries where costs of labour are low while drilling costs are high.

Advantages:

- A very large effective diameter compared to wells and horizontal drains.
- Radial drain holes can be drilled from inside adit to intercept a much larger number of water bearing discontinuities.
- More effective than horizontal drains or wells because the full length of the adit is usually situated just below the failure surface, where it contributes most to slope stability.

Disadvantages:

- Practical only in fair to good bedrock conditions. Support problems preclude the use of this technology in overburden or badly broken ground.
- Location of the slip surface should be well defined so that the drainage adit can be positioned for maximum effect.
- Development time will be much longer than installation of horizontal drains.

Cost Comparison: The total cost of a groundwater control program will depend on the drainage method selected, size of the area to be dewatered, ground conditions, complexity of the hydraulic conductivity distribution, the time span over which dewatering will be required, and long term stability of the pit wall. For comparative purposes, *Table 2.2* presents the range of costs that one might experience when dewatering a single 500 m wide design sector with each method. Horizontal drains generally provide the lowest cost solution, followed by dewatering wells, and ultimately drainage adits.

Table 2.2 Approximate Costs of Dewatering with Most Common Methods

Dewatering Technology	Cost per m	No. Required	Length (m)	Total Cost ($ million)
Horizontal Drains	$60 - $100	100-200	50-150	0.3-3.0
Vacuum Option				0.05-0.2
Wells	$1,000-$2,000	5-15	50-150	0.25-4.5
Drainage Adit	$2,000-$3,600	1-2	500-1500	1.0-5.4
Vacuum Option				0.05-0.1

2.7 SUMMARY

This chapter has provided a brief overview of open pit mining operations and how those operations can be affected by groundwater seepage into the pit. Potential impacts that were addressed include slope stability, berm erosion, trafficability, blasting, production water and environmental concerns. The discussion then turned to a review of modern dewatering methods, including an evaluation of the advantages, liabilities and typical installation costs associated with each. It was concluded that horizontal drains frequently provide the most cost effective dewatering solution; however, the costs associated with all three drainage methods are high, $0.5 to $2.5 million is usually spent by mines to depressurize a single design sector.

When addressing the issue of whether or not to invest in some form of groundwater control program, mine management and supporting engineering staff are faced with a technically complex and risky decision. The risk-cost-benefit approach, introduced in the following chapter, provides a rational framework for analyzing this complex problem that has been shown to involve many related and inter-disciplinary issues.

CHAPTER 3 RISK-COST-BENEFIT ANALYSIS

3.1 INTRODUCTION

This chapter provides an overview of the complete risk-cost-benefit framework. The objective is to show how decision analysis is used to identify the most cost effective design strategy from a limited set of proposed slope design and dewatering options. The various components of the framework, that include geostatistics, analysis of groundwater flow, evaluation of slope stability and economic assessment, are also described briefly to show how each component fits into the global scheme of the framework. Having laid the foundation for the framework in this chapter, *Chapters 4* through *6* will then examine the technical aspects of the principal framework components.

3.2 DECISION ANALYSIS

Decision analysis is a tool used in many engineering disciplines to make design and operating decisions in complex situations where the best design or operating strategy is not intuitively obvious (Massmann and Freeze, 1987, Baecher, 1980, Whitman, 1984). The analysis involves the definition of an economic objective function, which is usually taken as the summation over an engineering time horizon of the net present value of all system risks, costs and benefits. The objective function is used as a measure of the worth of various design options. The optimal design strategy is identified as the strategy that maximizes the value of the objective function.

The decision analysis approach adopted in this framework is based on earlier research at The University of British Columbia by Massmann and Freeze. To avoid duplication of material in an area where this dissertation makes no research contribution, only the basic elements of decision analysis logic will be presented in this section. The interested reader is referred to *Chapter 2* of Massmann's (1987) dissertation for a more detailed treatment of the subject matter.

A decision problem occurs whenever there is a choice between two or more alternative courses of action that result in different consequences.. Consider a typical open pit design problem involving three possible design alternatives: 1) leave slope design unchanged, 2) flatten slope and 3) introduce a dewatering system. Complete characterization of this decision problem usually involves four components:

- *Decision Variables* define the list of possible design alternatives, e.g. flatten slope or leave slope unchanged, and introduce dewatering program or do not dewater.

- *Consequences* describe the final outcome of the decision, e.g. slope fails or slope remains stable.

- *State Variables* describe parameters that will impact on the consequences, but are beyond the control of the decision maker. Site conditions are typically considered state variables, e.g. hydraulic conductivity distribution, shear strength parameters, etc.

Figure 3.1 Decision Tree for Example Design Problem

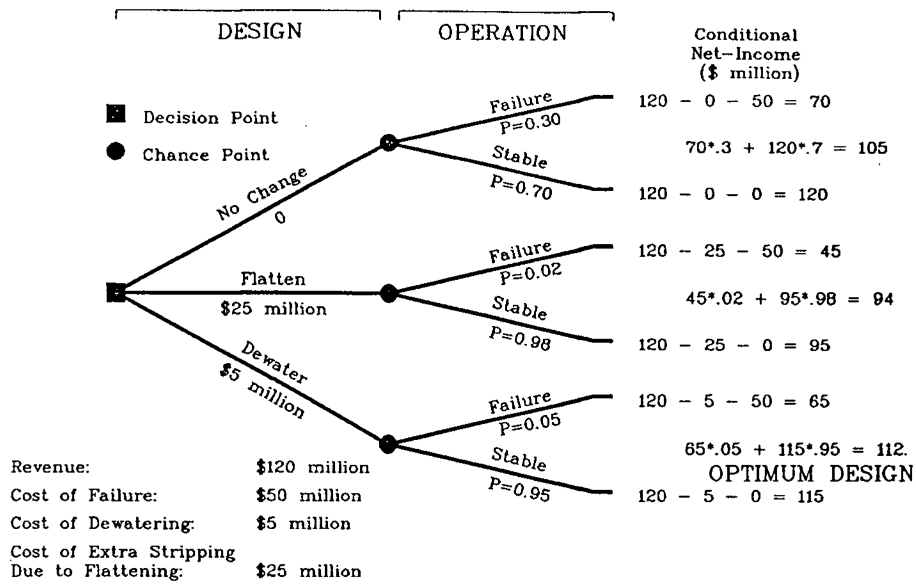

- *Constraints* may be imposed on the decision problem to limit the number of viable design variables (e.g. overall slope must be shallower than 45° to prevent ravelling), or to guarantee that certain unacceptable consequences do not materialize under any circumstances (e.g. probability of failure must be less than 20%).

For the decision problem considered in this thesis, the relationship between decision variables, consequences, state variables and constraints, as well as the selection process used to identify the optimum design alternative is best illustrated with a simple decision tree, as shown in *Figure 3.1.* The decision problem typically involves a limited number of design alternatives, each alternative being represented by a single branch emanating from the square decision node or trunk, found at the extreme left of the decision tree. Each design branch ends at chance node, where nature would determine the actual site conditions, and ultimately, whether the particular design will result in stability or failure. Since site conditions are usually uncertain to some degree, design performance cannot be predicted exactly a priori. However, it is possible, given statistical information about each state variable, to predict the probability that a particular design will result in stability or failure.

In the illustrative example considered in *Figure 3.1,* the 30% probability of failure for the original design is reduced to 5% by dewatering, and to 2% by slope flattening. Clearly, slope flattening is the best design in terms of stability. However, an economic analysis is required to identify which of the three design options will maximize profit for the mine operator. Formulation of the economic model will be the theme of the following section.

3.3 FORMULATION OF OBJECTIVE FUNCTION

Before a comparison study can be conducted to identify the optimum design alternative, it is necessary to express the consequences associated with each design in terms that can be used to compare the relative value of each option in an unbiased and consistent manner. In the field of system optimization, this frame of reference is known as the objective function.

In an open pit mine, the primary objective of virtually all activities is to maximize production and achieve the greatest possible profit, subject of course to constraints regarding worker safety and damage to the environment. Therefore, it is natural to express the objective function in terms of profit. In the most general sense, mine profitability is influenced by three categories of parameter uncertainty. The first category considers ore grades and recoveries, as these can differ significantly from exploration projections. The second category consists of uncertain economic factors. Included in this group are world metal prices, interest rates, tax laws, changes in marketing contracts, and fluctuations in salaries and commodities such as explosives, fuel, electric power and tires. The third category of parameter uncertainty is comprised of geotechnical factors that will impact on slope stability. These factors include shear strength parameters and hydrologic conditions. Because the objective of this dissertation is to investigate the importance of groundwater control on mine profitability, only geotechnical factors will be treated in a stochastic manner. Ore grades and economic factors will be treated as deterministic parameters; with each deterministic parameter assigned a single "most representative" value.

Because all economic factors are held constant, it is more convenient to express the objective function in terms of expected net income, rather than profit. In this context, expected net income is defined as the difference between revenue generated by the sale of concentrate, less all operating costs required to produce the concentrate, less monetary risks associated with slope failure.

$$\text{Expected Net Income} = \Sigma\text{Benefits} - \Sigma\text{Costs} - \Sigma\text{Risks} \qquad \textit{Equation 3.1}$$

Unlike profit, net income does not include adjustments for capital financing, taxes, etc.; therefore, it provides a simpler, crisper definition for the objective function of this study. The following sub-sections identify the many economic components considered within the benefit, cost and risk categories.

3.3.1 SYSTEM BENEFITS

The stream of benefits realized from a particular design alternative is the revenue received from the sale of mineral concentrate mined over the design period. Revenue is a function of: amount of ore mined, ore grade, recovery realized by the mill, and price received for the concentrate. The amount of ore produced from the open pit will depend on the size and shape of the ore deposit, the maximum depth of the pit, and the pit wall angle. Because ore grades, recoveries and metal prices are factors over which the geotechnical engineer has no control, they are treated as fixed deterministic coefficients in the calculations.

In this framework, all economic calculations are performed automatically with computer program SG-RCB. The following algorithm is utilized in the computer program to estimate revenue:

- A single vertical section is selected to represent the design sector. It is assumed that the entire section has a constant width in the third dimension and that all properties remain constant in that dimension. The section is then divided into a finite number of equal size blocks, typically 10x10 m to 25x25m in size, depending on the size of the pit.

- A user friendly data interface in SG-RCB is used to associate each block with an ore grade, the push-back during which it will be mined, and digability characteristics.

- Using the above information, the computer calculates the total tonnage in each block, whether the block constitutes ore, how much economic mineralization is present within the block, how much mineralization can be recovered, and what monetary value should be assigned to the block. The total revenue per push-back is obtained by summing the block values for all blocks that will be mined during the particular pit expansion.

3.3.2 SYSTEM COSTS

A large number of costs are incurred by the mine operator during production. It is useful to divide these costs into two broad categories: operating costs and dewatering costs.

Operating costs are defined as all costs of mining and processing the ore. The costs include:

- engineering design
- blasting
- excavation
- transport to crusher and waste dumps
- milling of ore
- environmentally sound disposal of waste rock and tailings
- numerous ancillary support tasks

The task specific operating costs are not tracked individually in this framework. Instead, operating costs are obtained based on total mining and milling costs per tonne because these statistics are more readily available than the detailed unit costs. Total mining costs include all costs associated with the extraction of ore and waste from the pit to the primary crusher. Total milling costs cover all expenses incurred to produce concentrate once the ore passes through the primary crusher.

Recall that operating costs are very dependent on the pit wall angle; due to the large increase in the amount of waste rock that must be blasted, excavated, transported out of the pit and disposed of as the pit wall angle is flattened.

Dewatering costs are defined as all costs associated with pit wall depressurization. The costs include:

- site investigation
- engineering design
- purchase of required equipment
- installation and development of horizontal drains or wells
- pumping costs
- monitoring and maintenance costs
- costs of water treatment

Dewatering costs will reflect design decisions made regarding the amount of site investigation performed to define hydrologic parameters, the type of dewatering system selected, the ground conditions, the spacing and location of the drains and/or wells, and the amount of water pumped.

3.3.3 SYSTEM RISKS

In the formulation of the objective function, monetary risk is defined as the expected cost of slope failure. In other words, risk is the product of the conditional cost that must be borne by the mine operator in the event of a slope failure, multiplied by the probability of the slope failure occurring.

Recall from *Section 2.4* that the consequences of slope failure may include:

- Clean up costs of removing failed material from pit.
- Lost production due to a blocked haul road or buried ore.
- Lost ore within the failure block that can no longer be separated from waste.
- Reduced cash-flow.
- Damaged equipment and services.
- Physical hazard to workers and mobile equipment in pit.

Estimates of the monetary consequences to be attributed to each of these factors will vary from design sector to design sector. Input from the mine planning department will usually be required to identify all potential impacts of slope failure in the design sector and realistically forecast the costs associated with those impacts.

Having described how benefits, operating costs and costs of failure are estimated in this framework, only probability of failure remains to be discussed before the definition of the objective function is complete. As estimation of the probability of failure is the key step that lies at core of this risk-cost-benefit framework, this issue is addressed separately in the following section.

Before moving on to the discussion of probability of failure, it is important to note that the expected value formulation does not predict the true net income that will be realized by the mine operator; it only provides a weighted average estimate of net income; the average being calculated over the two possible outcomes (i.e. stable wall or failure). The net income that will actually be achieved by the mine operator is conditional, it will depend on whether or not a slope failure is experienced. If no failure is experienced, net income will likely be significantly higher than in the case a failure does develop.

While conducting the decision analysis, it is worthwhile to consider the conditional net income projections in the analysis, as these projections indicate how the mine will prosper if the pit wall remains stable, or alternately, if failure does develop. If the costs of failure are sufficiently high to create economic hardship for the company (e.g. premature mine closure), then mine management may perceive that the true consequences of failure are much higher than indicated by the narrow scope of this analysis. Although not considered in this dissertation, utility theory (cf. Lindley, 1971; Fischoff, et al, 1981; Crouch and Wilson, 1982; Freeze et al, 1990) could be introduced to make corrections for this risk-averse behaviour.

It should also be noted that in many situations where decision analysis has been applied in the past, the formulation of an objective function was not straightforward. Complications frequently encountered include multiple objectives, an adversarial decision involving several parties (Massmann and Freeze, 1987), and risks that are not easily quantified in terms of monetary value, e.g. a threat to human life or welfare (Baecher, 1980). Although some external issues can also affect operating decisions at open pit mines (e.g. regulatory agencies, unions, Workmen's Compensation Board, etc.), the design problem considered here is almost ideal in that the formulation of the objective function is straightforward; the mine operator is the primary party to make and to be affected by the consequences of decisions, and most decisions are made to achieve the primary objective, to maximize profitability at the mine site.

3.4 COMPONENTS OF THE RISK COST BENEFIT FRAMEWORK

In this framework, probability of failure is calculated using a Monte-Carlo simulation approach. This section presents a global overview of the methodology; subsequent chapters will address the technical details of the individual framework components that include geostatistics, groundwater flow and slope stability.

Stability of a pit wall is influenced by slope configuration, shear strength properties of individual geologic horizons through which the failure surface will pass, and pore pressure conditions along the failure surface[1]. In order to properly evaluate how each of these factors will impact on the probability of failure, each step of the stability analysis must be orchestrated so that all necessary input will always be available at the completion of the preceding step. *Figure 3.2*, a flow chart of the risk-cost-benefit framework, illustrates the sequence of analytical steps adopted in this framework.

Data Collection and Interpretation: As shown in *Figure 3.2*, the analysis begins with collection and interpretation of field data required to construct the groundwater flow, slope stability and economic models. Because the list of necessary parameters is extensive, individual items will not be addressed here. *Section 7.2* of the sensitivity study and *Appendix E* provide two practical examples of the types and quantities of information that are required to conduct a risk-cost-benefit analysis of dewatering options.

Geostatistical Analysis: Formulation of a reasonable stochastic description of the hydraulic conductivity field is the most demanding aspect of the data collection and interpretation effort. In order to obtain a sufficiently large data base that will yield meaningful statistics, it is usually necessary to collect hydraulic conductivity information from all available sources, e.g. pump tests, slug tests, grain-size analyses, consolidation tests, geologic logs, etc. Once all local measurements are evaluated, a geostatistical analysis is conducted to estimate the mean, variance and semi-variogram function of the hydraulic conductivity field. Whenever some form of preferentially oriented fabric is detected during subsurface investigations (e.g. bedding, joint sets, foliation, etc.), it is also necessary to identify the degree of anisotropy that is introduced within the auto-correlation structure. During the case history study at Highland Valley Copper for example, it was shown that the hydraulic conductivity field was correlated over much larger distances parallel to bedding than across bedding.

Simulation of Hydraulic Conductivity Field: Having quantified all necessary input parameters, the Monte-Carlo simulation begins. The first step in the simulation involves generating a large number of realizations of the hydraulic conductivity field. The objectives are: 1) to generate each realization so that it duplicates all important features of the geologic environment being modelled, 2) to effectively reproduce the specified geostatistical structure in each realization, and 3) to reproduce the appropriate level of prediction uncertainty at each estimation point over the ensemble of realizations.

A number of simulation techniques have been pioneered in recent years to achieve this objective. The available options, and their distinguishing attributes, are explored in *Chapter 4.*

Prediction of Pore Pressures: A two dimensional, saturated/unsaturated, finite element model of groundwater flow is used to predict the pore pressure distribution in the pit wall for each realization of the hydraulic conductivity field. Given the complete hydraulic conductivity distribution, boundary conditions and pumping strategy, the model uses an iterative procedure based on the free surface approach pioneered by Neuman (1973) to solve for the hydraulic head and pore pressure at each finite element node in the flow domain. The theory, unique features, and capabilities of the stochastic groundwater flow model are presented in *Chapter 5.*

---

[1] Dynamic effects due to blasting or earthquake loading can also be important, but are not be considered in this dissertation.

Figure 3.2 Flow Chart Illustrating Key Steps in Risk-Cost-Benefit Framework.

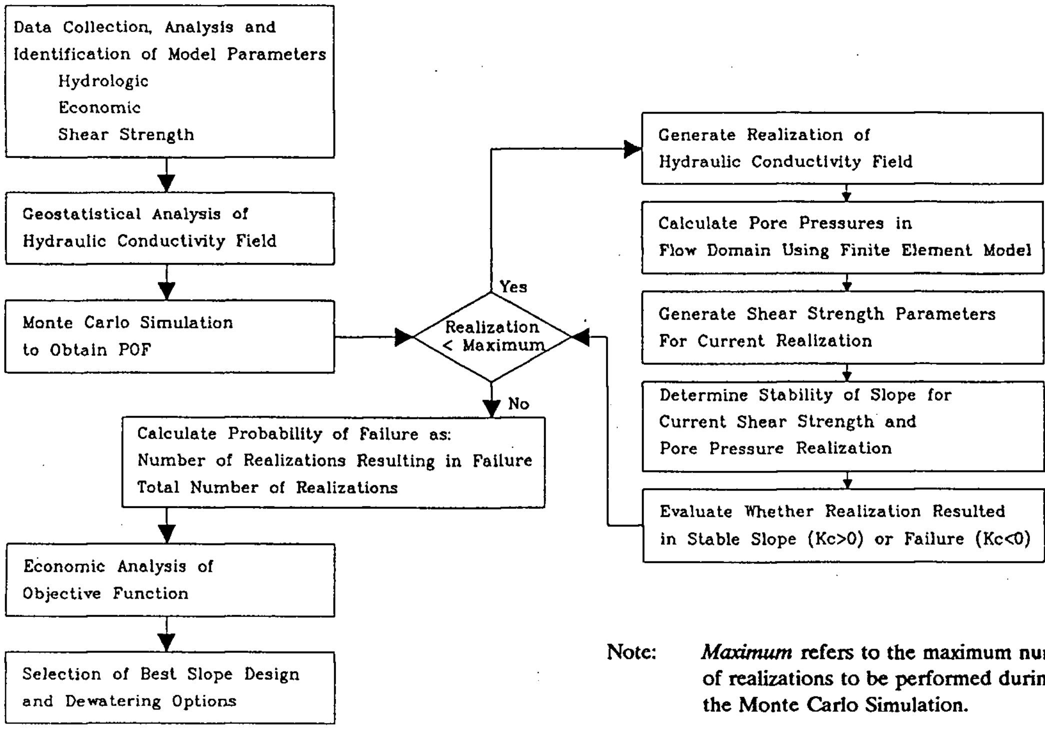

Note: *Maximum* refers to the maximum number of realizations to be performed during the Monte Carlo Simulation.

Simulation of Shear Strength Parameters: Having defined the pore pressure field, the next step in the analysis involves the generation of shear strength parameters for the current realization. Using mean and standard deviation statistics for cohesion and friction angle that must be specified for each geologic horizon, a Gaussian random number generator is used to select a unique cohesion and friction angle for each geologic horizon that will apply for the current realization.

Analysis of Slope Stability: A two dimensional method slices based on Sarma's (1979) analysis technique is used to determine whether the pit wall design will remain stable or result in failure under the current realization of shear strength and pore pressure. The Sarma method simultaneously solves the equations of horizontal and vertical force equilibrium, moment equilibrium and a failure criterion for each slice to obtain K_c, the critical horizontal acceleration factor that indicates whether or not the resulting slope will be stable. If K_c is positive, the slope will remain stable; if K_c is negative, the realization will result in failure. *Chapter 6* provides a more complete discussion of the theory underlying Sarma's method and documentation that outlines how pore pressures predicted by the finite element model are incorporated in the stability analysis.

Estimation of Probability of Failure: Having completed the stability evaluation of each realization and determined whether the particular realization will result in stability or failure, the probability of failure is calculated as the ratio of the number of realizations resulting in failure, divided by the total number of realizations in the ensemble.

Economic Analysis: In this step of the analysis the benefit, cost and risk terms are assessed for the design under consideration, and substituted into *Equation 3.1* to solve for the expected net income. Recall from *Section 3.3* that in this framework, expected net income serves as the objective function that is used to measure the worth of each design option.

Figure 3-1, the decision tree illustration presented earlier in this chapter, provides a concise example of the calculations involved. First, one design alternative is selected from the available options. Conditional net incomes are then calculated for both stable and failure scenarios. As demonstrated in the figure, the monetary worth of each possible combination of decision variable, state variable and consequence can be determined by simply following the branches of the decision tree to the desired terminus and summing up all benefits, costs and risks along the route. For example, assuming the slope remains stable, the conditional net income for the dewatering design is $115 million. The expected net income is then obtained by multiplying each of the two conditional net incomes by the corresponding probabilities of failure, and summing the two results (e.g. expected net income for the dewatering only option is $112.5 million).

Selection of Best Design: In order to identify the best slope configuration and dewatering alternative, the entire calculation process outlined above is repeated for each design under consideration. Once a value of the objective function is computed for each design, selection of the best design strategy simply involves choosing the design that results in the highest value of expected net income. Given the specified level of uncertainty in field parameters, this design alternative is expected to generate the greatest profit from mining activity in the design sector, on average.

In the example presented in *Figure 3-1,* the dewatering only alternative is expected to result in the highest net income of the three options considered ($112.5 million), given the likelihood of failure associated with each design.

3.5 SOFTWARE MODULES

Personal computer software is utilized extensively in each step of the risk-cost-benefit framework, from field data interpretation to economic evaluation. A major part of the research effort summarized in this dissertation involved the development of custom software modules to carry out the four principal tasks that comprise the risk cost benefit framework, i.e. *SG-Stat* for geostatistical analysis, *SG-Flow* to model groundwater flow, *SG-Slope* to analyze slope stability and *SG-RCB* to conduct the economic analysis. Five other software modules were later incorporated in the framework to facilitate various aspects of data management and interpretation, especially during the case history study of the dewatering design at Highland Valley Copper. This section provides a very brief overview of each module, and an indication where the program fits in the global scheme of the risk-cost-benefit framework.

Figure 3.3 identifies the various data analysis and modelling functions that comprise the risk-cost-benefit framework. The software modules that are used to conduct each aspect of the analysis are also shown (highlighted in double boxes).

SG-CoreLog was developed to efficiently process large amounts of geologic data normally generated during exploration drilling programs. Once information is entered in the data base, *SG-CoreLog* can also be used to generate graphic strip logs and geologic cross-sections. The program was used extensively by the author during the case history study of Highland Valley Copper to interpret the complex overburden stratigraphy that exists at the site.

SG-Pump has been developed as a practical working tool to analyze drawdown data from a large number of pump tests conducted at Highland Valley Copper. Based on the Jacob-Cooper semi-log method of analysis, the program has been enhanced to also permit analysis of stepped drawdown tests, i.e. where the pumping rate is periodically increased as the test progresses. An aquifer response module has also been incorporated in the program. This module, based on the Theis (1935) solution, is used to predict the drawdown response for any user specified pumping rate once transmissivity and storativity parameters are known.

Figure 3.3 Flow Chart Illustrating Software Modules.

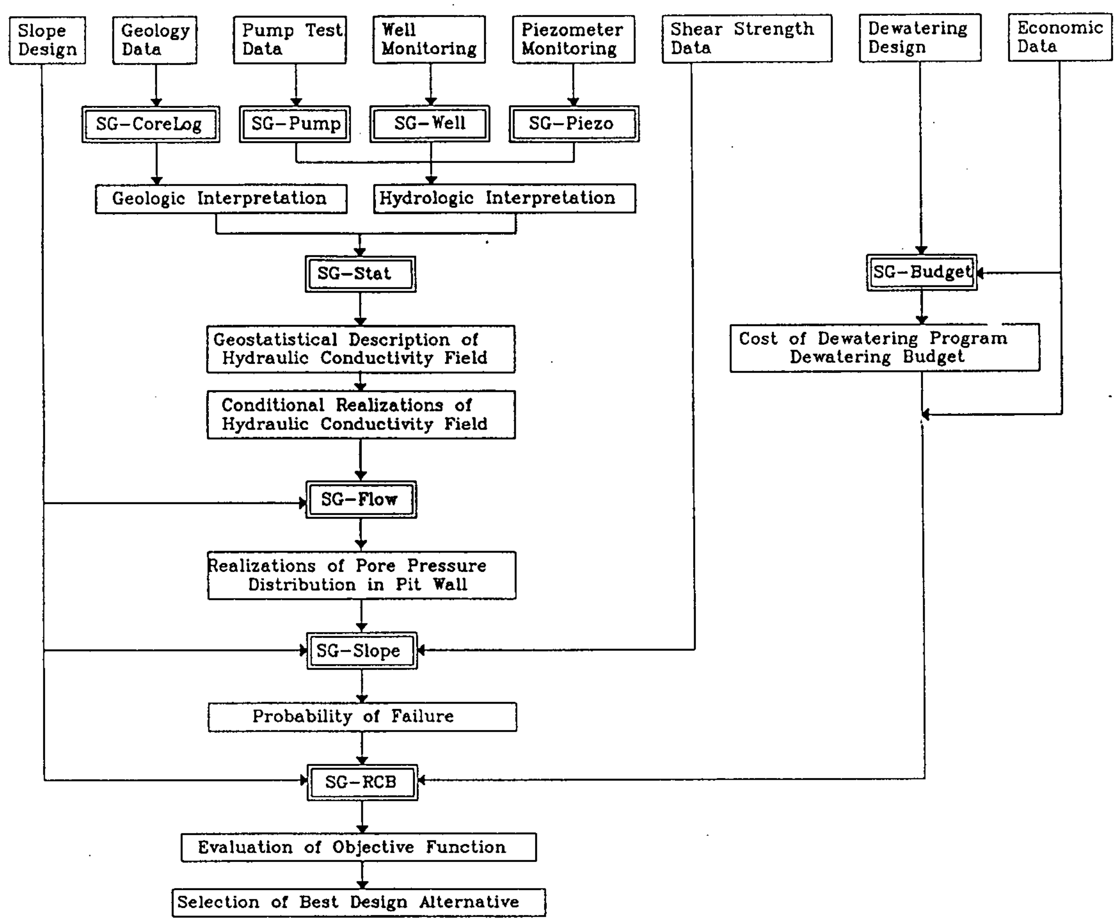

SG-Well serves as a data base and graphic display module to store and analyze large amounts of well monitoring data that are generated as part of daily or weekly monitoring programs. The module is capable of storing an unlimited number of monitoring records, accessing any stored information in seconds, and displaying the data in a number of easy to interpret graphic formats (e.g. time graphs, bar graphs, XY graphs). The module was developed to organize and interpret the thousands of well monitoring records that have been collected at Highland Valley Copper since 1984.

SG-Piezo serves essentially the same function as *SG-Well*, except that it is used to store and interpret water level observations from piezometer monitoring networks.

SG-Budget was developed to provide a fast and accurate method of forecasting the costs of future dewatering programs at Highland Valley Copper. Given an outline of the dewatering plan, including the completion depth of each well, well diameter, expected flow rate, etc.) the program automatically calculates the development and operating costs for each installation. A year by year summary of costs and flow rates is also provided for planning purposes.

SG-Stat is a modular program used to conduct all aspects of the geostatistical analysis of hydraulic conductivity data. Capabilities of the program include:

- Structural analysis to identify the mean, variance and semi-variogram statistics of raw field data.
- Kriging estimation to obtain the best linear unbiased estimate of hydraulic conductivity at each prediction node and the associated estimation error based on available field data.
- Stochastic simulation to generate hydraulic conductivity realizations that possess the desired auto-correlation structure as well as reflecting an appropriate amount of variability at each prediction point over the ensemble of realizations (i.e. simulated values located close to measurement points should show little variability over the ensemble of realizations while simulated values far from supporting data should possess somewhat more).
- Ability to simulate complex geologic deposits that may possess several distinct geologic horizons (e.g. layered aquifer/aquitard sequence or distinct fault zone) and sedimentary stratification that may result in an anisotropic auto-correlation structure.

Chapter 4 provides a complete description of *SG-Stat,* the underlying theoretical concepts, and numerous examples of the software capabilities.

SG-Flow is the two dimensional saturated/unsaturated finite element model of groundwater flow that has been developed to predict pore pressures in the pit wall. Given a description of the hydraulic conductivity field, the pit wall configuration, and the location of all pumping wells or horizontal drains, the program predicts the steady state pore pressure distribution that will be established. Interfaces have been developed to *SG-Stat* and *SG-Slope* so that hydraulic conductivity realizations generated by *SG-Stat* are automatically imported into the program and pore pressure realizations are automatically accessed from *SG-Slope*.

SG-Slope is a two dimensional slope stability program based on Sarma's (1979) method of slices. The program is capable of conducting both the stochastic method of analysis to obtain a probability of failure, as well as the more conventional deterministic analysis to obtain factors of safety. The effects of groundwater on stability can be evaluated in one of three ways: 1) drained analysis, 2) Dupuit assumptions and 3) pore pressures from finite element model. *Chapter 6* provides a more detailed description of the underlying theory and unique capabilities provided by this program.

SG-RCB is the final program in the framework. It is used to conduct the economic risk-cost-benefit analysis once all of the necessary input data has been compiled (i.e. probability of failure, costs of dewatering program, etc.). Given the ore grade distribution, the pit development plan, the critical failure geometry for each pit expansion, the associated probability of failure, the dewatering plan and a gamut of economic parameters, *SG-RCB* evaluates the revenue, the operating costs and monetary risks that will be realized during each push-back. Expected net income, is then reported for each push-back and for the entire mining cycle. Besides using the computed objective function to identify the best pit design and dewatering strategy, statistics calculated by *SG-RCB* can also be used to quantify the economic consequences of slope failure during each pit expansion so that mine management can accurately judge the importance of stable pit walls in the design sector.

A user friendly software interface and easy to interpret colour graphics have been incorporated in all nine software modules. Time saving features of the user interface include on screen menus, on-line help and graphic data entry. Graphic data entry involves painting input data (e.g. hydraulic conductivity field, boundary conditions, slice geometry) directly on the screen rather than keying the information into a data file. The guiding motivation behind the extra programming effort was to disseminate the contributions made in this research not only through this dissertation and subsequent technical papers, but through practical software that future researchers and practitioners will be able to apply to similar design problems. To this end, several of the software modules are already being used in other graduate research at The University of British Columbia, as practical analytical tools in a number of consulting firms and at Highland Valley Copper, and as teaching tools in the core curriculum of the geological engineering program at U.B.C.

All of the software modules that constitute the RCB framework, including ***SG-Stat***, ***SG-Flow***, ***SG-Slope*** and ***SG-Risk*** have been circulated in the public domain. Diskettes containing the software, including both source code and executable code have been provided to the UBC Geology Library. However, the software user must accept all responsibility for the accuracy of the modules for his particular design problem. Also, technical support for the software is not provided.

3.6 SUMMARY

This chapter has provided an overview of the complete risk-cost-benefit framework and a summary of the decision making processes that are used to identify the most cost effective slope design and dewatering strategy from a limited number of design options. The discussion began with an introduction to the decision analysis approach adopted in the framework. A decision tree was used to illustrate the basic decision making logic. Expected net income was then identified as the preferred objective function, one that can be used to compare the relative economic value of each design option in an unbiased and consistent manner. It was shown that net income can be calculated as the sum of all system benefits, less operating costs, less monetary risks of failure. The various economic components that must be considered in the calculation of the benefits, costs and risks were then briefly listed. Of the three terms, monetary risk was shown to be the most difficult to evaluate because it requires estimates of both economic consequences of failure and probability of failure.

The risk-cost-benefit framework was then broken down into nine basic steps, including:

- Data collection and interpretation
- Geostatistical Analysis
- Simulation of Hydraulic Conductivity Field
- Prediction of Pore Pressures
- Simulation of Shear Strength Parameters
- Analysis of Slope Stability
- Estimation of Probability of Failure
- Economic Analysis
- Selection of Best Design

The tasks that are conducted during each of the above analysis steps were reviewed briefly to provide the reader with an understanding of the global framework before addressing the various task specific issues, including geostatistics and simulation, groundwater flow modelling and slope stability in following chapters. Finally, the four computer software modules that are needed to carry out this risk-cost-benefit analysis (*SG-Stat, SG-Flow, SG-Slope* and *SG-RCB*), as well as a number of auxiliary data interpretation programs, were introduced in the last section of this chapter.

CHAPTER 4 GEOSTATISTICS

4.1 OVERVIEW

Subsurface conditions are variable in space, and frequently highly uncertain. When designing a pit wall, the primary objective of the geotechnical team performing the site investigation is to characterize subsurface conditions in a satisfactory manner that will result in a reliable and economic design. An equally important objective is to quantify the uncertainty associated with each parameter estimate, and to predict how the uncertainty will impact on the economics of the pit wall design.

Index properties commonly recorded during geotechnical investigations may include grain size, fracture spacing, RQD, and hydraulic conductivity measurements. Observations of these properties on surface exposures, drill cores and cutting samples suggest that physical properties of the soil or rock mass are spatially variable because measurements tend to fluctuate as observations are taken along a traverse or bore hole (see *Figure 4.1*). In most cases the physical properties are also spatially *autocorrelated;* measurements taken close to each other are more strongly correlated with one another than measurements taken far apart.

Geostatistics provides a powerful set of tools for estimating hydraulic conductivity at selected points in an autocorrelated flow domain based on a limited set of field data. The data may include pump tests, slug tests, grain size analyses and other soft data such as geophysical results. The geostatistical tools can also be used to estimate the degree of uncertainty associated with each hydraulic conductivity prediction. This chapter provides a summary of existing geostatistical tools that have been adopted in this *Risk-Cost-Benefit framework* to generate realizations of the hydraulic conductivity field that are required for Monte Carlo Simulation. *Figure 4.2* is an organization chart that outlines the topics that will be addressed on the following pages and how they are related. For the most part, the technical material presented in this chapter is drawn from Journel and Huijbregts (1978), De Marsily (1984) and Clifton and Neuman (1982).

Section 4.2 introduces essential statistical concepts that provide the basic building blocks for geostatistics. These include: *mean, variance, covariance* and *semi-variogram*. Unique terminology has evolved in the domain of mining geostatistics to describe the semi-variogram. The meaning of several important terms including: *nugget effect, sill,* and *range* is also given.

Section 4.3 explains how the experimental *semi-variogram* is constructed from field data, and how it is used to describe the natural variability of the hydraulic conductivity field. Emphasis is placed on exploring how the shape of the semi-variogram reflects the correlation structure of the hydraulic conductivity field. A small set of simple mathematical functions have been developed to model the experimental semi-variogram. *Section 4.3* presents the most common of these functions and suggests simple rules of thumb for quickly selecting model coefficients that will result in a good fit to the experimental semi-variogram.

Figure 4.1 Hydraulic Conductivity Profile in Borehole

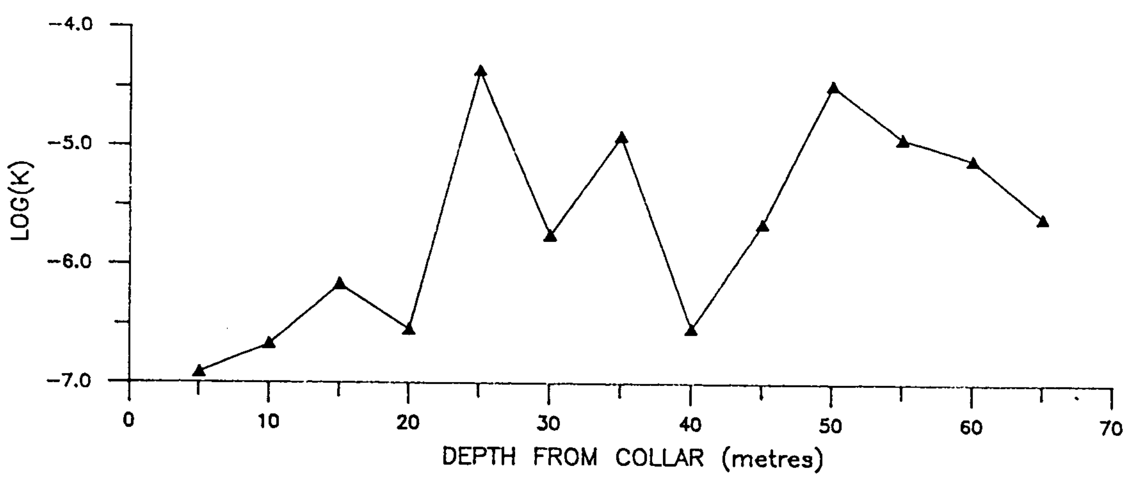

Figure 4.2 Organization Chart - Geostatistics

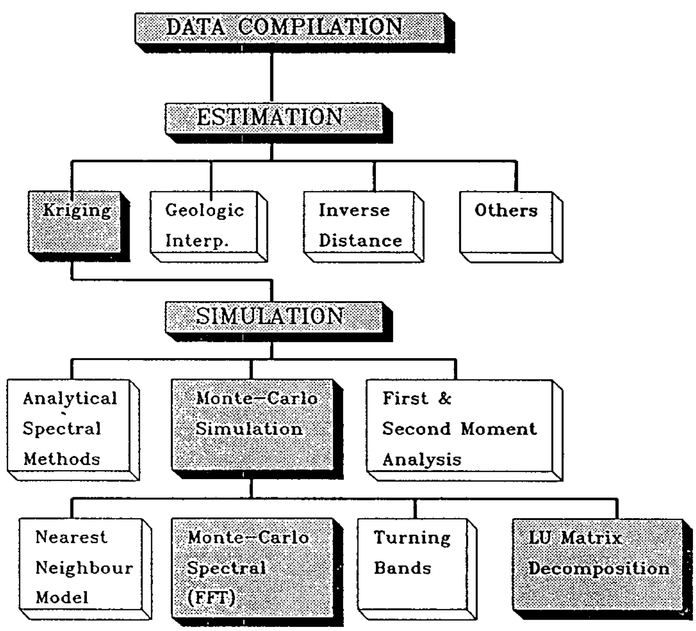

Section 4.4 introduces *Kriging*, a popular method of parameter estimation. *Kriging* is an averaging method that results in the *Best Linear Unbiased Estimate*. The meaning and significance of *BLUE* is reviewed briefly as are the fundamental assumptions on which *Kriging* is based. Each Kriging estimate is associated with an estimation error. *Section 4.4* also examines the physical meaning of each term in the *Kriging Error* equation and shows how estimation uncertainty is affected by quantity, location, size, relative orientation and measurement error of available data. *Kriging variance* distributions are prepared using a number of different sampling strategies to illustrate the most significant relationships between geology, sampling geometry, and uncertainty.

Section 4.5 introduces *simulation*, a tool that is used to generate a large number of hydraulic conductivity realizations from available statistics. The realizations serve as input for the *Monte Carlo* analysis of groundwater flow, slope stability, and ultimately, probability of pit wall failure. *Conditional* and *unconditional* simulation methods are defined and practical guidelines are given as to when each simulation method should be used. A number of simulation techniques have evolved for generating realizations. *Section 4.5* provides a brief review of the available techniques. An expanded discussion of the theory underlying the *Fast Fourier Transform* (FFT) and *LU Matrix Decomposition* simulation methods that are utilized in this framework is presented in *Appendices B* and *C*. The examples in *Section 4.5* demonstrate that the *FFT* simulation method has many advantages over the other simulation approaches commonly used by groundwater researchers today. Therefore, application of the *FFT* method to the generation of auto-correlated hydraulic conductivity fields is one of the key research contributions of this chapter. A few remarks about verification and practical examples of grid size and flow domain selection in relation to the semi-variogram model complete the discussion in this section.

The quantity and quality of information increases dramatically as a project matures from conceptualization, through site investigation, to design and construction. With the aid of an illustrative example, *Section 4.6* shows how the geostatistical model presented in this chapter can be applied at each stage of the design process to evaluate all available information and to assist in making logical design decisions as new information is revealed. Because the worth of additional data, and in particular, a suitable stopping rule that will indicate when enough field data has been collected to complete the pit wall design safely, are both intimately linked to the economic component of the *Risk-Cost-Benefit analysis*, a discussion of data worth is not presented until the sensitivity discussion in *Chapter 7*. At that point all of the necessary tools will be in place to evaluate and compare the various sampling strategies with the *Risk-Cost-Benefit framework*.

4.2 BASIC STATISTICS

Before introducing the techniques of *kriging* and simulation, and showing how these methods can be applied to dewatering system design, it is necessary to review a few of the underlying statistical foundations. In this section the terms *mean, variance, standard deviation, covariance, variogram, semi-variogram, stationarity, intrinsic hypothesis, sill, range,* and *nugget effect* will be presented. To maintain a coherent focus, the presentation will be organized as a statistical analysis of a geologic profile.

Figure 4.3 is a contour map of the log hydraulic conductivity field that will be referenced in this section. Geologic materials are naturally variable because they are deposited in dynamic environments that undergo change throughout the period of deposition. Once deposited, the materials are further subjected to complex stress histories that are controlled by irregular tectonic and climatic events. It is for these reasons that geologic materials exhibit variability. The irregular hydraulic conductivity fields such as the field portrayed in *Figure 4.3* are reflections of variability in the physical composition and structure of the deposit. Furthermore, the actual value of hydraulic conductivity at any given point cannot be predicted with certainty unless a measurement is taken nearby or the hydraulic conductivity field is sufficiently homogeneous to allow extrapolation of distant data.

Today, deterministic models of groundwater flow such as USGS-MODFLOW and PC-SEEP are used widely to predict pore pressures in complex engineered structures such as open pit walls and earth dams (Sumner 1987, Krahn, 1987). The deterministic models require that a single value of hydraulic conductivity be specified for each cell in the flow domain, even if that value is not known with confidence. Because it is assumed that all input data is known exactly, output from deterministic simulations does not yield any information about the possible error of model predictions.

Over the past fifteen years researchers, and more recently practitioners, have adopted statistical methods for characterizing variability of the hydraulic conductivity field and incorporating the parameter uncertainty into *stochastic* models of groundwater flow (Freeze, 1975, Clifton & Neuman 1982, Delhomme, 1983). In stochastic groundwater literature hydraulic conductivity, $Y(x_i)$, is frequently considered as a *spatially autocorrelated, log-normally distributed* random variable. Instead of working with $Y(x_i)$ directly, it becomes more convenient to define $Z(x_i)$ as $log_{10}[Y(x_i)]$ since the new random variable will be normally distributed. At each point x_i in the flow domain the random variable $Z(x_i)$ is not known for certain; but the range of likely values can be described by a *probability density function*. The geostatistical techniques described in this chapter require that the probability density function be a Gaussian Normal distribution specified by mean m and standard deviation σ. The hydraulic conductivity field is *autocorrelated* because $Z(x_i)$ changes gradually from point to point, unless a discontinuity such as a geologic contact or major fault is present.

In this framework, Monte Carlo simulation provides the vital link that incorporates parameter uncertainty into the groundwater flow model. Monte Carlo simulation generates a large number of realizations of the desired output variable, the hydraulic head field. The uncertainty in hydraulic head prediction at each point in the flow domain, calculated by statistical analysis over all realizations, gives the analyst an indication of how input parameter uncertainty ultimately influences reliability of the groundwater flow model predictions. Such uncertainty predictions cannot be achieved with deterministic analysis. The biggest advantage of the stochastic approach is realized when probabilistic output from the groundwater flow analysis is utilized as input into an economic decision making component of the risk-cost-benefit framework to compare merits of different dewatering strategies.

The first step in this demonstration is to discretize the hydraulic conductivity field into an array of gridded point values. This step, illustrated in *Figure 4.4,* is analogous to conducting a permeability testing program on a regular grid. The next step is geostatistical characterization of the observed correlation structure.

Figure 4.3 Log Hydraulic Conductivity Contours

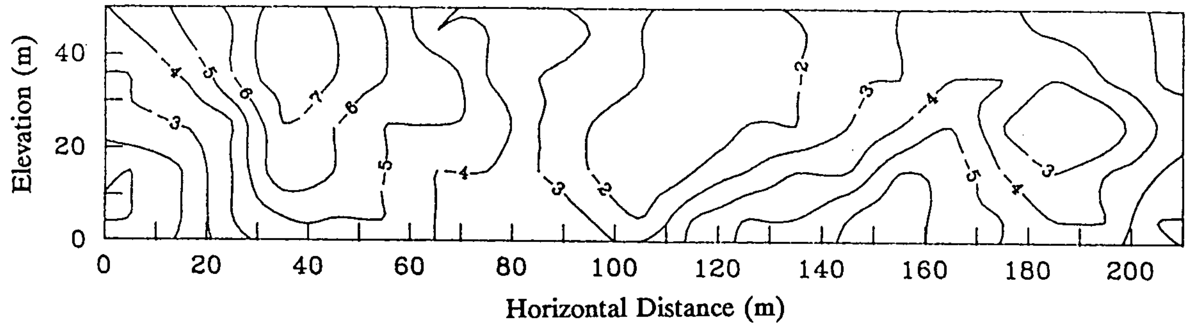

Figure 4.4 Hydraulic Conductivity Field Discretized into Cells

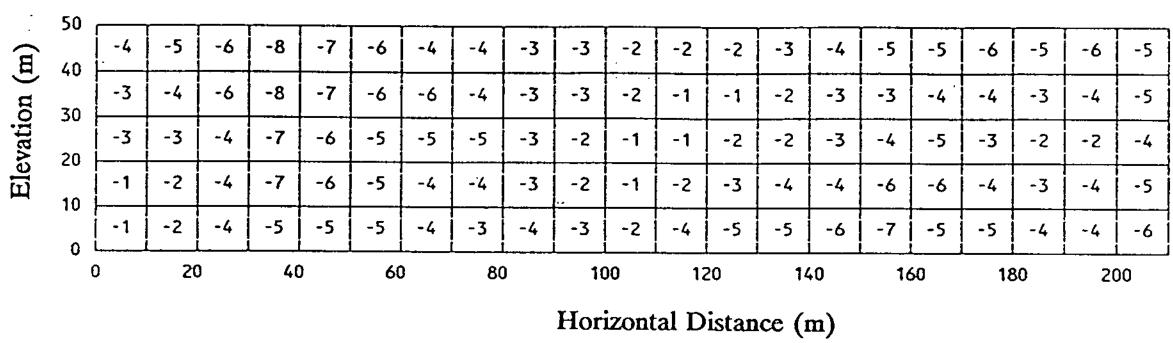

4.2.1 GEOSTATISTICAL TERMINOLOGY DEFINED

Ensemble: An ensemble is a set of realizations of the random field (e.g. hydraulic conductivity). Because each realization in the ensemble is generated from one set of statistics, on average all realizations will have the correlation structure, but actual parameter values at a fixed point in space will vary from realization to realization in accordance with the level of estimation uncertainty associated with each estimation point.

Mean: This parameter is defined as the expectation of the random variable, $Z(x_i)$:

$$M = E[Z(x_i)] \qquad \textit{Equation 4.1}$$

where $E[\,]$ denotes the expected value operator. For the problem at hand, log hydraulic conductivity, $Z(x_i)$, is not known everywhere in the flow domain. Therefore, the expectation $E[Z(x_i)]$ cannot be determined and the mean must be estimated from available hydraulic conductivity measurements, $z(x_i)$:

Figure 4.5 Normal PDF - Mean & Variance Defined

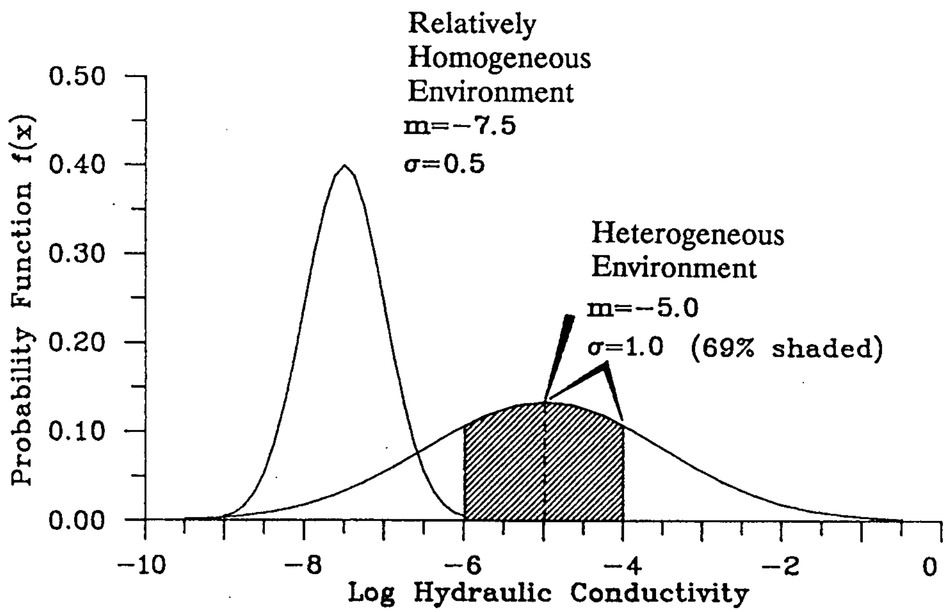

$$m = \frac{\sum_{i=1}^{I} z(x_i)}{I}$$ *Equation 4.2*

The mean of the discretized geologic profile in *Figure 4.4*, calculated with *Equation 4.2*, is *-3.98*.

Variance: Variability of the log hydraulic conductivity field about its mean value is described by its *variance*, σ^2. Variance is defined as the expected value of the squared difference between a local value of the random variable $Z(x_i)$ and the mean value M, when averaged over the entire domain:

$$\sigma^2 = E[\{Z(x_i) - M\} \cdot \{Z(x_i) - M\}]$$ *Equation 4.3*

The variance operator, given by the right hand side of *Equation 4.3*, is frequently abbreviated as $VAR[Z(x_i)]$. For a set of I discrete data points such as the set portrayed in *Figure 4.4*, the variance can be calculated by:

$$\sigma^2 = \frac{\sum_{i=1}^{I} \{z(x_i) - m\}^2}{I}$$ *Equation 4.4*

Standard deviation: Defined as the square root of variance, this parameter is useful for relating variability to the shape of the *PDF*. If data is normally distributed, *69%* of samples will fall within *±1* standard deviation of the mean, 95% within 2σ, and *99.7%* within 3σ (see *Figure 4.5*). Sedimentary deposits that exhibit a high degree of heterogeneity such as glaciofluvial sediments will have a relatively large σ and a broad *PDF*, while homogeneous strata (e.g. evaporite deposits) will have a smaller σ and a tighter *PDF*. Statistics compiled from the literature by Freeze (1975) suggest that the standard deviation of log hydraulic conductivity ranges from *0.2* for very homogeneous strata to *2.0* for highly heterogeneous strata. The standard deviation of the discretized geologic profile in *Figure 4.4* is *1.66*.

Figure 4.6 Characteristics of Covariance & Semi-Variogram

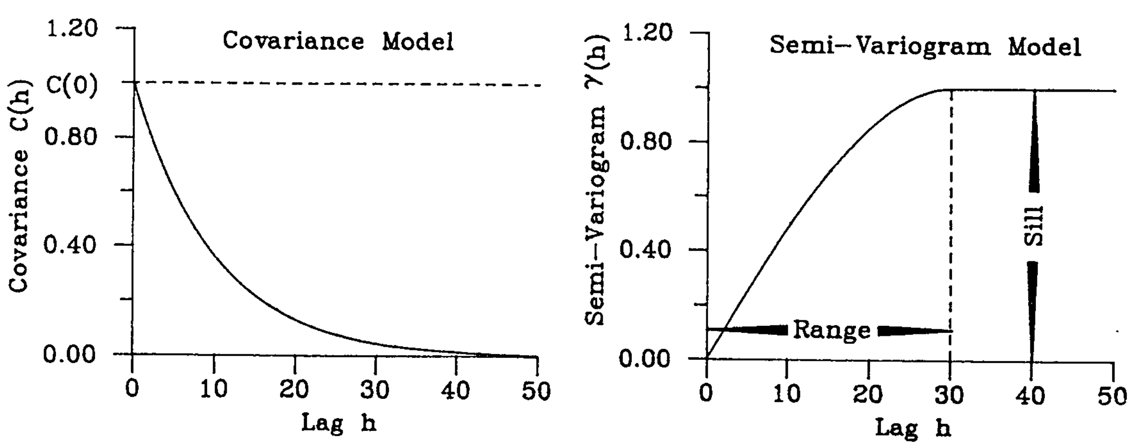

Covariance: This parameter is a measure of spatial correlation over a separation vector[1] ***h***. Symbolized by $C[h]$, the covariance is defined as:

$$C[h] = E[\{Z(x_i) - m\} \cdot \{Z(x_i + h) - m\}] \qquad \textit{Equation 4.5}$$

When two points x_i, x_j are strongly correlated, log hydraulic conductivity $Z(x_i)$ will be very similar to $Z(x_j)$. Therefore, the product $\{Z(x_i) - m\} \cdot \{Z(x_j) - m\}$ will always be positive and $C[h]$, the expectation of the product will be significantly greater than 0. On the other hand, for longer lags over which points are no longer correlated, some product terms $\{Z(x_i) - m\} \cdot \{Z(x_i + h) - m\}$ will be negative, others will be positive, and the net result will be a covariance value very close to 0. When $\boldsymbol{h}=0$ *Equation 4.5* simplifies to the expression for variance, hence variance is often designated $C[0]$. The left side of *Figure 4.6* presents a graph of a typical covariance function. The maximum value, $C[0]$, occurs at the origin, the function then decays to 0 at some distance over which hydraulic conductivity ceases to be correlated.

Variogram: Represented by $2\gamma[h]$, the *variogram* is defined as the variance of first order increments[2]:

$$2\gamma[h] = VAR[Z(x+h) - Z(x)] \qquad \textit{Equation 4.6}$$

The variogram can be interpreted as the estimation variance of predicting $Z(x)$ by $Z(x+h)$.

Semi-Variogram: Defined as one half of the variogram, the *semi-variogram* function $\gamma(\boldsymbol{h})$ can also be used to characterize the observed correlation structure. Indeed, it will be shown below that the semi-variogram and covariance are so closely related to be equally applicable when dealing with stochastic fields that do not exhibit spatial drift. As shown on the right side of *Figure 4.6* the semi-variogram function begins at the origin and then increases to a maximum value of $C[0]$ at the maximum distance over which the data is correlated.

---

[1] Separation vector ***h*** is frequently referred to as *lag* in the stochastic literature.

[2] First order increment is the difference $[Z(x+\boldsymbol{h})-Z(x)]$.

Before the relationship between the semi-variogram and covariance can be explored in detail it is necessary to review three commonly applied assumptions about the degree of stationarity exhibited by the log hydraulic conductivity field. The discussion is very brief, additional details are provided in *Appendix A.1.*

Stationarity: This condition requires that all statistical properties, including *mean, variance, covariance* and higher order moments be constant and independent of location ***x***.

2nd Order Stationarity: Less restrictive than strict stationarity, this condition requires only that the first two moments of the random variable be stationary. The mean and variance of the log hydraulic conductivity field must be constant over the flow domain and the covariance must be dependent only on the length and orientation of the separation vector ***h***, not on the location ***x***.

Intrinsic Hypothesis: Less stringent than the hypothesis of *2nd Order Stationarity*, the *intrinsic hypothesis* requires only that the variance of first order increments be finite and that the increments themselves be second order stationary. In *Appendix A.1* it is shown that the intrinsic hypothesis is useful for analyzing problems where variability in the log hydraulic conductivity field continues to increase with increasing size of the sampling domain and a finite variance *C[0]* cannot be defined over the size of the flow domain being analyzed.

If geostatistics is to provide meaningful simulation results at least one of the above hypotheses must be applicable to the random variable *Z(x)*. In practice, the hypothesis of 2nd order stationarity can be applied to most field problems. The intrinsic hypothesis is required only for situations where the dimension of the flow domain is shorter than the distance over which the random variable is correlated or a hidden trend is present that cannot be filtered out prior to the geostatistical analysis.

Sill: For log hydraulic conductivity fields that are *2nd order stationary* the experimental semi-variogram will increase to a *sill* value equal to the variance *C[0]* and then remain at that plateau for all increasing lags (see *Figure 4.6*). When the sill is not observed, *C[0]* cannot be defined, and the log hydraulic conductivity field will not be *2nd order stationary* at the scale of the flow domain. In that case, only methods based on the *intrinsic hypothesis* can be utilized to analyze the data.

Range: This parameter is defined as the lag at which the *sill* is first encountered and the covariance function vanishes. As shown in *Figure 4.6*, the range is the lag distance at which the hydraulic conductivity field ceases to be correlated.

Nugget Effect: Recognized as a discontinuity in the semi-variogram or covariance function at the origin, the *nugget effect* can be caused by variability in the log hydraulic conductivity field at a scale smaller than the sampling interval or by random measurement errors. The term is originally derived from analysis of gold bearing deposits where samples with very high gold grades occur directly adjacent to samples with background gold values. The experimental semi-variogram for such deposits, illustrated in *Figure 4.7*, appears discontinuous near the origin, jumping from 0 at the origin to a finite nugget variance at the first non-zero experimental lag point (equal to sample interval).

Figure 4.7 Semi-Variogram & Covariance Function with Nugget Effect

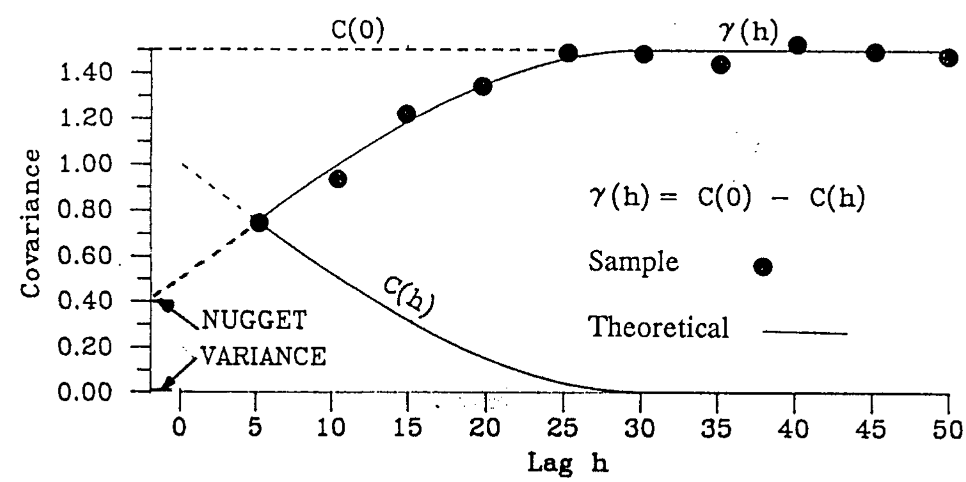

4.2.2 RELATIONSHIP BETWEEN γ(h) & C(h):

If the log hydraulic conductivity field is second order stationary then the variance *C[0]* exists and a relationship between the semi-variogram and covariance can be derived. Starting with a definition of the variogram given by *Equation 4.6*, writing the variance operator explicitly, and recognizing that the expectation of the first increment is *0* since the field is second order stationary yields:

$$2\gamma(h) = E[\{Z(x+h) - Z(x)\}\cdot\{Z(x+h) - Z(x)\}] \qquad \textit{Equation 4.7}$$

Expanding the product, taking the expectation of each term, recognizing that $E[Z(x)^2]$ is equal to $E[Z(x+h)^2]$ since the hydraulic conductivity field is second order stationary gives:

$$\gamma(h) = E[\{Z(x)\}^2] - E[Z(x)\cdot Z(x+h)] \qquad \textit{Equation 4.8}$$

Introducing m^2 and $-m^2$ on the right side of the equation yields the desired expression.

$$\gamma(h) = \{E[\{Z(x)\}^2] + m^2\} - \{E[Z(x)\cdot Z(x+h)] + m^2\} \qquad \textit{Equation 4.9}$$

Substituting the expressions for *C[0]* and *C[h]* given by *Equations 4.3* and *4.4* results in the relationship between the semi-variogram and the covariance function:

$$\gamma[h] = C[0] - C[h] \qquad \textit{Equation 4.10}$$

Equation 4.10 states that the semi-variogram is a mirror image of the covariance function, shifted upward by the constant value *C[0]*. The concept is illustrated in *Figure 4.7*. When *C[0]* exists, it is a trivial matter to switch from one parameter to the other.

4.3 VARIOGRAM MODEL

Analysis of the correlation structure begins with construction of an experimental semi-variogram or covariance function from field data. A mathematical function that duplicates the essential features of the experimental semi-variogram is then selected to represent the observed correlation structure. A number of parametric estimation techniques including maximum likelihood and restricted maximum likelihood can be used to automate the parameter selection process (Kitanidis, 1983, Kitanidis and Lane, 1985, Wagner and Gorelick, 1989, Jury and Russo, 1989). However, experiments conducted by this author (see *Section 4.4.7*) have demonstrated that simulations of the types of correlated hydraulic conductivity fields being considered here are not sensitive to the exact shape of the semi-variogram function as long as the function is reasonable. Since, in this case, the additional accuracy of parametric estimation methods is not required, a simpler manual model matching approach to semi-variogram fitting is adopted.

This section presents the algorithm utilized in *SG-STAT*[3] to calculate the experimental semi-variogram. Several paragraphs are devoted to explaining irregular behaviour of the experimental semi-variogram that is frequently observed at lags approaching the maximum dimension of the flow domain.

4.3.1 EXPERIMENTAL SEMI-VARIOGRAM

The experimental semi-variogram is constructed by defining *10* to *20* contiguous lag intervals H_k at which the semi-variogram function will be evaluated. Each lag interval is selected so that it spans approximately *1/10* to *1/20* of the longest dimension in the flow domain. If data is collected on a regular grid pattern, a lag interval equal to the distance between adjacent samples is selected. Since the demonstration data in *Figure 4.4* is discretized on a *10x10 m* grid, semi-variogram intervals are selected as follows: H_1 *5→15,* H_2 *15→25,* H_3 *25→35* ... H_{21} *205→215.* For each interval H_k, the average of all point semi-variograms

$$\gamma_{point\ ij} = \{Z(x_i) - Z(x_j z)\} \cdot \{Z(x_i) - Z(x_j)\} \qquad \text{Equation 4.11}$$

whose lag h_{ij} falls within the interval H_k is taken to represent the value of the experimental semi-variogram for lag H_k, applied at the midpoint of the interval. *Figure 4.8* is a graph of the experimental semi-variogram calculated for the demonstration data in *Figure 4.4.* The *sill* value, selected to pass through the middle of the sinuous semi-variogram trace observed at longer lags, is approximately equal to the sample variance, *2.78.* The range is picked at *50 m*, the lag at which the experimental semi-variogram is first equal to the sill. The correlation distance indicated by the range is consistent with the distance over which hydraulic conductivity appears to be correlated in *Figure 4.3.*

The shape of the experimental semi-variogram reveals a wealth of information about the correlation structure of the corresponding hydraulic conductivity field. *Figure 4.9* illustrates some frequently observed semi-variogram characteristics. The physical significance of each pattern is discussed below:[4]

Parabolic Behaviour at Origin: Characteristic of very regular spatial variability, parabolic behaviour is observed when adjacent samples are strongly correlated.

Linear Behaviour at Origin: Frequently observed, this behaviour occurs when the correlation structure is somewhat irregular or when the sampling interval is too coarse to capture details of the correlation structure.

---

[3] *SG-STAT* is a geostatistical software package developed by the author as part of this thesis research to analyze hydrogeologic data.

[4] Journel (1978) provides a more complete treatise on this subject.

Figure 4.8 Experimental Semi-Variogram for Demonstration Profile

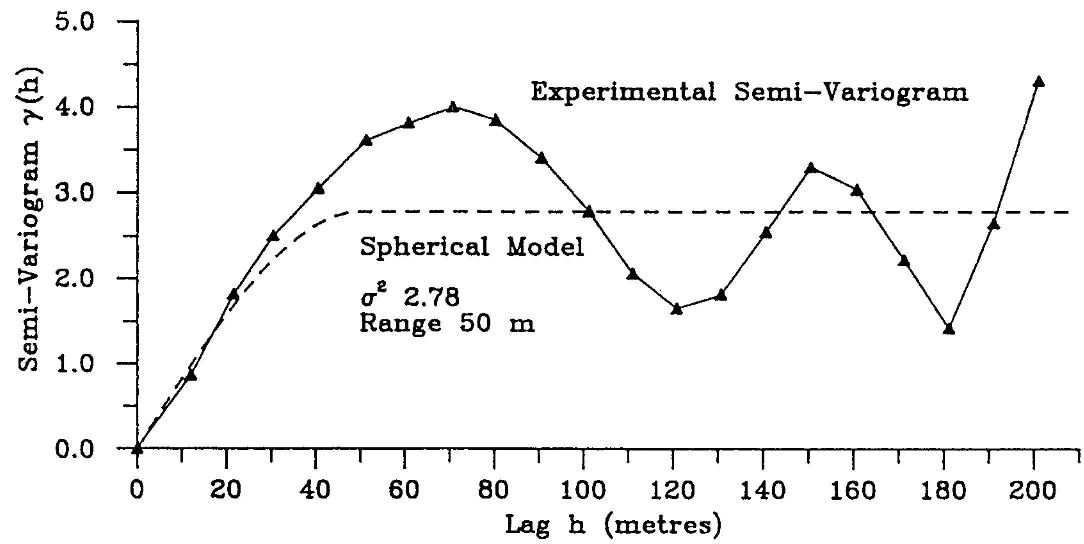

Discontinuity at Origin: Indicates presence of nugget effect; even samples taken very close together are not perfectly correlated. Nugget effect can be caused by measurement errors or small scale variability in the log hydraulic conductivity field.

Pure Nugget Effect: Indicates total lack of correlation between adjacent log hydraulic conductivity measurements. Equivalent to *white noise* phenomenon in physics. Encountered in hydrogeology when permeability tests are performed using a sampling interval that is longer than the range of the geologic deposit.

Sill: Confirms that hydraulic conductivity field is 2nd order stationary. No trend is present.

Semi-Variogram Increasing at Large Lags: Suggests that a trend exists in the hydraulic conductivity field or the range is significantly larger than the maximum dimension of the domain sampled.

Sinuosity: Also observed in *Figure 4.8*, *sinuosity* reflects the waviness or periodicity of the hydraulic conductivity field. For example, the semi-variogram peak at *70 m* in *Figure 4.8* occurs because many of the point semi-variograms $\gamma_{\text{point ij}}$ for this lag are taken between the extreme low conductivity zone in the upper left corner of *Figure 4.3* and the very high conductivity zone in the central portion of the geologic profile. Sinuosity of the semi-variogram becomes less pronounced when samples are collected over a larger area since local periodicity effects cancel and any two maxima/minima cannot dominate.

Domain Size Effects: Can lead to significant distortion of the experimental semi-variogram at large lags approximately equal to the maximum distance of the flow domain. For example, hydraulic conductivities in both the extreme left and extreme right of *Figure 4.3* are close to the mean value of *-4*. Since there appears to be strong correlation between these points the experimental semi-variogram is very low. On the other hand, if a maximum is present at one end of the domain, and a minimum at the other, the experimental semi-variogram will shoot up well above the sill. As a practical rule of thumb, the semi-variogram model should be fitted only to experimental semi-variogram points that are based on at least *30* supporting pairs of point-semi variograms. As an additional safeguard, the semi-variogram model should not be considered reliable beyond $\frac{1}{2} D_{max}$, the maximum dimension of the flow domain (Journel, 1978).

Figure 4.9 Semi-Variogram Behaviour at Origin & Large Distances

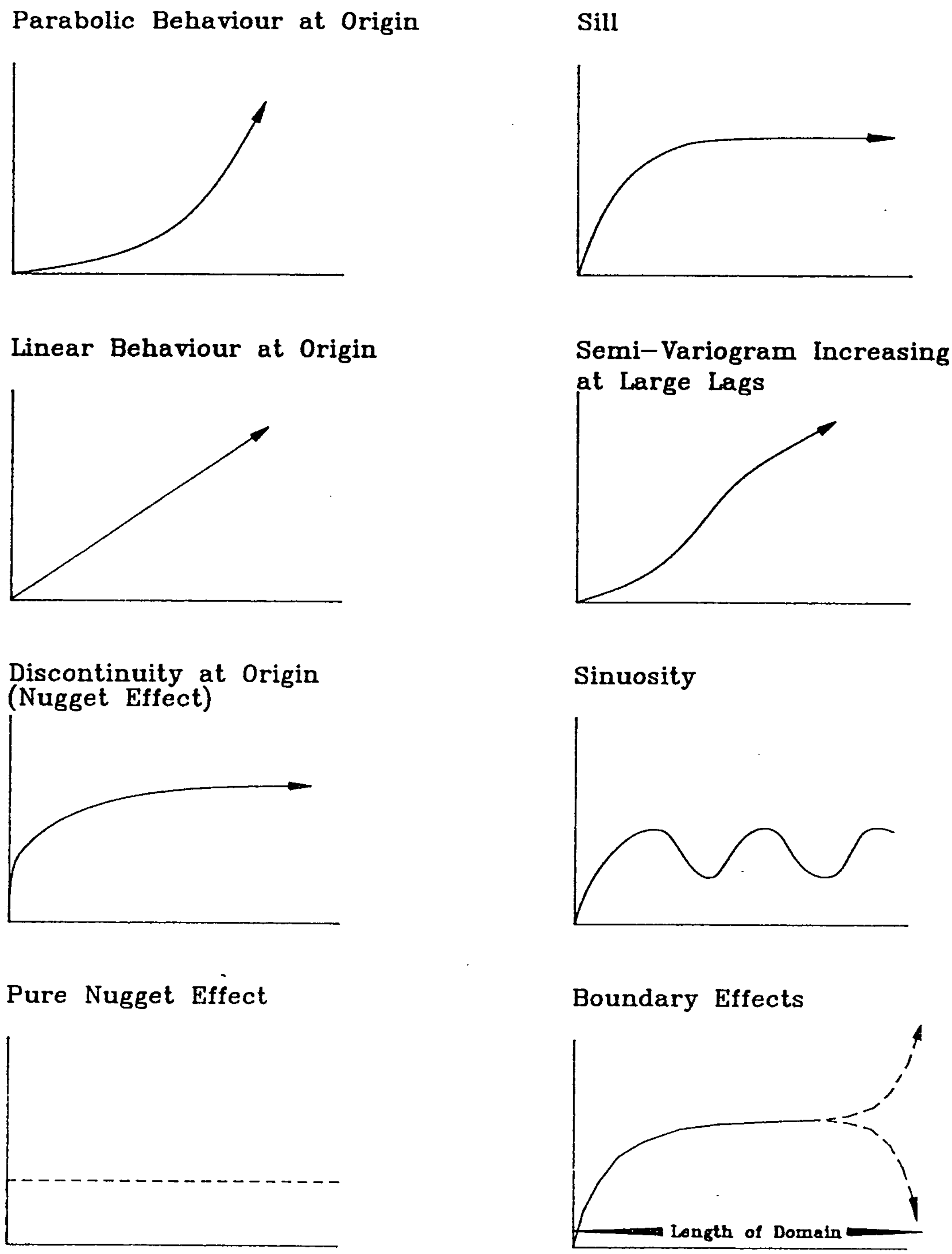

4.3.2 VARIOGRAM FUNCTIONS

To apply information about the nature of the correlation structure contained in the experimental semi-variogram to problems of estimation and simulation, it is necessary to describe the experimental semi-variogram in terms of a continuous mathematical function that can be evaluated at any lag $\boldsymbol{h}$. Geostatistical practitioners have found that in most cases a reasonable fit to the experimental semi-variogram can be obtained by selecting the corresponding model from a limited set mathematical functions that includes: *linear, spherical, exponential, Gaussian, power,* and *nugget* models. The standard *semi-variogram models* can be combined to fit complex experimental variograms for which a satisfactory match cannot be obtained with a single semi-variogram model. For example, the nugget model could be combined with a spherical model to reproduce the semi-variogram structure illustrated in *Figure 4.7.*

Not all functions $f(\boldsymbol{h})$ provide suitable semi-variogram or covariance models. To be acceptable, $-\gamma(\boldsymbol{h})$ must be *conditionally positive definite* and if $C[\boldsymbol{h}]$ exists, it must be *positive definite*. Consider making an estimate of the true log hydraulic conductivity, $Z(x)$, by any linear combination of I measured data, $z(x_i)$:

$$Z^*(x) = \sum_{i=1}^{I} \lambda_i \cdot z(x_i) \qquad \textit{Equation 4.12}$$

To be physically meaningful, the variance of the estimate must be greater than or equal to zero.

$$VAR[Z^*(x)] = \sum_{i=1}^{I}\sum_{j=1}^{I} \lambda_i\, \lambda_j \cdot (-\gamma[\boldsymbol{h}_{ij}]) \geq 0 \qquad \textit{Equation 4.13}$$

Appendix A.2 provides the derivation of *positive definite* conditions and additional insight.

Equations for the six standard semi-variogram models are presented below; suggestions for initial parameter settings are also given. Needless to say, each of the standard models satisfy the *conditionally positive definite* requirement.

Linear Model: $\gamma(h) = A \cdot h \qquad A \geq 0$

The linear model fits well to experimental semi-variograms that are intrinsic only, without a well defined sill. The model can also be used in combination with other semi-variogram models to simulate an increasing experimental semi-variogram at large lags. An increase in coefficient A steepens the semi-variogram profile. A suitable starting point is σ^2/D_{max}.

Spherical Model:

$$\gamma(h) = \sigma^2 \cdot (1.5 \cdot h/a - 0.5 \cdot a^3/h^3) \qquad 0 \leq h \leq a$$
$$\gamma(h) = \sigma^2 \qquad a > h$$

The spherical model provides a suitable match for experimental semi-variograms with a well developed sill $C[0]$. It is the only standard model that does not continue to increase at large lags by definition. When fitting this model, σ^2 should be set to the observed sill and a to the observed range.

Exponential Model: $\gamma(h) = \sigma^2 \cdot (1 - exp(-h/a)) \qquad a > h$

The exponential model can be used to simulate most experimental semi-variograms that increase rapidly at the origin and then gradually flatten out. Although the exponential model attains σ^2 only at infinity; for all practical purposes, a sill occurs at $h \approx 3 \cdot a$, where the variogram is already equal to 95% of the sill value. If the experimental semi-variogram exhibits a sill a suitable starting point can be achieved by setting σ^2 to the observed sill value and a to $1/3$ of the range. If a sill is not present, set a to $1/3\ D_{max}$ and σ^2 to the maximum value of the experimental semi-variogram.

Gaussian Model: $\gamma(h) = \sigma^2 \cdot (1 - exp(-h^2/a^2)) \qquad a > h$

The Gaussian model increases very gradually at the origin and then rises quickly to a sill at $h \approx 2a$. The model is suited to simulating experimental semi-variograms that exhibit parabolic behaviour at the origin, suggesting that a very strong and regular correlation structure is present. Setting σ^2 equal to the experimental sill and a equal to ½ the range generally results in a good starting point for the fitting procedure.

Power Model: $\gamma(h) = a \cdot h^b$ $a > h$

The power model is generally reserved for experimental semi-variograms that do not attain a sill over the lag distances sampled. The power coefficient, b, controls how quickly the semi-variogram model levels off to a sill. Values of b less than 0.6 are generally required if the experimental variogram levels off at large lags. Also, b must always be less than 2 since values larger than 2 result in a variogram model that is not *positive definite*. Reasonable starting values for this semi-variogram are: $b = 0.5$, $a = \sigma^2/(D_{max})^{1/4}$.

Nugget Effect Model: $\gamma(h) = C_{nugget}$

The nugget model is used almost exclusively in conjunction with other semi-variogram models to simulate a discontinuity at the origin of the experimental semi-variogram. When a discontinuity is present, the nugget variance C_{nugget} is set equal to the y-intercept of the experimental semi-variogram. One of the other standard models is then added to the nugget semi-variogram to simulate the experimental behaviour at non-zero lags.

Figure 4.10 illustrates the characteristic shapes of the standard semi-variogram models. The standard model that best matches the shape of an experimental semi-variogram is selected to represent the correlation structure of the sampled log hydraulic conductivity field. Once a suitable model is selected, the model parameters are adjusted until the model results in a good fit to the experimental semi-variogram points. In some instances, semi-variogram models have to be combined in a composite model in order to achieve a good fit. In *Section 4.6* it will be shown that estimation and simulation of hydraulic conductivity fields is not sensitive to the exact shape of the semi-variogram, as long as it captures the dominant features of the experimental data.

Figure 4.10 *Standard Variogram Models*

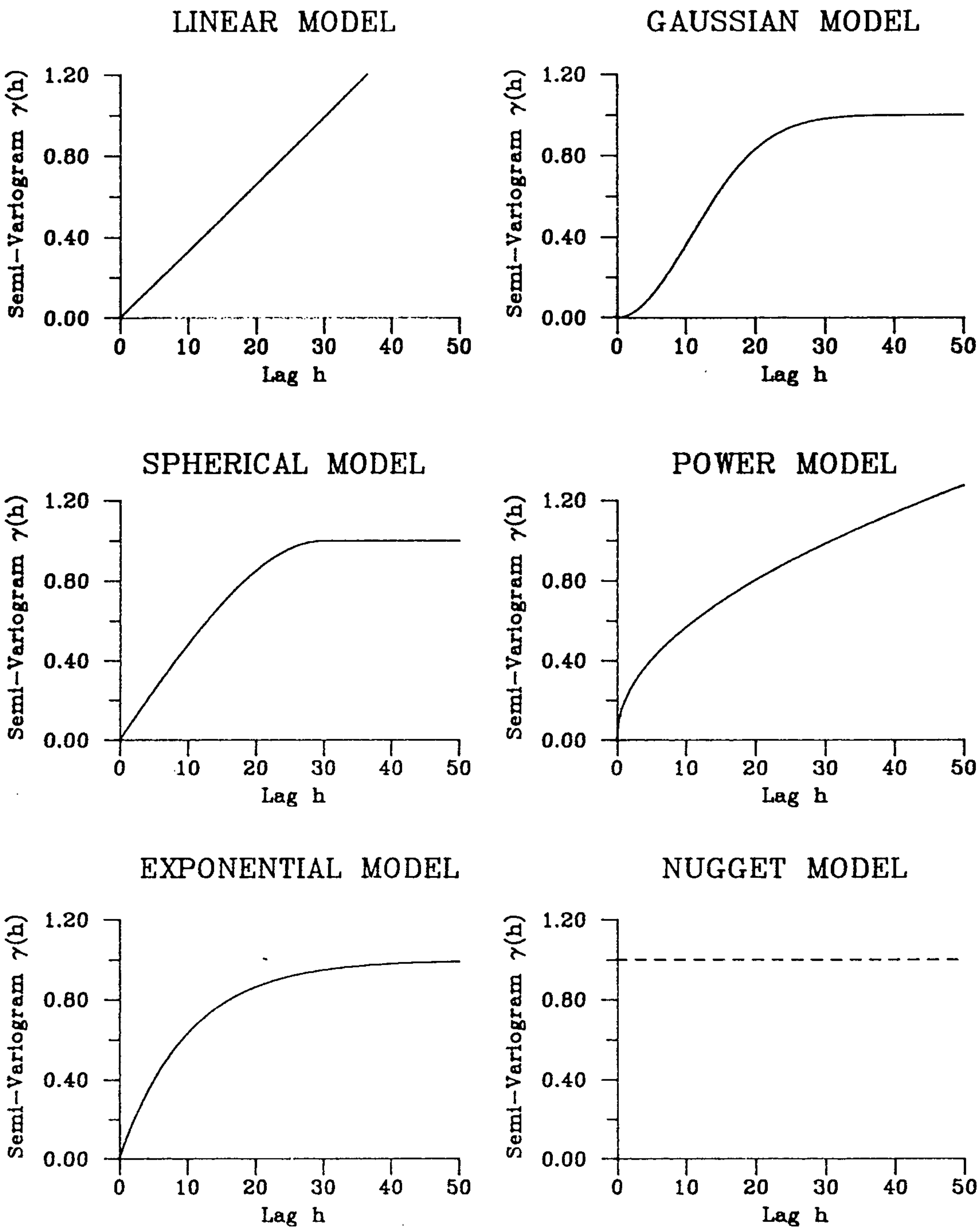

4.4 ESTIMATION

Numerical models of groundwater flow, such as the finite element model used in this framework to predict pore pressures in the pit wall, require that the hydraulic conductivity field be specified at every point in the flow domain. Pump tests, slug tests, and virtually all other subsurface measurements provide only local parameter values that are valid at discrete points or over small volumes relative to the size of the flow domain. The primary objective of such measurements however, is not to ascertain the exact value of hydraulic conductivity at a point; rather, it is to provide hard data that can be used to estimate hydraulic conductivity values everywhere in the flow domain. Today, the hydrologist can select from a large number of averaging methods that have been designed to estimate a continuous function from a set of such discrete measurements. The methods include hand contouring, method of minimum curvature, method of polygons, inverse distance weighting and *kriging*. Of these, *kriging* is the estimation method of choice. Unlike other estimation strategies that assign weights based exclusively on the relative geometry between sample and prediction point, *kriging* weights are influenced by both sample geometry and the correlation structure of the parameter being predicted.

This section begins with an introduction to the philosophy of *kriging*, followed by a brief discussion of why it is the *Best Linear Unbiased Estimator.* The mechanics of *kriging* are then introduced, together with a summary of some of the strengths and weaknesses of the method, and suggestions as to when the method should and should not be used. One of the biggest advantages of *kriging* is that the variance of estimation errors, calculated as part of the *kriging* process, indicates the degree of uncertainty associated with each *kriging estimate*. This section develops an expression for the variance of estimation errors and examines how the equation is affected by changes in sampling strategy. A verification of the *Kriging* program developed as part of this thesis research and several practical examples based on the familiar demonstration problem first introduced in *Section 4.2* and on the Avra Valley Aquifer in southern Arizona are presented in the final subsection of this section.

4.4.1 PHILOSOPHY OF KRIGING

Given a set of log hydraulic conductivity measurements $z(x_i)$, the objective of estimation is to use the data to estimate as accurately as possible actual log hydraulic conductivity values, $Z(X)$ at locations where no measurements exist given available supporting data. The more sophisticated estimation methods define the estimator, $Z^*(X)$, as a weighted combination of available data:

$$Z^*(X) = \lambda_1 \cdot z(x_1) + \lambda_2 \cdot z(x_2) + \lambda_3 \cdot z(x_3) + \ldots\ldots \lambda_i z(x_i) \qquad \textit{Equation 4.14}$$

Figure 4.11 Location of Estimation Volume and Supporting Measurement Points

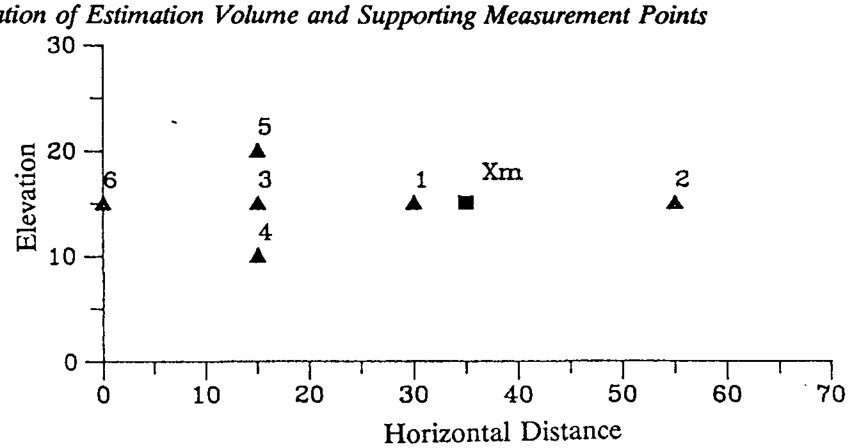

The difference between the various estimation methods lies in how the weights, λ_i, are determined.

Presented below is a list of desirable attributes that should be possessed by the estimation method if it is to yield the best possible estimates. *Figure 4.11* portrays an array of sample locations x_i surrounding a central prediction volume centred on x_m. This figure will be referenced on several occasions to illuminate the most important concepts.

- The method should be unbiased. On average, the estimation error, $\{Z^*(x) - Z(x)\}$, should be equal to zero.
- The method should honour data. Measured values $z(x_i)$ should be reproduced by the estimate $Z^*(x_i)$.
- The weighting scheme should be influenced by the distance between measurements and the prediction volume. Measurements closest to the prediction volume should be assigned larger weights (e.g. $\lambda_1 > \lambda_2$ on *Figure 4.11*).
- The weighting scheme should be influenced by the correlation structure of the log hydraulic conductivity field, as indicated by the shape of the experimental semi-variogram. More weight should be assigned to a measurement in a strongly correlated medium than to an equi-distant measurement in a medium exhibiting weak correlation.
- The weighting scheme should preserve symmetry of sample locations, $\lambda_4 = \lambda_5$.
- The weighting scheme should be influenced by relative geometry of the measurement points relative to each other. If two measurements are equi-distant from the prediction volume and one sample is isolated while the other is in proximity to other data points, the isolated sample should be weighted more heavily since each sample in the cluster carries much the same information, e.g. $\lambda_2 > \lambda_3$.
- Samples separated from the prediction volume by a distance greater than the range are not correlated with V_m; therefore, they should not influence the prediction, except when contributing to the global mean. Since x_6 is well beyond the range *(25 m)*, λ_6 should be approximately equal to 0.
- The method should be able to quantify the uncertainty associated with each estimate.

Estimation weights provided by *Kriging* satisfy each of these requirements. As a preliminary example, *Table 4.1* lists the *kriging weights* for each support point in *Figure 4.11*. The negative value of λ_3 appears erroneous at first glance; however, it is correct. *Section 4.4.4* explains why kriging assigns negative weights for certain sample configurations.

Table 4.1 Kriging Weights for Sampling Array

SAMPLE LOCATION:	x_1	x_2	x_3	x_4	x_5	x_6
DISTANCE TO X_m:	*5.00*	*20.00*	*20.00*	*20.61*	*20.61*	*35.00*
KRIGING WEIGHT:	*0.8003*	*0.1436*	*-0.0486*	*0.0041*	*0.0041*	*0.0963*

4.4.2 KRIGING IS BLUE

The acronym *BLUE* stands for *Best Linear Unbiased Estimator.* This section explores why *kriging* is *BLUE* and why *kriging* generally results in estimates that are more accurate than those of other estimation methods. *Kriging* is a *linear* estimator because $Z^*(X)$ is formed from a linear combination of supporting data[5]:

$$Z^*(X) = \sum_{i=1}^{I} \lambda_i z(x_i) \qquad \textit{Equation 4.15}$$

The resulting estimates are *unbiased* because one of the conditions imposed by *kriging* when calculating the optimal set of estimation weights is that on average, the prediction error should be equal to zero:

$$E[Z^*(X) - Z(X)] = 0 \qquad \textit{Equation 4.16}$$

Kriging is the *best* linear estimator because it yields estimates that have the smallest possible variance of estimation error, $VAR[Z^*(X) - Z(X)]$. In the following section it will be shown that the unknown *kriging* weights are determined by solving a system of simultaneous linear equations known as the *kriging system*. A brief explanation of why the *kriging system* guarantees the minimum variance of estimation errors will also be presented.

4.4.3 MECHANICS OF KRIGING

This section presents a brief overview of the key steps that lead to the development of the *kriging system*. For completeness, the full derivation is presented in *Appendix A*. As was pointed out in the previous section, the objective of *kriging* is to find a set of weights λ_i that will result in an unbiased estimate $Z^*(X_m)$ with the minimum variance of estimation errors.

In *Appendix A.3* it is shown that the unbiased condition leads to the constraint:

$$\sum_{i=1}^{I} \lambda_i = 1 \qquad \textit{Equation 4.17}$$

By invoking the assumption that the log hydraulic conductivity field is 2^{nd} *order stationary* and the definition of *covariance* given by *Equation 4.5*, *Appendix A.4* derives an expression for the estimation variance at prediction point X_m:

$$\sigma_m^2 = C_{av}[X_m, X_m] - 2\{\sum_{i=1}^{I} \lambda_i \cdot C_{av}[X_m, x_{mi}]\} + \sum_{i=1}^{I} \sum_{j=1}^{J} \lambda_i \lambda_j \cdot \{C_{av}[x_{mi}, x_{mj}] + \delta_{ij} \cdot \sigma_i \cdot \sigma_j\} \qquad \textit{Equation 4.18}$$

From *Equation 4.18* it is seen that σ_m^2 is a function of:

- Average covariance, $C_{av}[X_m, X_m]$, over prediction volume V_m.
- Average covariance, $C_{av}[X_m, x_{mi}]$, between V_m and each supporting data point x_{mi}.
- Average covariance between the individual data points, $C_{av}[x_{mi}, x_{mj}]$
- Variance of measurement error at each data point, σ_i^2.
- The unknown *kriging* weights λ_i.

---

5 Nonlinear estimators that include higher order terms such as $z(x_i)^2$ in the expression for $Z^*(X)$ are available, but are not used extensively in practice because they are complicated and require more information about the correlation structure of the parameter being estimated.

Each of the average covariance terms above can be evaluated provided the *semi-variogram* model and the location, size and shape of the prediction and support volumes are known.

The desired kriging weights are calculated by solving for the global minimum of σ_m^2 with respect to each λ_i, subject to the non-bias constraint given by *Equation 4.17*. Using the method of *Lagrange Multipliers*, the non bias constraint can be introduced into *Equation 4.18*. A set of equations that can be solved for λ_i and μ is obtained by taking the $I+1$ partial derivatives $\partial/\partial\lambda_i(\sigma_m^2)$ and $\partial/\partial\mu(\sigma_m^2)$, and setting each derivative equal to 0. This procedure results in $I+1$ simultaneous linear equations known as the *kriging system*:

i=constant $$\sum_{j=1}^{J} \lambda_j \cdot C_{av}[x_{mi}, x_{mj}] + \lambda_i \cdot \sigma_i^2 + \mu = C_{av}[X_m, x_{mi}]$$ *Equation 4.19*

$$\sum_{i=1}^{imax} \lambda_i = 1$$ *Equation 4.20*

The *kriging system* can be expressed in matrix form. For example, for $J=3$:

$$\begin{bmatrix} C(x_1,x_1)+\sigma_1^2 & C(x_1,x_2) & C(x_1,x_3) & 1 \\ C(x_2,x_1) & C(x_2,x_2)+\sigma_2^2 & C(x_2,x_3) & 1 \\ C(x_3,x_1) & C(x_3,x_2) & C(x_3,x_3)+\sigma_3^2 & 1 \\ 1 & 1 & 1 & 0 \end{bmatrix} \cdot \begin{bmatrix} \lambda_1 \\ \lambda_2 \\ \lambda_3 \\ \mu \end{bmatrix} = \begin{bmatrix} C(X_m,x_1) \\ C(X_m,x_2) \\ C(X_m,x_3) \\ 1 \end{bmatrix}$$ *Equation 4.21*

Equation 4.21 is then solved for the unknowns, λ_i and μ with any linear equation solver subroutine. When the calculated *kriging* weights are re-introduced into *Equation 4.15*, the resulting expression for $Z^*(X_m)$ becomes the best linear unbiased estimate of the true log hydraulic conductivity over the prediction volume V_m, based on available support.

To demonstrate how kriging is applied to analysis of real data, imagine that a permeability measurement program is conducted on the geologic profile presented in *Figure 4.4*. The program consists of packer tests at *15 & 35 m* elevations in six vertical bore holes and eleven permeability estimates based on grain size analysis of test pit samples obtained just below the ground surface. Since the open pit mine will be located on the left side of the profile, hole spacings are tighter in that area to provide better geologic control. *Figure 4.12* portrays the resulting data array.

The shape of the experimental semi-variogram constructed only from sample data resembles the semi-variogram in *Figure 4.6* that was constructed from the entire data array. A spherical model with a sill at *0.278* and a range of *50 m* provides a close fit to the observed experimental structure. A contour map of the resulting kriged estimate of the log hydraulic conductivity field is illustrated in *Figure 4.13*. The contour pattern of the estimated field reproduces the actual profile provided in *Figure 4.3* reasonably well, especially on the left half of the profile where measurements are closely spaced together, at distances approximately equal to ¼ of the range.

4.4.4 PROPERTIES OF KRIGING

Smoothing Behaviour: *Kriging* is a smoothing process. To minimize estimation variance, the *kriged* surface passes through the central or expected value at each prediction point, never through values that deviate significantly from the mean. Therefore, a *kriged* log hydraulic conductivity field will always show much less variability than the actual field from which the samples were collected. *Figure 4.14* illustrates the smoothing behaviour in one dimension. The solid line represents the true log hydraulic conductivity profile in a bore hole, the dots indicate locations where point measurements were conducted, and the dashed line indicates the resulting *kriged* profile.

Figure 4.12 Location of Hydraulic Conductivity Measurement Points - Packer Tests & Test Pits

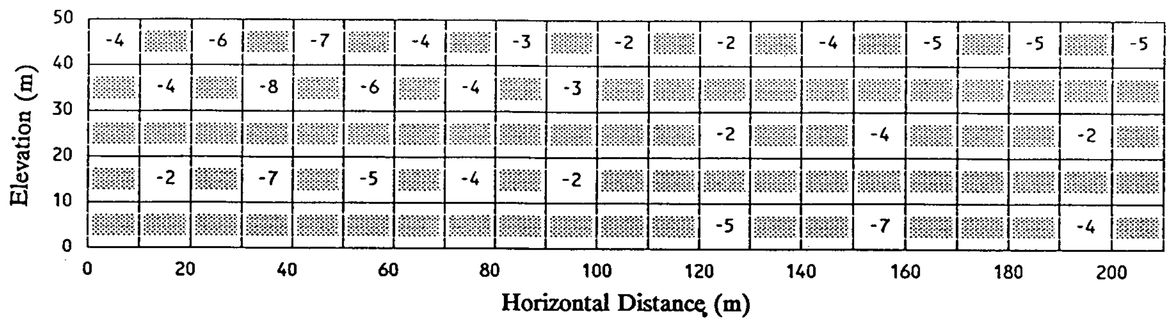

Figure 4.13 Kriged Estimate of Hydraulic Conductivity Field

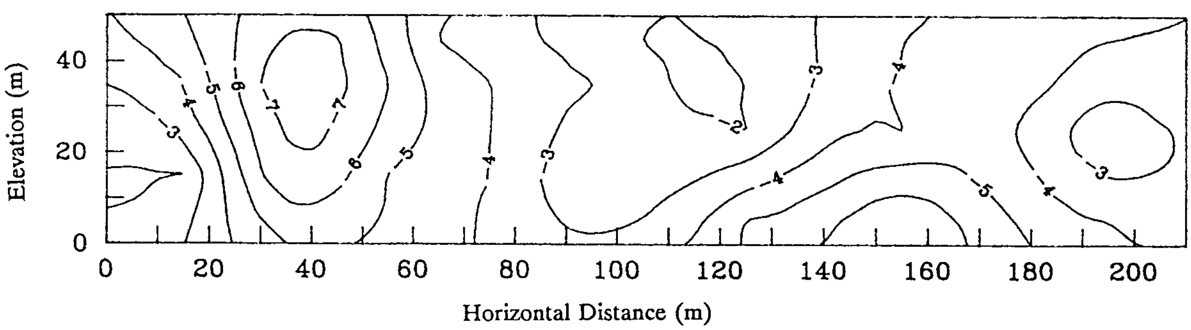

The smoothing behaviour that makes *kriging* ideal for applications such as predicting average copper grades in an open pit mine or representative log hydraulic conductivities in the pit wall, may detract from it's applicability in situations where the physical process being modelled is controlled by extreme values of the kriged parameter. Two examples of the latter processes include prediction of contaminant travel times (where most of the contaminant mass will follow flow paths that pass through the most permeable lenses in the deposit) and studies of mechanical dispersion (where variability in hydraulic conductivity results in flow velocity contrasts responsible for dispersing the contaminant concentration). Fortunately, the simulation techniques presented in *Section 4.5* provide a mechanism whereby the natural high frequency variability of the hydraulic conductivity field can be re-introduced in the realizations.

Figure 4.14 Smoothing Effect of Kriging

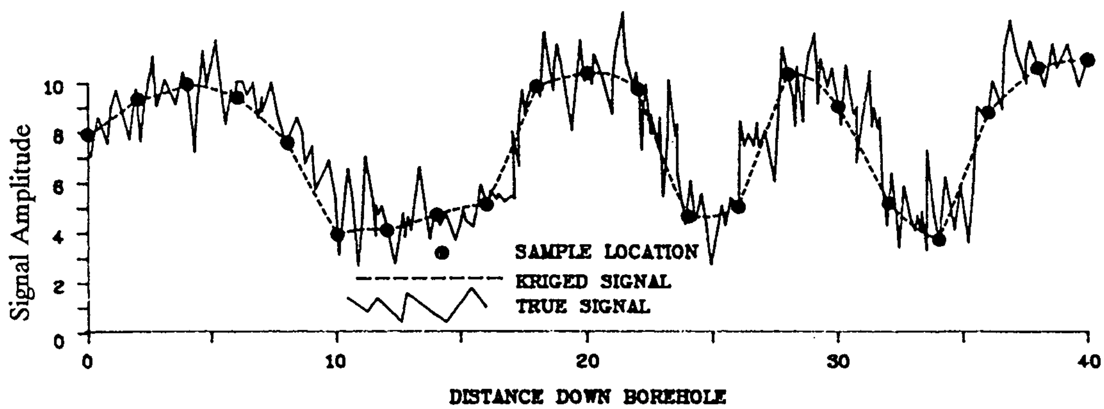

Negative Kriging Weights: Negative weights are permitted in kriging. They occur frequently at measurement points that are screened from the prediction point by other data. At the same time, the *kriging system* increases the kriging weight of the closer point that is providing the screen, thereby placing the greatest emphasis on the closest data. For example, in *Figure 4.11* sample location x_2 is assigned a negative kriging weight of *-0.0486* while point x_1 is assigned a very large positive weight, *0.8003.*

Lack of Support: This condition develops when a prediction point is isolated and all supporting measurements are located at a distance further than the range. Since none of the supporting data are correlated to the prediction point, *kriging* will assign equal weights to all supporting data; the estimate will thus be equal to the mean value of the supporting measurements. This property of *kriging* suggests that hydraulic conductivity measurements should be spaced at distances significantly shorter than the range in areas of interest if *kriging* is to yield accurate estimates of the hydraulic conductivity field unless inverse methods are utilized to enhance the hydraulic conductivity estimates (e.g. hydraulic head measurements, temperature data).

Estimation at Measurement Point: Kriging is an exact interpolator. When estimating a log hydraulic conductivity value over exactly the same volume as is used for a supporting measurement, kriging will recover the measured value by setting the corresponding weight to *1.0* and all other weights to *0.* However, if log hydraulic conductivity is being estimated over a large block while supporting measurements are taken over much smaller volumes, then the resulting estimate may not have the same value as a measurement point located in the center of the prediction block. Also, if some of the supporting data points are clustered together, then the weights of those points will be reduced to account for duplication of information.

Kriging with a Moving Neighbourhood: In instances when a spatial drift is recognized, resulting in a hydraulic conductivity field that is not second order stationary, kriging can still be utilized by limiting the selection of supporting data to a smaller "moving neighbourhood" in which the field can be treated as second order stationary. In some instances, it may be advantageous to remove the drift prior to kriging.

4.4.5 ESTIMATION ERROR

The variance of estimation errors, given by *Equation 4.18* and reproduced below, provides confidence intervals on the accuracy of each *kriging estimate*. Assuming that the hydraulic conductivity field is *log-normally distributed* and either the *intrinsic hypothesis* or the *hypothesis of 2nd order stationarity* is valid, *69%* of kriging estimates should fall within ± 1 standard deviation σ_m of the true log hydraulic conductivity, 95% within $\pm 2\sigma_m$, and 99.7% within $\pm 3\sigma_m$.

$$\sigma_m^2 = C_{av}[X_m, X_m] - 2\{\sum_{i=1}^{I} \lambda_i \cdot C_{av}[X_m, x_{mi}]\} + \sum_{i=1}^{I} \sum_{j=1}^{J} \lambda_i \lambda_j \cdot \{C_{av}[x_{mi}, x_{mj}] + \delta_{ij} \cdot \sigma_i \cdot \sigma_j\} \qquad \textit{Equation 4.18}$$

To understand how support and prediction volume geometry affects the estimation error it is necessary to explore the physical significance of each term in *Equation 4.18.*

Starting at the extreme left, $C_{av}[X_m, X_m]$ represents the natural variability of the hydraulic conductivity field and the variance reduction effects of increasing sample volume. $C_{av}[X_m, X_m]$ is defined as the average value of the covariance function, evaluated between all possible pairs of points *(a,b)* in prediction volume V_m. In practice, the expression for $C_{av}[X_m, X_m]$ is approximated by discretizing V_m into an array of *A* points (typically *6x6*) and then averaging the covariance between each pair of these points.

$$C_{av}[X_m, X_m] = \frac{1}{V_m^2} \int_{V(a)} \int_{V(b)} C[a,b]\, \partial a\, \partial b = \frac{1}{A^2} \sum_{a=1}^{A} \sum_{b=1}^{A} C[a,b] \qquad \textit{Equation 4.22}$$

When the prediction volume is a point, *Equation 4.22* reduces to *C[0]*, the variance of the log hydraulic conductivity point process, as defined in *Equation 4.3*. However, as size of the prediction volume increases, covariances over some lags *h(a,b)* become significantly smaller than *C[0]*, and the average covariance is reduced. This mechanism, illustrated in *Figure 4.15*, accounts for the *variance reduction factor* (Van Marcke, 1983), whereby estimation variance decreases with increasing size of the estimation volume.

Figure 4.15 Calculating Average Covariance $C_{av}[Xm, Xm]$

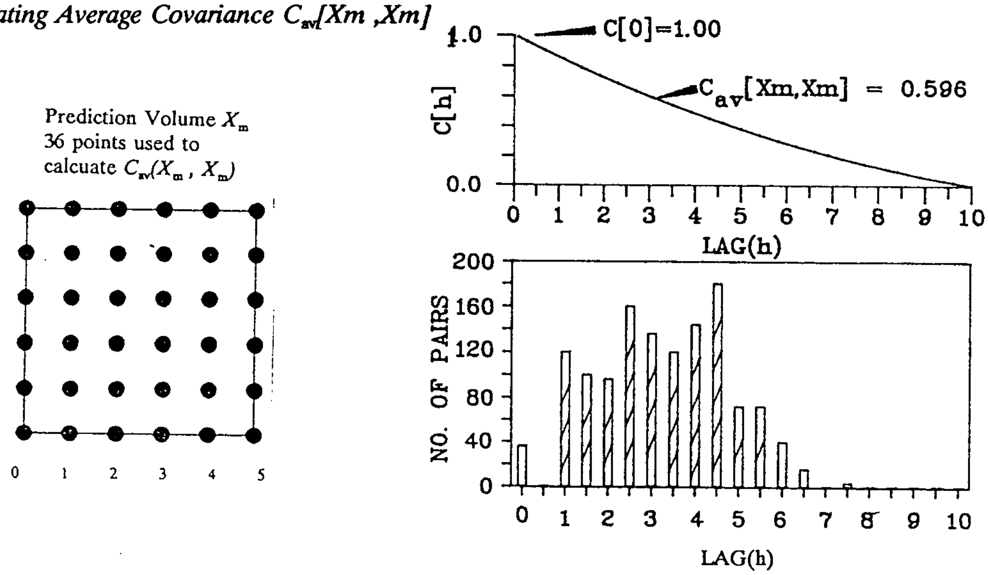

Figure 4.16 Increased Uncertainty due to Duplication of Information.

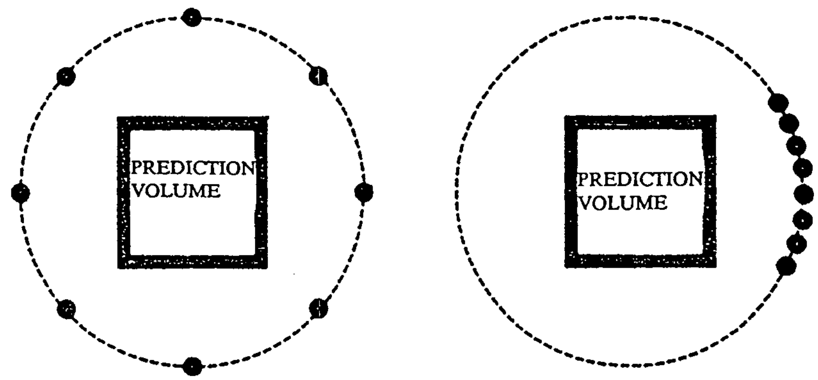

The second term in *Equation 5.18*, $-2\{ \Sigma\ \lambda_i \cdot C_{av}[X_m, x_{mi}]\}$ accounts for reduction in estimation uncertainty due to supporting measurements. $C_{av}[X_m, x_{mi}]\}$ represents the average covariance between prediction volume V_m and support volume v_{mi}. Since covariances between closely spaced points are large, measurement points situated closest to X_m will make the largest contribution to uncertainty reduction. Once again, the average covariance between prediction volume and support point can be obtained by discretizing the volumes into arrays of points, evaluating the covariance between each possible pair, and taking the average. In situations where the support volumes are significantly smaller than the prediction volume, it suffices to discretize only V_m and treat v_m as a point value.

The third term in *Equation 4.18*, $\Sigma\ \Sigma\ \lambda_i\ \lambda_j \cdot \{C_{av}[x_m, x_{mj}]\}$, is a correction factor that adjusts for duplicated information. When support points are correlated, both measurements carry information about the hydraulic conductivity field in the immediate neighbourhood. The second term in *Equation 4.18* does not recognize this fact and reduces σ_m^2 more than it should. The third term is needed to increase the covariance back to the correct level. To illustrate this concept, consider the scenario in *Figure 4.16*. One prediction point is surrounded by a ring of 8 equally spaced support points, a second prediction point is supported by 8 measurement points all clustered closely together on one side. Although the second term in *Equation 4.18* will be the same for both data configurations, the third term will ensure that the ring sampling configuration results in a better estimate with a smaller variance of estimation errors.

The final term, $\Sigma\ \Sigma\ \lambda_i\ \lambda_j \cdot \{\ \delta_{ij} \cdot \sigma_i \cdot \sigma_j\ \}$, corrects for measurement errors at each supporting sample location x_{mi}. By increasing σ_m^2 when supporting data is unreliable, this term accounts for the fact that a set of exact measurements reduce uncertainty more than a set of noisy measurements taken at the same locations.

In summary, the uncertainty of *kriging* estimates is influenced by the following factors:

- Nature of the correlation structure, represented by $C[h]$ *or* $\gamma[h]$.
- Size of prediction volume.
- Number of supporting measurements.
- Proximity of supporting measurements to prediction volume.
- Proximity of supporting measurements to each other.
- Measurement errors, resulting in noisy data.

Figure 4.17 Contour Plan of Variance of Estimation Errors for Point Estimates.

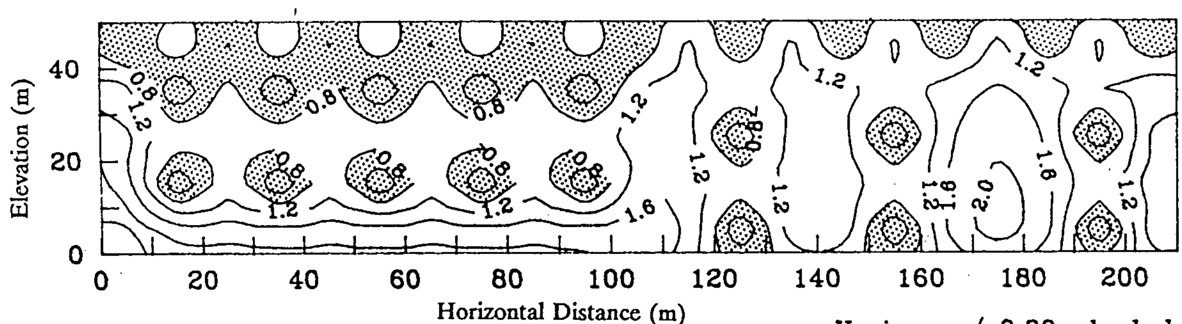

Figure 4.17 presents a contour plot of σ_m^2 for the sampling array used in *Figure 4.12*. To demonstrate the effect of measurement errors it is assumed that test pit data was subject to measurement errors with a standard deviation $\sigma_{test\ pit}=0.5$ while packer test data is exact, $\sigma_{packer}=0.0$. As expected, the estimation uncertainty is lowest in the vicinity of bore holes and test pits. At packer test locations the variance is *0;* log hydraulic conductivity is known with certainty at those points. At test pit locations some uncertainty still exists since hydraulic conductivity estimates based on grain size are not exact. The largest uncertainty occurs in the lower right corner of the profile where measurements are separated by as much as *40* m.

The contour map illustrated in *Figure 4.17* is based on variances of estimation errors associated with kriging predictions at a point. The influence of a larger prediction volume on estimation uncertainty can be seen in *Figure 4.18*, prepared for kriging estimates over a *10x10 m* block. Since the range is only *50 m*, this larger block size represents a sizeable fraction of any portion of the flow domain over which hydraulic conductivities are correlated. Because the blocks are relatively large, the *variance reduction factor* (introduced in *Section 4.4.5*) leads to a substantial reduction in uncertainty. Unfortunately, since the reduction in uncertainty is achieved by utilizing a larger averaging volume, it is achieved at the expense of model resolution.

Note that in areas very close to measurement locations (unshaded in *Figure 4.18*) estimation uncertainty actually increases. The increase can be explained as follows: when a point measurement is taken in the center of a block, hydraulic conductivity will be known exactly at that point and the point estimation variance will be 0; while the average hydraulic conductivity over the entire block will still be somewhat uncertain.

Figure 4.18 Contour Plan of Percent Variance Reduction for 10x10 m Block Estimates.

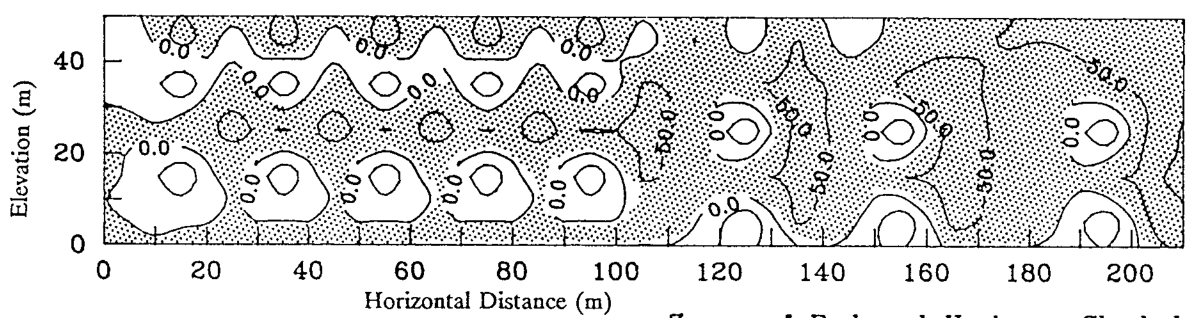

4.4.6 VERIFICATION

The standard procedure for verifying a *kriging* model (de Marsily, 1986) is to systematically remove one measurement point from the data base and then estimate that point based on the remaining data. This procedure, referred to as *Jack-Knifing*, yields *M* observations of the actual estimation error $\{Z^*(x_m) - z(x_m)\}$. If the *kriging* model is valid the mean of the estimation error, m_e should be approximately equal to *0* since *kriging* is an unbiased estimator:

$$m_e = \frac{1}{I} \cdot \sum_{m=1}^{M} \{Z^*(x_m) - Z(x_m)\} \approx 0 \qquad \textit{Equation 4.23}$$

Furthermore, the variance of estimation errors, σ_m^2, given by *Equation 4.18*, gives an indication of the confidence interval of the kriging estimate at each prediction point. σ_m^2 is not stationary, it varies from prediction point to prediction point, depending on the amount and geometry of supporting data. If the *kriging* estimate is to be verified at the *95%* confidence interval, then *95%* of the observed errors $\{Z^*(x_m) - z(x_m)\}$ should fall within $\pm 2\sigma_m$ of m_e.

De Marsily (1986) provides a simpler procedure for verifying the kriging results. He suggests that the magnitude of the actual estimation error at each measurement point should be coherent with the uncertainty predicted by the kriging system for that point, as indicated by the variance of the estimation error σ_m^2. The kriging model will be coherent if the average ratio of the square of the estimation error divided by σ_m^2 is approximately equal to 1.0.

$$\sum_{m=1}^{M} \frac{\{Z^*(x_m) - Z(x_m)\}^2}{\sigma_m^2} \approx 1 \qquad \textit{Equation 4.24}$$

If the *coherency ratio* given by *Equation 4.24* is significantly greater than *1.0* then the actual magnitude of estimation errors is larger than the magnitude of errors predicted by kriging. This situation occurs if the semi-variogram model chosen to simulate the actual autocorrelation structure is too strongly correlated at short lags (e.g. if a Gaussian model is chosen to represent an experimental variogram with a strong nugget effect). If the coherency ratio is significantly smaller than *1.0* (e.g. < *0.9*) then the kriging estimates are more accurate than expected based on the specified semi-variogram model. Coherency ratios less than 1.0 are observed when the semi-variogram model has more variability than the experimental variogram that it is supposed to represent (i.e. when the model plots above the experimental semi-variogram).

In conclusion, kriging estimates of the hydraulic conductivity field can be trusted for dewatering design if:

- The mean estimation error is approximately equal to *0.0.*
- Approximately *95%* of the kriging predictions fall within $\pm 2\sigma_m$ of measured values.
- The coherency ratio is approximately equal to *1.0.*

Because the verification steps presented above are based on statistics, application of the procedures to flow domains with a small number of data points can lead to unpredictable and erroneous results since the statistics may then be strongly affected by one or two extreme values.

Table 4.2 and *Figure 4.19* present results of the verification procedures for the demonstration problem analyzed in this section. The mean estimation error, *0.03*, is very close to *0*, suggesting that kriging did yield an unbiased estimate of the actual hydraulic conductivity field. The histogram of normalized estimation errors, portrayed in *Figure 4.19*, shows that all estimation errors were smaller than $\pm 2\sigma_m$; therefore, the model is valid at the 95% confidence interval. The coherency ratio for this problem is equal to *0.77*. In this case kriging performed better than expected, most likely because excess variability was introduced into the semi-variogram model. When

Table 4.2 Results of Verification Calculations at Measurement Points

Mean of Sample Data:	*-4.29*	Variance of Measurements:	*1.75*
Mean of Kriging Estimates:	*-4.26*	Variance of Kriging Estimates:	*1.21*
Mean of Estimation Errors:	*0.03*	Variance of Estimation Errors:	*1.36*
Percent Errors < $2\sigma_m$:	*100%*	Coherency Ratio:	*0.78*

Figure 4.19 Histogram of Normalized Estimation Errors at Measurement Points

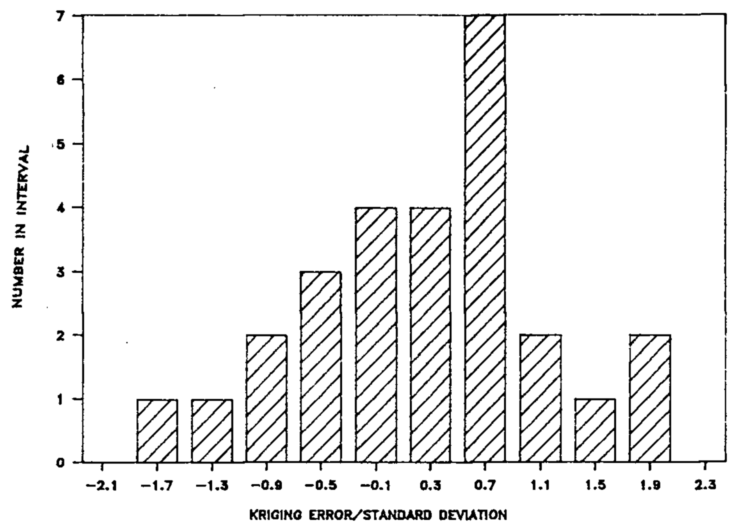

Figure 4.20 Histogram of Normalized Estimation Errors at all Grid Points

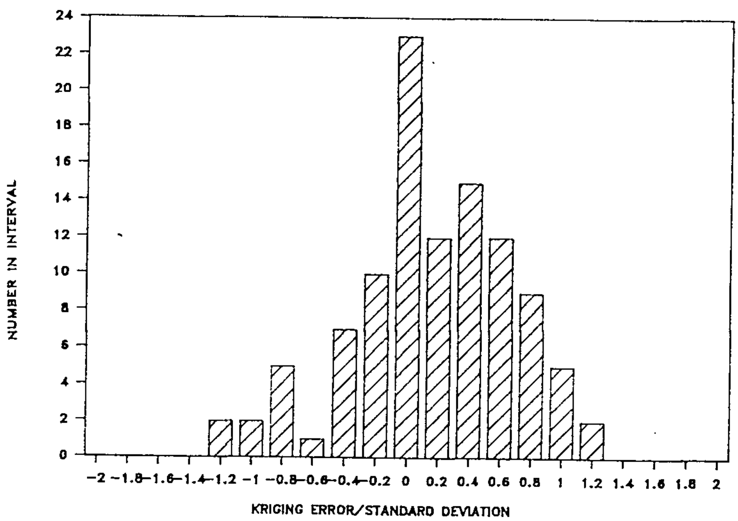

kriging larger sets of actual field data, the coherency ratio typically falls much closer to *1.0* when a well fitting semi-variogram model is chosen, typically in the range *0.90* to *1.10*.

The demonstration problem presented in this section is atypical in that the actual value of log hydraulic conductivity is known at each grid point in the flow domain (e.g. *Figure 4.4*). This makes it possible to compare kriging estimates to actual values not only at available measurement points, but at each point in the flow domain. *Figure 4.20* presents a histogram of normalized estimation errors for all *105* grid points in the flow domain. The figure shows that kriging did a very good job in reproducing the actual hydraulic conductivity field; *96%* of errors were less than $\pm 1\sigma_m$ in magnitude.

4.4.7 CASE HISTORY & FITTING SEMI-VARIOGRAM

Thus far, all examples have been limited to analysis of a very simple hypothetical problem. The example presented in this section will illustrate how kriging can be applied to analysis of real hydrologic data. Selection of semi-variogram models that fit the experimental structure will be one of the focal points of the discussion. The example is based on a case history of aquifer characterization documented by Clifton & Neuman (1982). Although that particular paper originates in the domain of groundwater resource management, the methodology can be applied equally to mining, geotechnical, water supply and environmental problems since the objective of accurately defining the hydraulic conductivity field is common to all. In fact, at Highland Valley Copper, development of groundwater resources for the concentration process is a key goal of the dewatering program.

Figure 4.21 shows the location of *45* water supply wells that intersect the northeast half of the Avra Valley aquifer in southern Arizona. Transmissivity values, obtained from analysis of pump test data, are reported beside each well location. The objective of kriging is to predict transmissivities throughout the study area. Transmissivity estimates are required for input into a numerical model of groundwater flow. In turn, the numerical model allows groundwater resource managers to look into the future and study aquifer response to different exploitation strategies before they commit to a water use policy.

Figure 4.21 Location of Transmissivity Measurements - Avra Valley

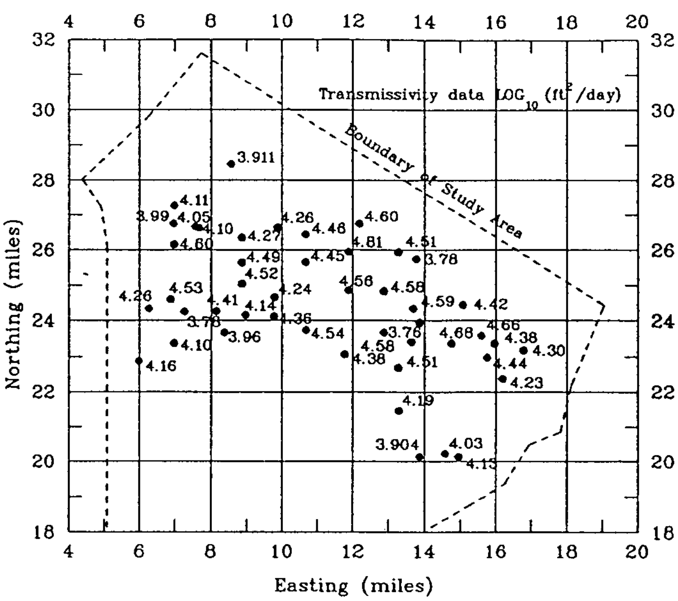

Figure 4.22 Experimental Semi-Variogram Structure and Six Possible Models

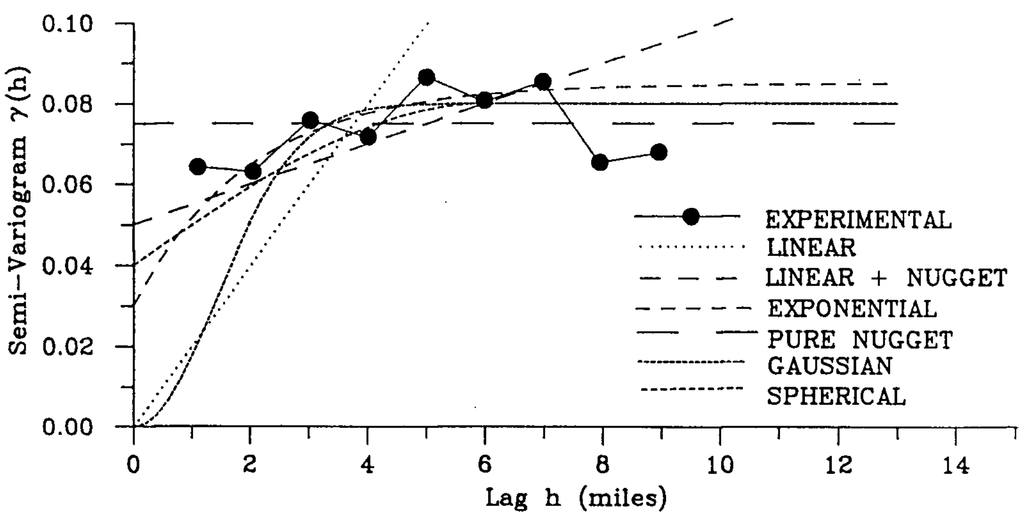

The experimental semi-variogram for this data set is illustrated in *Figure 4.22.* A nugget effect is apparent. Clifton & Neuman attribute the nugget variance to a combination of measurement errors and heterogeneity in the aquifer at scales smaller than *1* mile. The semi-variogram reaches a sill of *0.08* at approximately *6* miles. A spherical or exponential model, combined with a nugget effect of *0.04* to *0.05* should provide a good fit to the experimental structure.

According to Journel (1978) selecting a semi-variogram model to represent the experimental structure is an art that does not lend itself to automation. More recently, parametric estimation methods have been developed to identify the best fitting semi-variogram model (Kitanidis, 1983, Kitanidis and Lane, 1985, Wagner and Gorelick, 1989). In either case, as well as capturing the general form of the experimental semi-variogram structure, the model should also incorporate important geologic information such as depositional anisotropy, lenticular structures, etc. As explained at the beginning of *Section 4.3*, the standard procedure for fitting an experimental variogram, which involves "eyeballing" different models and then adjusting model parameters until a suitable match is found (Journel, 1978, Clark, 1979, De Marsily, 1986) has been adopted in this framework. To facilitate this fitting approach, a graphics intensive variogram module was incorporated in the SG-STAT program. By programming the computer to automatically re-plot the semi-variogram model over the experimental structure each time model parameters are adjusted SG-STAT helps the user select the best semi-variogram quickly and efficiently.

Because kriging is *robust* estimation results are not sensitive to the exact shape of the semi-variogram model as long as it captures the main characteristics of the semi-variogram. However, when the experimental variogram is very irregular and/or the nugget variance intercept can be picked only roughly, as is the case in *Figure 4.22*, a large number of models seem to provide a reasonable fit. In such situations, the verification procedures described in the previous section can provide a simple means for testing the goodness of fit of semi-variogram models. A semi-variogram model will provide reliable parameter and uncertainty estimates if the following verification conditions are satisfied when comparing kriging estimates at measurement points to observed values:

- The average estimation error at the measurement points is approximately equal to *0.0*. This condition confirms that the semi-variogram model resulted in an unbiased estimate.

- The average variance of estimation errors at measurement points, $VAR[Z^*(x_m) - Z(x_m)]$, is less than the dispersion variance of the data, i.e. kriging reduces uncertainty. The semi-variogram model that has the smallest variance of estimation errors provides the most accurate kriging estimates. However, this model may not be the best choice for the geostatistical simulation if it results in an unrealistic assessment of estimation uncertainty.

- The kriging results are significant at the *69%* and *95%* confidence intervals. Ideally, at least *69%* of estimation errors, $|Z^*(x_m) - Z(x_m)|$, should be no larger than one standard deviation of the expected estimation error, $1\sigma_m$, and *95%* of kriging estimates should fall within $\pm 2\sigma_m$ of measured values. In practice, the observed percentages may fall below these targets by a few percent and still yield acceptable results, especially if small data sets are being used.

- The coherency ratio is approximately equal to *1.0*. If the estimation uncertainty indicated by kriging is consistent with observed estimation errors, the coherency ratio should fall within the range *0.9* to *1.1*. Deviations outside this range indicate that the estimation variances calculated by kriging are not reliable and could lead to errors in risk assessment of the slope design.

To be acceptable the semi-variogram model should satisfy each of the four criteria listed above. If a number of models meet the acceptability conditions then the best semi-variogram model can be selected by identifying the model that yields the highest confidence interval percentages and a value of the coherency ratio that is closest to *1.0*.

To illustrate how the above procedure can be used to identify the most suitable semi-variogram model six different models were defined. Each of the models is plotted in *Figure 4.22*. Model coefficients are presented in *Table 4.3*. Obviously, some of the semi-variograms provide a very poor fit in comparison to the others. The poor fitting models were included to illustrate the robust nature of kriging and to demonstrate the sensitivity of the verification procedure to screening poor models.

***Table 4.3** Coefficients for Semi-Variogram Models*

NO.	*MODEL*	σ^2	COEFFICIENT A	NUGGET VARIANCE
1	Linear & Nugget	n/a	0.005	0.05
2	Exponential	0.055	2.000	0.03
3	Pure Nugget	n/a	n/a	0.08
4	Gaussian	0.080	2.000	0.00
5	Spherical	0.040	6.000	0.04
6	Linear	n/a	0.020	n/a

Results of the verification analysis are presented in *Table 4.4* for each semi-variogram model. The most significant results are also compiled on four bar charts in *Figure 4.23*.

- *Figure 4.23A* indicates that the mean estimation error is very close to zero for all six semi-variogram models (mean error is less than *1%* of transmissivity values). This is expected since kriging should always yield unbiased estimates.

Figure 4.23 Results of Verification Analysis

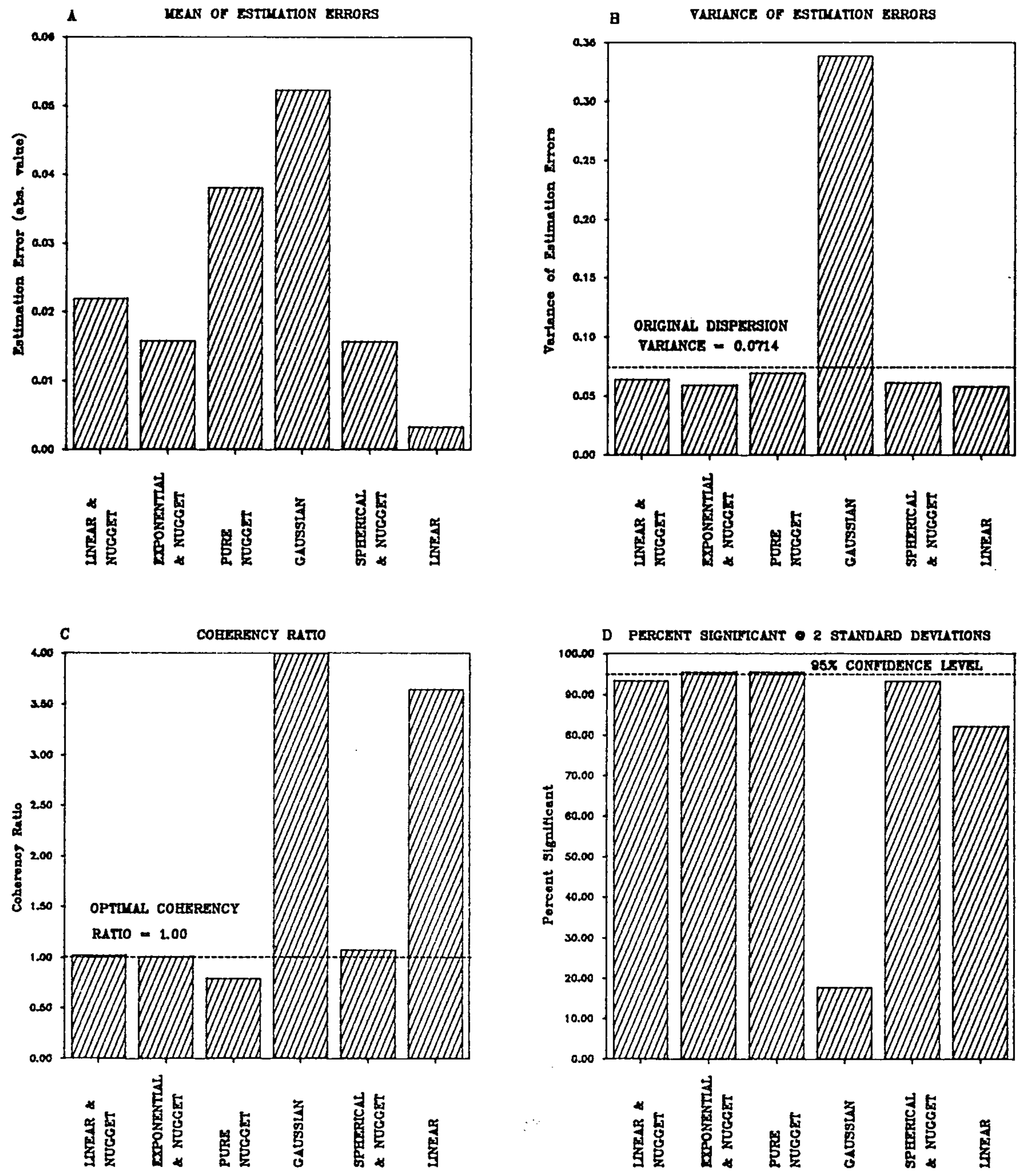

Table 4.4 Results of Verification Analysis

	LIN+NUG	EXPON	PURE NUG.	GAUSS.	SPHERICAL	LINEAR
MEAN OF OBSERVED DATA	4.31	4.30	4.30	4.30	4.30	4.30
MEAN OF KRIGING ESTIMATE	4.33	4.31	4.34	4.35	4.31	4.30
MEAN ESTIMATION ERROR	0.02	0.01	0.03	0.05	0.01	-0.00
VARIANCE OF OBSERVED DATA	0.07	0.07	0.07	0.07	0.07	0.07
VAR. OF KRIGING ESTIMATE	0.01	0.01	0.00	0.33	0.01	0.03
VAR. OF ESTIMATION ERROR	0.06	0.05	0.06	0.33	0.06	0.05
COHERENCY RATIO	1.03	1.01	0.79	152.75	1.07	3.64
SIGNIFICANT @ 1 SD (>69%)	66.67	77.78	77.77	15.55	66.66	53.33
SIGNIFICANT @ 2 SD (>95%)	93.33	95.56	95.55	17.77	93.33	82.22

- A comparison of dispersion variances of the observed data to the variance of kriging estimates confirms that kriging is a smoothing process since the kriging variance is substantially smaller (except for Gaussian model).

- *Figure 4.23B* shows the actual variance of estimation errors for each model. Kriging reduced estimation uncertainty for all models except the Gaussian where the variance of estimation errors increased from *0.0714* to *0.3388*. This large increase is due to the fact that the Gaussian model assigns very large weights to the closest data points and ignores data further afield. The large nugget variance observed in the Avra Valley Aquifer indicates that data points separated by more than *1* mile are poorly correlated; therefore, relying on the closest measurement yields a much poorer estimate of transmissivity than the average of several observations located further afield. Also, due to the short range (*6* miles) only a small set of supporting measurements exist for most supporting points. The large nugget variance and lack of supporting data in close proximity to estimation points explain why kriging point estimates reduces uncertainty by only *15%* on average (variance of estimation errors reduced from *0.0714* to approximately *0.060*). *Figure 4.24*, a contour map of variances of block estimation errors shows that kriging does a much better job at reducing estimation variance when transmissivity estimates are predicted for 1x1 mile. Kriging would also be more effective if fill-in data was available to define the shape of the experimental semi-variogram at lags shorter than *1* mile, thereby eliminating the large nugget variance.

- The coherency ratio is plotted in *Figure 4.23C* for each model. This is the most useful statistic for selecting the best fitting model. The figure shows that the *Gaussian* and *Linear* models are not acceptable since their ratios are much greater than *1.0*. The large values of coherency ratio indicate that these two models instruct the kriging program to assign far too much weight to nearby measurement points and not enough weight to data points further afield. The coherency ratio of the pure nugget effect model is *0.7916*. A value less than *1.0* confirms that this semi-variogram model introduces more variability than is actually present in the experimental structure. Coherency ratios for the three semi-variogram models that provide a reasonable fit (linear & nugget, spherical & nugget, and exponential & nugget) all have semi-variogram ratios approximately equal to *1.0*.

- The 69% and 95% significance tests confirm that the same three models yield transmissivity estimates that are consistent with corresponding predictions of estimation uncertainty. *Figure 4.23D* indicates that the Gaussian and linear models fail this acceptability test.

The exponential & nugget model will generate the most reliable kriging estimates for the Avra Valley Aquifer. It satisfies all four acceptability conditions, results in the highest scores in the significance tests and has a coherency ratio that is very close to 1.0. It is of interest to note that the *Mean Estimation Error* and *Variance of Estimation Error* statistics presented in *Table 4.4* indicate that all three semi-variogram models that fit the experimental structure yield acceptable kriging estimates, the exponential model is only slightly better than the spherical model, which in turn is slightly better than the linear & nugget model. This observation confirms the *robustness* of kriging, that the method is not sensitive to the exact shape of the semi-variogram as long as it captures the essential characteristics of the experimental structure.

Figure 4.25 presents a contour map of kriged transmissivities that is based on the exponential and nugget model. Measurement locations and transmissivities observed at those locations are also plotted on the figure. Although the kriged contours correspond to the measured values in most cases, there are some discrepancies, i.e. some measurements are not bound by the correct contour intervals. This is because kriging is an exact interpolator only when point values are being estimated and the prediction point is located exactly at the sample location. In this case, transmissivities were kriged over blocks 1x1 mile in areal extent. Since kriging assigns an average transmissivity value from several nearby measurement points to each block center, the kriged value may differ substantially from any given measurement, especially if the measurement is an extreme value.

The contour pattern in *Figure 4.25* matches the results obtained by Clifton and Neuman (1982) reasonably well, although minor deviations are present. The deviations can be attributed to the fact that Clifton & Neuman used a larger block size and different block orientation for their analysis.

Figure 4.24 shows a contour map of the standard deviations of estimation errors for the Avra Valley Aquifer. The standard deviation of the original log transmissivity measurements is *0.2672*. This standard deviation is an indicator of estimation uncertainty prior to geostatistical analysis. Kriging reduces the standard deviation of estimation errors by *50* to *66%*. The solid contours in *Figure 4.24* represent the standard deviations obtained by SG-STAT, the dotted contours were obtained by Clifton & Neuman (1982). The contour intervals correspond reasonably well, although the standard deviations obtained by Clifton and Neuman are approximately *10-15%* smaller. This discrepancy can be explained by the variance reduction factor since the blocks used by Clifton and Neuman were approximately four times larger.

Figure 4.24 Contours of Kriged Transmissivity Estimates - Avra Valley

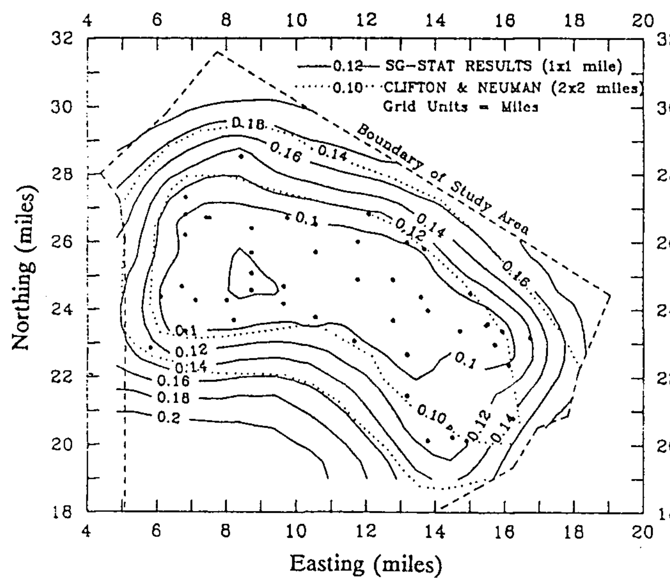

Figure 4.25 Standard Deviations of Estimation Errors for 1x1 Mile Blocks - Avra Valley

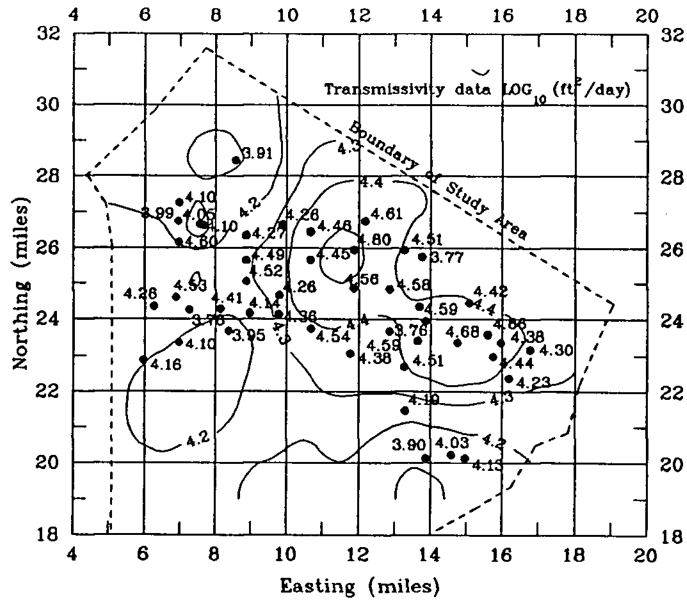

4.5 SIMULATION

Material properties controlling groundwater flow are often spatially variable and always uncertain. Deterministic models of groundwater have been used extensively to predict aquifer response to system stresses such as dewatering. *Deterministic* models assume that input parameters are known exactly everywhere in the flow domain. Hydrogeologists have recognized that predictive capabilities of deterministic models are often limited. This deficiency is attributed to the fact that it is often not possible to accurately quantify subsurface conditions in a deterministic manner; much of this difficulty stems from the natural variability of geologic deposits, the rest from data sets that are typically sparse and often include substantial measurement errors. In order to obtain more realistic predictions of hydraulic head and/or flow rates that include estimates of prediction uncertainty, hydrogeologists have turned to stochastic analysis.

Stochastic models of groundwater flow account for parameter variability during analysis. Instead of being specified as a single representative value (the case in deterministic analyses), each input parameter is treated as a random variable with a known mean and variance. In addition, most modern stochastic models treat input parameters as autocorrelated stochastic processes. Output variables of stochastic models, such as predictions of hydraulic head, are also probabilistic in character. Some models calculate the complete probability distribution function at each prediction point, others calculate only the first two moments.

In this framework, geostatistical simulation is the first step of a multi-facetted stochastic analysis that includes parameter characterization, groundwater flow modelling, slope stability assessment and economic analysis. The goal of geostatistical simulation is to create a digital model of sub-surface conditions that will duplicate actual log hydraulic conductivity values, natural variability, and estimation uncertainty as accurately as possible given available hydraulic conductivity measurements and geologic information. Ultimately, output from the simulation, the ensemble of log hydraulic conductivity realizations, will contribute to a realistic assessment of the risk of pit wall failure.

Simulation of groundwater flow has evolved steadily since the advent of powerful computer hardware in the

1960's. During that time, many significant advances have broadened our understanding of spatial variability of porous media and how the variability influences groundwater flow. *Section 4.5.1* provides a historical perspective of these advances, focusing on key discoveries that lead to the evolution of stochastic simulation techniques. Because the discussion provides but a glimpse of each technique, frequent references are made to papers providing greater insight.

Stochastic methods can be classified as to whether they generate realizations that are conditioned on available data or realizations that do not reproduce measured values at sample locations. *Section 4.5.2* examines the differences between unconditional, conditional and inverse techniques and suggests at what stage of dewatering design each approach should be used.

Three classes of stochastic analysis techniques have been developed: 1) spectral analytical method, 2) first & second moment analysis, and 3) Monte-Carlo simulation. The first part of *Section 4.5.3* briefly examines the unique characteristics of each analysis method; emphasis is placed on application of the method to dewatering system design. Of the available approaches only Monte Carlo simulation is capable of simulating the complex parameter distributions and geometry conditions encountered on real pit wall design problems. Therefore, the second part of *Section 4.5.3* presents a brief overview of the most common methods for generating spatially auto-correlated realizations that are required by the Monte Carlo approach. The methods include nearest neighbour, Fast Fourier Transform (FFT), Turning Bands Method (TBM), and Lower-Upper (LU) matrix decomposition.

The simulation module of *SG-STAT* can utilize the LU approach or a spectral approach based on the FFT. *Section 4.5.4* presents the fundamental concepts required for a basic understanding of the LU technique, including a discussion of its advantages and limitations. Less pertinent material, including a derivation of the equations and a detailed discussion of simulation difficulties, is presented in *Appendix B*.

The alternate simulation technique adopted in this framework, based on the FFT, also possesses a number of very desirable characteristics. Although the method is well known in the domains of geophysics and graphic image processing, it has not been used in groundwater applications. Therefore, *Appendix C* provides a comprehensive review of this simulation approach and its many powerful attributes.

Methods for verifying the reliability of the simulation model are presented in *Section 4.5.5*. As well as presenting the standard verification tests this section presents a new method based on the average semi-variogram.

In *Section 4.5.6* practical examples of simulation results illustrate how characteristics of the ensemble of realizations are affected by changes in sampling strategies and different semi-variogram models. This section also explores how grid density can influence the accuracy of simulation results.

4.5.1 HISTORICAL OVERVIEW

Stochastic theory was developed in the 1920's to study random components of white light and electrical noise. The most significant contributions of that time were: 1) formulation of the autocorrelation function by Taylor (1920), and 2) derivation of Wiener-Khintchine theorem (Wiener, 1926, Kenrick, 1929, Khintchine, 1934). By linking the autocorrelation function to the amplitude spectrum through the Fourier transformation, this theorem paved the way for subsequent development of stochastic methods in the spectral domain.

Although Warren and Price (1961), were the first researchers to apply stochastic methods to problems in flow through porous media as it applied to petroleum reservoir engineering, wide application of stochastic methods in the geological sciences began only after Matheron and Krige introduced the theory of geostatistics to the mining industry, where over the next decade, the methodology blossomed into a complete theory for estimation and simulation of mineral resources now known as geostatistics (Matheron 1967, 1973, Journel, 1974, Journel & Huijgbrets 1978).

The hydrogeologic community began to investigate and apply stochastic methods in earnest with the publication of a paper by Freeze (1975). Results obtained from his stochastic analysis of one-dimensional flow cast into doubt the validity of accepted deterministic flow models when applied to real soils and geologic formations. Freeze suggested that:

- It may not be possible to define an equivalent uniform porous medium (required for deterministic analyses) that acts in every sense like the actual non-uniform one.

- Consideration of spatial variability may lead to very large fluctuations in computed values of hydraulic head.

- As a result, deterministic models that do not account for parameter variability may suffer from very large errors.

In a parallel development, Gelhar and his co-workers developed stochastic simulation methods based on spectral analytical techniques that could be applied in two and three dimensions (Gelhar, 1976, Bakr et al., 1978, Gutjahr et al., 1978). With their multi-dimensional stochastic model they were able to demonstrate that the large variability of head predictions observed by Freeze in one dimension is reduced dramatically when the flow domain is extended to two or three dimensions. Gelhar and his co-workers also recognized that hydraulic conductivity behaves as an autocorrelated random variable, and incorporated this into their model. The major advantage of their approach lay in the fact that by developing closed form solutions that did not require huge computing power of modern computers they were able to analyze two and three dimensional stochastic problems years before affordable computer power was available to analyze these problems with a numerical approach.

Smith and Freeze (1979a, 1979b) developed a Monte Carlo approach to simulating two dimensional flow through spatially autocorrelated media. Their model, based on a nearest neighbour stochastic generator (see *Section 4.5.3*), was able to overcome many of the limitations of the analytical spectral approach utilized by Gelhar and his co-workers. In fact, the Monte Carlo simulation approach has been adopted by hydrologists as the standard method for analyzing groundwater problems that involve complex geometry, boundary conditions and/or highly variable hydraulic conductivity fields

Delhomme (1979) recognized that uncertainty of hydraulic head predictions could be reduced by conditioning each realization of the hydraulic conductivity field on available measurements. To condition the realizations, Delhomme utilized the geostatistical tools developed by Matheron for evaluation and simulation of ore reserves, including kriging and simulation via the turning bands method. He also suggested that variability of head predictions could be further reduced by including head data in the conditioning process.

Using a rigorous inverse method, Neuman and Yakowitz (1979) demonstrated that further conditioning of simulated hydraulic conductivity fields on measurements of hydraulic head could result in a dramatic reduction in the variability of hydraulic conductivity predictions, especially in portions of the flow domain where hydraulic conductivity measurements were infrequent. Clifton and Neuman (1982) provide an excellent case history that demonstrates the application of the inverse method to the Avra Valley aquifer in southern Arizona.

Recent developments include the development of maximum likelihood procedures for establishing the correlation structure (Kitanidis, 1983, Kitanidis and Lane 1985), application of stochastic methods to well field optimization (Wagner and Gorelick, 1987, 1989), and an increased awareness of the large data requirements for accurate determination of the semi-variogram model (Jury and Russo, 1989).

This thesis demonstrates how uncertainty in sub-surface conditions impacts on the economics of operating an open pit mine. It builds on recent research efforts that have been directed at incorporating output from stochastic simulation models into comprehensive decision making frameworks. The intention of the risk based decision frameworks is to develop practical tools that will help engineers to identify the most desirable design strategy in complex situations where sub-surface conditions are highly uncertain. Baecher et al. (1980) demonstrate the use of stochastic methods in assessing the risk of dam failure, Massmann and Freeze (1987) describe a risk based engineering design approach for the evaluation of new waste management facilities.

4.5.2 UNCONDITIONAL SIMULATION, CONDITIONAL SIMULATION AND INVERSE

Stochastic simulation can be conducted on one of three levels, depending on the type and amount of supporting data that is available. The three simulation levels include 1) unconditional simulation, 2) conditional simulation, and 3) inverse method. Each of the methods is briefly discussed below.

UNCONDITIONAL SIMULATION: This technique captures the natural variability of the deposit, i.e. each realization possesses the correlation properties specified by the statistical model, including the mean, the variance and the semi-variogram or covariance structure. However, as the name unconditional simulation suggests, the simulated field is not conditioned on the location of actual data. This means that measurements do not affect prediction uncertainty in the immediate area of the measurement point, they only affect global statistics. Since the simulated surface is not constrained to reproduce measured values at sample locations, the simulated field will generally appear markedly different to the measured profile. Because the location of data is not considered, the histogram of simulated values, taken over the ensemble of realizations, will be approximately the same at each estimation point. Furthermore, since unconditional simulation does not make full use of available data, the estimation error associated with each unconditionally simulated prediction point will be larger than the estimation error that would be obtained if available measurement data was fully utilized.

CONDITIONAL SIMULATION: This technique generates realizations that incorporate the desirable attributes of both kriging and unconditional simulation. Globally, the simulation method ensures that the correlation structure observed in field data is reproduced. Locally, the conditioning process ensures that each realization honours all available data, i.e. that the simulated surface passes through each measured value. The variability of simulated values at a fixed location in space, when observed over the ensemble of realizations, will in most cases differ markedly from one location to the next. This is because the variability of simulated values is based on the variance of estimation errors obtained during kriging. Variability in the simulated hydraulic conductivity field will generally be slight at simulation points with abundant supporting data, and large in areas where little or no data is available. The maximum variance of conditionally simulated realizations will always be less than or equal to the variance taken over an ensemble of unconditional realizations.

INVERSE METHOD: In many situations, a further reduction in simulation uncertainty can be realized if the simulated log hydraulic conductivity values are conditioned on available head measurements as well as hydraulic conductivity data (Neuman & Yakowitz, 1979). Studies of the Contraro aquifer by Binsariti (1980) and the Avra Valley aquifer by Clifton & Neuman (1982) have shown that variance reducing effect of inverse modelling can be significantly larger then that of kriging. At present, the inverse method has not been incorporated into the framework described in this thesis. A future extension of the design framework in this direction would prove useful during analysis of problems where a reasonable number of reliable head measurements are available.

To illustrate the important difference between conditional and unconditional simulation, consider the surface representation of the demonstration hydraulic conductivity field[6] shown in *Figure 4.26A*. In particular, note the location of pronounced high and low hydraulic conductivity zones. These appear as ridges and troughs in the perspective drawing. Also note the degree of local roughness and large scale waviness of the surface; these characteristics are indicative of the strength of the correlation structure over short and long distances.

---

[6] Actual hydraulic conductivity values were first presented in *Figures 5.2 & 5.3*.

Figure 4.26 Surface Representations of Hydraulic Conductivity Field

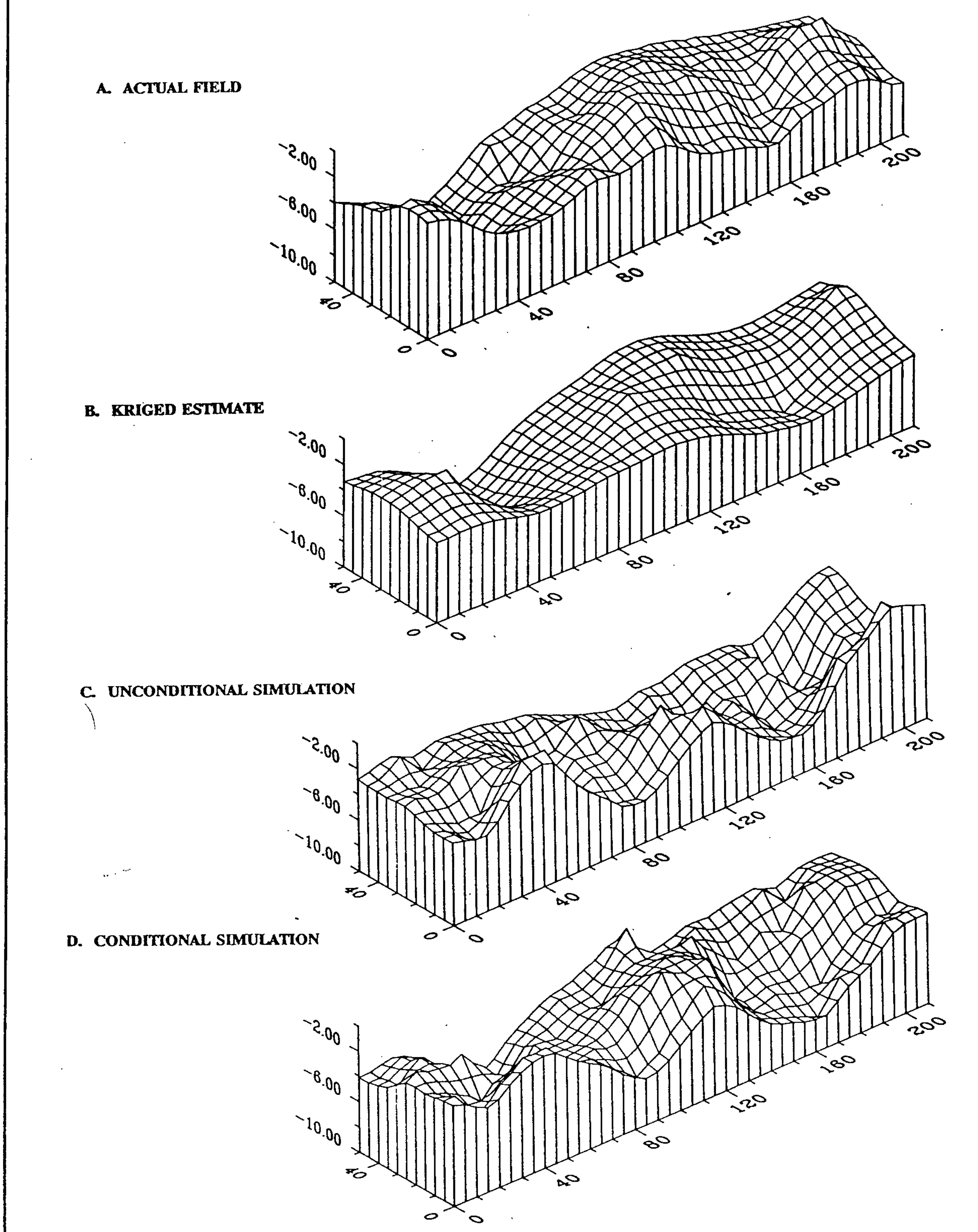

Figure 4.26B is surface representation of the log hydraulic conductivity estimate obtained upon kriging the data set shown in *Figure 4.12*. Although the kriged surface captures the large scale features of the true hydraulic conductivity field, the kriged surface is much smoother. This indicates that the kriging estimate failed to reproduce the natural variability of the deposit.

Figure 4.26C portrays one unconditional realization of the hydraulic conductivity field. Note that the small scale roughness and large scale waviness of the unconditional surface are very similar to the true surface. This indicates that actual correlation structure has been successfully reproduced. However, the location of topographic features differs markedly. For example, the pronounced topographic high at coordinates *(120,40)* that is present in the actual surface is not recreated in the simulation.

Figure 4.26D portrays a conditional realization that is based on the same statistical model as *Figure 4.26C*. Once again, the true correlation structure appears to have been recreated successfully. More important; however, is the way the conditional realization honours measured values, i.e. topographic features are accurately reproduced wherever measurements are available. In areas that lack support, each hydraulic conductivity realization may deviate substantially from the unknown true value and from other realizations, since prediction uncertainty is highest at these locations.

Conditional simulation should be utilized for design purposes as soon as a reasonable amount of data is available to condition realizations. This is important since the exact location of high permeability zones can have a significant effect on pore pressures acting on the failure surface. Unconditional simulation should be reserved for initial feasibility studies when none or very little data is available. In such cases, statistics describing the expected correlation structure must be specified based on previous experience and engineering judgement. Although such analyses are not fully reliable, in general they will indicate the degree of stability problems that can be expected at the proposed mine site. The management can then make a better informed decision as to how much capital should be invested in a detailed site investigation program.

4.5.3 REVIEW OF SIMULATION METHODS

In order to classify the numerous stochastic methods cited in the previous section it is useful to define three classes of techniques for the solution of stochastic equations of groundwater flow: 1) spectral analytical methods 2) first & second moment analysis, and 3) Monte Carlo simulation.

ANALYTICAL SPECTRAL TECHNIQUES: In this analytical perturbation approach, pioneered by Gelhar (1976), and expanded by Bakr et al. (1978), Gutjahr et al. (1978), and Mizel et al. (1982) the spatial covariance function of the log hydraulic conductivity field is expressed as a spectral density function in the wave number domain. By introducing the spectral density function directly into the partial differential equation governing flow it is possible to deduce closed form expressions for corresponding spectral density functions of hydraulic head and flux. An inverse Fourier transform is then utilized to obtain the covariance functions of head or flux in the space domain. Advantages of the spectral method include: 1) a closed form expression of the statistical properties of the hydraulic head distribution, and 2) a continuum representation of the correlation structure that is more realistic than the discontinuous, block discretized representations obtained by numerical methods. Unfortunately, the continuum approach also limits the applicability of this method to relatively simple problems.

FIRST AND SECOND MOMENT ANALYSIS: This numerical technique, developed by Sagar (1978) and extended by Dettinger and Wilson (1981) and Townley (1984) introduces parameter and boundary condition uncertainty only after the system of finite difference or finite element equations relating unknown heads to hydraulic conductivities and boundary fluxes is formulated. By neglecting the higher order terms of a Taylor series expansion of the matrix equation Sagar (1978) developed expressions for the expected value and variance of hydraulic head at each node. The resulting method is computationally much more efficient than the Monte Carlo approach because the system of matrix equations has to be solved only once. This characteristic makes first and second moment analysis ideal for solution of transient flow problems that would otherwise result in a very large computational burden. However, Dettinger and Wilson (1981) state that the use of first and second moment methods must be limited to portions of flow domain where 1) input parameters have relatively small variances, and 2) truncating effects of boundary conditions do not impose a skewness on the distribution function of hydraulic heads. Also, it has been recognized that the method tends to truncate the tails of the output parameter probability density functions.

MONTE CARLO SIMULATION: This technique provides a powerful tool that makes it possible to model groundwater flow within any hydraulic conductivity field exhibiting natural variability, even if variances are large (Smith & Freeze, 1979). To be effective, Monte Carlo simulation requires a large number of realizations of the hydraulic conductivity field; each *realization* is a picture of subsurface conditions that possesses the same scale of variability as the natural deposit. The prediction uncertainty of output variables (i.e. head and/or flux) is determined by analyzing the distribution of head/flux values at each node over the ensemble of realizations. If the simulation is to yield valid results, statistics calculated over the ensemble of realizations should duplicate the level of estimation uncertainty predicted by the estimation model at each prediction point.

A number of methods are available to generate realizations that possess the desired correlation structure. The methods differ in ease of implementation, types of multi-dimensional covariance models that can be utilized, computational speed, and memory requirements. These characteristics are reviewed below for the four most common generation techniques. In the review, computational speed will be indicated by the approximate number of operations required to generate R realizations while memory requirements will be measured by the dimension of the largest data array required. P will designate the number of points to be generated for each realization.

Nearest Neighbour Method: First applied to groundwater analysis by Smith and Freeze (1979), this method relates hydraulic conductivity values in each block to its four nearest neighbours. The resulting expression for the covariance matrix, $[C]$, is a function of α, the autoregressive parameter expressing the degree of spatial dependence of the central block on its neighbours. Mantoglou and Wilson (1982) point out that the nearest neighbour approach is thus limited to a single covariance model that is not directly related to common covariance models such as the exponential or spherical. Furthermore, the model is difficult to fit to correlation structures observed in field data and to account for the variance reduction effects of block discretization.

Implementation of the nearest neighbour method is the least complicated of the methods discussed in this section. It requires a decomposition of one symmetric matrix of size (PxP) and repeated multiplications of the decomposed matrix by a random vector. Memory requirements are dictated by the amount of memory required to store the (PxP) weight matrix. Computational speed is on the order $P^3 + R \cdot P$, with P^3 operations required for the matrix inversion and $R \cdot P$ operations for each random vector multiply. Realizations that incorporate field measurements can be obtained by a conditioning filter that operates on the output of the nearest neighbour model (Smith and Schwartz, 1981).

Monte-Carlo Spectral Methods: All spectral methods rely on the fact that any covariance function in the space domain can be transformed to an equivalent representation in the wave number domain. In fact, spatial fields that possess the same autocorrelation structure will also possess an identical amplitude spectrum. However, conversion of a two dimensional covariance model from the spatial domain to an equivalent spectral domain representation can prove difficult via the analytical approach. Mantoglou and Wilson (1982) provide analytical expressions of spectral forms for several common covariance models. Once the amplitude spectrum representation is available, any number of unconditional realizations can be generated by specifying a random phase delay for each spectral amplitude, and then converting the amplitude spectrum back to the space domain. Conditioning of realizations on field measurements can be performed independently once the unconditional realizations are generated. The conditioning procedure is described in *Section 4.5.4*.

A Monte-Carlo simulation method that utilizes an analytical spectral representation of the covariance function was first utilized for hydrologic applications by Meija and Rodriguez-Iturbe (1974) to investigate rainfall processes. In their study, Meija and Rodriguez-Iturbe utilized a covariance model based on a modified Bessel function for which a very simple analytical expression exists for the amplitude spectrum in the wave number domain. To obtain realistic realizations of rainfall intensities, Meia and Rodriguez-Iturbe selected random values of the amplitude spectrum for each realization, as well as random phase delays for each amplitude. Amplitude spectrum randomness was also incorporated in their model to yield realizations that exhibited noise in the covariance function as is observed in real data. If the amplitude spectrum is treated in a deterministic manner (constant for any lag) then all realizations will yield exactly the same covariance structure.

A more practical method of generating realizations in the spectral domain is to utilize the FFT. Although Mantoglou and Wilson (1982) suggested that the FFT would be more efficient than the analytical spectral method that they utilize for generating autocorrelated one dimensional line processes, actual application of the FFT method has not been demonstrated in the groundwater literature as far as this author can establish.

In the FFT method, the amplitude spectrum representation of the covariance model is obtained by applying a forward FFT to the two dimensional covariance model in the space domain. As in all other spectral approaches, realizations are generated in the wave number domain by randomly selecting a phase angle for each amplitude spectrum. Finally, an inverse FFT is utilized repeatedly to convert spectral realizations back to the space domain.

The FFT method is very easy to implement provided a two dimensional FFT subroutine is available. The biggest obstacle is coding an algorithm to transform the 2-D covariance model into an indexed array compatible with the FFT subroutine. The memory requirement is $2P$, far smaller than any of the matrix inversion methods. The computational speed is of the order $(1+R)\cdot\{P\cdot\log_2(P)\}$. The memory and speed requirements make the FFT method very attractive for generating large, production realizations on personal computers where memory is limited and execution speed is substantially slower than in main-frame or work station environments.

To date, the power of the FFT stochastic method has not been tapped in groundwater hydrology. To explore the advantages and limitations of this approach, a FFT simulator was developed, incorporated into SG-STAT, and utilized to generate a number of large and complex realizations. Some of the most interesting simulation results are presented in *Appendix C* of this dissertation, together with a detailed outline of the FFT methodology that can be referenced when implementing this method for other applications.

Turning Bands Method: Introduced as a geostatistical tool for simulation of ore deposits in three dimensions by Matheron (1973), the TBM has been adapted by Mantoglou and Wilson (1982) to generation of two dimensional realizations. The basic concept of the TBM is to transform a multi-dimensional simulation into a sum of a series of equivalent one-dimensional simulations. This transformation makes the method extremely attractive for generating large, three dimensional simulations that frequently contain thousands of points. To create such multi-dimensional realizations the process only requires that a relatively small number of one dimensional realizations be generated (i.e. 15), with each 1-D realization possessing an appropriate 1-D correlation structure. The multi-dimensional realization is then obtained by orthogonally sampling each one dimensional realization at the point closest to the simulation point, and then computing the average of all samples (see Journel and Huijgbrets, 1978, pp. 498-504).

Identification of an appropriate covariance model for the one-dimensional line process that will reproduce the multi-dimensional covariance structure is not straight forward in the spatial domain, especially in two dimensions. To overcome this difficulty, Mantoglou and Wilson (1982) derived a very simple expression that can be used to perform the conversion in the spectral domain.

$$A_{1D}(w) = \tfrac{1}{2}\,\sigma^2 A_{2D}(w) \qquad \text{Equation 4.25}$$

Mantoglou and Wilson (1982) used *Equation 4.25* to convert two dimensional, analytical expressions for a number of standard covariance models into equivalent one dimensional spectral representations. To produce the necessary one-dimensional autocorrelated line processes in the spatial domain from the amplitude spectrum, their approach utilizes a well established technique based on the inverse Fourier transform[7] (Rice, 1954, Shinozuka, 1971, Meija and Rodriguez-Iturbe, 1974). Recently, Tompson et.al. (1989) implemented the Turning Bands generator to analyze spatial variability in the third dimension.

Computationally, the two dimensional TBM, as described by Mantoglou and Wilson (1982), is the most efficient of all unconditional stochastic generators, provided the hurdle of determining a suitable one dimensional amplitude spectrum can be overcome. Total memory required by this method is $n \cdot h$, where n represents the number of one dimensional line processes utilized, and h the number of harmonics used to define the amplitude spectrum. The number of operations required to obtain a set of TBM realizations is of the order $R \cdot P^{1/4}$. Although the TBM method cannot generate realizations conditioned on field data directly, unconditional TBM realizations can be conditioned on field data after the realizations are generated.

This author believes that an FFT approach to deriving the one dimensional amplitude spectrum could be used to overcome the difficulty of determining the appropriate covariance model in the spectral domain with much less effort than the analytical methods utilized by Mantoglou and Wilson (1982). In the proposed FFT approach, a forward FFT could be used to obtain the two dimensional representation of the amplitude spectrum. *Equation 4.25* could then be applied to obtain the corresponding one dimensional form. Any number of autocorrelated line processes could then be generated with an inverse FFT. Finally, the turning bands procedure could be utilized to transform the multiple one dimensional realizations into a single realization in two dimensions.

LU Matrix Decomposition Method: Based on a Cholesky decomposition of the covariance matrix, this technique provides the most versatile simulation tool relative to the other methods documented in this section (Scheurer and Stoller, 1962, Clifton and Neuman, 1982). The main advantage of this technique is that conditional realizations can be generated directly, without first generating unconditional realizations and then conditioning those realizations on available data. In addition, the variance reduction factor can be incorporated very easily in this method by accounting for prediction and sample volume effects when constructing the covariance matrix (see *Section 4.4.5*). The one drawback of the LU approach is the large memory and computational overhead required to store and decompose the covariance matrix; memory requirements are of size $\frac{1}{2}P^2$; computational speed to generate R realizations is of order $P^3 + R \cdot P$ when a standard Cholesky algorithm is used to decompose the covariance matrix. The computational overhead can be reduced by using decomposition methods that take advantage of the sparse nature of the covariance matrix (I. Cavers, personal communication). *Section 4.5.5* presents the underlying theory and shows how the LU method has been implemented in SG-STAT to generate both conditional and unconditional simulations.

Table 4.5 summarizes the most important characteristics of the stochastic generators reviewed in this section. The efficiency of each stochastic simulator is strongly dependent on the number of points to be generated. The sum of expressions in columns "*Unconditional Realizations*" and "*Conditional Overhead*" indicates the total order of operations required to generate an ensemble of realizations for any set of parameters P,R,h,N. The figures under the heading "*Unconditional Benchmark*" compare the order of operations required to generate 500 unconditional realizations, each realization containing 1024 simulated points. The figures confirm the findings of Mantoglou and Wilson (1982), who demonstrated that the Turning Bands Method is by far the most efficient technique for generating large number of unconditional simulations. However, the same pattern does not hold true for conditional simulations. In most simulation methods, conditioning is performed only after the unconditional realizations are generated using kriging with a moving neighbourhood of the nearest N

---

[7] The theory of simulation methods based on the Fourier transform is reviewed in *Section 5.5.4* under the heading *Generating Realizations.*

Table 4.5 Performance Parameters for Simulation Methods

METHOD	MEMORY	UNCOND. REALIZ.	COND. OVERHEAD	UNCON. BENCH	COND. BENCH	VARIANCE FACTOR	ANISOTROPY IMPLEMENT
Nearest Neighbour	P^2	$P^3 + R \cdot P$	$N^3 \cdot P \cdot R$	1.07E+9	1.59E+9	approx.	easy
Spectral	$2h^2$	$(1+R)P \cdot h$	$N^3 \cdot P \cdot R$	1.64E+7	5.28E+8	approx.	difficult
FFT	2P	$(1+R)P \cdot \log_2(P)$	$N^3 \cdot P \cdot R$	5.13E+6	5.17E+8	approx.	easy
Turning Bands	$n \cdot h$	$R \cdot P^{1/2}$	$N^3 \cdot P \cdot R$	1.60E+4	5.12E+8	approx.	difficult
LU Decomposition	$\frac{1}{2}P^2$	$P^3 + R \cdot P$	0	1.07E+9	1.07E+9	approx.	easy

MEMORY :	Indicates the size of the largest data array required.
UNCOND. REALIZ.	Indicates order of operations required to generate unconditional realizations.
COND. OVERHEAD	Indicates order of operations required to condition realizations on measurements once realizations generated.
UNCON. BENCH	Gives order of operations required to generate 500 unconditional realizations on a square grid containing 1024 points (32x32). P=1024, R=500, h=32, N=10
COND. BENCH	Gives order of operations required to generate 500 conditional realizations over same grid.
VARIANCE FACTOR	Suggests how well method accounts for variance reduction factor due to volume effects.
ANISOTROPY IMPLEMENT	Suggests level of difficulty experienced in implementing method for generation anisotropic realizations.

P = Number of simulation points R = Number of realizations
h = number of frequency harmonics N = number of points in kriging neighbourhood

measurement points. Comparison of the order of operations required to generate unconditional and conditional simulations demonstrates number of operations required to condition the realizations is frequently much larger than the number of operations required to generate the unconditional realizations. Therefore, the conditional simulation is not sensitive to the efficiency of the conditioning method. This conclusion is supported by the fact for the benchmark problem considered in *Table 4.5* the least and most efficient methods were separated by a ratio of only 3:1.

The information presented in this section clearly demonstrates that LU matrix decomposition is the most versatile technique for generating conditional simulations of the type required during the detailed planning stage of dewatering system and pit wall design. With this generator it is possible to implement procedures that account for conditioning on available pump test measurements, recognized anisotropies in the hydraulic conductivity field, and variance reduction due to volume effects at only slightly more computational overhead than is required by other simulation methods. However, during feasibility and initial pit wall design studies very little hydrologic information is typically available. In these situations it is expedient to utilize the most efficient unconditional simulation methods such as the TBM or FFT since the computational burden can be reduced by many orders of magnitude.

4.5.5 LU MATRIX DECOMPOSITION METHOD

In the review of available simulator options presented in *Section 4.5.3*, it was concluded that LU matrix decomposition is the recommended technique for generating conditional simulations of the type required during the detailed planning stage of dewatering system design. This section first summarizes the most important theoretical concepts underlying the LU method; a complete derivation of all equations is presented separately in *Appendix B* for the reader interested in a more complete presentation of the material. Next, the section explains why the LU method is capable of generating conditional simulations in one step, whereas all other simulation methods require a separate conditioning step in order to achieve the same end result. Finally, this section points out a number of pit-falls that can be encountered with this method; details of the problems and suggested remedies are provided in *Appendix B*.

THEORY: Some degree of uncertainty is associated with the prediction of log hydraulic conductivity at each simulation point. The objective of Monte Carlo simulation is to accurately reproduce that uncertainty over the ensemble of realizations. Recall that prediction uncertainty is a function of the covariance model and the number, size, and location of supporting measurements. *Section 4.4.5* demonstrated that prediction uncertainty at simulation point X_m is given by the variance of estimation errors *(Equation 4.18)*. Symbolized by C_{mm}, this variance is stored on the main diagonal of the covariance matrix for each simulation point. *Appendix B* demonstrates that the approach used to develop *Equation 4.18* can also be used to obtain a similar expression *(Equation B.13)* for all off-diagonal entries in the covariance matrix. These off-diagonal entries in *[C]* provide a complete description of the autocorrelation structure; they incorporate all of the features of the selected covariance model as well as any covariance reduction effects due to the presence of supporting data.

CONDITIONING: The LU decomposition method is the only simulation technique that directly exploits all of the information contained in *[C]*. Because *[C]* is positive-definite and symmetric it can be decomposed into a product of upper and lower triangular matrices *[U] & [L]*, where *[L]* is equal to the transpose of *[U]*. The decomposition can always be computed via the Cholesky algorithm, provided *[C]* satisfies the above requirements. Once *[U]* is determined, any number of realizations $\{Z_r\}$ can be obtained from

$$\{Z_r\} = \{Z^*_u\} + [U]\{N\} \qquad \textit{Equation 4.32}$$

by generating a new *{N}* vector for each realization. In *Equation 4.32*, *{N}* represents a vector of *M* independent random numbers selected from a Gaussian normal population with mean *0* and variance *1*, $\{Z^*_u\}$ represents the appropriate vector of expected log hydraulic conductivity values.

The LU method uses exactly the same simulation approach to generate both conditional and unconditional simulations; however, the input parameters differ markedly. For unconditional realizations, each entry in $\{Z^*_u\}$ is set equal to the global expectation of hydraulic conductivity, m. When measurements are available kriging provides a much better estimate of the expected hydraulic conductivity at each simulation point. Therefore, the vector of kriging estimates, $\{Z^*_k\}$, is utilized in *Equation 4.32* when generating conditional realizations.

Each entry in *[C]* will also differ, depending on whether the covariance matrix is conditioned on data or not. Entries in the conditional matrix will generally be smaller in magnitude than their unconditional counterparts, although the amount of variance and covariance reduction will depend on the amount and geometry of supporting data. As a matrix equation, the expression for each unconditional realization is given by:

$$\{Z_u\} = \{m\} + [U]_u\{N\} \qquad \text{Equation 4.33}$$

The corresponding equation for each conditional realization is:

$$\{Z_k\} = \{Z^*_k\} + [U]_k\{N\} \qquad \textit{Equation 4.34}$$

Figure 4.27 illustrates the important difference between the standard two step conditioning process[8] used by all other simulation methods, and the one step conditioning process utilized in the LU approach. Briefly, the standard procedure involves replacing the random, low frequency oscillations by similar conditioned oscillations that pass through the data points. The LU method generates the conditional realization directly: the conditioned low frequency oscillations are contained in the vector of kriging estimates, the high frequency, autocorrelated noise is generated by decomposition of the conditioned covariance matrix. Since all covariance matrix coefficients *Cmn* decay to zero whenever either simulation point X_m or X_n coincides with a sample locations, all autocorrelated noise realizations will have zero variability at these locations. Upon adding the noise realization to the kriged estimate, each resulting conditional realization is thus guaranteed to pass through all measurement points.

---

[8] Conditioning procedure described at end of *Appendix C*.

Figure 4.27 Differences between Standard and Lu Conditioning Techniques

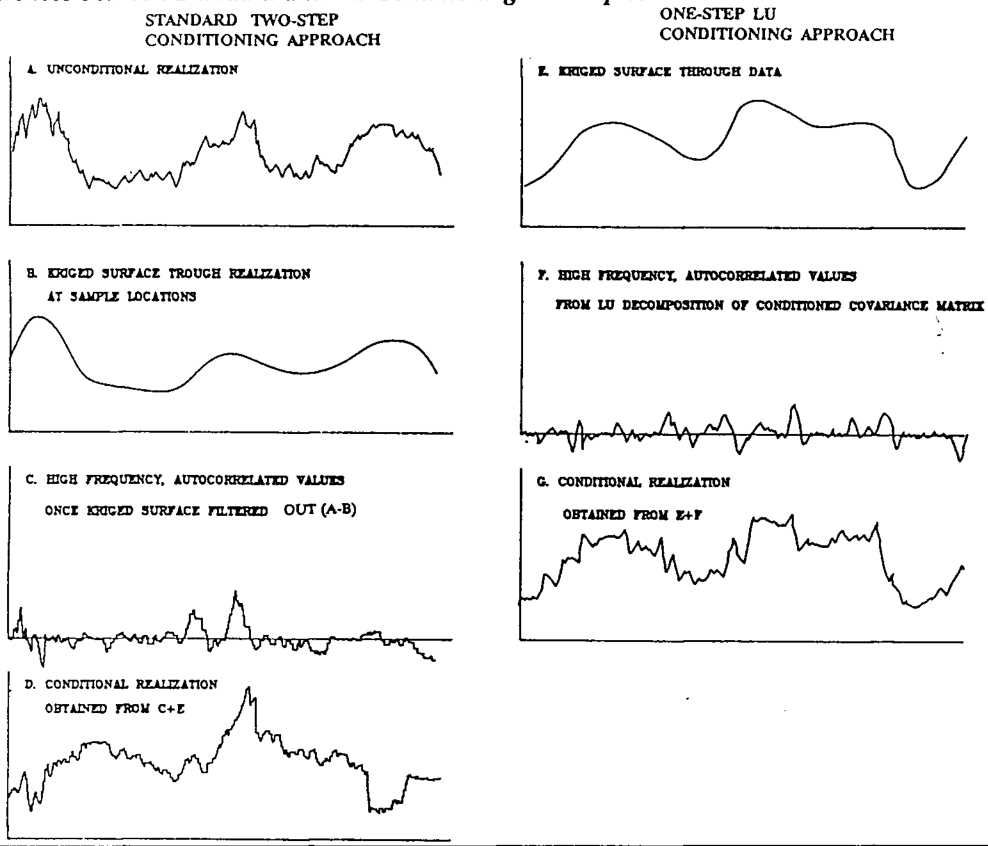

IMPLEMENTATION DIFFICULTIES: Decomposition of the covariance matrix via the Cholesky algorithm will fail if *[C]* is not positive-definite. *Appendix B.3* explores the requirements for positive-definite matrices and identifies the most common reasons why some covariance matrices fail these requirements. The appendix shows that lack of positive-definite characteristics can be brought about in three ways:

- Failure to partition known simulation points (i.e. where variances are 0) out of simulation equations. Cholesky decomposition will fail because some main diagonal entries will be equal to zero, resulting in divide by zero errors during the decomposition.
- When dealing with very small positive variances (i.e. simulation points with lots of support), round-off errors can lead to computed variances that are equal to or slightly smaller than zero, when in fact they should be greater than zero. Once again, this destroys the positive definite nature of *[C]* and results in divide by zero errors.
- Selection of an invalid one or two dimensional covariance model that does not satisfy positive definite conditions.

Error traps have been introduced in the SG-STAT computer code to warn users when non positive-definite conditions are detected. The program then makes one pass at attempting to restore the positive definite structure by increasing diagonal entries slightly at problem locations.

This sub-section has demonstrated the most important features of the LU matrix decomposition technique. Simplicity, ease of implementation, one step conditioning, and exact representation of variance and covariance reduction effects make this the preferred method for conditional simulation.

4.5.5 VERIFICATION OF SIMULATION RESULTS

The objective of simulation is to generate realizations of hydraulic conductivity that will possess the same statistical characteristics as the actual hydraulic conductivity field. In particular, the selected simulation method should generate realizations that reproduce the following statistics:

- The average value of log hydraulic conductivity over any single realization should be approximately equal to mean value observed in the field.
- The variance of generated values over any single realization should be approximately equal to dispersion variance observed in field data.
- The covariance structure observed in any single realization should be similar to the covariance model used to generate the realizations.
- Estimation variance at each prediction point in the domain, computed over the ensemble of realizations, should be approximately equal to the variance of estimation error for that point, i.e. the simulation should reproduce estimation uncertainty. For conditional simulations, the desired estimation uncertainty at each prediction point is given by $\sigma_m^2(X_i)$, the kriging variance of estimation error. For unconditional simulations, the target estimation uncertainty is equal to the dispersion variance observed in field data. The latter variance is the same for all estimation points.

VERIFICATION: Verification of simulation results involves confirming that each of the four requirements listed above has been satisfied. Once the realizations have been generated, the mean, variance and covariance structure are computed over each realization, followed by the variance of realized values at each prediction point. Finally, the calculated values are compared to target values in order to determine whether the simulation model is valid. *Figure 4.28* presents the results of these steps for a typical unconditional simulation for both LU decomposition and FFT methods. *Table 4.6* lists the desired simulation statistics.

Table 4.6 Desired Statistics For Simulation

Domain Size:	16x16	Covariance Model:	Spherical
Cell Size:	1x1	Realization Mean:	5.0
Number of Points:	256	Realization Variance:	1.0
Number of Realizations:	200	Range:	4.0
		Sill:	1.0

Realization Mean: Plots *A* and *B* indicate that both LU decomposition and FFT methods generate unbiased realizations that reproduce the desired mean on average. However, the actual mean observed in any single realization tends to vary about the target value; between 4.6 to 5.6 for the LU method and 4.8 to 5.2 for the FFT generator.

Realization Variance: Plots *C* and *D* present the standard deviations obtained for each realization. Once again, the cumulative average curve indicates that the desired variance of *1.0* is reproduced on average, but the variance obtained for any single realization fluctuates around the target value. Note that realizations generated by the FFT method (Plot *D*) reproduce the desired variance much more closely than realizations generated by Lu decomposition (Plot *C*).

Covariance Model: Plots *E* and *F* illustrate typical covariance structures for a single realization. Both simulation methods reproduced the sill, the range and the shape of the covariance model accurately; the FFT method tends to reproduce the covariance model somewhat more closely than the LU method over the ensemble of realizations.

Ensemble Variance: Plots G and H present the average standard deviation error, calculated over each point in the flow domain, as a function of the number of realizations used to form the ensemble. The standard deviation error at a single point in the domain is the difference:

$$E_{sd} = |\sigma_{Desired} - \sigma_{Obtained}| \qquad \textit{Equation 4.35}$$

Plots G and H show the value of this error when averaged over all 256 simulation points. The two methods do an equally good job at reproducing the desired estimation variances. Both methods require a minimum of approximately *50* realizations to accurately reproduce simulation point variability. In this case, the minimum standard deviation error in generating the hydraulic conductivity field (approximately *0.07)* is reached after *100* realizations. It appears that use of more than 100 realizations in the ensemble is not necessary in this case; however, a similar test should be conducted on hydraulic head statistics to confirm that the variance of the output parameters has also converged to the minimum level.

NUMBER OF REALIZATIONS: Because the optimal number of realizations appears to be dependent on the size of the flow domain and the characteristics of the covariance model, the optimum number of realizations should be identified by generating a large number realizations (e.g. *200* to *300*), constructing a graph similar to Plots G and H, and identifying the number of realizations at which the graph becomes asymptotic. If the graph trace continues to decline even at the maximum number of realizations then additional realizations should be used in the simulation if higher accuracy is desired. In all cases tested, the optimal number of realizations fell between *100* and *200.*

SIZE OF DOMAIN: Validity of simulation results is very sensitive to the size of the flow domain in relation to the range of the hydraulic conductivity field being simulated. Realization statistics begin to diverge from target values once the range approaches approximately ¼ to ½ the maximum dimension of the flow domain (D_{max}). As explained below for each statistic, the errors develop because hydraulic conductivity values become correlated over a large portion of the flow domain.

When the range is longer than ½ *Dmax* the mean log hydraulic conductivity for any single realization may be significantly higher or lower than the target value, depending on whether the generator arbitrarily assigns a high or low value over most of the flow domain. Plots A and B in *Figure 4.29* illustrate this effect for the LU and FFT generators. The plots show that progressively larger deviations from the target mean are observed as the *Range/Length Domain* ratio increases. The *FFT* generator (Plot B) appears to be much less sensitive to this effect than the LU method (Plot A).

Plots C and D in *Figure 4.29* show that the realization variance decreases steadily from the target value as the range increases beyond ½ D_{max}. The error is caused by the fact that once a majority of simulated values in any realization become correlated the variance is no longer calculated over the full spectrum of possible hydraulic conductivity values, but rather over a narrower range of correlated values generated for that particular realization.

The covariance model continues to be reproduced accurately at short lags as the range increases; however, at long lags it tends to diverge from the model since an insufficient number of simulation points is available to calculate the covariance structure.

Plots E and F in *Figure 4.29* show that the accuracy to which point variances are reproduced over the ensemble of realizations is also sensitive to the *Range/Length Domain* ratio, although the increase in error is not severe (increasing from *7%* of σ_m to *10%* as the ratio increases from *0* to *1*). The FFT method is more sensitive to this effect because as the range increases the spectral information is stored in a progressively decreasing band of low frequencies close to the origin (see *Figure C.3* in *Appendix C*). Since progressively fewer harmonics are used to store the amplitude spectrum the discretization resolution suffers and errors are introduced.

Figure 4.28 Results of Simulation Verification - Example Problem

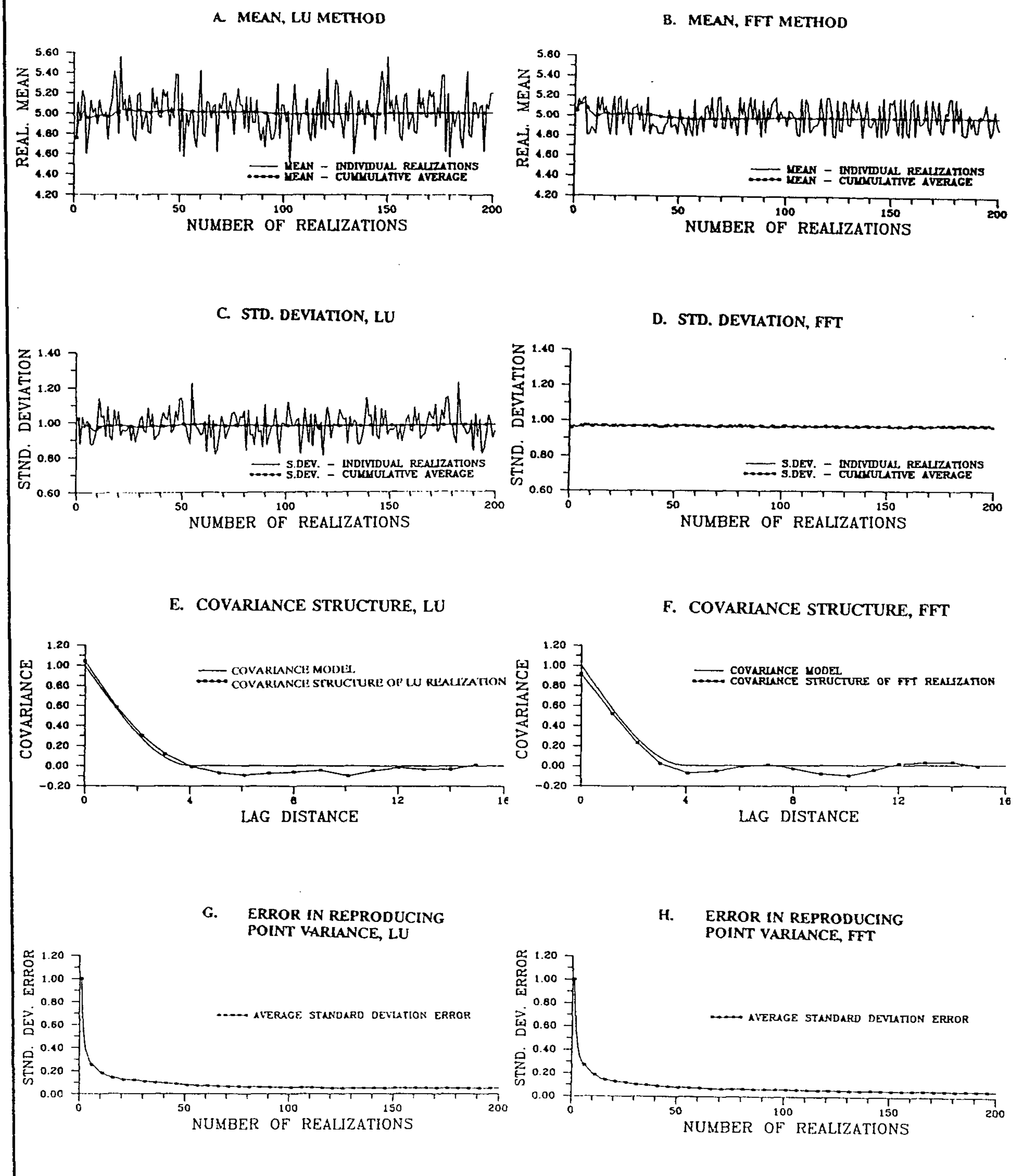

Furthermore, once the range exceeds the length of the flow domain the covariance function is truncated at the domain boundary during the *FFT* transformation. Once this point is reached, realizations generated by the FFT method are no longer based on the same covariance model; therefore, they rapidly diverge from desired statistics (see Plot *F* in *Figure 4.29*).

GRID SIZE: To investigate whether grid density influences the accuracy of simulation statistics, both the LU and FFT simulation methods were used to generate realizations for *2x2*, *4x4*, *8x8*, *16x16* and *32x32* size domains. In order to focus only on the effect of changing grid density, the range was specified as ¼ of the dimension of the flow domain in each of the simulations. The results, presented in *Figure 4.30* show that the simulations are not sensitive to grid density once the domain exceeds *4x4* cells. When a very coarse grid is selected (e.g. *2x2*) the realization mean (Plots *A* and *B)* and realization variance (Plots *C* and *D*) deviate from target values because there is an insufficient number of points that can be used to calculate reliable realization statistics.

All six plots in *Figure 4.30* suggest that simulation accuracy appears to remain fairly constant once the number of cells exceeds *64*. This result suggests that grid size effects should not influence the accuracy of the groundwater flow simulation, since the finite difference or finite element grids used in groundwater flow models tend to have a more than adequate number of cells for reliable calculation of realization statistics.

Although realization statistics are not influenced by grid size, selection of this parameter is still a very important factor in the overall simulation since it controls the resolution of the simulation model. If the grid size selected is too coarse, the realizations will not reproduce the detail of the covariance model at short lags; if it is too fine, storage requirements may exceed the capacity of the computer. The following points should be considered when selecting the size of the geostatistical grid:

- The geostatistical grid should coincide with the finite element grid used for groundwater flow simulations. Minimum and/or maximum cell size may be dictated by accuracy requirements or memory limitations of the groundwater flow model.

- The cell size should be sufficiently small to reproduce the smallest structural details of interest (e.g. given that the range over which hydraulic conductivity is correlated is 20 m, then the simulation grid should be smaller than 5 m, otherwise variance reduction due to volume effects will be very significant).

- The cell size should be somewhat larger than the volume of supporting measurements. Use of smaller cell sizes increases the computational burden without improving accuracy of the geostatistical simulation.

This sub-section has demonstrated that the degree to which simulation statistics reproduce the desired statistics is dependent on the type of simulation method, the size of domain simulated in relation to the range, and to a much lesser extent, the grid size used for the simulation. The output of the geostatistical simulation model can be used with confidence as input into the analysis of groundwater flow and slope stability provided that the four verification conditions

- reproduce mean hydraulic conductivity in each realization
- reproduce dispersion variance in each realization
- reproduce correlation structure in each realization
- reproduce estimation uncertainty at each simulation point

are fully satisfied. The above checks have been implemented in the verification module of SG-STAT to facilitate the process. It is recommended that a verification be performed during each geostatistical analysis to confirm that the simulated conditions conform to all available information of actual subsurface conditions at depth.

Figure 5.34 Sensitivity of Simulation Statistics to Range/Length Domain Ratio

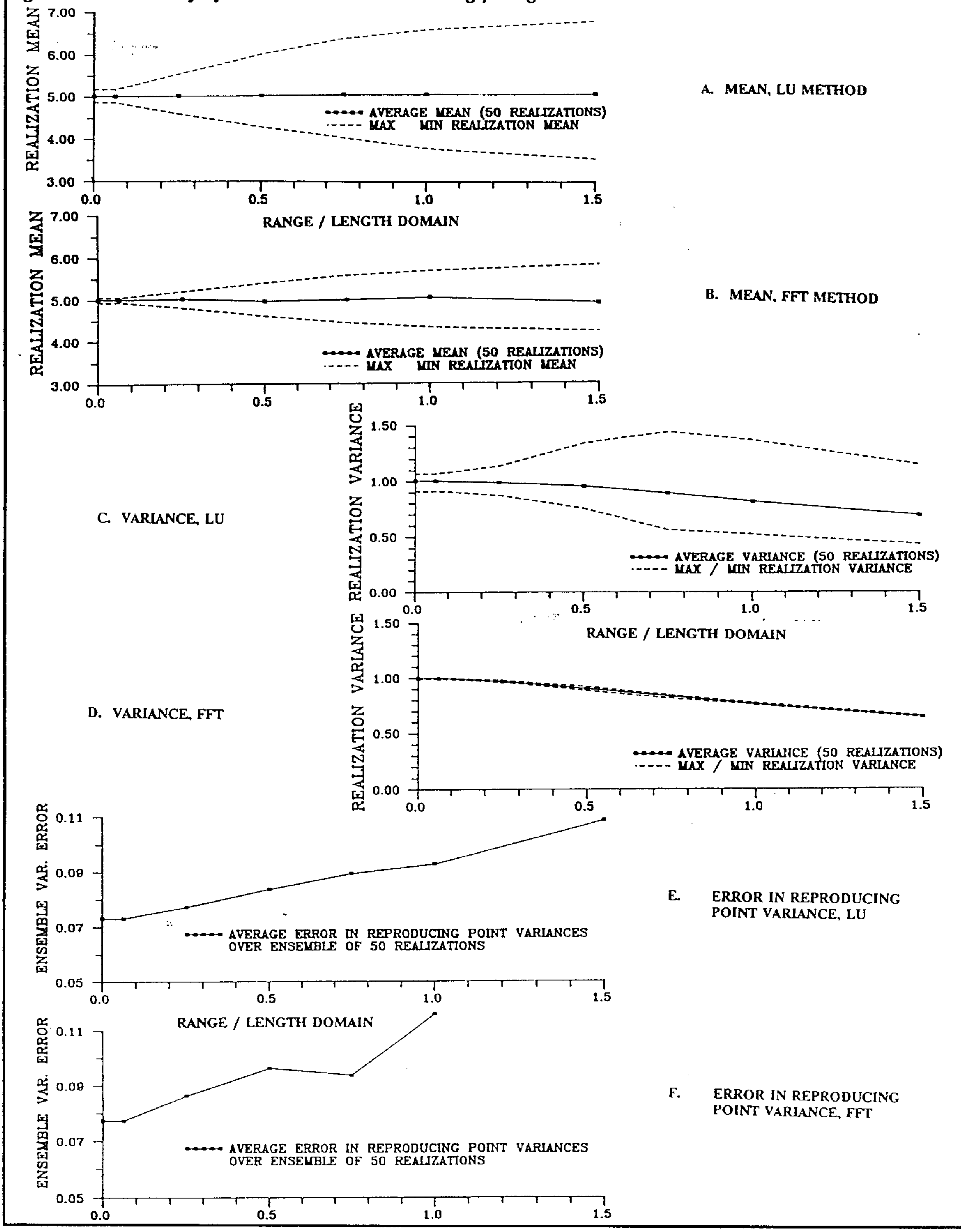

Figure 4.30 Sensitivity of Simulation Statistics to Number of Cells in Domain

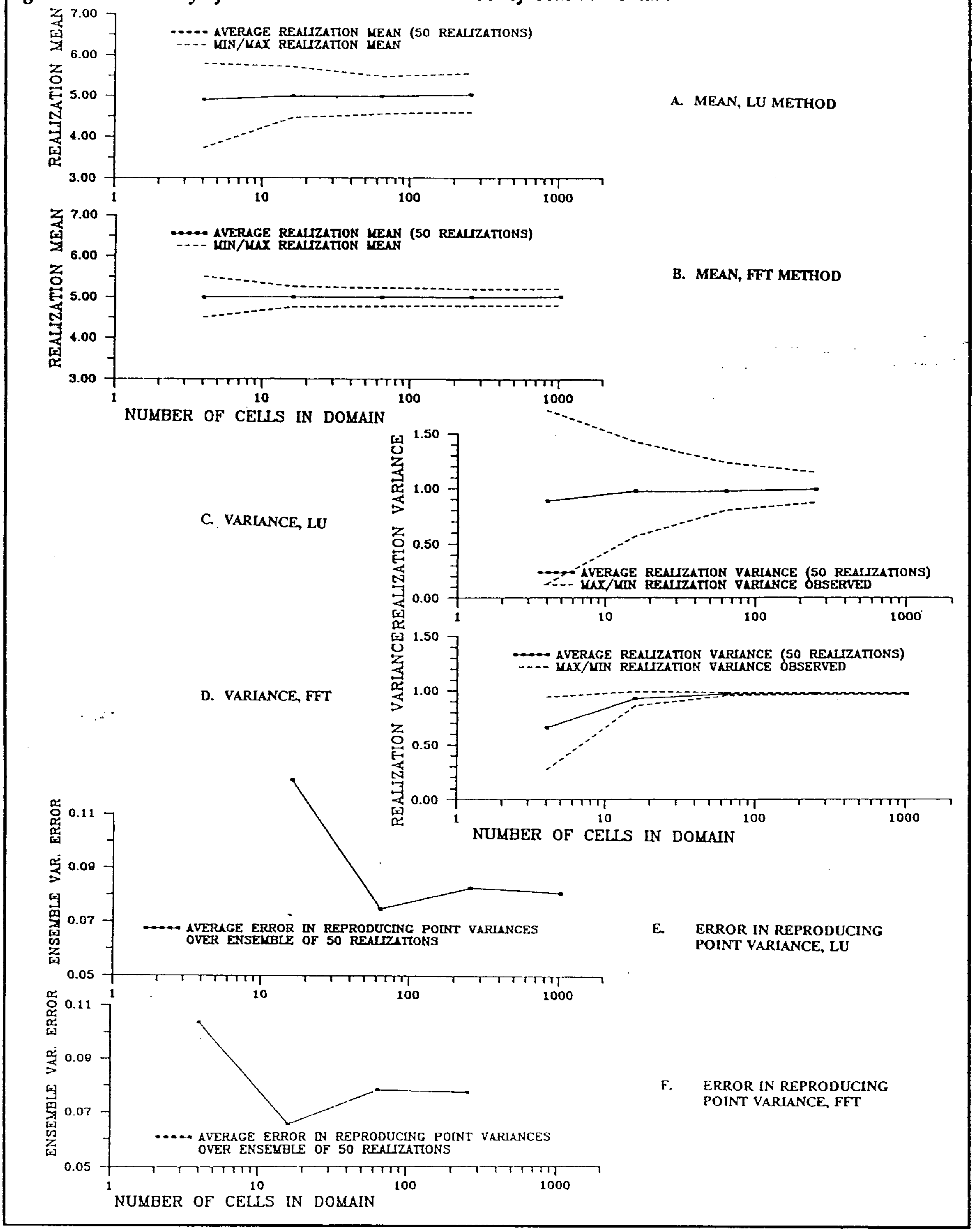

4.6 GEOSTATISTICS AND DESIGN

Thus far, the discussion in this chapter has focused on presenting the theory underlying the estimation and simulation techniques utilized in this thesis and on verification methods that can be used at each step of the analysis to confirm that simulated values are consistent with information collected in the field. This section suggests how the geostatistical approach presented in previous sections can be incorporated at each step of the project evaluation and design process, from feasibility study, through site investigation, production, and ultimately reclamation.

FEASIBILITY STUDY: The feasibility phase of pit wall design normally begins once exploration results confirm that there is sufficient grade and volume in the ore body to consider development. At this early stage in the project sufficient geotechnical data is not available to complete a detailed pit wall design study; however, the stochastic design approach should still be adopted for the following reasons:

- The stochastic analysis will provide an estimate of the likelihood of encountering favourable, intermediate, or poor sub-surface conditions at depth. This information can be input into the stability analysis to predict the anticipated range of pit wall angles and dewatering requirements that will be required, and ultimately, used to evaluate the economic viability of the proposed project.

- Once established, the stochastic model of the pit wall can be used to evaluate different exploration and development strategies prior to allocating site investigation resources (e.g. What pit wall angle is expected to yield maximum profitability? Does it appear that dewatering will be required? Is stability more sensitive to hydraulic conductivity data or shear strength data? Are a large number of slug test measurements more valuable than a few large scale pump tests?)

- By adopting the stochastic design approach early in the program, a well organized data base and analysis system will be in place well in advance of the site investigation process. The procedures can then be used to analyze new data as soon as it becomes available and modify exploration and design strategies accordingly . Since consistency in data requirements and analytical procedures will be maintained from one exploration stage to the next, the pit wall design will proceed much more efficiently.

To construct the initial geostatistical model, the geotechnical engineers must first become familiar with existing geologic information obtained during exploration drilling, including all geologic logs, sections, maps and reports. Interaction between the geotechnical team and the exploration geologists working on the property should also play an important part in this process.

Having defined the anticipated geologic environment, the geotechnical team must draw on experience from related projects to estimate the likely range of each design parameter. For the groundwater simulation, the parameters to be estimated include the mean, variance and autocorrelation structure of the log hydraulic conductivity field in each major geologic unit.

Once adequate values for each of these statistics is obtained, one of the unconditional simulation methods described in *Section 4.5* can be used to generate realizations of sub-surface conditions that will possess the expected statistical properties. Finally, Monte Carlo analysis of groundwater flow and slope stability will provide an indication of the probable risk of failure and economic viability associated with the various design alternatives.

SITE INVESTIGATION: The objective at this stage of the design process is to define the ultimate pit wall configuration and mining plan as accurately as possible prior to commencing production, although it is recognized that the plan will likely be revised as additional information and experience becomes available during the production phase.

Site investigation will typically involve a number of geotechnical borings, mapping of surface exposures and geophysical reconnaissance. Collection of the complete suite of shear strength and hydraulic conductivity tests is standard procedure in each drill hole. Data requirements for the hydraulic conductivity portion of the analysis include:

- Definition and geologic characteristics of the major geologic units.
- Estimation of the mean hydraulic conductivity values and variability of those values about the mean.
- Estimation of the range over which hydraulic conductivity values are correlated, including possible anisotropies.

On most projects, the hydraulic conductivity data base will be relatively sparse since the majority of exploration resources are generally directed to proving ore reserves at this early stage of mine development. Fortunately, recent advances in packer testing and multiple port piezometer technology make it possible to obtain a large number of hydraulic conductivity measurements in a single borehole. If available, such measurements can be used to establish the mean, variance, and autocorrelation structure in the vertical direction. However, in many situations a large number of direct hydraulic conductivity measurements will not be available. In these cases, it is necessary to infer the spatial distribution of hydraulic conductivity values from available geologic information. The Highland Valley Copper case history in *Chapter 9* provides an example of the latter technique.

Once the hydraulic conductivity tests are analyzed the results must be incorporated in the geostatistical data base. In the past, one of two philosophies have been be adopted to construct the new data base: 1) Kriging, based on classical statistics, and 2) Bayesian updating based on Bayesian statistics. Freeze et al. (in press) provide a complete discussion of the philosophical and quantitative differences between these two approaches. Important to this discussion is the fact that the classical Kriging approach (as applied by Delhomme, 1979 and de Marsily, 1984) does not provide a mechanism for including subjective prior estimates of hydraulic conductivity based on soft data (e.g. geologic information, geophysics, and experience) in the geostatistical data base. Kriging estimates and simulation realizations can be generated only after the first set of hydraulic conductivity measurements are completed. Thereafter, measurements taken during subsequent exploration phases are simply added to the data base to create a larger sample. On the other hand, Bayesian updating does recognize the value of subjective prior estimates in design and provides a mechanism whereby these estimates serve as the starting values in the simulation process. As measurements become available during subsequent exploration stages, they are used to update the initial subjective prior estimates. Freeze et al. (in press) point out that for sparse data sets, the subjective prior will continue to play a role in the later estimates. Presented below, is a list of the advantages of adopting one or the other of the two approaches for the particular problem addressed in this thesis.

- Due to the sparse nature of hydraulic conductivity data sets, any form of statistical analysis becomes practical only if subjective information is included, especially during the feasibility stage of mine design when the most important design decisions have to be made. Therefore, the Bayesian philosophy is desirable.

- The mining community is very familiar with kriging, since the method is used on a routine basis for grade control in most large open pit mines. This author is convinced that practitioners in the mining industry will be more likely to accept and adopt the conclusions of this research if they are familiar with the methodology used to obtain those conclusions.

- Kriging, based on the semi variogram is more robust than the Bayesian updating scheme since it can be utilized even if a covariance model cannot be defined over the scale of the field problem being analyzed.

- Literature describing the application of kriging to the type of parameter estimation performed in this thesis is much richer than literature describing the Bayesian approach.

Although the Bayesian philosophy adopted by Massmann & Freeze (1987) and Freeze et al. (1990) would provide the most effective stochastic method of updating the hydraulic conductivity data base, the geostatistical computations in this thesis are based on the less sophisticated ordinary kriging equations presented in *Section 4.4*. The resulting methodology possesses most of the desirable attributes noted above. Bayesian prior subjective estimates are treated just as if they were actual measurements. A large "measurement error" is associated with each estimate to account for the large estimation uncertainty associated with the subjective prediction. As actual measurements are taken, they are added to the geostatistical data base in the kriging sense, rather than used to update prior subjective estimates[9]. In situations where actual measurements coincide with, or fall close to earlier subjective estimation points, the subjective estimates are removed from the data base. This author believes that the above approach is justified; because, if properly performed, a hydraulic conductivity measurement should always yield a much more accurate value of the true hydraulic conductivity at a test location than a prior subjective estimate based on imprecise geologic and/or geophysical data.

Having updated the geostatistical data base, the information is used to generate a new set of realizations of the hydraulic conductivity field. As in the feasibility stage, the realizations provide input into the Monte Carlo simulation model of groundwater flow, slope stability, and economic analysis. At the site investigation stage the model is used to evaluate a number of viable pit wall design and dewatering design alternatives, and identify the strategy that will result in the most profitable design. Conditional simulation should be used during this simulation step in order to take full advantage of estimation variance reduction due to field measurements.

PRODUCTION: In order to recover the very high costs associated with start up (e.g. mill, crusher, trucks, etc.) and fully extract available ore from the deposit, most open pit mines must stay in production for many years, frequently several decades. A tremendous amount of data and experience is generally accumulated during that time. Just as production blast hole assays are used to update the earlier geostatistical model that was initially based on exploration assay results, so should new hydraulic conductivity measurements be added to the hydraulic conductivity data base. The entire pit design should also be reviewed periodically in light of new information, and modified accordingly as required.

RECLAMATION: The geostatistical model will also prove very valuable during the final years of production when reclamation of the open pit is being considered in detail. The model can be used to evaluate stability of the slopes once the dewatering program is halted, rates of flooding, and long term impacts on the hydrology of the immediate vicinity.

---

[9] Technically, this distinction is not required since the Bayesian updating scheme will yield exactly the same statistics as the kriging scheme provided the new measurement is exact, i.e. the conditional probability *P[sample=A | condition=A]* is equal to *1.0*.

4.7 SUMMARY

The stochastic risk-cost-benefit framework presented in this thesis allows the analyst to explicitly account for the natural variability in sub-surface conditions and to evaluate how uncertainty in parameter estimates will influence the economics of any proposed pit wall design. The simulation model of the hydraulic conductivity field that is generated by the simulation techniques presented in this chapter provides the necessary statistical description of the variability and uncertainty of sub-surface conditions that is required in order to conduct the risk-cost-benefit analysis. In short, the geostatistical analysis serves as the first and most important step in using the risk-cost-benefit approach to rationally select the most cost effective exploration, pit wall design, and dewatering strategies during each phase of mine planning and development.

This chapter and supporting appendices documented in detail how Geostatistics have been applied to the problem of predicting hydraulic conductivity values in the pit wall. In sequence, the contents have addressed each of the specific tasks that must be performed during a geostatistical simulation. The tasks include:

- Structural analysis, definition of semi-variogram model.
- Kriging estimation, computation of estimation uncertainty.
- Verification of estimation model.
- Simulation
- Verification of simulation model.

Section 4.2 provided a brief introduction to the unique terminology utilized in geostatistics. Emphasis was placed on the similarities and differences between the two tools that can be used to describe the autocorrelation structure: 1) the semi-variogram, frequently utilized in mining geostatistics, and 2) the covariance function, frequently used in groundwater hydrology.

Section 4.3 described the standard procedure for obtaining the experimental semi-variogram from field data, followed by a list of the six most common semi-variogram models used in modern geostatistics. A set of practical guidelines that help to speed up fitting of these models to the experimental structure were also presented.

Section 4.4 introduced kriging, a very popular estimation technique that possesses many desirable features. Besides providing the best linear unbiased estimate at each prediction point, the kriging equations can also be used to compute the level of uncertainty associated with each kriging estimate. Much of *Section 4.4* was devoted to explaining the many processes that influence the magnitude of estimation uncertainty, including the variance reduction factor. It was shown that unlike other estimation methods, kriging can account for each of these processes in a complete and concise manner. Verification of the kriging model is an important step that is frequently overlooked. Three standard verification tests were described and demonstrated in *Section 4.4*. Each of the kriging attributes described in *Section 5* has been implemented in the estimation module of SG-STAT. A practical example that demonstrated how SG-STAT can be applied to a real world estimation problem of predicting transmissivities in the Avra Valley aquifer was presented at the end of the kriging section.

Section 4.5 introduced geostatistical simulation, a set of stochastic methods that are capable of generating realizations of sub-surface conditions that capture the essential statistical characteristics of the actual hydraulic conductivity field. After a brief overview of the most important contributions on this subject, *Section 4.5* examined the differences between unconditional and conditional simulation and explained why conditional simulation methods are preferred whenever a reasonable amount of field data is available.

Section 4.5 also reviewed the good and bad points of the five simulation methods utilized in groundwater hydrology. It was concluded that while the LU matrix decomposition method is the most versatile technique for generating conditional simulations of the type required during the detailed planning stage of the dewatering system design, the Turning Bands or Fast Fourier Transform methods are much more efficient for generation of unconditional realizations of the type required during the feasibility study phase of the design.

A major part of *Section 4.5* was devoted to reviewing the performance of a simulation method based on the Fast Fourier Transform. Because the FFT technique, first applied to problems in groundwater hydrology in this thesis, is very fast and capable of generating very large realizations with complex covariance structures, it is expected to find extensive use as a simulation tool in years to come, especially in industry where access to large main frame and work station computers is limited. The LU matrix decomposition method was also described in detail as it was used to generate all conditional simulations in this thesis.

Verification procedures that can be used to confirm whether an ensemble of realizations conforms to input statistics were presented in the final simulation sub-section. To be considered as valid, each realization in the ensemble must reproduce the desired mean, variance and covariance model. As well, the variance of the simulated log hydraulic conductivity value at each prediction point, must reproduce the desired variance of estimation error for that point, when calculated over the ensemble of realizations. A detailed comparison of the FFT and LU simulation methods showed that the FFT method is more effective at reproducing each of these statistics, especially when a large number of points is generated. Furthermore, this study concluded that the degree to which simulation statistics reproduce input parameters is also dependent on the size of the flow domain in relation to the range, and to a lesser extent, on the grid size used for the simulation. As a rule of thumb, the flow domain should be at least twice as long as the range, and the grid size should be smaller than ¼ of the range in order to accurately reproduce the desired covariance structure. In case the maximum length of the flow domain is smaller than twice the range, an accurate analysis can still be conducted by treating the hydraulic conductivity field as a non-stationary system.

Finally, *Section 4.7* described how the geostatistical techniques presented in this chapter should be applied at each stage of the pit wall design process, from feasibility study, through site investigation, production, and ultimately to reclamation. Use of these new techniques will result in a more efficient and reliable pit wall and dewatering system design, and in the long term, a much more profitable mining operation.

Although the most important contributions of this thesis research arise from the analysis of results obtained during application of the complete framework to practical design problems, several contributions worth noting have arisen specifically from the research in reported in this chapter. These include:

- Pioneering use of the Fast Fourier Simulation method to the analysis of problems in groundwater flow.

- Implementation of the geostatistical techniques described in this chapter into SG-STAT, a comprehensive, user friendly and graphics intensive software module that will prove very useful to practitioners in the mining industry and to hydrogeologists who are required to provide estimates of sub-surface properties from limited exploration data.

CHAPTER 5 GROUNDWATER HYDROLOGY

5.1 OVERVIEW

As open pits are frequently excavated well below the original water table, estimating water pressures on the failure surface is a key factor in evaluating the stability of pit walls. This chapter demonstrates how SG-FLOW, a stochastic model of groundwater flow developed as part of this research effort, is utilized in this framework to predict the distribution of water pressures that will develop in the pit wall for any dewatering option under consideration.

The first modelling step requires the formulation of a well posed boundary value problem (BVP), one that will provide an accurate representation of the actual groundwater flow system. *Section 5.2* examines the various aspects of formulating the BVP, including:

- Region to be analyzed
- Governing equation of flow
- Boundary Conditions
- Representation of sources and sinks within the flow domain (i.e. wells, horizontal drains)
- Characterization of the hydraulic conductivity field

Although the actual flow problem is three dimensional, a simpler two dimensional representation is used in this study to reduce the computational burden. Several approximations must be made in transforming the 3D problem to an equivalent 2D representation, including geologic continuity in the third dimension and a continuous line sink representation of each row of pumping wells or drains. *Section 5.2* also examines the effect of these approximations on the subsequent accuracy of model predictions.

As the position of the water table is not known a priori, it must be determined as part of the solution. Two methods have been developed for solving the free-surface problem, including the deforming mesh approach and the saturated/unsaturated approach, adopted in SG-FLOW. *Section 5.3* provides a brief overview of the iterative techniques utilized to solve for the position of the water table. The saturated/unsaturated approach requires that hydraulic conductivities in the unsaturated zone be reduced as a function of negative pore pressures. As the characteristic curve that defines the relationship between negative pressure and hydraulic conductivity is frequently unavailable, *Section 5.3* also investigates sensitivity of the solution to approximations in the shape of this function.

The pattern of water pressures that will develop in the pit wall is strongly influenced by geologic conditions (e.g. a pervious gravel lens or an essentially impervious gouge zone). A unique feature of the SG-FLOW program is it's ability to incorporate these discrete structures in the stochastic analysis. *Section 5.4* describes how this feature has been implemented in the computer program. Several examples are also presented to illustrate the potential impacts of typical geologic structures on slope stability.

Figure 5.1 3D Schematic of Typical Dewatering Design

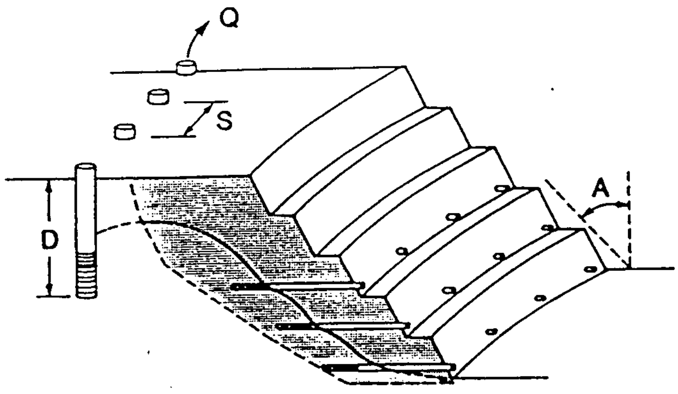

5.2 BOUNDARY VALUE PROBLEM

Figure 5.1 is a schematic of a typical dewatering design problem. The objective of the groundwater flow model is to forecast the position of the water table and water pressures on the failure surface given the spacing (S), depth (D) and pumping rate (Q) of all wells and horizontal drains.

Although the groundwater flow system is three dimensional, the computer model utilized in this framework is limited to two dimensions for the following reasons:

- Since the slope stability component of the framework is two dimensional, a full 3D representation of the pore pressure field is not required.
- A complete 3D analysis would pose memory and processing speed requirements well beyond the capacity of the current generation of personal computers.[1]
- Because exploration holes are usually drilled along section lines radiating outward from the center of the pit, a reasonable amount of geology and hydrology data can be compiled for a 2D analysis, whereas large data gaps frequently occur between individual sections in a 3D representation.

In the 2D representation of the flow system only a single vertical slice of unit thickness is considered. It is assumed that this slice is representative of conditions in the third dimension. *Figure 5.2* illustrates a typical 2D boundary value problem.

[1] If analyzed in 3D, the simulation would require a sophisticated model containing thousands of finite element nodes. If N is used to designate the total number of nodes, the geostatistical component of the analysis would then involve inversion of a covariance matrix of size N^2, containing several million entries. The memory, and especially, processing speed requirements clearly exceed the capacity of 386 based personal computers.

Figure 5.2 2D Representation of Boundary Value Problem

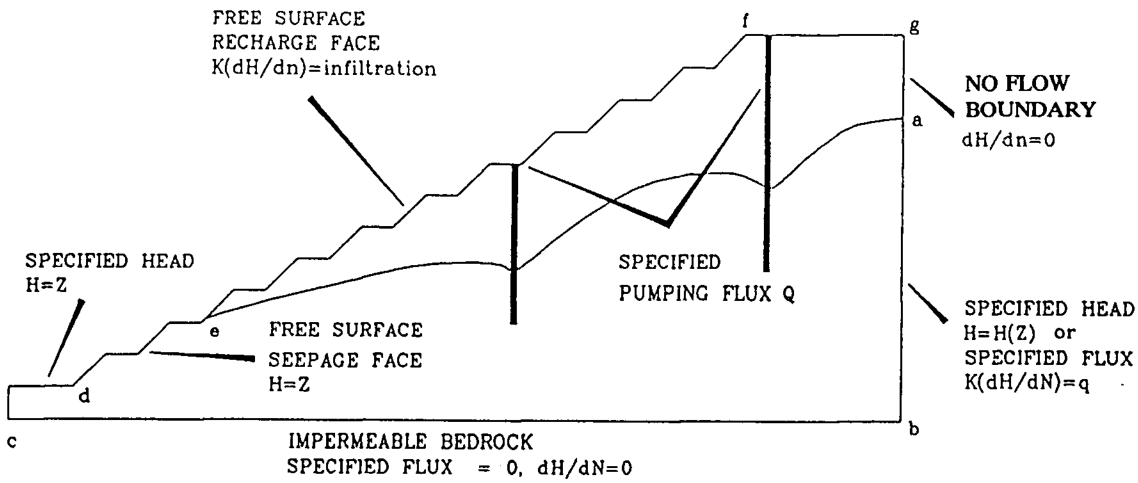

5.2.1 Flow Equation and Boundary Conditions

The long term distribution of hydraulic heads within the flow domain can be obtained by solving the 2D steady state equation of groundwater flow

$$\frac{\partial}{\partial x}\left(\frac{K_x \partial h}{\partial x}\right) + \frac{\partial}{\partial y}\left(\frac{K_y \partial h}{\partial y}\right) = 0 \qquad \textit{Equation 5.1}$$

subject to appropriate boundary conditions imposed on the perimeter of the flow domain, as shown in *Figure 5.2* and briefly described below. The vertical boundary *(a-b)*, located at a reasonable distance behind the pit crest can be represented as a specified flux or specified head boundary, depending on site conditions. The basal boundary *(b-c)* is usually selected to coincide with the top of a low permeability layer (e.g. at the overburden/bedrock contact) and represented as a no flow boundary. Because sump pumps usually maintain the water table at the pit floor, the segment *(c-d)* is represented by a specified head boundary with head equal to elevation. The pit face *(d-f)*, the horizontal boundary segment behind the pit crest *(f-g)* and the short vertical segment extending from the ground surface to the water table form a special free surface boundary for which one of two boundary conditions can apply. Below the exit point[2] *(e)* the free surface boundary *(d-e)* becomes a seepage face, represented by specified head boundary with head equal to elevation. Above the exit point the free surface boundary segment *(e-g)* is treated as a recharge face, with recharge flux equal to the infiltration rate. The final boundary segment *(g-a)* is represented by a no-flow boundary, as it is assumed that all infiltration in this portion of the flow domain will move vertically toward the water table.

[2] The point where the water table detaches from the ground surface and the unsaturated zone begins.

Figure 5.3 Illustration of Finite Element Mesh

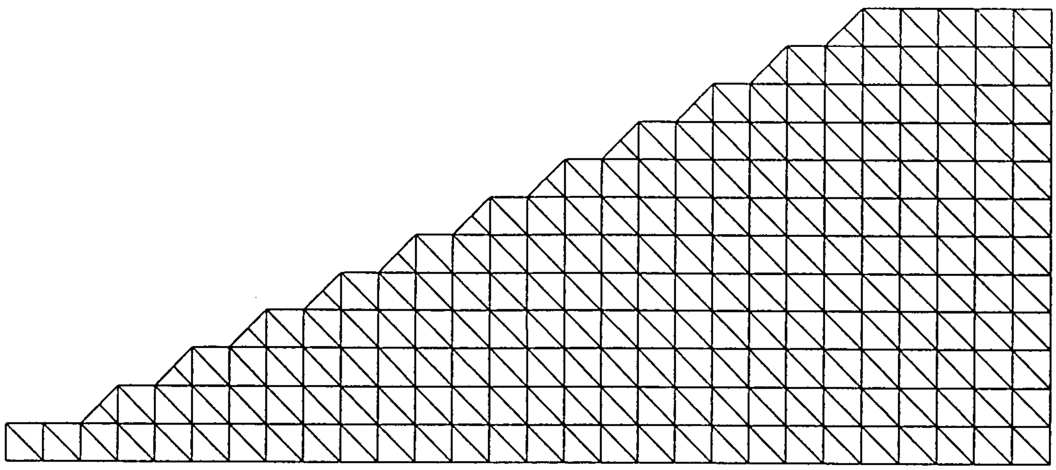

5.2.2 The Finite Element Method

The steady state groundwater flow equation, *Equation 5.1*, can be solved analytically for flow fields with relatively simple geometries, boundary conditions and material properties. Modelling of groundwater flow in the pit wall presents a much more complex flow problem that necessitates a numerical solution in the form of a finite difference or finite element model. The finite element method is used in this study.

In general terms, the finite element procedure involves discretizing the entire flow domain into a large number of triangular elements, as shown in *Figure 5.3*. Each element can be associated with a different set of boundary conditions and physical parameters. The differential equation describing groundwater flow in the entire flow domain is approximated with a large set of linear equations, one for each element. The resulting set of simultaneous linear equations can then be solved for the unknown hydraulic head values at each node of the finite element mesh with a linear equation solving algorithm such as Cholesky decomposition.

The finite element method has become a familiar tool in groundwater hydrology over the past decade. Because a large number of texts provide details of the standard modelling approach (c.f. Lapidus and Pinder, 1982, Remson et.al. 1971) the remainder of this discussion will focus only on the non-routine aspects of the groundwater flow model, including treatment of flow in the unsaturated zone, representation of wells on a 2-D section and the stochastic modelling approach.

5.2.3 Representation of Wells and Horizontal Drains

In the 2D finite element model, dewatering wells are represented by a column of one or more pumping nodes, with each node withdrawing a fixed fraction of the total flux. For example, consider a design sector 500 m in width in which a single row of five wells will be developed, orthogonal to the section line. Furthermore, it is estimated that each well will pump 50 l/s. The average pumping rate per unit width will then be 0.5 l/s. Assuming that a column of five pumping nodes is used to represent the row of wells, then a withdrawal rate of 0.1 l/s will be assigned at each node.

The flow rate emanating from a set of horizontal drains is a function of the hydraulic conductivity of the surrounding soil mass, the hydraulic head distribution behind the pit wall and the spacing of individual drains. Since the dewatering system operator has no control over the flow rate from the horizontal drain system once the drains are installed, horizontal drains cannot be represented by a set of internal pumping nodes (except if they are placed under vacuum, in which case they behave as horizontal dewatering wells). In this finite element model, each row of horizontal drains is represented by a row of finite elements for which hydraulic conductivities are increased by two to three orders of magnitude, depending on the spacing of individual drains. This modelling approach was adopted because it is more conservative than representing each row of drains by as an internal seepage face, where hydraulic head is set equal to elevation. Although the seepage face approach is representative of conditions within the drain, it is generally not representative of conditions in the surrounding soil mass, especially when a coarse nodal spacing is utilized in the finite element model (e.g. 10 to 25 m spacing).

Figure 5.4 Plan View Showing Well Locations and Piezometric Surface

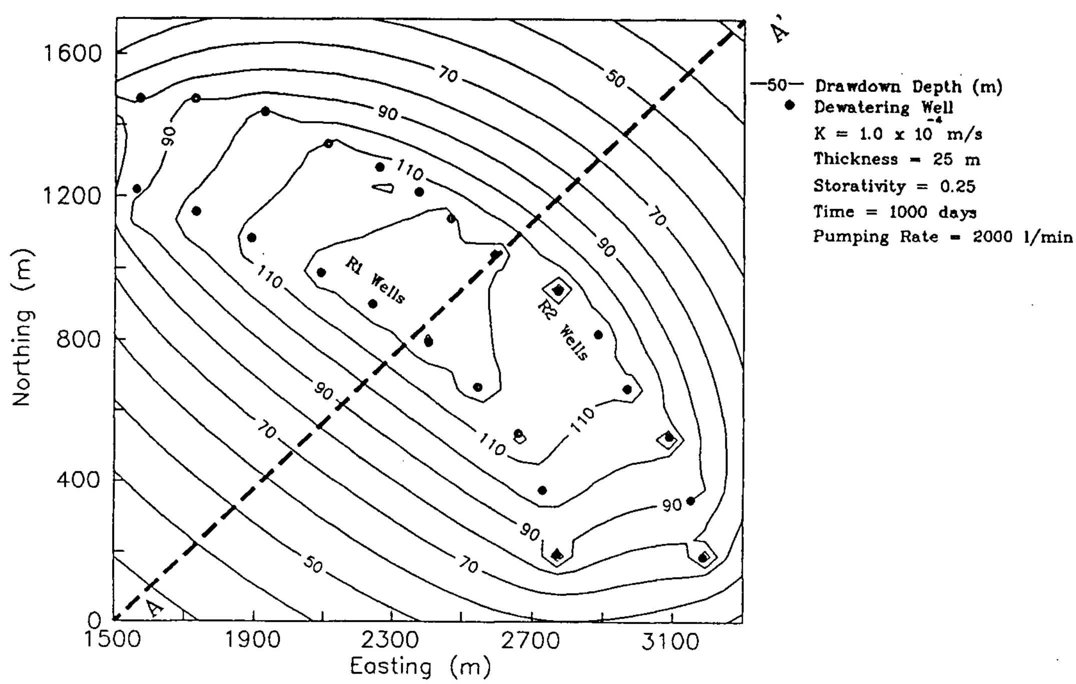

Figure 5.5 Piezometric Profiles on Section A-A'.

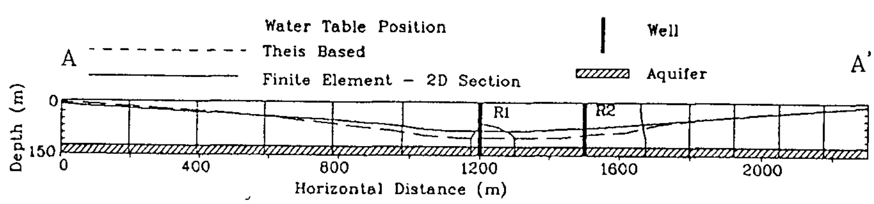

Although the 2D representation of wells and horizontal drains is best suited to analysis of seepage into long linear excavations such as those encountered in coal and tar sand strip mines, a simple verification study confirmed that the simplified approach provides sufficient accuracy for analysis and design of dewatering system geometries encountered in conventional open pit mines which are generally circular or elliptical in plan view. The verification involved a comparison of the drawdown response predicted by superposition of Theis solutions for a number of individual wells spaced as shown in *Figure 5.4* to the long term profile obtained from a 2D finite element analysis along section line A-A'. In the 2D finite element analysis each row of wells was represented by a column of pumping nodes; with the cumulative pumping rate set equal to the average pumping flux of the row per unit thickness of the pit wall.

Figure 5.4 also shows the shape of the drawdown cone as predicted by the Theis superposition method after 1000 days of pumping. In this scenario, the response of individual wells is masked by the combined response of all wells, resulting in a smooth, elongated drawdown cone. *Figure 5.5* illustrates a cross section view through the drawdown cone along line A-A'. The piezometric surface predicted by the Theis superposition method is indicated by a dashed line while the piezometric surface profile predicted by the 2D finite element method is indicated by a solid line. Although the two profiles are not identical, there appears to be sufficient agreement between the two surfaces to conclude that the 2D representation of the dewatering system will provide results that are sufficiently accurate for design purposes as long as the variability in subsurface geology in the third dimension is sufficiently small to be treated as homogeneous over the width of the design sector.

5.3 FLOW IN THE UNSATURATED ZONE

In the unsaturated zone, hydraulic conductivity decreases as a function of moisture content and negative pressure head. Because an accurate representation of the coupling between tensor components K_{ij} and pressure head is one of the key issues in modelling of groundwater flow in the pit wall, this section focuses on this issue, outlining the basic theory and the simulation approach adopted in SG-FLOW.

Since the position of the water table is not known a-priori, and is in fact free to move anywhere within the flow domain, the boundary value problem of groundwater flow in the pit wall is known as a free surface problem. Because the position of the free surface and the extent of the unsaturated zone are issues of concern in a number of engineering design problems (e.g. seepage through dams, contaminant migration, infiltration and slope stability) reliable numerical methods have been developed to calculate the position of the water table for any arbitrary set of geologic conditions and surface geometry. The solution methods follow one of two lines: 1) a free surface approach that ignores groundwater flow above the water table, or 2) a saturated/unsaturated approach that accounts for groundwater movement in both the saturated and unsaturated zones. Both methods are reviewed below; however, only the saturated/unsaturated approach has been implemented in this framework.

5.3.1 Free Surface Approach

The free surface approach considers only flow within the saturated zone. In this approach, first developed by Taylor (1967), Finn (1967) and later refined by Neuman (1978) the upper boundary of the flow domain is formed by the water table or free surface. Since the true position of this boundary is not known, a systematic iterative approach is adopted to determine the shape of the free surface as a part of the solution. First, an initial guess is made as to the water table location. Using the standard finite element formulation, the hydraulic head distribution is then computed over the entire flow domain. Given that at the free surface total head equals elevation head and pressure head is zero by definition, the computed values of pressure head at each node on the free surface boundary are used to determine whether the free surface should be shifted upward or downward during the subsequent iteration. If pressures are positive, the water table is moved upward, if they are negative the water table is moved downward. The iterations continue until the maximum elevation adjustment at any free surface node drops below a specified tolerance.

In most free surface algorithms, entire columns of the finite element mesh are stretched upward or compressed downward as dictated by results of the pore pressure calculations. As a result, each element within the mesh can shift significantly from it's original position as well as becoming somewhat deformed. This characteristic of the free surface method presents difficulties when attempting to model heterogeneous or anisotropic geologic conditions. Although Neuman (1978) developed a sophisticated mesh deformation algorithm that permitted him to analyze problems involving two or three geologic layers (e.g. flow through an earth dam), the classic deforming mesh approach cannot be used for stochastic problems where hydraulic conductivity differs for each element and it is required that the shape and size of each element remain constant.

A recent paper by Schwartz and Crowe (1985) introduced a refined free surface approach whereby the mesh deformation is limited only to the top row of finite elements while all others remain undisturbed. Whenever an element is stretched beyond it's maximum height a new element is introduced. Since the majority of elements remain undisturbed, this method is more suitable for incorporation in a stochastic framework. Unfortunately, the presence of two or more free surfaces in a single vertical profile, as would occur with a perched water table or unsaturated wedge in a pit wall, also present difficulties. In fact, this author is not aware of any free surface programs capable of modelling this aspect of unsaturated flow.

5.3.2 Saturated/Unsaturated Approach

The saturated/unsaturated method of analysis was developed to overcome the handicaps inherent in the free surface approach. In this method, groundwater flow is analyzed in both the saturated and unsaturated zones.

As illustrated in *Figure 5.6A*, below the water table all pore spaces are fully saturated. Flow can occur throughout all connected voids in the soil mass and the hydraulic conductivity is at its maximum (saturated) value. If the available water is not sufficient to completely fill all of the pores, capillary forces will retain available water in the smallest voids while the larger voids will drain, as shown in *Figure 5.6B*. Since water flow can occur only through water filled voids, effective hydraulic conductivity, K_u, will decrease as the soil becomes progressively drier. Also, negative (tensile) pore pressures will develop in the soil mass because gravitational forces acting on the fluid will be balanced by capillary forces at the soil-water interface.

Figure 5.6 Cause of Reduced Hydraulic Conductivity in Unsaturated Zone

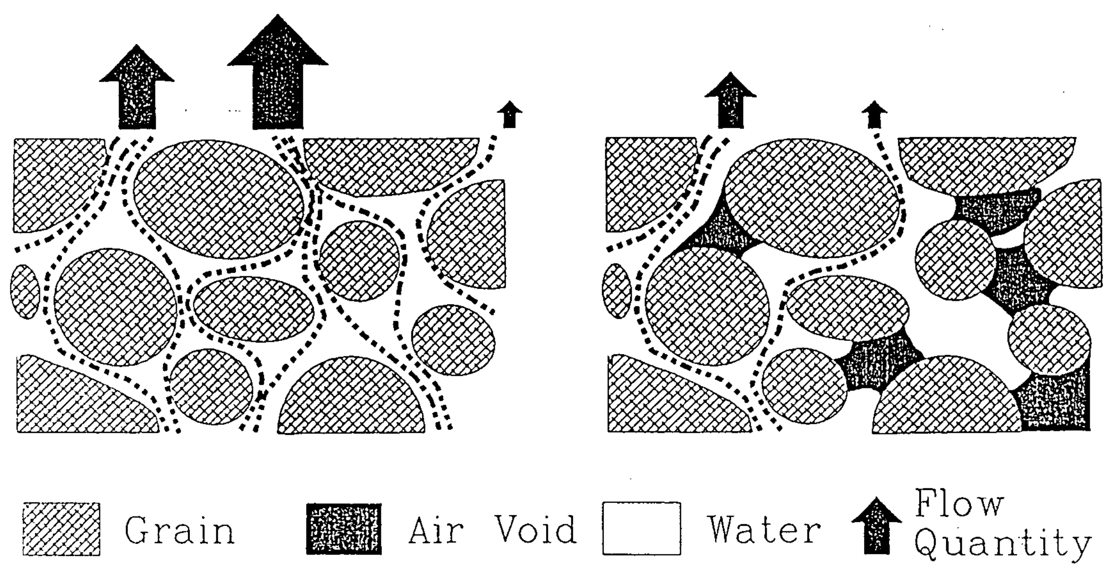

Figure 5.7 Characteristic Curves Defining Unsaturated Behaviour (after Freeze & Cherry, 1978)

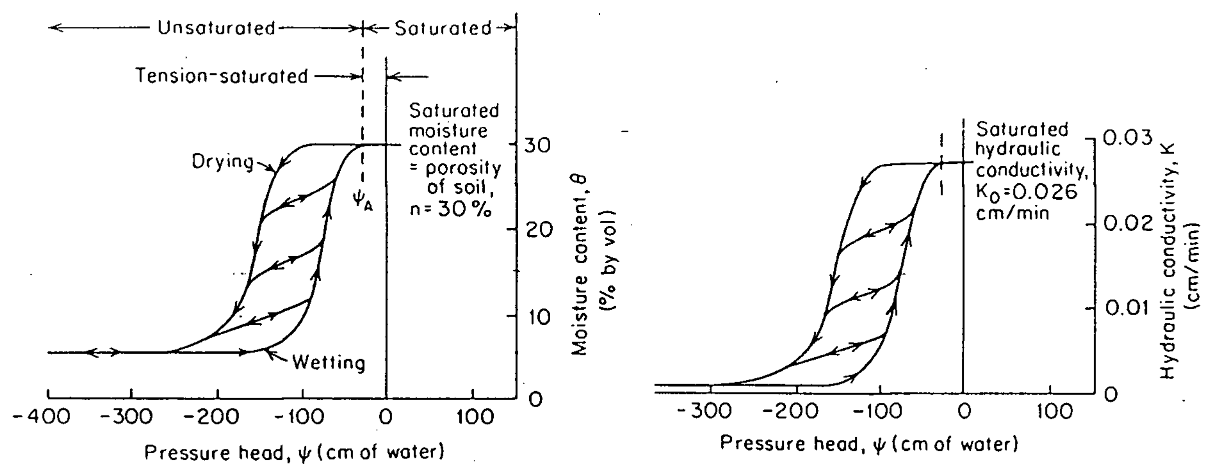

Figure 5.7 illustrates how the physical properties of a soil, including moisture content, hydraulic conductivity and pressure head in the pore space are related. The characteristic curve relationship between K_u and pressure head ψ is utilized in the saturated/unsaturated model to correctly account for flow in the unsaturated zone. An iterative approach is required. First, an initial guess is made regarding the position of the water table and the likely ψ distribution within the unsaturated zone. Next, hydraulic conductivities in all finite elements that experience negative pressure heads are reduced according to the appropriate characteristic curve. After each hydraulic conductivity adjustment the entire head distribution is re-evaluated. This iterative process is repeated until all nodal pressure heads converge to steady values.

Because the boundary condition along the pit-face seepage face boundary is a function of the dependent variable ψ and cannot be determined a priori, the iterative scheme must also adjust the boundary conditions on the seepage face with each iteration. In *SG-FLOW*, the iterative strategy proposed by Neuman (1972) is utilized. The position of the water table is initially guessed. Then for the first iteration, the value of ψ is set equal to zero along the seepage face and this segment of the slope is treated as a specified head boundary. Then, the nodal flux per unit area, Q, is set equal to the infiltration rate along the unsaturated portion of the pit-face (recharge face) and this segment is treated as a specified flux boundary. The flow equation is then solved with the expectation that the newly calculated values of Q will indicate that flow is directed out of the slope only along the seepage face segment of the boundary, and the newly calculated values of ψ will be negative only at boundary nodes along the recharge face. If these expectations are not met, the boundary conditions at the errant nodes are redefined to agree with the new solution. This procedure is repeated until the solution converges.

Because measurement of the characteristic curve response requires sophisticated laboratory analysis, the relationship is not routinely determined as part of hydrogeologic investigations. Therefore, a number of sensitivity analyses were conducted to determine whether the saturated/unsaturated numerical model could still be used when detailed information on the shape of the characteristic curve was not available.

Figure 5.8 Boundary Value Problem Used to Test Sensitivity to Characteristic Curve

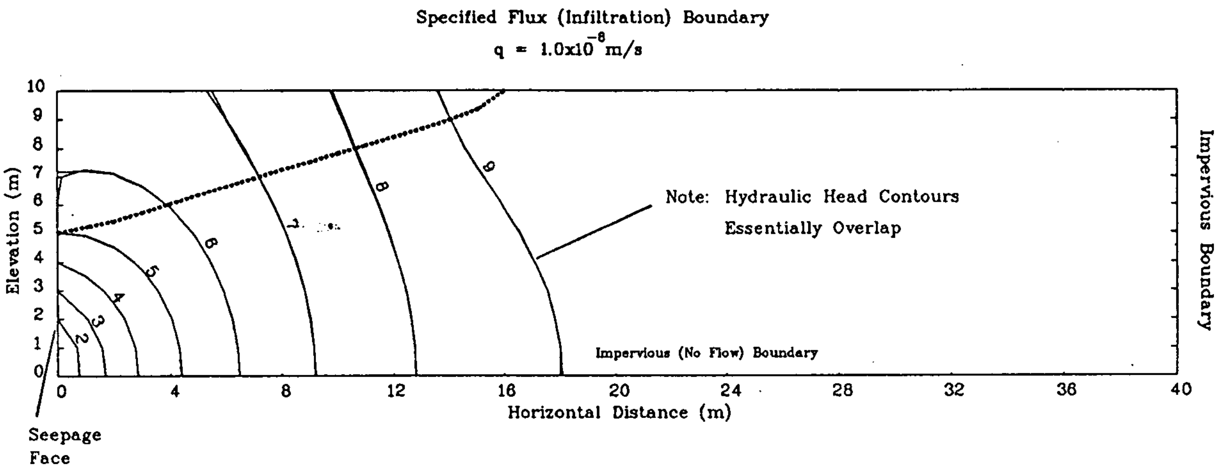

The sensitivity studies showed that the pore pressure response and the predicted position of the water table are not affected by the shape of the characteristic curve for mine scale groundwater flow problems. The pore pressure response is not sensitive to the shape of the characteristic curve because the thickness of the unsaturated zone is usually much greater than the width of the transition zone above the water table where K changes from a fully saturated to an essentially unsaturated condition. Consider the simple groundwater flow problem illustrated in *Figure 5.8*. Analysis of this problem using a single K_{sat} and characteristic curves representative of sand and clay materials resulted in essentially the same steady state hydraulic head distribution and water table position.

5.4 *IMPORTANCE OF GEOLOGY AND K_{SAT}*

Although the shape of the characteristic curve was not critical in the sensitivity analysis, the starting K_{sat} value certainly was. *Figure 5.9* shows the predicted water table for two K_{sat} scenarios, one corresponding to a sand horizon ($K_{sat} = 1x10^{-5}$ m/s, the other to a silt ($K_{sat} = 1x10^{-7}$ m/s). When the flow domain is composed of sand the water table remains at depth, controlled by the specified head boundary along the left margin of the flow domain; groundwater flow remains essentially vertical through the unsaturated zone. When silt is considered the saturated hydraulic conductivity approaches the infiltration rate. The water table rises to the ground surface and ponding occurs on the right half of the flow domain. These results demonstrate the importance of determining the mean hydraulic conductivity as accurately as possible prior to modelling the groundwater flow system.

Discrete geologic structures such as an impervious fault zone, a thin clay bed, or a highly permeable gravel aquifer can also impact on the resulting pore pressure distribution without influencing overall hydraulic conductivity statistics. *Figure 5.10* presents three scenarios that illustrate how geologic structures can distort the classic "flow-net" head distribution. *Figure 5.10A* shows the homogeneous flow-net solution, *B* shows how a discontinuous lens of high permeability material reduces pore pressures in the toe area, *C* illustrates how a low permeability fault zone along the failure surface increases pore pressures.

In the ideal stochastic model, realizations of the hydraulic conductivity field for each distinct geologic unit would be generated independently from separate sets of statistics. In practice, sufficient statistical data and programming difficulties dictate a more pragmatic approach. In computer program *SG-FLOW* distinct geologic structures can be introduced as deterministic "overlays" that either increase or decrease hydraulic conductivity by a specified amount wherever a particular geologic structure is known to exist. For example, when modelling a distinct gravel lens in a sand aquifer, hydraulic conductivities of all associated elements might be increased by two orders of magnitude. This way, the desired hydraulic conductivity contrast is introduced while maintaining the variability and correlation structure in each horizon.

Figure 5.9 Influence of Changing K_{sat} on Position of Water Table

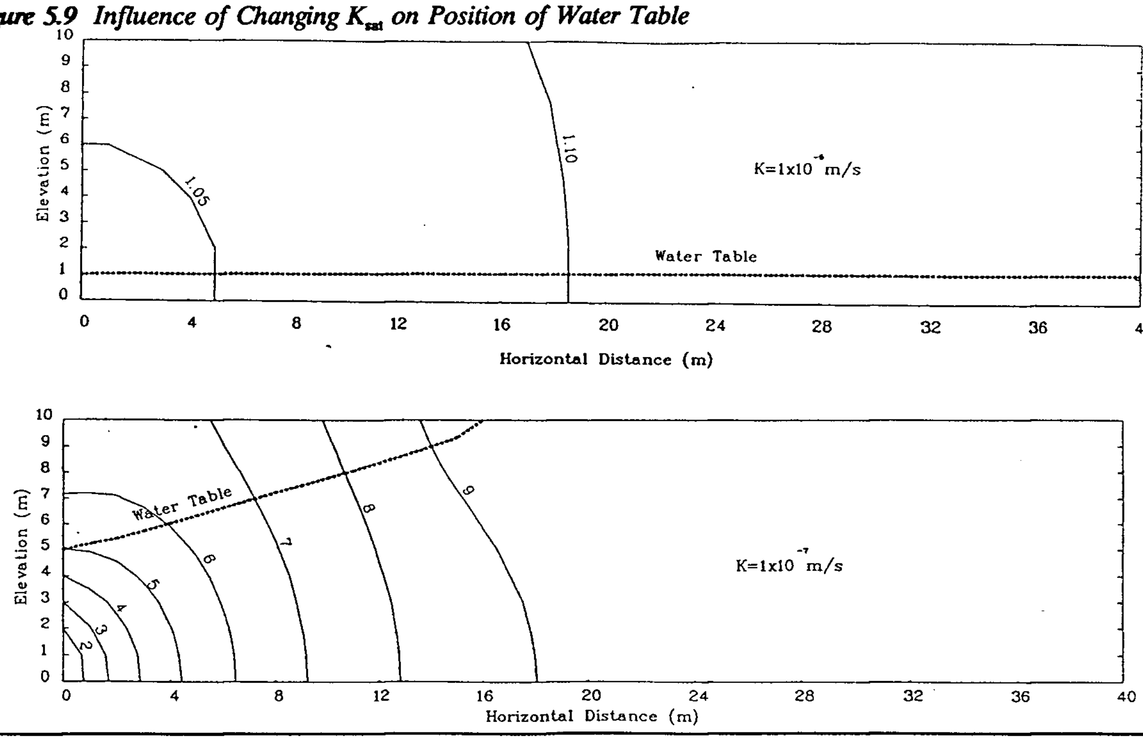

Figure 5.10 Influence of Geologic Structure on Pore Pressure Distribution

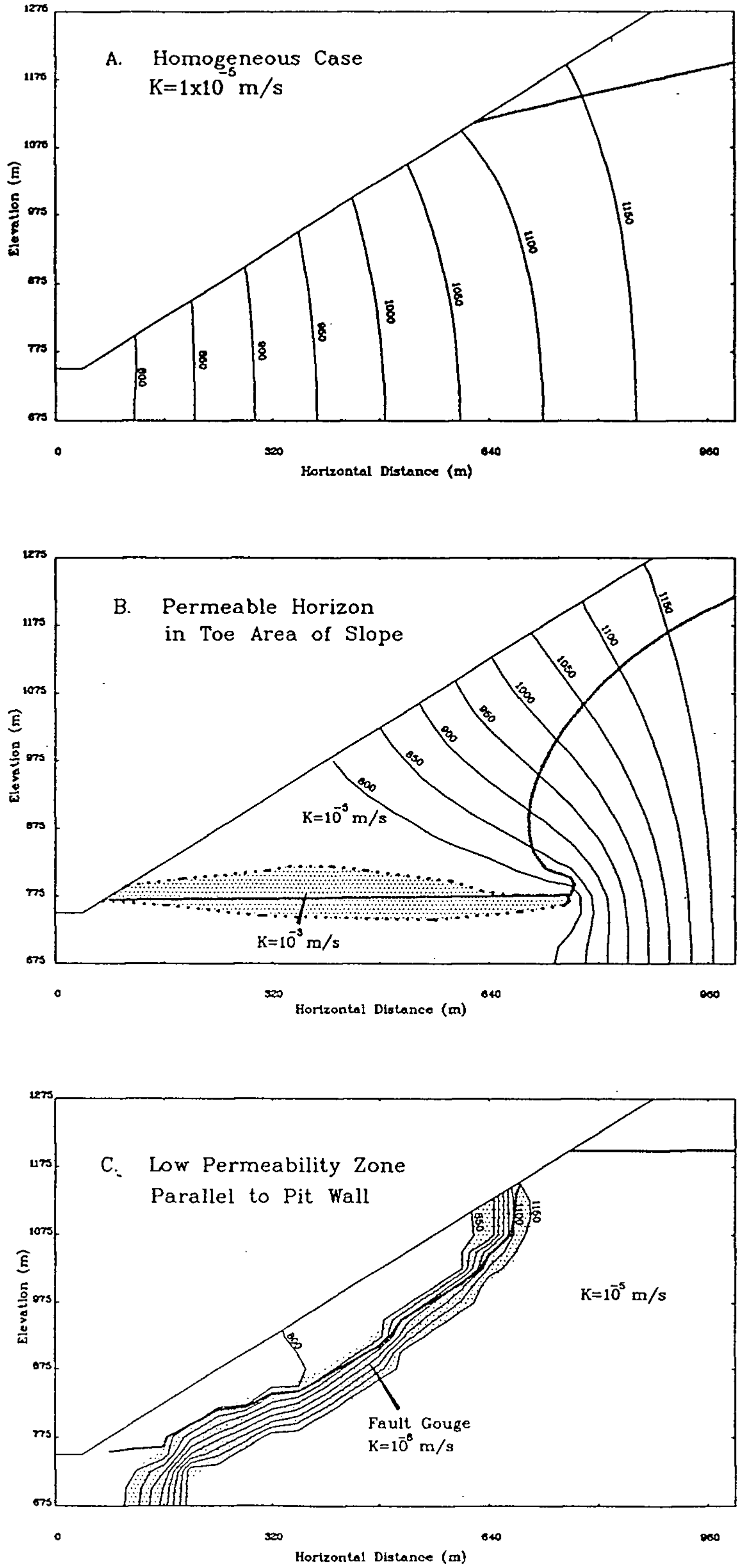

5.5 STOCHASTIC GROUNDWATER FLOW MODELLING

Thus far, the discussion of groundwater flow has been considered in a deterministic sense. In other words, it has been assumed that all input parameters for the computer model are known exactly. In practice, many input parameters that are required to complete a dewatering system analysis are uncertain to some degree. In particular, the distribution of hydraulic conductivities in the sub-surface is frequently the most uncertain data set, known only at a few points in the flow domain where measurements have been taken.

The geostatistical methods that have been adopted in this framework to account for this uncertainty have been described in *Chapter 4*. In the Monte-Carlo simulation approach, these methods are used to generate a large number of conditional realizations of the hydraulic conductivity field based on the available data. The stochastic analysis of groundwater flow, the next logical step in the analysis, simply involves using the SG-FLOW finite element model repeatedly to solve the BVP for each realization of the hydraulic conductivity field. The resulting pore pressure distributions can then be evaluated to estimate the most likely pore pressure at each node in the flow domain and the corresponding degree of uncertainty associated with that estimate. The key objective is to establish how uncertainty in sub-surface conditions affects our ability to predict the pore pressure distribution in the pit wall, and ultimately, the probability of slope failure.

A number of sensitivity studies have been completed to investigate how changes in mean K, standard deviation of K and range of correlation influence the resulting pore pressure distribution, the probability of slope failure and the degree of monetary risk. The results of these sensitivity studies are presented in *Section 7.5* of this thesis.

5.6 SUMMARY

This chapter provided a brief overview of the finite element computer model that is used to predict the distribution of pore pressures that are likely to develop for any proposed pit dewatering strategy.

The first portion of this chapter described how the problem of groundwater flow in the pit wall was transformed into a two dimensional boundary value problem. The applicability and limitations of simplifying the problem to two dimensions were also discussed, especially the approach used to accurately simulate the effect of a 3D array of dewatering wells or horizontal drains in the 2D section model.

Next, the subject of flow in the unsaturated zone was examined in detail. Both the free surface (deforming mesh) and saturated/unsaturated modelling approaches were reviewed. The saturated/unsaturated approach is utilized in SG-FLOW because it is easier to implement in a stochastic framework since the boundaries of each finite element remain fixed in space instead of deforming across zones of differing hydraulic conductivity.

In the saturated/unsaturated model hydraulic conductivity of the unsaturated soil mass (above the water table) decreases as a function of moisture content, as specified by the characteristic curve. As determination of this function requires detailed laboratory testing; it is generally not obtained during routine geotechnical investigations at open pit mines. Fortunately, sensitivity studies conducted as part of this research have shown that when considering large scale groundwater flow problems the distribution of pore pressure in the pit wall is not sensitive to the shape of the characteristic curve.

On the other hand, geologic horizons or structures of contrasting hydraulic conductivity (e.g. fault zones, gravel lenses, etc.) can have a pronounced effect on the distribution of pore pressures in the pit wall. In SG-FLOW these distinct structures are introduced as deterministic "overlays" that either increase or decrease the hydraulic conductivity by a specified amount wherever a particular geologic structure is known to exist.

The final section of this chapter described how SG-FLOW has been implemented in the framework to analyze groundwater flow problems in situations when the hydraulic conductivity field is uncertain. The stochastic analysis simply involves solving the specified BVP repeatedly for a large number of realizations and updating the hydraulic head statistics. The effect of the resulting pore pressure distributions on the probability of slope failure is addressed in the next chapter.

CHAPTER 6 SLOPE STABILITY

6.1 OVERVIEW

Probability of failure is the most important and complex factor in the assessment of monetary risk due to pit wall failure. This chapter discusses how limit equilibrium stability analysis and Monte Carlo simulation techniques are used to estimate this essential parameter.

Stability of a pit wall is entirely dependent on local geologic and groundwater conditions. These include: shear strength of materials, orientation and continuity of faults, joints and other discontinuities, groundwater pore pressures, and slope geometry. Specialized methods of analysis have been developed to estimate the factor of safety (F) of a pit wall for the most common modes of failure. Although most of the methods are based on the principle of limit equilibrium, they differ significantly in the assumptions made to resolve the problem of static indeterminacy. The principle of limit equilibrium and a general formulation of the problem common to all methods of slices are discussed in *Section 6.2*. *Section 6.3* then examines some of the most popular methods of stability analysis; emphasis is placed on assumptions, accuracy, and computational efficiency inherent in each method. Closing remarks discuss the practical reasons why Sarma's method was selected for incorporation in this framework.

Mechanics of Sarma's method of slices are introduced in *Section 6.4*. Starting with the basics, the system of linear equations used by Sarma is derived. A simplified numerical procedure for solving the equations is then presented. The relationship between critical acceleration K_c and factor of safety is explored and a new iterative procedure for calculating F is presented. Sensitivity of F to the orientation of slice boundaries and the problem of negative stresses are two very important topics that are only briefly mentioned in the literature. The final paragraphs in this section examine these problems in greater detail.

In the past decade geotechnical engineers have developed probabilistic methods that explicitly consider uncertainty and variability of geologic and hydrologic parameters in the stability assessment of pit walls. Instead of measuring stability in terms of the conventional factor of safety, these methods measure stability in terms of probability of failure. Section 6.5 examines the concept of probability of failure and shows how it is related to the factor of safety.

The destabilizing influence of groundwater pore pressures on open-pit walls has long been recognized by geotechnical engineers. Section 6.6 describes briefly how groundwater pore pressures calculated by *SG-FLOW* are incorporated in the Sarma analysis. Practical examples that illustrate how dramatic improvements in stability that can be realized through properly engineered groundwater control programs are presented later in the sensitivity and case history chapters of this dissertation.

6.2 LIMIT EQUILIBRIUM ANALYSIS

Slope failures in open pit mines can be categorized into six basic failure modes: planar, wedge, block, circular, toppling, and buckling. These basic modes of failure are illustrated in *Figure 6.1*. Some slides must be classified as compound; with the upper part of a slide mass controlled by one failure mode and the lower part with another. Planar, wedge, and block modes of failure; where sliding occurs along one or more well defined discontinuities, are most common in weakly to moderately jointed rock. The circular mode of failure is frequently observed in pit walls excavated in heavily jointed rock or unconsolidated overburden and in waste dumps. Toppling and buckling modes of failure are less common in general, because discontinuities must fall in a narrow range of orientations relative to the pit wall in order to result in a kinematically admissible failure mechanism. Large volume, multiple bench failures that impact on mine production can generally be classified as planar, wedge, or circular.

During the past twenty years a wide spectrum of methods have been developed to assess slope stability. The methods are based on one of two solution techniques: limit equilibrium or stress - strain continuum. Methods based on the stress - strain approach require that the pit wall behave as a continuum, subsurface geologic conditions be accurately known, and elastic properties of each geologic unit be well defined. Because discontinuities introduce modelling complications that are difficult to overcome and data obtained from geotechnical drilling programs is typically insufficient to accurately describe the deformation response of the pit wall, stress - strain methods are not applied to stability analysis of pit walls except in special circumstances.

Figure 6.1 Modes of Pit Wall Failure

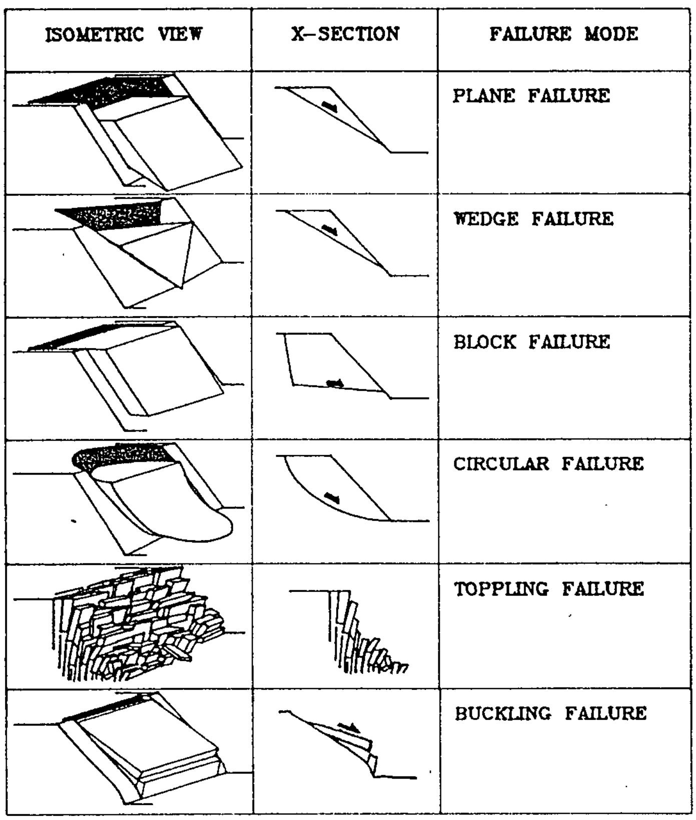

Methods based on the principle of limit equilibrium are conceptually simpler and require much less input data to assess stability of a potential failure block. These methods usually measure degree of stability in terms of the factor of safety, F, although other stability indicators such as critical acceleration factor, K_c, are also applied. Before defining factor of safety two stress states must be introduced. First, mobilized shear stress, τ_m, is defined as the state of shear stress that develops on the failure surface due to gravitational and external loading. Second, available shear strength, s, is defined as the maximum shear stress that can develop along the base of the failure block before a condition of incipient movement is induced. For a stable slope, where F is greater than 1.0, the mobilized shear stress required to counteract gravitational forces and maintain the free body in equilibrium is a fraction of available shear strength, the maximum shear stress that can develop on the failure surface for any given normal stress σ. Available shear strength can be expressed as a function of normal stress , either by the linear Mohr-Coulomb failure criterion:

$$s = c + \sigma \cdot tan(\phi) \qquad \textit{Equation 6.1}$$

or by non linear equations such as the Hoek -Brown empirical failure criterion (Hoek, 1983).

Factor of Safety is then defined as the ratio of mobilized shear stress on the failure surface to the available shear strength. In other words, F is the factor by which available shear strength must be reduced in order to bring the failure block into a state of equilibrium with the mobilized shear stress.

$$\tau_m = s \,/\, F \;=\; c/F \;+\; \sigma \cdot tan(\phi)/F \qquad \textit{Equation 6.2}$$

Limit equilibrium techniques have been developed to evaluate stability of each of the six basic failure modes; the techniques include: method of circles (Taylor, 1937), method of slices (Fellenius, 1936), wedge solution (Londe, 1969), and method of columns (Unger, 1983) . Other researchers subsequently introduced more sophisticated variants of the original solution strategies to overcome some of the simplifying assumptions inherent in the original methods.

A limit equilibrium technique that is well suited to analyzing one type of failure mechanism cannot in general be applied to study all others. The method of slices was chosen to evaluate slope stability in this framework. The technique was selected for three reasons:

- The method is very flexible, it can be used to evaluate stability of design sectors where planar, circular, or wedge failures with large included angles (greater than 120 degrees according to design charts presented by Hoek, 1981) are anticipated.

- The method has modest data requirements. All necessary shear strength, groundwater, and failure surface geometry information can be obtained from standard geotechnical exploration programs.

- The method is well established and familiar to most mining and geotechnical practitioners. It has been applied to a full range of slope stability problems in open pit mines around the world. Many well documented case histories are available for calibration purposes.

Before examining the most popular methods of slices in the following section and introducing the Sarma method of slope stability analysis that is used in this framework in Section 6.4, it is important to review the basic principles that all methods of slices have in common; and more importantly, to explore why the method of slices approach results in a statically indeterminate problem. In order to obtain a solution to this problem some assumptions have to be made; it is in these assumptions that the various methods of slices differ.

The first step in analyzing a potential slope failure is to identify the failure surface. In weakly to moderately jointed rock, the failure surface will often develop along a major, throughgoing discontinuity such as a fault plane. The location and orientation of these surfaces can usually be established. In heavily jointed rock masses and overburden slopes, the critical failure surface is much more difficult to predict. Search methods have been developed for estimating the location of the critical failure surface; these will be discussed in Section 6.8. At this point it will be assumed that the failure surface is well defined. Once the failure block is identified a representative two dimensional cross section is constructed as shown in *Figure 6.2*. The failure block is then divided into a series of slices. Permissible slice shapes depend on the actual method of slices used. All methods of slices require that each slice be a quadrangle or triangle with linear slice boundaries. Most methods also require that slice boundaries be vertical.

Figure 6.2 Failure Block Divided Into Slices

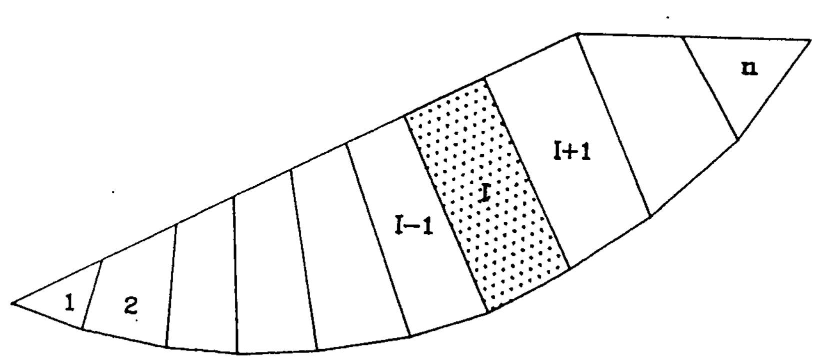

Body forces acting on each slice are then identified, as illustrated in *Figure 6.3*. The magnitude and line of application of gravitational and water pressure forces are known. The magnitudes of normal and shear reaction forces acting on the base and sides of each slice are unknown, the lines of thrust of the normal forces are also unknown. *Table 6.1* lists the unknowns as a function of the number of slices, *n*, used to define the failure block.

Figure 6.3 Body Forces Acting on Slice

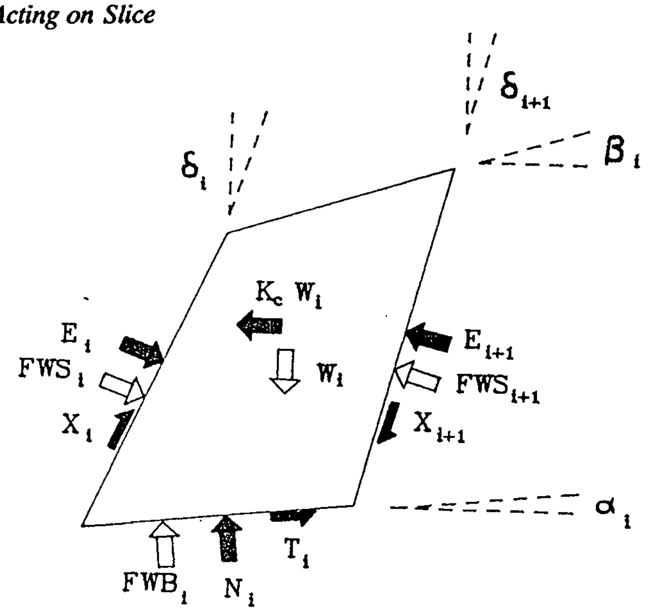

Table 6.1 Unknown Forces and Available Equations

FORCE	DEFINITION	NUMBER	EQUATION	NUMBER
X_i	Side Shear Side i	n-1	Vertical Equilibrium	n
E_i	Normal Force Side i	n-1	Horizontal Equilibrium	n
Z_i	Point of Application of E_i	n-1	Moment Equilibrium	n
T_i	Base Shear Force	n	Failure Criterion - Base	n
N_i	Base Normal Force	n		
L_i	Point of Application of N_i	n		
F	Factor of Safety	1		
	Total Unknowns:	***6n-2***	***Total Equations:***	***4n***

The total number of unknowns, *6n-2*, must be resolved as part of the solution procedure for calculating F. Equations that can be used to solve for the unknowns include horizontal and vertical force equilibrium, moment equilibrium, and some form of failure criterion on the slice base. One complete set of equilibrium equations is available for each slice n; therefore, the total number of available equations is $4n$. Because there are $2n$-2 more unknowns than independent equations the method of slices problem is statically indeterminate. If a solution is to be obtained $2n$-2 independent assumptions must be made.

Finally, the solution should meet all conditions of acceptability: 1) all normal stresses should be compressive, 2) shear stresses must not exceed the maximum shear strength as predicted by the selected failure criterion, and 3) lines of thrust of normal forces must be physically admissible.

6.3 METHODS OF LIMIT EQUILIBRIUM ANALYSIS

The first widely applied method of slices was introduced by Fellenius in 1936. Since that time many variations have been developed, each using a different set of assumptions to make the problem statically determinate. Possible sets of assumptions include:

- n points of application of base normal forces.
- n-1 points of application of interslice normal forces.
- n-1 functional relationships between the magnitudes of interslice normal forces and interslice shear forces.

A method is considered *rigorous* when the solution satisfies all conditions of equilibrium in every slice and *simplified* when all conditions of equilibrium are not satisfied in one or more slices. In order to obtain a *rigorous* solution the number of assumptions made must exactly equal the number of unknowns (e.g. Sarma method) or an iterative procedure must be used to find a solution that satisfies all assumptions as well as all equations of equilibrium (e.g. Bishop's Rigorous method). In *simplified* methods one extra assumption is introduced to facilitate the theoretical or computational effort necessary to obtain a solution (e.g. Janbu Generalized Procedure), or some equilibrium conditions are not considered (e.g. Fellenius). When the number of assumptions exceeds the number of unknowns then the problem becomes over-constrained and a solution that satisfies all conditions of equilibrium cannot, in general, be obtained. In practice, simplified methods have been widely accepted for design studies because they markedly reduce the computational effort, while yielding factor of safety results that are only a few percent in error from rigorous analyses for many failure surface geometries (Bishop, 1955, Morgenstern, 1965). The most popular methods of slices and the underlying assumptions were reviewed by Duncan (1973), Fredlund (1977,1981) and Sarma (1979). Key points presented in these discussions are summarized in *Table 6.2* and examined in greater detail below.

Table 6.2 Methods of Slices and Associated Assumptions

METHOD	RIGOROUS SIMPLIF.	NUMBER UNKNOWNS	NUMBER EQTNS.	NUMBER ASSUMPTS.	ASSUMPTIONS
Fellenius	simplified	*2n+1*	*2n+1*	*0*	Interslice shear forces X_i and interslice normal forces N_i are assumed equal to 0. Moment equilibrium of slices not considered in analysis.
Bishop Simplified	simplified	*6n-2*	*4n-1*	*2n-1*	Interslice shear forces X_i are assumed equal to 0, line of thrust of base normal forces is assumed to pass through center of slice base (L_i specified). Horizontal equilibrium of slices not considered in analysis.
Bishop Rigorous	rigorous	*6n-2*	*4n*	*2n-1*	Magnitudes of interslice shear forces X_i are assumed, lines of thrust of base normal forces L_i must pass through center of slice base. Iterative procedure is used to find a set of X_i that satisfy all equilibrium conditions.
Janbu Generallized Procedure	simplified	*6n-2*	*4n-1*	*2n-1*	Line of thrust of base normal forces L_i must pass through center of slice base, points of application of interslice normal forces Z_i are assumed. Moment equilibrium equation for last slice *n* is not utilized.
Morgenstern and Price	rigorous	*6n-1*	*4n*	*2n-1*	Line of thrust of base normal forces L_i must pass through center of slice base. Additional unknown Ω is introduced so number of equations plus assumptions will equal number of unknowns. Functional relationship between interslice shear forces and interslice normal forces is specified ($X_i = \Omega f(x) E_i$).
Spencer	rigorous	*6n-1*	*4n*	*2n-1*	Line of thrust of base normal forces L_i must pass through center of slice base. Functional relationship between interslice shear forces and interslice normal forces of form $X_i = E_i \tan(\Theta)$ is assumed. Iterative procedure is then used to find a value of Θ that satisfies all equilibrium equations.
Sarma	rigorous	*6n-2*	*4n*	*2n-2*	Line of thrust of interslice normal forces Z_i must pass through center of slice side. Shear strength on interslice boundaries assumed to be fully mobilized; functional relationship between X_i and E_i given by Mohr-Coulomb failure criterion.

6.3.1 FELLENIUS METHOD

As one of the earliest and simplest method of slices algorithms, the Fellenius method assumes that no interslice forces are present. Furthermore, because moment equilibrium of the slices is not considered in the analysis the points of application of the base normal forces L_i need not be established. Under these assumptions the total number of unknowns is $2n+1$:

• normal forces N_i	n
• shear forces T_i	n
• factor of safety	1
total	$2n+1$

Equations used to solve for the unknowns include:

• force equilibrium in normal direction	n
• force equilibrium in shear direction	n
• definition of factor of safety	1
total	$2n+1$

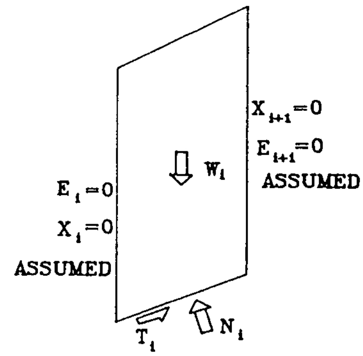

Figure 6.4 Force Distribution - Fellenius Method

Calculation of factor of safety proceeds as follows:

- calculate base normal forces N_i from force equilibrium in normal direction.
- calculate base shear forces T_i from force equilibrium in shear direction.
- calculate factor of safety F from the shear strength definition of factor of safety (*Equation 6.2).*

The method is general, in that it can be applied to two dimensional failure surfaces of any geometry. Although vertical slice sides are implied in the original development, inclined slice boundaries can also be invoked. Because the method does not satisfy moment equilibrium in each slice it is a simplified method of solution. Due to the simplifying assumptions made the method underestimates the factor of safety by 5 to 20 percent (Craig, 1979).

6.3.2 BISHOP'S RIGOROUS METHOD

This algorithm, restricted to analysis of truly circular failure surfaces and vertical slice boundaries, was the first to fully satisfy all conditions of equilibrium. In Bishop's rigorous method the magnitude of all *n-1* interslice shear forces X_i is assumed. To ensure that all lines of thrust of base normal forces pass through the center of the failure circle, the method further assumes that all n base normal forces are applied at the center of each linear slice base as illustrated in *Figure 6.5.* A total of *2n-1* assumptions is made. The full set of *6n-2* unknowns and *4n* equations listed in *Table 6.1* is utilized in this method. Because one extra assumption is made a closed form solution for all unknowns cannot be achieved. Instead, an iterative procedure is utilized whereby the assumed magnitudes of interslice shear forces are systematically adjusted until all conditions of equilibrium are satisfied. The solution strategy utilized by Bishop is:

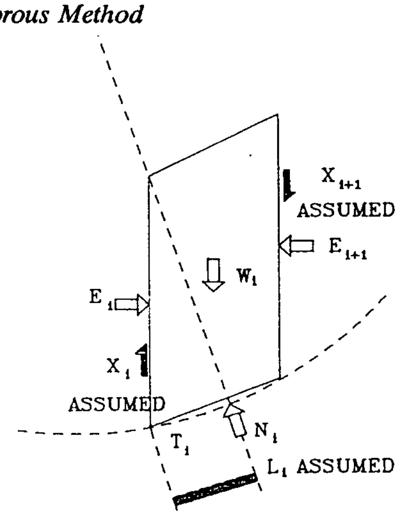

Figure 6.5 Force Distribution - Bishop's Rigorous Method

- assume line of thrust of base normal forces L_i
- assume magnitude of interslice shear forces X_i
- calculate base normal forces N_i from vertical force equilibrium. Use Mohr - Coulomb relationship to express T_i in terms of N_i.
- calculate base shear forces T_i from Mohr-Coulomb failure criterion.
- calculate interslice normal forces E_i from horizontal force equilibrium of first *n-1* slices.
- calculate factor of safety *F* from overall moment equilibrium about center of circle.
- calculate line of thrust of interslice normal forces Z_i from moment equilibrium of individual slices.
- check tangential equilibrium of final slice, if not satisfied adjust magnitudes of assumed X_i and repeat iterative procedure.

6.3.3 BISHOP'S SIMPLIFIED METHOD

Figure 6.6 Force Distribution - Bishop's Simplified Method

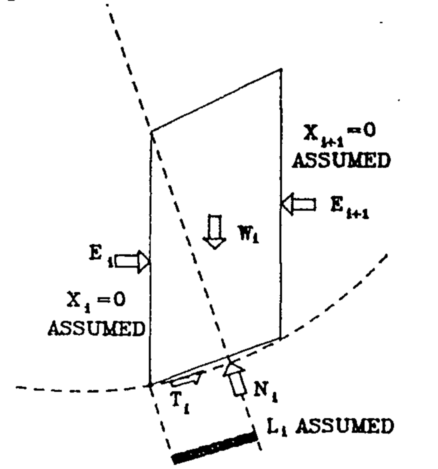

Prior to the introduction of computers, the iteration process of adjusting interslice shear forces proved too time consuming to make Bishop's Rigorous method practical. However, while conducting trial analyses with the new method, Bishop observed that after the initial estimate of X_i, the factor of safety typically changed by less than 1 percent as a result of subsequent adjustments to the interslice shear forces. Bishop recognized that his simplified procedure yielded acceptable values of *F* at a fraction of the computational effort, and could be used as a convenient and routine method for slope stability assessments.

The original Bishop Simplified algorithm is again restricted to truly circular failure surfaces and vertical interslice boundaries. However, Fredlund (1975) has extended the procedure to include non-circular problems. The assumptions used include: *n-1* assumptions that all interslice shear forces X_i are equal to zero (resultants of all interslice forces are horizontal), and *n* assumptions that lines of thrust of all base normal forces pass through the centers of the slice bases and the center of the failure circle. The total number of assumptions is *2n-1*. The following procedure is used by Bishop to calculate *F*:

- Vertical force equilibrium is used to calculate *Ni*, the Mohr-Coulomb failure criterion is invoked to express T_i in terms of N_i in the equation.
- Mohr-Coulomb equation is used to obtain T_i.
- Moment equilibrium of all external forces about the center of the failure circle is then invoked to solve for *F*.

In order to obtain *F*, the Bishop Simplified procedure uses *2n+1* equations to solve for *2n+1* unknowns. The magnitude of interslice normal forces E_i and their point of application, Z_i must be obtained only if the analyst wishes to check whether the solution is acceptable. In that case, horizontal equilibrium of the first *n-1* slices is used to solve for E_i, and moment equilibrium of the first *n-1* slices is used to obtain Z_i. *2n-1* assumptions and only *4n-1* of the *4n* available equations are invoked to solve for the *6n-2* unknowns. Because the final equation, horizontal equilibrium of slice *n*, is not met the solution is not rigorous. However, the resulting error is small for circular failure surfaces and the factor of safety obtained with Bishop's Simplified method is generally acceptable (Sarma, 1979, Wright, 1973).

6.3.4 JANBU'S GENERALIZED PROCEDURE

Figure 6.7 Force Distribution - Janbu's Generalized Method

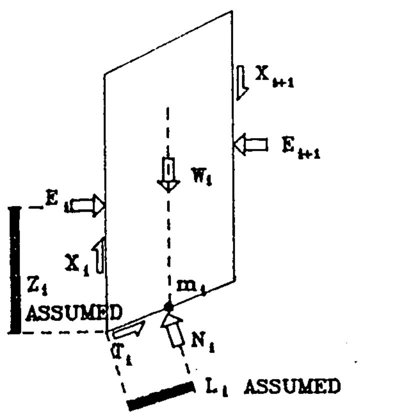

Janbu's method, introduced in 1954, is a method of slices capable of analyzing any general failure surface. For a time it was believed that the method satisfied all conditions of equilibrium (Janbu, 1957, Duncan 1973). In subsequent years it was recognized that the method failed to satisfy moment equilibrium of the final slice (Morgenstern, 1965; Sarma, 1979); therefore, it could not be considered a rigorous solution. This did not detract from the method finding wide application in practice because predicted factors of safety seemed accurate and computations based on the working formulae developed by Janbu were sufficiently simple for all calculations to be performed by hand. It was not until eleven years later that Morgenstern (1965) developed a truly rigorous, generalized method of slices. By comparing his results to those predicted by Janbu's method he was able to show that failure to satisfy all conditions of equilibrium could result in the factor of safety being in error by as much as 8% in certain cases.

To make the problem statically determinate, the Janbu method assumes that the line of thrust of the base normal force passes through the point m_i, defined by the intersection of the line of thrust of the weight vector and the slice base, as shown in *Figure 6.7.* The method also assumes that the point of application of each interslice normal force E_i is known, specified by Z_i. The total number of assumptions is $2n-1$. Since one extra assumption is made the method is not rigorous.

The solution strategy used by Janbu proceeds as follows:

- A new parameter t is defined as the rate of change in the magnitude of interslice shear force X as a function of horizontal position x. $t = \delta X/\delta x$.
- To start the iterative process it is assumed that $t=0$; therefore, the magnitude of X_i is constant for all slices.
- Vertical force equilibrium is used to solve for the base shear forces T_i. The Mohr-Coulomb equation is used to express N_i in terms of T_i.
- The Mohr-Coulomb equation is invoked to solve for N_i.
- Horizontal force equilibrium of the first $n-1$ slices is used to solve for interslice normal forces E_i.
- Moment equilibrium of the first $n-1$ slices is used to solve for new values of X_i.
- Using the new values of T_i, new values of the spatial derivative t_i are calculated. If the values do not match the initial assumed values then the iterative cycle is repeated until t converges.
- Finally, F is calculated from overall horizontal force equilibrium (a linear combination of horizontal equilibrium of final slice and equilibrium of all other slices that has already been satisfied).
- The only remaining equation, moment equilibrium equation of the final slice, is not used or satisfied.

6.3.5 METHOD OF MORGENSTERN AND PRICE

The algorithm of Morgenstern and Price, introduced in 1965, was the first to provide geotechnical engineers with a fully rigorous method of slices capable of analyzing failure surfaces of any arbitrary shape. To make the problem statically determinate, the method assumes that each of n base normal forces are applied at m_i, the point defined by the intersection of the slice base and the line of thrust of the weight vector W_i, as illustrated in *Figure 6.8.* Morgenstern and Price also assume that interslice shear forces and interslice normal forces can be related by:

$$X_i = \Omega f(x) \cdot E_i \qquad \textit{Equation 6.3}$$

A reasonable form of the function $f(x)$ must be specified as the first step in the analysis. The functional form can be derived from elastic theory, in-situ stress measurements, or based on the intuitive assumption that the ratio between shear and normal forces at the slice interface should increase with increasing curvature of the failure surface, as illustrated in *Figure 6.9.* Morgenstern and Price (1965) found that the factor of safety is not sensitive to the form of $f(x)$ as long as the function is reasonable.

Figure 6.8 Force Distribution - Morgenstern-Price Method

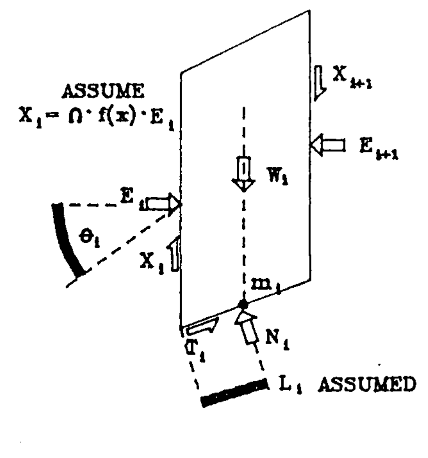

Since the number of equations available *is 4n* and the number of assumptions made is *2n-1* an extra unknown, Ω, is introduced in order to match the number of unknowns to the number of available equations and assumptions (*6n-1*). The value of Ω is calculated in the solution process.

The solution procedure is outlined below; the reader is referred to the original paper by Morgenstern and Price (1965) for a complete description.

Figure 6.9 Function f(x) Relating Interslice Shear and Normal Forces

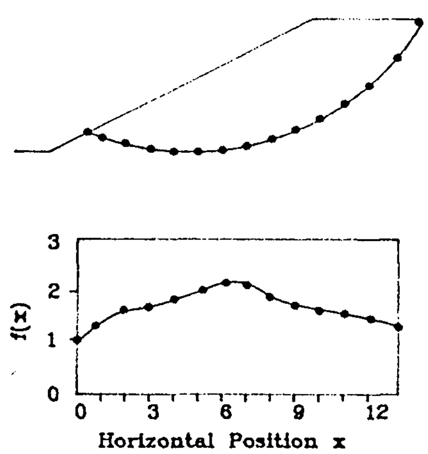

- Slope is divided into a finite number of slices, separated by vertical boundaries.
- The form of function $f(x)$ is specified.
- For each slice, equations for moment equilibrium about point m_i, force equilibrium in normal direction, force equilibrium in shear direction and Mohr-Coulomb failure criterion are combined to produce two governing differential equations. The first equation contains unknowns E_i, F, and Ω and numerous geometry defined parameters. The second equation contains unknowns E_i and Z_i.
- Initial values of F and Ω are assumed.
- The first governing differential equation is integrated over each slice to calculate the magnitude of E_i at each slice interface.
- Once E_i is established the second governing differential equation is used to calculate the point of application of the interslice normal forces Z_i.
- The computed value of E_n is compared with the boundary condition on the final slice. If the computed force does not match the boundary condition F and Ω are systematically adjusted and the solution process is repeated until convergence is obtained.

Because the method involves an iterative procedure that requires simultaneous adjustment of two parameters the solution procedure is complex and computationally demanding. For circular surfaces, the factor of safety obtained with this method compares favourably with Bishop's Simplified method, even though the assumed internal stress distributions are markedly different. Internal deformation is much more prevalent in non-circular failures; therefore, F becomes more sensitive to stress conditions on internal slice boundaries. It is not surprising that factor of safety values obtained by the rigorous method of Morgenstern - Price can differ by as much as 8% from values predicted by simplified methods that make less realistic internal stress assumptions.

6.3.6 SPENCER'S METHOD

Spencer's rigorous method, first introduced in 1967, relies on some key findings published by Morgenstern and Price only two years before. In their method of analysis, Morgenstern and Price assume that interslice shear and normal forces are related by the equation:

$$X_i = \Omega f(x) E_i \qquad \textit{Equation 6.4A}$$

They conclude that the factor of safety is not sensitive to the form of assumed function $f(x)$ as long as the function is reasonable. In essence, Morgenstern and Price specify that the resultant of interslice forces at each slice boundary is oriented at angle θ_i, given by:

$$\theta_i = Arctan(X_i/E_i) \qquad \textit{Equation 6.4B}$$
$$= Arctan(\Omega f(x))$$

Since different values of $f(x)$ can be specified at each interslice boundary, the orientations of interslice resultants can differ.

Figure 6.10 Force Distribution - Spencer's Method

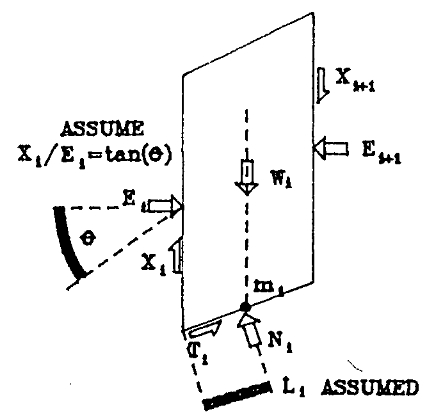

Spencer's method assumes that all interslice resultant forces are oriented at the same angle θ (see *Figure 6.10*). The actual value of θ is not specified; rather, the angle is introduced as an extra unknown that must be determined as part of the solution procedure. As in the Morgenstern - Price method, Spencer assumes that the lines of thrust of each base normal force N_i pass through the point m_i, defined by the intersection of the slice base and the line of thrust of the weight vector W_i. The total number of assumptions is $2n-1$ and the standard $4n$ equations are available. Since θ is introduced as an extra unknown the total number of unknowns is $6n-1$; because the number of equations and assumptions matches number of unknowns exactly the solution is rigorous.

The iterative solution procedure developed by Spencer is considerably simpler than the procedure of Morgenstern and Price as only one parameter is adjusted. Although originally developed to analyze circular slopes, Wright (1974) extended the procedure accomodate non-circular failure modes. The solution strategy is:

- Circular slope is divided into a finite number of slices, separated by vertical boundaries.
- An initial value of angle θ is assumed.
- For each slice, equations for force equilibrium in normal direction, force equilibrium in shear direction and Mohr-Coulomb failure criterion are combined to develop an expression for Q_i, the resultant of all internal body forces acting on slice *i*. Each equation contains unknowns θ, F, and numerous known geometry defined parameters.
- Using the assumed value of θ, Spencer's method invokes overall force equilibrium of internal forces in direction θ to calculate F_{force} and overall moment equilibrium about the center of the failure circle to calculate F_{moment}.
- The two factors of safety, F_{force} and F_{moment} are then checked for convergence. If they do not match then θ is adjusted and the entire calculation procedure is repeated until convergence is achieved. The two factor of safety functions and the point of intersection that defines the true values θ and F are illustrated in *Figure 6.11.*
- Once θ and F are established, the remaining unknowns E_i, X_i, Z_i, N_i and T_i are calculated by invoking force and moment equilibrium equations and assumptions for each slice.

Figure 6.11 Relationship Between Factor of Safety and Resultant Angle θ

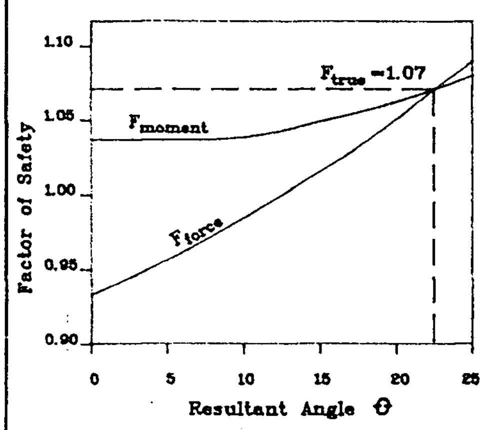

6.3.7 SARMA'S METHOD

Figure 6.12 Force Distribution - Sarma's Method

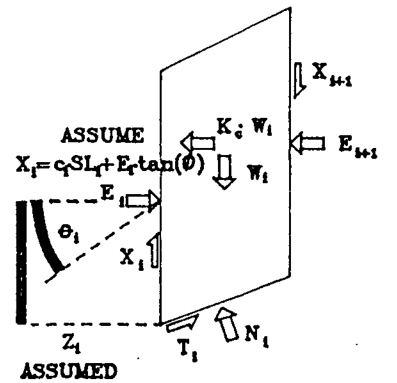

Sarma's method, introduced in 1979, is a rigorous two dimensional method of slices that incorporates the most of the desirable features of the aforementioned methods in a single algorithm, including analysis of non-circular failure surfaces and geologically complex, heterogeneous slopes. In addition, Sarma's method provides two very useful features that were not previously available: 1) because inclined slice boundaries are permitted the method can analyze slopes where internal deformation will occur along existing planes of weakness within the rockmass, and 2) because the method results in a system of *6n-2* linear equations in *6n-2* unknowns, the solution algorithm is conceptually simple and computationally efficient.

To make the stability problem statically determinate Sarma's Method assumes that the point of application of each interslice normal force E_i is located in the center of the slice boundary, and interslice shear and interslice normal forces are related by the Mohr-Coulomb failure criterion. The total number of assumptions made is *2n-2*.

Sarma's method introduces a new dimensionless stability indicator, critical horizontal acceleration K_c. The product of critical horizontal acceleration and slice weight, $K_c \cdot W_i$, defines an extra, non existent horizontal force (e.g. seismic loading) that would have to be applied to each slice to bring about a condition of limiting equilibrium. The force is assumed to act through the center of mass of each slice, as illustrated *Figure 6.13*. If K_c is positive, the extra force $K_c \cdot W_i$ is applied in the direction of slip; since an extra destabilizing force is required to induce a condition of incipient failure the slope is stable when the extra force is not present. On the other hand, if K_c is negative the extra force force would have to be applied in the direction opposing slip to prevent failure and the slope is unstable. When K_c is equal to zero, the slope is in a state of limiting equilibrium ($F=1$). Because K_c replaces F as the stability indicator the total number of unknowns remains *6n-2*.

Although K_c and F are equally valid indicators of slope stability, analysis results presented in terms of F are much more useful because a very large number of case histories, experimental studies, and empirical design procedures have evolved around this parameter. To address this concern, Sarma (1979) developed an iterative procedure that can be used to calculate F once K_c and all unknown forces are established. By comparing results of a large number of stability analyses Sarma and Bhave (1974) also derived an approximate linear relationship between K_c and F. Both procedures will be examined in greater detail in *Section 6.4.3*.

Since factor of safety is defined as a ratio of mobilized shear stress divided by shear strength, it always leads to complex, non-linear equations for F that contain a ratio of two or more unknown forces. A closed form solution to these equations cannot in general be achieved; therefore, most rigorous methods based on the factor of safety expression use some form of iterative procedure to solve the equations. K_c on the other hand, appears only as an extra unknown external force on each slice. Since it is not multiplied or divided by any other unknowns all equilibrium equations remain linear; the solution of these equations is straight forward.

The solution strategy utilized by Sarma (1979) and Hoek (1986) is outlined below. It combines force equilibrium and Mohr-Coulomb equations to form a single closed form expression for K_c. Moment equilibrium equations can be invoked after K_c is calculated to determine the point of application of base normal forces and check whether the solution is acceptable.

- Slope is divided into finite number of slices. Slice boundaries can be inclined.
- Geometric relationships are utilized to compute known body forces that include slice weight, groundwater forces on the slice base, and groundwater forces on the slice sides. The points of

application of these forces are also computed.

- Equations for horizontal force equilibrium, vertical force equilibrium, Mohr-Coulomb failure criterion on slice bases, and the assumed Mohr-Coulomb relationship between interslice shear forces are combined and manipulated into one closed form equation that can be solved for K_c.
- Once K_c is known a derived recurrence equation can be invoked to solve for interslice normal forces E_i. The failure criterion relationships and force equilibrium equations for each slice can then be used to determine the magnitudes of the other unknown forces X_i, N_i, and T_i. (Note: alternately, the entire system of linear equations can be solved simultaneously for all unknowns with an equation solver program such as LU decomposition.)
- The point of application of each base normal force L_i can be computed from the moment equilibrium equations for each slice.
- An acceptability check is conducted to confirm that all normal stresses should be positive and the points of application of the base normal forces must fall on the slice base, preferably in the middle third.

6.3.8 SELECTION OF METHOD FOR INCORPORATION IN FRAMEWORK

Selection of the most useful method of stability analysis for incorporation in this risk-cost-benefit framework was a two step process. First, a list containing all essential features was compiled, then a process of elimination was used to select the best method. The list of desirable attributes is presented below, the features are listed in relative order of importance. A brief explanation indicating why each feature was considered necessary is also given.

- It should be possible to analyze any general failure surface, including planar, circular and non-circular failure modes. Failures in weakly to moderately fractured rock develop along one or more pre-existing discontinuities. Failures in homogeneous materials including highly fractured rock, soil slopes and waste dumps will fail in a circular fashion. Since both types of geologic conditions are anticipated in mine environments the method of analysis must be general.
- The method must be rigorous. Because simplified methods do not satisfy all conditions of equilibrium, factor of safety and/or probability of failure estimates can be significantly in error. An error in the probability of failure estimate will lead to an erroneous estimate of monetary risk. Ultimately, the error could result in the wrong design procedure being selected.
- The method must be computationally efficient. A solution algorithm that relies on an iterative procedure should be avoided if possible. Computational efficiency is essential because a very large number of stability analyses must be performed during a single Monte-Carlo simulation.
- The method must be capable of computing factor of safety when required so well established pit design procedures based on factor of safety can be referenced.
- It must be possible to specify different shear strength parameters on each slice base and side so geologically complex, heterogeneous slopes can be analyzed.
- Inclined slice boundaries should be permitted. It will then be possible to accurately analyze rock slopes where internal deformation will occur along known planes of weakness within the failure block.
- Some form of search procedure for the critical failure surface must be allowed. This step is important when dealing with highly fractured rocks or soils where the likely failure surface cannot be predicted by geotechnical investigation techniques.

The first two selection criteria precluded Bishop's, Fellenius' and Janbu's methods from further consideration. The selection was thus restricted to the methods of Morgenstern - Price, Spencer, and Sarma. Of these three, Sarma's method was selected because it appeared to be the simplest and most efficient algorithm. It was anticipated that development of a computer program based on Sarma's algorithm would be straight forward, as would linking of the stability program to a finite element groundwater flow model that predicted pore pressures in the pit wall.

It should be noted that the general limit equilibrium method (Fredlund, 1983) incorporates many of the aforementioned limit equilibrium slope stability methods into a unified software framework that is ideal for comparing and evaluating the individual methods. Comparison of the results provided by Sarma's method to the results generated by this methods in the general package is a future research objective for this author.

6.4 MECHANICS OF SARMA'S METHOD

A new computer program, *SG-Slope*, was developed, verified, and then incorporated into the framework presented in this thesis. Although the program is based on the methodology introduced by Sarma (1979) and expanded by Hoek (1986), it deviates significantly from the closed form solution approach presented in those papers. Instead, the system of linear equations is solved directly with an LU (lower-upper) decomposition scheme. The governing equations and the numerical procedure used by *SG-Slope* to obtain a solution are reviewed in *Sections 6.4.1 and 6.4.2.*

The importance of calculating the factor of safety F, as well as K_c has been discussed. A singular point is always present in the function relating the two stability indicators. When this singular point occurs near K_c some iterative procedures for calculating F (e.g. Hoek, 1986) may become unstable. A new iterative procedure was developed to overcome the problem of instability. The procedure is described in *Section 6.4.3.*

The occurrence of negative normal stresses on any slice side or base renders a solution unacceptable. *Section 6.4.4* examines the most common causes of negative stress problems and suggests some simple remedies. Sarma (1979) and Hoek (1986) briefly mentioned that the factor of safety can be sensitive to the orientation of slice boundaries. *Section 6.4.4* explores this problem in more detail, and suggests some guidelines for selecting the most appropriate slice orientation.

A solution is also unacceptable if the calculated line of thrust of any base normal force fails to pass through the corresponding slice base. *Section 6.4.5* reviews the common causes of moment acceptability problems and suggests several rules of thumb to reduce the likelihood that such problems develop.

6.4.1 GOVERNING EQUATIONS

In *Section 6.3* it was stated that Sarma's method leads to a system of *6n-2* equations in *6n-2* unknowns. Six equations are associated with each slice i: 1) horizontal equilibrium, 2) vertical equilibrium, 3) Mohr-Coulomb criterion on slice base, 4) assumed Mohr-Coulomb Criterion on slice side, 5) assumed line of thrust of interslice normal force E_i, and 6) moment equilibrium. Each equation will be derived for a general slice i, illustrated in *Figures 6.13 & 6.14*. All unknown forces and lines of thrust acting on slice i are defined in *Figure 6.13*, the *6* unknowns actually associated with slice i are highlighted with solid fills. *Figure 6.14* defines all known body forces and their points of application. The forces include slice weight, groundwater forces, and external applied forces such as tensioned cable anchors.

Figure 6.13 Unknowns Associated with Slice i

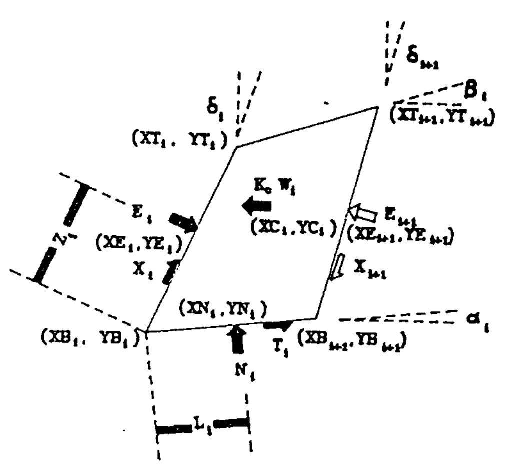

Figure 6.14 Known Forces and Points of Application - Slice i

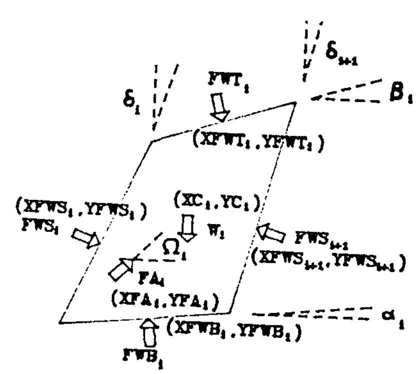

Before proceeding with the main derivations, it is necessary to adopt several conventions concerning the indexing of unknowns and expected directions of thrust.

- The left side of slice i is called side i, the right side is side $i+1$.
- Interslice forces acting on the left side of slice i are associated with that slice, interslice forces acting on the right side are associated with slice $i+1$.
- Slices are numbered sequentially from left to right starting with slice 1 at the toe of the slope, proceeding to slice n at the crest.
- The positive direction of all forces is indicated by the arrows in *Figure 6.13*. If negative magnitudes are calculated for any force, then the actual direction of thrust is reversed.

It is also necessary to express the coordinates of each body force in terms of user specified corner point coordinates XB_i , YB_i , XT_i , YT_i. (XFA_i, YFA_i) are given. Expressions for (XE_i, YE_i) and (XN_i, YN_i) are obtained from elementary geometric relationships *(Equations 6.5 & 6.6)*. Expressions for the center of mass (XC_i, YC_i), and the points of application of the water forces $(XFWB_i, YFWB_i)$, $(XFWS_i, YFWS_i)$, $(XFWT_i, YFWT_i)$ are obtained by calculating the centroid of the appropriate surface area or water pressure distribution. A general subroutine that calculates the area and centroid of any closed prism was developed and incorporated in *SG-SLOPE* for this purpose.

$$XE_i=(XT_i - XB_i)/2 \qquad \textit{Equation 6.5A}$$
$$YE_i=(YT_i - YB_i)/2 \qquad \textit{Equation 6.5B}$$
$$XN_i=XB_i+L_i\cdot cos(\alpha_i) \qquad \textit{Equation 6.6A}$$
$$YN_i=YB_i+L_i\cdot sin(\alpha_i) \qquad \textit{Equation 6.6B}$$
$$SL_i=[(XT_i - XB_i)^2+(YT_i - YB_i)^2]^{1/2} \qquad \textit{Equation 6.7}$$
$$BL_i=[(XB_{i+1} - XB_i)^2+(YB_{i+1} - YB_i)^2]^{1/2} \qquad \textit{Equation 6.8}$$

The six controlling equations are given below. To facilitate solving the first four equations numerically all unknown variables are isolated on the left side; known forces are brought to the right.

Horizontal Equilibrium:

$$X_i\cdot sin(\delta_i)+E_i\cdot cos(\delta_i)-N_i\cdot sin(\alpha_i)+T_i\cdot cos(\alpha_i)-X_{i+1}\cdot sin(\delta_{i+1})-E_{i+1}\cdot cos(\delta_{i+1})-K_c\cdot W_i=HE_i \qquad \textit{Equation 6.9A}$$
$$HE_i=-FWS_i\cdot cos(\delta_i)+FWB_i\cdot sin(\alpha_i)-FWT_i\cdot sin(\beta_i)+FWS_{i+1}\cdot cos(\delta_{i+1})-FA_i\cdot cos(\Omega_i) \qquad \textit{Equation 6.9B}$$

Vertical Equilibrium:

$$X_i\cdot cos(\delta_i)-E_i\cdot sin(\delta_i)+N_i\cdot cos(\alpha_i)+T_i\cdot sin(\alpha_i)-X_{i+1}\cdot cos(\delta_{i+1})+E_{i+1}\cdot sin(\delta_{i+1})=VE_i \qquad \textit{Equation 6.10A}$$
$$VE_i=FWS_i\cdot sin(\delta_i)-FWB_i\cdot cos(\alpha_i)+FWT_i\cdot cos(\beta_i)-FWS_{i+1}\cdot sin(\delta_{i+1})-FA_i\cdot sin(\Omega_i) \qquad \textit{Equation 6.10B}$$

Mohr-Coulomb Failure Criterion - Slice Base:

$$T_i - N_i\cdot tan(\phi_{bi})=MCB_i \qquad \textit{Equation 6.11A}$$
$$MCB_i=c_{bi}\cdot BL_i - FWB_i\cdot tan(\phi_{bi}) \qquad \textit{Equation 6.11B}$$

Mohr-Coulomb Failure Criterion - Slice Side (assumed):

$$X_i - E_i\cdot tan(\phi_{si})=MCS_i \qquad \textit{Equation 6.12A}$$
$$MCS_i=c_{si}\cdot SL_i - FWS_i\cdot tan(\phi_{si}) \qquad \textit{Equation 6.12B}$$

Point of Application - Force E_i (assumed):

$$Z_i=0.5\cdot SL_i \qquad \textit{Equation 6.13}$$

ım: *Equation 6.14*

$$
\begin{aligned}
0= &- X_i \cdot sin(\delta_i) \cdot (YE_i - YB_i) + X_i \cdot cos(\delta_i) \cdot (XE_i - XB_i) \\
&- E_i \cdot cos(\delta_i) \cdot (YE_i - YB_i) - E_i \cdot sin(\delta_i) \cdot (XE_i - XB_i) \\
&+ N_i \cdot sin(\alpha_i) \cdot (YN_i - YB_i) + N_i \cdot cos(\alpha_i) \cdot (XN_i - XB_i) \\
&- T_i \cdot cos(\alpha_i) \cdot (YN_i - YB_i) + T_i \cdot sin(\alpha_i) \cdot (XN_i - XB_i) \\
&+ X_{i+1} \cdot sin(\delta_{i+1}) \cdot (YE_{i+1} - YB_i) - X_i \cdot cos(\delta_{i+1}) \cdot (XE_{i+1} - XB_i) \\
&+ E_{i+1} \cdot cos(\delta_{i+1}) \cdot (YE_{i+1} - YB_i) + E_{i+1} \cdot sin(\delta_{i+1}) \cdot (XE_{i+1} - XB_i) \\
&+ K_c \cdot W_i \cdot (YC_i - YB_i) - W_i \cdot (XC_i - XB_i) \\
&- FWS_i \cdot cos(\delta_i) \cdot (YFWS_i - YB_i) - FWS_i \cdot sin(\delta_i) \cdot (XFWS_i - XB_i) \\
&+ FWB_i \cdot sin(\alpha_i) \cdot (YFWB_i - YB_i) + FWB_i \cdot cos(\alpha_i) \cdot (XFWB_i - XB_i) \\
&- FWT_i \cdot sin(\beta_i) \cdot (YFWT_i - YB_i) - FWT_i \cdot cos(\beta_i) \cdot (XFWT_i - XB_i) \\
&WS_{i+1} \cdot cos(\delta_{i+1}) \cdot (YFWS_{i+1} + YB_i) + FWS_{i+1} \cdot sin(\delta_{i+1}) \cdot (XFWS_{i+1} - XB_i) \\
&- FA_i \cdot cos(\Omega_i) \cdot (YFA_i - YB_i) + FA_i \cdot sin(\Omega_i) \cdot (XFA_i - XB_i)
\end{aligned}
$$

L SOLUTION PROCEDURE

three step calculation procedure to solve for K_c and check on acceptability of the solution. ystem of *4n-1* linear equations is constructed, utilizing the first four governing equations for) internal forces are associated with side *1* the Mohr-Coulomb failure criterion for side *1* is system of equations can be written in matrix form:

$$[A_{ij}] \cdot \{U_i\} = \{RHS_i\} \qquad \textit{Equation 6.15}$$

matrix of known directional coefficients, $\{U_i\}$ represents the vector of *4n-2* unknown body nown K_c, and $\{RHS_i\}$ represents a vector of known force summations. *Table 6.3* illustrates n of equations for a general 3 slice problem.

decomposition subroutine is used to solve *Equation 6.15* for the vector of unknowns $\{U_i\}$. known forces are calculated during this step it is possible to determine whether the slope is the negative stress acceptability criterion is satisfied.

of Linear Equations for Sarma Method

X_2	E_2	N_2	T_2	X_3	E_3	N_3	T_3	K_c				
$in\,\delta_2$	$-cos\,\delta_2$	0	0	0	0	0	0	W_1		N_1		HE_1
$os\,\delta_2$	$sin\,\delta_2$	0	0	0	0	0	0	0		T_1		VE_1
	0	0	0	0	0	0	0	0		X_2		MCB_1
	$-tan\,\phi_{s2}$	0	0	0	0	0	0	0		E_2		MCS_2
δ_2	$cos\,\delta_2$	$-sin\,\alpha_2$	$cos\,\alpha_2$	$-sin\,\delta_3$	$-cos\,\delta_3$	0	0	W_2		N_2		HE_2
$s\,\delta_2$	$-sin\,\delta_2$	$cos\,\alpha_2$	$sin\,\alpha_2$	$-cos\,\delta_3$	$sin\,\delta_3$	0	0	0	$\cdot$	T_2	=	VE_2
	0	$-tan\,\phi_{b2}$	1	0	0	0	0	0		X_3		MCB_2
	0	0	0	1	$-tan\phi_{s3}$	0	0	0		E_3		MCS_3
	0	0	0	$sin\,\delta_3$	$cos\delta_3$	$-sin\,\alpha_3$	$cos\,\alpha_3$	W_3		N_3		HE_3
	0	0	0	$cos\,\delta_3$	$-sin\delta_3$	$cos\,\alpha_3$	$sin\,\alpha_3$	0		T_3		VE_3
	0	0	0	0	0	$-tan\,\phi_{b3}$	1	0		K_c		MCB_3

In the third step of the calculation procedure moment equilibrium is invoked for each slice to calculate the point of application of each base normal force, described by the unknown L_i. A final check is performed to confirm that each point (XN_i, YN_i) is located within the corresponding slice base. Once K_c is calculated and all acceptability criteria are satisfied an iterative subroutine may be summoned to evaluate the corresponding F.

6.4.3 ITERATION PROCEDURE TO CALCULATE *F*

Slope assessment results reported in terms of the familiar factor of safety are more useful to geotechnical and mining engineers than results reported in terms of K_c. Sarma (1979) showed that F_{actual} could be obtained by systematically adjusting shear strength on all slice surfaces by the ratio $1/F$ until the imaginary horizontal force required to maintain stability vanished, at point $K=0, F=F_{actual}$. When applying Sarma's method to a number of practical stability problems Hoek (1986) discovered that more than one value of F may satisfy the equations and *"under certain circumstances, the iteration technique used in this program (and all other iteration techniques tried during the development of the program) will choose the incorrect solution"*. This section examines the cause of the convergence problem and describes a new algorithm that successfully converged to the correct F in all cases tested.

The relationship between dimensionless acceleration K and F is illustrated in *Figure 6.15* for a typical slope analysis. The function relating the two parameters is discontinuous; a horizontal asymptote separates the upper, physically based portion of the curve from the lower mathematically related portion. Additional horizontal asymptotes may also appear in the lower part of the function to a maximum limit of one asymptote for each interslice boundary. For a given value of F there is only one corresponding value of K that satisfies all equations; but the converse is not true, for a given value of K several roots F may exist. As shown in *Figure 6.15*, the point K_c will always plot on the $F=1$ horizontal axis and F_{actual} will always plot on the $K=0$ vertical axis. Since the actual factor of safety is physically based it must also fall on the upper portion of the F vs K curve.

Figure 6.15 Functional Form Relating K and F

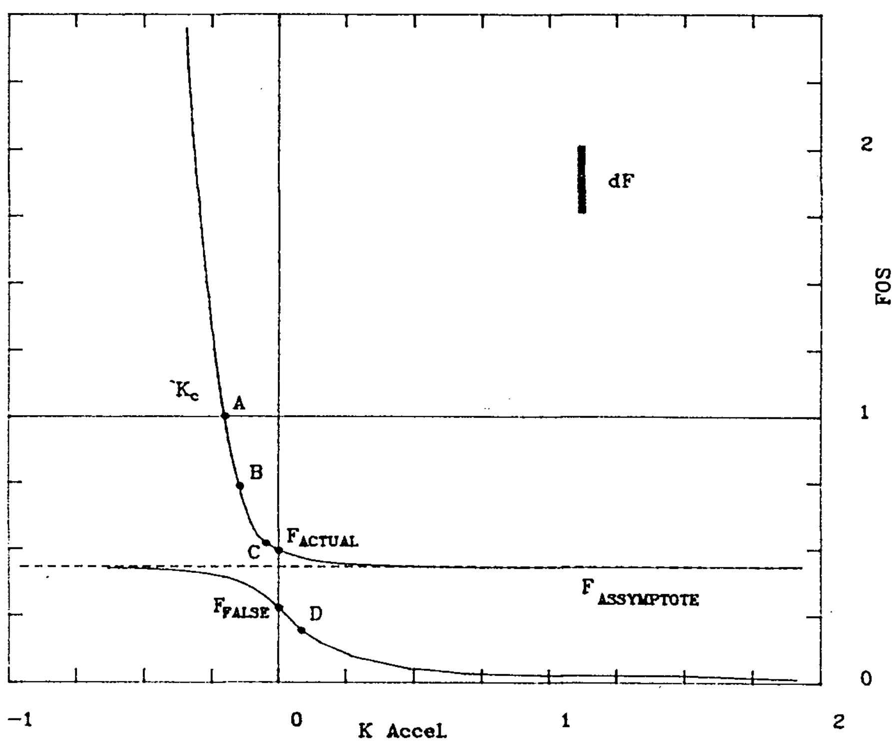

Conceptually, F_{actual} can be calculated by starting at the point $K_c, 1$, then gradually adjusting shear strength parameters on all slice boundaries by the ratio $1/F$ until the corresponding K vanishes. In *Figure 6.15* for example, K_c is negative, indicating that the slope is unstable; an imaginary horizontal force must be applied in the direction opposing slip to prevent failure. If the imaginary force is removed shear strength on all slice surfaces must be increased to maintain a condition of limiting equilibrium; therefore, F_{actual} must be less than unity. If F is gradually decreased to values F_A, F_B, F_C the desired point $K=0, F=F_{actual}$ will be systematically approached.

Numerical instability problems arise when F_{actual} is only slightly larger than $F_{asymptote}$. When the trial value of F falls below the unknown value $F_{asymptote}$, at point F_D for example, some iteration schemes may unknowingly jump across the discontinuity to the lower portion of the curve. The iteration process may then continue along the lower curve until the solution converges at F_{false}, the wrong factor of safety. Alternately, the iteration process can become unstable, bouncing back and forth between the upper and lower curves with ever increasing error. If an iteration scheme is to converge unconditionally to F_{actual} it must guarantee that F_{trial} never drops below $F_{asymptote}$ and the iterative process does not jump to the lower curve.

The actual cause of the first asymptote can be recognized when the magnitudes of interslice and base reaction forces are plotted as a function of F_{trial}. *Figure 6.17* shows these forces for an active-passive spoil pile failure illustrated in *Figure 6.16*. As F_{trial} is reduced from a starting value of *1.5*, the shear strength parameters are gradually increased by the ratio *1/F*. To satisfy the Mohr-Coulomb failure criterion the line of thrust of all base and side reaction force resultants must always be oriented at angle ϕ. As ϕ is increased the resultants must rotate as illustrated in *Figure 6.18*. At the same time the forces must also satisfy vertical and horizontal force equilibrium of the slice. When F_{trial} approaches $F_{asymptote}$ all three equations can be satisfied simultaneously only if the magnitude of all forces gets very large. At a critical point further reductions in F_{trial} result in a sudden reversal in the direction of the side and base resultants, generally from compressive to tensile stress conditions. To maintain horizontal equilibrium the direction of the imaginary horizontal force must change from a very large positive force to a very large negative force. In *Figure 6.15* the sudden force reversal appears as an asymptote; K jumps from a very large positive value to a very large negative value.

Figure 6.16 Geometry of Spoil Pile Failure

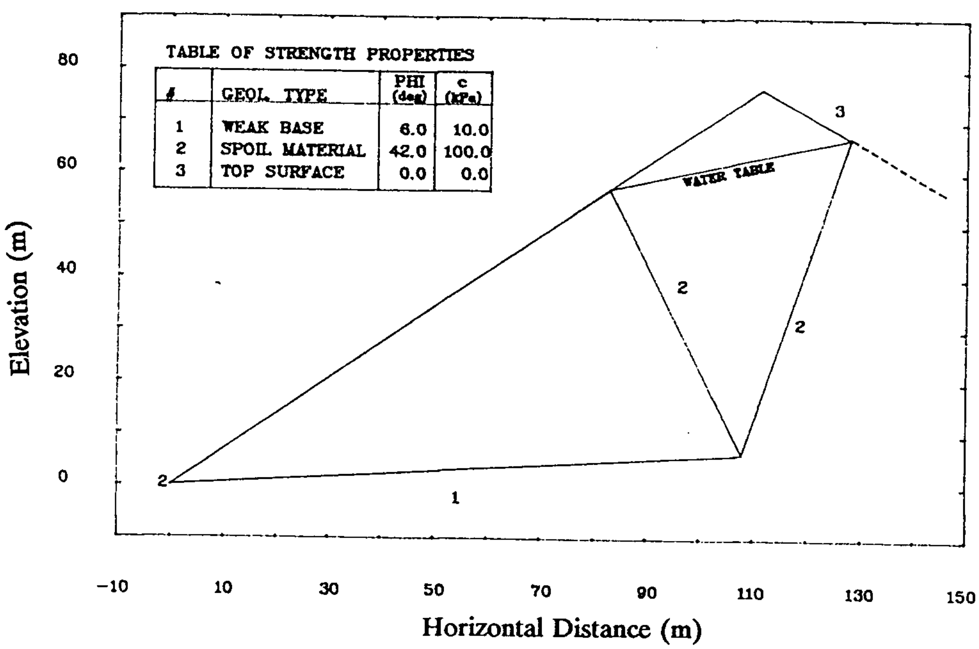

Figure 6.17 Magnitude of Reaction Forces with Changing FOS

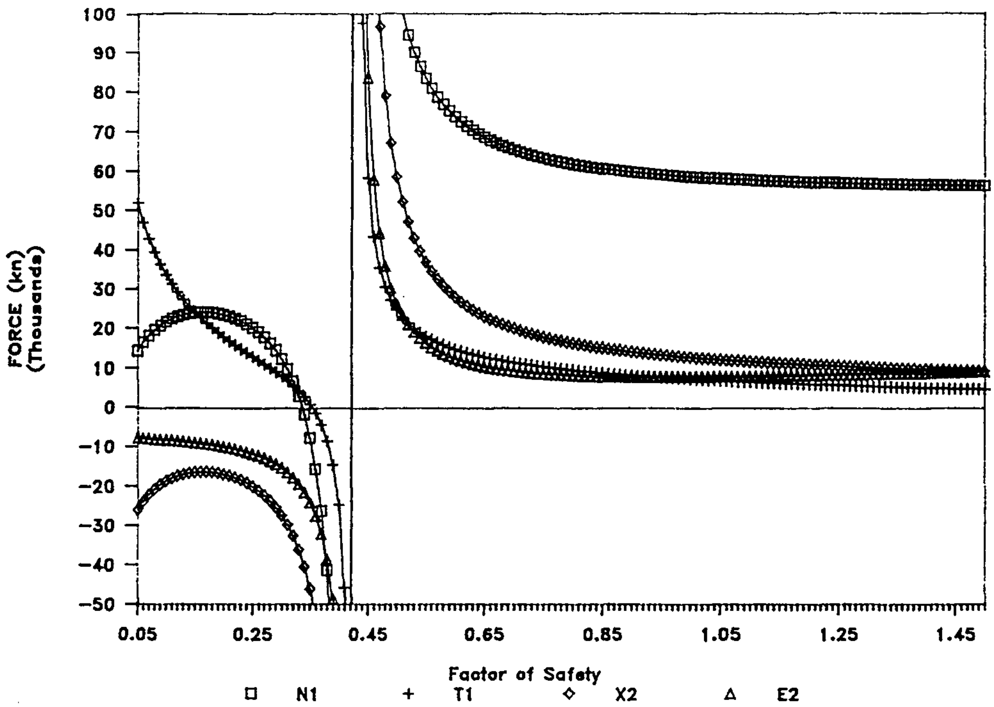

Figure 6.18 Force Vector Diagram For Slice 1

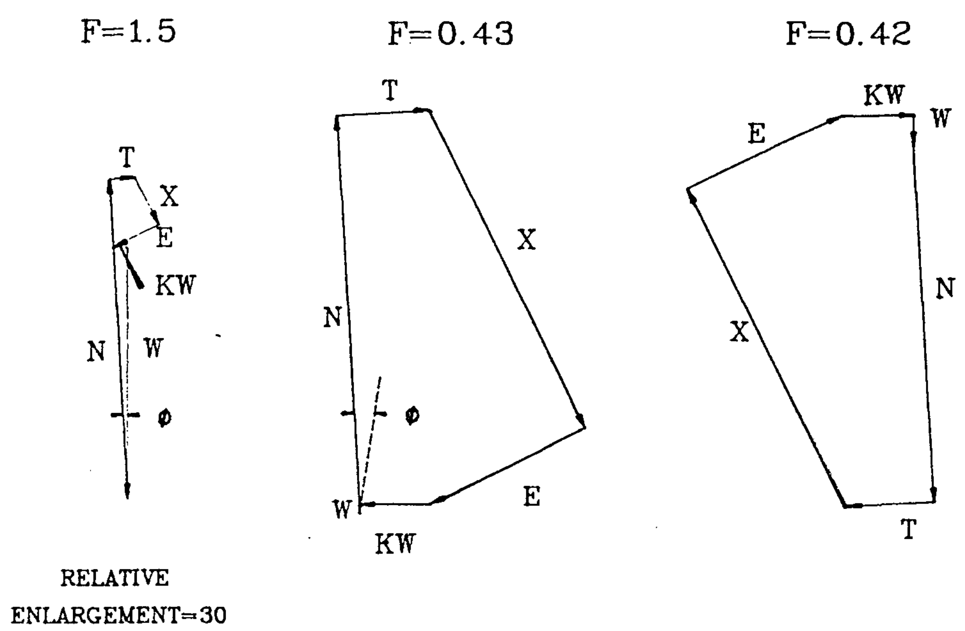

Two algorithms have been developed to detect the presence of an asymptote and eliminate the convergence problems encountered in all previous slope stability programs based on Sarma's method.

In the first procedure K values are calculated for ten regularly spaced values of F_{trial} between 0 and 2.5. Starting at the top of the physically based curve, the slope of each increment between adjacent trial points is calculated until the increment straddling $K=0$ is reached. If the slope of each increment tested is shallower (less negative) than the slope of the previous increment the curve is monotonic and all trial points likely fall on the upper, physically based curve. In that case the point $0,F_{actual}$ is located somewhere between the end points of the interval straddling $K=0$. An iterative linear interpolation scheme is used to quickly converge to that point. If on the other hand, the slope of any single increment becomes steeper (more negative) than the slope of the previous increment the lower trial point of that interval must have jumped to the lower curve. To prevent the jump from occurring dF is reduced by a factor of 5 and the iteration process is restarted at the upper trial point of the problem interval. In all cases tested, setting $dF=0.05$ was sufficient to ensure that F_{trial} values did not fall below $F_{asymptote}$ and the iterations always converged to F_{actual}.

Proximity to an asymptote can also be detected by a sudden increase in the sum of reaction force magnitudes, as illustrated in *Figure 6.19*. If the sum increases by more than 50% from the initial value calculated at $F_{trial}=2.5$ an asymptote is indicated and dF is reduced. Unfortunately, the band width of the force spike is narrow; therefore, the method is not 100% reliable since the presence of an asymptote can be missed if the sampling interval dF is wider than the band width of the spike.

Figure 6.19 Graph of Reaction Force Summation

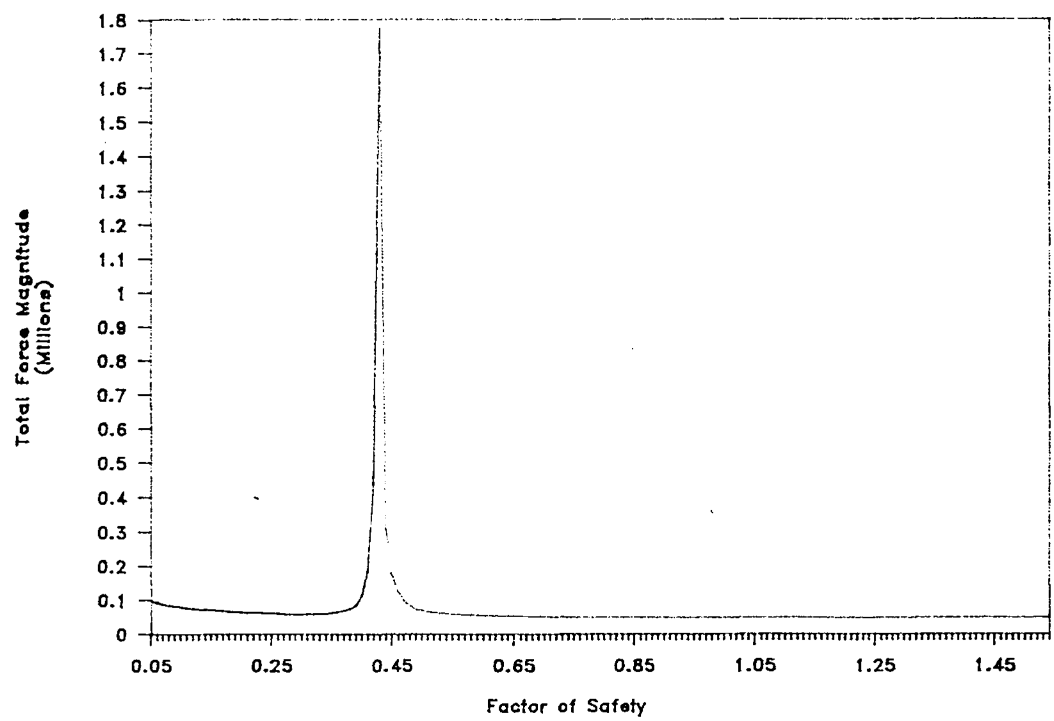

To provide fast, reliable convergence to the correct factor of safety *SG-SLOPE* uses both asymptote detection procedures in series. The less reliable force magnitude method is invoked first since it can often detect an asymptote as F_{trial} approaches $F_{asymptote}$, whereas the slope method can detect an asymptote only after F_{trial} drops below $F_{asymptote}$ to the lower curve. If an asymptote is detected by either method the iteration step dF is reduced.

In *Section 6.3.7* it was stated that F is more useful as a design parameter than K_c because a very large number of case histories, experimental studies and empirical design procedures have evolved around the factor of safety concept. Unfortunately, the iteration procedure for calculating factor of safety is computer time intensive since the system of force equations has to be solved repeatedly, once for each F_{trial} iteration. A 386 series computer requires approximately 15 seconds to 1 minute to converge to F_{actual}, depending on the number of slices and whether F_{actual} is close to the first asymptote. Since stochastic probability of failure analyses require assessments of stability for a large number of realizations of strength parameters and groundwater conditions the computational burden can become excessive, up to 17 hours on a 386 series processor for a Monte-Carlo simulation of 1000 realizations.

To calculate probability of failure more efficiently *SG-SLOPE* uses K_c instead of F to indicate whether a slope is stable or unstable for each Monte Carlo realization. The K_c procedure is more efficient because the system of force equations has to be solved only once for each realization instead of 5 to 20 times.

Sarma and Bhave (1974) identified an empirical relationship that can be used to estimate F_{actual} for design purposes if K_c is known. By calculating both K_c and F_{actual} for a large number of slopes and plotting results on an X-Y graph similar to *Figure 7-20* they observed that the two parameters were approximately linearly related, the equation that described the best fitting straight line through their data points is:

$$F = 3.333 * K_c + 1.000 \qquad \textit{Eqn. 6.16}$$

To test whether the relationship is valid for large rock slope failures of the type encountered in open pit mines both K_c and F_{actual} were calculated for nine large rock slides described in the literature. Each slide was analyzed under three different groundwater scenarios: dry, 50% saturated, and fully saturated. Results of the analyses are plotted in *Figure 7-20*. The small scatter in data points, especially in the principal region of interest between (K_c=*-0.1,F=0.7*) and (K_c=*0.1,F=1.3*) where slopes are metastable, confirms that an approximate linear relationship does exist. The best fitting straight line for the test data is given by:

$$F = 2.759 * K_c + 1.039 \qquad \textit{Eqn. 6.17}$$

Figure 6.20 F vs. K_c Scatter Plot

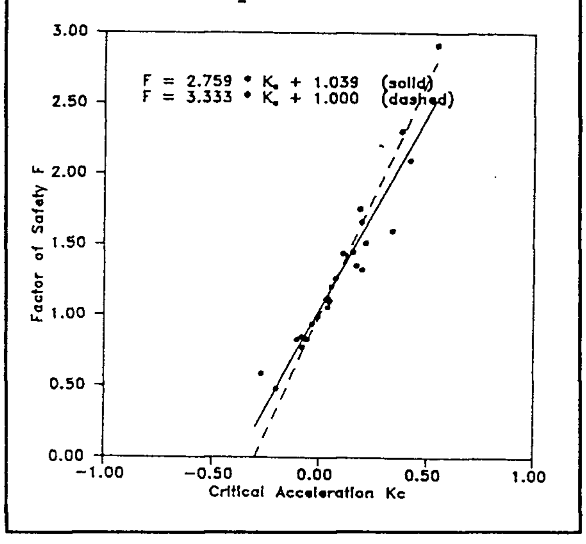

Figure 6.21 Error in Estimate of F

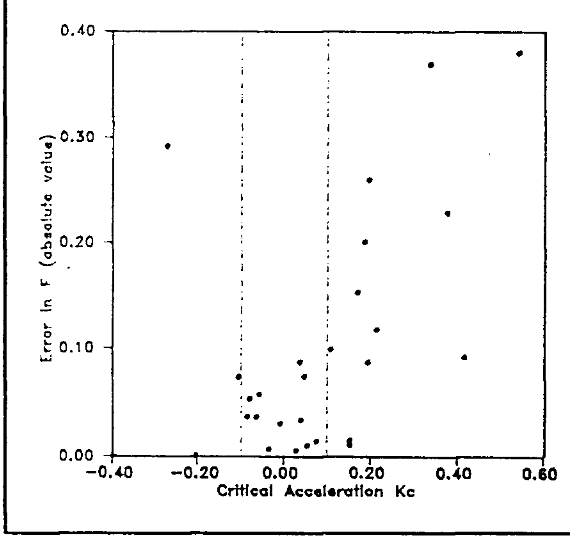

It can be seen in *Figure 6-20* that the difference in factor of safety as predicted by the two equations is not large in the principal region of interest. The difference in regression coefficients can probably be attributed to the fact that *Equation 6.17* is based on a small, less representative sample size than used by Sarma and Bhave, and the test equation was not constrained to pass through the theoretical point ($K_c=0.0, F=1.0$).

Figure 6-21 is a plot of the error in F as predicted by *Equation 6-16* when compared to the true factor of safety calculated by the iterative method. The figure shows that the linear equation is not reliable over the full range of K_c; the maximum error in F is as high as 0.4; however, in all test cases where K_c fell in the principal region of interest the error in estimating F by the linear equation was less than *0.1*. It can be concluded that estimates of the mean factor of safety based on the computationally efficient linear equation method provide additional useful information about the stability of a pit wall during stochastic analyses, but only in the range K_c=-0.1 to *0.1*. If K_c falls outside that range then the time demanding iteration technique must be used to obtain an accurate estimate of the mean factor of safety if such an estimate will allow the design engineer to make a more confident risk assessment.

6.4.4 ACCEPTABILITY PROBLEMS WITH NEGATIVE STRESS

Because Sarma's method uses equations of force and moment equilibrium to calculate the unknown slice forces, conditions of static equilibrium will always be satisfied. However, before F or K_c values calculated by *SG-SLOPE* can be used in a pit wall design the results must be checked to confirm that conditions of acceptability are satisfied; that the state of stress in the soil or rock slope is physically possible.

Because soils and fractured rock materials have very low tensile strength negative effective stresses cannot be supported. Under tensile or "negative" effective stress conditions the soil or rock particles are pulled apart at the grain contacts. As soon as negative stresses are applied tensile cracks develop in the materials and the stresses are dissipated through deformation. The first acceptability condition requires that all base and interslice normal effective stresses be positive.

If negative effective stress conditions are calculated on one or more slice bases or slice sides the corresponding F or K_c results must be considered suspect. In many such cases, a more critical failure surface with a considerably lower factor of safety can be found by logical adjustments to the slice geometry.

The most common conditions that result in the development of negative stresses are listed below in point form. With supporting illustrations from historic land slides and pit-wall failures, each condition is then explored in greater detail.

- Crest region too strong - tensile crack
- Pore pressure reduction at crest
- Toe region excessively strong
- Slice boundaries not placed in critical orientation
- Extreme surface roughness

Tensile Cracks: Negative stresses develop on slice boundaries if the crest region of a slope failure is stronger than the toe. By developing tensile stresses, the model transfers part of the load to the stronger crest region. If a strong crest condition occurs in the field, a tensile crack will develop and the toe region will fail. If a strong crest condition is encountered the correct factor of safety can be calculated by limiting the stability analysis to the lower portion of the pit wall. *Figure 6.22* shows the computed force vectors for a representative cross section of Dutchman's Ridge landslide on the Columbia River. To illustrate the development of negative stress conditions the crest region was artificially strengthened by increasing the friction angle on the fault scarp from 33.4 to 45.0 degrees on the uppermost two slices. The model indicates that negative stresses develop on sides *6*, *7* and *8*, just below the strong crest region. The factor of safety is *0.942*. *Figure 6.23* illustrates the force distribution obtained when only the lower, less stable portion of the slide was analyzed. In this case, all effective stresses are positive. As expected, the resulting factor of safety, *0.874*, is substantially lower.

Figure 6.22 Force Vectors, Dutchman's Ridge with Strong Crest

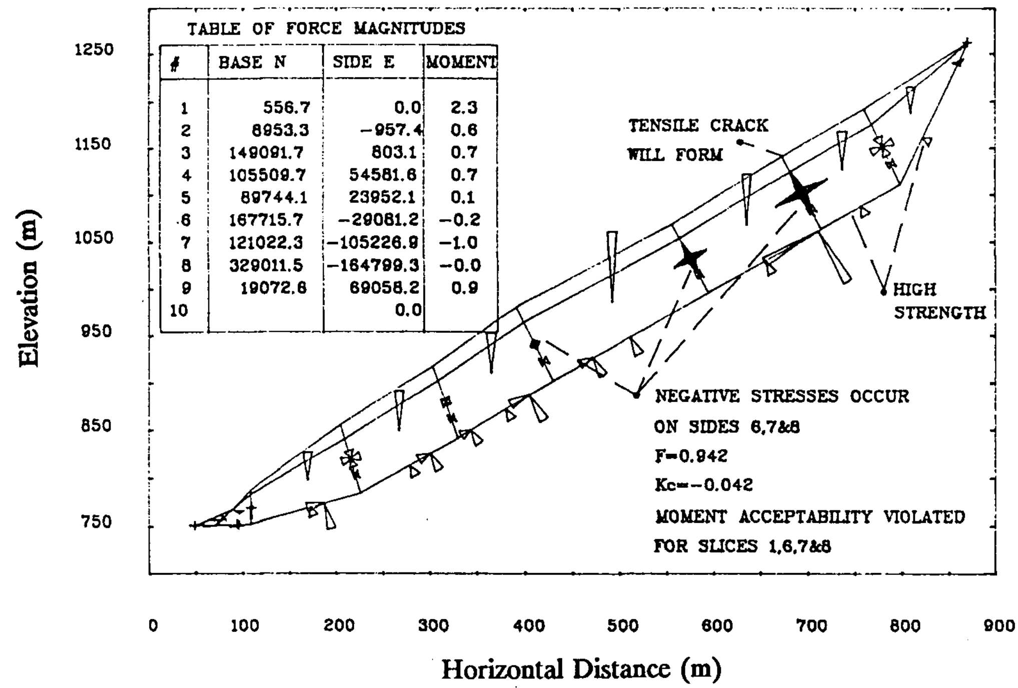

Figure 6.23 Force Vectors, Toe Region of Dutchman's Ridge

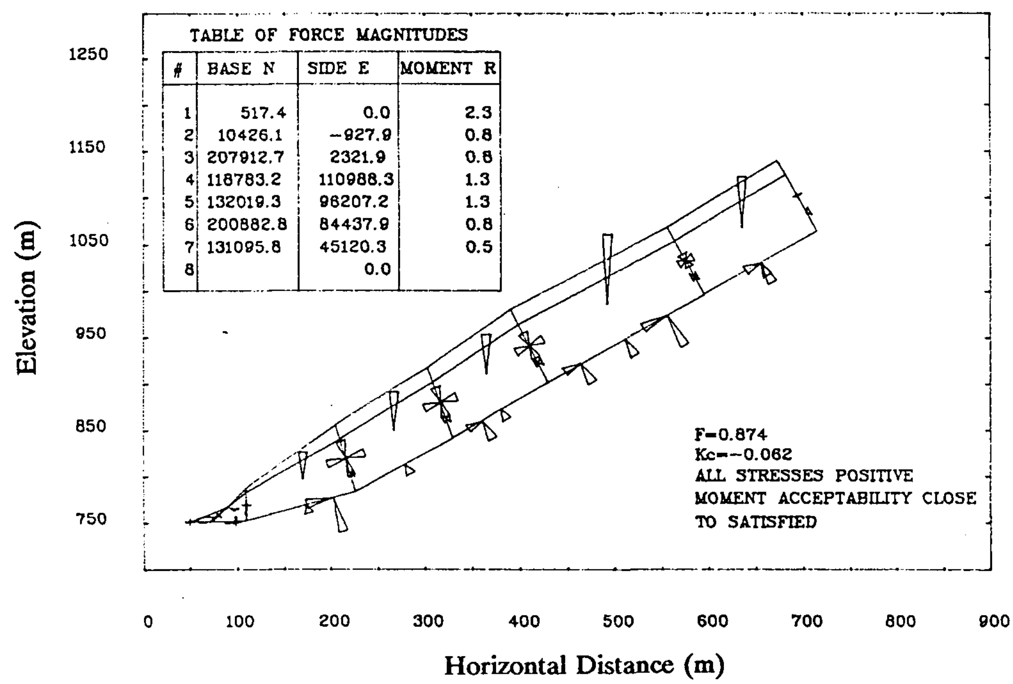

Pore Pressure Reduction at Crest: Low pore water pressures in the crest region of a pit-wall failure will increase effective stresses on the basal failure plane, making the crest region stronger. As in the previous subsection, the result is once again that the crest is too strong; however, the cause is water pressure, not shear strength. Under such conditions, *SG-SLOPE* may calculate tensile stresses on slice boundaries that separate the stable crest region from the unstable toe. *Figure 6.24* shows the force distribution calculated for Dutchman's Ridge when low pore pressures are specified in the crest region and the friction angle along the entire basal fault zone is set to 33.4 degrees. As expected, *SG-SLOPE* predicts development of negative effective stresses in the central portion of the slope where the pore pressures change from high to low.

Results of this simulation indicate that a dewatering program initiated in the toe region of a failure will be more effective in stabilizing a slide than a similar program initiated in the crest region, even if the water table is everywhere near the ground surface. When pore pressures are reduced in the toe region an increase in shear strength due to increased effective stresses can support loads transmitted by compressive stresses from the entire slide mass. When pore pressures are reduced in the crest the increase in strength cannot be transmitted to support the lower portion of the slide since tensile cracks will develop.

Figure 6.24 Force Vectors, Dutchman's Ridge with Reduced Pore Pressures at Crest

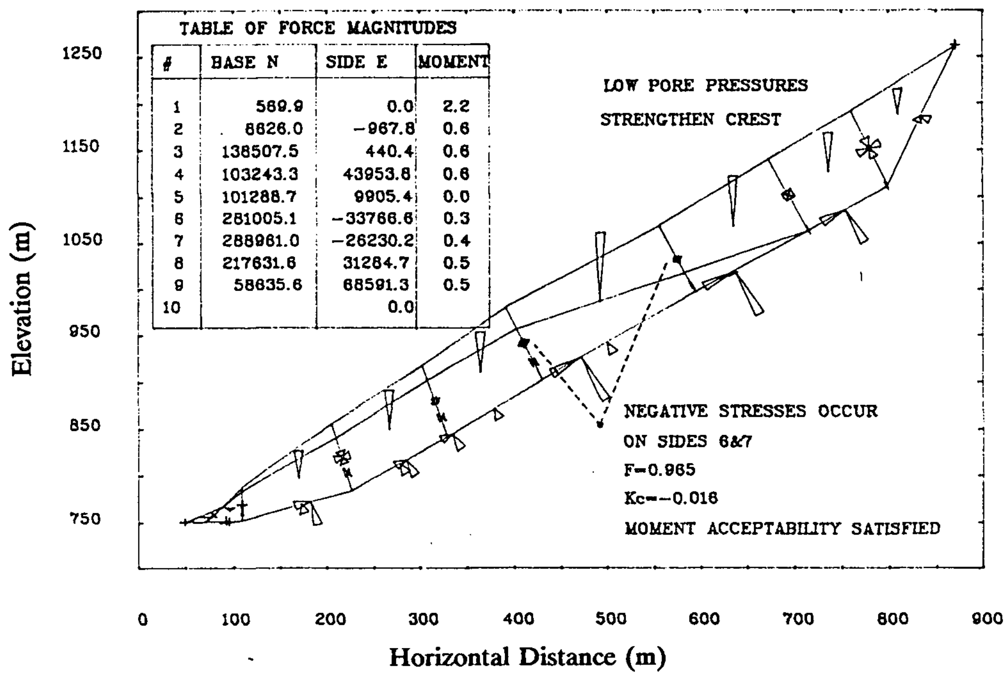

Toe Strength and Orientation: Tensile stress conditions will develop on slice bases in the toe region of a slide if a more critical failure surface is present above the high strength surface selected in the analysis. An artificially strong toe will occur if curvature of the failure plane is too tight or the friction angle assigned in the toe area is significantly higher than on the remainder of the basal plane. *Figure 6-25* illustrates a typical problem. A large earth embankment is constructed against a coarse aggregate retaining wall. The factor of safety for the geometry and strength parameters given in *Figure 6-25* is 2.090. Negative stresses are predicted at the base of slice 2. The tensile stress condition suggests that the embankment is more likely to fail along a slip circle that daylights at the top of the retaining wall, shown in *Figure 6-26*. Analysis of the circular failure gives $F = 0.878$ and all effective stresses predicted by *SG-SLOPE* are positive.

Figure 6.25 Force Vectors, Embankment with Strong Toe Region

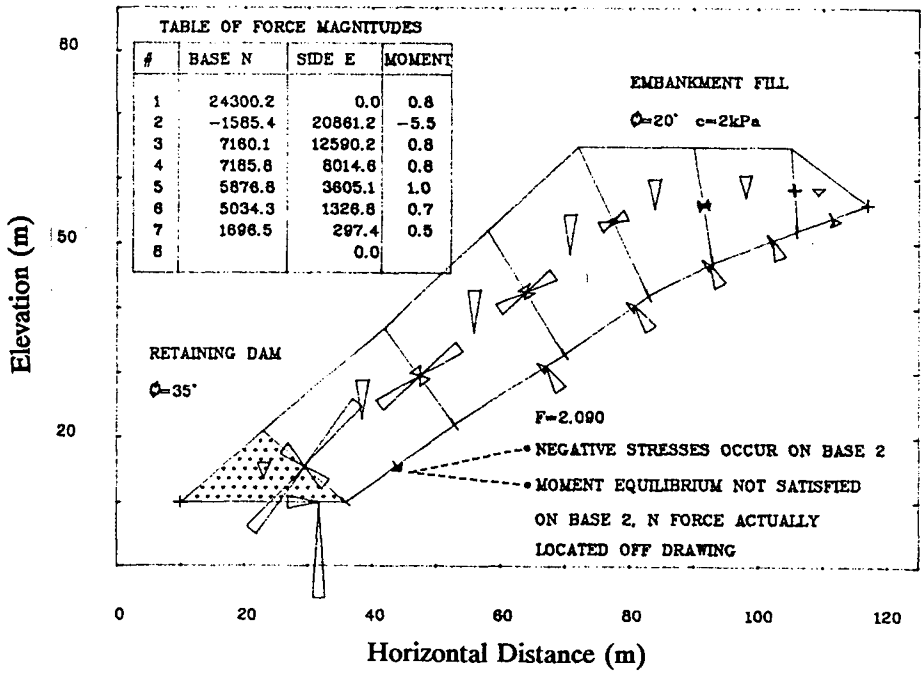

Figure 6.26 Force Vectors, Circular Failure in Embankment above Retaining Wall

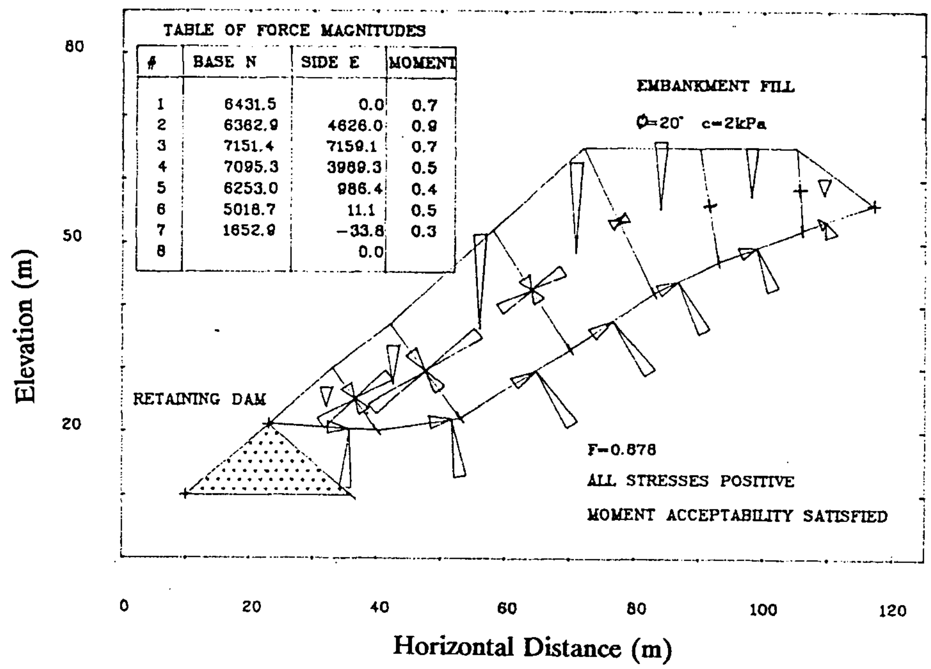

Side Orientations not Critical: Negative stresses may develop on a slice side or adjacent slice base if the specified orientation of the side is not critical (resulting in the lowest possible factor of safety). An example of non-critical side orientation is illustrated in *Figure 6.27.* The geometry is once again based on *Dutchman's Ridge*. In this example it is assumed that slice separation is controlled by one of two joint sets: *set A,* oriented approximately normal to the failure plane and *set B,* inclined at approximately 30 degrees to the normal. First, side orientations corresponding to joint *set A* were specified on all slice sides (e.g. *Figure 6-24*). Under fully drained conditions the solution yielded a factor of safety of *1.206* and positive effective stresses were calculated for all surfaces. When side *6* was rotated to the *set B* orientation as shown in *Figure 6.27, SG-SLOPE* predicted negative stresses on base *6,* just uphill from the inclined slice side. The factor of safety increased to 1.245. Rotation of slice boundaries during analysis of other pit wall failures also resulted in development of negative stresses, always on slice bases just uphill of the slice side being rotated. The program consistently over-estimated the true factor of safety whenever negative effective stresses were observed.

Figure 6.27 Negative Stresses Caused by Wrong Slice Orientation

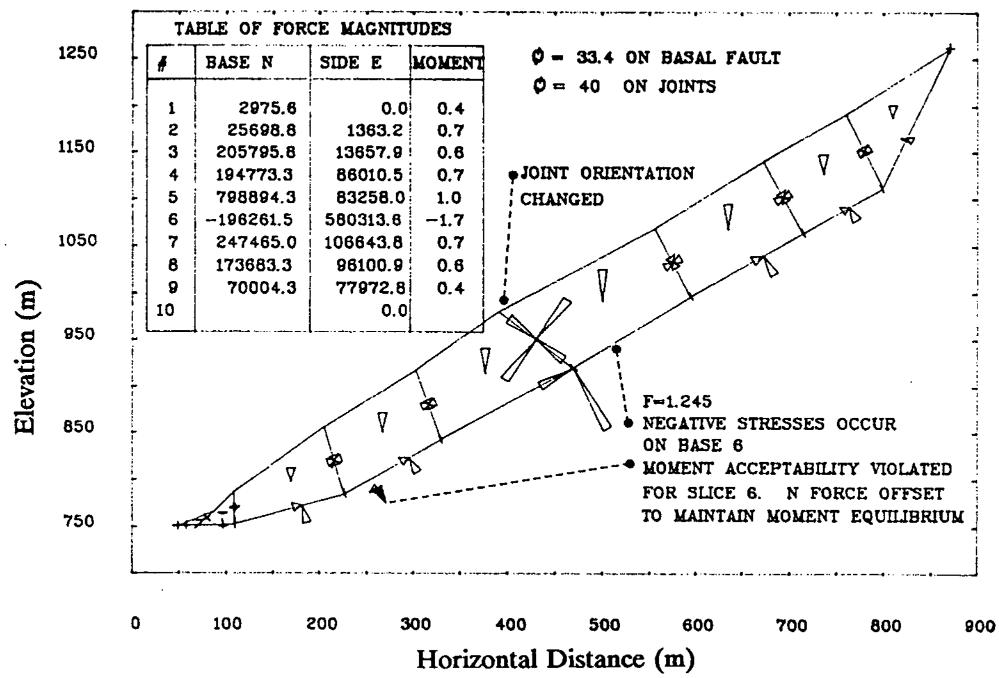

#	BASE N	SIDE E	MOMENT
1	2975.6	0.0	0.4
2	25698.8	1363.2	0.7
3	205795.8	13657.9	0.6
4	194773.3	86010.5	0.7
5	798894.3	83258.0	1.0
6	-196261.5	580313.6	-1.7
7	247465.0	106643.8	0.7
8	173683.3	96100.9	0.6
9	70004.3	77972.8	0.4
10		0.0	

Since inappropriate orientation of slice boundaries can lead to negative stresses and erroneous stability results, the relationship between slice orientation and effective stresses on the adjacent slice base was explored in greater detail for the *Dutchman's Ridge* failure geometry. The objective: to develop a simple rule of thumb for selecting slice orientations that define the critical slice geometry. In the experiment orientations of each slice boundary were systematically adjusted by *5* degree increments. *Figure 6.28* illustrates results of the sensitivity study.

To facilitate explanation of the results it is necessary to introduce a new parameter, *offset angle*. *Offset angle* is defined as the angle measured from the basal failure plane normal to the slice side under consideration. *Offset angle* is positive if the slice side is steeper than the normal and negative if the side is shallower (see lower left corner of *Figure 6.28*).

Figure 6.28 Normal Stress vs. Angle of Slice Side

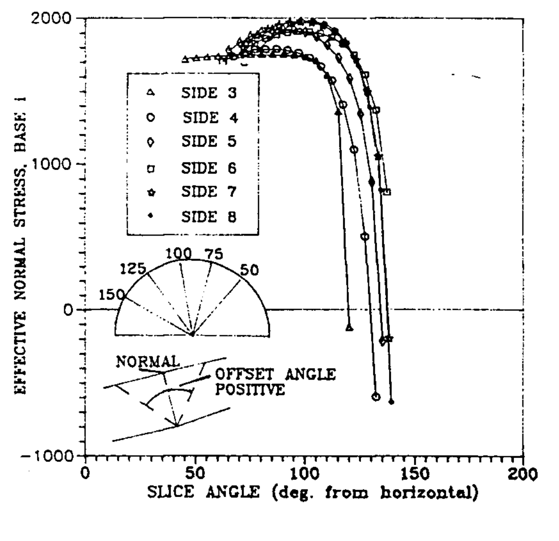

Figure 6.29 Factor of Safety vs. Angle of Slice Side

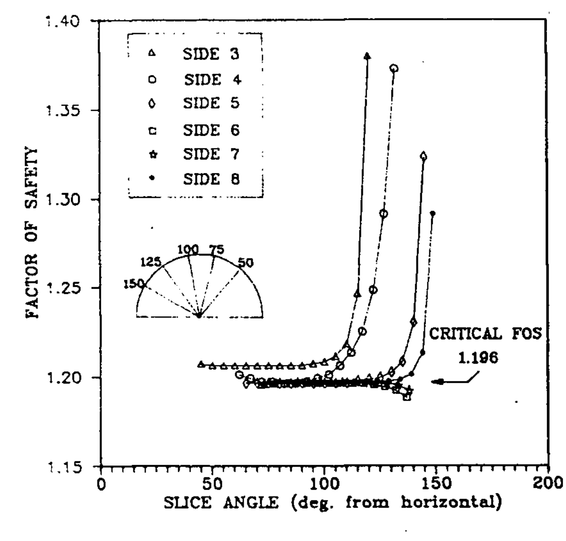

Negative stresses did not develop on adjacent slice bases until slice sides were inclined at angles greater than *120* degrees at the toe of the slope and *130* degrees at the crest; in all cases the offset angles were more negative than *-25* degrees. The limited scope of this study suggests that in order to avoid development of negative stresses, slice boundaries should be selected so that they have positive, or only slightly negative offset angles. In fact, for the near planar slope geometry associated with *Dutchman's Ridge*, critical slice orientations occurred at moderately positive offset angles, in the range *+15* to *+30* degrees.

Figure 6.29 shows how the calculated factor of safety changes as orientation of each slice is adjusted. The nearly flat trough in each curve indicates that there is a broad range of orientations for each slice side for which the factor of safety remains close to the critical value. The practical implications of the results presented in *Figures 6.28 & 6.29* can be summarized as follows:

- Negative stresses do not develop on slice bases until large offset angles are specified on slice sides.
- Factor of safety is not sensitive to orientation of slice boundaries over a wide range of side orientations. In most cases, a reasonable estimate of the true factor of safety can be attained without adjustment of slice side orientations if care is taken when defining the initial slice geometry.
- When selecting slice orientations in homogeneous materials, slices should be oriented radially or at small positive offset angles. For planar failures, critical slice orientations seem to occur at offset angles of +15 to +30 degrees.
- When defining slice geometry for rock slopes where deformation may be controlled by existing discontinuities extra caution must be exercised. Existing discontinuities should define the location of slice sides if oriented at positive or small negative offsets. If the discontinuity is oriented at a large negative offset, then block separation through intact rock or random joints may be critical, especially if negative stresses are predicted on the slice base adjacent to the unfavourably inclined discontinuity.

Extreme Surface Roughness: Hoek (1986) observed that "*A rough or irregular failure surface can also give rise to negative stress problems if it causes part of the sliding mass to be significantly more stable than an adjacent part.*" Development of crevasses over irregularities at the base of a glacier is a classic example of this mechanism in action. Tests of a number of failure geometries reveal that in many cases irregularities must be extreme if negative stresses are to develop. *Figure 6.30* illustrates a typical example where a substantial irregularity did not lead to the development of negative stresses. The geometry is a classic circular failure, but the Y_b coordinate of side *6* is shifted to introduce a large convexity in the failure surface. Contrary to expectations, *Figure 6.30* indicates that all stresses remain positive, even when high pore pressures are introduced on all slices.

Figure 6.30 Force Vectors for Irregular Failure Surface

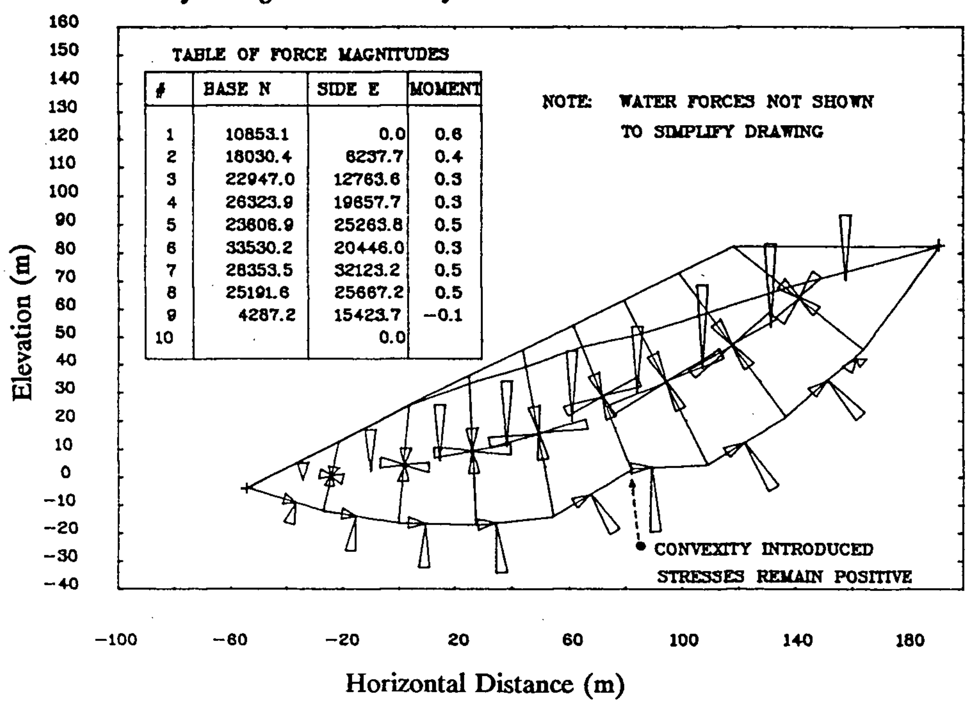

#	BASE N	SIDE E	MOMENT
1	10853.1	0.0	0.6
2	18030.4	6237.7	0.4
3	22947.0	12763.6	0.3
4	26323.9	19657.7	0.3
5	23606.9	25263.8	0.5
6	33530.2	20446.0	0.3
7	28353.5	32123.2	0.5
8	25191.6	25667.2	0.5
9	4287.2	15423.7	-0.1
10		0.0	

6.4.5 MOMENT ACCEPTABILITY PROBLEMS

After all forces are calculated *SG-SLOPE* satisfies moment equilibrium of each slice by calculating the length of the moment arm L_i necessary to bring slice *i* into moment equilibrium about the point (xb_i, yb_i) as shown in *Figure 6.13.* To be physically acceptable, the point of application of the base normal force N_i must be located somewhere on the slice base, preferably in the middle third. To check whether this acceptability condition is met *SG-SLOPE* calculates the ratio RM_i, defined as the moment arm L_i divided by the length of the slice base. To be acceptable, RM_i must be in the range *0* to *1.* Moment acceptability problems can be attributed to two causes:

- Tall, narrow slices
- Inappropriate orientation of slice sides

Tall-Narrow Slices: To maintain moment equilibrium $Ni\,L_i$ must balance the resultant moment induced by all other body forces acting on slice *i.* If tall, narrow slices are selected N_i will be relatively small so a very large moment arm L_i may be required. To avoid moment acceptability problems the height to width ratio should be *2:1* or smaller for all slices. *Figure 6.31* illustrates the slice geometry used by Hoek (1986) to analyze an unstable pit wall in a large open pit coal mine. In this example, moment equilibrium of slice *3* can be satisfied only if a very large moment arm is used and moment acceptability is violated. (*SG-SLOPE* calculated: $RM_i=222.54$, $F=1.154$ for this example). *Figure 6.32* shows the pit wall geometry after adjustments were made to satisfy moment acceptability on all slices (all $RM_i<1$). The factor of safety for the adjusted geometry increased by *2%* to *1.176*.

Slice Side Orientation: Inappropriate slice orientation can also result in violation of the moment acceptability condition. Severe violations in moment acceptability are commonly accompanied by development of negative stresses. Both problems can usually be resolved by rotation of the appropriate slice side so that the offset angle is slightly positive.

The previous example illustrates that factor of safety is not sensitive to violations in the moment acceptability condition. F is much more sensitive to changes in failure surface geometry and surface topography. It is likely that the *2%* difference in F observed in the above example can be attributed to very small changes in the shape of the basal failure surface resulting from adjustments to the slice side geometry rather than to actual changes in the length of the moment arm. To obtain reliable stability assessment results the following rules of thumb should be followed when first defining slice geometry.

- Use an adequate number of slices to accurately describe the basal failure plane and surface topography.
- If possible, orient slice sides so that all sides have a small positive offset angle. If discontinuities dictate slice orientation check the solution for negative stresses before relying on results.
- Keep slices as thick as possible. Try to maintain a height to width ratio smaller than *2:1*; but not at the expense of reduced resolution in the definition of the basal failure surface.

Figure 6.31 Coal Mine Geometry with Narrow Slice at Toe

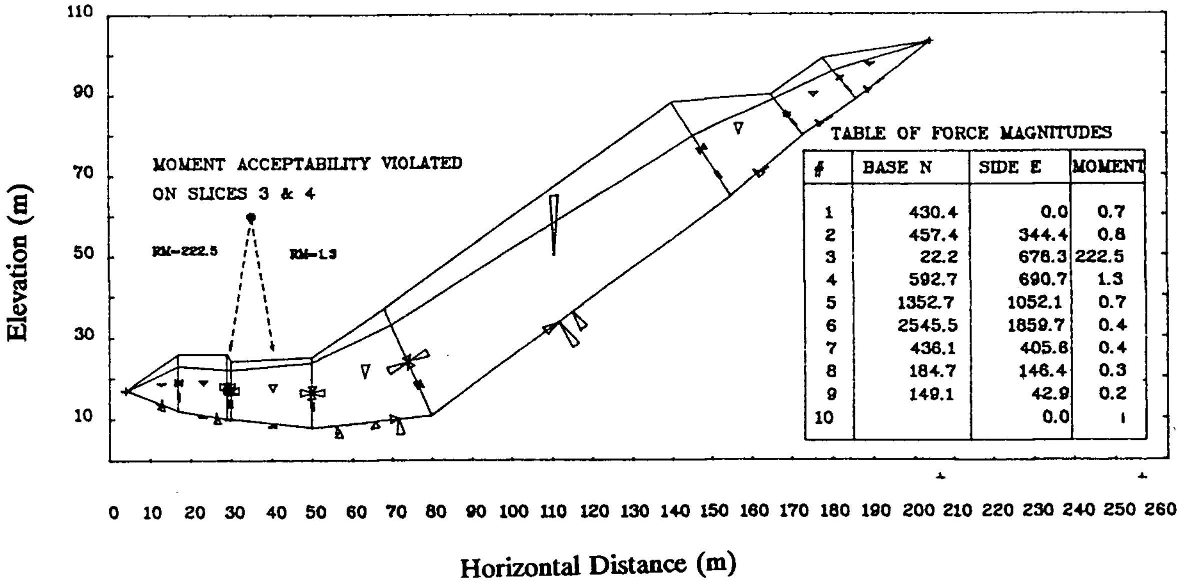

Figure 6.32 Coal Mine Geometry that Satisfies Moment Acceptability

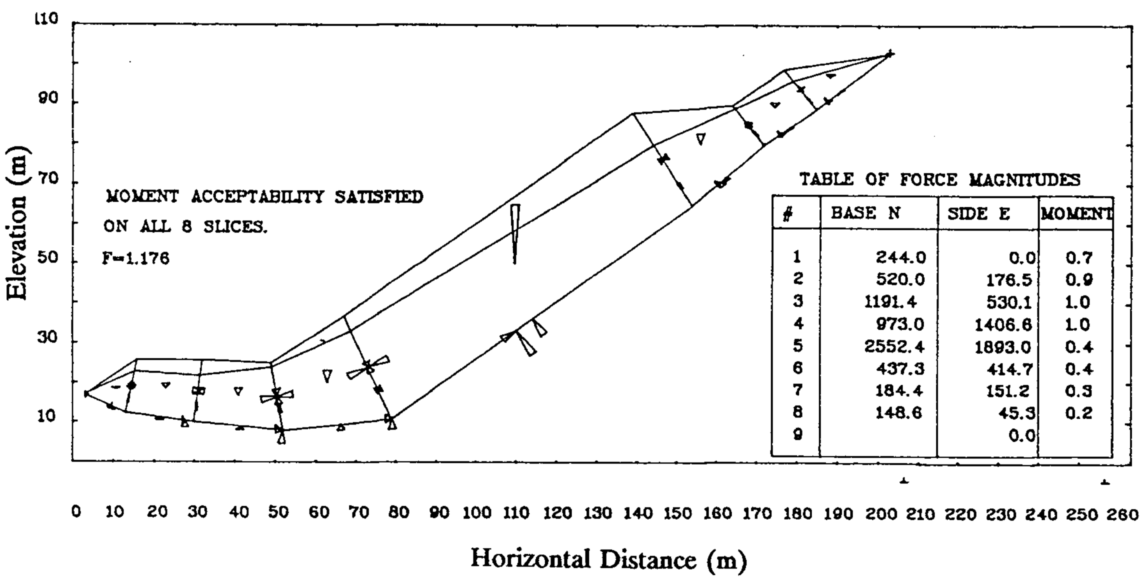

6.5 PROBABILITY OF FAILURE

In the disciplines of soil and rock mechanics slope stability has historically been measured in terms of the factor of safety. Defined as the ratio of resisting forces divided by destabilizing forces, F is a deterministic stability indicator that is greater than unity when a slope is stable, equal to unity when a slope is in a state of limiting equilibrium and less than unity a slope is considered unstable.

The factor of safety concept has proved useful for classification of slope performance. Based on experience gained from the performance of a very large number of pit walls from around the world, most slopes today are designed with a factor of safety of 1.1 to 1.5. Slopes with factors of safety greater than 1.5 are considered overly conservative while slopes with factors of safety lower than 1.1 are thought to have a very high likelihood of failure.

Probability of failure is an alternate method of evaluating slope stability. In Canada, the probability of failure concept was promoted to practitioners in the mining industry in the early 1980's (CANMET Slope Manual); however, it did not gain widespread popularity at the time because it did not seem to provide any significant advantages over the factor of safety concept. As well, the concept lacked the extensive performance data base associated with the Factor of Safety.

With the introduction of risk based engineering design this situation will likely change. As demonstrated in the sensitivity study and case history components of this thesis the risk based design approach can identify the optimum risk level and the most cost effective design strategy for each unique mine environment. Because evaluation of the monetary risk term requires an estimation of the probability of failure, the popular factor of safety concept cannot be utilized.

As illustrated in *Figure 6.33*, there is an indirect relationship between factor of safety and probability of failure. Accepting that parameters controlling slope stability are uncertain, a unique factor of safety does not exist. Rather, the factor of safety results in a continuous probability distribution for which a mean and a variance can be defined. The distribution mean serves as a relative indicator of stability. For example, slope B, associated with the F distribution in *Figure 6.33B* would be less stable than the slope in *Figure 6.33A*. The distribution variance is indicative of input parameter uncertainty. The more uncertain are input parameters, the broader the distribution. For example, considerably more uncertainty exists in the stability assessment of slope C (depicted in *Figure 6.33C*) than slope A.

Probability of failure is defined as the area under the factor of safety distribution situated to the left of $F=1.0$ (shaded in *Figure 6.33*). In the Monte-Carlo approach adopted in this framework, the probability of failure is calculated by generating a large number of realizations of shear strength and hydrologic conditions, evaluating the factor of safety for each realization, and then dividing the number of realizations that resulted in failure by the total number of realizations in the ensemble.

As can be seen in comparing *Figures 6.33A,B* and C, the probability of failure can increase if entire F distribution shifts to the left as depicted in *Figures 6.33A* and B. For example, this case would arise if exploration revealed that shear strength parameters are lower than expected. An increase in the probability of failure can also be brought about by an increase in uncertainty resulting in a broadening of the F distribution and a large portion of the area falling to the left of $F=1.0$. This mechanism, referred to as the *"tail effect"* in subsequent sections of this dissertation is illustrated in *Figures 6.33A* and C.

As shown in the previous examples, there is not a direct correspondence between factor of safety and probability of failure. However, suitable guidelines for slope design, couched in terms of probability of failure can be established in exactly the same way as they were established for the factor of safety. Once these guidelines are in place and a large data base of experience is attained, the probabilistic design approach will likely replace the standard approach based on the factor of safety. However, until that time is at hand, all slope designs based on the risk-cost-benefit framework approach should also be evaluated with the conventional factor of safety approach to ensure that the resulting slope design is sufficiently stable.

Figure 6.33 Probability Distributions Showing Relationship Between POF and F.

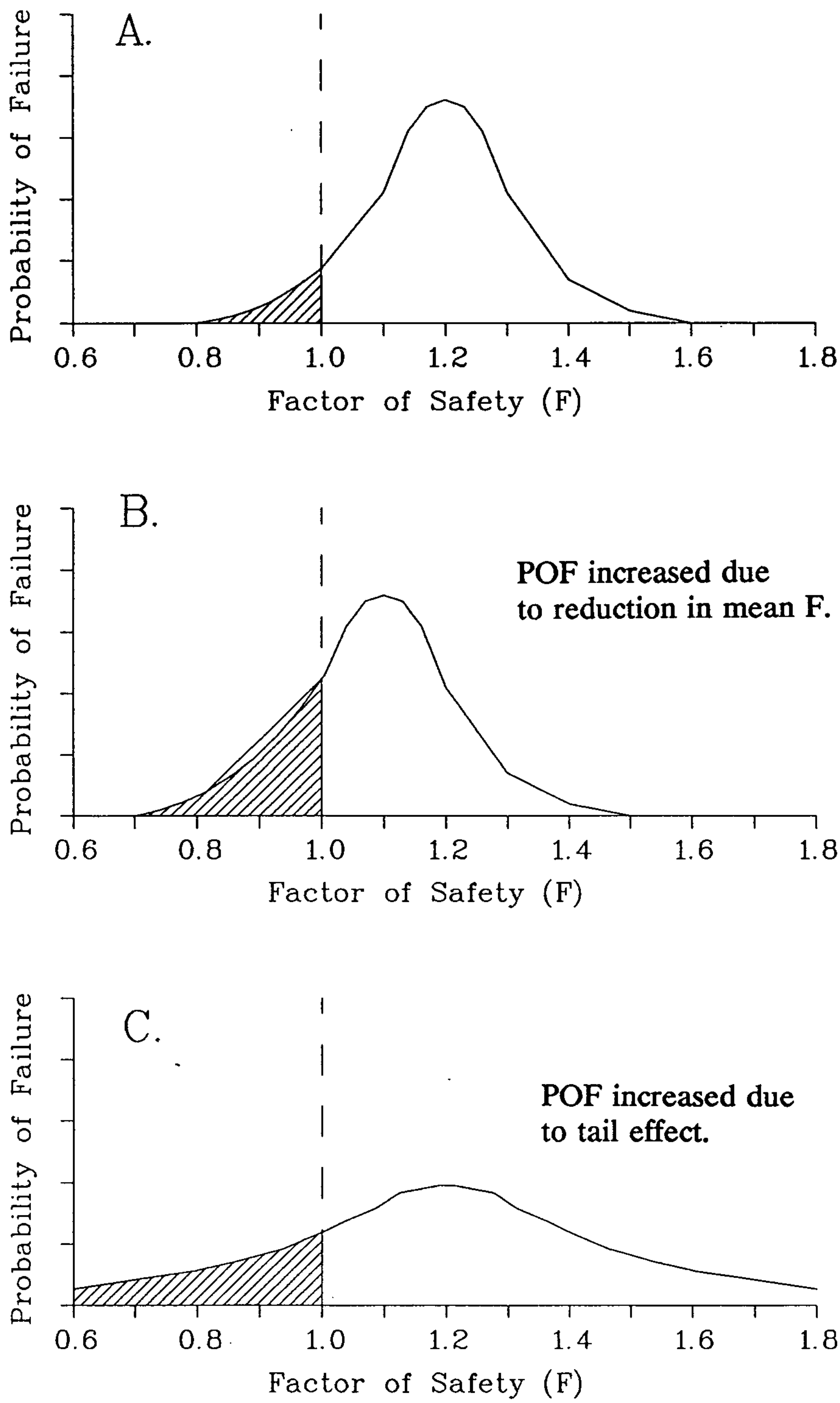

6.6 INCORPORATING PORE PRESSURES IN ANALYSIS

Most slope stability analysis programs introduce the influence of groundwater on slope stability by invoking the Dupuit assumptions (i.e. pressure head on failure surface is indicated by vertical distance to water table). Because such an approach can lead to serious errors when complex, heterogeneous geologic conditions are encountered a more accurate method of accounting for the influence of groundwater has been incorporated in this framework.

The previous chapter described how the *SG-FLOW* finite element program computes the hydraulic head and pressure head distributions everywhere in the pit wall. *Figure 6.34A* provides an example of a typical pore pressure distribution. In computer program *SG-SLOPE*, this distribution is accessed to determine the pore pressure acting on key points along the failure surface and inter-slice boundaries. As shown in *Figure 34B*, six equally spaced points are used to fully define the pore pressures acting on the slice base. The resultant water forces FWB_i and FWS_i are then determined by intergrating the water pressure over the entire area. The resultant forces *FW*, known to act through the centroid of each corresponding pore pressure distribution are then introduced in *Sarma's* formulation as known body forces.

Figure 6.34 Determining Water Forces Acting on Slice

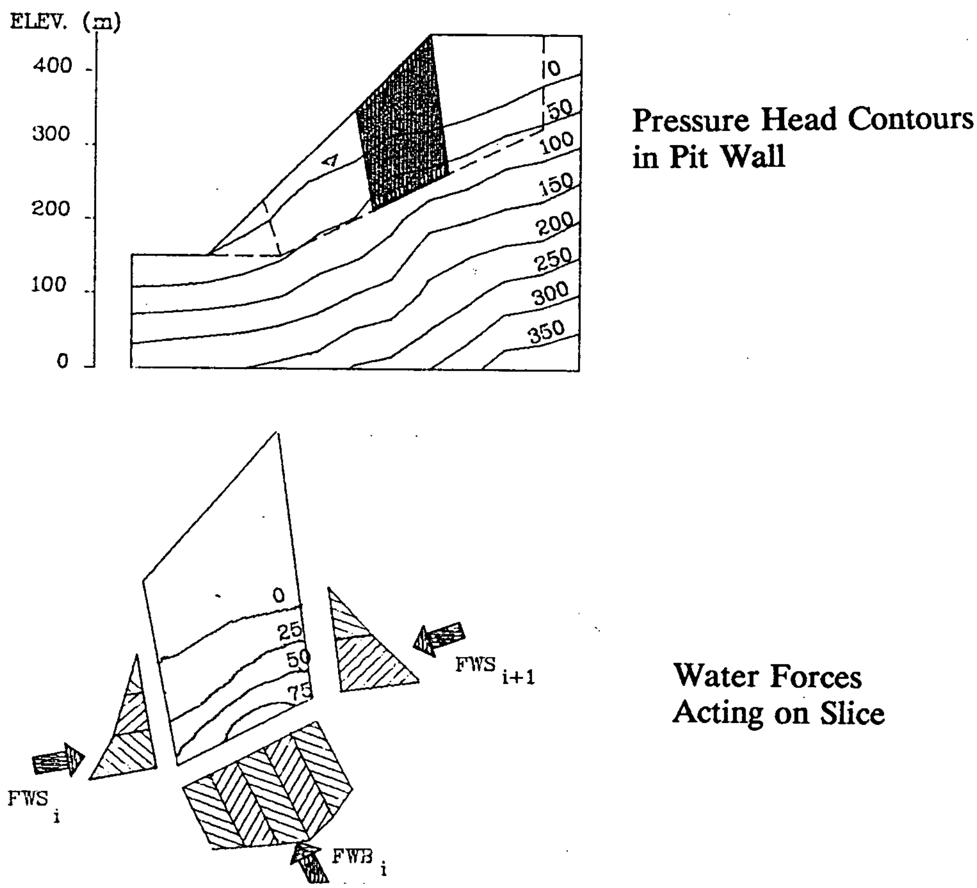

6.7 SUMMARY

This chapter presented the theory underlying *Sarma's* two dimensional, limit equilibrium approach to analyzing slope stability. The method was selected for implementation in this framework based on a review of the most popular two dimensional method of slices algorithms which revealed that Sarma's method was the simplest and most efficient algorithm for analyzing the circular and non-circular problems that would be encountered.

The system of linear equations that must be solved in order to determine the critical acceleration ratio K_c and the factor of safety was developed from first principles and a new numerical approach was implemented to solve these equations, thereby avoiding the need to derive a complicated closed form solution.

Sarma's method does not yield F directly, instead an iterative scheme involving progressive reduction of shear strength parameters by the ratio 1/FOS is required to solve for this parameter. Previous researchers (Hoek, 1986) have noted that in some cases the iterative process may converge to the wrong FOS. The cause of this instability was investigated. It was determined that the instability develops when the true factor of safety is situated close to an asymptote in the K vs. F function. Also, the previously unexplained cause of the asymptotic behaviour was shown to be caused by a sudden reversal in the direction of interslice shear forces from compressive to tensile.

A number of conditions that can lead to the development of negative stresses and moment acceptability problems on one or more slice boundaries were identified and guidelines were presented to overcome these acceptability problems by carefully selecting the most appropriate slice geometry.

CHAPTER 7 SENSITIVITY STUDY

7.1 OVERVIEW

The process used in this thesis research for evaluating different pit wall and dewatering design alternatives consists of four stages:

- Data collection and geostatistical interpretation
- Prediction of the pore pressure distribution in the pit wall for each dewatering alternative
- Slope stability analysis to predict probability of failure for each pit design
- Risk-cost-benefit analysis to evaluate expected profitability of proposed pit design

The analysis techniques used in each of the above stages of the pit wall design have been documented independently in earlier chapters. When coupled together, the techniques form a comprehensive framework that can be used to evaluate different pit wall design and dewatering strategies and to identify the design that will lead to maximum profit for the operator of the open pit mine. By utilizing the framework in sensitivity mode, it is possible to explore how each of the many input parameters (hydrologic data, shear strength parameters, economic parameters, ore grades, pit angles, dewatering design, etc.) have an impact on the overall economics of the mining operation. The studies described in this chapter were conducted by perturbing the parameter under investigation while maintaining all other parameters fixed. Recognizing that the sensitivity study is being performed on a non-linear system, this pertubation approach is truly accurate only for small perturbations, so many of the sensitivity results presented on the following pages may be very approximate. Never-the-less, sensitivity analysis permits the analyst to assess the relative significance of each input parameter or design decision (e.g. is it more important to reduce uncertainty in shear strength parameters or in hydraulic conductivity estimates, or, is it more economical to reduce probability of failure by dewatering than by reducing the pit wall angle).

The purpose of this chapter is to report on the most significant and interesting findings of the sensitivity studies conducted as part of this thesis research, findings that will help geotechnical engineers to identify mine sites where groundwater control is beneficial, to specify which input parameters are the most important for design, to recommend the type of dewatering system required, to estimate the necessary dewatering budget, and to demonstrate how the capital invested in dewatering will increase profitability of the mining operation.

The objective of this chapter is not to overwhelm the reader with an endless list of sensitivity results. Rather, the sensitivity analysis presented on the following pages considers a problem that resembles actual site conditions in the overburden pit wall at Highland Valley Copper (HVC). This has made it possible to apply findings of the sensitivity study directly to the actual dewatering design (see case history, *Chapter 8*). Since ground water control in the thick overburden strata is the most improtant design issue, the scenario consists of a large overburden pit wall for which a circular mode of failure is anticipated.

Figure 7.1 Organization Chart for Chapter 7

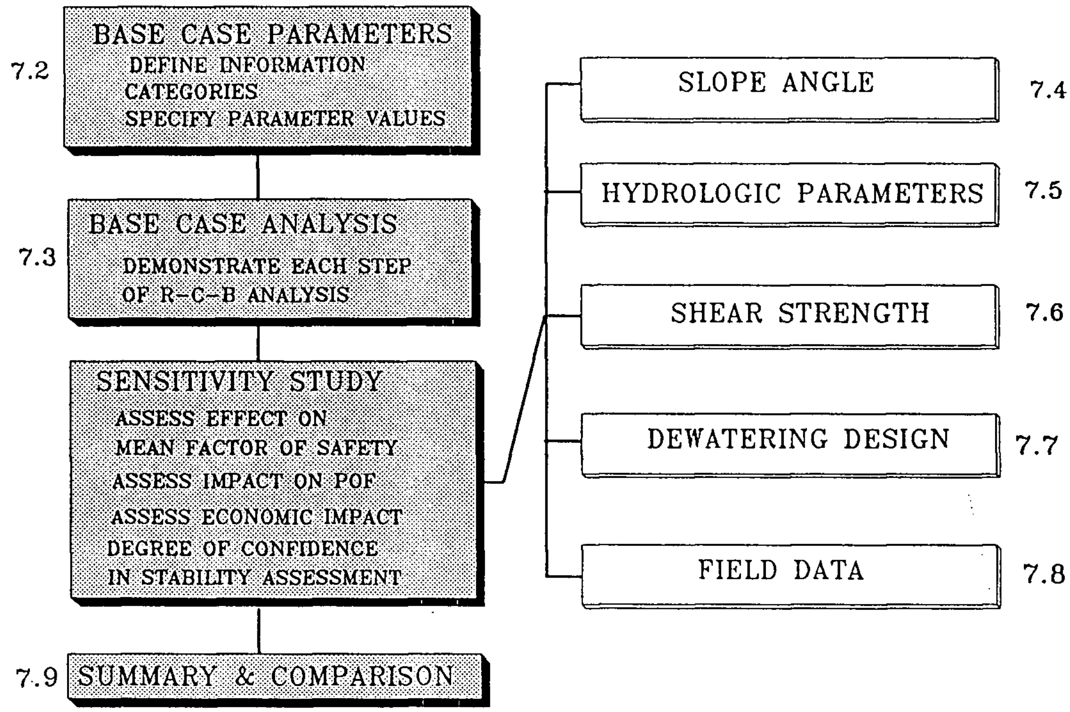

Although applicable to most overburden slopes where a circular mode of failure is anticipated, the conclusions reported in this chapter should not be extrapolated to the design of dewatering systems in bedrock where groundwater flow is restricted to open fractures and/or cavities in the rock mass and failure is most likely to occur along one or more major discontinuities. However, each of the analytical techniques utilized in this framework could just as easily be applied to the analysis of pit wall and dewatering requirements in bedrock, provided that the rock mass is sufficiently fractured such that it can be considered as an equivalent continuum for groundwater flow.

Figure 7.1 presents an overview and organization chart of the topics to be covered under each section heading in this chapter. The following paragraphs outline the material discussed under each heading.

Section 7.2 provides a detailed description of the hydrologic, strength and geometric parameters for the base case scenario. The pit wall design, mining sequence and dewatering plan are also fully described.

To illustrate the risk-cost-benefit framework in its entirety, *Section 7.3* presents and discusses the intermediate results obtained during each of the four basic steps in the analysis of the base case data; in subsequent sensitivity analyses only the final economic results are usually reported.

Section 7.4 explores the importance of geotechnical input in the formulation of an open pit mine plan. Design recommendations that fall in the realm of the geotechnical engineer include pit wall angles and dewatering requirements. These design recommendations affect the economics of the open pit mine in two ways: 1) reductions in slope angle will dramatically increase the stripping ratio and associated excavation costs, and 2) changes to the slope angle and to the dewatering design will alter the probability of failure term, p_f, in the risk-cost-benefit objective function. *Section 7.4* first investigates how net income and profitability are influenced by the projected probability of slope failure. Next, *Section 7.4* demonstrates that through careful balancing of the probability of failure constraints against stripping ratio, geotechnical analysis and design can identify the optimal pit wall angle that will maximize profitability of the mining operation. Finally, *Section 7.4* illustrates that groundwater control provides an alternate method of reducing the probability of failure, a method that proves much more cost effective than reductions in the slope angle in many circumstances.

Effectiveness of a particular dewatering program is influenced by geologic conditions in the subsurface. *Section 7.5* investigates the sensitivity of the economic model to changes in hydrogeologic parameters. These parameters include: mean hydraulic conductivity, hydraulic conductivity contrast, correlation length, and stratification.. The objective of *Section 7.5* is to ascertain which hydrogeologic parameters are the most important and must therefore be determined accurately during the site investigation phase of the pit wall design. Although geostatistics provides a very useful tool for describing hydraulic conductivity fields that are statistically homogeneous, results based on a purely geostatistical description of measurements can lead to significant design errors if known geologic features such as large faults are not incorporated in the hydraulic conductivity model. *Section 7.5* also provides an example that clearly illustrates the importance of accurate geologic interpretation.

A major portion of the material in this thesis has been devoted to quantifying the degree of uncertainty that is associated with each hydraulic conductivity estimate. However, it must be recognized that hydraulic conductivity is not the only uncertain input parameter. Shear strength, ore grade, metal prices and operating costs are also uncertain and should be treated as stochastic variables in the analysis. However, as the emphasis of this research is geotechnical, only hydrologic and shear strength parameters will be treated as stochastic variables; all other geometric and economic parameters will be considered in a deterministic sense. *Section 7.6* investigates the sensitivity of the economic model to shear strength parameters, in particular, to changes in the mean and variance of the friction angle and cohesion parameters. A comparison is then made of the economic impact of reducing the degree of uncertainty in shear strength parameters vs. reducing the degree of uncertainty in hydrogeologic parameters. Results of this comparison are used to formulate a rule of thumb for allocation of site investigation resources between hydrogeologic and shear strength measurements.

It was stated earlier that results of the sensitivity studies presented in this chapter will demonstrate that a thorough groundwater control program can dramatically increase profitability of an open pit mine. *Section 7.7* describes how to determine the optimum amount of capital to invest in groundwater control. Logic suggests that there must be a point of limited return when additional investment in the dewatering system is no longer justified. *Section 7.7* illustrates how this point can be identified for the base case scenario and then investigates whether the amounts of capital allocated for groundwater control should increase as the pit matures and the overburden pit wall increases in height. The economic effect of utilizing steeper slope angles in the early stages of mine design will also be investigated in this section.

Section 7.8 briefly examines the importance of the number and location of hydrogeologic measurements. The analysis presented in this section is very primitive; by testing different sampling strategies on a hypothetical "known" profile it is shown that the investigation strategy can have a very significant influence on subsequent profitability and operational problems in the open pit mine. A much more detailed study of the worth of field data is currently being conducted at The University of British Columbia by B. James and R.A. Freeze.

Figure 7.2 Schematic of Ore Deposit

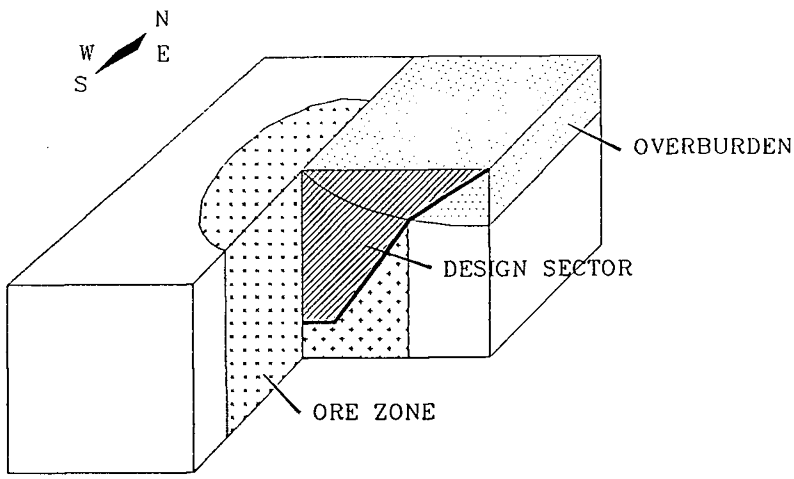

7.2 *BASE CASE PARAMETERS*

This section describes the hypothetical pit design problem that will be analyzed in this sensitivity study. The zone of mineralization is assumed to be a large copper porphyry deposit whose size, shape and grade bears some resemblance to a number of British Columbia's larger open pit copper mines. As illustrated in *Figure 7.2*, the ore deposit is cylindrical in shape. The zone of economic mineralization is approximately 900 m in diameter and open at depth. The ore grades are richest in the cylinder's core, becoming progressively poorer in outer shells of the cylinder.

The hypothetical ore deposit is situated on the southern flank of a broad, gently sloping glacial valley. Much of the valley has been infilled with a thick, relatively homogenous glacio-lacustrine deposit. The unconsolidated silty sand has buried the eastern half of the ore body in as much as 300 m of overburden. The sensitivity study presented in this chapter will be limited to a single design sector. The location of the design sector is indicated by diagonal hatching in *Figure 7.2*. This sector has been selected for analysis because it contains the thickest sequence of unconsolidated material from which the pit wall will have to be excavated.

The information specified for this hypothetical base-case data set has been carefully selected so that both quantity and quality of data are consistent with information typically available at the completion of a mine feasibility study when the decision is made to proceed with development of the ore body.

It is assumed that exploratory drilling on the centre line of this design sector has defined the location of the high, medium, and low grade ore zones and the position of the overburden bedrock contact as illustrated in *Figure 7.3*. The grade limits for each interval are given in *Table 7.1* under the heading *Geology - Ore Grade*.

Furthermore, it is assumed that information obtained during the exploratory drilling program was also used to define the average unit weight of the overburden and bedrock, as well as the digability characteristics of each material. The base case values for these parameters are listed in *Table 7.1* under the heading *Geology - Rock/Overburden Type*. *Figure 7.4* shows the hypothetical distribution of soft, medium and hard ground.

Figure 7.3 Geologic Section Showing Ore Grade and Ovb. Bedrock Contact

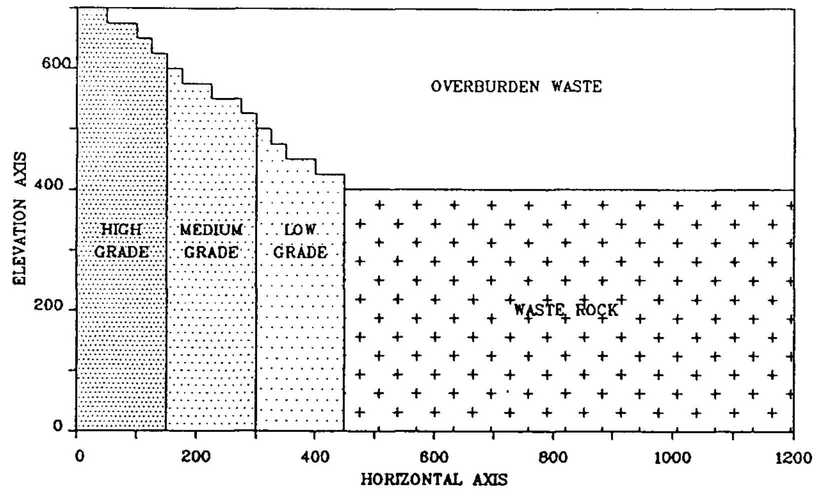

Figure 7.4 Section Showing Digability Characteristics of Subsurface

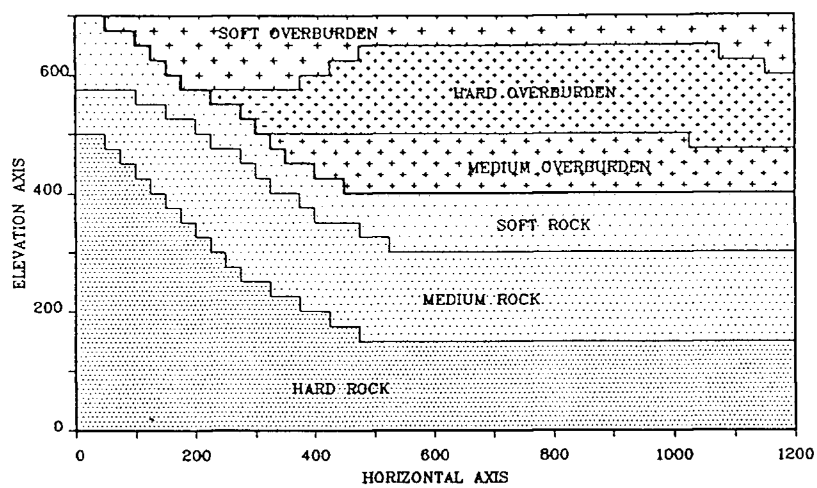

Assuming that a number of undisturbed soil samples were collected in each exploration drill hole and shear strength tests were performed on the samples, the *Slope Stability* section of *Table 7.1* lists base case statistics for both friction angle and cohesion parameters. Since the overburden material appears homogeneous, a circular mode of failure is anticipated.

It is assumed that at this stage of mine development, hydrogeologic information is limited to a small number of slug tests and initial water level measurements taken from recently installed stand-pipe piezometers. Relying on a sound geologic interpretation and experience from other projects, the consulting hydrogeologist would be able to provide initial values for each of the hydrogeologic parameters reported in *Table 7.1*. It is recognized that each hydrogeologic parameter estimate is likely associated with a large degree of estimation uncertainty; the influence of this uncertainty on the economics of the pit wall design will be one of the key issues of the sensitivity investigation. In order to complete the economic calculations that are used to estimate the expected profitability of each pit wall / dewatering system design a number of unit cost parameters must also be specified. These parameters include the unit cost of mining a tonne of rock or overburden, the cost of milling a tonne of ore, percent mill recovery and the price received by the mine operator for the copper concentrate. Realistic values for each of these parameters are tabulated under the headings *Economic Parameters* and *Production Costs* in *Table 7.1*.

With the exception of the dewatering design parameters that are described later in this section, *Table 7.1* summarizes all of the base-case input parameters required to carry out the complete risk-cost-benefit analysis for the selected design sector. In each of the sensitivity studies presented later in this chapter, all input parameters will be set to the base-case values listed in *Table 7.1* unless otherwise specified.

Having defined all of the geologic, shear strength, and hydrologic data it is now necessary to specify the base-case pit wall design, dewatering plan and mining sequence. The base-case mining plan calls for the ore body to be mined over a time span of 25 years in a series of concentric shells or *pits*, numbered *PIT 1* to *PIT 5* in *Figure 7.5*. The bedrock pit walls are to be excavated at 45 degrees from the horizontal, the overburden pit walls, expected to be significantly weaker, are to be excavated at 30 degrees. Double benches, 25 m in height are to be maintained throughout. The pit limits of each 5 year pit have been selected with care so that the mining rate will remain approximately constant at 22 million tonnes per year in this design sector from one pit to the next.

Figure 7.5 Section Showing Pit Limits at 5 Year Intervals

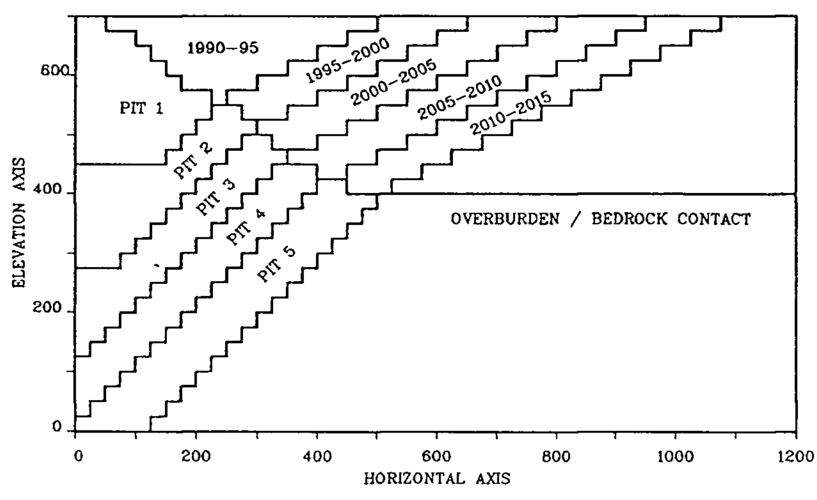

Table 7.1 Input Parameter List for RCB Analysis

PARAMETER	LOWER LIMIT	UPPER LIMIT	BASE CASE
1. GEOLOGY – ORE GRADE			
Size of ore body (billion tonnes)	0.5	5	2.4
Shape of ore body	vein	massive	zoned
massive			
planar vein			
zoned			
Orientation of ore body	horizontal	vertical	vertical
horizontal			
vertical			
inclined parallel to pit wall			
inclined orthogonal to pit wall			
Average grade (%Cu equivalent)	0.4	0.8	0.6
Grade Intervals (%Cu equivalent)			
waste	0.0	0.2	0.1
low grade	0.2	0.5	0.4
medium grade	0.5	0.7	0.6
high grade	0.7	1.0	0.8
Nature of ore/waste transition	sharp	pockets	gradational
sharp boundary			
local pockets			
gradational boundary			
2. GEOLOGY – ROCK/OVERBURDEN TYPE			
Location ovb. bedrock contact	inc. prll.	inc. ortho.	inc. ortho.
horizontal			
inclined parallel (inc. prll.)			
inclined orthogonal (inc. ortho.)			
Angle ovb. bedrock contact (degrees)	0.0	45.0	10.0
Height ovb. slope (meters)	10.0	300.0	200.0
Type of overburden deposit	homogeneous	stratified	homogeneous
Digability characteristics rock (%)			
hard	0	50	47
medium	20	50	33
soft	0	50	20
problem	0	20	0
Digability characteristics ovb. (%)			
hard	0	40	35
medium	20	70	35
soft	0	40	30
problem	0	20	0
Unit weight rock (tonnes/m ^ 3)	3.0	4.5	3.5
Unit weight ovb. (tonnes/m ^ 3)	1.8	2.5	2.2

Table 7.1 cont. Input Parameter List for RCB Analysis

PARAMETER	LOWER LIMIT	UPPER LIMIT	BASE CASE
3. SLOPE STABILITY			
Anticipated failure mechanism			circular
circular			
planar			
block			
toppling			
composite			
Critical failure surface	shallow	deep	medium
shallow seated			
medium seated			
deep seated			
Mean friction angle (degrees)	18	32	26
Stnd. dev. friction angle (degrees)	0	4	2
Mean cohesion (kN/m^2)	0	100	50
Stnd. dev. cohesion	0	20	10
4. HYDROGEOLOGY			
Type of flow system			homogeneous
aquifer / aquitard			
homogeneous			
Mean hydraulic conductivity (m/s)	1E−8	1E−4	1E−6
Stnd. dev. log hydraulic cond.	0	2	0.5
Correlation Range (metres)	0	1000	200
Anisotropy ratio range (vert./hor.)	0.01	1.0	1.0
Semi−variogram model	nugget	Gaussian	Spherical
nugget			
exponential			
spherical			
Gaussian			
Boundary condition inflow face	head	flux	head
specified head (metres)	floor elev.	crest elev.	675
specified flux (m^3/s/m^2)			
Recharge rate on slope (cm/yr)	0	200	0
Recharge rate in uplands (cm/yr)	0	200	50
Initial water table position (metres)	floor elev.	crest elev.	675
5. ECONOMIC PARAMETERS			
Cut of grade (%Cu equivalent)	0.10	0.20	0.20
Inflation rate each period (%)	0.0	12.0	10.0
Interest rate each period (%)	5.0	15.0	10.0
Price received for Cu concentrate ($/kg)	0.88	1.76	1.40

Table 7.1 cont. Input Parameter List for RCB Analysis

PARAMETER	LOWER LIMIT	UPPER LIMIT	BASE CASE
6. PRODUCTION COSTS			
Mining hard rock ($/tonne)	1.20	3.40	2.30
Mining medium rock ($/tonne)	1.10	3.20	2.10
Mining soft rock ($/tonne)	1.00	3.00	1.90
Mining problem rock ($/tonne)	4.00	12.00	8.00
Mining hard ovb. ($/tonne)	0.85	2.40	1.60
Mining medium ovb. ($/tonne)	0.78	2.25	1.50
Mining soft ovb. ($/tonne)	0.70	2.10	1.40
Mining problem ovb. ($/tonne)	2.80	8.40	6.00
Milling ore ($/tonne)	3.00	5.00	4.00
Mill recovery (%)	80	92	89
7. PIT DESIGN			
Size ultimate pit (billion tonnes)	0.5	5.0	2.4
Radius ultimate pit (metres)	500	1500	1066
Depth ultimate pit (metres)	100	900	700
Production rate (million tonnes/yr)	20	150	90
Frequency pit designs (yrs.)	2	5	5
Expected life of mine (years)	15	30	24
Pit angle bedrock	30	50	45
Pit angle overburden	20	35	30
Height design sector (metres)	100	500	300
Width design sector (metres)	200	1000	500
8. DEWATERING SYSTEM DESIGN (see detailed summary that follows)			
9. SUBSURFACE MEASUREMENTS			
Type of measurement			
Geotechnical logging	none	each hole	each hole
Shear strength tests	none	every 10 m	every 20 m
Sieve analyses	none	every 5 m	none
Slug tests in piezo	none	5 per hole	3 per hole
Pump tests in well	none	1 per well	none
Geophysical logging	none	each hole	none

A slope stability analysis of the 30 degree overburden pit wall indicates that the pit wall will be unstable unless a comprehensive groundwater control program is implemented. Therefore, the base-case pit design will include a 4.8 million dollar dewatering system consisting of 25 dewatering wells to be completed over a 20 year period between 1990 and 2010. *Figure 7.6* illustrates the location of the dewatering wells in plan view. The year in which each well will come on-line is also indicated. *Figure 7.7* shows the location of each row of dewatering wells on section, each 5 year pit limit is also shown in the figure. The position of each row of wells has been selected so that the active wells will always be located as close as possible to the active mining area, not hundreds of meters back of the pit crest from where they would provide very marginal pore pressure reduction on the potential failure surface.

Figure 7.6 Plan View of Well Locations for Base Case Pit Design

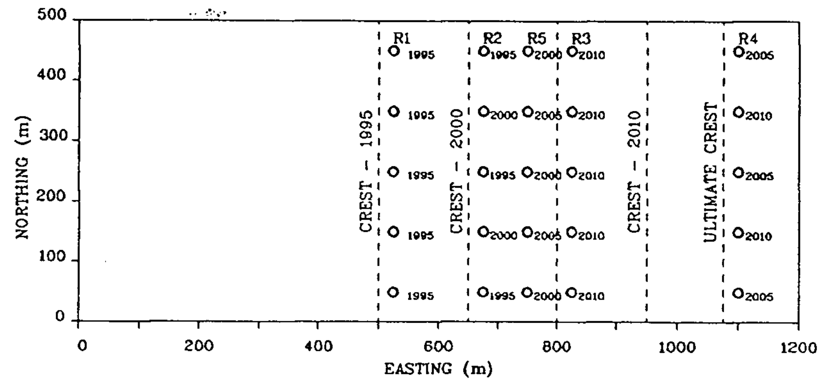

Figure 7.7 Section Showing Location of Wells Relative to Pit Limits

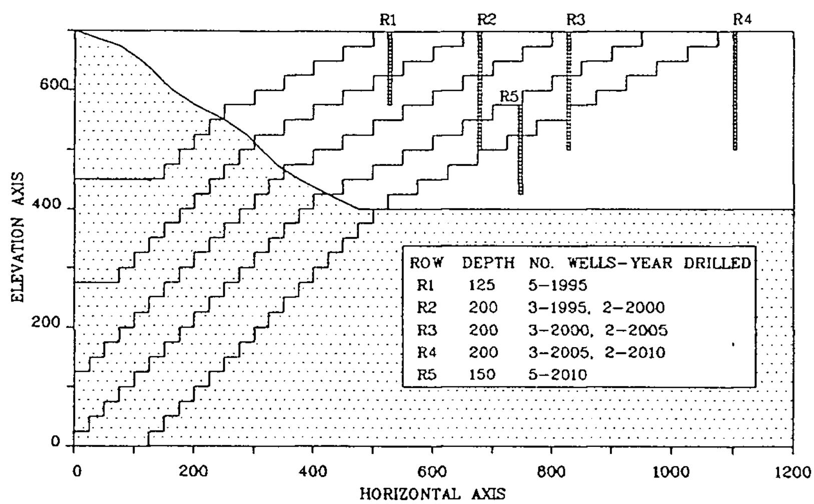

The expected costs of the base-case groundwater control program are summarized in *Table 7.2*. Besides reporting the total net cost of groundwater control, *Table 7.2* also breaks down the dewatering costs for each five year design period into the following categories: development costs, operating costs, and a water supply bonus.

Table 7.2 Base Case Dewatering Costs for Sensitivity Study

YEAR FROM	YEAR TO	WELLS DRILLED	TOTAL METRES	DEVELOP. COST	OPERATING WELLS	PUMP RATE (m^3/day)	OPERATING COST	SUPPLY BONUS	TOTAL COST
1990	1995	8	1150	1447367	8	5178	272395	209036	1510726
1995	2000	5	925	1001527	13	9264	434760	373988	1062299
2000	2005	5	925	1003616	13	11172	487230	451014	1039832
2005	2010	7	1150	1342107	15	12806	552165	516978	1377294
2010	2015	0	0	0	10	8174	374785	329984	44801

Development costs are a function of the number of wells drilled, the depth of each well, the casing diameter, and the design pumping rate. *Tables 7.3* and *7.4* give unit costs for the many materials and services required during the development of each well. The unit costs listed in these *Tables* were used when calculating the base-case well development costs given in *Table 7.2*. Computer program *SG-BUDGET*, developed at Highland Valley Copper, was utilized for all development cost calculations. Operating costs include all costs associated with running, monitoring and maintaining all active wells in peak working condition. By far the largest of these costs is electric power required for running the pumps. Realistic unit costs for each operating cost category are listed at the bottom of *Table 7.3*.

***Table 7.3** List of Unit Costs for Well Diameter Independent Items*

ITEM	UNIT	UNIT COST
Pump Test	$/unit	9900
Lower Pump	$/unit	1650
Lift Pump	$/unit	2475
Rig Time	$/hour	165
Well Head Labour	$/unit	3960
Pump <750 gpm	$/unit	12000
Pump >750 gpm	$/unit	18000
Starter <750 gpm	$/unit	2000
Starter >750 gpm	$/unit	8000
Cable	$/m	20
Electric Power	$/m^3/day/yr	27.5
Maintenance	$/well/yr	10000
Monitoring	$/well/yr	2500
Water Supply Bonus	$/m^3/day/yr	40.37

Table 7.4 List of Unit Costs for Well Diameter Dependent Items

ITEM		16 INCH	12 INCH	10 INCH	08 INCH	06 INCH
Drill and Case	$/m	187	144	127	116	94
Cut Shoe	$/u	2640	2640	2640	2200	2200
String Casing	$/m	0	121	100	88	73
Casing Left	$/m	132	90	61	51	33
Screens	$/m	0	307	220	187	165
Blanks	$/m	0	77	55	43	30
Drop Pipe	$/u	0	0	0	209	44
Discharge Head	$/u	0	0	0	1346	1038
Gate Valve	$/u	0	0	0	932	560
Check Valve	$/u	0	0	0	1209	620

In order to produce copper concentrate, modern mills require vast quantities of water, ranging from 3,000 to 8,000 USGPM. Local surface water supplies are often not sufficient to meet this demand. Under such circumstances the mine must either pipe water from the nearest major river or lake, or develop local groundwater supplies. In either case, the cost of obtaining adequate water supplies will appear as a noticeable fraction of the mill's annual operating budget. By utilizing groundwater from the pit dewatering system, a mine can significantly reduce, if not eliminate, its external water requirements and associated costs, thereby realizing a *water supply bonus*. The net total cost of groundwater control is then defined as the sum of all development and operating costs less the water supply bonus.

Having defined all dewatering parameters, the last step in formulating the base-case problem is to quantify the consequences of pit wall failure. Using the calculation methods described in *Chapter 3*, the expected cost of pit wall failure can be estimated if the total failure volume and probability of failure are defined for each 5 year pit limit. *Figure 7.8* outlines the approximate boundaries of the failure volume for each overburden pit wall; the analytical procedures for estimating the probability of failure for each of these failure blocks are described in the following section.

Figure 7.8 Section Showing Approximate Location Critical Failure Surfaces

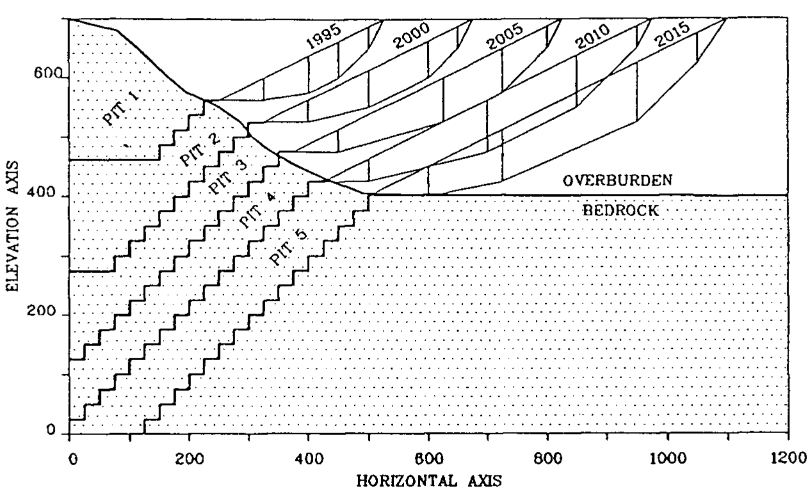

7.3 BASE CASE ANALYSIS

This section describes each of the four key steps involved in the risk-cost-benefit analysis of a pit wall and dewatering design. These steps include: 1) prediction of the hydraulic conductivity field, 2) prediction of the pore pressure distribution, 3) estimation of probability of failure, and finally 4) economic assessment. For illustrative purposes, the analysis is conducted for the base-case scenario described in the previous section.

In the base-case scenario, hydraulic conductivity measurements were conducted only at a small number of piezometer port locations. By combining the measurements with the geologic interpretation it is possible to estimate the statistical parameters that describe the distribution of the log hydraulic conductivity field, including the mean, variance and range. Because much of the hydrogeologic information was derived from geologic inference, the unconditional LU-decomposition simulation method, described in *Section 5.5*, was utilized to generate the large number of equally likely realizations of the hydraulic conductivity field that are required for the Monte Carlo analysis of groundwater flow. Although the location and shape of low and high permeability zones differed from one realization to the next, the statistics of each log hydraulic conductivity realization closely matched the expected statistics of the actual hydraulic conductivity field. *Figure 7.9* illustrates the distribution of low and high hydraulic conductivity zones for a typical realization. A total of *100* realizations were generated to serve as input for the Monte-Carlo analysis of groundwater flow. Although this number of realizations is believed to be adequate in this instance, significantly more realizations (e.g. 500 to 1000) may be required when the tails of the probability distribution need to be accurately reproduced (e.g. contaminant transport problems).

In order to obtain a realistic range of pore pressure distributions in the pit wall during each stage of pit development it is necessary to repeatedly solve a complex boundary value problem that involves an intricate hydraulic conductivity field, the action of dewatering wells, and an undetermined water table position in a saturated-unsaturated flow field. *Figure 7.10* is a schematic of the boundary value problem for the ultimate pit geometry. The computer program *SG-FLOW*, described in *Chapter 5* is capable of modelling each of these complexities. It was utilized to compute the resulting pore pressure distribution for each of the 100 hydraulic conductivity realizations. *Figure 7.11* illustrates the hydraulic head distribution that was computed by *SG-FLOW* for the hydraulic conductivity realization shown in *Figure 7.9*. The position of the water table is also indicated in the figure. Note the reduced pore pressures in the vicinity of *R4* and *R5* rows of dewatering wells (indicated by depressions in the water table) and the distorted shape of the equipotentials, induced by the significant hydraulic conductivity contrasts.

Figure 7.9 Realization of Hydraulic Conductivity Field (log_{10} scale)

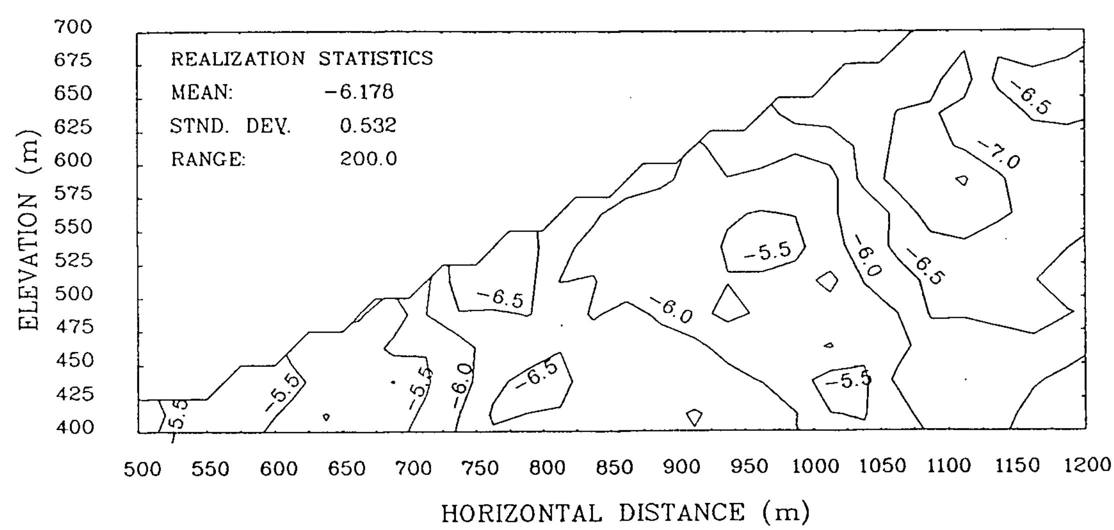

Figure 7.10 Boundary Value Problem - Ultimate Pit Configuration

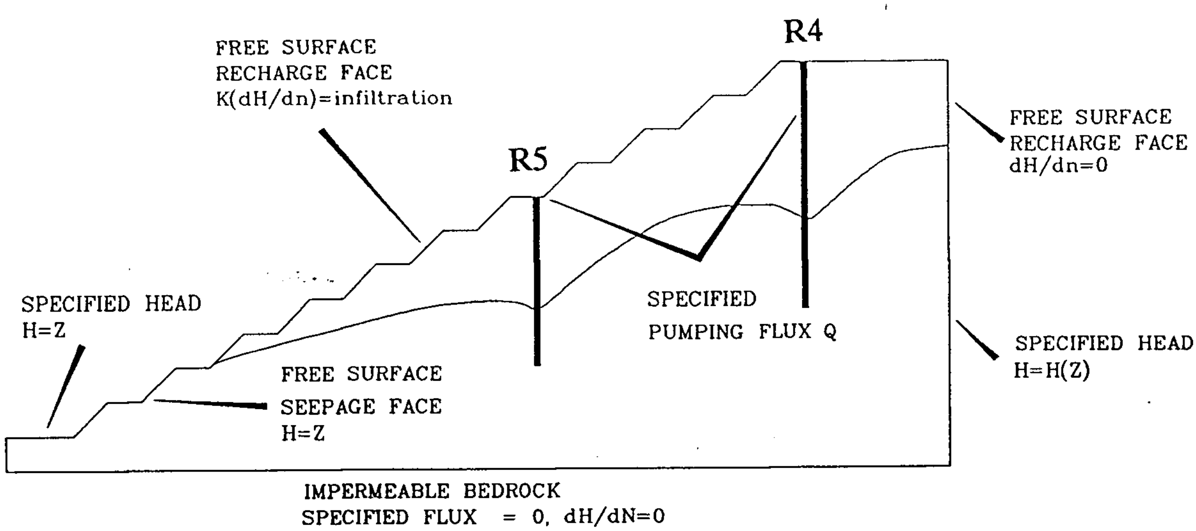

Figure 7.11 Computed Hydraulic Head Distribution

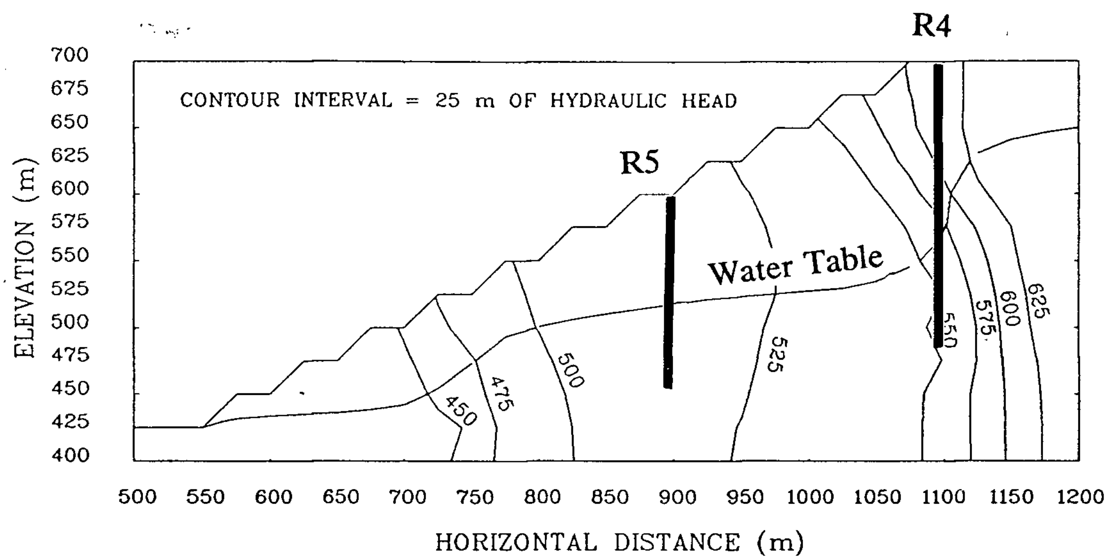

Figure 7.12 Contour Plot of Standard Deviation in Pressure Head

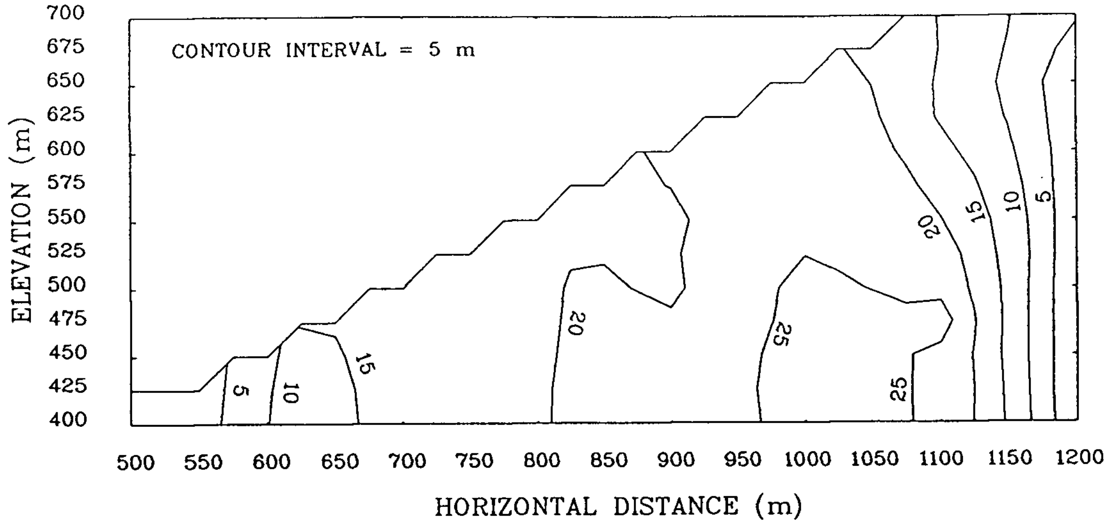

As expected, each realization of the hydraulic conductivity field results in a somewhat different pore pressure distribution in the pit wall. The large degree of variability is clearly illustrated in *Figure 7.12.* This figure is a contour plot of the standard deviation in pressure head computed at each node in the flow domain over the 100 pore pressure realizations. The variability in pressure head predictions is smallest adjacent to the left and right boundaries of the flow domain. This behaviour, first recognized by *Freeze, (1978)*, is due to the fact that the hydraulic head values are constrained by the presence of the two specified head boundaries applied on the inflow and outflow face (see *Figure 7.10*). On these boundaries, the heads are assumed to be known with certainty.

Having established the likely range of pore pressures in the pit wall, the third step in the analysis requires that the probability of failure be estimated for the pit wall at each of the five stages of development shown in *Figure 7.8.* Using a Monte Carlo approach, the *SG-SLOPE* model described in *Chapter 7* was utilized to calculate the critical acceleration coefficient, K_c, for each of the 100 realizations of groundwater pore pressures and shear strength parameters. Although treated in a stochastic manner, the shear strength parameters are assumed to remain constant over each slice boundary and to be uncorrelated from one slice boundary to the next. The bar graph in *Figure 7.13* illustrates the K_c distribution computed for the ultimate pit wall. Recall that positive values of K_c indicate that the slope is stable for the specified input conditions and negative values indicate that the slope is unstable.

The probability of failure was obtained for each pit wall by simply dividing the number of realizations that resulted in failure by the total number of realizations analyzed. *Figure 7.14* summarizes the probabilities of failure for each of the 5 year pits for the base case dewatering scenario. The probabilities of failure are very low, especially in the first fifteen years of operation. The results indicate that the proposed dewatering design will definitely reduce pore pressures to acceptable levels; the first three stages of the groundwater control system in fact appear to be over-designed. In *Section 7.7* it will be shown that the most effective dewatering programs allocate less capital for dewatering in the early stages of mine development, and shift it to an increased dewatering effort during the later stages as the pit approaches it's ultimate depth.

Figure 7.13 Histogram of K_c Coefficients for Ultimate Pit Failure

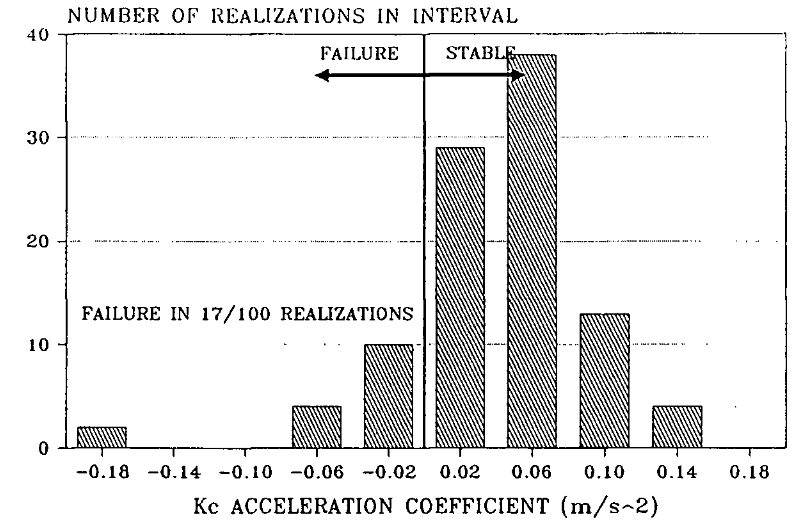

Figure 7.14 Probability of Failure of Pit Wall - 5 year stages

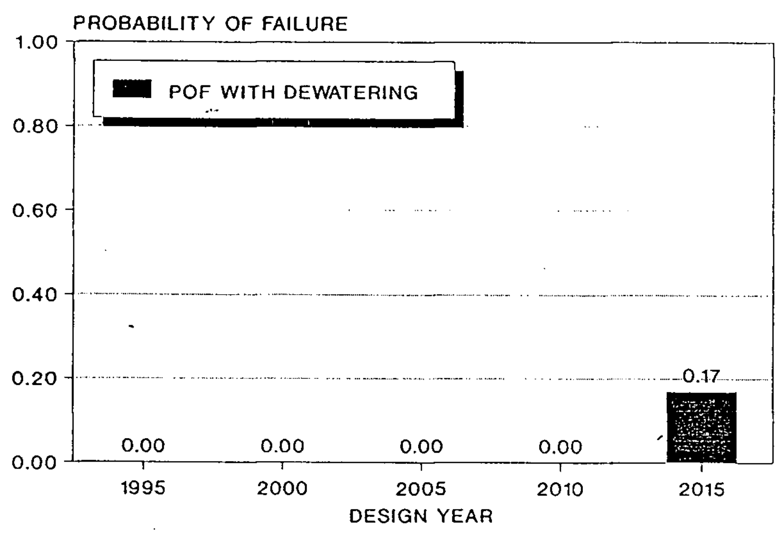

The final step in the analysis is to evaluate the economics of the proposed pit design, to ascertain how net income will be influenced by the proposed stripping ratio, probability of failure, and cost of the dewatering program.

As outlined in *Chapter 3*, the economic analysis begins with an assessment of the total tonnages that are to be excavated during each 5 year push-back. The volume calculations are performed twice, first assuming that no pit wall failure occurs during the push back, followed by a calculation assuming that a full pit wall failure does develop. Results of the conditional tonnage calculations are reported in *Table 7.5*. In the economic formulation, the costs of cleaning up a slope failure are always associated with the subsequent push-back; therefore, the initial push-back is associated with a zero failure volume and costs of clean-up.

Table 7.5 Projected Tonnages for Each Push-Back, With & Without Failure

PUSH-BACK	YEAR FROM	YEAR TO	TOTAL	STABLE (millions of tonnes)	CLEAN UP
1	1990	1995	103.69	103.69	0.00
2	1995	2000	104.34	89.47	14.88
3	2000	2005	103.03	82.03	21.00
4	2005	2010	128.84	97.34	31.50
5	2010	2015	140.44	101.94	45.50
6	2015	ABANDON	0.00	0.00	55.13

The analysis then proceeds to the calculation of the conditional costs and revenues for both stable and failed scenarios. *Table 7.6* summarizes the results for each push-back, including:

- *MINE NO FAIL:* Cost of mining entire push-back if no failure occurs.
- *MINE STABLE:* Cost of mining stable rockmass if failure does occur.
- *MINE CLEANUP:* Cost of excavating failed overburden.
- *MILL:* Cost of milling ore.
- *DEWATER:* Cost of installing and operating dewatering program.
- *REVENUE:* Revenue obtained from sale of copper concentrate.

Table 7.6 Projected Conditional Costs and Revenue, with & without Failure

PUSH-BACK	MINE NO FAIL ($ million)	MINE STABLE ($ million)	MINE CLEAN UP ($ million)	MILL ($ million)	DEWATER ($ million)	REVENUE ($ million)
1	180.16	180.16	0.00	236.25	1.45	569.66
2	203.15	181.80	89.25	284.38	1.00	645.97
3	198.12	165.05	126.00	240.63	1.00	512.42
4	242.13	193.05	189.00	266.88	1.34	528.77
5	274.53	215.12	273.00	358.75	0.00	637.80
6	0.00	0.00	330.75	0.00	0.00	0.00

Figure 7.15 Net Incomes per Push-Back, Conditional and Expected.

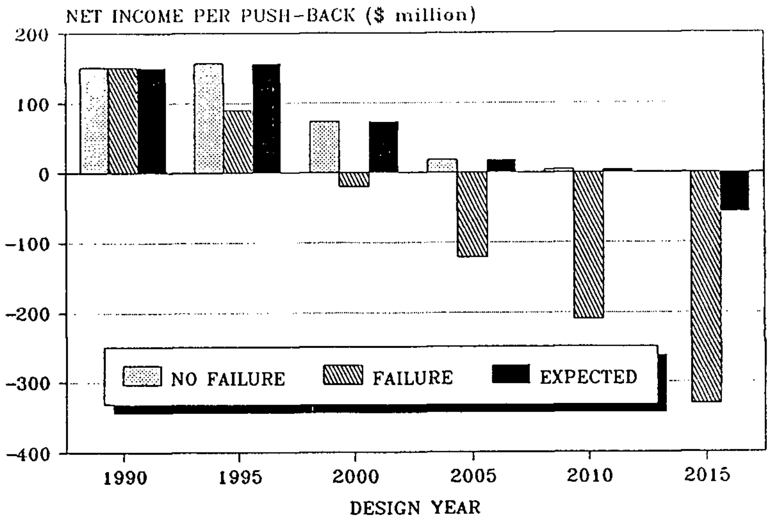

The last calculation in the economic analysis involves estimating the expected net income for each push-back (revenue less operating costs). *Figure 7.15* illustrates the projected values of net income for each 5 year push-back. The figure is obtained by computing the conditional net income for both the no failure and the failure scenarios, and then multiplying each intermediate result by the appropriate probability. The solid bars indicate the expected net income, which serves as the reference parameter for comparing the various design alternatives in this thesis. For this design sector, the expected net income exceeds $150 million during the first two push-backs. Net income then drops steadily as the stripping ratio increases to an expected profit of $3 million in the final push-back, and a potential loss of $50 million if the mine plan required that a failure of the ultimate pit wall would have to be cleaned up to access ore at lower levels in other sectors.

It is very important to recognize that the actual net income generated from mining each 5 year pit will not equal the expected net income; the actual value will depend on whether a failure does or does not occur during the push-back. If a failure does not occur, then the net income will be equal to the value indicated by the dotted bars, if a failure does occur then the net income will be equal to the hatched bars.

Notice that the consequences of failure are particularly severe during mining of the *2010* pit ($205 million loss) and failure of the *2015* ultimate pit wall ($320 million loss). The losses are large because the total tonnages of overburden that would have to be cleaned up are considerable, exceeding 45 and 55 million tonnes respectively. This suggests that any design procedure such as dewatering, that reduces the probability of failure at a cost that is far lower than the cost of cleaning up the failure is going to be extremely attractive. Also, in the case when a failure does occur in the ultimate pit wall, the operator will most likely close the mine early and forgo mining the last remaining ore rather than face the very large clean up costs that would have to be incurred.

In summary, the proposed base-case design appears very profitable, the expected net income over the life of the mine is $348 million, the maximum net income of $405 million occurs at the completion of the fifth push-back in the year 2015. The probability of failure is low during each push-back, never exceeding 17%. In the next section it will be shown that the low probability of failure is in fact a direct result of the aggressive $4.79 million dewatering program that has been incorporated in this design. It will also be demonstrated that as designed, the mine would be less profitable in the short term without the dewatering program, and that in the long term it would experience very heavy losses.

It is very important to note that for the overburden pit wall scenario being analyzed here, the overburden material that constitutes the failure block has no economic value. That will not be the case in situations when the failure block is comprised of ore. In that case, there would also be a significant loss of revenue associated with any failure. The loss of revenue would stem from the fact that it would no longer be possible to conduct accurate grade control when cleaning up the rubble; therefore, most of the ore would be shipped as waste. For this reason, maintaining a low probability of failure is especially important in situations where all or part of the failure block has economic value.

7.4 IMPACT OF GEOTECHNICAL DESIGN DECISIONS

The costs of mining waste rock are very large, and the costs associated with the clean-up after a major slope failure are even larger. Therefore, any design recommendation that reduces the stripping ratio while maintaining the probability of failure at the same level, or vice versa, will have a very positive impact on the profitability of the open pit mine. This section describes how sound geotechnical and hydrogeologic analysis is an effective way of realizing these positive changes.

Consider the hypothetical base case pit design described in *Section 7.2*. Without geotechnical input on the shear strength and hydrologic conditions that will be encountered, the probability of failure of the pit wall during each of the five push-backs could fall anywhere between 0 and 1. *Figure 7.16* illustrates the full spectrum of potential economic outcomes as a function of the unknown probability of failure. If stability conditions are exceptionally good this design sector could generate a windfall profit of 404 million dollars; on the other hand, if conditions are unfavourable, repeated slope failures could lead to an unacceptable loss of $440 million. An enterprise with such a gamut of possible economic outcomes would preclude participation of all but the most speculative investors unless further steps were taken to reduce the risk of economic failure.

Prior to development, prudent mining companies will commission a thorough geotechnical investigation to ascertain the actual subsurface conditions, and follow up with a detailed slope stability and economic analysis of a number pit wall configurations. The latter step is performed in order to identify the optimal slope angle, one that balances the increased risk of slope failure against the monetary benefits of a reduced stripping ratio.

To demonstrate how this important optimization step might be carried out in practice, the analysis described in the previous section was repeated for three additional slope configurations, at 20, 25, and 30 degrees from the horizontal. In each of the latter scenarios, it was assumed that groundwater control would not be utilized. *Figure 7.17* summarizes the results of the four slope stability analyses. As expected, the probability of failure decreases as the slope angle is flattened. For example, without drainage, the ultimate pit wall has an 86% probability of failure at 30 degrees. At 25 degrees the p.o.f. decreases to 78%, a further 5 degree flattening results in a dramatic reduction in POF to 5%.

Figure 7.16 Projected Net Income - Importance of Probability of Failure

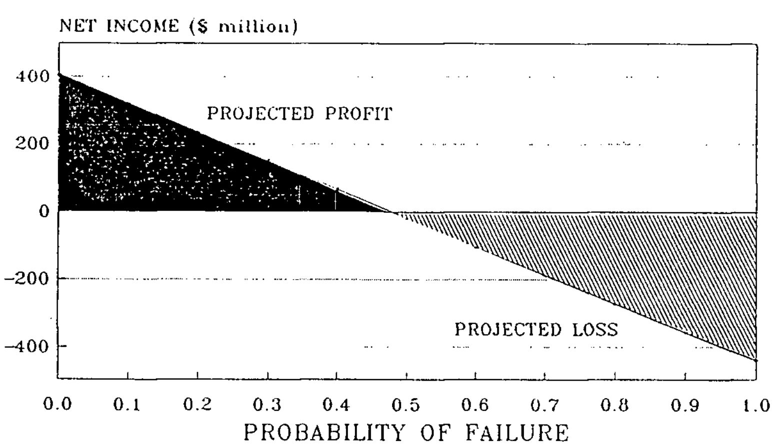

Figure 7.17 Probabilities of Failure for each Slope Design

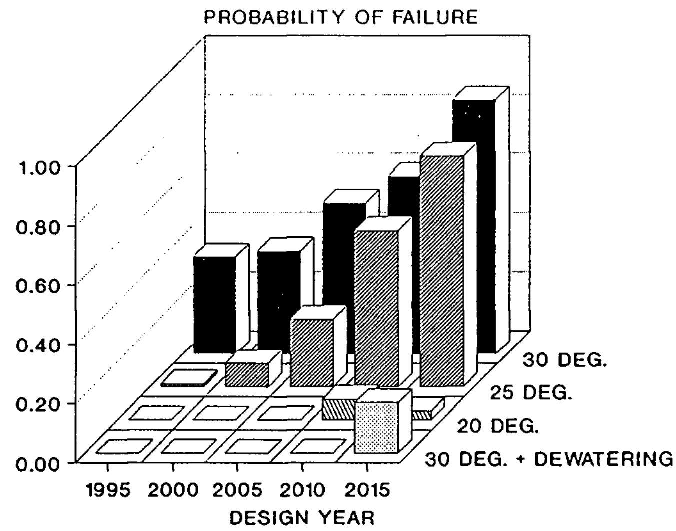

Also of interest in *Figure 7.17*, is the systematic increase in the probability of failure with increasing slope height. This trend is due to increasing pore pressures experienced in the critical toe area as the pit deepens. The trend suggests that it may be beneficial to utilize steeper slope angles in the early stages of mine development and then cut back as the size of the pit wall increases. This design concept will be investigated further in *Section 7.7.*

Having calculated the probabilities of failure for each design, it is still not obvious which of the three designs would yield maximum profits. The 30° design would result in the minimum stripping ratio, but it suffers from a very high probability of failure while the 20° design results in a acceptable probability of failure, but a very large stripping ratio. An economic analysis is required to discern the optimal design alternative.

Figure 7.18, a graph of the expected net-income per push-back for each of the four design alternatives summarizes the results of the economic analyses. The corresponding monetary values are given in *Table 7.7.*

Figure 7.18 Expected Net Income per Push-Back, Four Different Scenarios

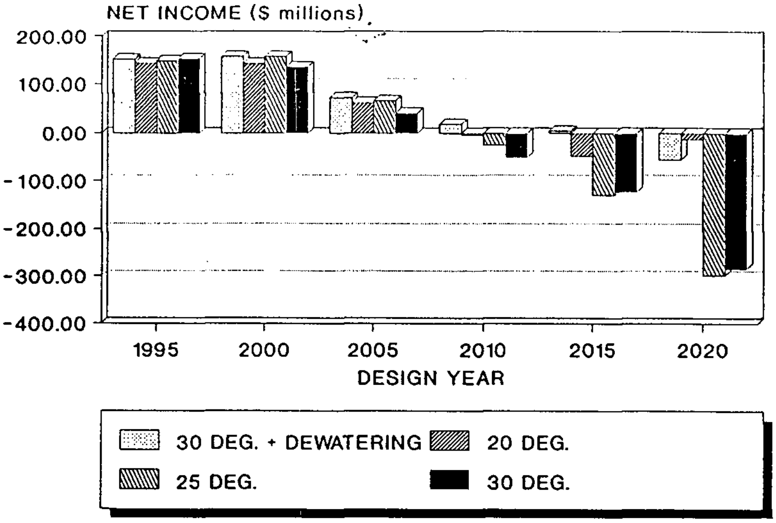

Table 7.7 Monetary Values of Expected Net Income per Push-Back

INCOME PER PUSH-BACK ($ millions)				
PIT YEAR	30 DEGREES + DEWATERING	20 DEGREES	25 DEGREES	30 DEGREES
1995	151.796	143.443	148.343	153.243
2000	157.444	143.220	157.416	136.038
2005	72.667	62.908	66.544	41.147
2010	18.420	-4.388	-24.972	-51.594
2015	4.515	-48.743	-130.251	-123.638
2020	-56.227	-12.915	-298.935	-284.445

The data in *Figure 7.18* shows that during mining of the first push-back (1995), the system would not be sensitive to the actual slope design. Only 8 million dollars separate the best design alternative (30° slope, no dewatering) from the worst (20° slope, no dewatering). The importance of choosing the best slope design becomes much more apparent as the pit deepens and the consequences of failure become more significant. If dewatering is not used, a 25° slope would appear optimal during the second and third push-backs to be completed in years 2000 and 2005. A further 5° reduction in slope angle to 20° would be necessary to maximize profit during excavation of the final two push-backs to be completed in years 2010 and 2015.

Figure 7.19 Expected Cumulative Net Income for Four Design Scenarios

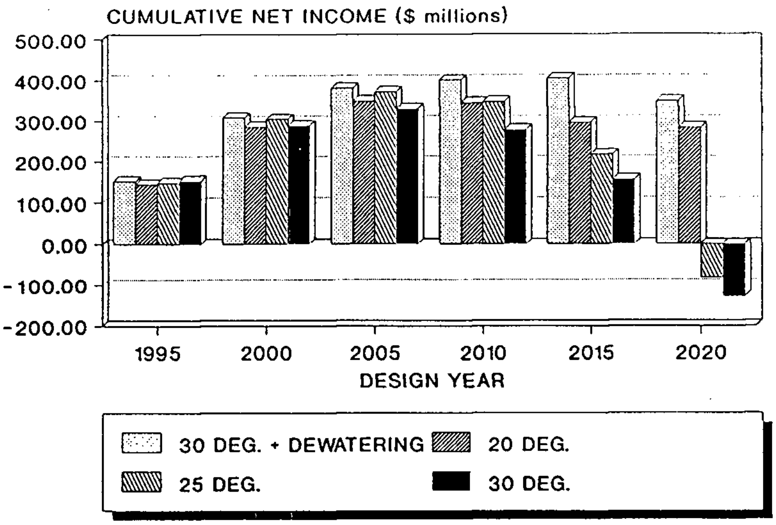

Table 7.8 Monetary Values of Cumulative Expected Net Income - Four Designs

CUMULATIVE INCOME ($ millions)				
PIT YEAR	30 DEGREES + DEWATERING	20 DEGREES	25 DEGREES	30 DEGREES
1995	151.796	143.443	148.343	153.243
2000	309.239	286.663	305.759	289.281
2005	381.906	349.571	372.303	330.428
2010	400.326	345.183	347.332	278.834
2015	404.841	296.440	217.081	155.196
2020	348.613	283.525	-81.854	-129.248

Figure 7.19 and *Table 7.8* present the expected cumulative net incomes for each design alternative. Assuming that the mine will be excavated to the ultimate pit limits, all failures will be cleaned up, and no groundwater control will be utilized, the results indicate that the mine can expect to realize a positive net income of $283 million in this design sector, but only if the overburden slope angle is flattened to 20°. Under the same assumptions, the 25 and 30° pits are expected to result in losses of 82 and 129 million dollars respectively. The same design strategy remains optimal even if the analysis is performed without considering the costs of cleaning up a potential failure of the ultimate pit wall, i.e. the mine is abandoned if a failure occurs during the final push-back.

The optimal slope angle for each push-back can be identified most easily when the cumulative net incomes are plotted as a function of slope angle, as shown in *Figure 7.20.* The optimal slope angle (located at the apex of each push-back curve) clearly migrates from 30° in 1995, to 25° in 2000 and 2005, to approximately 23° in 2010 and 20° for the ultimate pit wall in 2015.

Figure 7.20 Expected Cumulative Net Income as a Function of Slope Angle

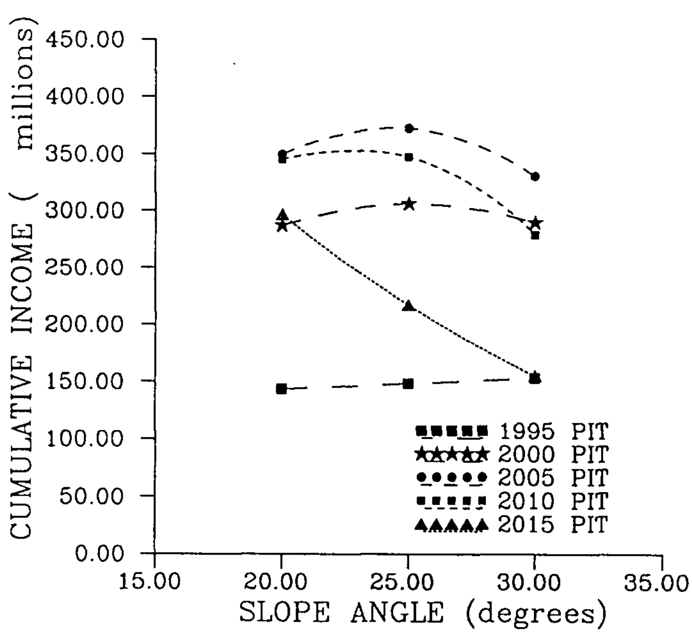

Thus far, it has been shown that the risk-cost-benefit framework described in this thesis provides a powerful tool that can be adopted by geotechnical and mining engineers to identify slope angles that will result in maximum profitability for the mining operation. More importantly, the results presented in *Figure 7.19* suggest that the framework can also be used to assess the economic merit of a groundwater control program.

The expected cumulative net income for the base case pit design is highlighted with a dotted pattern in *Figure 7.19*. Recall that this design called for a 30° slope angle and a $4 million groundwater control program. This design is expected to generate by far the largest net incomes during the final four push-backs (a total of $404.8 million by 2015). By the time the mine is completed in 2015, the aggressive groundwater control program is expected to result in operating cost reductions in excess of 108 million dollars. By adopting the groundwater control program the mine can realize a 38% increase in net income over the next best slope design that does not make any provisions for groundwater control.

The findings presented in the above paragraphs demonstrate that the risk-cost-benefit framework described in this thesis provides a systematic and rational approach to the selection of the optimal pit design, including recommendations for both slope angle and capital investments in groundwater control. Furthermore, the findings indicate that for the particular base case scenario described in this section, groundwater control would result in an impressive $108 million dollar reduction in operating costs during the life of the mine. The remainder of this sensitivity study will investigate whether the same degree of economic benefit can be expected from dewatering programs over a much wider range of potential site conditions. But, before moving on to the sensitivity study, two minor points pertinent to the applicability of conclusions presented in this section remain to be clarified.

First, for the vertically zoned ore body analyzed in this scenario, the expected net incomes per push-back decrease steadily as the pit deepens due to increases in stripping ratio and probability of failure (refer to *Figures 7.3, 7.5 and 7.18*). In fact, *Figure 7.18* suggests that mining should cease by the year 2005 in this sector since heavy losses, or at best marginal profits, are expected during the final two push-backs. However, this may not be the best mining strategy if valuable ore still remains at depth in other design sectors. The optimum size of the ultimate pit can be identified only upon completion of a similar analysis for each design sector in the pit, followed by a synthesis of the design sector results into a single economic model of the entire pit.

Second, it should be noted that a much larger portion of total revenue will be realized in the final few push-backs if the ore body is a oriented in the horizontal plane (e.g. coal seam, gold reef, or tar sand). Maintaining stability of the ultimate pit wall will become even more important in such circumstances.

7.5 SENSITIVITY TO HYDROLOGIC PARAMETERS

Results of earlier risk-cost-benefit analyses of the base-case geologic environment suggest that a dewatering program would be extremely cost effective for that particular geologic setting and slope configuration. However, it is not possible to draw far reaching conclusions regarding the effectiveness of groundwater control programs in the general case from a single analysis. Clearly, conventional dewatering methods will not be effective in some geologic environments. For example, in highly impermeable geologic formations such as massive clays or unfractured shale sequences, well yields can be less than 1 USGPM. At such low pumping rates, hundreds of years would be required to depressurize the pit wall.

The objective of this section is to investigate how performance of a given dewatering program is influenced by local hydrogeologic conditions. In particular, this section will examine the sensitivity of the probability of failure and economic parameters to changes in: 1) mean hydraulic conductivity, 2) variance in hydraulic conductivity, and 3) range of hydraulic conductivity correlation. The primary goal of this sensitivity study will be to identify, whenever possible, a range of values for each hydrogeologic parameter over which satisfactory dewatering performance can be expected.

In order to evaluate the total economic benefit of the base case dewatering program, the preceding analyses calculated the probability of failure and economics for each push-back. The sensitivity calculations that follow have been conducted only for the 2015 ultimate pit wall configuration. This simplification made it possible to concentrate on the functional relationship between drawdown response and the various hydrogeologic parameters without simultaneously analyzing five sets of results. Of course, any conclusions drawn from the ultimate pit wall analysis can also be applied to pit configurations during the earlier push-backs. Since the revenue generated during the final push-back will remain constant and is in fact much smaller than operating costs in this design sector (i.e. mining during the final push-back will result in a loss in this sector), the monetary worth of the dewatering design will be measured in terms of reduced operating costs, rather than net income.

Three types of graphs will be utilized to present the sensitivity results in this section and in the shear strength sensitivity study that follows. First, an X-Y graph (e.g. *Figure 7.23*) that plots mean factor of safety vs. the parameter under investigation is most useful for illustrating the relative increase in stability as shear strength or groundwater conditions improve.

Second, a three dimensional plot (e.g. *Figure 7.25*) is used to illustrate the effect of uncertainty in input parameters on reliability of the stability evaluation. Each 3D plot presents a number of FOS distributions, one for each test value of the parameter under investigation. Each FOS distribution represents a histogram of 100 factor of safety values; one factor of safety is computed for each realization of the hydraulic conductivity field and shear strength parameters. The number of realizations in each interval is indicated on the Z axis, the factor of safety on the X axis, and the parameter under investigation on the Y axis. Please note that in order to present the data from the optimum viewing angle, the X & Y tick marks are reversed, increasing from right to left and from back to front. In each figure, there are three basic things to watch for:

- A shift in the position of the distribution peak from right to left indicates an overall increase in stability as the parameter is varied.
- A flattening of the FOS distribution (increase in standard deviation of FOS values) indicates greater uncertainty in the stability assessment, resulting from increased uncertainty in one or more input parameters.
- The number of realizations that resulted in failure (indicated by the area located to right of the FOS=1.0 axis) is indicative of the probability of slope failure. Note that the probability of failure can increase in one two ways: 1) as the entire distribution shifts to the right, as is the case when the

mean factor of safety decreases, or 2) as the FOS distribution broadens and a larger proportion of the total area falls to the right of FOS = 1.0.

The response of both probability of failure and economic risk to changes in the parameter under study are presented in the third and final type of graph (e.g. *Figure 7.24*). Since the value of monetary risk is directly proportional to the probability of failure (risk = POF·cost of failure) the same graph can be used to illustrate both parameters. The probability of failure is obtained by referring to the axis found along the left margin of the area figures, the monetary risk values are obtained by referring to the axis on the right.

7.5.1 SENSITIVITY TO MEAN HYDRAULIC CONDUCTIVITY

To investigate how a typical dewatering system might perform in a wide range of geologic environments, the complete risk-cost-benefit analysis was performed repeatedly for the ultimate pit wall configuration and failure geometry illustrated in *Figure 7.7*. During each run, the mean hydraulic conductivity was changed by one order of magnitude. As can be seen in *Figure 7.21*, the range of hydraulic conductivities tested, from $1x10^{-10}$ to $1x10^{-2}$ m/s covers all but the most pervious and impervious geologic deposits.

All other parameters were set to the base-case levels specified in *Table 7.1*. Also recall from *Section 7.2* that the base-case dewatering design consists of three rows of five wells, with each well pumping a maximum of 150 USGPM. A Theis analysis suggests that a well yield of this magnitude could be sustained from a 50 to 70 m thick, silty sand aquifer.

To demonstrate the effect of the dewatering system on pore pressures in the pit wall, *Figure 7.22* shows the approximate position of the water table for each hydraulic conductivity scenario, when averaged over 100 realizations. Notice that the base case groundwater control program appears to be effective in reducing pore pressures for hydraulic conductivities in the range of $1x10^{-8}$ m/s to $1x10^{-6}$ m/s. *Figure 7.23* illustrates the mean factor of safety for each hydraulic conductivity value. Note that the mean FOS increases substantially over the range of hydraulic conductivities for which dewatering is effective.

Figure 7.21 *Range of Values of Hydraulic Conductivity for Different Geologic Environments (after Freeze & Cherry, 1979)*

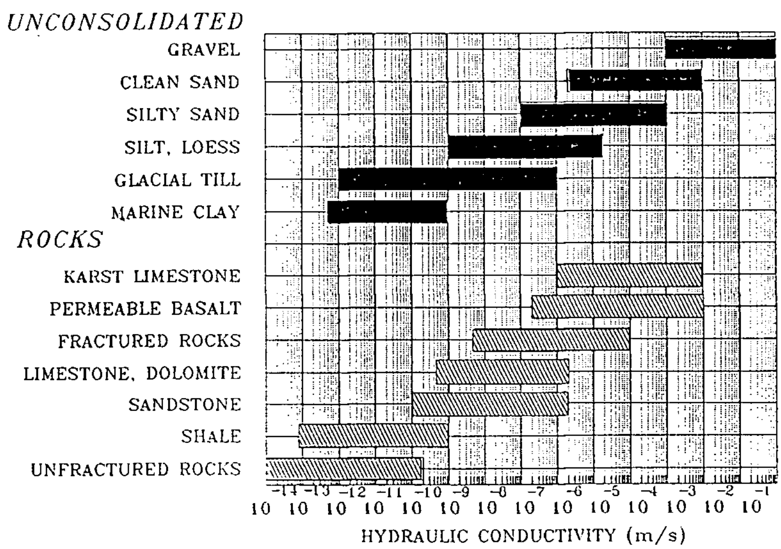

Figure 7.22 Avg. Position of Water Table - Varying Hydraulic Conductivity

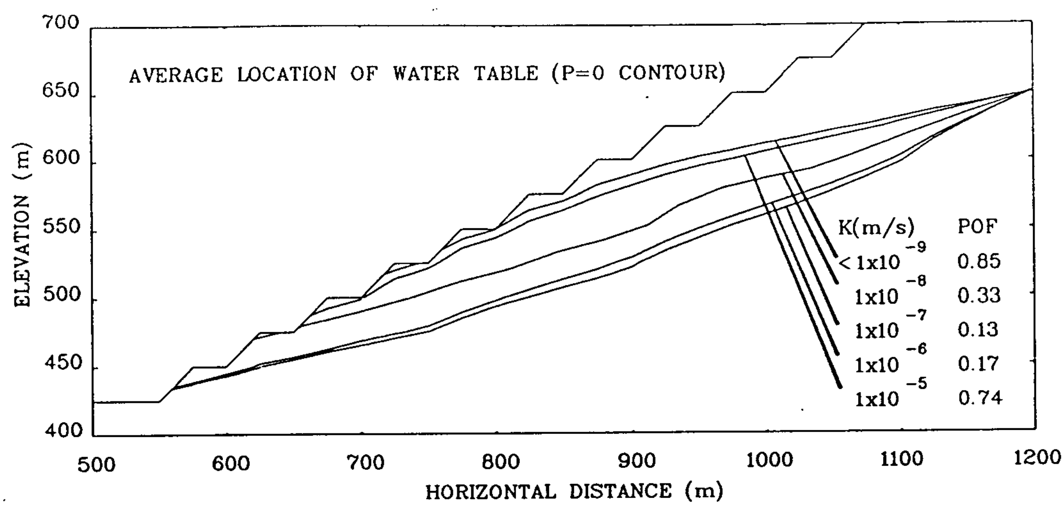

Figure 7.23 FOS vs. Mean Hydraulic Conductivity for Specified Pumping Scheme

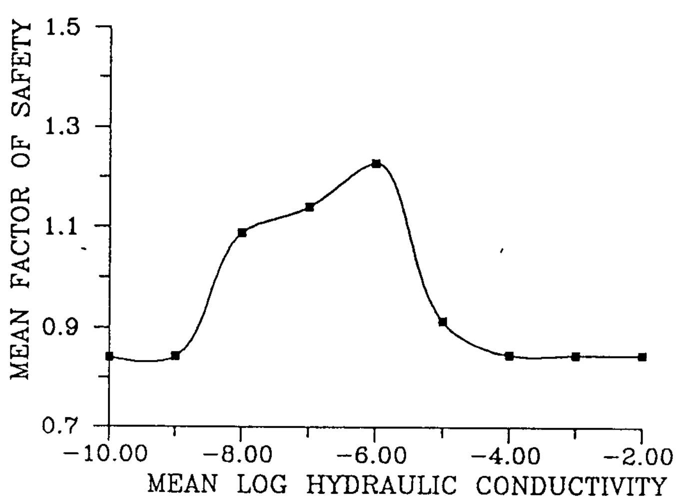

Figure 7.24 Sensitivity of POF and Monetary Risk to Changes in Mean Hydraulic Conductivity

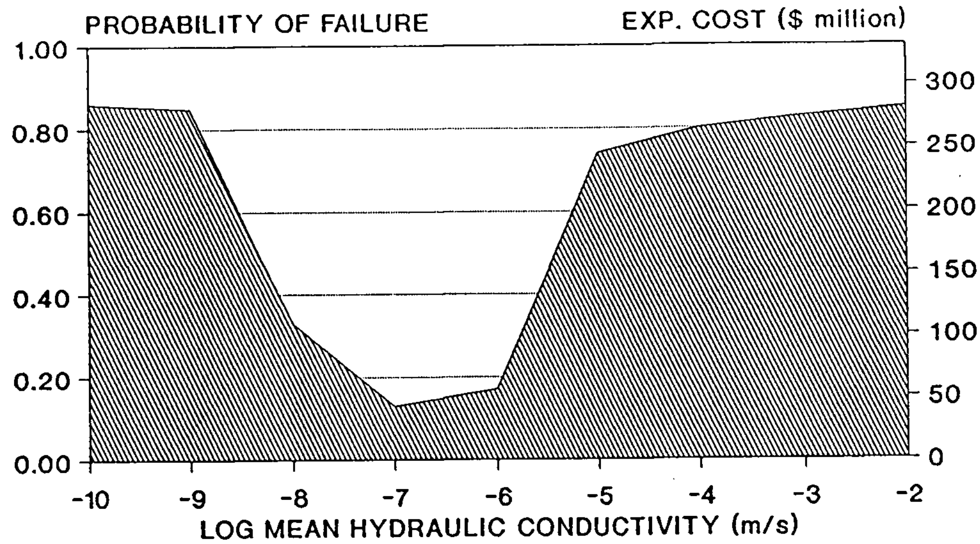

Figure 7.24 presents the probabilities of failure that were obtained for each hydraulic conductivity scenario. As one would expect, there is a close correspondence between the range of K's for which dewatering resulted in a significant reduction in probability of failure and the range showing a large reduction in pore pressures.

The computer simulations indicate that the base-case dewatering program would fail to effectively depressurize the pit wall if the mean hydraulic conductivity fell below $1x10^{-8}$ m/s. This situation would arise because the seepage into each well bore would not be sufficient to keep the pump impellers submerged, even if pumping rates were reduced to as little as 1.5 gpm (Recall from *Chapter 5* that the SG-FLOW computer model automatically reduces the discharge flux at a pumping node whenever negative pore pressures are established, indicating that the immediate area has been completely dewatered). These results suggest that dewatering with conventional wells will not be effective if the mean hydraulic conductivity of the geologic unit falls below $1x10^{-8}$ m/s.

Having studied the data presented in *Figure 7.24*, one may wonder whether a dewatering scheme that maintained the pumps submerged by utilizing very low pumping rates could depressurize the pit wall effectively in impervious geologic strata. Although the results of the SG-FLOW steady state seepage analysis indicate that such a scheme would be effective in theory, in practice, the steady state drawdown response would only be achieved after tens, if not hundreds of years of pumping. Alternate depressurization schemes such as closely spaced, vacuum assisted horizontal drains would have to be utilized to achieve significant levels of depressurization.

Results of the computer simulations also indicate that the base-case dewatering program would fail to achieve substantial levels of pressure reduction if the mean hydraulic conductivity exceeded $1x10^{-6}$ m/s. In highly pervious geologic horizons, pumping rates much larger than 150 USGPM would be required in order to effectively depressurize the aquifer. For example, if the mean hydraulic conductivity was $1x10^{-4}$ m/s, the seepage and stability analysis indicates that pumping rates of 1000 USGPM would be required in all 15 wells before the pore pressure reductions resulted in a significant drop in the probability of failure. Experience from Highland Valley Copper corroborates the numerical simulation results: each of the two dewatering wells situated in a coarse sand aquifer on the property must be pumped at 1000 to 1500 USGPM before a substantial draw-down response is observed in adjacent piezometers.

Once the ultimate pit wall configuration is attained in the upper 300 m overburden portion of the pit wall in 2015, no further operating costs will have to be incurred in the design sector unless a failure develops. In the event that a full wall failure does develop, the consequences would be very serious. Assuming that the slope fails along the 2015 circular failure surface shown in *Figure 7.8* and involves the full width of the design sector, it would encompass approximately 55 million cubic meters. The cost of cleaning up the failure rubble is estimated at $330 million.

The monetary risk of failure[1] associated with the base-case slope angle and dewatering design can also be obtained from *Figure 7.24* for each value of mean hydraulic conductivity by referring the monetary axis plotted along the right margin of the figure. The results suggest that the base-case ultimate pit wall design will present an acceptable risk only if the mean hydraulic conductivity falls in the range $5x10^{-8}$ to $1x10^{-6}$ m/s.

In summary, the value of mean hydraulic conductivity will determine the effectiveness of any groundwater control program. Results of this sensitivity study suggest that dewatering will not be effective if the mean hydraulic conductivity falls below $1x10^{-8}$ m/s or above $1x10^{-5}$ m/s. In the first case, the strata becomes sufficiently impervious as to reduce the yield of each pumping well to a trickle. In the second case, lack of resistance to flow in the subsurface will result in the development of a very extensive draw-down cone around each pumping well. Huge quantities of water would have to be pumped to achieve desired draw-downs. Besides resulting in very high pumping costs, such dewatering efforts could also present severe environmental problems that include: 1) disposing of the water, 2) reducing or drying up other domestic and industrial groundwater supplies in the area, and 3) adverse effects on surface hydrology. Instead of utilizing dewatering wells, groundwater control would likely be achieved by grouting or a dredge would be employed to excavate below the water table.

7.5.2 SENSITIVITY TO STANDARD DEVIATION OF HYDRAULIC CONDUCTIVITY

Recall from *Section 5.2.1* that the standard deviation of the log hydraulic conductivity field, σ, indicates the degree of fluctuation of K about the mean value. Also recall from that section that a standard deviation of 0.2 indicates very homogeneous strata, while a σ of 2.0 is typical in very heterogeneous deposits. The objective of this subsection is to investigate how natural variability in subsurface geologic conditions will impact on the effectiveness of a groundwater control program.

In order to investigate this impact, the base-case scenario was analyzed for seven different standard deviation values: 0.1, 0.22, 0.32, 0.50, 0.70, 1.00 and 1.41. Once again, the variance of both strength parameters was set to 0 while all other parameters were held at the initial base-case levels. Since a base-case value of 200 m was specified for the range, zones of high and low hydraulic conductivity generated in each realization were typically 100 to 200 m in size (see *Figure 7.9* for example).

Figure 7.25 presents a three dimensional plot of the FOS histograms obtained during each of the seven runs. In the figure, notice the FOS distribution is very tight when the standard deviation in LOG(K) is low, the variance then increases rapidly as the standard deviation in LOG(K) increases.
The inset diagram in *Figure 7.25* shows that the mean factor of safety remains nearly constant at a value of 1.1 in all seven runs, while *Figure 7.26* shows that there is a striking increase in the probability of failure from 0.03 to 0.41. The direct cause of the observed increase in POF is easily identified in *Figure 7.25*. As the standard deviation in log(K) increases, the pore pressure distributions become more variable and the tails of the FOS distribution move outward. As a result, computed factor of safety values for more and more realizations fall to the right of the FOS = 1.0 axis, and the probability of failure increases. In subsequent sections, this process is referred to as the *tail effect*.

---

1 Recall that monetary risk, or expected cost of failure, is defined as the product of the cost of failure and the probability of failure.

Figure 7.25 FOS Distributions for Several Levels of Standard Deviation in K

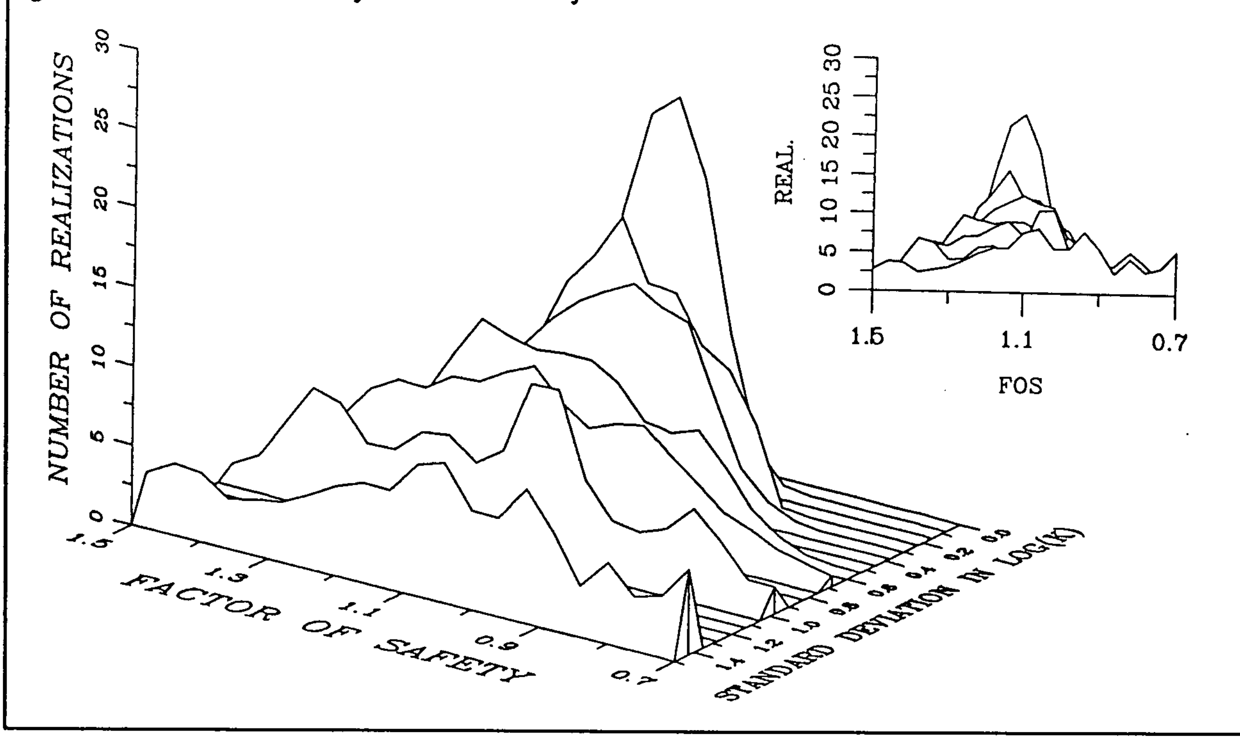

Figure 7.26 Sensitivity of P.O.F. and Monetary Risk to Changes in Standard Deviation of Hydraulic Conductivity

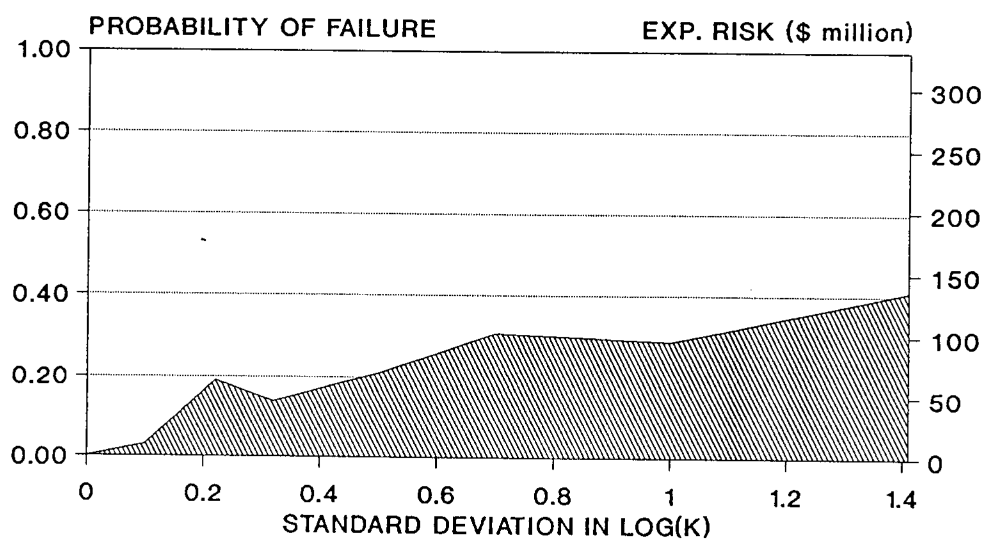

The observed increase in both the factor of safety variance and the probability of failure can be explained as follows. When σ is small, each realization of the hydraulic conductivity field will be almost the same as all others, and the position of the water table will deviate only slightly, hence the tight FOS distribution. On the other hand, when σ is large, each hydraulic realization will be very different from the others, as will the computed pore pressure distribution and factor of safety. *Figures 7.27* and *7.28* substantiate this hypothesis. Both figures are contour plots of the standard deviation in pressure head response at each node in the flow domain. For a very small standard deviation in hydraulic conductivity (i.e. 0.1), *Figure 7.27* shows that pore pressures varied by less than 7.5 m from realization to realization over most of the flow domain. *Figure 7.28* shows that the uncertainty in the pore pressure response increased dramatically when variability in the hydraulic conductivity field was increased to $\sigma = 1.41$.

Figure 7.27 Contours of Standard Deviation in Pressure Head for $\sigma = 0.1$

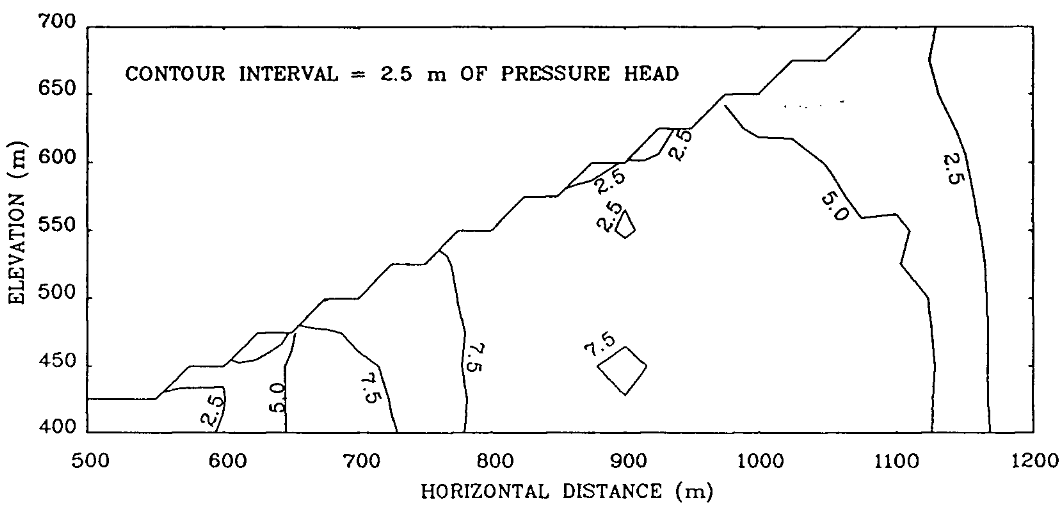

Figure 7.28 Contours of Standard Deviation in Pressure Head for $\sigma = 1.41$

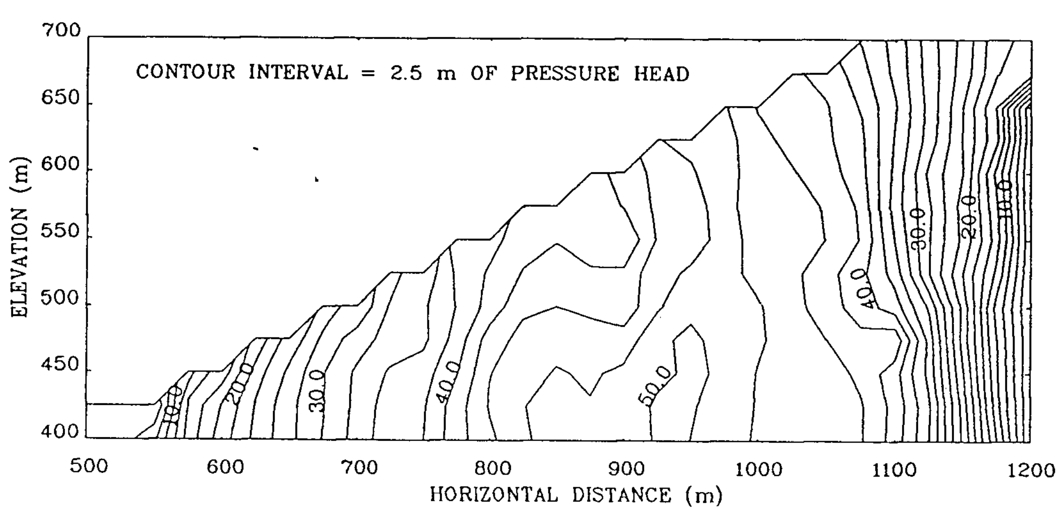

Sensitivity of the economic system to changes in the standard deviation of the hydraulic conductivity field is also portrayed in *Figure 7.28* in terms of the monetary risk of slope failure. Although the economic system is less sensitive to the standard deviation in K than it is to changes in mean K, the differences in the expected effect of dewatering between a homogeneous and heterogeneous system are still substantial, exceeding 125 million dollars. In *Section 7.8* it will be shown that when faced with a highly heterogeneous system, the risk term can be reduced to acceptable levels by implementation of a detailed permeability testing program.

The previous paragraphs clearly demonstrate a major advantage of the probabilistic design approach in geologic environments where uncertainty exists in one or more of the input parameters. By utilizing only average or representative parameter values and a constant factor of safety (e.g. 1.1), engineers adopting the factor of safety (i.e. deterministic) design philosophy will fail to differentiate between the low risk situation when all parameters are known accurately, and the high risk situation when parameters are uncertain. In the preceding example, the monetary value of the difference in risk between these two scenarios exceeds 125 million dollars, approximately 30% of the total net income from this design sector.

8.5.3 SENSITIVITY TO RANGE OF CORRELATION

Recall from *Section 5.2.1* that the range is a measure of the distance over which the hydraulic conductivity field is correlated. A small range value is indicative of a geologic environment with many small, discontinuous lenses of high and low permeability[2]. A large range value is indicative of large, continuous zones of impervious and highly permeable materials. The objective of this subsection is to ascertain how the level of spatial continuity in the hydraulic conductivity field impacts on the performance of a groundwater control program.

In order to carry out this sensitivity study, the base-case scenario was analyzed for seven different values of the range, including: 25, 50, 100, 200, 400, 500 and 750 m. *Figure 7.29* shows the distribution of the 100 factors of safety computed for each range. The two dimensional perspective graph inset in *Figure 7.29* indicates that the mean factor of safety remains essentially constant at 1.1. However, the spread of FOS values about the mean increases with increasing range.

Once again, the increase in the variance of FOS values is caused by increased variability in the pore pressure response from realization to realization as the range increases. When the range is small (i.e. 25 m), each realization of the hydraulic conductivity field will appear as a mosaic of many local fluctuations. When analyzed on the scale of a large pit wall, these local variations become insignificant; the computed pore pressure distribution fluctuates very little from realization to realization, indicating that the system is behaving almost as if it was homogeneous. Since pore pressures remain nearly constant, the corresponding FOS distribution is very tight and the probability of failure is small.

When the range increases to 200 m or more, the position of the heterogeneities will have a tremendous influence of the pore pressure distribution observed in each realization. If a high K lens is predicted in the toe area it will drain naturally by gravitational forces. Pore pressures will be low over much of the slope and a high FOS value will be obtained for that realization. Alternately, if a low K lens is predicted there, it will act as a dam, increasing pore pressures and raising the position of the water table over much of the slope. As indicated in *Figure 7.30*, an increase in the range raises the probability of failure to approximately 25% as a result of the tail effect.

---

[2] As a rule of thumb, the maximum dimension of each lens will be approximately equal to the range.

Figure 7.29 FOS Distribution for Several Values of Range

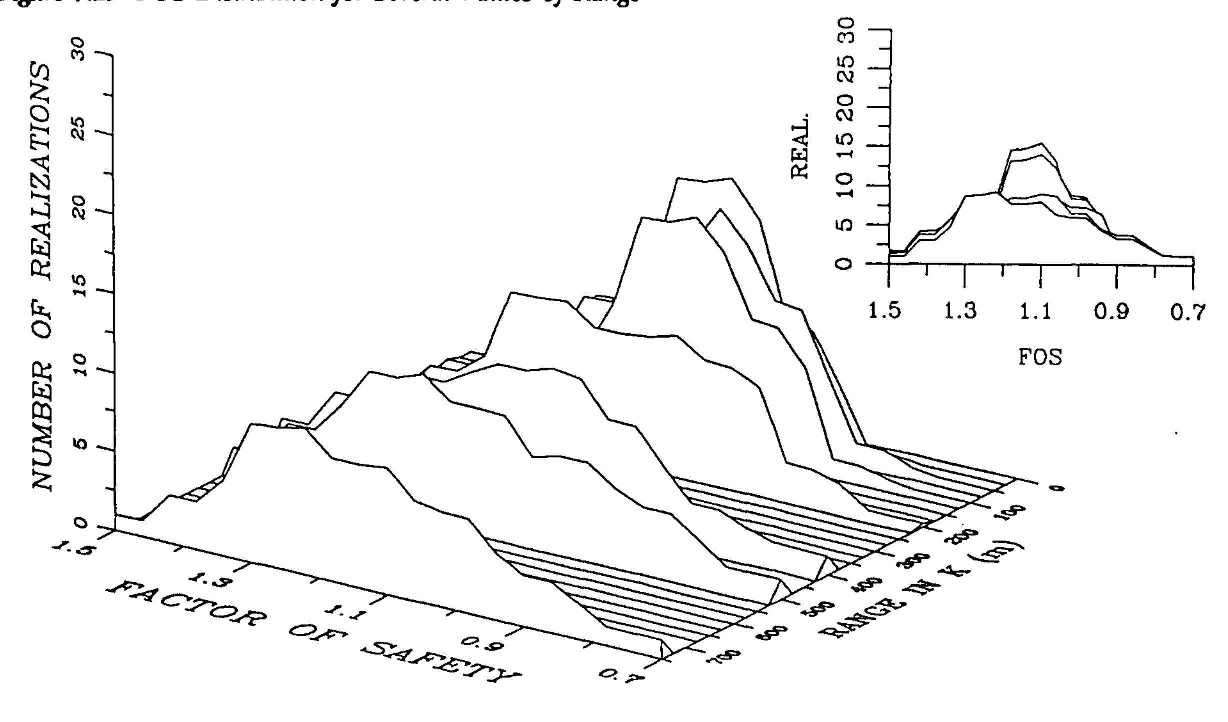

Sensitivity of the economic system to variations in the range is also given in *Figure 7.30* in terms of monetary risk of slope failure. The effect of the range appears less significant than that of the mean hydraulic conductivity or the standard deviation in K. However, in this case the results must be interpreted very carefully.

The tight FOS distribution for small values of range in *Figure 7.29* indicates that the actual factor of safety and probability of failure can be estimated reasonably accurately when zones of low and high K are small. If the range is large on the other hand, the degree of stability and dewatering requirements cannot be predicted accurately without a detailed hydrogeologic investigation. The results plotted in *Figure 7.30* indicate that there is 20% probability of encountering a highly unfavourable hydraulic conductivity distribution in the pit wall if the range exceeds 200 m. If the geology is indeed unfavourable, then there will be every likelihood of failure unless the in-situ hydraulic conductivity distribution is identified and a dewatering program is designed specifically for observed conditions. Additional slope flattening may also be required to minimize the risk of failure.

These results emphasize the importance of characterizing subsurface conditions, especially the location of high K and low K zones, once the size of these zones becomes significant relative to the size of the pit wall (e.g. when the range is greater than one fifth of the maximum dimension of the flow domain). By conducting a detailed geologic investigation, a permeability testing program, and a conditional numerical simulation of groundwater flow, it will be possible to determine whether actual subsurface conditions are very favourable and little dewatering is required (e.g. realizations with FOS = 1.3) or conditions are unfavourable and slope flattening is required even with the dewatering program (e.g. realizations with FOS = 0.7). The worth of site characterization will be investigated further in *Section 7.8*.

Figure 7.30 *Sensitivity of POF and Monetary Risk to Changes in Range of Correlation of Hydraulic Conductivity Field*

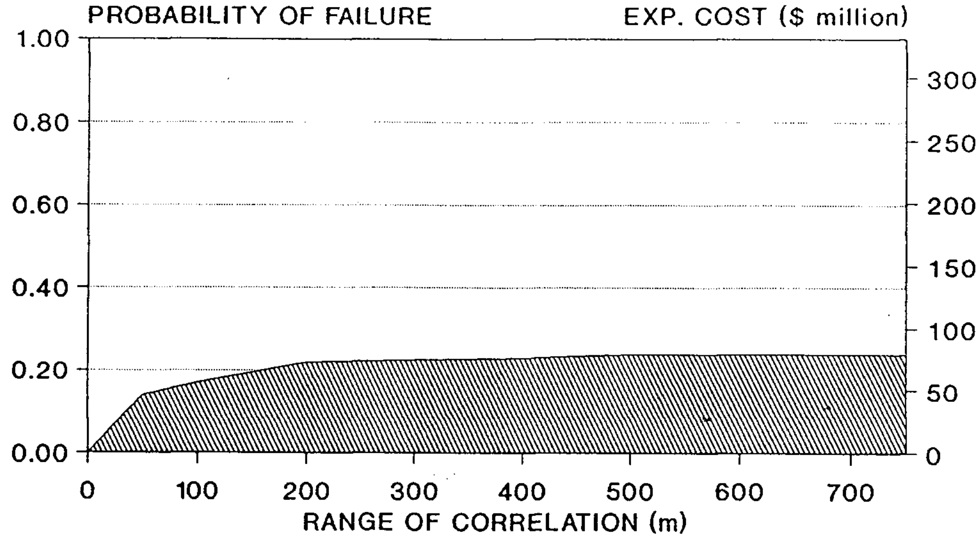

7.6 SENSITIVITY TO SHEAR STRENGTH PARAMETERS

The degree of stability of a pit wall is controlled by both groundwater pore pressures and shear strength conditions on the failure surface. System sensitivity to hydrogeologic parameters was investigated in the previous section. This section examines how stability of the pit wall is influenced by shear strength parameters, including friction angle and cohesion. In each case, the sensitivity analysis is performed over the full range of strength values normally encountered in overburden materials. A likely range of friction angle and cohesion values is listed in *Table 7.8* for the most common soil and rock types. Key topics that are discussed in this section include: 1) the effect of parameter uncertainty, 2) the relative importance of friction angle vs. cohesion data, and ultimately, 3) the relative importance of hydrologic data vs. strength data.

To filter out the large variations in computed factors of safety that are introduced as a result of fluctuations in the hydraulic conductivity field from realization to realization, all of the sensitivity runs in this section were conducted using a single pore pressure distribution[3].

7.6.1 SENSITIVITY TO MEAN FRICTION ANGLE

To assess the influence of the friction angle parameter on pit wall stability and economics, the base case scenario was analyzed for eleven possible values of friction angle, spaced uniformly between 25 and 35°. As can be seen in *Table 7.9,* this range of friction angle values spans almost all overburden and rock types. Results of the sensitivity study, presented in *Figure 7.31,* show that the mean factor of safety increases from 0.8 to 1.3 as the friction angle is varied. The increase in FOS appears linear over the range of friction angles tested; the mean factor of safety increases by 0.05 for each one degree change in ϕ. The corresponding probability of failure distribution is plotted in *Figure 7.32.* The transition from a probability of failure of 0 to a POF of 1 occurs very rapidly between 28 and 30 degrees as the tight FOS distribution shifts from stable to unstable. The transition would be somewhat more gradual if variability in pore pressure was also introduced in the analysis.

---

3 The pore pressure field computed for a homogeneous slope with $K=1x10^{-6}$ m/s and base case dewatering program was utilized.

Table 7.9 Typical Properties for Soil and Rock (Modified after Table 1, Hoek & Bray, 1981)

MATERIAL	UNIT WEIGHT Saturated (kN/m^3)	UNIT WEIGHT Dry (kN/m^3)	FRICTION ANGLE (degrees)	COHESION (kN/m^2)
SOIL MATERIALS				
GRAVEL				
Gravel, uniform grain size	22	20	34-37	0
Sand and gravel, mixed grain size	19	17	38-45	0
SAND				
Loose sand, uniform grain size	19	14	28-34	0
Dense sand, uniform grain size	21	17	32-40	0
Loose sand, mixed grain size	20	16	34-40	0
Dense sand, mixed grain size	21	18	38-46	0
CLAY				
Soft Bentonite	13	6	7-13	10-20
Very soft organic clay	14	6	12-16	10-30
Soft, slightly organic clay	16	10	22-27	20-50
Soft glacial clay	17	12	27-32	30-70
Stiff glacial clay	20	17	30-32	70-150
Glacial till, mixed grain size	23	20	32-35	150-200
ROCK MATERIALS				
BLASTED/BROKEN ROCK				
Basalt	22	17	40-50	0
Chalk	13	10	30-40	0
Granite	20	17	45-50	0
Limestone	19	16	35-40	0
Sandstone	17	13	35-45	0
Shale	20	16	30-35	0
INTACT ROCK				
Hard igneous rocks granite, basalt, porphyry	25-30	25-30	35-45	35000-55000
Metamorphic rocks quartzite, gneiss, slate	25-28	25-28	30-40	20000-40000
Hard sedimentary rocks limestone, dolomite, sandstone	23-28	23-28	35-45	10000-30000
Soft sedimentary rock sandstone, coal, chalk, shale	17-23	17-23	25-35	1000-20000

Figure 7.31 Sensitivity of Mean FOS to Changes in Friction Angle

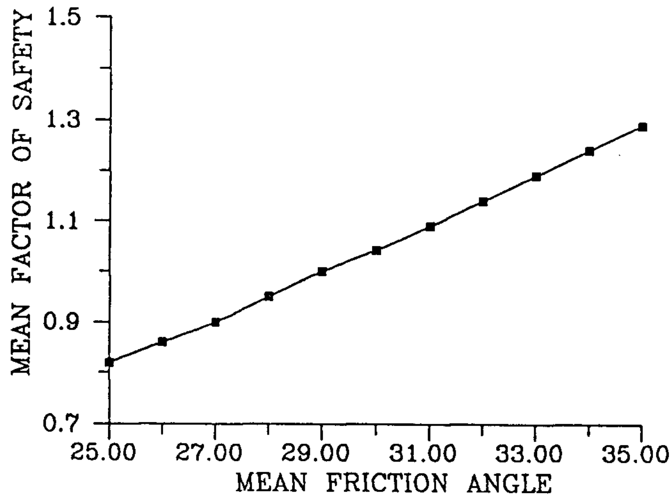

Figure 7.32 Sensitivity of P.O.F. and Risk to Changes in Mean Friction Angle

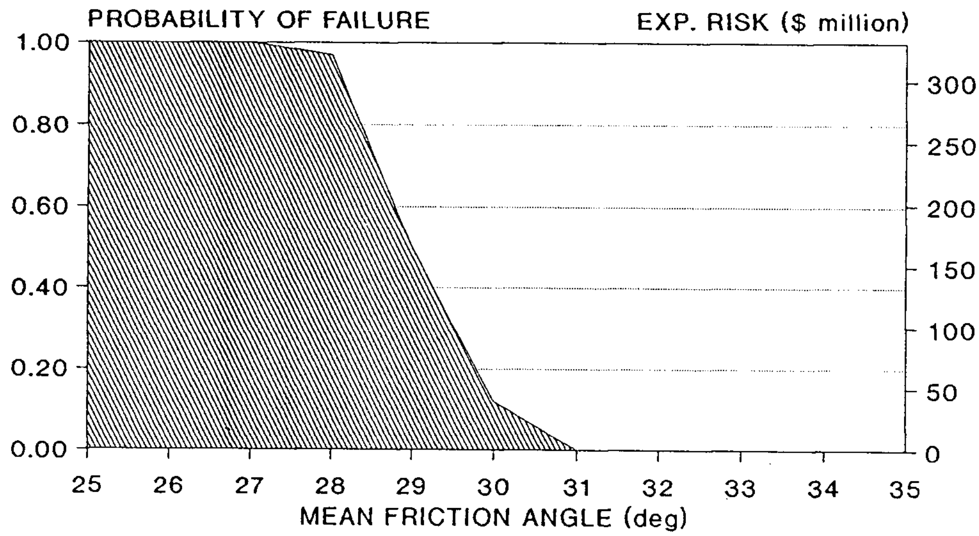

The economic consequences of failure, given by the monetary risk term in *Figure 7.32*, make it vital to determine the mean friction angle as accurately as possible by laboratory testing. Friction angle estimates based on material type, typically accurate to ±3° in consolidated overburden, are not adequate for design purposes.

7.6.2 SENSITIVITY TO STANDARD DEVIATION IN FRICTION ANGLE

The standard deviation of the friction angle distribution serves as an indicator of parameter uncertainty, including both inherent spatial variability and statistical uncertainty in the true value (Benjamin & Cornell, Pg. 632). Assuming that a mean friction angle of 30° has been identified during the site investigation, the objective of this sub-section is to determine how the level of uncertainty in ϕ about the mean value will affect the probability of failure. The spread of standard deviation values analyzed covers the full spectrum of likely values, from 0 to 3°. In the first case, the friction angle would be known exactly, in the second case the friction angle estimate would be associated with an error of ±6° at a 95% confidence interval.

In order to focus on the effect of uncertainty in the friction angle, the deterministic pore pressure distribution was used once again in all runs. The resulting FOS distributions for each level of uncertainty in ϕ are plotted in *Figure 7.33*. As expected, the FOS distribution becomes progressively more dispersed as the standard deviation in ϕ increases, the standard deviation in FOS increases from 0 to 0.08 over the interval tested. The probability of failure, plotted in *Figure 7.34*, also increases from a minimum of 0 to a maximum of 0.29; the increase is due to the widening tail effect described at the beginning of this section. The sensitivity results suggest that if possible, the standard deviation in ϕ should be reduced to less than 1.5° in order to attain a reliable stability assessment (standard deviation in FOS < 0.05). The monetary worth of friction angle measurements is indicated in *Figure 7.34*. By reducing uncertainty in the friction angle determination to ±1° (sdev ϕ=0.5), the risk associated with failure of the ultimate pit wall can be reduced by $90 million.

Figure 7.33 *FOS Distribution for Several Levels of Uncertainty in Friction Angle*

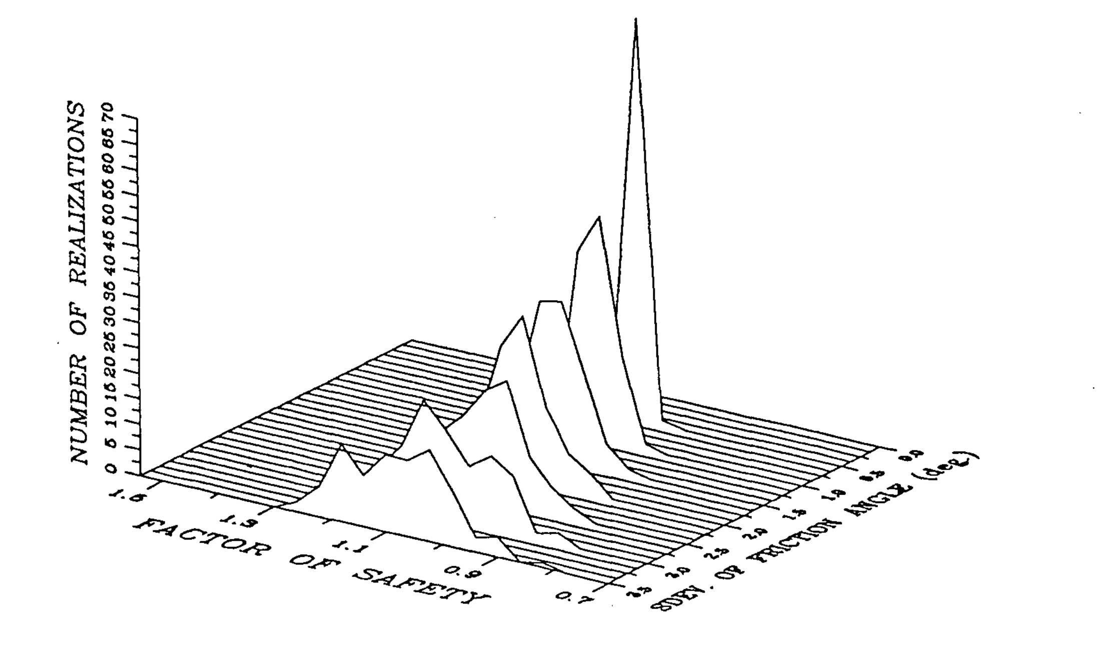

Figure 7.34 *Sensitivity of POF and Risk to Changes in Standard Deviation of ϕ*

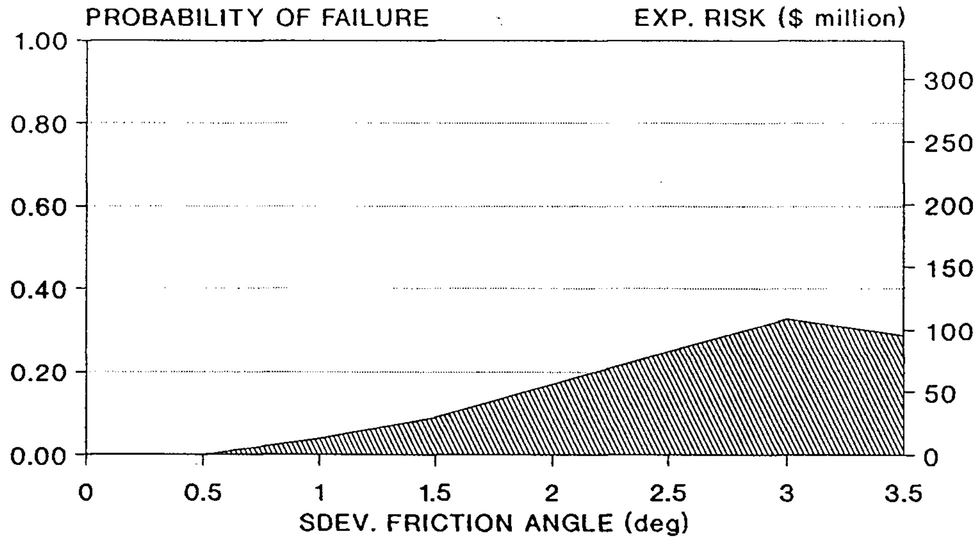

7.6.3 SENSITIVITY TO MEAN COHESION

Table 7.9 also presents cohesive strength values for a wide variety of overburden and bedrock materials. In clay rich soils cohesive strength is a function of clay mineralogy and organic content, it can range from 10 to 250 kN/m^2. In coarse grained or *cohesionless* soils that lack clay mineral content (e.g. clean gravels, sands, and some silts) significant cohesive strength does not develop. Parameter estimates for stability analysis can be obtained from triaxial tests performed in the laboratory, or in some cases, vane shear tests performed in the field. Care must be taken to perform the tests under appropriate stress and drainage conditions.

To assess the effect of cohesion on stability, the base-case slope was analyzed repeatedly using the full range of possible cohesion values encountered in overburden materials. *Figure 7.35* shows that the mean factor of safety increases from 0.91 to 1.45 over the range of trial c values. The functional relationship between FOS and cohesion is linear, an increase of 18.5 kN/m^2 is required to raise the mean factor of safety by 0.05. The effect on the probability of failure is illustrated in *Figure 7.36*. Notice that the probability of failure drops to 0 much more quickly than in *Figure 7.32*. Since a base-case friction angle of 30° was utilized in this sensitivity study, only a slight increase in cohesion is required to bring about a condition of stability.

Figure 7.35 *Sensitivity of Mean FOS to Changes in Cohesion*

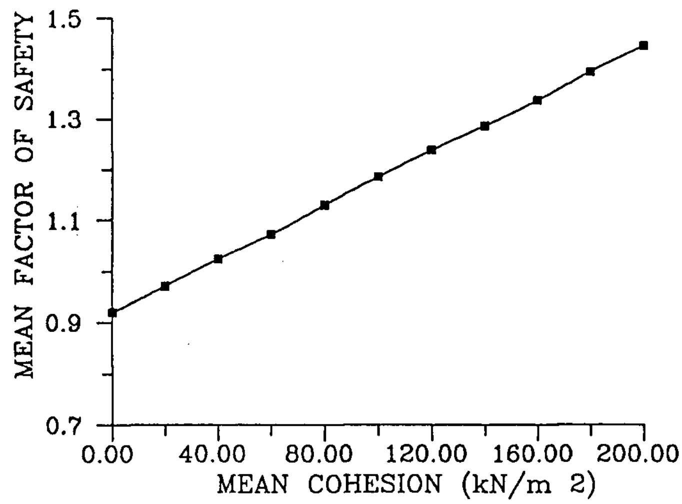

Figure 7.36 *Sensitivity of POF and Risk to Changes in Mean Cohesion*

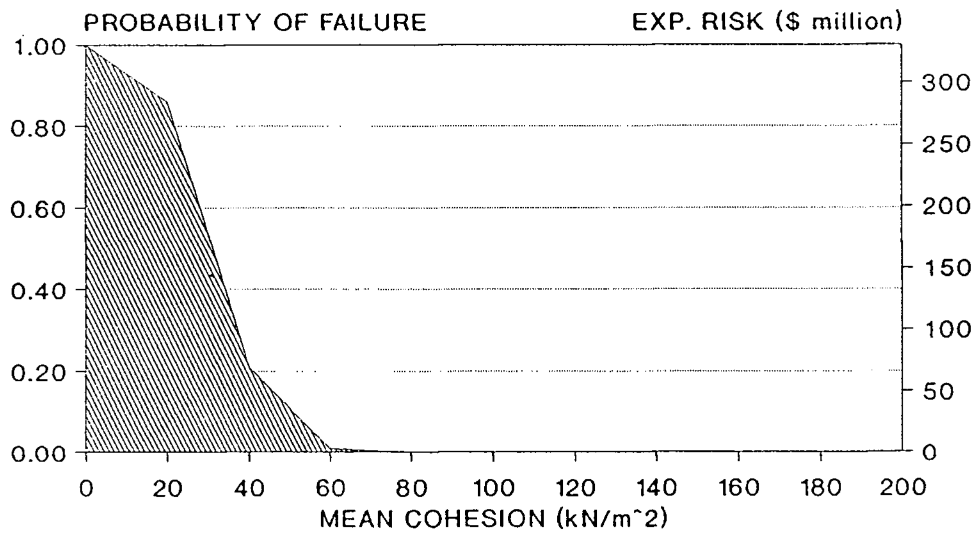

7.6.4 SENSITIVITY TO STANDARD DEVIATION IN COHESION

In this study, the base-case scenario was analyzed for a number of realistic levels of uncertainty in cohesive strength. Results of the analysis are summarized in *Figures 7.37* and *7.38*. *Figure 7.37* indicates that the mean FOS remains constant at approximately 1.05, consistent with earlier results. Once again, the FOS distribution becomes more dispersed as the level of uncertainty in the input parameter is elevated (the standard deviation in FOS increases from 0.01 to a maximum value of 0.08). The probability of failure and monetary risk response shown in *Figure 7.38* is very similar to the friction angle response illustrated in *Figure 7.34*. As was the case with friction angle data, the risk associated with a large degree of uncertainty in cohesive strength is substantial. The monetary risk drops very quickly, becoming relatively inconsequential as uncertainty in the parameter is reduced to a standard deviation of less than 15 kN/m^2.

Figure 7.37 *FOS Distribution for Several Levels of Uncertainty in Cohesion*

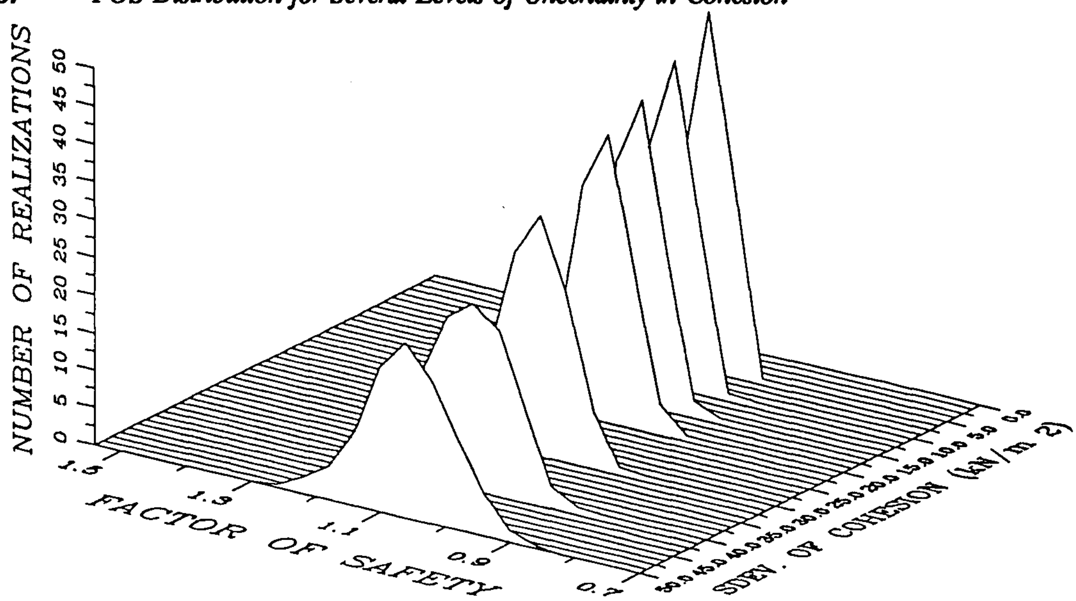

Figure 7.38 *Sensitivity of POF and Risk to Changes in Standard Deviation of Cohesion*

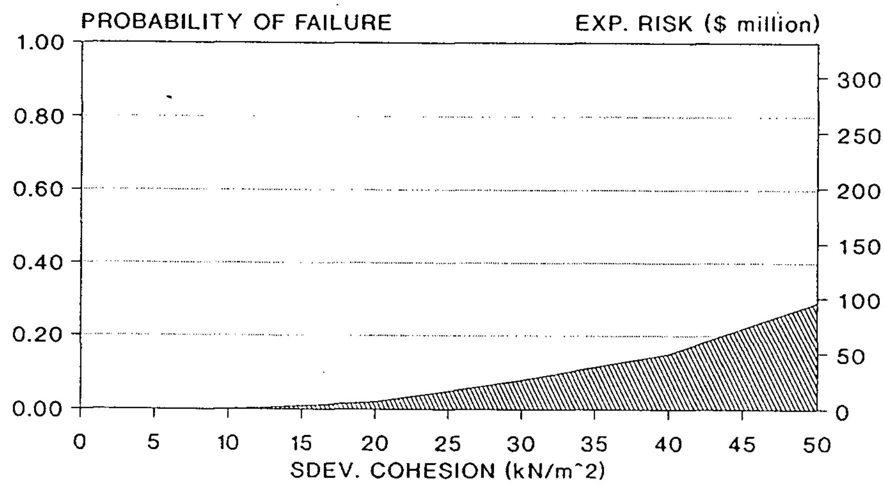

7.6.5 EVALUATION OF SENSITIVITY RESULTS

The sensitivity studies reported in *Section 7.6* have investigated how changes in the mean and standard deviation of strength parameters would affect stability of the ultimate pit wall. The objective of this subsection is to summarize those results and put them into perspective by comparing changes in stability that were observed as each parameter was varied.

Adjustments to either the mean friction angle, or to mean cohesion resulted in dramatic changes to the mean factor of safety and to the probability of failure. Both parameters appeared to be equally important for the ultimate pit wall failure analyzed; adjusting ϕ over the full range of possible values resulted in an increase of 0.5 in the mean factor of safety, the same increase was realized by adjusting c from 0 to 200 kN/m^2. Since the mean factor of safety increased linearly as either strength parameter was varied, it was possible to relate sensitivity of the mean factor of safety to both parameters directly: an increase of 1° in ϕ has the same stabilizing effect as an increase of 18.5 kN/m^2 in c. An examination of the Mohr-Coulomb equation

$$s = (\sigma - u) \cdot \tan(\phi) + c \qquad \textit{Equation 7.1}$$

indicates that cohesion will become progressively more important as effective stresses decrease. Relatively low magnitudes of effective stress can occur in one of two ways: 1) from reduced levels of confining stress (i.e. small, shallow failures), or 2) from increased levels of pore pressure on the failure surface. Conversely, when analyzing very large landslides (e.g. Downie slide) where effective stresses on the failure surface will be substantial, much more emphasis should be placed on accurate measurements of friction angle than on measurements of cohesion.

The degree of confidence that can be placed in a stability assessment is entirely dependent on how widely the factors of safety computed for each realization are dispersed about the mean FOS value for that particular simulation. The amount of dispersion is indicated by the standard deviation of the FOS distribution. When the standard deviation in FOS is small (i.e. 0.025) then the actual factor of safety is likely to be very close to the mean value; conversely, when the standard deviation is large, the true factor of safety cannot be predicted precisely.

The sensitivity results presented in this section and in *Section 7.5* have demonstrated repeatedly that the amount of dispersion in the FOS distribution escalates rapidly with increases in the degree of uncertainty of any input parameter. *Figure 7.39* illustrates the observed response in the standard deviation of the FOS distribution to changes in the level of uncertainty associated with each input parameter. During this set of sensitivity studies, the standard deviation of each input parameter was increased incrementally from 0 to some realistic maximum value. The maximum standard deviations were selected so as to be representative of typical levels of uncertainty that result when estimating parameters based on limited geologic information and no measurements. *Table 7.10* summarizes the range of uncertainty selected for each parameter.

Table 7.10 Standard Deviations and Confidence Intervals in Input Parameters

PARAMETER	MAXIMUM STND. DEV.	MAXIMUM RANGE
Log Hydraulic Conductivity (m/s)	1.4	+/- 2.8
Friction Angle (degrees)	3.0	+/- 6.0
Cohesion (kN/m^2)	50.0	+/- 100

Figure 7.39 Response of Standard Deviation in FOS to Changes in Uncertainty of Input Parameters

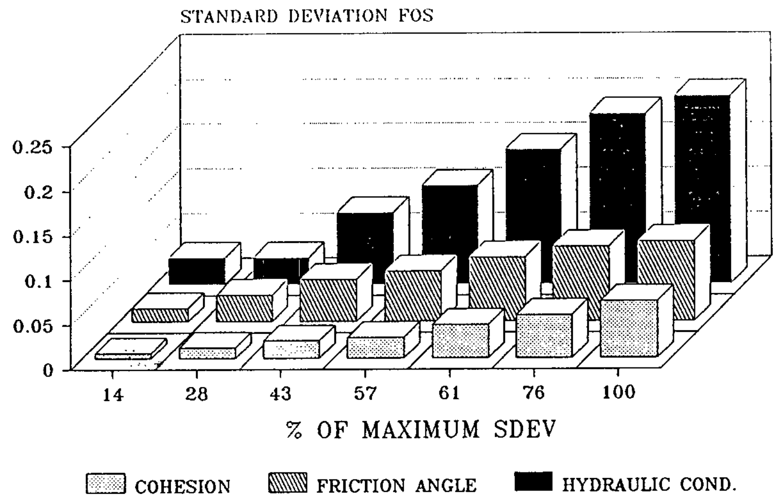

In the case of *Figure 7.39*, the effect of uncertainty in the hydraulic conductivity estimate appears much more significant than uncertainty in friction angle or cohesion. In part, this behaviour due to modelling *K* as a spatially distributed random variable, and *c* and ϕ as uncorrelated random variables, with one set of strength parameters randomly selected for each slice interface. Also, the large increase in variability of the FOS distribution that was observed as the variability in *K* was increased is due to the fact that the sensitivity study was conducted in a geologic environment that exhibited a strong degree of spatial correlation in the hydraulic conductivity field (range = 200 m). As described in *Section 7.5.3*, large zones of contrasting hydraulic conductivity values result in highly unpredictable pore pressure distributions. The trends observed in *Figure 7.39* suggest that a thorough geologic/hydrogeologic investigation that identified the mean hydraulic conductivity and the location of all high K and low K zones would be more valuable than a detailed shear strength testing program. In this case the hydrogeologic investigation has the potential to reduce monetary risk by as much as $130 million.

In geologic environments where the hydraulic conductivity field is less continuous, the effect of uncertainty in the mean value of the hydraulic conductivity field would become less critical. A comparison of *Figures 7.26, 7.30, 7.34* and *7.38* suggests that for the base-case slope geometry, uncertainties in mean hydraulic conductivity, in the location of high K & low K zones, in the mean friction angle, and in the mean value of cohesion all have approximately the same maximum impact on slope stability.

During the sensitivity studies presented thus far, only the parameter under investigation was treated in a probabilistic manner. In order to filter out the effects of other input parameter uncertainties, the standard deviations of all other parameters were set to 0. However, in a real slope design situation, there will most likely be some non-zero level of uncertainty associated with each input parameter. *Figure 7.40* illustrates the FOS distributions that result as the level of uncertainty is increased in mean K, ϕ and *c* simultaneously from 0 to the maximum values given in *Table 7.10*. The most important point to recognize in *Figure 7.40* is that the FOS distribution becomes more dispersed, and at a much faster rate than is the case when only one parameter is uncertain. Analysis results indicate that the standard deviation of all three input parameters must be reduced to less than 28% (2/7) of maximum values before the mean factor of safety can be predicted to ±0.1 accuracy (i.e. the standard deviation in FOS reduced to less than 0.05 at the 95% confidence interval).

Figure 7.40 Response of FOS Distribution to Combined Increases in Uncertainty of K, ϕ, and c

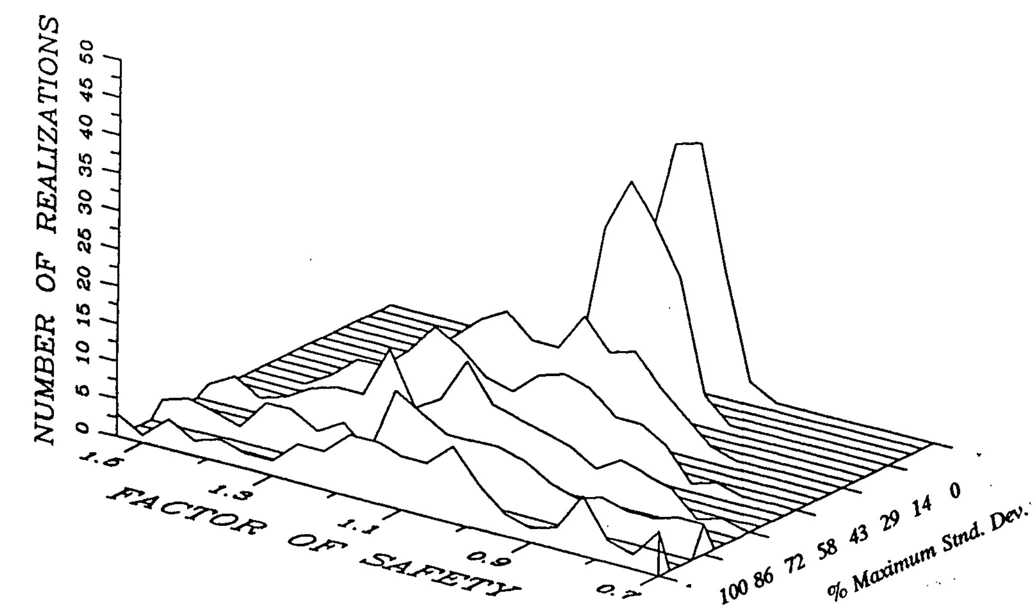

The corresponding probability of failure and monetary risk distribution is plotted in *Figure 7.41*. Once again, note that uncertainty in input parameters results in a large increase in the probability of failure due to the tail effect; as always, the increase in POF is associated with a very substantial increase in economic risk.

Figure 7.41 Sensitivity of POF and Monetary Risk to Combined Changes in Standard Deviation of K, ϕ and c.

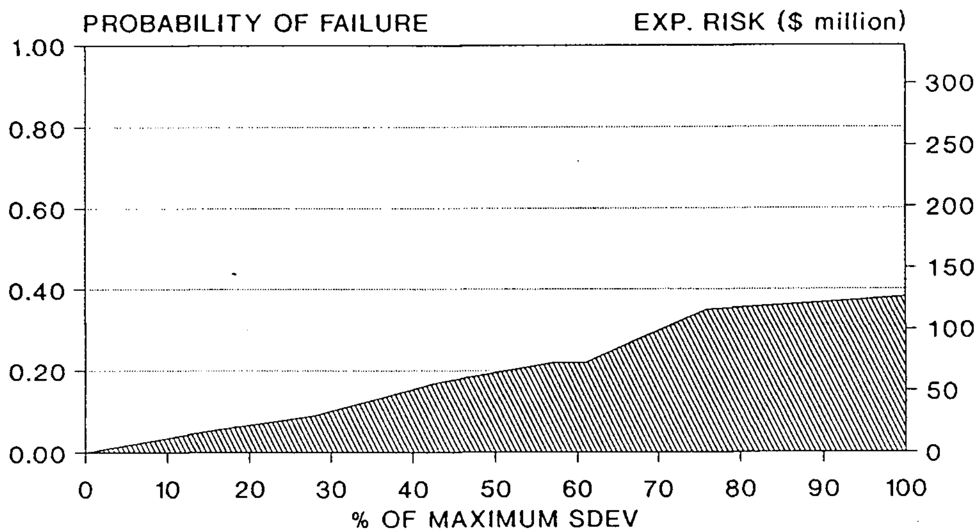

In conclusion, this section has demonstrated that accurate and abundant hydrogeologic and shear strength data is required in order to reduce the monetary risk associated with failure of the ultimate pit wall. In the particular case analyzed, hydraulic conductivity data appears to be twice as valuable as shear strength data due to the strong spatial correlation of the hydraulic conductivity field. In more variable geologic environments, hydrogeologic and shear strength information will be of approximately equal value. In this scenario, the value of friction angle data was approximately equal to the value of cohesion data; however, the relative importance of these two parameters is highly dependent on the size of the failure and pore pressure conditions. In general, cohesion contributes less to overall shear strength when a slide is very large and/or when drained conditions prevail. And of course, cohesion will not influence stability when dealing with failure through cohesionless materials (i.e. gravels, sands, some silts, broken rock, or movement along a smooth discontinuity).

Finally, it is important to note that the primary purpose of this sensitivity study was not to identify correlations or rules of thumb that can be applied blindly from one slope stability analysis to the next. Rather, the objective of this section has been to illustrate how the risk-cost-benefit framework described in this thesis can be applied to identify the relative importance and approximate monetary value of hydrogeologic and shear strength data in each particular situation.

7.7 SENSITIVITY TO DEWATERING DESIGN

Feasibility of the base-case dewatering program was investigated in *Section 7.4.* In that section it was concluded that the proposed four million dollar dewatering program would result in a $108 million reduction in expected operating costs over the operating life of the mine when compared with the best pit design that did not utilize a groundwater control program. The base-case dewatering program is clearly economically feasible, whether the dewatering program is also optimal will be investigated in this section, first for the ultimate pit wall and then over the entire production life of the mine.

7.7.1 IMPACT OF DEWATERING ON ULTIMATE PIT STABILITY

The base-case dewatering program reduced the probability of failure of the ultimate pit wall to 0.17. The economic risk associated with that level of probability of failure, 56.2 million dollars, is still substantially higher than the cost of the dewatering program. It would appear that a denser, more costly dewatering program could be justified.

To investigate this hypothesis six different dewatering programs were tested. As indicated in *Table 7.11* the programs differed in the number of wells utilized and the total dewatering budget. *Figure 7.42* shows the average water table position for each simulation. The corresponding costs of dewatering and probabilities of failure are also tabulated in the figure. Note that the relationship between the number of wells utilized and the level of pressure reduction attained is not linear. The largest drop in the water table is attained with the first four wells. Thereafter, progressively steeper hydraulic gradients are established, and larger quantities of water must be removed to attain the same increment of drawdown.

Table 7.11 Design Parameters and Costs for Several Dewatering Programs

RUN #	ACTIVE ROWS	TOTAL WELLS	WELLS PER ROW	TOTAL DEWT. COST ($ millions)	P.O.F.	OPERATING COST ($ millions)
1	NONE	0	0	0.00	0.86	284.44
2	R4,R5,R6,R7	4	1	1.08	0.57	189.61
3	R4,R5,R6	15	5	3.05	0.17	59.27
4	R4,R5,R6,R7	12	3	3.25	0.06	23.10
5	R4,R5,R6,R7	16	4	4.06	0.04	17.30
6	R4,R5,R6,R7	20	5	5.42	0.01	8.73
7	R4,R5,R6,R7	40	10	12.05	0.00	12.05

Results of the economic analysis are presented in *Figure 7.43.* In that figure the expected operating costs, including both the monetary risk associated with the clean-up effort and the cost of groundwater control are plotted against the cost of dewatering. The monetary risk decreases rapidly with the initial dewatering effort as the dewatering budget is increased from 0 to $3 million because, as can be seen in *Figure 7.42,* the first 12 wells ($3.25 million budget) are responsible for 70 to 80% of maximum pore pressure reductions attained by the most expensive dewatering system analyzed. Additional dewatering expenditures beyond $3.25 million continue to yield marginal reductions in probability of failure and associated reductions in risk, but only to a maximum dewatering budget of $5.42 million. This budget level results in the optimum dewatering design because it minimizes expected operating costs in the sector. *Figure 7.43* shows that further capital investment in dewatering is not economically justified because it results in a gradual increase in expected operating costs as dewatering expenditures begin to outweigh the economic benefits of improved slope stability.

Figure 7.42 Average Water Table Positions for Test Dewatering Design Programs

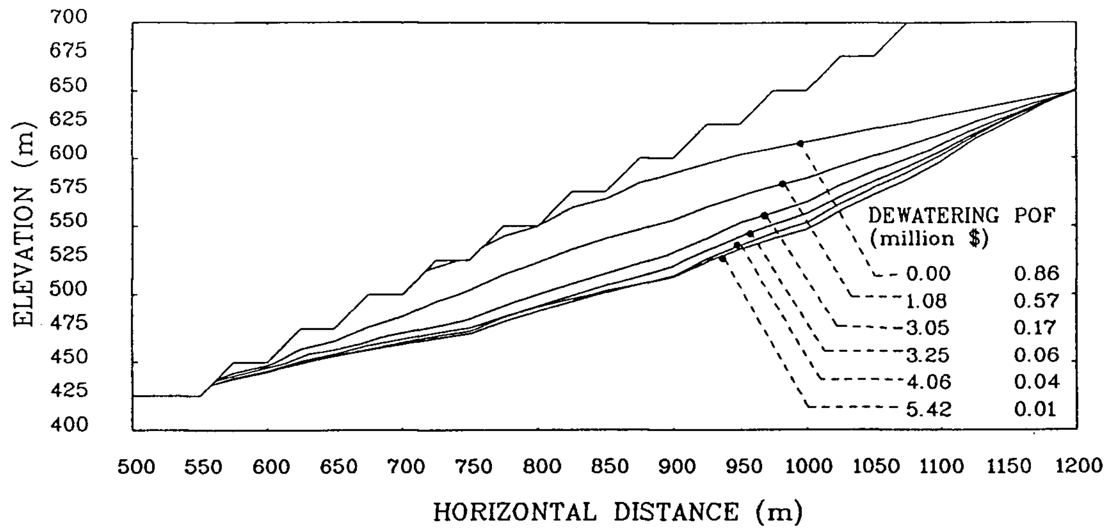

Figure 7.43 Expected Operating Costs as a Function of Dewatering Budget

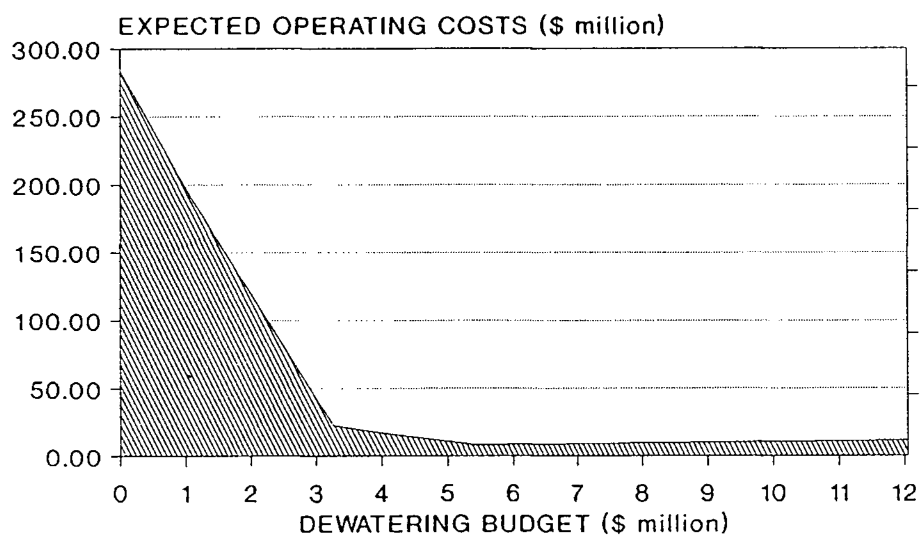

7.7.2 STEEPENING SLOPE ANGLE IN EARLY PITS

A systematic increase in the probability of failure with increasing slope height was recognized in *Section 7.4* (see *Figure 7.17*). Based on the observed trend it was suggested in that section that it may be beneficial to utilize steeper slope angles in the early stages of mine development and then cut back as the depth of the pit increases. Increased cash-flow in the early stages of production would be the principal benefit of this design strategy. Since less overburden waste would have to be mined in the early pits, mine equipment could be concentrated on mining ore and increased production would be realized. Alternately, if the mill was already running at capacity then fewer shovels and haulage units would be required during mining of the early pits; reductions in both capital and operating costs would be realized. Either scenario would result in increased cash-flow during the critical early years of the mine. This would allow the mine to pay back outstanding start-up loans faster, substantially reducing the total interest paid.

The objective of this sub-section is to investigate whether such a strategy is valid. To assess the economic benefit of steeper pit walls, a new slope design was prepared for the sector and evaluated with the risk-cost-benefit framework. The slope angles utilized for each 5 year pit are listed under the *ANGLE STEEP* heading in *Table 7.12*. The 1995 pit was steepened by a maximum 10°, the 2000 pit by 7.5°. In order to maintain stability during the early push-backs and reduce the probability of failure from 0.17 to 0.01 for the ultimate pit wall (utilizing optimum design described in *Section 7.7.1*), the overall dewatering budget was increased from \$5.14 to \$9.29 million.

Table 7.12 Slope Angles, Dewatering Costs and Net Incomes for Design Alternatives Analyzed

DEWATERING COSTS & NET-INCOME PER PUSH-BACK ($ millions)							
PIT YEAR	ANGLE BASE-CASE	ANGLE STEEP	EWAT. COS BASE-CASE	EWAT. COS STEEP DES.	NET INCOME 30 DEG. NO DEWATERING	NET INCOME BASE-CASE DEWATERING	STEEP DES. AGGRESIVE DEWATERING
1995	30.0	40.0	1.45	3.56	153.243	151.796	163.157
2000	30.0	37.5	1.00	0.42	136.038	157.444	164.504
2005	30.0	35.0	1.00	1.47	41.147	72.667	85.496
2010	30.0	32.5	1.34	1.30	-51.594	18.420	11.807
2015	30.0	30.0	0.35	2.54	-123.638	4.515	-26.894
2020	30.0	30.0	0.00	0.00	-284.445	-56.227	-3.307
TOTAL:			5.14	9.29	-129.249	348.615	394.763

The expected net incomes for each push-back are illustrated in *Figure 7.45* for the steep design, as well as for the base-case design with dewatering (all pits at 30 degrees), and the base-case design with no dewatering. Exact monetary values are also presented in *Table 7.12*. The data indicates that the steep design does lead to increased cash flow during the first three push-backs: \$11.36 million in 1995, \$7.06 million in 2000, and \$12.82 million in 2005. Cash flow is then reduced during the final two push backs as the overburden walls are cut back.

Figure 7.46 illustrates the cumulative net income for the three design alternatives. Once again, note that the steep design results in higher net incomes during the first three push-backs. More important, because the steep design reduces the risk of failure of the ultimate pit wall through enhanced dewatering efforts, it leads to a \$46.14 million increase in total net income (13%) over the original base-case design with dewatering.

Figure 7.44 Expected Net Income per Push-Back, Steep Design & Two Other Scenarios

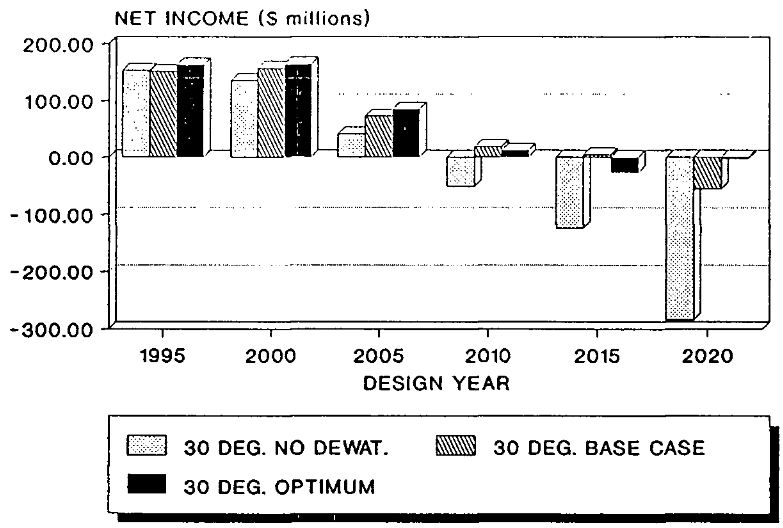

Figure 7.45 Expected Cumulative Net Income for Steep Design and Two Other Scenarios

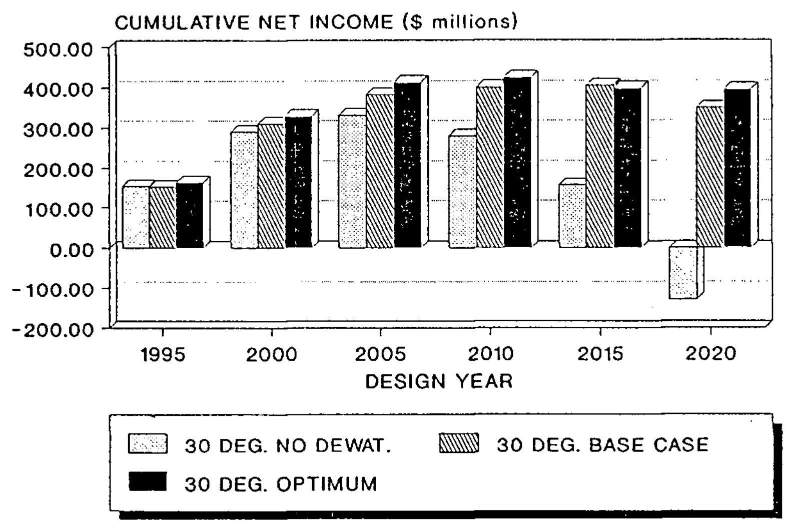

7.8 SENSITIVITY TO FIELD DATA

The sensitivity studies presented thus far have demonstrated that it is possible to identify an optimum slope angle and dewatering strategy based on the limited information given in *Section 7.2.* The data base utilized in those sensitivity studies was limited because it did not include any information about the distribution of individual geologic horizons in the sub-surface. Associated with the deficiency in geologic information, was a lack of knowledge regarding the spatial distribution of high and low hydraulic conductivity horizons and shear strength zones. It is important to know whether availability of such information would lead to a more profitable slope design, and if so, at what point would the expenses of site investigation outweigh the benefits of increased efficiency and reduced monetary risk.

The objective of the sensitivity studies presented in this section is to investigate the impact of hydraulic conductivity measurements on the effectiveness of the groundwater control program, and ultimately, on the profitability of open pit mines. The approach utilized will be very simple; it will not include an exhaustive evaluation of the worth of data, rather it will provide a single illustrative example of how hydraulic conductivity measurements result in further increases in expected net income for the familiar base-case design problem.

7.8.1 EFFECT OF DATA ON CONFIDENCE IN THE STABILITY ASSESSMENT

In a real mining situation there will be only one unique distribution of geologic horizons beneath the surface, only one unique spatial distribution of hydraulic conductivity values. The hydraulic conductivity distribution will remain uncertain, except where penetrated by exploratory drill holes from the surface. It has been shown earlier (see *Sections 7.5.2, 7.6.2 & 7.6.4*) that the degree of confidence that can be placed in a slope stability assessment depends on the level of uncertainty associated with each input parameter, as well as the validity of the slope stability model (i.e. the critical failure mode). The smaller that uncertainty, the tighter the FOS distribution, and the more confident the resulting stability assessment. The goal in this study is to illustrate the relationship between density of hydraulic conductivity measurements and the degree of confidence in the stability assessment.

Instead of conducting a general sensitivity study, the approach used here will be to simulate the effects of a real site investigation on the probability of failure, and ultimately on the expected economic outcome. To simulate a real *unknown* hydraulic conductivity distribution, a single unconditional realization of the hydraulic conductivity field was generated from the base-case hydrogeologic statistics given in *Table 7.1.* A complete risk-cost-benefit assessment was then conducted for three levels of site investigation effort:

A. NO DATA: statistics of hydraulic conductivity field estimated from available geologic information and from experience at other similar sites.

B. LOW DENSITY: hydraulic conductivity tests conducted at 50 m spacings in each drill hole, drill holes spaced at 200 m intervals.

C. HIGH DENSITY: hydraulic conductivity tests conducted at 50 m spacings in each drill hole, drill holes spaced at 100 m intervals.

The locations of permeability test intervals and observed $LOG_{10}(K)$ values are presented in *Figure 7.46* for each level of site investigation effort. *Figures 7.47 A,B & C* illustrate the corresponding distributions of estimation variances of the hydraulic conductivity field for each site investigation program. In case *A*, no measurements were available; therefore, realizations of the hydraulic conductivity field had to be generated with the unconditional simulation technique. Since the hydraulic conductivity estimates were not conditioned on data, estimation uncertainty was the same everywhere in the domain. In cases *B* and *C*, the simulation was conditioned with measured values shown in *Figure 7.46.* In case *B*, measurements at the indicated test locations have reduced variances somewhat, from 0.25 to less than 0.20 over most of the domain, and to less than 0.15 over

Figure 7.46 Location of Hydraulic Conductivity Measurements & Observed Values

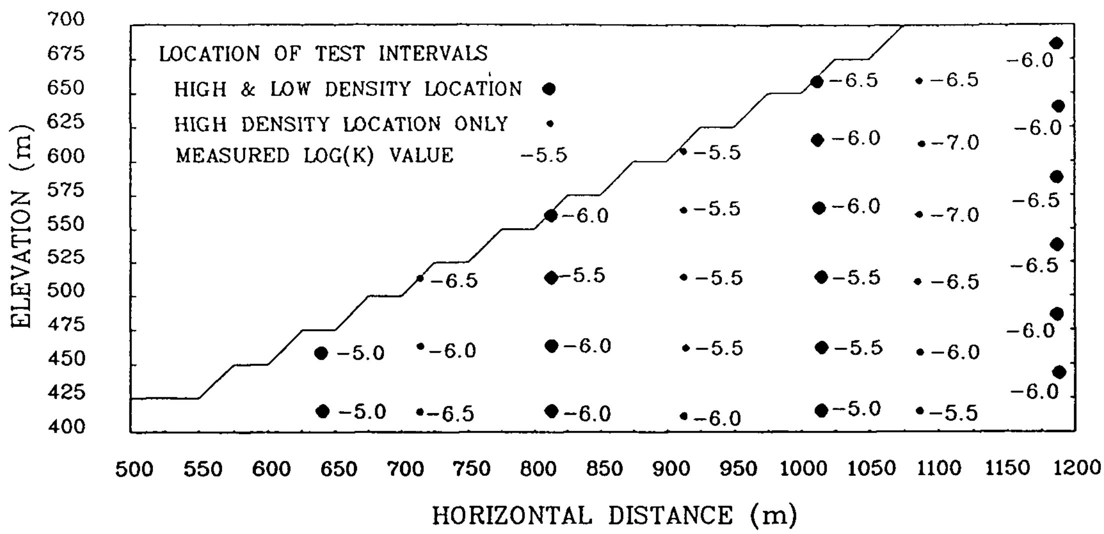

approximately ½ of the domain. In case *C*, measurements at the indicated locations have resulted in a very significant reduction in variances, from 0.25 to less than 0.10 over most of the flow domain (because standard deviation is defined as the square root of variance the average reduction in the standard deviation in K is less dramatic, decreasing from 0.50 to 0.26).

The uncertainties in pressure head predictions for each site investigation scenario are illustrated in *Figures 7.48 A,B & C.* Each figure presents a contour plot of the standard deviations in pressure heads observed during the corresponding simulation. As expected, case *A* resulted in the highest levels of variability in simulated pressure heads because the location of high K and low K zones was not constrained by measurements, and could therefore vary significantly from realization to realization. On the other hand, the high density sampling program reduced uncertainty in pressure head predictions by approximately 65%.

For comparison, *Table 7.13* lists the relative reduction in uncertainty (as measured by standard deviations) for both simulated hydraulic conductivities and simulated pressure heads at each level of site investigation effort. Note that in this case there is approximately a one to one correspondence between the reduction in hydraulic conductivity uncertainty and the reduction in uncertainty of simulated pressure heads. Additional research would be required to determine whether this relationship holds true in the general case.

Table 7.13 Reductions in Uncertainty Due to Measurements

SCENARIO	MEAN SDEV K	% REDUCTION SDEV K	MEAN SDEV HEAD	% REDUCTION SDEV HEAD
NO DATA	0.50	0	20	0
LOW DENSITY	0.38	24	15	25
HIGH DENSITY	0.26	48	7	65

Figure 7.47 Variance in Estimating K for Three Levels of Measurements

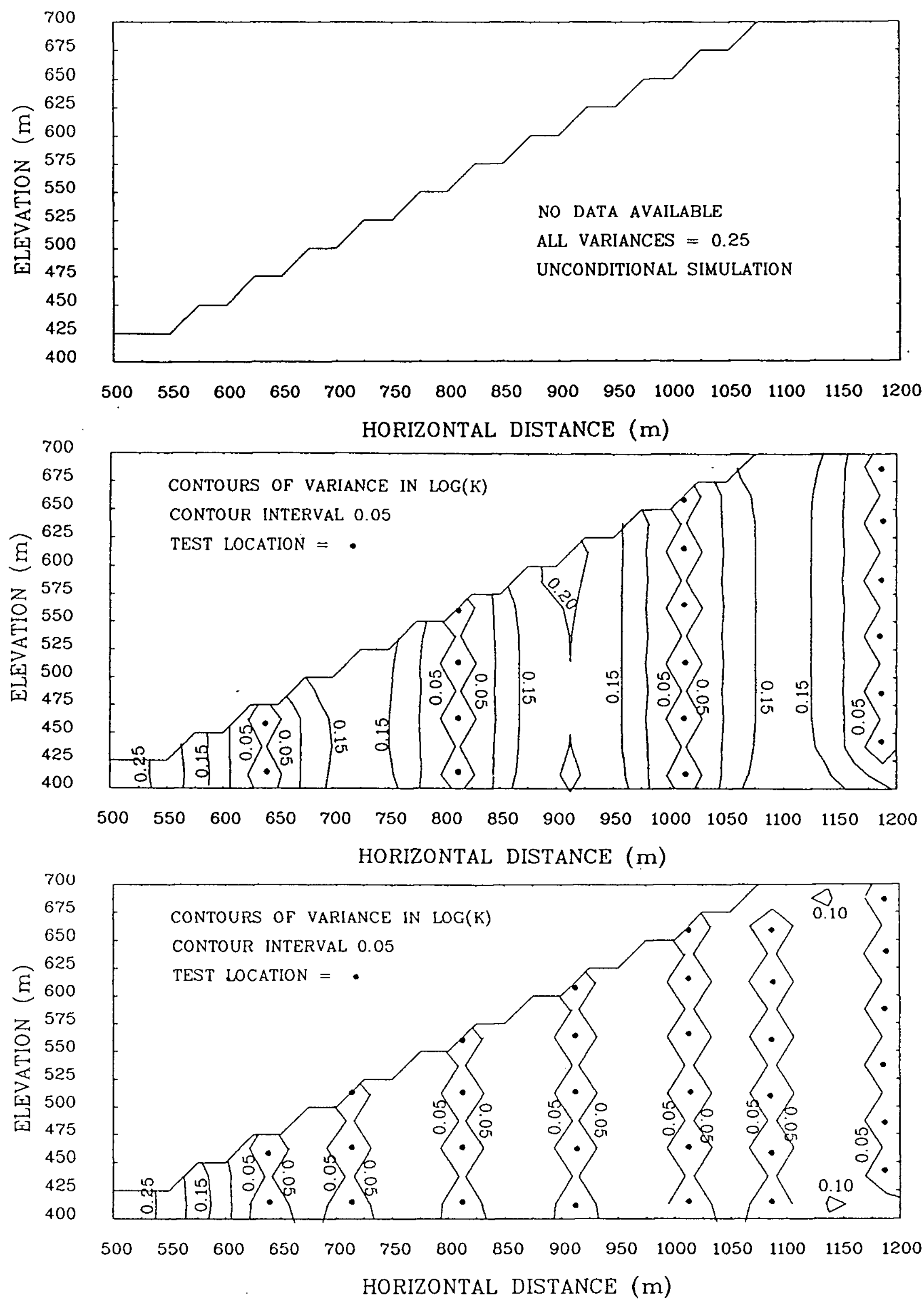

Figure 7.48 Contours of Standard Deviation in Estimated Pressure Head for Three Levels of Measurement

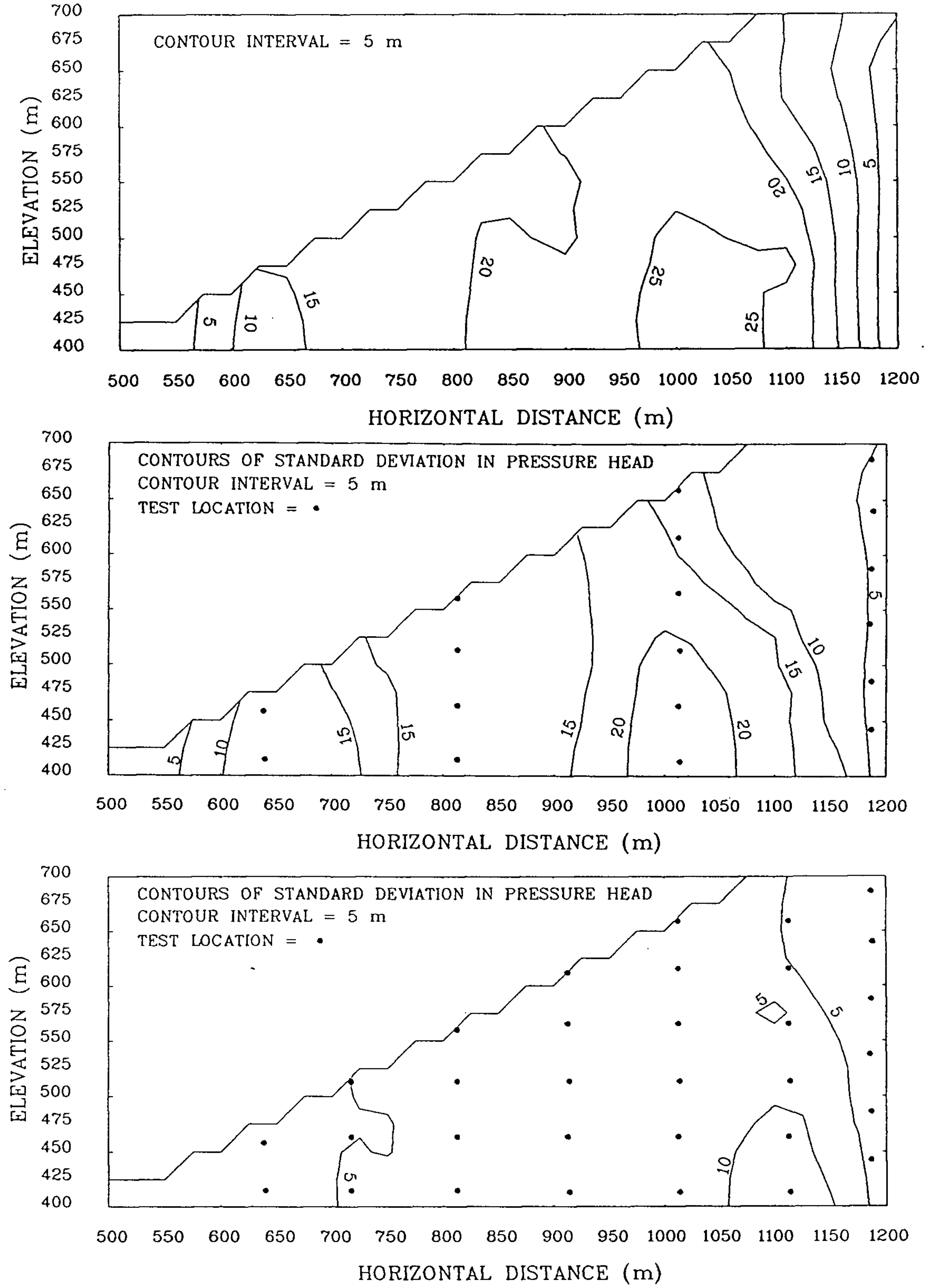

Figure 7.49 FOS Distributions for Three Levels of Measurement Networks

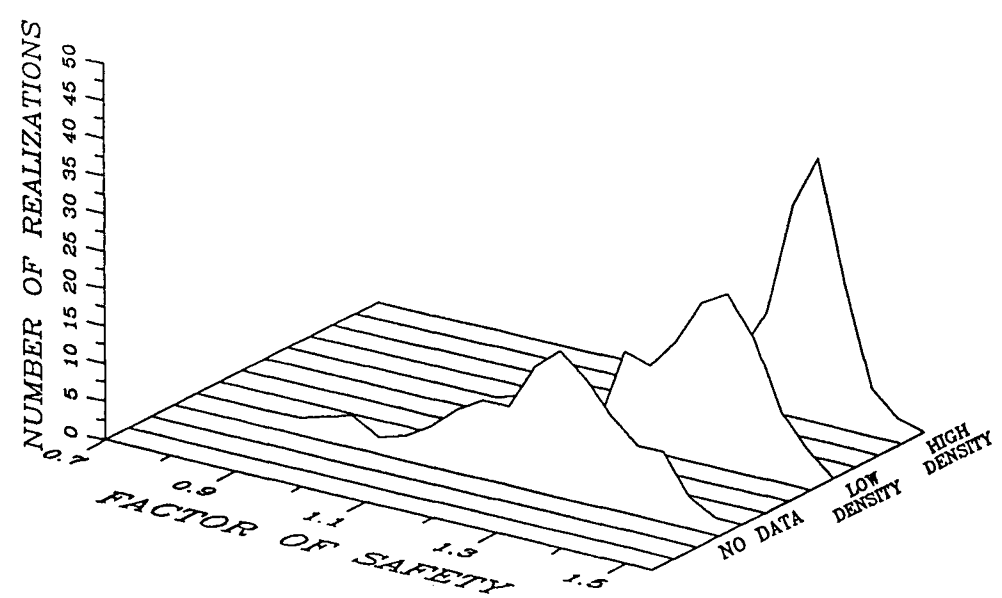

The effect of hydraulic conductivity measurements on the degree of confidence in the slope stability assessment is best understood by examining *Figure 7.49*. This figure shows the resulting FOS distribution for each level of site investigation. The FOS distribution becomes progressively less dispersed as more hydraulic conductivity measurements become available, increasing the accuracy of the stability assessment.

Results of the slope stability analysis indicate that the probability of failure drops quickly from 0.03 to 0.00 as data from the low density sampling program is introduced in the analysis. In this case, the reduction in POF can be attributed to two factors:

First, the initial low density sampling results confirm that the sub-surface geology is favourable. The observed log(K) values indicate that lenses of relatively high hydraulic conductivity are situated in the critical toe area, and in the central part of the slope through which the circular failure surface will pass. Wells located in these horizons, as well as natural seepage, would bring about substantial reductions in pore pressures along most of the failure surface. A shift in the mean factor of safety from 1.23 for the no data scenario to 1.33 for the low density scenario confirms the presence of favourable geologic conditions.

Second, because the hydraulic conductivity data leads to a reduction in the variability of computed pressure heads from realization to realization, thereby reducing the amount of dispersion in the FOS distribution, the probability of failure is lowered due to the tail effect.

7.8.2 MONETARY WORTH OF A SITE INVESTIGATION PROGRAM

The monetary worth of a site investigation program clearly depends on the test results obtained. If the test results indicate that the hydraulic conductivity distribution is more favourable than expected then the slope angle can be steepened, and/or the dewatering effort reduced. Both cost saving measures can be implemented while maintaining the same risk of failure. On the other hand, if the site investigation indicates that conditions are worse than expected, then the slope will have to be flattened or the dewatering budget will have to be increased in order to maintain stability. Finally, if the investigation indicates that conditions are pretty much as expected, then the original slope design will not be modified. In this section posterior analysis will be used to investigate the worth of data.

Before proceeding to an evaluation of the worth of data for each scenario, it is necessary to define the term *regret*, that will be used to measure the worth of data. Regret is defined as the difference between the maximum net income that could be attained if given perfect information, and the optimum expected net income based on currently available information. The concept of regret is complex; a brief example here might help to clear the muddy waters. Consider the ultimate pit wall design illustrated in *Figure 7.50A*. Prior to conducting a detailed hydraulic conductivity testing program, the probability of failure is estimated at 0.05. Using the revenue and cost coefficients given in *Figure 7.50*, the prior expected net income is estimated at $50 million. Upon conducting the testing program it is discovered that hydraulic conductivity conditions are much worse than anticipated. As a result, the probability of failure of the original design increases to 0.20. The posterior expected net income for the original design is $20 million. In light of the new data, the slope angle is reduced by 5 degrees (*Figure 7.50B)*, increasing operating costs by $20 million, and reducing the probability of failure to the original level of 0.05. The expected net income of the new design is $30 million. The reduction in expected regret is given by the difference in expected net income of the updated slope design ($30 million) and the posterior expected net income of the original slope design ($20 million). In this simple illustration the monetary worth of the testing program proves to be $10 million.

Figure 7.50 Concept of Regret

ORIGINAL DESIGN – PRIOR ANALYSIS		REVISED DESIGN – POSTERIOR	
REVENUE:	150	REVENUE:	150
OPERATING COSTS	90	OPERATING COSTS	110
PRIOR RISK:	10	POSTERIOR RISK	10
EXPECTED NET INCOME:	50	EXPECTED NET INCOME:	30

ORIGINAL DESIGN – POSTERIOR	
REVENUE:	150
OPERATING COSTS	90
POSTERIOR RISK	40
EXPECTED NET INCOME:	20

30 – 20 = 10

REDUCTION IN EXPECTED REGRET

Figure 7.51 Monetary Worth of Three Site Investigation Strategies

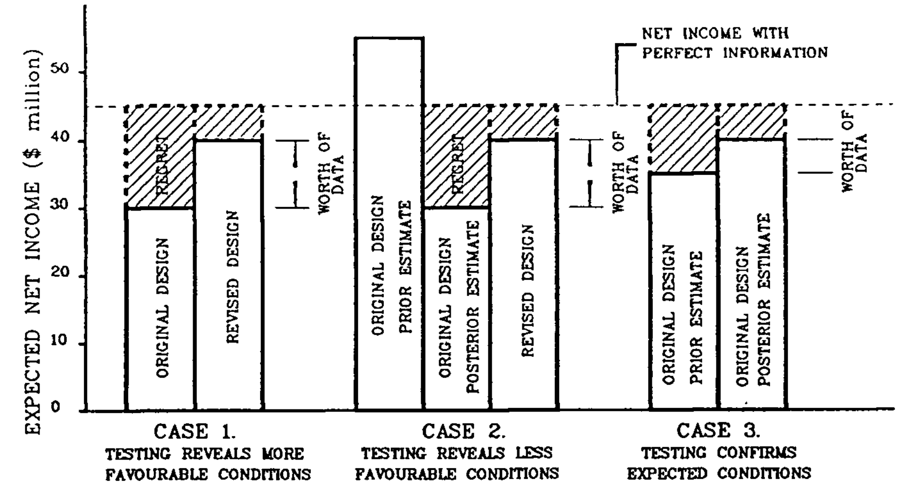

Having defined regret, the discussion turns to the analysis of the three possible sampling outcomes (i.e. 1) conditions more favourable, 2) conditions less favourable and 3) conditions as expected. In the first case, the monetary worth of data can be equated to the increase in expected net income (which in this case is equivalent to the reduction in monetary risk, since both revenue and operating costs remain unchanged). In the second case, the site investigation reveals that conditions are worse than anticipated; therefore, expected net income actually decreases as a result of sampling. In such a situation, the worth of data is best measured in terms of reduction in expected regret. In the third case the slope design will remain unchanged. Therefore, monetary worth of the data is limited to a possible reduction in risk that stems from increased confidence in input parameters (i.e. the reduction in parameter uncertainty leads to a lower input parameter variance and a tighter output parameter probability density function which in turn leads to reduced risk due to the tail effect). *Figure 7.51* illustrates how the monetary worth of data can be identified in each of the three situations described above. Note that in each case, the worth of data can either be measured in terms of the difference between expected net income for the original design and the expected net income for the improved design, or in terms of the difference between expected regret for the original design and expected regret for the improved design.

Having briefly introduced worth of data, the concept can be applied to the three site investigation strategies documented in *Section 7.8.1.* In the analyses that follow it is assumed that the ultimate pit wall configuration has been attained in this sector and no additional revenue will be generated; therefore, the worth of data is directly proportional to the reduction in monetary risk associated with the clean-up of a full wall failure. Results of the economic analysis are presented in *Table 7.14.*

Table 7.14 Cost of Data Collection and Posterior Worth of Data

SCENARIO	P.O.F.	COST OF DATA ($ million)	EXPECTED OPRTN. COSTS ($ million)	NET WORTH OF DATA ($ million)
NO DATA	0.03	0.00	15.34	0.00
LOW DENSITY	0.00	0.66	6.07	9.92
HIGH DENSITY	0.00	1.38	6.80	9.18

In the no data scenario, funds have not been allocated to hydraulic conductivity testing. Uncertainty as to the actual values of hydraulic conductivity in general, and suitability of the recommended dewatering program in particular, results in a substantial monetary risk of failure ($9.92 million). The total expected cost, including both monetary risk and dewatering cost is $15.34 million.

In low data density scenario, $655 thousand has been allocated for hydraulic conductivity testing (5 holes per row, 200 m spacing between rows, all holes to bedrock). The testing program confirms that actual geologic conditions are favourable and that the recommended dewatering program will reduce the probability of failure to 0.0. Since the monetary risk of failure is zero, the expected operating costs for this scenario include only the costs of site investigation ($0.655 million) and dewatering ($5.42 million). The total cost is $6.07 million. Therefore, the monetary worth of the low density testing program is $9.92 million (15.34-6.07+0.655). Since the reduction in risk substantially outweighs the cost of obtaining the measurements, the low density testing program is economically justified.

In the high data density case, $1.38 million is allocated to site investigation (5 holes per row, 100 m spacing between rows, all holes to bedrock). In this case, the additional measurements serve only to further reduce uncertainty in the hydraulic conductivity estimate and the stability assessment. However, since the probability of failure, already at 0.00 can be reduced no further, the additional expenditure associated with the high density sampling program is not justified unless the slope design is to be modified. Without modifying the slope angle or dewatering design, the total cost of site investigation and dewatering for the high density program is $6.80 million. Clearly, the low density program is superior because it results in the same level of risk while costing $0.733 million less than the high density program.

In summary, this sensitivity study has demonstrated that additional hydraulic conductivity measurements can be justified as long as the cost of obtaining the data is less than the corresponding increase in expected net income or expected reduction in regret. However, the argument presented in this sub-section painted an incomplete picture of the worth of data because the dewatering design was not adjusted as additional information became available. In the following sub-section it will be shown that the worth of hydraulic conductivity data can be further increased if the dewatering plan is modified in response to new measurements.

When making the decision on whether or not to conduct further site investigation, actual test results will not be available; therefore, the terminal analysis approach utilized above to demonstrate the worth of data cannot be used to justify the expenditure. Fortunately, preposterior analysis (Benjamin & Cornell, 1970) provides a method of calculating the expected worth of data based on current information. Because such analysis is beyond the scope of this thesis it will not be discussed; the interested reader is referred to Maddock (1973) for additional insight.

7.8.3 USING DATA TO IMPROVE DEWATERING DESIGN

In order to design an efficient dewatering system that reduces pore pressures to target levels at minimum cost it is necessary to understand the geologic conditions in the sub-surface. First, a good working knowledge of the hydraulic conductivity distribution is essential in order to develop a realistic computer model of the groundwater flow system. Once established, the computer model can then be used to compare different dewatering strategies and to select the dewatering design that is best suited to the actual site condition.

A good understanding of the geology will also permit the hydrogeologist to:

- Locate wells in relatively permeable strata. Wells will then have a large radius of influence. They will also produce maximum quantities of production water for the mill.

- Select the optimum spacing between wells. Relatively impermeable zones require that wells be spaced close together in order to successfully depressurize the entire area.

- Identify the optimum completion depth for each well. The target completion depth will depend on the location of high permeability horizons and the expected depth of the failure surface.

- Make realistic estimates of the total yield on a year by year basis. This information will facilitate planning for alternate production water supplies.

Although the first set of hydraulic conductivity measurements and conditional computer simulations will most likely lead to improvements in the dewatering design, the investigation and design process should be continued only as long the costs of additional testing and engineering services are smaller than the incremental increase in expected net income resulting from modifications to the dewatering design. Ideally, each trial design should be analyzed with the complete stochastic analysis; however, because such analyses are very time consuming, a simpler deterministic approach based on the kriged hydraulic conductivity field is recommended to quickly screen a large number of design alternatives. The top two or three designs can then be evaluated thoroughly with the complete stochastic simulation.

In the deterministic approach, kriging is used to generate the best unbiased linear estimate of the hydraulic conductivity distribution. The kriged distribution is used to construct a single numerical model of sub-surface geology. The numerical model is used to establish the pressure reducing potential of each proposed dewatering design. The computed pore pressure distribution is input into the Sarma slope stability model, together with the most likely shear strength parameters, and used to compute a single factor of safety. In the final analysis step, a selection criterion based on a reasonably high factor of safety and a relatively low dewatering cost is used to narrow the field for the detailed stochastic analysis to two or three designs.

To illustrate how hydraulic conductivity measurements can be used to fine tune the dewatering design, consider the hydraulic conductivity distribution illustrated in *Figure 7.52*. This distribution was generated by kriging the low density measurements given in *Figure 7.46*. The hydraulic conductivity distribution is favourable for two reasons: 1) natural drainage of the high conductivity zone in the toe area will reduce the need for wells, 2) depressurization of the narrow, high conductivity zone at coordinates 825, 500 will reduce pore pressures over a large portion of the failure surface.

Four dewatering designs will be analyzed during this study:

A. No dewatering wells.
B. Original base case dewatering design.
C. Dewatering design considered optimal in *Section 7.7.1.*
D. New dewatering design adjusted in light of the low density data.

Recall that in *Section 7.7.1* no site specific hydraulic conductivity measurements were available; therefore, the optimum design had to be based on an unconditional simulation of groundwater flow. In light of the favourable results obtained during the low density testing program, conditional analysis of that dewatering program will most likely show that it is substantially over-designed.

Figure 7.52 Estimate of Hydraulic Conductivity Field Based on Low Density Testing Program

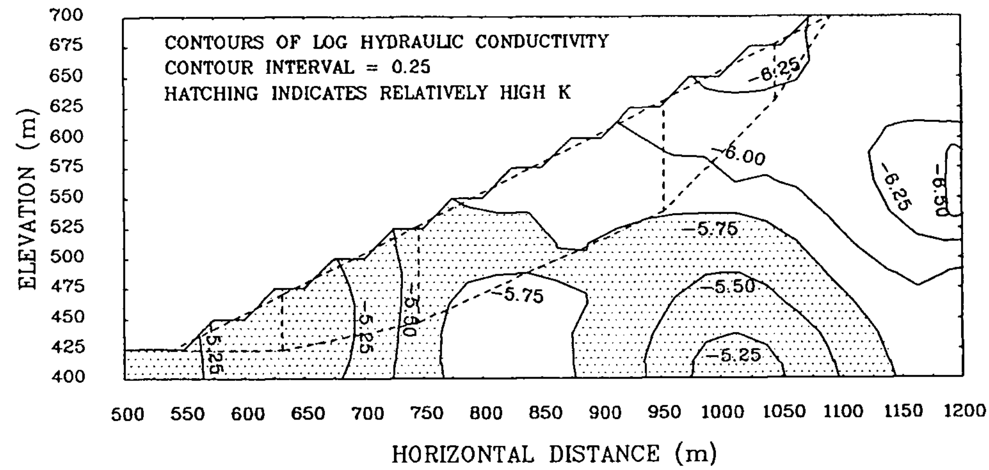

On the other hand, the new dewatering design makes full use of the low density hydraulic conductivity measurements. It utilizes a fewer wells per row in the toe region, wells in the central region are completed only to the base of the high conductivity horizon, and wells from the crest have been shifted down slope in order to intercept the high conductivity horizon.

Figures 7.53 A through *D* show the steady state hydraulic head distributions that result from each of the four dewatering designs. *Table 7.15* lists the corresponding dewatering costs and computed factors of safety. If design A is selected, no dewatering will be performed. Pore pressures will remain high over much of the failure surface and the factor of safety will be unacceptably low (1.07). Design B, the original base-case design, appears to depressurize the slope effectively, increasing the factor of safety to 1.27. However, much of the dewatering budget is wasted on development and operation of the deep wells in the crest region where substantial pore pressure reduction is not required. The new dewatering design (D) is clearly more effective than design B because it increases the factor of safety to 1.28 while costing substantially less. The old optimum design (C) increases the mean factor of safety only marginally from 1.28 to 1.29 at cost of nearly three million. It is very likely that this marginal increase in FOS is not economically justified; however, a complete stochastic analysis is required to confirm that the new design (D) is in fact superior to old optimum strategy (C). A stochastic analysis of design D confirms that the probability of failure remains at 0.0. The subsequent economic analysis shows that due to the modifications in the dewatering design, expected operating costs of the ultimate pit push-back are further reduced from 6.07 million to 3.04 million dollars.

Table 7.15 Costs and Factors of Safety for Dewatering Designs A to D

DESIGN NUMBER	DEWATERING PROGRAM	INVESTIGATION COSTS	DEWATERING COSTS	FACTOR OF SAFETY
A	NONE	0.00	0.00	1.07
B	BASE-CASE	0.00	3.05	1.27
C	OLD OPTIMUM	0.65	5.42	1.29
D	NEW DESIGN	0.65	2.39	1.28

Figure 7.53 Hydraulic Head Distributions for Dewatering Designs A to D

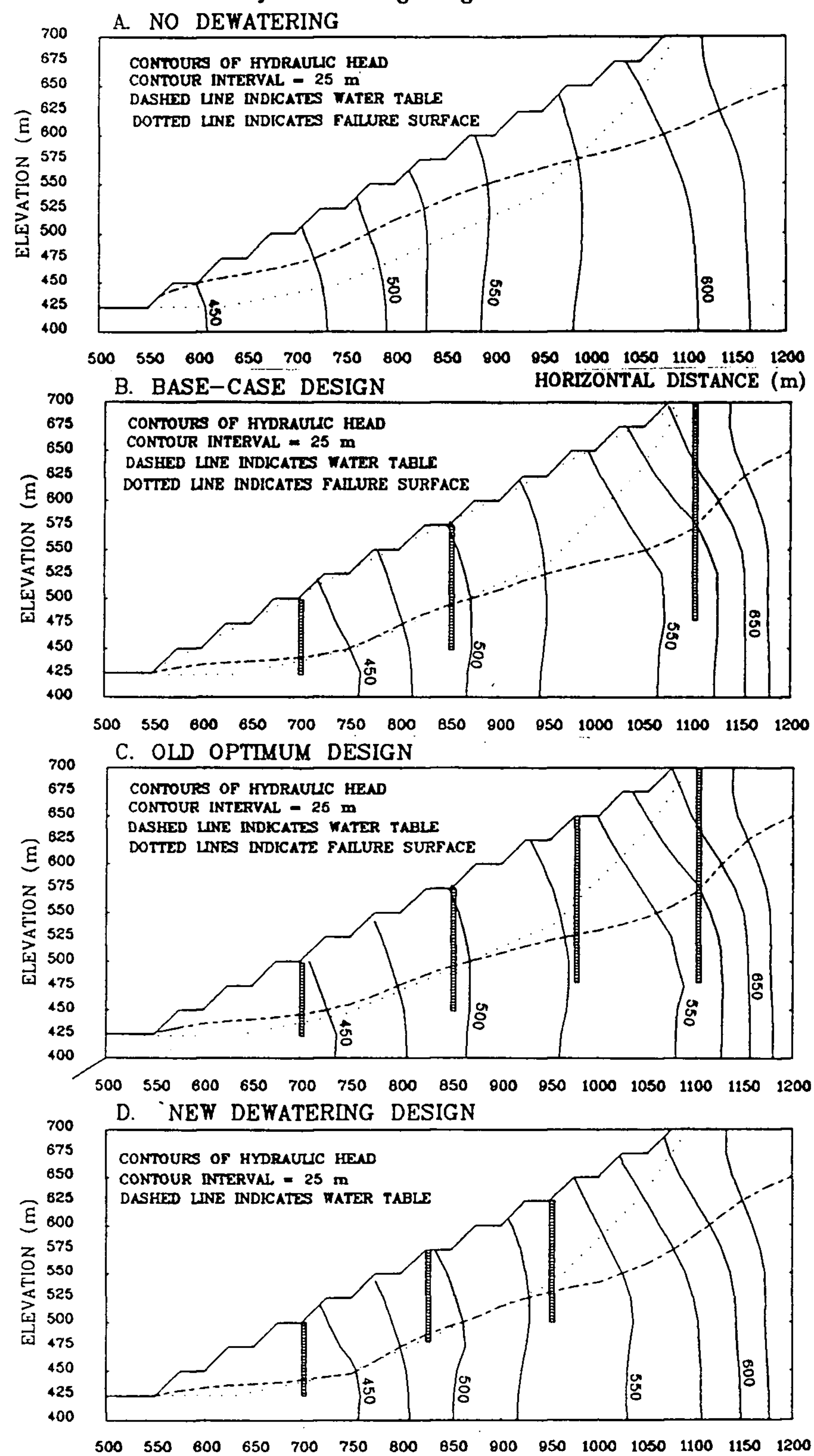

7.9 SUMMARY

Through a series of comprehensive sensitivity studies, this chapter has demonstrated how the various aspects of geotechnical slope design can influence the profitability of an open pit mine. In sequence, the discussion focused on the following key topics:

- The Risk-Cost-Benefit methodology; in particular, the steps involved in successfully applying the methodology to a realistic design problem.
- The influence of overall slope angle on probability of failure, and ultimately, on mine profitability.
- The controlling influence of local hydrologic conditions on the effectiveness of any dewatering program.
- The relative importance of shear strength parameters vs. hydrogeologic data on the overall stability assessment.
- A systematic procedure for identifying the optimum dewatering strategy.
- The monetary worth of hydraulic conductivity measurements, and how the measurements should be utilized to attain the most effective dewatering design.

Section 7.2 provided a complete list of geologic, hydrogeologic, slope design and economic parameters that are required in order to carry out a complete risk-cost-benefit assessment of any dewatering design strategy. *Section 7.2* also served to define the base-case scenario that was referred to in subsequent sensitivity studies. When formulating the base-case scenario, the range of values for each input parameter was carefully selected so that the quantity and quality of the data would be consistent with information typically available at the completion of the initial mine feasibility study. Furthermore, many base-case parameters were selected so that the base-case scenario would resemble actual conditions at Highland Valley Copper, thereby permitting results of the sensitivity study to be directly applied to the case history analysis in *Chapter 9.*

Section 7.3 illustrated the four key steps involved in applying the risk-cost-benefit framework to the analysis of slope angle and dewatering design. The steps included:

- Prediction of the hydraulic conductivity field.
- Estimation of the pore pressure distribution.
- Slope stability analysis to determine probability of failure.
- Economic assessment to determine expected net income of the proposed design.

During the analysis it was determined that the base case design would be expected to generate positive net income during each push-back; however, by far the largest contributions would be realized during the first two push-back cycles. Furthermore, the analysis indicated that a failure of the ultimate pit wall would prove very costly for the mine; therefore, any design improvements (i.e. more site investigation, reduction in slope angle, additional dewatering) that further reduced the probability of failure from 17% would likely prove economically attractive.

Section 7.4 investigated how changes to the overall slope angle would affect the profitability of the mine. The sensitivity study focused on three alternate slope configurations at 20, 25 and 30°. In all three designs no provisions were made for groundwater control. It was determined that without dewatering, the 20° design would be expected to generate the maximum net income; however, that level of income was 38% lower than would be expected for the base-case dewatering design. The base-case dewatering design would permit the mine to steepen the pit walls by 10° while maintaining approximately the same risk of failure.

It was also recognized in *Section 7.4* that the probability of failure generally increases with increasing slope height. This trend was attributed to two independent processes: 1) the effects of cohesion become less significant as confining stresses increase, and 2) larger pore pressures are developed in the critical toe area of the slope.

As a result of this phenomenon, it was suggested that it may be beneficial to utilize steeper slope angles in the early stages of mine development.

Section 7.5 examined how performance of a given dewatering program is influenced by local hydrologic conditions. In particular, the sensitivity study explored how dewatering performance is affected by changes to mean hydraulic conductivity, to the degree of variability in the hydraulic conductivity field, and to the range of hydraulic conductivity correlation.

It was established that dewatering by conventional methods is likely to prove effective only if the mean hydraulic conductivity falls between $1x10^{-8}$ m/s and $1x10^{-5}$ m/s. If the geologic strata is less permeable then the maximum attainable well yields will not be sufficient to depressurize the pit wall in the time allotted, if it is more permeable then enormous quantities of water will have to be pumped in order to achieve a substantial draw-down cone. Furthermore, because the draw-down cone will be very extensive, such massive dewatering could lead to adverse environmental impacts.

A sensitivity study of the effects of changing the hydraulic conductivity standard deviation indicated that accuracy of the stability assessment is strongly dependent on the variability of the hydraulic conductivity field. The pore pressure response became less and less predictable as the level of heterogeneity was increased during the simulation. The uncertainty in the pore pressure field propagated through each step of the analysis, ultimately increasing the monetary risk of failure. These results suggest that an abundance of hydraulic conductivity measurements will be much more valuable in geologic environments with highly contrasting zones of hydraulic conductivity.

A study of system sensitivity to changes in range revealed similar results. It was discovered that increases in the range (i.e. increasing the size of individual horizons of high and low conductivity) contributed to pronounced reductions in the degree of confidence in the stability assessment. These results suggest that a detailed hydrogeologic investigation will be much more valuable if the range is relatively large. As a rule of thumb, the system becomes sensitive to hydraulic conductivity contrasts once the range exceeds approximately 1/5 of the maximum dimension of the flow domain.

A comparison of the relative economic impact of changes in mean K, in the variance of K, and in the range indicates that mean hydraulic conductivity is by far the most critical parameter because it determines whether or not groundwater control will be successful.

Section 7.6 explored the role of shear strength parameters in the risk-cost-benefit assessment. The primary objective of this section was to determine whether accurate shear strength information was more, less or equally important as hydrogeologic data. During the analyses it was determined that the degree of stability is very sensitive to both friction angle and cohesion. The particular slope geometry analyzed appeared to be equally sensitive to changes in both c and ϕ. However, it was recognized that for small slides in cohesive soils cohesion would control stability, while friction angle effects would dominate for very large slides or in failures through cohesionless materials.

To determine the relative importance of friction angle, cohesion and hydraulic conductivity data a series of sensitivity studies were conducted whereby the standard deviation of one parameter was varied over the full range of likely values while the other two parameters were held constant (standard deviation set to 0). It was discovered that for the base-case scenario analyzed, uncertainty in hydraulic conductivity estimates would lead to the largest uncertainty in the stability assessment. This observation would suggest that hydraulic conductivity data would be the most valuable. However, a combined sensitivity analysis that gradually increased the level of uncertainty in all three parameters simultaneously demonstrated that the accuracy of a stability assessment cannot be substantially reduced by concentrating the investigation effort on measurements of one parameter only. A balanced site investigation strategy that reduces uncertainty in K, ϕ, and c proportionately will be most effective in increasing the degree of confidence of the stability assessment. As a rule of thumb, there should be a one to one correspondence between the number of shear strength tests and hydraulic conductivity tests performed in each bore hole to attain the optimum balance.

Section 7.7 examined how the economic picture would be affected by adjustments to the dewatering design. It was shown that the largest reductions in pore pressures are typically achieved by the first few wells. Thereafter, progressively steeper hydraulic gradients are established and larger pumping rates (i.e. more wells or larger pumps) are required to attain further reduction in pore pressures. A point of diminished returns is eventually reached whereby further additions to the dewatering system are no longer justified because the incremental development and operating costs begin to exceed the marginal increases in expected net income that result from improved slope stability. The bottom line: a low budget dewatering program will be justified in most circumstances, but a detailed risk-cost-benefit assessment is required to determine the optimum dewatering budget.

Based on an earlier observed trend that the probability of failure increases with increasing slope height, *Section 7.7* also investigated whether slopes should be cut steeper during the early stages of mine development. It was concluded that such a strategy would be beneficial because it would increase cash flows during the critical early years of mine operation. Of course, proper slope design would still have to be practised to ensure that pit walls are not over-steepened.

Section 7.8 examined the importance hydraulic conductivity measurements. The discussion focused on three related themes. First, the section explored how measurements influence the level of confidence in a stability assessment. The second theme illustrated how the monetary worth of data can be identified. Finally, the material demonstrated how hydraulic conductivity measurements can be used to fine tune the dewatering design in response to actual site conditions.

Using conditional simulation methods, the first part of *Section 7.8* demonstrated that by reducing uncertainty in the hydraulic conductivity field, variability in predicted heads will also be reduced. Ultimately, measurements lead to a substantial tightening of the factor of safety distribution, increasing the level of confidence in the stability assessment. It was shown that measurements can affect the probability of failure in two ways. First, by reducing uncertainty in input parameters and tightening the FOS distribution, the probability of failure will be reduced due to the tail effect. Second, if measurements indicate that conditions are much better or much worse than expected, the entire FOS distribution will shift. The probability of failure will of course increase or decrease, depending on the direction of the translation.

The second part of *Section 7.8* explored the worth of hydraulic conductivity data. Because the worth of data is a complex topic outside the scope of this research effort the discussion was brief and by no means complete. To illustrate the worth of data, *Section 7.8* presented a very simple example that analyzed three levels of site investigation effort: 1) no data, 2) low density program, and 3) high density program. The following criterion was used to decide whether or not each level of the monitoring program was justified: "Additional testing is justified as long as the total incremental cost of the monitoring program is less than the increase in net expected income that arises from the new information". The increase in net expected income can stem from increases in revenue, reductions in operating costs, and/or reductions in monetary risk. Using this criterion it was shown for the example considered that while the low density testing program would be worthwhile the high density monitoring program would not be economically justified.

The third part of *Section 7.8* demonstrated that much of the value of a hydraulic conductivity testing program is realized only when the new information is used to improve the original dewatering design, fine tuning it to actual site conditions. It was shown that a deterministic approach can be adopted to screen a large number of potential adjustments to the dewatering system quickly and efficiently, narrowing the field to two or three most favourable designs. The time demanding stochastic analysis is only required to make the final design selections among the favourable options.

The primary objective of this thesis research is to develop an analytical method that can be used to evaluate the monetary worth of a groundwater control program in an open pit mine, a method that has the capability to determine how much capital should be allocated for groundwater control in order to achieve maximum profits. It is hoped that the results of the numerous sensitivity studies presented in this chapter demonstrate that this objective has been attained. In addition, it has been shown how sensitivity studies can advance our understanding of the role each input parameter and design variable plays in the overall economic picture and how much data is required in order to achieve an adequate understanding of sub-surface conditions to complete a dewatering design. The development of the design tool illustrated in this chapter is the most important research contribution of this thesis.

CHAPTER 8 CASE HISTORY

8.1 OVERVIEW

Groundwater control is an important component of mining operations at Highland Valley Copper (HVC), especially in the thick sequence of overburden materials in the north eastern quadrant of the pit. A groundwater control strategy for the overburden pit wall was first mapped out in 1984 (Brown & Erdman, 1984), and subsequently updated in 1988 in light of new geologic information (Sperling & Brennan, 1988). This chapter describes how the risk-cost-benefit framework introduced earlier in this thesis has been used to evaluate the current overburden dewatering strategy. Several alternate groundwater control plans were also analyzed to determine whether the dewatering plan could be further modified in order to enhance stability of the pit wall and to realize additional reductions in expected operating costs. To avoid repetition, the analysis presented in this chapter has been limited to design sector R3, one of five design sectors currently defined in the overburden of the Valley Pit. Sector R3 has been selected for analysis because the thickest sequence of unconsolidated material, 225 m of saturated overburden, will have to be excavated in that sector.

Section 8.2 provides an overview of mine operations at HVC. The discussion touches on the mine's history, on site location and lay-out, on the regional geology, and on several other topics that will help to place the detailed analysis of design sector R3 that follows into perspective relative to the entire mining operation.

Section 8.3 reviews the current geologic interpretation. Although the section begins with a brief description of bedrock geology that is required for the economic analysis, the theme switches quickly to the latest interpretation of overburden geology at the mine site in general, and in design sector R3 in particular. Because the available density of hydraulic conductivity measurements is not sufficient to obtain accurate estimates of the range of correlation and anisotropy, the geologic interpretation was utilized for this purpose.

Section 8.4 presents all available hydraulic conductivity data for design sector R3. The information was derived from several sources including: pump tests, long term well yields, consolidation tests, grain size analyses, and estimates based on descriptions of drill cuttings. Section 8.4 also reports the results of the geostatistical analysis. Statistical parameters that are specified include: the mean hydraulic conductivity, variance of the hydraulic conductivity field, the estimated range of correlation, and an estimate of the directional anisotropy.

Section 8.5 describes the current Valley Pit mine plan and slope design, with emphasis on slope angles and slope heights in design sector R3 during each of the six push-backs. The current overburden groundwater control plan, including the drilling schedule, anticipated well yields, and dewatering budget is also outlined in this section. Once again, the discussion focuses on dewatering efforts in design sector R3.

Section 8.6 describes how computer program SG-FLOW was used to predict the pore pressure distribution in the pit wall for each pushback. The section begins with a discussion of the boundary value problem, followed by an outline of the steps used to generate realizations of the hydraulic conductivity field. A verification study of the 1987 pore pressure distribution is then presented, and finally, the model is used to predict the pore pressure distributions for the 1992, 1997 and ultimate slope configurations.

Section 8.7 documents the slope stability analysis. The discussion begins with a summary of available shear strength data. The data base includes results of the recently completed strength tests on samples from the extensive black clay horizon, as well as results of earlier tests on the upper glaciofluvial strata. Parameters that are reported for each major geologic unit include mean friction angle, mean cohesion, and the confidence level associated with each parameter estimate. The discussion then focuses on identification of the critical failure surface for each slope geometry. The discussion concludes with a review of the probabilistic stability evaluation results for the 1987, 92, 97 and ultimate slope configurations.

Section 8.8 presents the findings of the risk-cost-benefit analysis of the current slope design and groundwater control plan for design sector R3. The probability of failure and expected net income are reported for each push-back. Results of this analysis provide the first indication as to whether HVC is likely to profit from additional dewatering efforts during each of the six pit expansions.

Using the current design as a starting point, *Section 8.9* evaluates the economic merit of increased dewatering efforts during excavation of the ultimate pit. After evaluating the expected net income for each design option, *Section 8.9* makes recommendations on how the groundwater control plan should be modified to achieve maximum profitability in design sector R3.

8.2 SITE ORIENTATION

HVC is a "world class" mining operation. It is currently the second largest copper mine in the world in terms of total tonnage mined per year. As shown in *Figure 8.1*, the mine is located 350 km northeast of Vancouver, British Columbia, and approximately 70 km west of Kamloops, the closest major municipality.

Ore is being mined in two pits on the property: at the mature Lornex pit, and at the new Valley pit. The study area that is described in this case history is situated in the Valley pit. Development of the Valley porphyry copper deposit commenced in 1982. When completed in approximately 20 years, the Valley pit will have a diameter of 2.5 km and a depth in excess of 750 m.

Figure 8.2, a contour map of the Highland Valley and surroundings defines topographic relief and drainage patterns. The valley is very broad and U shaped, the highlands of the Bethseida Plateau rise approximately 1000 m above the valley floor. The mine, indicated by concentric ellipses in *Figure 8.2*, is situated on the southwest flank of the Highland Valley. Pleistocene glacial activity buried the northern half of the ore body under a thick blanket of overburden material. *Figure 8.3* illustrates the location of the overburden in relation to the ore deposit and the ultimate pit wall. The 1988 pit profile is also shown. Notice that the upper 225 m of the ultimate pit wall will be excavated in saturated overburden material.

The primary objective of the overburden dewatering program is to maintain stability in the very high overburden pit walls by reducing pore water pressures. Groundwater control is also required to limit seepage into the pit. It is expected that uncontrolled seepage would lead to serious erosion of berms and very poor operating conditions for the truck and shovel fleet. Not all impacts of groundwater on operations are detrimental; because local surface water supplies are limited, most of the process water required by the mill must be pumped 30 km from the North Thompson River at a cost that exceeds $1,100,000 per annum. As the dewatering wells come on line local groundwater resources are providing a significant proportion of the water requirement and substantial reductions in water supply costs are being realized.

Figure 8.1 Map of British Columbia Showing Location of Highland Valley Copper

Figure 8.2 Topographic Map of Highland Valley and Surroundings

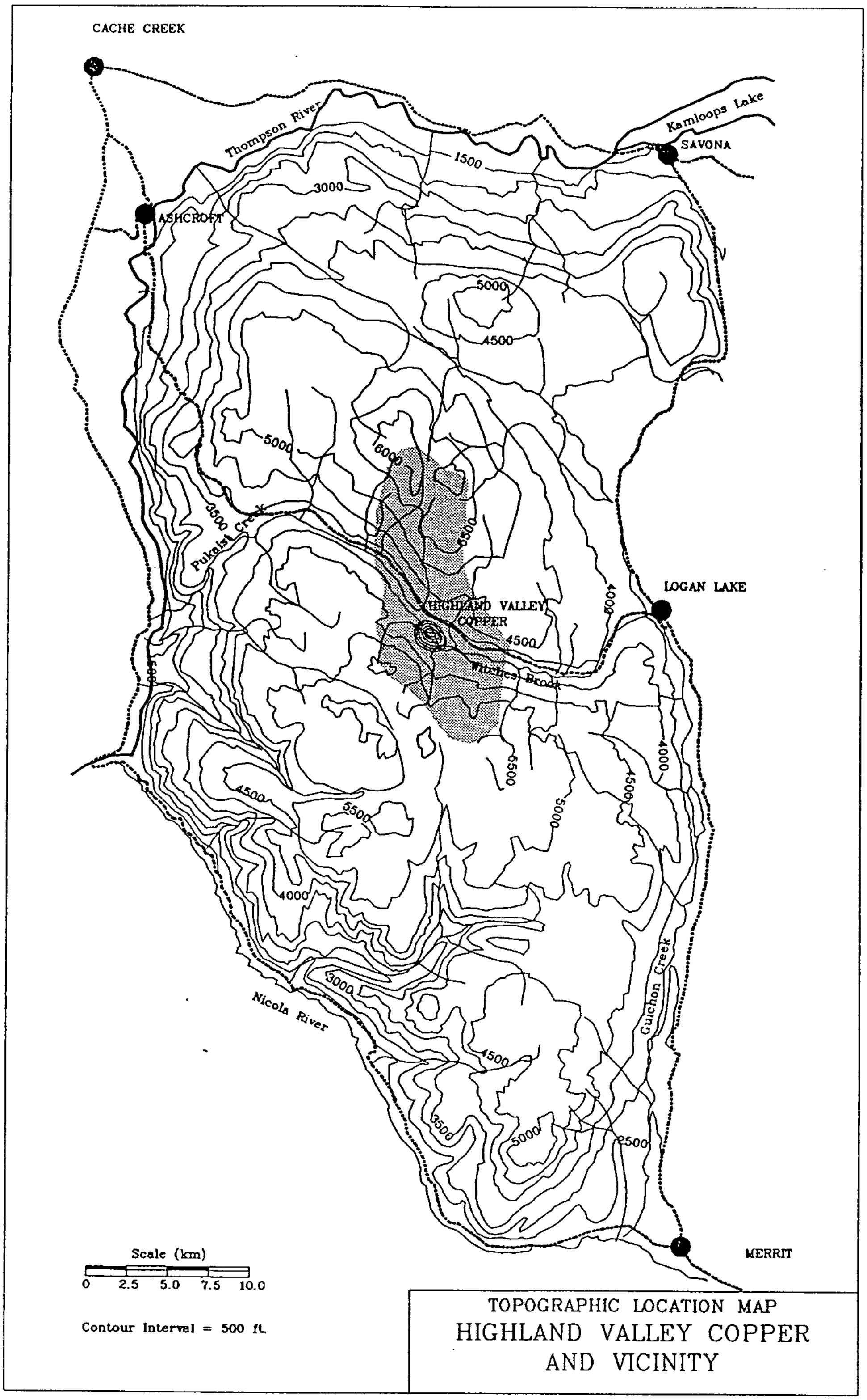

Figure 8.3 Geologic Cross Section of Valley Pit, Looking Northwest

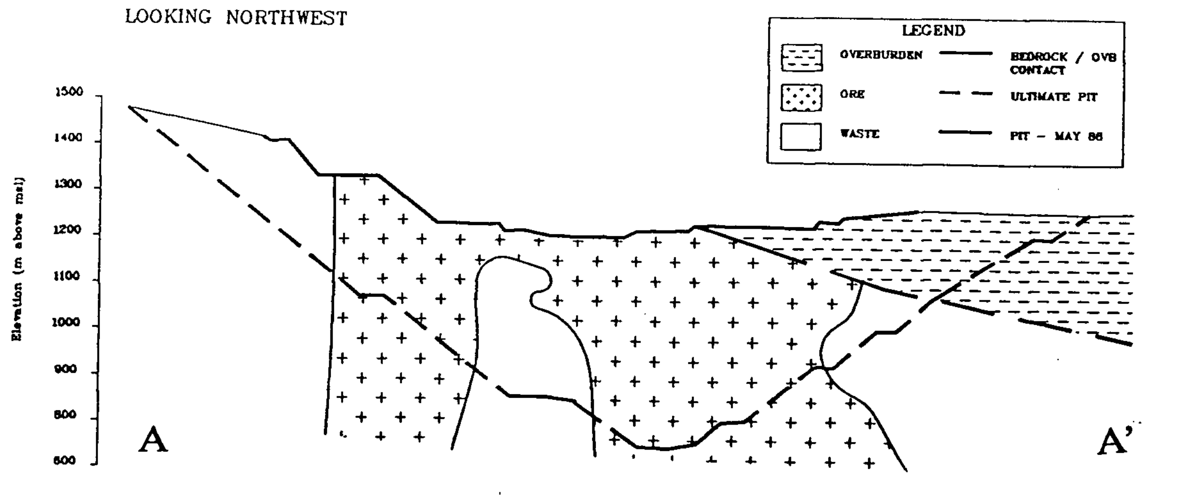

As of December 1988, the dewatering system consisted of 21 wells. *Figure 8.4* shows the location of the wells in relation to the 1988 pit limits. Most of the existing wells are located within the ultimate pit limits, these wells will eventually be lost as the pit is expanded. Many new wells will be required to adequately dewater the extensive aquifer horizons at depth. The shaded region in *Figure 8.4* identifies the location of design sector R3 that is analyzed in this study.

Figure 8.4 Plan Showing Outline of 1988 Pit, Existing Wells, and Design Sector R3

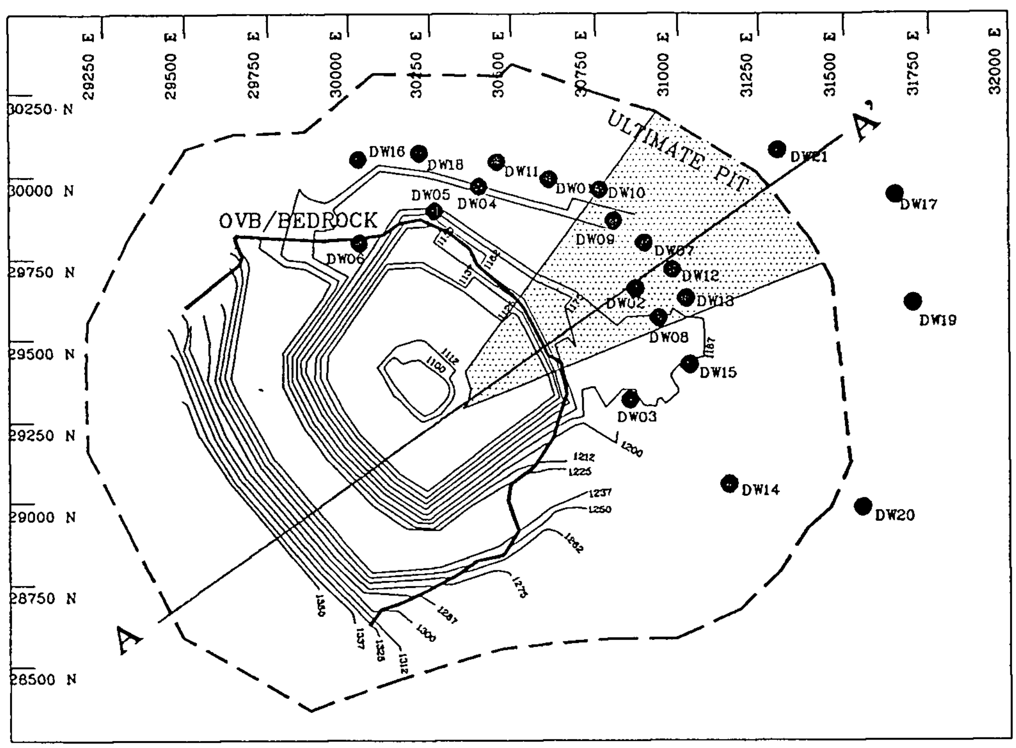

8.3 GEOLOGIC INTERPRETATION

The objective of this section is to present the latest interpretation of overburden and bedrock geology, with special emphasis on portions of the interpretation that will impact on the risk-cost-benefit evaluation of design sector R3.

The bedrock geology is understood well at HVC. This understanding is the result of an extensive, ongoing ore definition drilling program. The program involves diamond drilling, detailed geologic logging, sampling and assaying of all ore intersections, and three dimensional geostatistical analysis of the assay results.

Prior to 1987, the overburden geology was understood much less clearly than the bedrock geology. At that time it was recognized that a better understanding of this subject was urgently required for two basic reasons: 1) overburden geologic conditions will impact on slope stability in approximately 25% of the pit, and 2) the distribution of aquifer and aquitard horizons, as well as the permeability characteristics of those horizons, will determine whether groundwater pore pressures can be successfully reduced by a dewatering system.

Over a two year period from May, 1987 through December, 1988, this author was responsible for organizing and conducting a detailed investigation of overburden geologic and hydrogeologic conditions in the Valley pit. The investigation involved:

- A detailed review of existing geologic data.
- Planning of an exploration drilling program to obtain additional data where information was considered inadequate.
- Detailed geotechnical logging of nine piezometers and well borings completed in 1987 and 1988.
- Entry of all existing geologic data into the SG-CoreLog geotechnical data base. The software was then used to generate printed logs, bar graphs, and geologic sections.
- Interpretation of all available geologic information to establish a comprehensive, three dimensional model of overburden conditions.

Presented below is a summary of the key findings of this investigation. Additional details, including logging procedures, geologic logs, bar graphs and sections are presented in Appendix E.

8.3.1 BEDROCK GEOLOGY

The Valley porphyry copper deposit is situated on the northeast flank of the Guichon Creek Batholith, an intrusive body approximately circular in cross section and 15 km in diameter. The host rock for the mineralization is the Bethsaida granodiorite. This bedrock unit is found to the west of the Lornex fault, while Bethlehem granodiorite occurs on the east side of the fault (see *Figure 8.7*). The tectonic activity that created this major regional discontinuity is also believed to be responsible for increasing the permeability of the Bethsaida unit sufficiently to permit circulation of the copper rich groundwaters that eventually deposited the chalcopyrite and molybdenite mineralization.

Figure 8.5 shows the location of the mineralized zones on geologic section R3. The ore zones, greater than 0.35% Cu, are indicated by the densely shaded pattern. Digability and hardness characteristics of the rockmass are shown in *Figure 8.6.* The "R" hardness categories used in the figure are based on the approximate classification of cohesive soil and rock (Hoek & Bray, 1981). Comparison of *Figures 8.5* and *8.6* suggests that the ore deposit is structurally controlled; the main zone of mineralization occurs in the highly fractured Osprey Shear Zone, the second, somewhat smaller zone of mineralization is associated with the narrower shear zone illustrated on the left side of *Figure 8.6.*

Figure 8.5 Geologic Section Showing Location of High Grade Ore Zones.

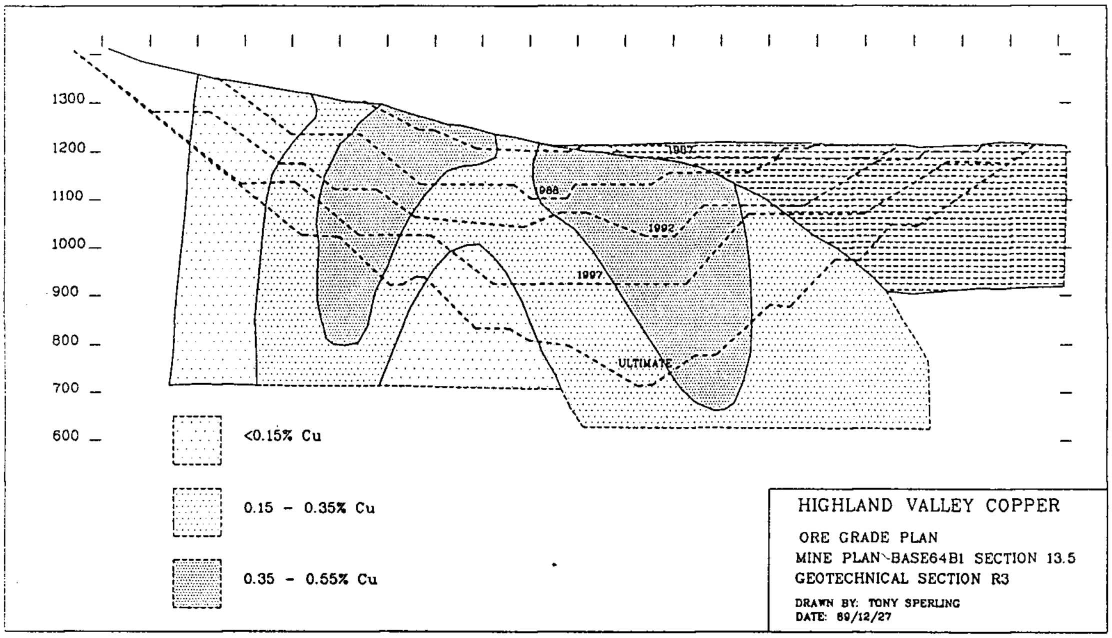

Figure 8.6 Section Showing Digability and Hardness Characteristics on Section R3.

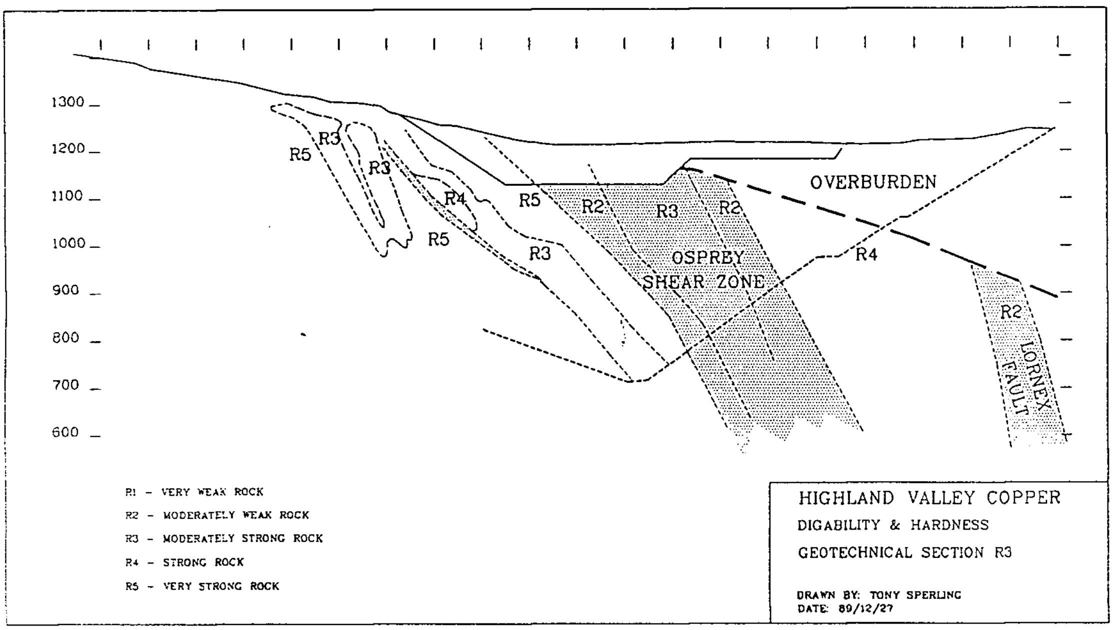

Figure 8.7 Contour Plan Showing Elevation of Overburden/Bedrock Contact

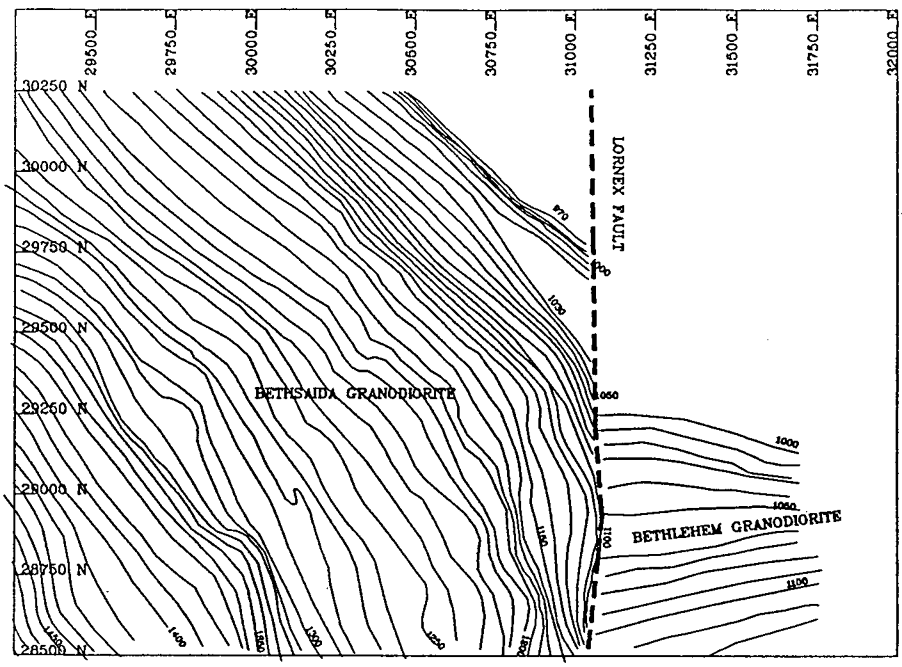

The ore distribution and hardness data presented above will be considered in the economic evaluation of design sector R3. In addition, the bedrock geology will also affect groundwater flow in the pit wall. Based on limited inspection of drill core and information provided by HVC geologists it appears that the bedrock is relatively impermeable to groundwater flow, except in zones of major fracturing and alteration (shaded in *Figure 8.6*). Observations of groundwater discharges from a large number of horizontal drains in the Lornex pit suggest that some parts of the shear zones are highly permeable while others are very tight. As a result, geologic staff at HVC have described the groundwater regime as "compartmentalized". In the computer model used in this analysis it will be assumed that the overburden/bedrock contact will be treated as an impermeable boundary for groundwater flow. The effects of this simplification, in particular, the possible impact of significant groundwater flow through the Osprey and Lornex shear zones should be evaluated in the near future. The shape of the overburden/bedrock contact, illustrated by elevation contours for the contact surface in *Figure 8.7*, is well defined over most of the mine area, based on a large number of drill hole intersections.

8.3.2 OVERBURDEN GEOLOGY

The thick overburden sequence that blankets the valley floor includes till deposits, fluvial sands and gravels, and glaciolacustrine silts and clays. The resulting overburden geology is complex. The fluvial sands and gravels form three relatively continuous aquifer horizons. Each aquifer is confined by much less permeable till and lacustrine silt and clay aquitards. The aquifers are water bearing, with existing dewatering wells yielding 400 to 6000 l/min. Twelve overburden units have been recognized in the Highland Valley to date. *Table 8.1* shows the stratigraphic succession of the horizons, as well as the approximate material composition of each unit. In the field the stratigraphic sequence is less ordered as individual layers thin out gradually or are abruptly truncated by paleooutwash channels. *Figure 8.8* illustrates the approximate extent of each unit on geologic section R3. In the broadest sense, the stratigraphy can be divided into two groups: 1) an upper group of relatively thin (20-50 m thick) layers of sand, silty sand, and till, and 2) a lower sequence of much finer silts and clays.

Originally, it was believed that the lower sequence was comprised of massive "Black Clay"; however, recent exploratory drilling (Sperling, 1988) has revealed that the sequence is also made up of a number of 20 to 50 m thick layers that vary in grain-size, colour, and mineralogical composition. More drilling and detailed geologic investigation will be required to identify the extent of each horizon and to determine whether any of the coarser grained horizons are sufficiently pervious to justify dewatering efforts.

Geologic horizons that will have the greatest impact on the dewatering program and pit wall design include: 1) silts and clays of the Lower Sequence, especially the location and continuity of weak layers and presence of pervious drainage layers that could be exploited for dewatering, 2) the Rust Aquifer (very high yields, potential for flooding if not sufficiently dewatered), and 3) the Main Aquifer (potential for high yields, good production water supply). Vibration induced liquefaction could threaten stability, but the threat is considered remote since the fine strata exhibit dilatant behaviour as a result of overconsolidation. Nevertheless, it is recommended that blast energy is minimized in production blasts at the overburden contact.

The overburden geology interpretation presented above is based on geologic logs from 21 wells and 19 piezometers, as well as limited information from surface exposures that were excavated prior to 1988. The interpretation is revised periodically as new information becomes available. To conduct this time demanding task efficiently, and to maintain consistency from year to year, a set of systematic data collection and analysis guidelines have been established. These guidelines are described very briefly in *Appendix E.*

Figure 8.8 Overburden Geology Interpretation - Design Sector R3

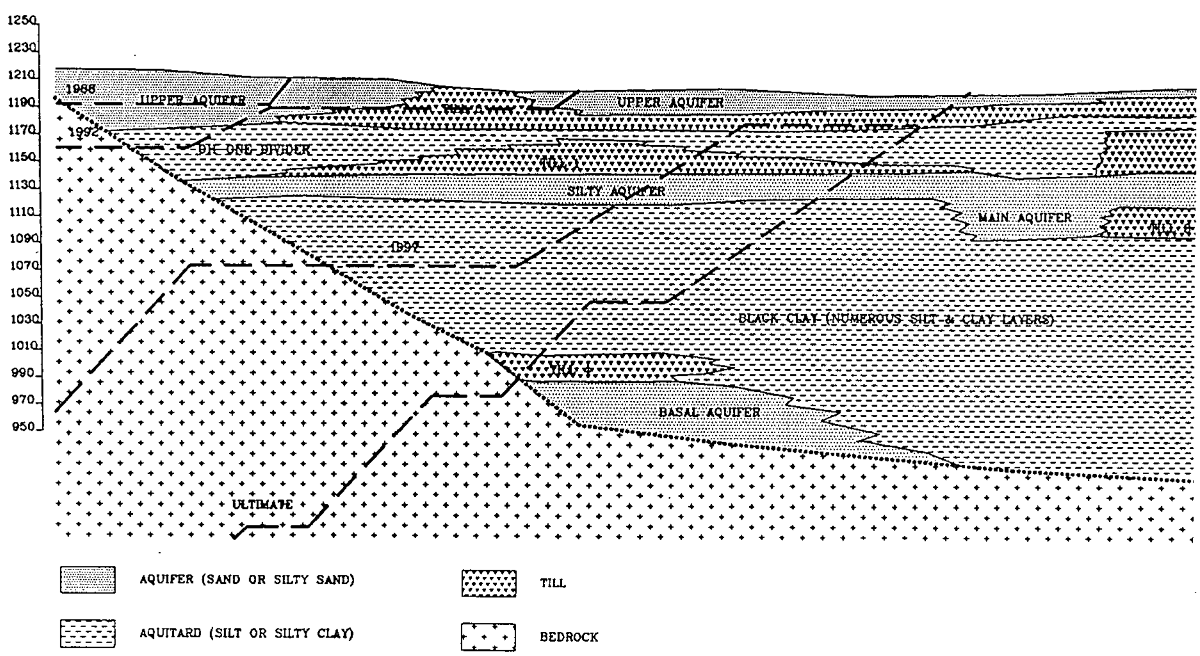

Table 8.1 Overburden Stratigraphy and Material Composition

UNIT	UNIT NAME	DESCRIPTION	AGE
1	Upper Aquifer	Predominantly silty sand, 10 to 20 m thick. Very Continuous. Water table drawn down below aquifer in vicinity of pit. Therefore, most of the horizon is unsaturated.	Youngest
2	Till – 0	Dense silt and clay, sandy, some gravel. Relatively impervious. Youngest till sheet deposited in Highland Valley. Semi–continuous. Thickness varies between 0 and 20 m. Plunges 1 degree to east.	
3	Oh–One Divider	Comprised of thin interbeds of silty sand, silt and clay. Thickness varies from 10 to 40 m. Unit plunges approximately one degree to east. Water bearing potential is limited because horizon is very silty.	
4	Till – 1	Composed of brown clayey silt, with some graded sand and gravel. Very continuous till sheet, thickness varies between 0 and 20 m. Acts as confining layer between Oh–One divider and Silty Aquifer.	
5	Silty Aquifer	Consists of graded silty sand with some gravel. Thickness ranges between 5 and 30 m, generally becoming thicker east of the Lornex Fault. Slight plunge to east. Colour generally brown. Deposition environment most likely braided glacial outwash plain.	
6	Till – 2	Dense silt and clay till, some sand and gravel. Colour generally grey. Thickness ranges from 0 to 35 m. Till sheet is widespread, but semi–continuous. Forms effective low permeability aquitard between overlying silty aquifer and underlying basal aquifer.	
7	Main Aquifer	Silty sand and gravel. Graded composition. Thickness varies between 10 and 40 m. This aquifer is a major fluvial deposit of glacial outwash. Well yields between 200 and 900 US GPM.	
8	Rust Aquifer	Coarse, granitic sand and gravel. Stained with characteristic rust colour. Contains numerous angular quarz grains. Maximum thickness is 35 to 65 m in vicinity of P18 and DW14 (see Fig. 8.3); however, aquifer thins rapidly to the north and to the west. Depositional environment is most likely an alluvial or outwash fan deposit. The source area was most likely to the south. Highest yielding aquifer in the overburden, yields as high as 1700 US GPM.	
9	Till – 3	Thin, discontinuous layer, 5 to 20 m in thickness. Always observed under thick channel deposits of Main and Rusty Aquifer. Most likely originated as basal lag material in depressions and channels carved by glacial activity through black silt and clay.	
10	"Black" Silt and Clay	Originally believed to be a single massive clay horizon. Recent drilling (Sperling, 1988) has shown that horizon consists of three thinner silt and clayey silt horizons.	
		Black silt with some clay and occasional fine sand layers. Upon exposure to air material oxidizes to characteristic olive green color.	
		Tan grey clay with some silt. Contains the finest grainsize materials. Expected to be highly impervious and to exhibit low shear strength.	
		Dark grey silt and clay with some fine and medium sand interbeds.	
11	Basal Till	Grey tan clay, with minor sand and gravel. Unit not widespread. Where present, thickness ranges from 3 to 20 m.	
12	Basal Aquifer	Silty sand with very little gravel fraction. Sand composed primarily of dark shale and volcanic fragments. Thickness between 5 and 50 m, decreasing to south. Source area most likely to north.	Oldest

8.4 HYDROGEOLOGY

This section examines groundwater flow conditions in the vicinity of the Valley pit. Beginning with a short review of surface water hydrology and the current interpretation of the groundwater flow system, the discussion then quickly focuses on the procedures used to define the hydraulic conductivity field in design sector R3. In order to conduct a Monte-Carlo simulation of groundwater flow, a detailed geostatistical description of the hydraulic conductivity field is required. At HVC, the geostatistical model was based on several different types of measurements that included: 1) long term well response to pumping, 2) short term pump tests, 3) sieve analyses, 4) consolidation tests, and 5) geologic data. The results of these measurements are summarized in this section, as are estimates of the accuracy associated with each type of measurement. Finally, the geostatistical analysis of the hydraulic conductivity data is described in detail, with emphasis on the determination of the parameters required for the stochastic computer model of groundwater flow, including: the mean, the variance, the correlation range, and the degree of directional anisotropy of the log hydraulic conductivity values.

8.4.1 SURFACE WATER HYDROLOGY

As shown in *Figure 8.3*, the Valley pit is situated very close to the topographic divide of the Highland Valley. Surface drainages to the northwest of the pit discharge into Pukaist creek. This creek flows in a westerly direction for approximately 20 km, ultimately discharging into the Thompson River. Surface run-off to the east of the mine originally flowed into Witches Brook, the brook then flowed eastward for 17 km to merge with Guichon Creek at Logan Lake. The extent of the surface and groundwater catchment basin is indicated by shading in *Figure 8.3*. The catchment area covers approximately 85 square kilometres.

The nearest long term meteorological station is located at Ashcroft. The mean annual precipitation at this station is 237 mm per year. Average seasonal precipitation trends for this weather station are illustrated in *Figure 8.9*. Note that the heaviest precipitation falls in mid-winter and during the summer months. A water budget analysis has been prepared based on the meteorological data from this weather station using the method of Thornthwaite and Mather (1957). The mean annual evapotranspiration is estimated to be 162 mm/yr, the mean annual water surplus is estimated to be 75 mm/yr. The water surplus includes both surface run-off and infiltration.

Seasonal precipitation trends at the mine site are expected to be very similar to Ashcroft; however, because the mine site is located on the Nicola Plateau actual precipitation rates are expected to be somewhat higher while evapotranspiration rates are expected to be somewhat lower. In the water balance calculations presented later in this thesis, it will be assumed that the average annual precipitation is 300 mm/yr, annual evapotranspiration is 120 mm/yr and the average annual water surplus is 180 mm/yr.

To determine how much of the surplus precipitation will actually recharge the groundwater flow system it is first necessary to determine the appropriate run-off coefficient *C*. The Highland Valley is located in the *Interior Douglas Fir* climatic zone that is composed of approximately 50% hilly woodland and 50% hilly pasture. The soil texture is assumed to be a loam to silt loam. According to the design charts published by the Ontario Ministry of Highways *(Table 8.2)*, the appropriate run-off coefficient for this area is 0.37. Therefore, of the estimated 300 mm/yr annual precipitation, approximately 111 mm/yr will leave the catchment as run-off. The remaining water surplus of 69 mm/yr will enter the groundwater flow system as recharge.

Based on the above water budget estimates and catchment area measurements, it is estimated that the annual groundwater recharge is 5.8 million m^3 per year. With the large water table depression that will develop as the size of the open pit increases, a significant portion of this recharge will ultimately flow into the Valley Pit. At present, the dewatering wells and sump pumps are extracting approximately 14 million m^3/yr. Based on this simple water budget analysis, HVC is mining local ground water resources. A more detailed analysis will be required to determine the long term impact of dewatering on water levels in the vicinity of the pit.

Figure 8.9 Average Monthly Precipitation - Ashcroft Weather Station

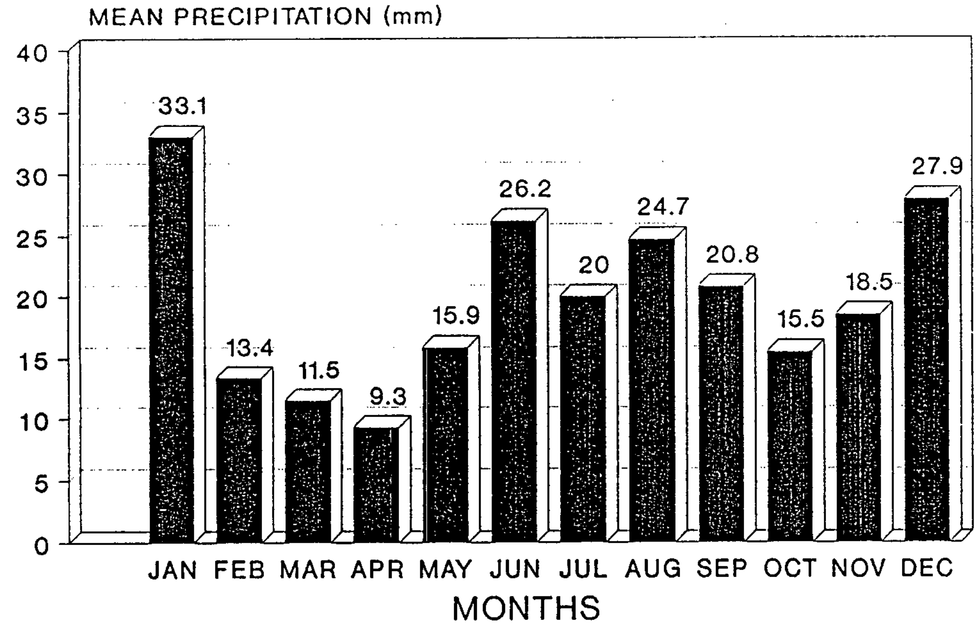

Table 8.2 Run-Off Coefficients (After Ontario Dept. of Highways Report 1979-08-10, Chart B4-3)

LAND USE & TOPOGRAPHY	SLOPE ANGLE	SOIL TEXTURE		
		OPEN SAND LOAM	LOAM AND SILT LOAM	CLAY LOAM AND CLAY
CROP				
FLAT	0 - 5%	0.22	0.35	0.55
ROLLING	5 - 10%	0.3	0.45	0.6
HILLY	10 - 30%	0.4	0.65	0.7
PASTURE				
FLAT	0 - 5%	0.1	0.28	0.4
ROLLING	5 - 10%	0.15	0.35	0.45
HILLY	10 - 30%	0.22	0.4	0.55
WOODLAND				
FLAT	0 - 5%	0.08	0.25	0.35
ROLLING	5 - 10%	0.12	0.3	0.42
HILLY	10 - 30%	0.18	0.35	0.52

Recently, many of the small creeks that flowed into Witches Brook have been diverted and utilized for the mine's process water supply. The diversion of tributaries to Witches Brook and dewatering of the surficial aquifers of Highland Valley have lead to a reduction in the flows in Witches Brook and Guichon Creek.

8.4.2 GROUNDWATER HYDROLOGY

The groundwater flow system in the Highland Valley is dominated by topography and the glacio-fluvial overburden horizons that blanket the valley floor. From below, the groundwater flow system is bounded by igneous intrusive bedrock that is believed to be relatively impervious. Recall from the previous subsection that approximately 23 percent of total precipitation is believed to enter the ground water flow system as infiltration. Much of the recharge occurs in the hills north and south of the pit. The water then flows down slope, eventually entering the thick overburden sequence that fills the valley floor.

Before the development of the Valley Pit the groundwater flow system was in a steady state condition. The presence of several small lakes and numerous marshes indicated that the water table was present at or very close to the surface (approximately 1210 m ASL). With the exception of the surficial aquifer, all overburden horizons were fully saturated. Piezometers installed prior to the development of the Valley Pit indicated that there was a very gradual horizontal gradient down-valley to the east and no discernible vertical hydraulic gradient.

As shown in *Figure 8.10*, excavation of the Valley Pit and the introduction of the dewatering wells has changed the groundwater flow regime in the upper sequence of sand, silty sand and till. A well defined drawdown cone has been established, centred on the inner ring of pumping wells that extends from DW16 to DW14. Piezometric levels in the lower sequence of silts and clays have remained essentially unchanged.

Realistic predictions of future piezometric responses can be achieved with the help of a computer model, but only if hydraulic conductivities, recharge rates, and other boundary conditions are well understood. The following subsections describe how water level monitoring data, pump testing results, and geologic logs were compiled to form a consistent statistical description of the hydraulic conductivity field.

8.4.3 ESTIMATES OF K FROM PUMP TESTS

All wells completed at HVC since 1987 have been pump tested prior to the installation of the production pump. The tests involve pumping the well continuously for a period of two to three days and monitoring the drawdown response in the well bore and at two or three nearby piezometer nests. Although pump tests were likely conducted in all wells, test data is available only for wells DW12, 14, 17, 18, 19 and 20A.

The drawdown responses observed in each of the tested wells are plotted in *Appendix E.3.1*. The time-drawdown data was analyzed with computer program *SG-PUMP*[1] to obtain estimates of transmissivity T and storativity S at each well location. Representative hydraulic conductivity values were then obtained by dividing T by the total screened interval in each well. The resulting conductivities are listed in *Table 8.3* under the heading "Conductivity - Pump Test". The conductivities ranged from 3.8×10^{-6} to 2.1×10^{-4} m/s, a range characteristic of clean to silty sands.

---

1 SG-PUMP is a computer program for analyzing stepped drawdown tests using the Cooper and Jacob (1946) semi-log method. The program was developed by the author in 1987-88 to analyze the pump tests at HVC.

Figure 8.10 Piezometric Contours in Main Aquifer (1988)

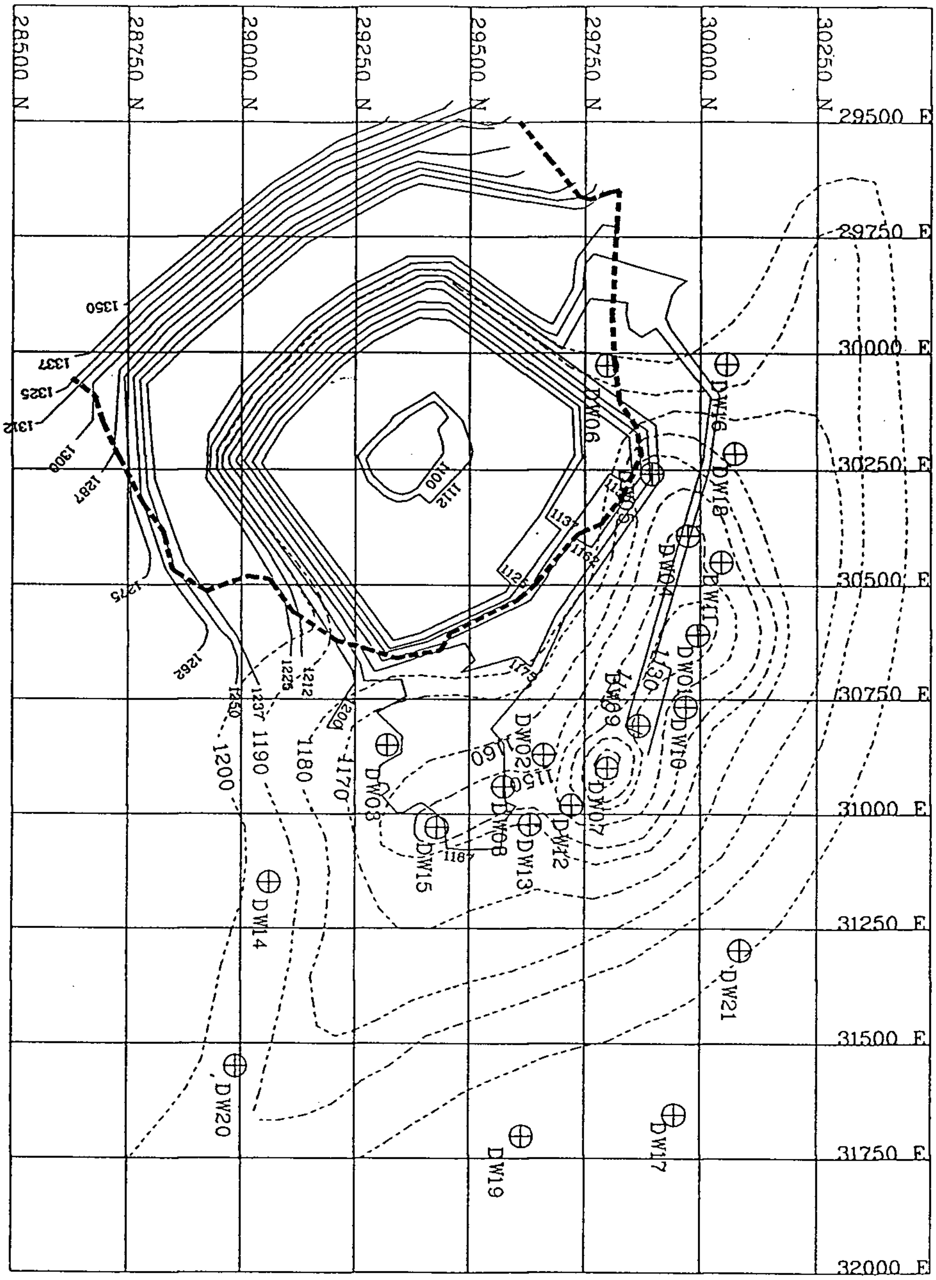

8.4.4 ESTIMATES OF K FROM LONG TERM WELL RESPONSE

Groundwater levels and pumping rates in wells have been monitored on a regular basis at HVC since 1984. Given the drawdown, pumping rate and the duration of pumping it is possible to back-calculate approximate aquifer transmissivities via the Theis equation if one assumes a reasonable value for storativity and that the well interaction effects of neighbouring wells are minimal. This approach was used to back-calculate *T* for each of the 20 overburden dewatering wells. Results of the back-calculations are presented in *Table 8.3* under the heading "Conductivity - Long Term". The estimates varied from 9.1×10^{-7} to 1.1×10^{-4} m/s, typical of clean to silty sands.

***Table 8.3** Hydraulic Conductivity Estimates of Aquifer Horizons*

WELL NUMBER	AQUIFER THICKNESS (m)	PUMPING RATE (L/min)	DRAW-DOWN (m)	TIME INTV. (days)	TRANS-MISSIVITY (m^2/s)	CONDUCTIVITY LONG TERM (m/s)	CONDUCTIVITY PUMP TEST (m/s)	RATIO OF K PUMP TEST/ K LONG TERM
DW01	20.30	341	24	730	5.0E-04	2.5E-05		
DW02	42.67	946	40	730	7.0E-04	1.6E-05		
DW03	12.20	170	60	730	7.0E-05	5.7E-06		
DW04	28.98	1041	80	730	3.0E-04	1.0E-05		
DW05	18.30	379	35	730	1.5E-04	8.2E-06		
DW06	9.15	284	23	365	3.0E-04	3.3E-05		
DW07	54.87	284	125	365	5.0E-05	9.1E-07		
DW08	67.05	246	80	730	8.0E-05	1.2E-06		
DW09	29.32	227	75	730	8.0E-05	2.7E-06		
DW10	29.32	662	70	730	2.5E-04	8.5E-06		
DW11	40.10	379	110	730	1.0E-04	2.5E-06		
DW12	16.00	454	85	187	2.0E-04	1.3E-05	2.9E-05	2.3
DW13	15.24	189	40	730	1.0E-04	6.6E-06		
DW14	44.10	6056	20	187	5.0E-03	1.1E-04	2.1E-04	1.9
DW15	36.60	946	90	365	3.0E-04	8.2E-06		
DW16	NA	0	0	0	NA	NA		
DW17	40.90	2271	40	187	1.0E-03	2.4E-05	9.1E-05	3.7
DW18	20.10	170	25	187	2.0E-04	1.0E-05	3.8E-06	0.4
DW19	18.30	568	50	365	3.0E-04	1.6E-05	2.4E-05	1.4
DW20	20.00	946	25	365	9.0E-04	4.5E-05	1.7E-04	3.9

As indicated in the last column of *Table 8.3*, conductivity estimates based on long term monitoring data compared favourably to pump test results. In five of six cases, the long term estimates of *K* underestimated the pump test results by a ratio of 2 to 3. This trend is likely caused by negative boundaries at a large distance from the pumping well. These boundaries will not be felt during a short term pump test, but will reduce yields and/or increase the drawdown response in the long term.

8.4.5 ESTIMATES OF K FROM LABORATORY TRIAXIAL TESTS

The potential impact of the lower silt and clay sequence on groundwater control and slope stability was first recognized in early 1987. At that time, no shear strength or hydrologic information was available for this geologic horizon as most wells did not penetrate the unit. Because the lower portion of any deep seated failure will occur in this horizon a good understanding of pore pressures and shear strengths in this horizon was required. A geotechnical drilling program was undertaken in 1988 to obtain this data. A total of five deep piezometer holes were drilled. Undisturbed thin-wall shelby tube samples were collected at regular intervals in the lower silt and clay sequence. A complete suite of geotechnical tests (moisture content, Atteberg Limits, grain size, consolidation, triaxial strength, direct shear strength) was performed on the samples. The laboratory testing program is described in detail in Golder Associates Report 872-1416.

Hydraulic conductivity values of the lower silt and clay sequence can be calculated directly from the computed coefficients of consolidation, C_v, if the soil compressibility, α, is known.

$$C_v = \frac{K}{\gamma \alpha} \qquad \textit{Equation 8.1}$$

Because α values were not reported by Golder, a value of 1.0×10^{-7} m^2/N was assumed in order to complete the calculation. Since compressibility is relatively constant for a given soil type, the error introduced by this assumption is believed to be small. *Table 8.4* reports the results of calculations. Conductivities in the lower silt and clay sequence (Units 10A and 10B) ranged from 6.7×10^{-12} to 2.1×10^{-10} m/s. This range of conductivities is normally observed in unweathered clays and very dense glacial tills. However, it is important to recognize the results of the consolidation tests may underestimate the actual *K* by several orders of magnitude since the tests are usually performed on the finer materials (i.e. avoiding sand stringers) and the consolidation loads are applied normal to layering (i.e. flow across stratification). Therefore, the tests establish effective vertical conductivity, while the parameter of interest, conductivity in the horizontal direction, is not measured.

Table 8.4 Hydraulic Conductivity Estimates of Lower Silt and Clay Sequence based on Rate of Consolidation.

Hole Number	Depth (m)	Cv (m^2/s)	Compress. (m^2/N)	Dry Density (Kg/m^3)	K (m/s)	LOG(K)	Unit #	Description
P15	24.07	2.3E-05	1.0E-08	1960	4.42E-09	-8.4	3	Oh-One Divider
P15	30.48	5.0E-05	1.0E-08	1510	7.41E-09	-8.1	3	Oh-One Divider
P17	154.53	1.3E-07	1.0E-07	1640	2.09E-10	-9.7	10A	Olive Green, Black Silt
P17	154.53	1.3E-07	1.0E-07	1740	2.22E-10	-9.7	10A	Olive Green, Black Silt
P17	164.89	9.1E-08	1.0E-07	1420	1.27E-10	-9.9	10A	Olive Green, Black Silt
P17	165.81	5.7E-08	1.0E-07	1220	6.82E-11	-10.2	10A	Olive Green, Black Silt
P20	118.07	7.9E-08	1.0E-07	1590	1.23E-10	-9.9	10A	Olive Green, Black Silt
P20	183.72	2.9E-08	1.0E-07	1450	4.13E-11	-10.4	10B	Grey Tan Silt and Clay
P20	183.72	8.8E-09	1.0E-07	1570	1.36E-11	-10.9	10B	Grey Tan Silt and Clay
P20	184.83	1.1E-08	1.0E-07	1490	1.61E-11	-10.8	10B	Grey Tan Silt and Clay
P20	184.83	4.4E-09	1.0E-07	1550	6.69E-12	-11.2	10B	Grey Tan Silt and Clay

Note: Representative compressibility values assumed, based on Table 2.5, Freeze and Cherry, 1979.

8.4.6 ESTIMATES OF K BASED ON GRAIN SIZE ANALYSES

Hydraulic conductivity can also be estimated from the grain size distribution. A number of equations have been proposed for this correlation. The Hazen equation:

$$K = A\, d_{10}^{\,2} \qquad \textit{Equation 8.2}$$

is one of the most widely applied. The equation relates K to d_{10}, the grain size diameter for which 10% (by weight) of the soil particles are finer and 90% are coarser. The coefficient A is equal to 0.01 if d_{10} is measured in mm and K is desired in m/s. Sieve analyses are routinely performed at HVC on potential water bearing horizons. A large number of sieve analyses have also been performed on the lower silt and clay sequence by Golder Associates. A representative grain size curve of each geologic horizon is presented in *Appendix E.3.2.* *Table 8.5* summarizes the spread of $\log^{10}(K)$ values obtained for each geologic unit from the Hazen analyses. Because grain shape and microscopic structure can influence the permeability in soils finer than very fine sand hydraulic conductivity estimates based on the Hazen equation are not reliable. Therefore, estimates of K for units 10A and 10B should be considered less representative than estimates obtained from the analysis of consolidation tests.

Table 8.5 Hydraulic Conductivity Estimates Based on Sieve Analyses

UNIT	UNIT NAME	LOG(K) LOW (m/s)	LOG(K) HIGH (m/s)
1	Upper Aquifer	NA	NA
2	Till 0	NA	NA
3	Oh-One Divider	-7.6	-7
4	Till 1	-6.3	-6.3
5	Silty Aquifer	-4.2	-3.8
6	Till 2	NA	NA
7	Main Aquifer	-4.2	-3
8	Rust Aquifer	-3.5	-3
9	Till 3	NA	NA
10A	Olive Green Silt	-9	-7
10B	Tan Grey Silt and Clay	-6.1	-9.4

8.4.7 SEMI-VARIOGRAM IN VERTICAL DIRECTION

Actual measurements of hydraulic conductivity or physical data that can be used to estimate K (e.g. grain size analyses) are limited to a few widely spaced intervals in each bore hole. Because this measurement density is not sufficient to determine the experimental semi-variogram in the vertical direction, the semi-variogram was estimated from available geologic information. A number of correlation strategies for relating geology to hydraulic conductivity were tested before a suitable method was identified. The chosen method involved assigning a geology coefficient, C_g, to each distinct soil horizon in a drill hole based on the primary, secondary, tertiary (PST) classification[2]. An empirical relationship

$$K = 0.2*C_g - 4.0 \qquad \textit{Equation 8.2}$$

was then used to calculate K as a function of C_g. *Equation 8.2* was developed by linear regression of data points for which both PST and K values were available. The distribution of C_g , K data pairs is illustrated in *Figure 8.11.* A trend between C_g and K is apparent in the figure, the maximum prediction error in LOG(K) is 0.73. The observed scatter of data points indicates that the method is frequently capable of estimating K to less than one half order of magnitude over the range of hydraulic conductivities for which calibration data is available.

Having determined that reasonable estimates of K can be obtained from geologic data, the technique was used to develop a hydraulic conductivity profile for each bore hole on section R-3. The hydraulic conductivity estimates were then analyzed with program SG-STAT to obtain semi-variograms in the vertical direction. The semi-variograms are illustrated in *Figure 8.12.* The similarity of the experimental semi-variograms from borehole to bore hole and the smoothness of the curves suggests that the estimation method described above is useful for determining the correlation structure.

---

2 Refer to *Appendix E.2.1* for explanation of classification system.

Figure 8.11 Log(K) vs. Geology Coefficient C_g

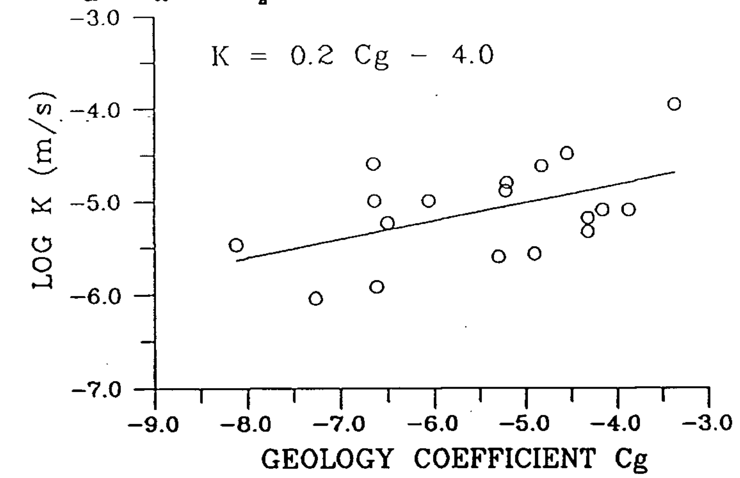

The experimental semi-variograms indicate that soil textures are correlated over distances up to 50 m in the vertical direction; however, the steep rise in the semi-variograms near the origin indicates that the strength of the correlation drops of rapidly after 10 m. The experimental semi-variograms are consistent with the geologic interpretation, thicknesses of individual geologic units typically vary between 10 and 40 m. A spherical semi-variogram model with a sill of 0.25 and a range of 50 m provides a good fit to most experimental semi-variograms depicted in *Figure 8.12.*

The semi-variograms for piezometers DP-15 to DP-20 that are illustrated in *Figure 8.12* were based on geotechnical logs prepared by the author in 1988. On the other hand, the semi-variograms depicted in *Figure 8.13* are based only on the driller's brief description of the cuttings, since the cuttings from these holes were not logged. The difference in the quality of the semi-variograms clearly shows the importance of proper data collection. Geologic logs can be used to estimate hydraulic conductivities and correlation statistics at HVC, but only if the cuttings are logged carefully by a qualified geologist.

8.4.8 SEMI-VARIOGRAM IN HORIZONTAL PLANE

The experimental semi-variogram for the horizontal plane was obtained from statistical analysis of the long term hydraulic conductivity estimates from each of the 20 dewatering wells. The locations of individual wells and the corresponding log hydraulic conductivities are shown in *Figure 8.14*. Contours of the kriged hydraulic conductivity surface are also presented in the figure. *Figure 8.15* illustrates the experimental semi-variogram that was obtained from analysis of the data with *SG-STAT*.

To establish that the selected correlation model is valid, the verification procedures described in *Section 4.4.6* were conducted. The verification involves systematically removing one measurement point from the data base and then estimating that point value based on the remaining measurements. The results of the verification are:

- The mean estimation error is -0.069. Since this error is close to 0.0 the verification confirms that the selected model results in unbiased estimates.
- The standard deviation of the 19 estimation errors is 0.4687. As expected, this standard deviation is smaller than the standard deviation of the measurements, determined to be 0.5311. In this case, kriging is successful in reducing estimation uncertainty by approximately 13%.
- The actual estimation errors obtained at each data point are reported in brackets in *Figure 8.14*. Note that the largest estimation errors occur at data points where extreme hydraulic conductivity values were measured (e.g. K=-3.9, -5.9, -6.0). This is because kriging is a smoothing function. It is not effective in reproducing the extreme highs and lows.

Figure 8.12 Semi-Variograms for Piezometers DP15-DP20.

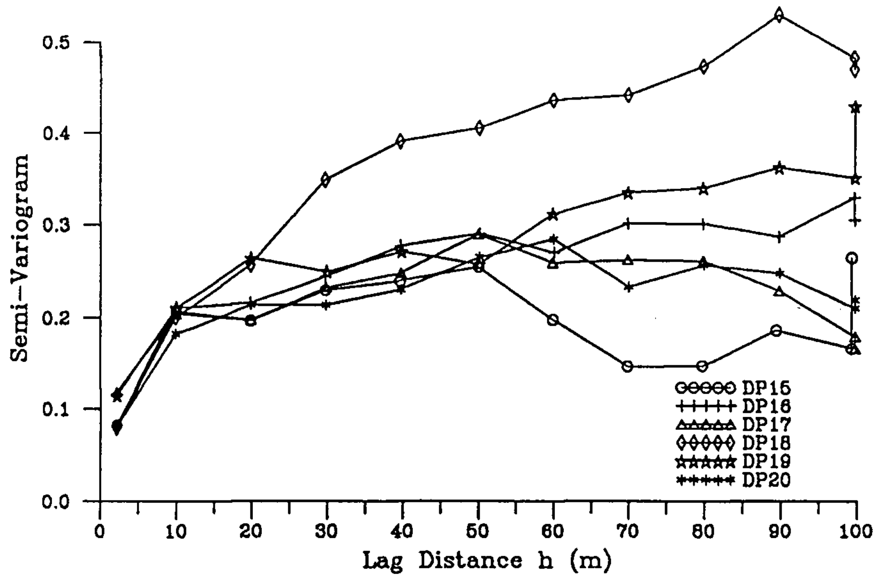

Figure 8.13 Semi-Variograms for Boreholes Without Proper Geologic Logging.

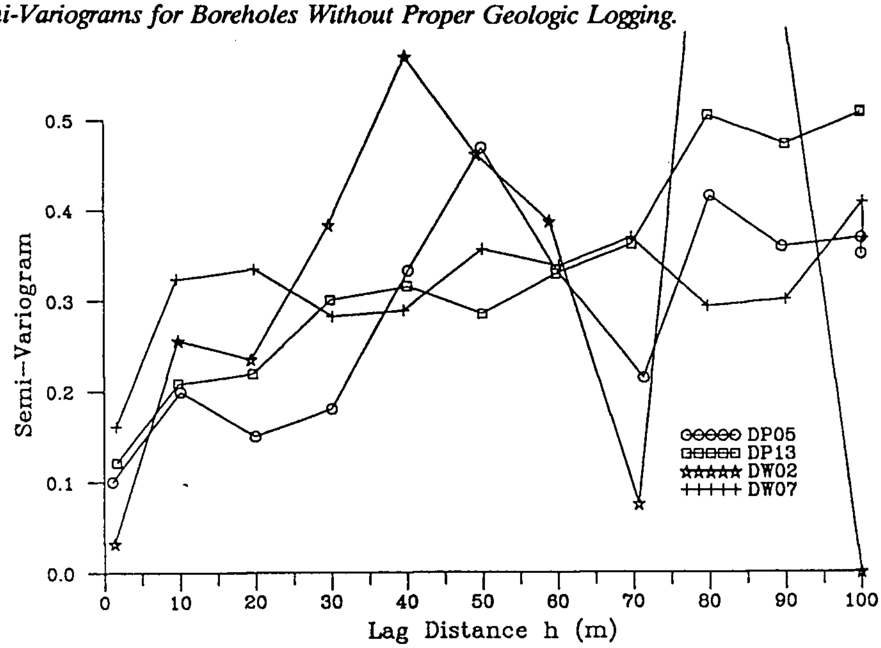

- The kriging results are close to being significant at the *69%* confidence interval (*63%* of the of the estimation errors $|Z^*(X_m) - Z(X_m)|$ were no larger than one standard deviation of the expected estimation error at each data point, σ_m). The kriging results are significant at the *95%* confidence interval as 100% of the estimation errors were smaller than $2 * \sigma_m$.
- The coherency ratio is *1.063*. Since this ratio falls within the range *0.9 - 1.1*, the kriging results are consistent with the predicted level of estimation uncertainty.

In summary, the semi-variogram model is acceptable because it satisfies all four verification criteria listed in *Section 4.4.6.*

Since the majority of screened intervals are located in the Main Aquifer, the semi-variogram is indicative only of the correlation structure in that unit. Unfortunately, the densities of measurements in all other geologic units on the property are not sufficient to construct individual semi-variograms; therefore, it was assumed that the Main Aquifer semi-variogram is representative of the horizontal correlation structure in all horizons.

The dashed line in *Figure 8.15* plots the spherical semi-variogram model that was chosen to represent the experimental correlation structure. The model parameters are: sill=0.35, nugget=0.05, range=1000 m. Beyond 1000 m, the experimental semi-variogram values begin to decrease. This trend is due to a lack of measurement points with separation distances larger than 1000 m. As shown in *Figure 8.14,* The most of the limited number of data points that are separated by more than 1000 m exhibit similar log(K) values.

As expected in a glaciofluvial depositional environment, the observed horizontal range of correlation, estimated at 1000 m, is much greater than the range in the vertical direction, estimated at 50 m. The anisotropy ratio (vertical:horizontal) is approximately 1:20.

Figure 8.14 Hydraulic Conductivity Measurements and Kriged Map of K Field.

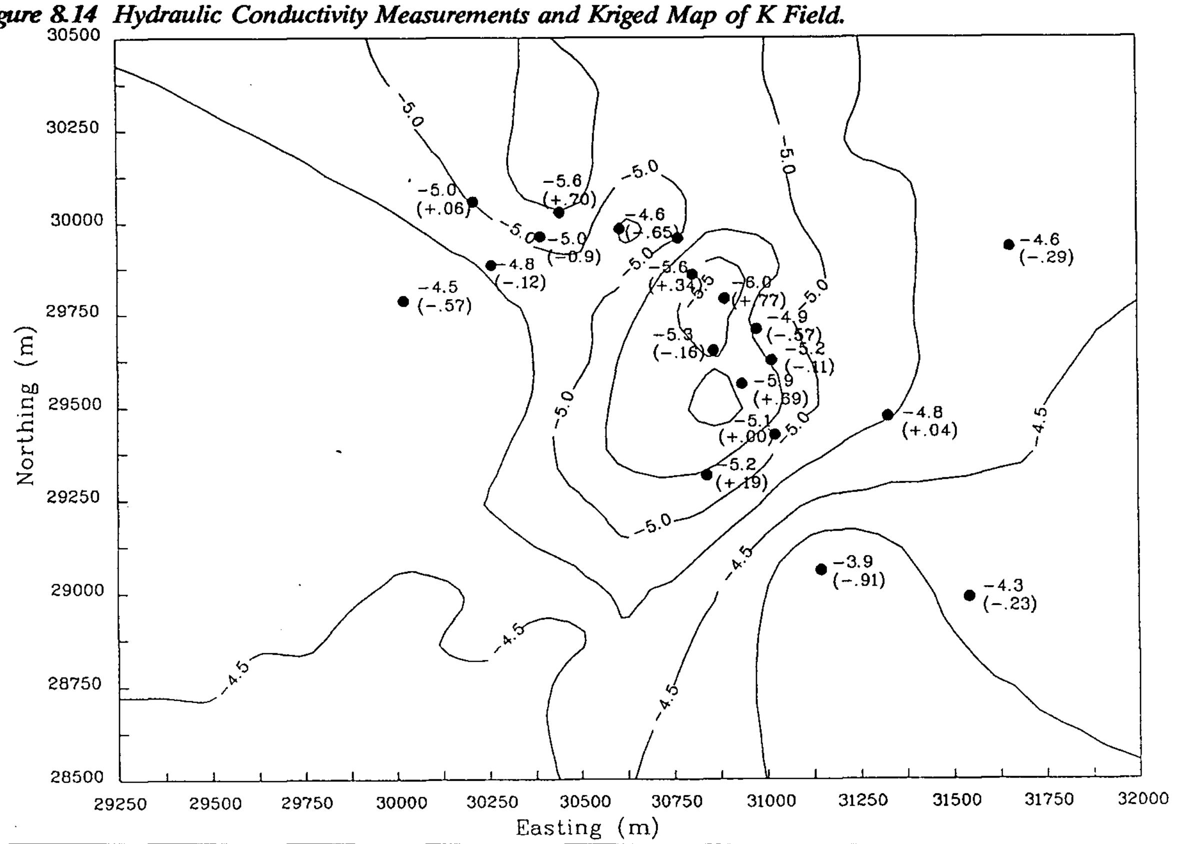

Figure 8.15 Semi-Variogram in Horizontal Direction.

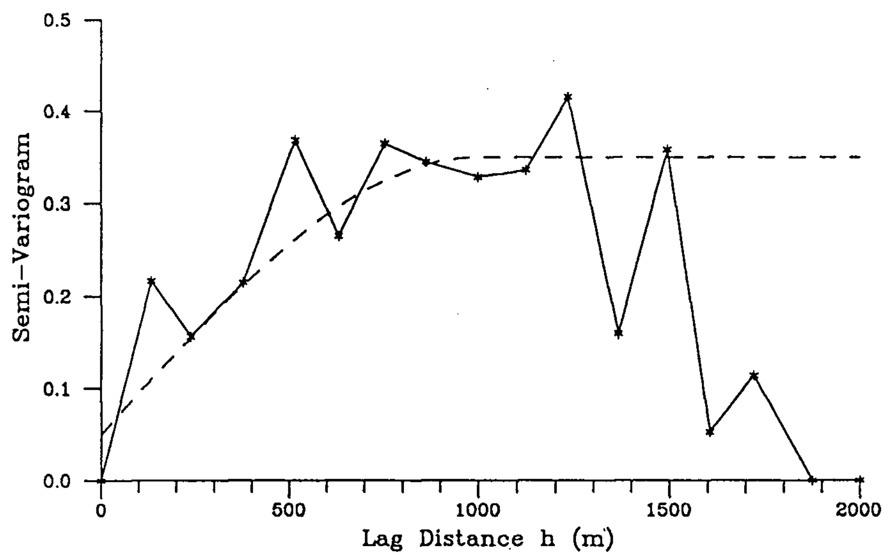

8.4.9 HYDRAULIC CONDUCTIVITY MODEL ON SECTION R-3

Table 8.6 presents a summary compilation of the likely hydraulic conductivity values for each geologic horizon, incorporating the numerous sources of hydraulic conductivity information thus far presented. Because the geologic interpretation in the upper sequence of sands, silty sands and tills is still uncertain, the stochastic model of the hydraulic conductivity that was used in this case history study differentiated only between the upper sand till sequence and the lower sequence of silt and clay.

The statistics describing the hydraulic conductivity field in each of the two sequences are given in *Table 8.6.* The information required to carry out the conditional Monte-Carlo simulation includes the mean, variance and correlation model, as well as all conditioning measurements. Figure 8.16 shows the approximate extent of the two geologic sequences, the location of nearby wells and piezometers, and the position of all hydraulic conductivity measurements on the section.

***Table 8.6** Summary of Hydraulic Conductivity Information for Each Geologic Horizon*

UNIT	UNIT NAME	Estimated Range of K LOG(K) LOW (m/s)	LOG(K) HIGH (m/s)	LOG(K) STATISTICS FOR UPPER & LOWER SEQUENCES	
1	Upper Aquifer	−6.0	−4.0	**Upper Sequence:**	
2	Till 0	−7.0	−5.0	Mean: (log m/s)	−5.5
3	Oh−One Divider	−7.6	−7.0	Stn.Dev. (log m/s)	0.75
4	Till 1	−7.0	−5.0	Range (m. hor.)	1000
5	Silty Aquifer	−6.0	−3.8	Anisotropy (v:h)	1:20
6	Till 2	−7.0	−5.0		
7	Main Aquifer	−6.0	−4.3	**Lower Sequence:**	
8	Rust Aquifer	−4.6	−3.0	Mean: (log m/s)	−9.5
9	Till 3	−7.0	−5.0	Stn.Dev. (log m/s)	0.75
10A	Olive Green Silt	−10.2	−8.0	Range (m. hor.)	1000
10B	Tan Grey Silt and Clay	−11.2	−9.4	Anisotropy (v:h)	1:20

Figure 8.16 Stochastic Model of Hydraulic Conductivity Field.

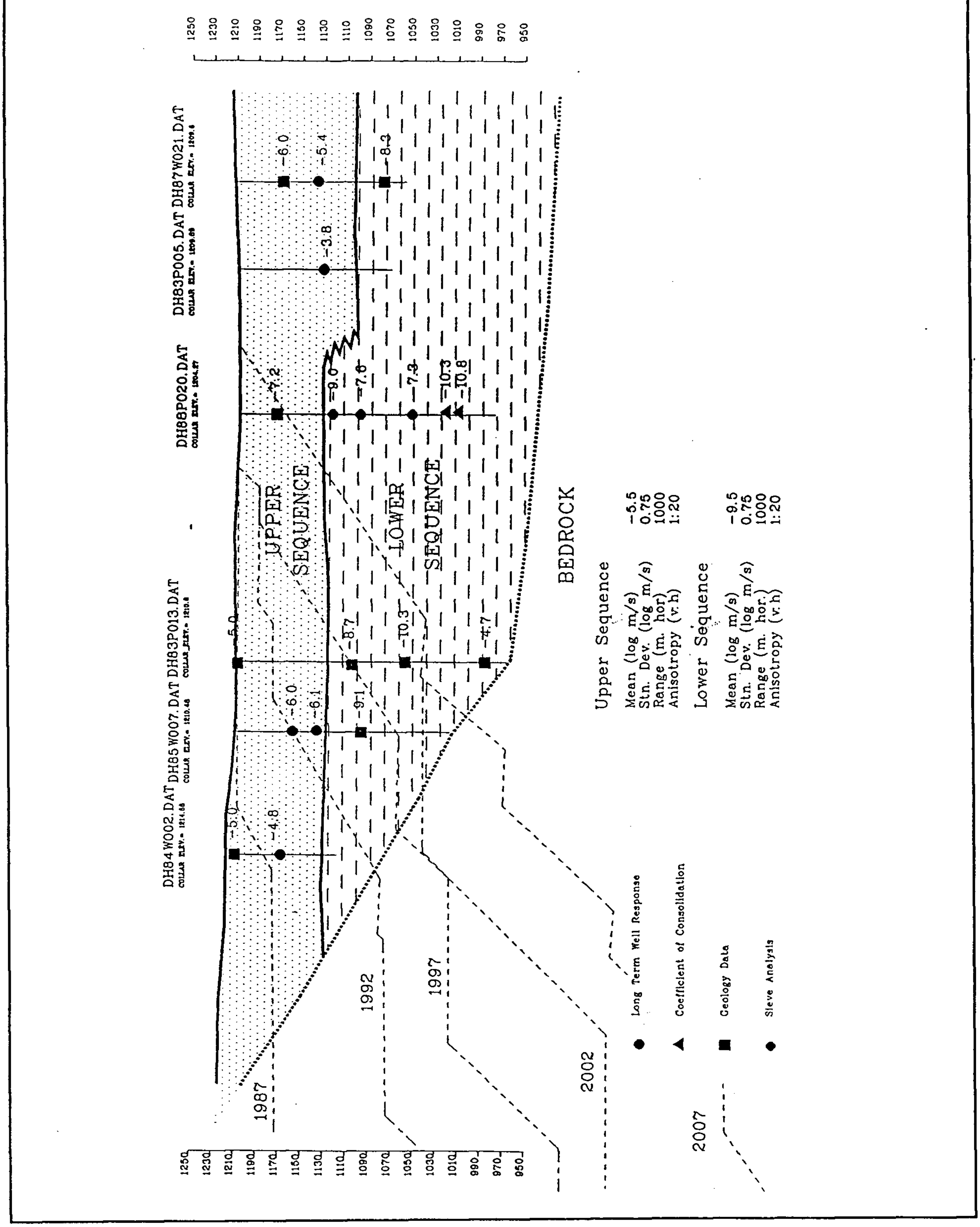

8.4.10 SELECTION OF BOUNDARY CONDITIONS WITH SIMPLE AQUIFER MODEL

Selection of realistic boundary conditions for the stochastic model of groundwater flow on section R-3 is an important component of the analysis because boundary conditions will have a strong influence on pore pressures in the flow domain. In the vertical section model, selection of two of three boundaries is straightforward while the third presents difficulties. The first boundary, to be applied along the pit face and crest, will be specified as a free surface boundary condition. The second boundary, to be applied along the granitic bedrock contact, will be specified as an impervious (zero flux) boundary condition. The third boundary, to be applied somewhere along the northeast margin of the flow domain is difficult to specify. Decisions have to be made regarding: 1) the horizontal distance separating the vertical boundary and the pit crest, 2) whether to treat the boundary as a specified head or specified flux boundary condition, and 3) the actual specified head or specified flux values to apply on the boundary.

A simple regional aquifer model was used to identify the appropriate boundary conditions by analyzing the development of the drawdown cone in the horizontal plane. The objective of the horizontal plane model was to predict the maximum extent of the regional drawdown cone once all wells are operational and to determine the steady state recharge fluxes across the aquifer boundaries. The model was limited to simulation of groundwater flow within the silty aquifer (see *Figure 8.8*), treating this horizon as a fully confined aquifer of constant thickness. Boundary conditions that were adopted in the model are illustrated in *Figure 8.17*. To the southwest the aquifer is bounded by granitic bedrock. This contact was represented as an impermeable boundary in the model. On the north side of the valley the aquifer is recharged by groundwater seepage from the highlands north of the mine site (see *Figure 8.3*). Therefore, a constant flux boundary condition was specified along the northern margin of the aquifer model. A recharge flux of 8×10^{-7} m/s per m^2 was specified on this boundary, based on recharge rates estimated from the water budget analysis reported in *Section 8.4.1*. Constant head boundary conditions of approximately 1200 m were assigned on the eastern and western boundaries of the flow domain. The hydraulic conductivity distribution within the aquifer was obtained by kriging the hydraulic conductivity estimates obtained from long term monitoring data. A contour map of the kriged hydraulic conductivity distribution that was utilized in the horizontal plane model is illustrated in *Figure 8.14*.

The boundary value problem described in the previous paragraph was solved with computer program SG-FLOW. To verify the simulation results, predicted heads were compared to 1987 piezometer data. The top window in *Figure 8.17* illustrates the predicted piezometric surface while the lower window presents a contour map of observed piezometric levels in the aquifer. The predicted head response duplicates the actual hydraulic head distribution reasonably well, considering that the model was not calibrated by repeatedly adjusting the hydraulic conductivity field to match the observed drawdown response.

The simulation results suggest that the northeast flow domain boundary should be located 500 to 750 m behind the perimeter wells and that 4.0×10^{-7} to 8.0×10^{-7} m^3/s is a reasonable flux across this boundary through pervious strata.

Figure 8.17 Comparison of Predicted and Observed Piezometric Levels - 1987.

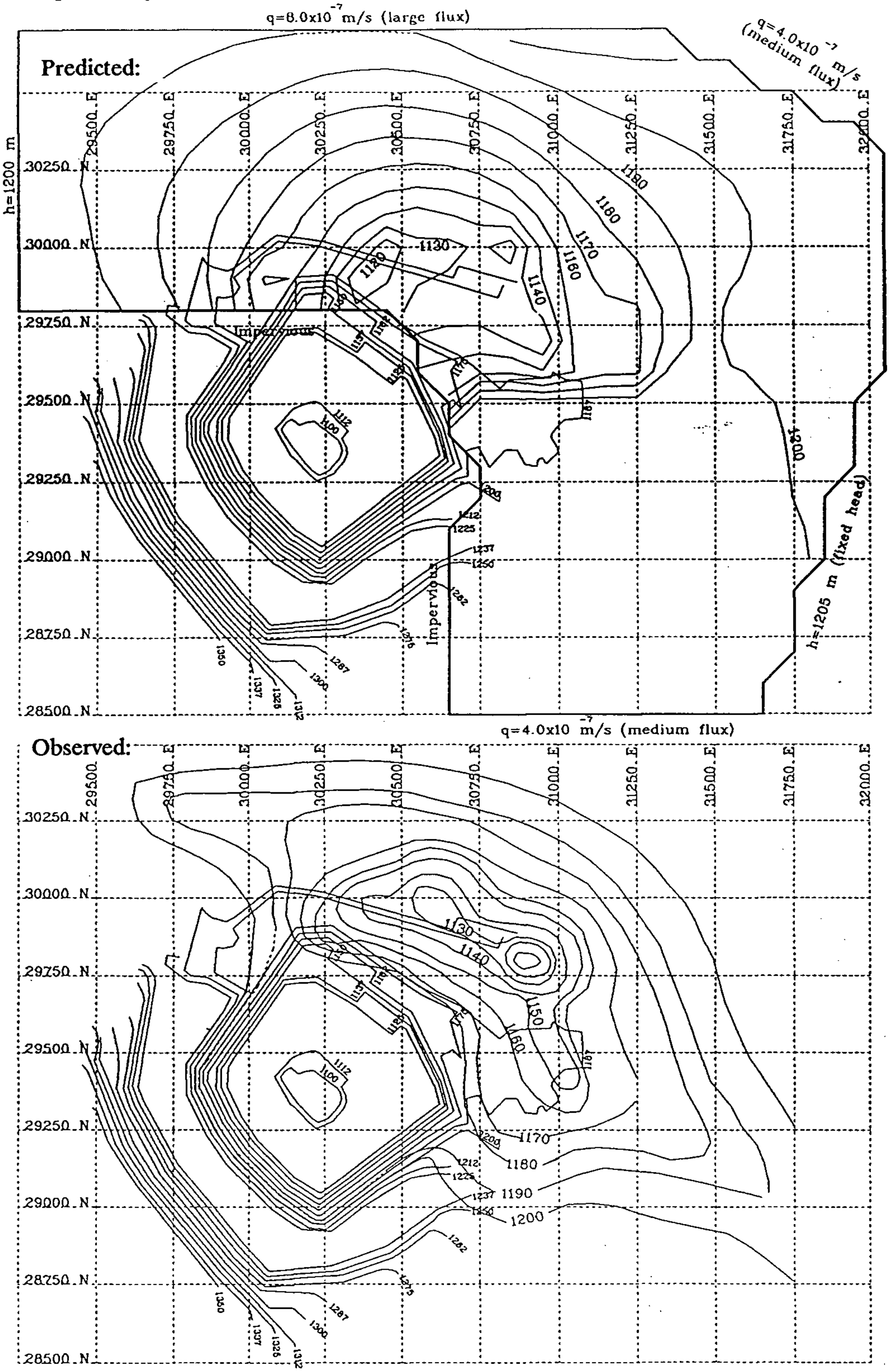

8.5 CURRENT PIT DESIGN AND DEWATERING STRATEGY

This section provides an overview of the current Valley Pit mine plan, with emphasis on the slope design and dewatering strategy in design sector R-3.

8.5.1 SLOPE DESIGN

The Valley Pit ore body will be developed in a series of seven concentric pit expansions. *Figure E.19* in *Appendix E.4* outlines the extent of each pit expansion relative to section R3. Because several expansion pits may be worked concurrently at different bench elevations, the actual pit profile will frequently be defined by a composite of two or three expansion pit plans. *Figure 8.18* illustrates the approximate outline of the pit limits along section R-3 in 5 year increments. The location of the overburden/bedrock contact is also shown in the figure. A more complete set of drawings that illustrate the progressive development of the pit in plan view are presented in *Appendix E.4.*

Overall slope angles of 25 to 28° are currently planned for final overburden slopes, with inter-ramp angles ranging from 31 to 35° between haul roads (F. Amon, personal communication). Similar slope angles will also be used in all expansion pits. However, the current pit design for sector R-3, taken from the Valley Composite Pit Mine Plan Base 64B1, Section 13.5, December 1988, utilizes an overall slope angle of approximately 31° in the overburden, and inter-ramp angles of 32 to 47°. It should be noted that the overburden slopes in this sector are significantly steeper than specified in the general mine design plan. It appears that the steepening in sector R-3 was caused by a downward shift in the latest interpretation of the overburden bedrock contact which has not been incorporated in the slope design. As a result, the bedrock slope angle of 47° has been utilized over the lower 90 m of the overburden slope surface. Also, it may be possible to improve slope stability by using different slope angles in the various overburden horizons, rather than one common slope angle for the entire pit wall.

The mine plan calls for steady development of the Valley Pit ore body over the next 15 to 20 years. Ore will be transported from the pit to the mill via a conveyor system that will climb from two portable primary crushers to the stockpile along a corridor in the southeast corner of the pit. As illustrated on the plans in *Appendix E.4.1*, the primary crushers and conveyors will be relocated periodically to a minimum elevation of 1000 m as the pit deepens. Waste rock and overburden will be trucked to the waste dumps along a haul road that will be situated in the northeast quadrant.

Figure 8.18 Development of Pit in 5 Year Increments - Section R3.

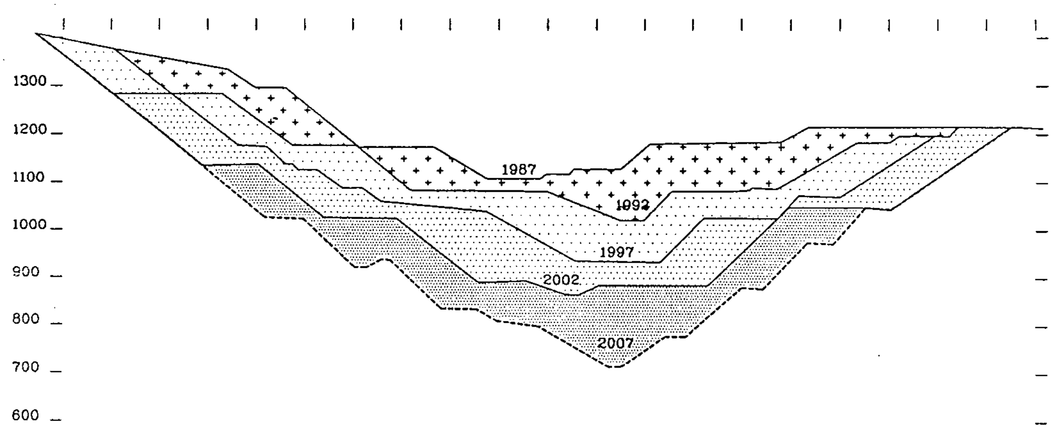

The upper 40% of the haul road will be constructed in the overburden portion of the pit wall. A major slope failure in the overburden would disrupt this vital traffic link by knocking out one or more ramps. Besides the obvious increase in stripping and longer haulage distances, a large overburden failure could also have serious economic consequences for HVC in terms of lost mine production and cash flow as a result damage to the haul road. The impact would be felt because the haul road will provide the only access for equipment, for removal of all waste material, and for transport of ore to the primary crusher and conveyor systems once mining progresses below 1000 m.

8.5.2 GROUNDWATER CONTROL OBJECTIVES AND CURRENT DEWATERING PLAN

In 1984, HVC commenced a comprehensive overburden dewatering program in the Valley Pit. The objectives of the dewatering program are:

- To depressurize the overburden and improve slope stability.
- To minimize seepage, erosion and piping failures at the pit face.
- To improve trafficability and material handling characteristics of the overburden material.
- To provide an alternate, lower cost supply of suitable process water for the mill.

As of December 1988, a total of 21 dewatering wells have been completed on the property. The majority of wells are located on the interior ring between DW06 and DW14. As earlier illustrated in *Figure 8.10*, the dewatering efforts have achieved a substantial drawdown cone in the northeast corner of the pit, with piezometric heads drawn below 1170 m over a fairly large area and below 1130 m in the center of the drawdown cone. Preliminary design studies by Sperling and Brennan (1988) indicate that continued dewatering efforts will be required in order to maintain target water levels as the pit expands. The long term dewatering goal identified in their study is to dewater all overburden horizons within a 200 m radius of the pit to less than 1110 m piezometric head. A total of 36 additional dewatering wells are planned in the future to attain these dewatering targets, the cost of the dewatering effort is estimated at $4.60 million. The wells are being developed in five concentric rings (R1 through R5), with each ring having between 8 and 17 wells. Well development will progress gradually outward from the interior ring, in step with the expansion of the pit. The active dewatering wells will always be situated close to pit crest where they contribute the most to improved slope stability.

The identification number, location and expected yield of all active dewatering wells for each 5 year planning interval are illustrated in *Figures E.20* to *E.22* of *Appendix E*. The technical report titled *Overburden Dewatering Strategy for Valley Pit, 1988-1994* (Sperling and Brennan, 1988) provides additional details of the base case dewatering plan that serves as the basis for this case history study.

8.6 STOCHASTIC MODEL OF GROUNDWATER FLOW

This section presents a summary of results from a numerical analysis of present and future groundwater pore pressures on geotechnical section R-3. The summary begins with a description of the boundary value problem, followed by an overview of the geostatistical tools that were used to generate the hydraulic conductivity realizations; an example of a typical realization is also presented. The section then documents how SG-FLOW was used to calculate the 1987 pore pressure distribution. The 1987 pore pressure predictions are reported and compared with the actual pore pressure response observed in piezometers to verify the computer model. In the last step of the groundwater flow analysis, SG-FLOW was used to predict the pore pressure distribution beyond year 2000. The final subsection discusses whether the current dewatering plan will be able to meet HVC's long term dewatering objectives.

8.6.1 DESCRIPTION OF BOUNDARY VALUE PROBLEM

The boundary value problem that was selected to represent the groundwater flow system on section R-3 is illustrated in *Figure 8.19.* The process of defining the dimensions of the flow domain and specifying appropriate boundary conditions is subject to engineering judgement. The following interpretations were used when constructing this model:

- The bedrock contact will serve as an impervious barrier to groundwater flow.
- As determined from the regional aquifer simulation in documented in *Section 8.4.10*, a recharge flux of 4.0×10^{-7} m^3/s was applied on the upper half of the specified flux boundary located on the right side of the flow domain. Across the lower half of the boundary the recharge flux was reduced to 4.0×10^{-11} m^3/s to reflect the reduced permeability in the lower silt and clay sequence.
- Because sump pumps will maintain the water table at the pit floor elevation, the pit floor was represented by a specified head boundary with head equal to elevation ($h=z$).
- A free surface boundary condition was applied on the pit face and on the upland surface.
- Realizations of the hydraulic conductivity field were generated from the statistical parameters reported in *Table 8.6*. Each realization was conditioned on available measurements, given in *Figure 8.16*.
- It was assumed that transient adjustments to the pore pressure field would happen sufficiently fast to justify the use of a steady state model. Results of verification studies reported in *Sections 8.4.10* and *8.6.3* support this assumption.
- As illustrated in *Figure 8.4*, the dewatering wells have been, and will continue to be, developed in concentric rows normal to section R-3. Recall that in *Chapter 5* it was shown that since the wells are spaced together closely, they can be represented as continuous line sink, with a specified pumping flux per unit length of drain normal to the section. Based on anticipated pumping rates, the pumping flux will vary between 5.0×10^{-5} m^3/s and 1.5×10^{-5} m^3/s per 1 m of a dewatering row.

Figure 8.19 Boundary Value Problem For Section R-3

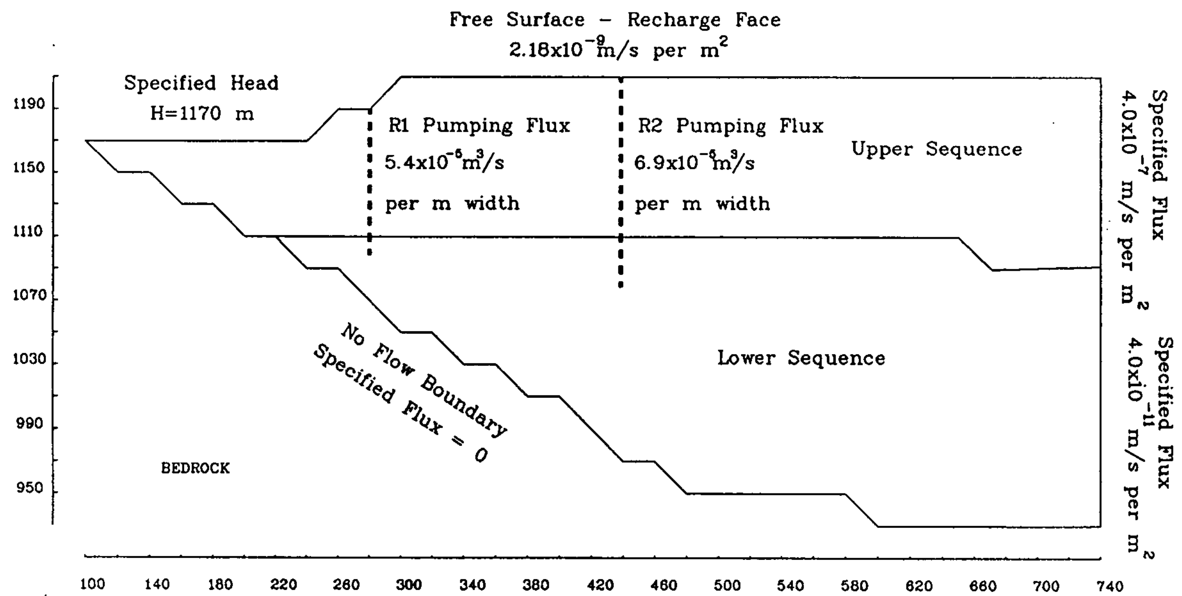

8.6.2 GENERATING REALIZATIONS OF THE HYDRAULIC CONDUCTIVITY FIELD

The hydrologic and geologic studies reported in *Section 8.4* have identified a number of important geologic characteristics that govern the movement of groundwater flow through the overburden. These characteristics include:

- Two distinct geologic sequences (i.e. upper sand, silt and till with high permeability and lower silt and clay with low permeability).
- Local variability of hydraulic conductivity within each sequence (i.e. 5 to 50 m thick beds and lenses within each sequence).
- Correlation of hydraulic conductivity field was observed in both horizontal and vertical directions. As is typical of fluvial deposits, the hydraulic conductivities were correlated more strongly in the horizontal plane, along bedding, than in the vertical plane, across bedding.

Because it was considered essential to replicate each of these characteristics in order to obtain valid results from the numerical model, the capabilities of computer program SG-STAT were enhanced to include generation of multiple geologic horizons with different mean *K*'s as well as anisotropic correlation structures.

Because a number of hydraulic conductivity measurements were available on section R-3, SG-STAT was executed in conditional simulation mode to reduce estimation uncertainty in the pore pressure predictions.

Figure 8.20 illustrates a typical realization of the hydraulic conductivity field. Note that each of the three desired geologic characteristics noted above have been successfully reproduced in the realization. In fact, the realization bears close resemblance to the geologic interpretation portrayed in *Figure 8.8*.

Figure 8.21 presents a map of the contours of variance of estimation errors. It is interesting to note that zone of reduced estimation uncertainty extends much farther in the horizontal direction than in the vertical as a result of the anisotropic correlation structure.

Figure 8.20 Typical Realization of Hydraulic Conductivity

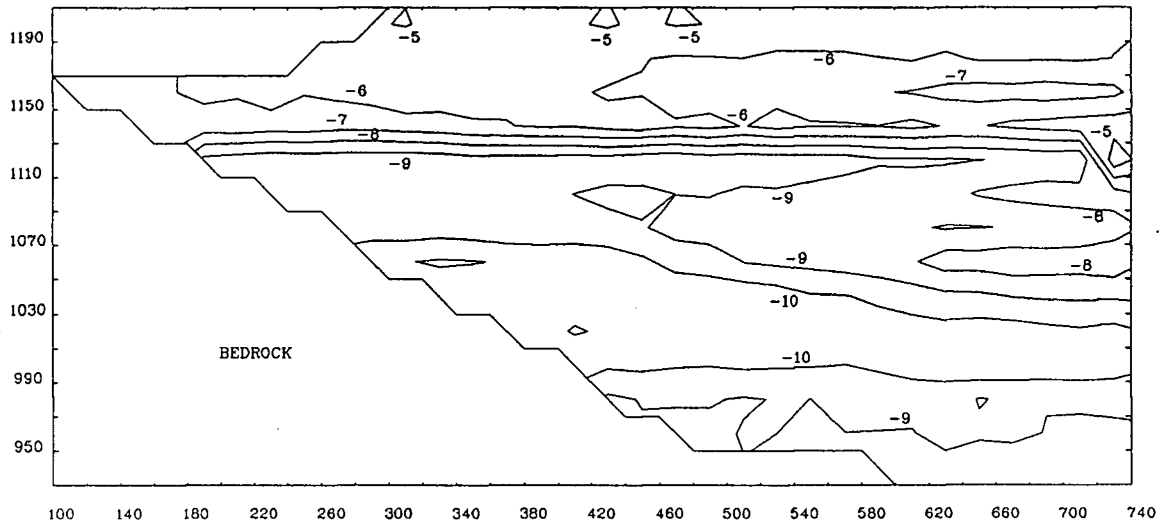

Figure 8.21 Contours of Variance of Estimation Errors

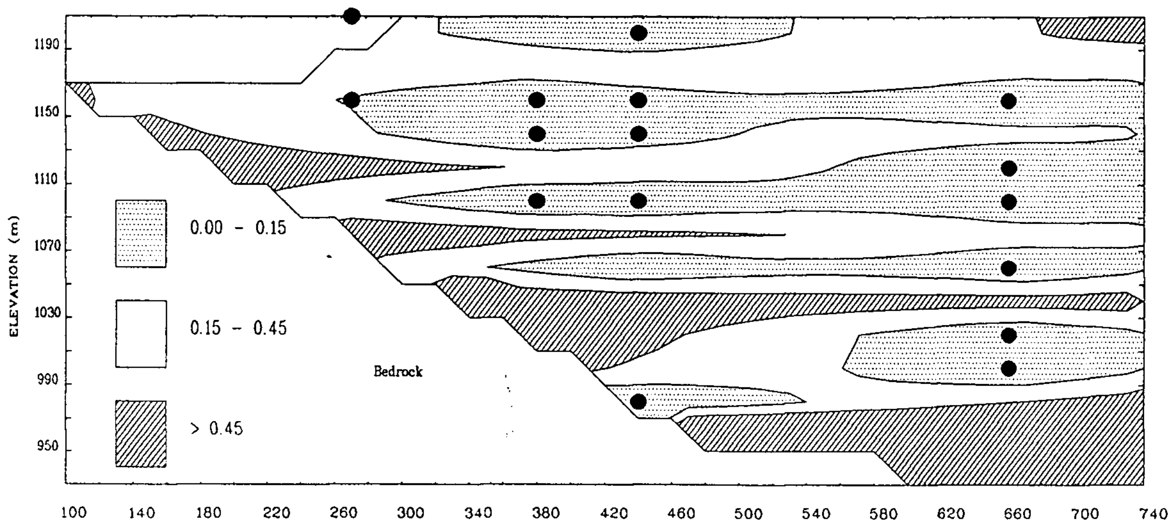

• Measurement Point

8.6.3 MODELLING OF 1987 CONDITIONS - A VERIFICATION

Verification is a key step in any computer modelling exercise. The objective of verification is to confirm that the computer model is working correctly and that the numerous input parameters that comprise the computer model are representative of actual sub-surface conditions. Because long term piezometer monitoring data is available at HVC, it was possible to verify the model predictions by comparing the predicted pore pressure field to the actual piezometric response.

The December 1987 pore pressure distribution was selected for the verification. The simulation involved the generation of 100 realizations of the hydraulic conductivity field. The pore pressure distribution was then calculated for each hydraulic conductivity realization. The boundary conditions illustrated in *Figure 8.19* were maintained during each simulation. The pumping fluxes for R1 and R2 wells reported in the figure are representative of actual pumping fluxes maintained on the rows of dewatering wells during 1987. *Figure 8.22* portrays the mean hydraulic head distribution for the simulation[3]. The mean piezometric surface for the Main Aquifer is also shown, represented by a dashed line while the actual piezometric surface is represented by a solid line. The relatively good fit between the predicted surface and the actual response indicates that the computer model is capable of predicting the pore pressure response to pumping stresses. However, it is recommended that the verification checks be continued periodically as new monitoring data becomes available to confirm the long range predictive accuracy of the model.

Figure 8.23 presents a contour map of the standard deviation of pressure head predictions at each node, calculated over the 100 realizations. The contours represent the degree of variability of the pressure head prediction at each point in the flow domain. The small standard deviation in pressure heads (less than 5 m) in the area of potential slope failure of the pit wall suggests that the destabilizing effect of groundwater can be accurately predicted for the 1987 slope configuration.

It is also interesting to note that the lowest uncertainty in head predictions occurs near the pit floor where the water table will be consistently maintained by a sump pump while the highest variability occurs at the specified flux boundary on the right side of the flow domain. Recall that during the sensitivity studies presented in *Chapter 7*, a specified head boundary condition was applied to on the right vertical boundary, artificially forcing the prediction uncertainty at the boundary to zero (see *Figure 7.48*). Comparison of *Figures 8.23* and *7.48* suggests that a specified flux boundary should be used in these slope stability analyses provided that reasonable flux levels can be determined and no natural geologic feature is present to justify a constant head boundary condition (e.g. tailings pond or lake). *Figure 8.23* also indicates that the pore pressure predictions are less accurate in the lower silt and clay sequence. This fact will have an impact on the uncertainty of slope stability estimates as the pit deepens and the critical failure surface begins to pass through the fine grained soils of the lower sequence.

8.6.4 MODELLING OF THE LONG TERM PORE PRESSURE RESPONSE

In the final step of the groundwater flow analysis, the SG-FLOW computer model was used to predict the pore pressure distribution at 5 year intervals over the life of the mine. The current dewatering plan described by Sperling and Brennan (1988) was used to determine the appropriate pumping fluxes during each interval.

The simulation results indicate that the drawdown cone will expand steadily as the pit deepens and additional wells are developed in coming years. By the year 1992, the upper aquifer/till sequence will be effectively dewatered to 1130 m, the elevation of the upper/lower sequence contact. In fact, during later simulations, pumping fluxes of most wells had to be reduced by a factor of 2 to 4 to prevent the wells from running dry. The pumping flux reduction indicates that in the long term, the proposed dewatering strategy will be more than

[3] Average hydraulic head at each node, calculated over 100 realizations.

Figure 8.22 Contour Plan of Mean Hydraulic Head on Section R-3 for 1987.

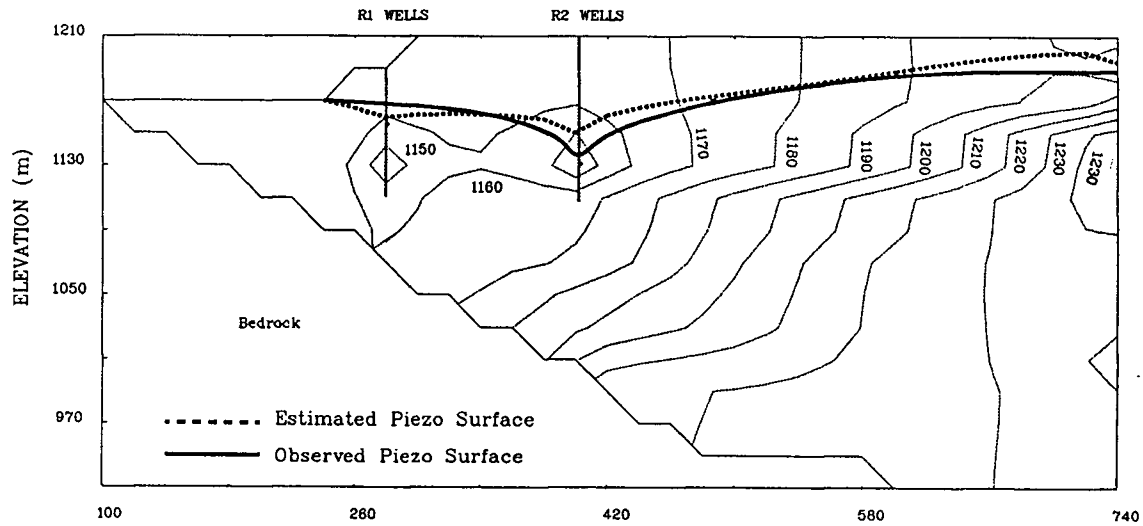

Figure 8.23 Contour Plan of the Standard Deviation in Predicted Pressure Head - 1987.

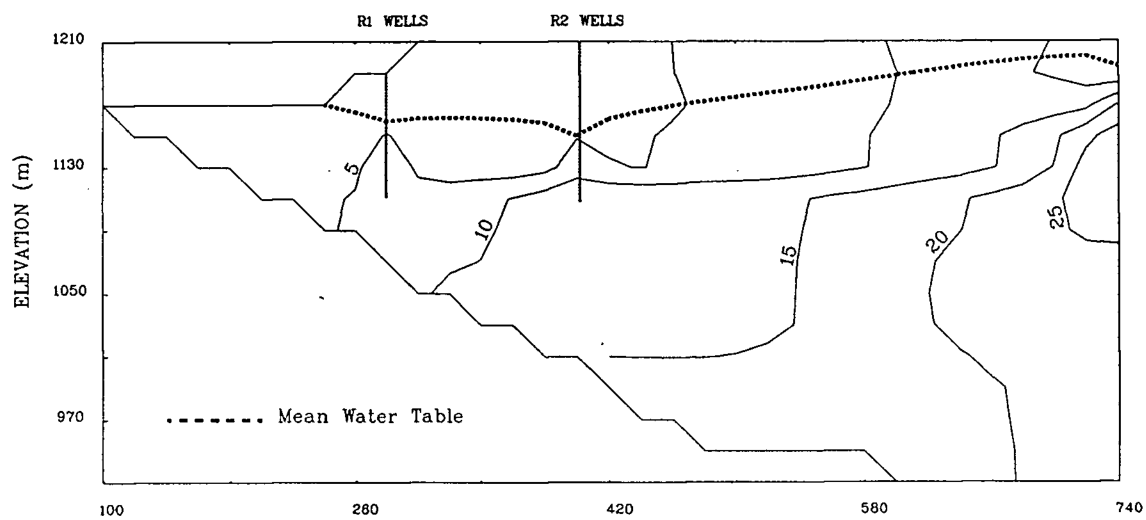

Adequate to maintain the upper sequence in a fully unsaturated state beyond 1992. It appears that the total number of wells required to dewater the upper sequence may be less than the number specified in the current HVC dewatering plan. However, this hypothesis must be confirmed with a transient aquifer model and water level monitoring to conclusively demonstrate that a dewatering scheme with fewer wells would be capable of drawing the water levels down within the required time horizon.

The expected hydraulic head distribution for the ultimate pit wall is illustrated in *Figure 8.24*. The water table position and the distribution of equipotentials indicate that the lower silt and clay sequence will not be significantly depressurized by the dewatering efforts because most wells will not penetrate the lower sequence. In fact, the very close spacing of equipotentials in the toe area indicates that over 60% of the pore pressure dissipation in the lower sequence will occur very close to the pit face. As a result, pore pressures along the basal failure surface may be as much as 40 m above hydrostatic in the long term, and even more in the short term.

In *Section 8.7* it will be shown that high pore pressures in the lower sequence, combined with very low shear strengths in unit 10B, will lead to instability of the ultimate pit wall unless steps are taken to reduce pore pressures in the toe area and/or to flatten the slope angle in the lower sequence. Past experience with deep wells at HVC has demonstrated that the dewatering technology will not be effective in depressurizing the fine grained soils. Horizontal drains developed within relatively high permeability sandy silt and sand stringers may provide the most effective dewatering alternative, especially if assisted by vacuum. However, additional studies will have to be conducted to establish that depressurization will be achieved sufficiently rapidly to have an impact on pore pressures while the pit wall is being constructed.

Figure 8.24 Contour Plan of Mean Hydraulic Head on Section R-3 for Ultimate Pit.

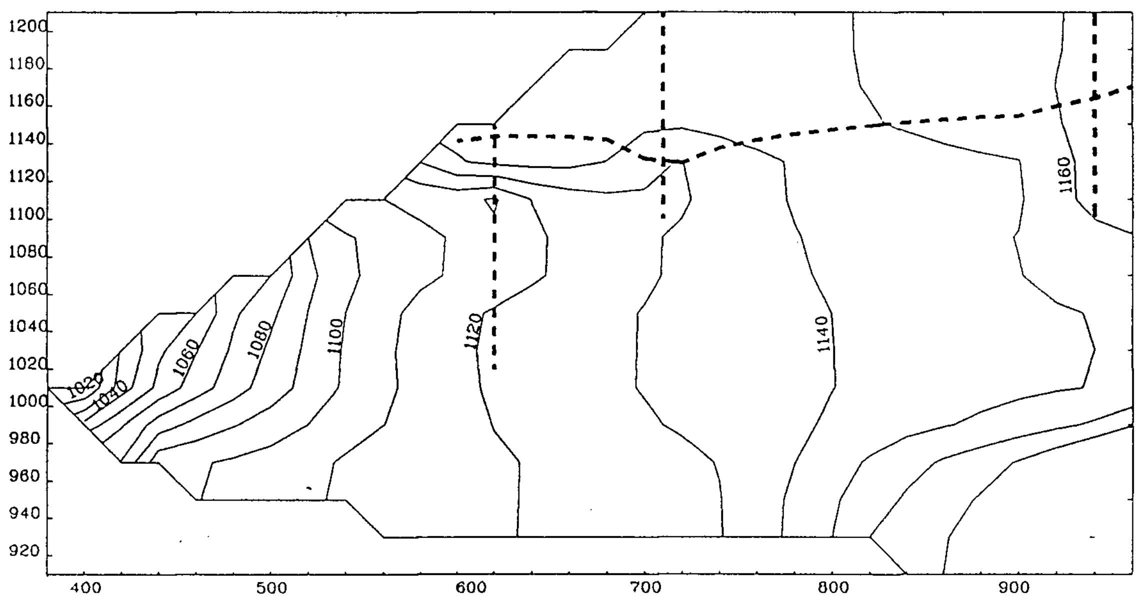

8.7 *SLOPE STABILITY EVALUATION*

This section provides insight as to the approach used to estimate the probability of failure for each pushback of the HVC pit wall. The discussion begins with a review of the stochastic shear strength parameters assigned to each geologic horizon. Several paragraphs are devoted to explaining how shear strength statistics were estimated from a very limited strength measurement population. Results of slope stability analyses are dependent of the geometry of the failure surface analyzed. The true stability index (FOS or POF) can only be determined from an analysis of the critical failure surface. A brief subsection is devoted to outlining the general procedure used to identify the critical failure surface for each slope geometry. Having identified the appropriate pore pressures, shear strength parameters, and critical failure surface for each geometry, computer program SG-SLOPE is used to estimate the probability of failure for each pushback. The remainder of this section focuses on the results of the stability evaluation, and more importantly, on an interpretation of the underlying geologic and hydrologic controls responsible for the observed results.

8.7.1 SHEAR STRENGTH DATA

Information on shear strength parameters in the overburden at HVC is limited to results of two geotechnical investigation programs conducted by Golder Associates. The first program, conducted in 1969, investigated shear strength parameters within the upper sequence of sand, silty sand and till. Results of that study, summarized in Golder Associates Report V6912-B, concluded that shear strength parameters $\phi'=36°$ $c'=0$ kPa were representative of this sequence.

As the design of the Valley pit evolved to include a deep overburden cut and the understanding of the overburden geology improved to include the lower silt and clay sequence, it became apparent that engineering properties of the lower sequence would also be required in order to evaluate slope stability. A second testing program was initiated in 1988 to identify shear strength parameters within this sequence.

A field sampling program was conducted in the summer of 1988 to obtain essentially undisturbed overburden samples for laboratory strength testing. The samples were then analyzed in the Golder Associates Vancouver laboratory. Shear strength tests included eleven consolidated undrained triaxial tests and four consolidated undrained direct shear tests. Other geotechnical tests, including visual inspection, grain size analyses, Atterberg limits, water contents, organic contents and x-ray diffraction were also performed. Detailed results of the analyses are presented in Golder Associates 1988 report 872-1416.

Table 8.7 presents a summary of the direct shear test and triaxial test results conducted by Golder. Strength parameters for both an effective stress analysis (effective residual friction angle ϕ'_r, effective residual cohesion c'_r) and a total stress analysis (residual undrained strength Su_r, undrained strength ratio Su_r/σ'_c) are reported. The Mohr-Coulomb residual strength envelopes of the test results are plotted in *Figure 8.25* as heavy dashed lines. Based on this limited data, the expected strength bounds for units *10A* and *10B* are also indicated in the figure. Because the number of strength measurements are not sufficient to obtain reliable estimates of the population mean and variance, the statistics were estimated as follows:

- The mean effective residual friction angle was approximated by the angle defined by the bisector of the shaded strength bounds, i.e. 18° for unit *10A* and 30° for unit *10B.*
- The standard deviation in friction angle was estimated from the half-with of the strength bounds envelope. In other words, it was assumed that the shaded area represents a 95% confidence envelope within ±2 standard deviations of the mean (i.e. 95% of shear strength tests will fall within shaded area).
- The mean effective residual cohesion was estimated from an average of all available cohesion intercepts. Once again, it was assumed that the observed range of cohesion intercepts define the bounds of the 95% confidence interval.

Table 8.7 Results of Triaxial Shear Tests by Golder Associates

Unit	BoreHole	Depth	ϕ'_r (deg)	c'_r (kPa)	σ'_c (kPa)	Su_r (kPa)	Su_r/σ'_c	Description
3	P15	24.07	37.3	0	343.5	NA	NA	Very dense to dense, grey to light brown silty fine sand.
3	P15	30.48	32	0	689	NA	NA	Very dense to dense, grey to light brown silty fine sand to to fine sand with some silt.
10A	P17	154.53	24.5	243	1752	483	0.28	Dark grey, very stiff, very fine sand laminated silt with trace clay (saturated).
10A	P17	154.53	24.5	243	2042	1130	0.55	Stage 2 test.
10A	P17	164.89	36.6	0	917	1028	1.12	Dark grey, very stiff silt and some clay (saturated). Laminated layers up to 1 cm thick.
10A	P17	165.81	36.6	0	2356	993	0.42	Dark grey, very stiff silt and some clay (saturated). Laminated layers up to 1 cm thick.
10A	P20	118.07	33.4	0	981	927	0.94	Grey to dark grey, stiff to very stiff silt with thin laminated fine sand layers.
10B	P20	183.72	20.7	145	699	370	0.53	Dark grey to grey, stiff silty clay with some laminated sand layers.
10B	P20	183.72	20.7	145	1794	643	0.36	Stage 2 test.
10B	P20	184.83	12.1	216	686	212	0.31	Tan grey silt and clay of high plasticity.
10B	P20	184.83	12.1	216	1806	431	0.239	Stage 2 test.

Parameters Defined:

ϕ'_r	Residual Effective Friction Angle
c'_r	Residual Effective Cohesion
σ'_c	Triaxial Test Isotropic Consolidation Stress
Su_r	Residual Undrained Strength
Su_r/σ'_c	Undrained Strength Ratio

Table 8.8 lists the statistics that have been adopted to describe the distribution of shear strength parameters within each of the major geologic sequences in this study. The accuracy of the parameters should be confirmed by additional shear strength testing and back analysis of berm scale failures as the mine develops and the various geologic horizons become exposed, especially since the triaxial tests determine shear strength in a direction that is oblique to stratification and may therefore not represent the minimum strength along the base of a block slide.

Figure 8.25 Mohr-Coulomb Strength Envelopes for Lower Sequence

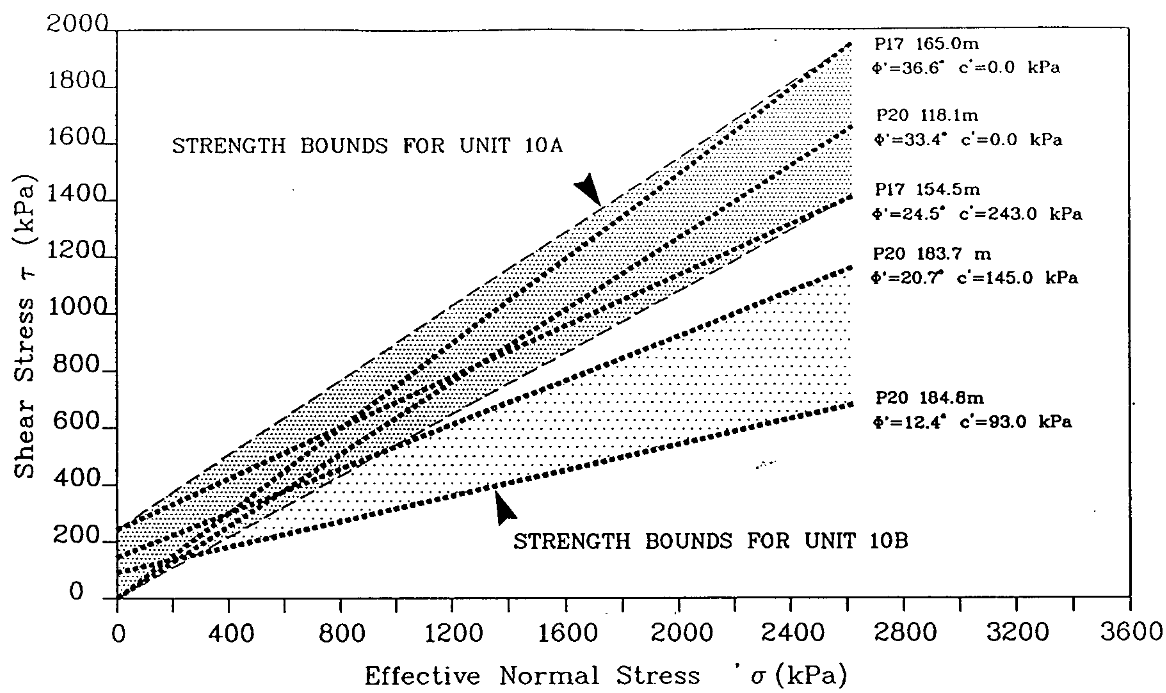

The laboratory shear strength of fine grained, cohesive soils is dependent on drainage conditions utilized during the test. In an undrained test, pore pressure changes induced by shearing are not permitted to dissipate while in a drained test, pore pressures are maintained at a constant level throughout the test. Shear strength parameters obtained from undrained tests are representative of in-situ soil strength in the short term, before any pore pressure changes induced by shearing can be dissipated. On the other hand, drained laboratory strength parameters duplicate long term in-situ strength conditions that occur after pore pressures within the soil mass have had an opportunity to return to steady state conditions dictated by the groundwater flow system.

Because the silts and clays of the lower sequence have been heavily overconsolidated, they tend to dilate on shearing. Dilative behaviour increases the pore volume, inducing temporary reductions in pore pressures and a corresponding increases in short term shear strength. However, over a period of time, the strength will decrease as the shear induced pore pressure reductions dissipate. As a result, slopes that may be very stable in the short term may become unstable in the long term.

The period of time during which short term conditions prevail is controlled by how quickly construction and shear induced pore pressure changes will dissipate. Because shear induced pore pressure changes initially occur only within the zone of shearing, and occasional relatively high permeability sand and silt lenses are known to exist within the lower sequence, any localized pore pressure reductions on the shear surface will probably dissipate quite quickly (weeks to months). For this reason, all stability analyses reported in this section were based on the long-term, effective stress approach and steady state pore pressures predicted by the analysis of groundwater flow.

Table 8.8 Shear Strength Parameters Adopted in This Study

GEOLOGIC SEQUENCE	COMPOSITION	$\phi'_{r\ mean}$	Sdev. ϕ'_r	$c'_{r\ mean}$ (kPa)	Sdev. c'_r (kPa)
Upper Sequence Units 1-9	Sands, silty sands and tills.	36.0	1.0	0.0	0.0
Lower Sequence Unit 10A	Silt.	31.5	1.0	121.5	60.8
Lower Sequence Unit 10B	Silt and clay.	17.0	2.1	119.0	13.0

8.7.2 DETERMINISTIC ANALYSES / CRITICAL FAILURE MODES

Before commencing the complete stochastic evaluation of stability that will involve analyses of groundwater flow, slope stability and economics, a simpler deterministic stability analysis was conducted for each five year pit design. The objective of the deterministic analysis was to identify the critical failure surface for each pushback and to obtain approximate factors of safety for comparison purposes. Input parameters and assumptions that were utilized in the analysis were as follows:

- The slope geometry for each pushback was taken from the current HVC mine plan (Base 64B1).
- Shear strength parameters were based on mean consolidated undrained residual values given in *Table 8.8.*
- The analyses were performed in terms of effective stress, i.e. it was assumed that all pore pressure changes induced by the excavation have been dissipated.
- Two groundwater scenarios were considered: In the first scenario, it was assumed that dewatering would only be effective in drawing the water table down to the top of the lower silt and clay sequence at 1110 m. In the second scenario, it was assumed that partial drainage would also occur within the lower silt and clay sequence, lowering the seepage point to approximately 1060 m.

Figure 8.26 illustrates the five potential ultimate pit failure surfaces that were analyzed during the critical failure surface search of the ultimate pit wall. FOS values for both water table configurations are also presented in the figure. The deterministic analysis results indicate that deep seated, full wall stability will be critical as failure mode 4 yields the lowest factors of safety for both water table scenarios. However, inter-ramp stability will also be of concern since factors of safety for failure mode 1 are only slightly higher. Because several computed FOS values for the high water table scenario are less than unity, these deterministic analyses provide the first indication that groundwater conditions within the lower silt and clay sequence will have a major impact on long term stability of the overburden walls. Since the overburden horizons are overconsolidated, and may therefore have a tendency to planar translational movement, additional stability analyses investigating the stability of planar and block failure modes are recommended.

A large number of deterministic slope stability analyses were also conducted by Golder Associates (Report 872-1416). In the Golder study, both total stress and effective stress stability analyses were performed to evaluate stability of the final pit wall. The analyses included a number of strength and water table scenarios, utilizing different combinations of upper bounds (peak) and lower bounds (residual) strength parameters obtained from the consolidated undrained triaxial and direct shear tests, and best case and worst case water table configurations. The factors of safety obtained during the analyses varied from 0.795 to 1.758. This wide range of computed factors of safety is a reflection of the large degree of uncertainty inherent in the shear strength parameters (peak vs. residual), drainage conditions (undrained or drained strength applicable), and the long term water table profile utilized in the analyses. The stability results presented in *Figure 8.26* compare favourably to the long term FOS values computed by Golder Associates.

Figure 8.26 Identification of Critical Failure Surface

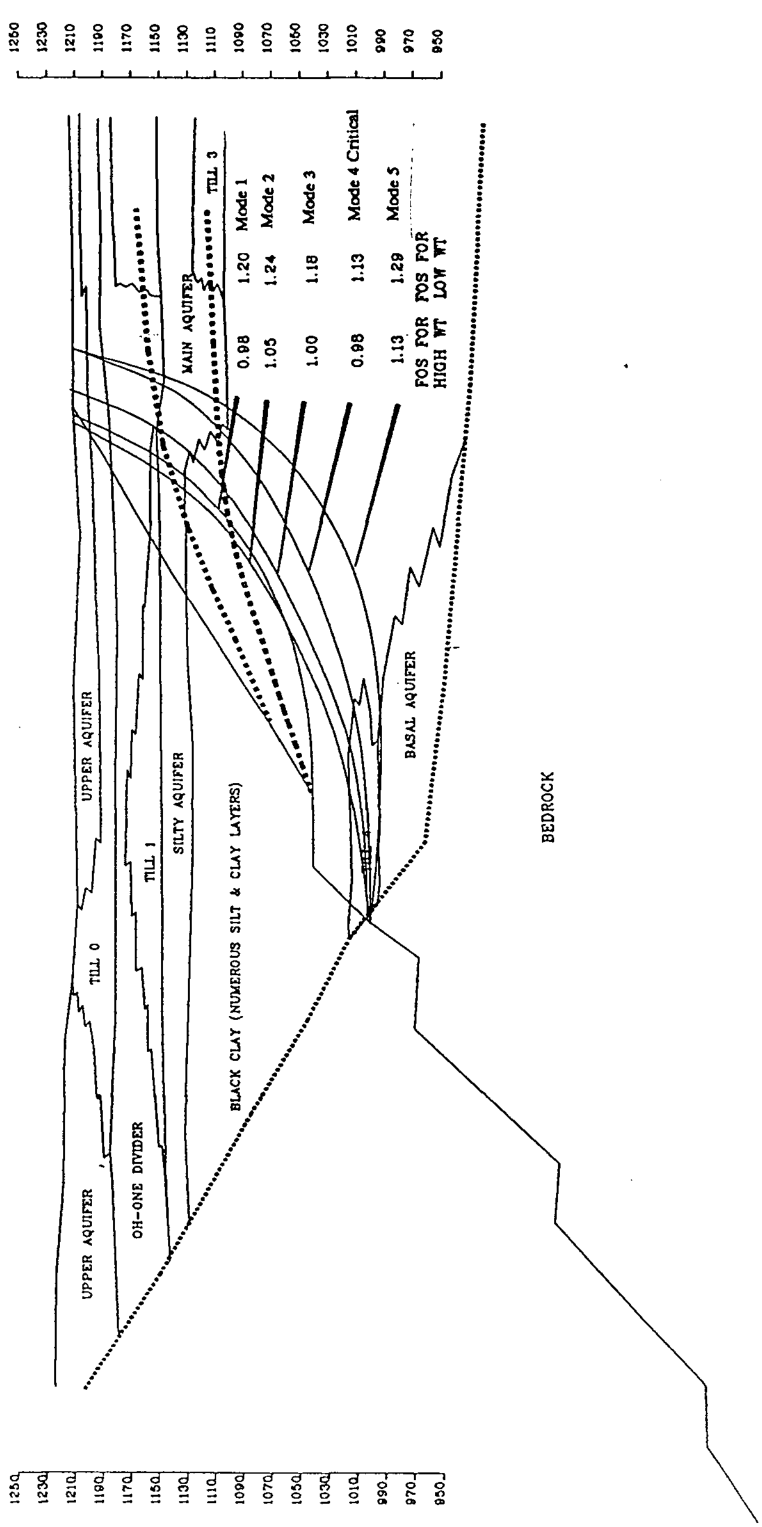

8.7.3 STOCHASTIC ANALYSES / PROBABILITY OF FAILURE

The final step in the slope stability evaluation involved the calculation of the probability of failure during each push-back. Each stability simulation was based on the analysis of 100 realizations of shear strength and groundwater conditions that can be expected during the corresponding stage of pit development.

Table 8.9 summarizes the results of the stability analyses, including the mean critical acceleration K_c, the standard deviation of K_c, the mean factor of safety, the FOS standard deviation, and the probability of failure. Histograms of the FOS distribution for each push-back are also shown in *Figure 8.27*.

Table 8.9 Summary of Slope Stability Analysis Results

YEAR	Kc MEAN	Kc SDEV.	FOS MEAN	FOS SDEV	POF
1987	0.88	0.10	3.94	0.32	0.00
1992	0.52	0.10	2.72	0.34	0.00
1997	0.18	0.08	1.59	0.28	0.02
ULT.	-0.14	0.03	0.55	0.11	1.00

The degree of uncertainty in the FOS estimates is indicated by width of the FOS histograms portrayed in *Figure 8.27* and quantified by the standard deviation of FOS values, reported in *Table 8.9*. The relatively large uncertainty in the FOS prediction ($\sigma_{FOS}=0.3$) during the first three pushbacks is due to the large uncertainty in shear strength parameters, and to a lesser extent, to possible estimation errors in the pore pressure distribution.

The results of this study indicate that overburden slopes in design sector R-3 will be very stable under assumed conditions until 1997. The stability analyses project a mean factor of safety in excess of 2.0 and a zero probability of failure during this period. The high degree of stability from 1987 to 1997 is attributed to the following factors:

- Any potential failure will involve only sands and tills of the upper sequence and unit 10A of the lower sequence, both relatively high strength horizons.
- The groundwater analyses indicate that dewatering will maintain the water table in the lower 50% of the slope so excessive pore pressures will not develop.

For the 1997 slope configuration, the analyses project a mean factor of safety of 1.59 and a probability of failure of 2%. Beyond 1997, stability conditions are expected to deteriorate rapidly. Under the assumed shear strength and groundwater conditions the mean factor of safety of the ultimate pit wall will be 0.55 and the probability of failure will be 100%. The decrease in stability can be attributed to the following factors:

- The lower portion of the failure plane will penetrate the very weak tan grey silt and clay horizon identified as unit 10B. Since the majority of resistance to shear originates along the flat portion of the failure surface, the impact will be very significant.
- Because the current groundwater control plan calls for dewatering only within the upper sequence, pore pressures in the lower sequence will continue to be very high, especially in the critical toe area.
- As the overburden slope is expanded to depth, stress levels on the failure surface will increase in proportion to the total overburden load. As a result, the cohesive contribution to shear strength, which is stress independent, will become progressively less significant.

The results of this stability assessment suggest that stability problems may develop in the overburden pit wall in design sector R-3 as the pit wall approaches the ultimate pit configuration and the potential failure surface shifts into the unit 10B horizon below 1020 m elevation. However, before accepting these findings, it is important to recognize that the preceding stability assessment was based on three key assumptions:

Figure 8.27 Histograms of FOS Distributions for 1987, 92, 97 and Ultimate Push-backs.

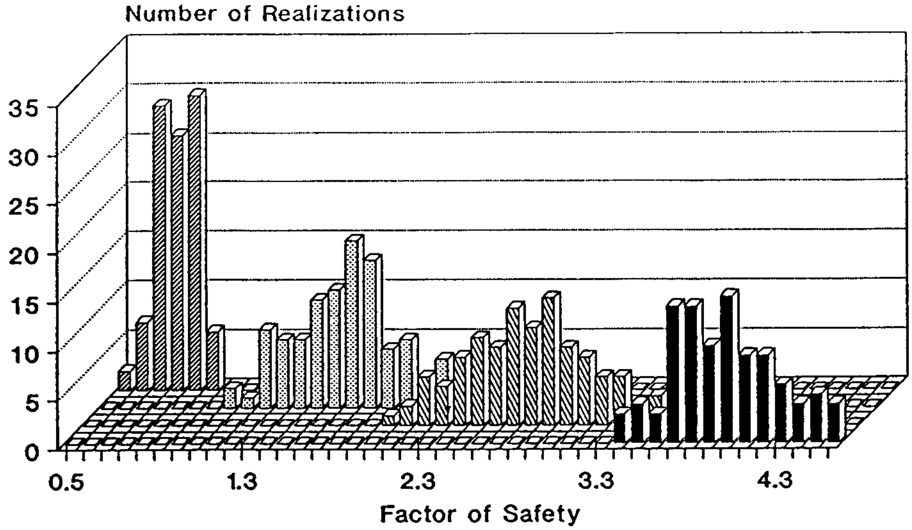

- First, it was assumed that the unit 10B horizon is continuous and that the low residual strengths observed in the two available shear tests on this unit are representative of the entire horizon.
- Second, it was assumed that the occasional sand layers which were observed in drill cores within the lower sequence are not continuous and will not contribute to widespread depressurization and formation of unsaturated wedges in the toe area.
- Third, it was assumed that shear induced pore pressure changes will dissipate relatively rapidly in relation to the time span during which the slope must remain stable; therefore, a long-term effective stress analysis of stability was considered appropriate.

The validity of these assumptions will have fundamental bearing on the stability results. For example, if sand horizons within the lower sequence are assumed to be continuous in the toe area of the ultimate pit wall, the computer models predict that stability would increase from a mean factor of safety of 0.55 to 0.97 while the probability of failure would decrease from 100% to 67%. Further investigations should be conducted to resolve these issues before a design commitment is made on the ultimate pitwall configuration in design sector R-3.

Before closing the discussion on slope stability, it should be noted that this stability assessment of the ultimate pit wall is less favourable than the findings of Golder's report 872-1416. The discrepancy is due to three factors:

1. The Golder analyses were conducted on a slope design with an overall slope angle of 25° while this analysis is based on the latest overburden slope design provided by HVC which adopted a 31° overall slope angle in design sector R-3.

2. The detailed groundwater modelling studies conducted as part of this thesis research suggest that without modifications to the groundwater control program, pore pressures in the ultimate pit wall will be slightly higher than this author's earlier pore pressure predictions (Sperling and Brennan, 1988) which were adopted in Golder's analyses.

3. All stability analyses in this study were conducted in terms of effective stress, utilizing pore pressure levels that may be expected in the long term, whereas many of the high FOS results obtained by Golder were based on dilatant, undrained pore pressure responses that are only appropriate in the short term.

8.8 RISK-COST-BENEFIT ANALYSIS OF EXISTING MINE PLAN

This section presents results of the economic risk-cost-benefit analysis for design sector R-3. The objective of the analysis was to determine the level of net income that will be generated in the design sector during each 5 year pit expansion. The net income projections were required to assess the relative significance of the monetary risk of slope failure and to serve as a benchmark for comparing with alternate slope design and dewatering strategies.

The economic analysis was conducted using the cost estimation procedures documented in *Chapter 3* of this thesis. Four pit profiles, based on the latest slope design for the sector, were considered in the analysis (1987, 1992, 1997 and ultimate). Probabilities of failure for each 5 year profile were based on results of the stochastic groundwater flow and stability analyses described earlier in this chapter. Because exact production costs and concentrate prices at HVC are confidential, this analysis was based on an approximate figures typical of large porphyry copper mines, kindly provided by the management of HVC. The complete data set, including geologic, slope stability, hydrogeologic, economic, pit design, dewatering system design, and monitoring parameters is summarized in *Table E.2* of *Appendix E.*

Table 8.10 lists the tonnages that will have to be excavated from sector R-3 during each push-back. Recall that in order to evaluate the consequences of failure, the volume calculations are performed twice, first assuming that no pit wall failure develops during the push-back (STABLE), and then assuming a failure does develop along the critical failure surface (TOTAL). The total amount of overburden that would be involved in a failure is reported under the heading CLEAN-UP. Note that the tonnages that would be involved in a failure increase very rapidly during the last two push-backs.

Table 8.11 lists the expected operating costs and revenues for each push-back. Because the costs of mining failed overburden are expected to be lower than those of mining undisturbed overburden based on discussions with mine management at HVC ($1.00 per tonne vs. $1.10 to $1.25 per tonne), the costs of clean-up are not prohibitive, typically only 25 to 50% of the costs of mining stable material. It is also interesting to note that over the life of the mine, the net costs of dewatering will come to less than 0.3% of the total operating costs.

The cost of a failure of the ultimate pit wall is projected at $46.2 million dollars. Whereas a failure of this magnitude during the final push-back would lead to an accelerated shut down at most mines because clean-up costs would outweigh remaining ore values, at HVC the clean-up cost would likely be justified as production will continue at lower levels of the Valley Pit long after the ultimate pit profile is established in the overburden.

Table 8.10 *Projected Tonnages to be Mined During Each Push-Back.*

PUSH-BACK	YEAR FROM	YEAR TO	TOTAL	STABLE	CLEAN UP
			(millions of tonnes)		
1	1982	1987	23.4	23.4	0.0
2	1987	1992	85.3	83.2	2.1
3	1992	1997	70.6	58.0	12.6
4	1997	2002	84.3	62.2	22.1
5	2002	ULT.	147.3	101.1	46.2

Table 8.11 Projected Conditional Costs and Revenue per Push-Back.

PUSH-BACK	MINE NO FAIL. ($ million)	MINE STABLE ($ million)	MINE CLEAN UP ($ million)	COST MILL ($ million)	COST DEWATER ($ million)	MINE REVENUE ($ million)
1984-1987	28.08	28.08	0	2.63	1.74	7.36
1987-1992	92.2	89.66	2.1	76.13	0.35	197.06
1992-1997	72.84	58.76	12.6	86.63	0.95	210.15
1997-2002	89.69	64.83	22.05	76.13	-0.26	193.79
2002-ULT	98.83	98.83	46.2	202.12	-0.26	448.91

Figure 8.28 Cumulative Net Incomes by Push-Back, Conditional and Expected.

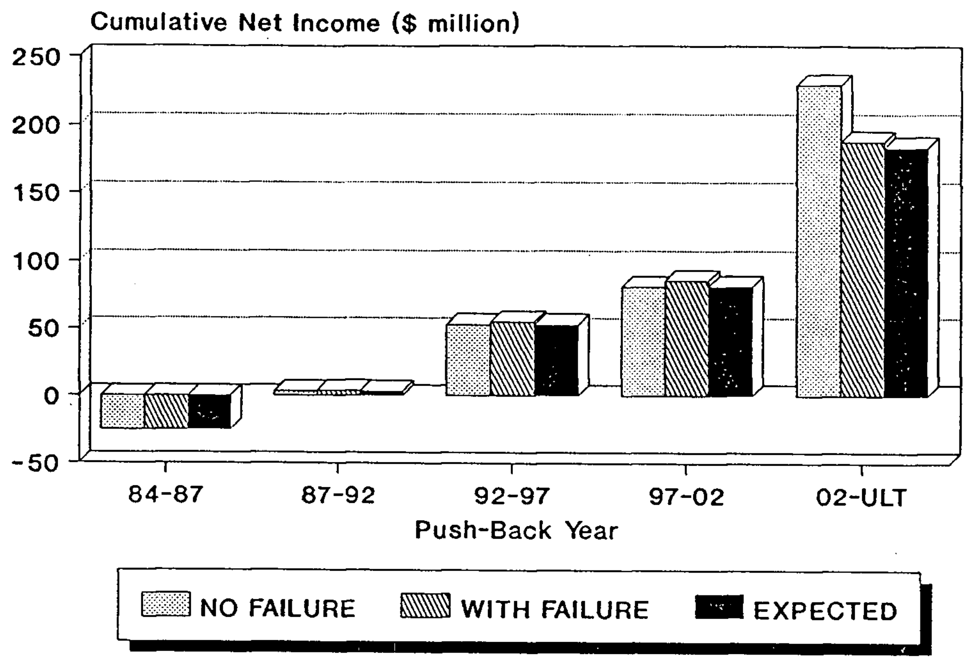

Table 8.12 Projected Expected Costs, Revenue and Net Income For Current Design

PIT	YEAR FROM	YEAR TO	POF	EXPECTED COST ($ million)	EXPECTED REVENUE ($ million)	EXPECTED NET INCOME ($ million)	CUMMULATIVE NET INCOME ($ million)
1	1982	1987	0.0	32.4	7.4	-25.1	-25.1
2	1987	1992	0.0	168.7	197.1	28.4	3.3
3	1992	1997	0.0	160.4	210.1	49.7	53.0
4	1997	2002	0.2	165.0	193.8	28.8	81.8
5	2002	ULT.	1.0	346.9	448.9	102.0	183.8

Table 8.12 summarizes the expected operating costs, revenue and net income while *Figure 8.28* shows the conditional net income projections in graphic format. The results indicate that a failure of one or more interior pits would involve a much lower level of economic risk since all failed overburden would have to be excavated during the next push-back anyway. However, the smaller interior pit failures could affect short term cash-flow while haul roads are re-established or buried ore is re-exposed at lower levels of the pit. These later factors have not been incorporated in the economic analysis.

In summary, expected net income based on the current slope and dewatering design is $183.6 million. The total monetary risk of slope failure is $50.6 million. Of the total, $46.2 million is associated with failure of the ultimate pit wall. Because the monetary risk of failure is high there appears to be good potential for improving the profitability in this design sector by flattening the overall slope angle and/or by some form of dewatering efforts in the critical toe area of the slope. The following section will investigate which of these design alternatives will result in the greatest increase in profit for HVC.

8.9 IMPROVEMENTS TO SLOPE DESIGN AND DEWATERING STRATEGY

In the previous sections it was shown that the probability of failure, and the monetary risk associated with the failure, would both be very high for the ultimate pit wall in the later years of operation at HVC. This section investigates whether modifications to the slope configuration and/or the dewatering program would result in increased profitability from this design sector.

Three design modifications will be considered in this study:

1. Making provisions for dewatering within the lower silt and clay sequence (e.g. horizontal drains).

2. Reducing the overall slope angle to 26° by eliminating the oversteepened portion of the ultimate pit wall.

3. Flattening the overall slope and making provisions for toe drainage.

The expected cumulative net income will be determined for each design alternative as a direct measure of the value of that particular design. Once the risk-cost-benefit is completed for each design option the three net-incomes will be compared against each other and to the $183.6 million net-income projected for the current design in order to identify the best slope angle and dewatering combination.

Because the analysis follows exactly the same lines as were used in the previous section, only the net income projections will be presented here.

8.9.1 TOE DRAINAGE ONLY

Pore pressures in the lower sequence are expected to remain high since planned dewatering efforts will focus only on the upper sequence. In order to improve stability further, this sub-section will investigate the economic feasibility of a horizontal drain groundwater control program within the lower sequence.

Unlike pumping wells that remove a specified flux from each node in the groundwater flow model, horizontal drains work by increasing the effective permeability of the soil or rock-mass. On small scale problems horizontal drains have traditionally been modelled as specified head line sinks ($\psi = 0$). However, such an approach leads can lead to erroneous results on large scale problems when the $\psi = 0$ condition may only be achieved in close proximity of the drain while in the model the condition would be applied over an entire row of elements that may be 25 m in size. To simulate the presence of drains more realistically, hydraulic conductivities of each row of finite elements within the lower sequence were increased by three orders of magnitude (mean log K values increased from -9.5 to -6.5).

Figure 8.29 Contour Plan of Mean Hydraulic Head on Section R-3 with Horizontal Toe Drains

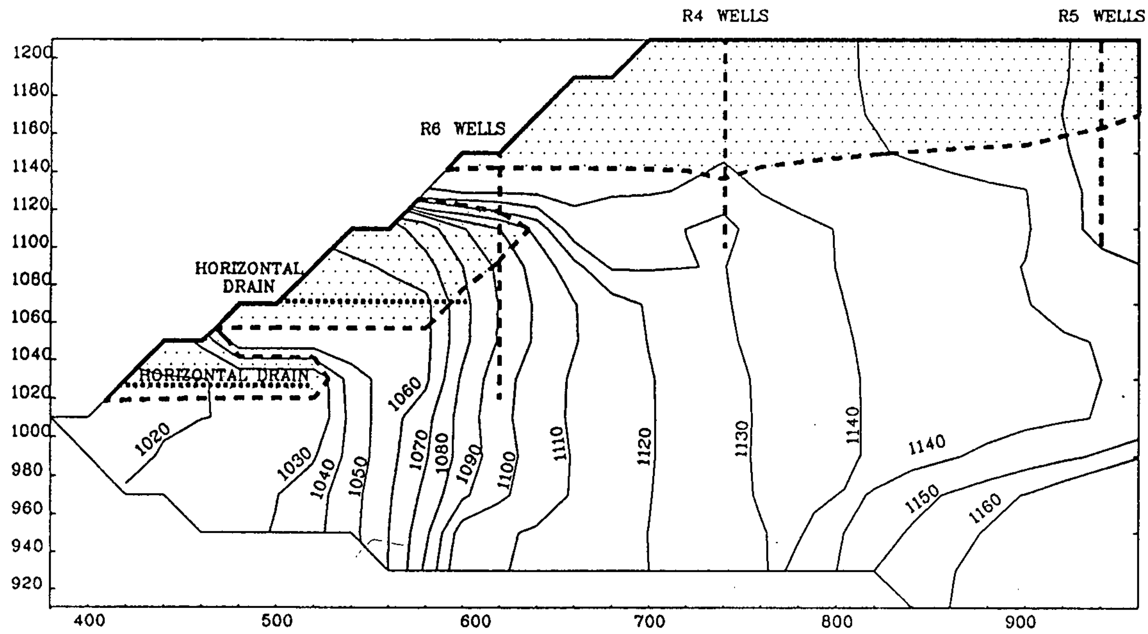

Figure 8.29 illustrates the predicted hydraulic head distribution in the slope. Note the development of unsaturated wedges in the toe area and the overall reduction in head relative to the no toe drainage design portrayed in *Figure 8.24*.

As a result of reduced pore pressures, the mean factor of safety of the slope increased from 0.55 to 0.96 and the probability of failure decreased from 100% to 67%. The monetary risk decreased from $46.2 million to $30.9 million and net-income for the final push-back increased from $102.0 million to $117.3 million less the capital and maintenance costs of the horizontal drainage program. The net income projections show that groundwater control in the toe area of design sector R-3 will be economically justified provided that the cost of the drainage program will be less than $15.3 million, and that the dewatering program can meet or exceed pore pressure targets indicated by the computer model. Since horizontal drains cost $60 to $100 per m, the strategy appears to be economic. However, a second important consideration is whether sufficient lead time will be available for the drains to reduce pore pressures to target levels.

8.9.2 FLATTENING SLOPE ONLY

This design modification involved flattening of the overburden slope below the proposed ramp at 1040 m elevation from 47° to 31° and a one degree reduction in the overall slope in the upper portion of the slope, from the ramp to the slope crest. As a result, the ultimate pit crest was pushed back by approximately 50 m and the total amount of stripping was increased from 101 to 116 million tonnes. The dewatering program was not modified, except for a slight offset for all wells to reflect the new slope geometry.

The stability analysis confirmed that the 5° flattening would improve slope stability considerably, increasing the mean factor of safety to 1.13 and reducing the probability of failure to 30%. As a result of the slope flattening, the expected net income for the final push-back increased from $102.0 million to $118.1 million. The increase can be attributed to a reduction in monetary risk from $ 46.2 million to $13.2 million.

8.9.3 FLATTENING TOE AND PROVISIONS FOR TOE DRAINAGE

The final design option implemented both slope flattening and toe drainage. Under this design, the mean factor of safety increased to 1.53 and the probability of failure dropped to 0. Since the stability analysis indicates that there is no physical risk of slope failure, the monetary risk also dropped to 0. The expected net income for the final push-back was projected at $131.3 million less costs of groundwater control.

8.9.4 EVALUATION OF DESIGN OPTIONS

Table 8.13 summarizes the key results of the risk-cost-benefit evaluation for the four design options. Based on projections of expected net income during the final push-back, all three alternate designs appear more attractive than current design. The best design alternative appears to be Case 3, calling for both flattening of the slope and toe drainage. The economic projections indicate that based on available information, the Case 3 design is expected to increase net income in design sector R-3 by $29.3 million dollars, less the cost of the horizontal drain program. The Case 3 design will be the best alternative provided that an effective toe drainage program can be implemented for less than $13.2 million dollars in this design sector. If drainage were to be more costly, then Case 2, flattening slope only, would become the best alternative.

***Table 8.13** Summary of Results for R-C-B Analysis of Design Options*

DESIGN OPTION	STABILIZING MEASURES	POF (%)	MONETARY RISK	EXPECTED NET INCOME
Current	No Extras	100	46.2	102.0
Case 1	Toe Drainage Only	67	30.9	117.3
Case 2	Flattening Only	30	13.2	118.1
Case 3	Flattening and Drainage	0	0.0	131.3

Assuming a conservative cost of $20,000 per 100 m long horizontal drain, the $13.2 million budget would provide sufficient funds to install 660 drains, providing enough coverage for five rows of drains at 5 m spacings across the entire design sector. Detailed modelling, and especially controlled field trial studies would be required to determine whether this level of horizontal drain coverage would be capable of achieving dewatering targets.

8.10 SUMMARY

This case history study has demonstrated that the risk-cost-benefit framework presented in this thesis can be used successfully to evaluate groundwater and slope design options at open pit mines and to identify the best design strategy from a number of alternatives. In a natural order of progression, the discussion focused on each major component of the case history study, including:

- Site orientation.
- Geologic interpretation, encompassing ore distribution, digability characteristics, and definition of the overburden stratigraphy.
- Hydrogeology, focusing on evaluation of recharge rates and estimation of statistical parameters to describe the hydraulic conductivity field.
- Current slope design and dewatering strategy for sector R-3.
- Stochastic modelling of the expected pore pressure distribution at each stage of pit development.
- Stability analysis, including a review of shear strength parameters, identification of critical failure surfaces, and an assessment of the probability of slope failure during each push-back.
- Economic risk-cost-benefit analysis of the current slope design.
- Assessment of design alternatives, including both reduction of the overall slope angle and dewatering the toe area of the ultimate pit wall.

Section 8.2 provided background information about mining operations at HVC. The objective was to set the stage for a more detailed description of the overburden dewatering efforts and to put the dewatering program into perspective relative to the numerous other facets of the mining operation.

Section 8.3 presented the latest geologic interpretation for the design sector. Emphasis was placed on documenting data that would be required to conduct the risk-cost-benefit analysis, including: the ore grade distribution, interpretation of the structural geology, and location of the overburden bedrock contact. Because sufficient hydraulic conductivity measurements were not available to estimate the range of correlation of the hydraulic conductivity field in the vertical direction, the interpretation of overburden stratigraphy was also utilized for this task.

Section 8.4 presented the hydrologic setting. The discussion began with an overview of the surface water hydrology. It was estimated that catchment recharge in the area is approximately 69 mm per year and that the total groundwater recharge of the watershed is 5.8 million m^3 per year. Because present pumping rates, estimated at 14 million m^3 per year, are significantly higher, HVC is actively mining local groundwater resources. A transient analysis will be required to assess how long the mine will be able to utilize groundwater for process water supplies before excessive drawdowns develop in the vicinity of the wells. A potential environmental impact on surface water supplies was also identified.

Much of the material presented in *Section 8.4* concerned estimation of representative hydraulic conductivities for each overburden horizon. A number of sources of hydraulic conductivity information were considered in formulating the stochastic model, including: pump tests, long term well response, laboratory triaxial tests, grain size analyses and empirical correlations to geologic information.

A geostatistical correlation study was also preformed to determine the distances over which hydraulic conductivities appear to be correlated. It was determined that in the horizontal plane, conductivities appear to be correlated over a correlation range of 1000 m while in the vertical direction the correlation range is only 50 m.

These results are consistent with the fluvial / lacustrine depositional environment which would naturally lead to much more continuity parallel to bedding. Based on the results of this analysis, a two layer stochastic hydraulic conductivity model was chosen to simulate the actual hydraulic conductivity distribution. The model consisted of an upper, relatively pervious sequence representing the thinly stratified beds of sand, silt and till, and a lower, relatively impervious sequence representing the thick glacio-lacustrine deposits of silt and clay.

A regional "plan view" aquifer model was used to obtain estimates of appropriate boundary flux levels for the cross section finite element model. The boundary condition calibration indicated that 4.0×10^{-7} to 8.0×10^{-7} m^3/s is a reasonable flux across the recharge boundary through pervious strata.

Section 8.5 described the current pit design and dewatering strategy for design sector R-3. The design calls for an overall slope angle of approximately 31° in the overburden, and inter-ramp angles of 32 to 47°. The slope is significantly steeper than the 26° overall slope angle planned in other overburden sectors of the pit. In this study it has been assumed that the apparent oversteepening is due to a downward shift in the latest interpretation of the overburden-bedrock contact which is yet to be incorporated in the slope design. As a result, the bedrock slope angle of 47° is still retained over the lower third of the overburden slope.

Section 8.6 documented the stochastic analysis of groundwater flow. After a brief description of the free-surface boundary value problem and the simulation methods used to generate the hydraulic conductivity field, the discussion focused on the characteristics of the hydraulic conductivity realizations generated by the model and how well they compared to the geologic interpretation. It was shown that in each realization, the stochastic model was able to duplicate all of the important features of the hydraulic conductivity field, including the hydraulic conductivity contrast between the upper and lower sequence, the natural variability within each sequence, the horizontal layering, and the continuity of lenses in both horizontal and vertical directions. Once constructed, the stochastic model was used in verification mode to predict December 1987 pore pressure levels observed in the HVC piezometer network. The predicted piezometric surface for the Main Aquifer was close to actual piezometric levels.

The model was then used to forecast the pore pressure distribution in Sector R-3 at 5 year intervals as the pit evolves to the ultimate configuration. The simulation results indicate the current dewatering strategy will be effective in dewatering the upper sequence, but pore pressures will remain high in the silts and clays of the lower sequence. In more detail, the results of the steady state analysis showed that the proposed cumulative pumping rate will exceed the aquifer yield of the upper sequence by a ratio or 4 to 8, but the pumping will have virtually no impact on pore pressures in the lower sequence. These findings suggest that fewer wells may be required to maintain the upper sequence dewatered to target levels than initially planned and some alternate drainage method may be required to reduce pore pressures in the lower sequence. A transient computer simulation is recommended to ascertain whether a reduced number of wells in the upper sequence, combined with horizontal drains in the lower sequence, would be capable of achieving target drawdown levels safely and at a sufficient rate to stay ahead of the pit expansion.

Section 8.7 presented the findings of the probabilistic slope analysis. The discussion began with a review of available shear strength data, much of which originated from the recent deep piezometer drilling program conducted by Golder Associates. Unit 10B, the tan-grey clay, was identified as a very weak horizon that may lead to stability problems once the toe of the overburden slope approaches 1020 m elevation. Representative statistics were estimated for each major geologic horizon, including the upper sequence, unit 10A of the lower sequence, and unit 10B of the lower sequence. It was noted that additional strength testing should be conducted in the future because the number of strength measurements in each unit were not sufficient to obtain reliable estimates of the population mean and variance.

The shear strength testing program, conducted by Golder Associates, revealed that the fine grained materials of the lower sequence tend to dilate during shear, and this dilation results in a short term increase in strength. In all slope stability analyses conducted as part of this case history study, it was assumed that the dilation induced pore pressure changes will dissipate relatively rapidly in relation to the time during which the slope must remain stable; therefore, the long-term effective stress approach to slope stability analysis was adopted for all analyses.

Probabilistic stability analyses for each 5 year push-back indicated that the pit wall in sector R-3 will be very stable until 1997, at which time stability will begin to deteriorate rapidly. The analyses also showed that as designed, the overburden portion of the ultimate pit wall will be unstable with a mean factor of safety of 0.55 and a probability of failure of 100%. The apparent instability of the ultimate pit wall was attributed to four factors:

- Oversteepening of the toe area as a result of changes in the projected depth to bedrock.
- A significant loss in shearing resistance once the failure surface penetrates unit 10B.
- Very high pore pressures in the lower silt and clay sequence.
- A gradual decrease in the relative importance of cohesive shear strength with depth as confining stress levels increase.

Section 8.8 presented the results of the economic risk-cost-benefit analysis for design sector R-3. The analysis was based on slope design, hydrologic and geotechnical parameters documented earlier in the thesis and on operating cost estimates considered typical of large open pit copper producers[4]. The results indicated that failure of the ultimate overburden pit wall will pose by far the greatest monetary risk in this design sector. The cost of failure was estimated at $46.2 million. Based on approximate production costs and prices, the expected cumulative net income for this design sector was projected at $183.8 million, with over 60% of the net income being generated during the last push-back.

Because the monetary risk of failure is very high, *Section 8.9* evaluated the feasibility of alternative designs that would lead to improved slope stability. Three alternatives were considered in the analysis: 1) dewatering the toe area with closely spaced horizontal drains while maintaining the current slope profile, 2) reducing the overall slope angle to 26° and not implementing the horizontal drains and 3) adopting both stabilizing measures.

The stability analysis results showed that dewatering of the toe would reduce the probability of failure to 67%, flattening the pit wall would result in a probability of failure of 30% and adopting both approaches would result in a zero probability of failure. The suitability of the alternate designs was evaluated by comparing corresponding projections of expected net income for the final push-back to the $102.0 million figure projected for the current design. The expected net incomes projected for each of the four design alternatives during the final push-back were:

Current	no extra provisions	$102.0 million
Case 1	toe drainage only	$117.3 million less cost of toe drainage
Case 2	flattening only	$118.1 million
Case 3	flattening and toe drainage	$131.3 million less cost of toe drainage

The net income projections suggests that of the design strategies considered, flattening of the slope, in combination with a horizontal drain drilling program in the toe area of the slope will result in the most profitable mining approach, provided that the horizontal drains will cost less than $13.2 million and that the drains will be capable of depressurizing the silt and clay to target levels.

---

[4] Exact production costs and concentrate prices were not made available for this study as they are considered confidential by Highland Valley Copper.

The findings of this case history study suggest that there is potential for attaining increased profitability and greater safety in design sector R-3 by modifications to the current mine plan. Summarized below is a list of suggested modifications to the current pit design and dewatering plan that have arisen from this risk-cost-benefit analysis:

- Re-evaluation of the overburden-bedrock contact and updating of all phases of the mine plan to reflect the latest information.

- Additional exploration drilling to better define the location, continuity and strength properties of the unit 10B tan grey silt and clay horizon.

- Additional shear strength testing of the lower sequence to confirm observed trends and to provide more reliable shear strength parameter statistics.

- Preliminary investigation of the feasibility of horizontal drains for depressurization of the lower silt and clay horizon, possibly through review of horizontal drain performance in silts and clays on other stabilization projects.

- Transient groundwater flow modelling of the upper sequence to establish whether a reduced number of dewatering wells will be capable of attaining target drawdown levels in advance of mining activity.

- Extension of the risk-cost-benefit analysis to other design sectors, especially sectors where overburden slopes will be smaller, to determine whether these slopes can be safely steepened or subjected to reduced groundwater control efforts without serious economic penalties.

CHAPTER 9 SUMMARY AND CONCLUSIONS

9.1 REVIEW AND SUMMARY OF DISSERTATION

Groundwater control programs have been implemented in many open pit mines around the world. In most cases, the objective of the dewatering programs has been to improve stability of pit walls that are experiencing progressive failure; in others, the dewatering programs have been justified in terms of improved operating conditions within the pit. Because groundwater control efforts are very expensive (dewatering programs typically cost several million dollars) and the resulting benefits have historically been expressed in terms of increased factors of safety rather than monetary units, mine management has been faced with a difficult decision when choosing whether a dewatering program should be implemented at their open pit mine, and if so, deciding how much capital should be allocated for groundwater control efforts.

The preceding eight chapters of this dissertation have presented a new risk-cost-benefit framework that can be used to evaluate and compare a number of different dewatering and slope design options in order to identify the strategy that is most likely to maximize profit for the mine operator. In the usual engineering approach, *Chapters 1* and *2* of this dissertation first identified the issues to be resolved and justified why they are important. The risk-cost-benefit approach to analyzing the design problem was then presented in general terms in *Chapter 3.* This overview served as an introduction to more detailed discussions of the four principal framework components that followed in subsequent chapters. The final sections of *Chapter 3* described the decision analysis methodology, *Chapter 4* focused on the geostatistical analysis and simulation of the hydraulic conductivity field, *Chapter 5* presented the model of groundwater flow, and *Chapter 6* discussed the slope stability method used to estimate the probability of failure. Having documented each component of the framework, *Chapter 7* then showed how the complete model can be used in sensitivity mode to explore how the various decision and state variables, including hydrologic measurements, shear strength data, economic parameters, slope angles, and dewatering designs can impact on mine profitability. Finally, *Chapter 8* demonstrated how the new framework has been applied to evaluate groundwater control options at Highland Valley Copper, the world's third largest open pit copper mine.

The remainder of this section presents a brief summary of the key issues that have been addressed in each chapter of this dissertation. *Section 9.2* then highlights the most important contributions of this research effort, contributions that will aid geotechnical engineers and hydrogeologists in implementing the most effective groundwater control systems open pit mines around the world.

9.1.1 REVIEW AND SUMMARY OF CHAPTER 1 - INTRODUCTION

Open pit mining is a capital intensive industry. Excavation and haulage costs alone typically range from 4 to 40 million dollars per year. To minimize the stripping ratio, mine operators continually strive to excavate pit walls as steep as possible while maintaining stability. If a large pit wall failure does develop, the mine will experience severe economic consequences, especially if the failure impedes or curtails normal production.

The objectives of the risk-cost-benefit framework documented in this dissertation were:

(1) To provide the mining community with a practical design tool that could be used to evaluate and compare proposed groundwater control plans and pit wall designs in order to identify the strategy that is expected to generate the greatest profit for the mine operator.

(2) To incorporate the latest engineering approaches to the analysis of each of the four design problems encountered in this framework, including: geostatistical interpretation, modelling of groundwater flow, slope stability analysis and economic analysis.

(3) To demonstrate how the framework was used in practice at Highland Valley Copper to determine future dewatering requirements.

(4) To implement all of the software modules into a user-friendly, graphically intensive software package that will execute on low cost personal computers, yet one that will have sufficient power to tackle realistic design problems.

9.1.2 REVIEW AND SUMMARY OF CHAPTER 2 - GROUNDWATER CONTROL IN OPEN PIT MINES

Canada is one of the world's largest and lowest cost mineral producers; however, the Mining Association of Canada forecasts that technological innovation will be required to keep the Canadian mining industry competitive in the global marketplace. This dissertation has shown that effective pit dewatering measures may provide one alternative for reducing operating costs and gaining a competitive advantage in international markets. The discussion on groundwater control began with a brief overview of the numerous activities that are a part of open pit mining. These include pre-production planning, the production cycle, and decommissioning and reclamation. Since the costs associated with these activities are high there is a strong economic incentive for designing pit walls as steeply as possible. Direct advantages of steep pit walls include reduced operating costs, smaller waste dumps and faster exploitation of the ore body. However, if a pit wall is oversteepened and a failure develops the mine will experience severe economic consequences that include lost production, costs of clean-up and buried ore.

In the traditional deterministic approach to pit wall design that utilizes the factor of safety concept to identify the steepest slope angle, the economic ramifications of the selected slope angle are not explicitly included in the geotechnical design process. On the other hand, in the risk-based approach proposed in this dissertation, balancing profitability against monetary risk becomes the key factor in identifying the optimum slope angle and probability of failure.

In many instances, a groundwater control program can increase profitability, either by reducing the monetary risk of slope failure, or by allowing steeper pit walls to be utilized without increasing the risk of slope failure. Other benefits of groundwater control may include: reduced slope erosion, improved trafficability, reduced blasting costs, and readily available supplies of production water.

To achieve the large scale dewatering that is required in open pit mines, a number of modern dewatering methods have been developed. These include horizontal drains, dewatering wells and drainage adits. *Chapter 2* reviewed the advantages, liabilities and typical installation costs of each system. It was concluded that horizontal drains frequently provide the most cost effective dewatering solution; however, the costs of all three methods are high; several million dollars are often spent by mining companies to dewater a single design sector.

9.1.3 REVIEW AND SUMMARY OF CHAPTER 3 - RISK-COST-BENEFIT ANALYSIS

Selection of the most suitable groundwater control and slope design strategy from a limited number of proposed design options is a classical decision analysis problem that involves decision variables, state variables, consequences and constraints. The goal in *Chapter 3* was to explain how the newly developed risk-cost-benefit framework is used to effectively analyze this problem.

An economic objective function that is used to measure the monetary worth of various design options lies at the heart of the framework. The objective function is expressed in terms of expected net income, defined as the difference between revenue generated by the sale of mineral concentrate, less all operating costs required to produce the concentrate, less all monetary risks associated with slope failure. Therefore, the three terms that must be evaluated in each analysis include benefits, costs and risks.

Benefits, defined as the revenue received from the sale of mineral concentrate are easily computed from production statistics that include production rate, ore grade, recovery and concentrate price. To facilitate the analysis, costs are broken down into operating costs that include costs of mining and milling, and dewatering costs, associated with the development and operation of the groundwater control system. Finally, monetary risk is defined as the expected cost of a slope failure, calculated as the product of the conditional cost that must be borne by the mine operator in the event of a slope failure, multiplied by the probability of the slope failure occurring. In the risk-cost-benefit framework the calculation of these terms is facilitated with computer program SG-RCB. The algorithm for this program was discussed in the chapter.

The complete risk-cost-benefit analysis involves nine analytical steps. The steps include:

(1) Collection and interpretation of data to construct the groundwater flow, slope stability and economic models.

(2) Geostatistical analysis of the hydraulic conductivity data to formulate an accurate stochastic description of the hydraulic conductivity field.

(3) Monte-Carlo Simulation of the hydraulic conductivity field to generate a large number of realizations of K that duplicate the important features of the geologic environment being modelled.

(4) Prediction of pore pressures in the pit wall with a two-dimensional, saturated-unsaturated, finite element model.

(5) Simulation of shear strength parameters.

(6) Analysis of slope stability, utilizing Sarma's method of slices and including the effects of the predicted pore pressure distributions.

(7) Estimation of the probability of failure from results of the above Monte-Carlo Simulation.

(8) Economic evaluation of the objective function.

(9) Selection of the most effective design strategy based on a comparison of R-C-B framework results for a number of design options.

From a technical perspective, geostatistical analysis, groundwater flow modelling, slope stability modelling and the economic evaluation of the objective function were the most challenging and complex aspects of the framework. Therefore, subsequent chapters of the dissertation focused on these four topics in more detail.

A major part of the research effort involved the development of custom software modules to carry out the various data processing and analysis tasks. The newly developed modules include *SG-Stat, SG-Flow, SG-Slope* and *SG-RCB*. *Chapter 3* provided a brief summary of the capabilities of each of these modules and described how the modules have been integrated into a comprehensive and flexible software package. During the software development considerable effort was devoted to incorporating a number of user friendly features in all of the modules, including colour graphics, menus, on-line help and graphic data entry. The motivation behind the extra programming effort was to enhance the software so that it could be used as another avenue of disseminating the contributions made in this thesis research to practitioners and researchers working on similar design problems.

9.1.4 REVIEW AND SUMMARY OF CHAPTER 4 - GEOSTATISTICS

When using numerical modelling to design a dewatering system in an open pit mine, it is necessary to estimate material properties such as hydraulic conductivity and shear strength in the entire flow domain from a limited set of measurements. Because these properties seldom remain constant in the subsurface due to natural geologic variability most parameter estimates are associated with some degree of estimation uncertainty, especially at estimation points that are not in proximity to measurement points. *Chapter 4* described how geostatistical methods have been incorporated in this framework to account for estimation uncertainty and to analyze how the uncertainty affects the risk component of the economic objective function.

The discussion in *Chapter 4* began with a review of the basic building blocks on which geostatistics are founded, including definitions of the mean, variance, covariance, semi-variogram, nugget effect, sill and range. Because the semi-variogram provides the fundamental description of the correlation structure this function was discussed in greater detail. It was shown that the experimental semi-variogram, constructed from field data, reveals a wealth of information about the correlation structure of the stochastic field being analyzed. Frequently observed semi-variogram responses that were discussed included:

- Parabolic behaviour at origin
- Linear behaviour at origin
- Discontinuity at origin
- Pure nugget effect
- Sill
- Semi-variogram increasing at large lag
- Sinuosity
- Boundary effects

Two practical rules of thumb for constructing experimental semi-variograms were reviewed. First, at least 30 supporting pairs of point semi-variograms should be available when fitting a semi-variogram model. Second, the semi-variogram model should only be considered reliable over distances shorter than ½ D_{max}, the maximum dimension of the flow domain. A number of semi-variogram models were then introduced, including linear, spherical, exponential, Gaussian, power, and nugget models.

In geostatistics, the process of predicting parameter values in the entire flow domain from a limited set of measurements is called estimation. In this framework, kriging has been selected to carry out estimation. Kriging is a very popular estimation technique that possesses many desirable attributes; it provides the best linear unbiased estimate (B.L.U.E.) and the kriging equations can be used to compute the level of uncertainty associated with each kriging estimate. It was explained that a number of processes affect the magnitude of estimation uncertainty. These processes include:

- Nature of the correlation structure
- Size of prediction volume (variance reduction factor)
- Number of supporting measurements
- Proximity of supporting measurements to prediction volume
- Proximity of supporting measurements to each other
- Measurement errors resulting in noisy data

Verification of kriging results is an important step that is frequently overlooked. Three standard verification tests (unbiased mean, 95% confidence interval and coherency ratio equal to 1.0) were described in *Chapter 4* and then illustrated with a practical example based on kriging transmissivities in the Avra Valley aquifer.

Since kriging is a smoothing or averaging process, it does not reproduce the natural variability of the hydraulic conductivity field. In order to establish how parameter uncertainty impacts on the monetary risk term it is necessary to carry out geostatistical simulation. Simulation is a set of stochastic methods that are capable of generating a digital model of sub-surface conditions that reproduces all essential statistical characteristics of the stochastic field. Two types of simulation models are recognized; unconditional models reproduce the correlation structure but do not duplicate observed values at measurement points while conditional models honour both correlation structure and measurements. Therefore, conditional simulation is preferred whenever a reasonable amount of data is available.

Before focusing in detail on the LU Decomposition and Fast Fourier Transform simulation methods that are used in the framework to carry out simulation, *Chapter 4* provided a brief review of simulation methods widely applied in groundwater hydrogeology, including analytical spectral techniques, first and second moment analysis, and Monte Carlo simulation. It was concluded that of these three modelling approaches only Monte-Carlo simulation is sufficiently robust to analyze problems with complex geometries and large input parameter variances.

Having identified Monte-Carlo simulation as the preferred simulation approach, *Chapter 4* then reviewed the advantages and disadvantages of five Monte-Carlo simulation methods, including:

(1) Nearest Neighbour
(2) Analytical Spectral
(3) Fast Fourier Transform
(4) Turning Bands
(5) Lu Matrix Decomposition

A comparison of memory requirements, computational overhead and ease of implementation suggests that LU Matrix Decomposition is the most versatile technique for generating conditional simulations of the type required during the detailed planning stage of dewatering system design. On the other hand the Turning Bands and Fast Fourier Transform methods are very efficient for conducting unconditional simulations during feasibility studies when very little conditioning data is available.

It was shown that verification of simulation results is an important step in the stochastic analysis. In order to consider the results of a Monte Carlo simulation valid, each realization in the ensemble must reproduce the desired mean, variance and semi-variogram model. Furthermore, the variance of the simulated log hydraulic conductivity field at each prediction point should reproduce the expected estimation error, as determined by kriging. A comparison of verification results from identical simulations using the LU Decomposition and FFT simulation methods showed that the FFT method resulted in more accurate simulations; however, both methods provided acceptable results. Furthermore, the verification study showed that the degree to which simulation statistics reproduce the input parameters is dependent on the size of the flow domain in relation to the range and on the grid size used for the simulation. As a rule of thumb, the shortest dimension in the flow domain should always be at least twice as long as the range and the grid size should be smaller than ¼ of range in order to accurately reproduce the desired covariance structure.

The geostatistical methods described in *Chapter 4* can be used at each stage of the pit wall design process, from feasibility study, through site investigation, production, and ultimately to reclamation. Use of the stochastic design approach in preference over the traditional deterministic approach will result in a more realistic dewatering system design, one that tracks the level of uncertainty that is associated with the input parameter estimates and translates the uncertainty into monetary risk. Once known, these risks can the be balanced against the costs of more detailed site characterization in order to identify the most cost effective exploration strategy.

9.1.5 REVIEW AND SUMMARY OF CHAPTER 5 - GROUNDWATER HYDROLOGY

Estimating water pressures in the pit wall is a key step in the RCB framework. *Chapter 5* described *SG-Flow*, the saturated/unsaturated finite element groundwater flow model that was developed as part of this research effort and utilized in the framework to determine the distribution of water pressures that will develop in the pit wall for any dewatering option under consideration.

The discussion in *Chapter 5* first focused on formulation of the boundary value problem, including the governing differential equation, representation of boundary conditions, discretization of the flow domain into triangular elements and the modelling approach used to represent wells and horizontal drains in the numerical model. Because a simpler two dimensional representation of the three dimensional flow system had to be adopted to reduce the computational burden, the representation of wells and horizontal drains was not straightforward. A simple verification study was carried out to ensure that the hydraulic head distributions obtained from the two dimensional cross section model were consistent with the expected head hydraulic response. The verification involved simulation of hydraulic heads in a pie shaped portion of an open pit. A single vertical cross section through the center of the wedge was selected for the analysis. The hydraulic head response predicted by the vertical cross section model was then compared to the Theis solution and to the head response in a two dimensional plan view model of the aquifer. The close similarity between all three piezometric distributions confirmed that the two dimensional cross-section representation is justified provided that geologic conditions are relatively homogeneous in the third dimension.

When modelling groundwater flow in the pit wall, the position of the water table cannot be determined *a priori* and must be determined as part of the solution. The resulting boundary value problem, known as a free surface problem, requires a calculation intensive iterative approach to obtain a solution. Because modelling of the free surface problem is not conducted routinely by most hydrologists, this aspect of the groundwater flow model was discussed in greater detail. The discussion involved a review of the two established solution strategies, including the deforming mesh approach and the saturated/unsaturated approach that was adopted in computer program *SG-Flow*. The saturated/unsaturated approach was selected for use in *SG-Flow* because it is easier to implement in a stochastic framework than the deforming mesh approach since all finite element boundaries remain fixed in space instead of deforming across zones of differing hydraulic conductivity.

Also, it was shown that in the saturated/unsaturated approach hydraulic conductivity in each cell in the unsaturated zone is adjusted as a function of moisture content and negative pore pressure. A sensitivity study was conducted to determine whether the predicted hydraulic head response is sensitive to the shape of the characteristic curve. The study showed that the pore pressure response and the predicted position of the water table are not affected by the shape of the characteristic curve for mine scale groundwater problems where the transition zone from fully saturated to unsaturated conditions is very narrow in comparison to the size of the flow domain.

The pattern of water pressures in the pit wall can be strongly influenced by discrete geologic structures such as a pervious gravel lens or an impervious zone of fault gouge. Because the geologic setting at Highland Valley Copper involved two distinct geologic horizons a geologic overlay feature was incorporated in *SG-Flow* to facilitate incorporation of discrete geologic structures in the stochastic model. The overlay feature is documented in detail in *Chapter 5*. Several hypothetical examples are also presented to demonstrate the importance of geologic conditions on the distribution of water pressures in the pit wall.

Finally, at the time of its development the *SG-Flow* computer model was unique in the integration of a saturated/unsaturated finite element flow model with a stochastic framework. Although it has not been used for this purpose to date, *SG-Flow* could be used to investigate the importance of hydraulic conductivity variability in the unsaturated zone. Also, development of the user friendly graphics interface for this program will provide educators with an ideal tool for demonstrating the concepts of stochastic groundwater flow.

9.1.6 REVIEW AND SUMMARY OF CHAPTER 6 - SLOPE STABILITY

Chapter 6 focused on *Sarma's* two dimensional method of slices that is used in the RCB framework to estimate the probability of failure. Sarma's methodology was selected based on a review of existing slope stability methods in general and two dimensional limit equilibrium algorithms in particular. In the review it was shown that the method of slices problem is statically indeterminate because there are *2n-2* more unknowns then available equilibrium equations. In order to resolve the indeterminacy *2n-2* independent assumptions must be made. It was shown that the various stability algorithms, including the methods of Bishop, Janbu, Morgenstern and Price, Sarma, and Spencer differ in the assumptions made to resolve the indeterminacy.

The *6n-2* limit equilibrium equations, including force equilibrium, moment equilibrium and failure criterion equations common to all methods were then developed from first principles. Also, instead of developing and programming a complex closed form expression for each unknown, it was recognized that the Sarma formulation leads to a set of simultaneous linear equations which can be solved more easily with a linear equation solver such as LU-decomposition.

Sarma's method does not yield FOS directly. Instead an iterative scheme involving progressive reduction of shear strength parameters by the ratio 1/FOS is required to solve for this parameter. Hoek (1986) noted that in some cases the iterative scheme used in his program may converge to the wrong FOS. *Chapter 6* investigated the cause of this instability. It was shown that the iteration instability develops when the true factor of safety is situated close to an asymptote in the FOS vs. K function. Also, the previously unexplained cause of the asymptotic behaviour was shown to be the result of a sudden reversal in the direction of interslice forces from compressive to tensile behaviour. Having established the cause of the instability, a more reliable iteration scheme was developed that converges to the correct FOS in almost all instances.

Because Sarma's method uses all available equations of force and moment equilibrium to determine the unknown slice forces conditions of static equilibrium are always satisfied. However, the calculated results may not be physically acceptable if negative stress conditions are predicted on one or more slice boundaries. In *Chapter 6* the five most common causes of negative effective stresses were identified. They included:

(1) Crest region too strong (tensile crack)
(2) Low groundwater pore pressures at crest.
(3) Excessive strength in the toe region.
(4) Extreme surface roughness.
(5) Slice boundaries not placed in critical orientation.

During the investigation of FOS sensitivity to slice orientation it was determined that the factor of safety is not sensitive to slice orientation. In most cases, a reasonable estimate of FOS can be attained without adjustment of slice side orientations provided that the initial slice geometry is specified such that all slice boundaries are oriented radially or at small positive offset angles (see *Section 6.4.4* for definition of offset angle). In case negative stresses are encountered during the analysis a more critical failure surface with a lower factor of safety can usually be found by logical adjustments to the slice geometry.

Furthermore, to be physically acceptable, the computed point of application of the base normal force N_i must be located somewhere on the slice base, preferably in the middle third. Tall narrow slices and inappropriate orientation of slice boundaries can lead to a physically unacceptable solution. It was discovered that in most cases, moment acceptability is accompanied by development of negative stresses.

In conclusion, the following guidelines should be used when first defining slice geometry:

- Use an adequate number of slices to accurately describe the failure plane and surface topography.
- If possible, orient the slice sides so that all sides have a small positive offset angle. If discontinuities dictate slice orientation check the solution for negative stresses before relying or results.
- Keep slices as thick as possible. Try to maintain a height to width ratio smaller than 2:1; but not at the expense of reduced resolution in the definition of the basal failure surface.

9.1.7 REVIEW AND SUMMARY OF CHAPTER 7 - SENSITIVITY STUDY

After all of the components of RCB framework were completed and verified the model was used in sensitivity mode in order to explore how each set of input parameters, including hydrologic data, shear strength parameters, pit angles and dewatering system specifications impact on the profitability of the mining operation. The objectives of the sensitivity study were:

(1) To demonstrate the application of the RCB methodology to a realistic design problem.
(2) To determine the level of risk reduction as well as operating cost increases associated with flattening for a typical open pit wall.
(3) To investigate how changes in mean hydraulic conductivity, variability in the hydraulic conductivity field and different correlation ranges impact on the economic objective function.
(4) To establish the relative importance of shear strength and hydrologic data on the overall stability assessment.
(5) To demonstrate how the framework was used to determine the most effective dewatering strategy from a small number of alternative designs for the base case geologic scenario.
(6) To examine the importance of number and location of hydrogeologic measurements.

The discussion began with definition of the base case scenario, including geologic conditions, ore grade distribution, digability characteristics, statistics describing the hydraulic conductivity field, boundary conditions on the flow domain, unit operating costs, concentrate prices and the mine development plan. A preliminary stability analysis indicated that a 30° degree pit wall will be unstable unless groundwater control is implemented; therefore, a comprehensive dewatering program involving 25 dewatering wells was incorporated in the base case design. Development and operating costs of the base case dewatering system were estimated between 1.0 and 1.5 million dollars for each 5 year design period during operation of the mine.

The first step in the RCB analysis of base case scenario involved simulation of the hydraulic conductivity field. In total, 100 unconditional realizations were generated from the statistics. The realizations were not conditioned because it was assumed that actual hydraulic conductivity measurements were very limited at the feasibility stage of design.

The second step involved prediction of water pressures in the pit wall for each realization of the hydraulic conductivity field, followed by a slope stability assessment to determine whether each realization resulted in stability or failure. The analysis results indicated that the probability of failure would be 17% during the final pit expansion. The same approach was then used to determine the probability of failure at 5 year intervals as the mine developed. It was determined that the probability of all earlier push-backs would be very low if the base case dewatering program and a 30° slope angle were utilized.

The subsequent economic analysis showed that the base case design would be profitable during each push-back; however, the largest profits would be realized during the first two pit expansions because stripping ratios were low and ore grades high. The economic analysis also showed that a pit wall failure during the final push-back would prove very costly for the mine operator. It was estimated that the costs of such a failure would exceed $300 million.

A sensitivity study was then conducted to investigate whether adjustments of the pit wall angle would improve profitability. Three alternate designs were considered: 20°, 25° and 30°. All three designs did not include dewatering measures. The analysis results showed that the objective function was not sensitive to the slope angle during first push-back from 1990 to 1995. However, with increased slope height the consequences of failure became more significant and marked differences in the objective function were noted when different slope angles were selected. For example, the projections indicated that the mine would attain a cumulative net income of $283 million if a stable 20° slope angle was selected while selection of a 30° would result in unstable pit walls and an operating loss of $129 million over the life of the mine. Finally, results of the aforementioned RCB analyses clearly show that in this case pit dewatering is economically justified.

The next sensitivity study examined the effect of mean hydraulic conductivity on dewatering system performance. It was shown that dewatering wells appear to be effective in a range of hydraulic conductivity from $1x10^{-8}$ m/s to $1x10^{-5}$ m/s. If the average hydraulic conductivity is lower than $1x10^{-8}$ m/s then the soil mass becomes so impervious as to reduce well yields to a trickle and effective depressurization will not be possible. On the other hand, if the average hydraulic conductivity exceeds $1x10^{-5}$ m/s then an extensive drawdown cone will develop and very large quantities of water would have to be pumped in order to achieve adequate drawdown.

A sensitivity study examining the effect of changing the standard deviation of the hydraulic conductivity field revealed that the probability of failure is sensitive to this parameter. As the variability in the hydraulic conductivity field increased the pore pressure response became progressively less predictable. Variability in the pore pressure response lead to more uncertainty in the stability assessment and an increased level of monetary risk due to the tail effect. Therefore, the sensitivity results confirm that hydraulic conductivity measurements that reduce estimation uncertainty will prove most useful in heterogeneous geologic environments.

The objective function response to changes in the correlation range provided results that were similar to the previous sensitivity study. It was found that increases in the range (i.e. increasing the size of individual lenses of high and low hydraulic conductivity) resulted in a less predictable pore pressure response and increased monetary risk. It was determined that individual hydraulic conductivity contrasts begin to affect the flow system once the range exceeds 1/5 of the maximum dimension of the flow domain.

Upon comparing the sensitivity results, it was concluded that mean hydraulic conductivity is by far the most important hydrogeologic parameter. In most cases, time and money for conducting the dewatering design is limited; therefore, site investigation efforts should aim to understand the geologic environment and to obtain representative hydraulic conductivity measurements from each geologic horizon whenever an opportunity arises. Standpipe piezometers should be installed in all exploration drill holes that encounter a significant interval of overburden, except in impervious formations where pneumatic or vibrating wire piezometers should be used in order to obtain a rapid response. Slug tests can then be conducted to determine in-situ hydraulic conductivity. In bedrock, a series of packer permeability tests should be considered after the completion of each exploration borehole.

The next stage of the sensitivity analysis focused on shear strength parameters. Upon evaluating the stability of the base case scenario over a full range of friction angles it was discovered that the probability of failure jumped from 0 to 100% quickly as ϕ increased from 28° to 30°. The economic objective function exhibited a similar response. Given the large economic consequences of failure, it is essential to establish the mean friction angle accurately by repeated laboratory testing. Friction angle estimates based on geology are not adequate.

Perturbation of mean cohesive strength over the full range of possible values from 0 to 200 kN/m^2 while holding ϕ constant at 30° revealed that probability of failure for the base case scenario was very sensitive to mean cohesion. Only a slight increase in cohesion was required to fully stabilize the pit wall and reduce the probability of failure to zero.

After evaluating and comparing the large number of sensitivity results it was concluded in *Chapter 7* that accurate and abundant hydrogeologic and shear strength measurements could reduce the monetary risk of failure of the ultimate pit wall. In the particular case analyzed, hydraulic conductivity data appeared to be twice as effective as shear strength data in reducing the dispersion in the factor of safety distribution (i.e. reducing the tail effect). This trend was attributed to strong spatial correlation of the hydraulic conductivity field which resulted in large variability in the predicted pore pressure response. In geologic environments where geology is correlated over shorter distances, hydrogeologic and shear strength data are expected to be equally effective in reducing uncertainty in the stability assessment. Furthermore, the risk reduction effect of a fraction perturbation of the friction angle was approximately equal to the risk reduction effect of an equivalent perturbation in cohesive strength; however, in the general case the relative importance of these two strength parameters will depend on the size of the failure and on pore pressure conditions. Cohesion contributes less to overall strength when a slide is very large and/or when drained conditions prevail.

Having established the importance of hydrologic and shear strength parameters in design, the next sensitivity study demonstrated that the RCB framework could identify the optimum dewatering strategy. The study involved repeated analysis of the base case scenario, except that the number of dewatering wells was progressively increased from 0 to 40. During the study, the largest reductions in pore pressure were achieved by the first few wells. Thereafter, progressively steeper hydraulic gradients were established and pumping requirements rapidly increased. A point of diminished returns was reached when the cost of the groundwater control system reached $5.4 million and started to exceed the marginal increases in expected net income. These results suggest that a low budget dewatering program is likely to provide significant economic returns with minimum risk; however, a detailed study would be required to identify the optimum level of capital expenditures for groundwater control.

Use of steeper pit walls during early push-backs was also investigated in the sensitivity study. It was concluded that increasing the slope angle during early push-backs would be beneficial because it would result in increased cash flow during the first 15 years of mine operation.

The importance of hydraulic conductivity measurements on design was the final theme of the sensitivity study. In the first part of this study unconditional simulation was used to generate a correlated hydraulic conductivity field which was then used to represent the unknown geologic environment. The complete RCB analysis was then conducted with three different levels of site investigation effort. The results showed that increased sampling lead to reduced uncertainty in hydraulic head estimates, which in turn lead to less variability in hydraulic head predictions and ultimately, a significant tightening in the FOS distribution. By increasing the engineer's confidence in the performance of the dewatering system and pit wall design due to the tail effect, sampling would permit him to adopt a less conservative design approach. Also, if measurements were to indicate that conditions were much better or much worse than expected the stability analysis would automatically reflect this through a corresponding reduction or increase in the probability of failure. Design modifications would then be required to achieve an optimum design.

In summary, the sensitivity study in *Chapter 7* demonstrated that the RCB framework can be used effectively to identify the most effective dewatering strategy given a limited amount of geologic and hydrologic information. It was also shown that the framework can be used to identify the most important input parameters for each specific dewatering problem and to establish the approximate monetary worth of data collection.

9.8 REVIEW AND SUMMARY OF CHAPTER 8 - CASE HISTORY

In the final thrust of this research effort the newly developed risk-cost-benefit framework was used to evaluate several dewatering strategies in design sector R3 at the recently opened Valley Pit, operated by Highland Valley Copper. The objective of this case history study was to demonstrate the steps involved in the practical application of the various analysis steps presented in this dissertation to a real design problem. The case history is not a design study; additional geotechnical analysis, including analysis of the full spectrum of failure modes and transient groundwater flow modelling will be required before the results of this RCB framework can be used with confidence to justify modifications to the current slope design and dewatering plan.

To achieve the aforementioned objective, *Chapter 8* provided a complete description of the case history study. The discussion began with a thorough review of site conditions, including regional topography, mine lay-out, and a brief overview of HVC's groundwater control program. A comprehensive dewatering program is required in the Valley Pit because the north half of the pit will be excavated through a 200 m thick sequence of overburden material that includes several saturated aquifer horizons.

The latest interpretation of bedrock and overburden stratigraphy was presented with the aid of several geologic cross sections. The overburden geology was shown to consist of the distinct sequences; an upper sequence of thinly layered aquifer and aquitard horizons, and a lower sequence of less pervious silty clay. The geologic interpretation was followed by detailed review of hydrologic conditions at the site. The review outlined the numerous techniques that were adopted to achieve a complete and accurate stochastic description of the hydraulic conductivity distribution at HVC. The hydraulic conductivity data base included:

- short term pump tests
- long term well response
- laboratory triaxial tests
- grain size analyses
- empirical correlations to geologic information

The data indicated that in the upper sequence the mean log hydraulic conductivity is -5.5 (3×10^{-6} m/s) with a standard deviation of 0.75. The correlation structure was shown to be strongly anisotropic, with a range of 1000 m in the horizontal direction and approximately 50 m in the vertical direction. In the lower sequence the mean log hydraulic conductivity is -9.5 (3×10^{-10} m/s) with a standard deviation of 0.75. Because the number of available measurements were not sufficient to determine the correlation structure in the lower sequence, the correlation statistics from the upper sequence were adopted for analysis.

Next, a simple regional aquifer model was used to identify the appropriate boundary conditions for the stochastic groundwater flow analysis. The regional aquifer model was used to determine the maximum extent of the drawdown cone around the pit once all wells become operational and to determine the steady state recharge fluxes across the aquifer boundaries. The model response confirmed that a recharge flux of 8.0×10^{-7} m/s identified during an earlier water budget analysis is realistic.

Having compiled all of the geologic and hydrologic data, HVC's current pit design and dewatering strategy was presented to provide a base case scenario for the risk-cost-benefit analysis. The strategy included an overall slope angle of 31°, full utilization of all existing dewatering wells and development of 36 new dewatering wells at an estimated budget of $4.6 million.

The RCB analysis of the base case scenario began with geostatistical simulation of the hydraulic conductivity field. In total, 100 conditional realizations of the hydraulic conductivity field were generated from statistics using computer model SG-STAT. The simulation results showed that hydraulic conductivity measurements were effective in reducing estimation uncertainty over much of the flow domain. The realizations compared favourably with the geologic interpretation of subsurface conditions. The model was able to duplicate the hydraulic conductivity contrast between the upper and lower sequence, the natural variability within each sequence, the horizontal layering, and the continuity of lenses in both horizontal and vertical directions.

Computer model *SG-Flow* was then used to calculate the hydraulic head distribution in the pit wall for December, 1987. Because the predicted head distribution compared favourably with actual hydraulic heads as observed in the monitoring network, it was concluded that the groundwater model appears to provide reasonable predictions in the short term.

SG-Flow was then used to predict the pore pressure distribution in the pit wall at 5 year intervals over the life of the mine using HVC's current dewatering strategy. The simulation results showed that the wells will be effective in dewatering the upper sequence, in fact a lesser number of wells may suffice to maintain the upper sequence dewatered beyond 1992. Detailed monitoring and a three dimensional transient aquifer model were recommended to confirm that a dewatering scheme with fewer wells would be capable of meeting long term dewatering objectives. The groundwater flow model indicated that pore pressures in the lower sequence will remain high, perhaps as much as 40 m above hydrostatic in the area of the basal failure surface.

A stability analysis of HVC's current slope design and dewatering strategy indicated that the pit wall in sector R-3 will be very stable until 1997, at which time stability will begin to deteriorate rapidly. An analysis of the ultimate pit wall configuration indicated that as designed the ultimate pit wall configuration will be unstable with a mean factor of safety of 0.55 and a probability of failure of 100%. The apparent instability of the ultimate pit wall was attributed to four factors:

- Over-steepening of the toe area as a result of changes in the projected depth to bedrock.
- Relatively low shear strength of unit 10B.
- Very high pore pressures in the lower silt and clay sequence.
- A reduction in the relative importance of cohesive shear strength with depth, due to the dominating role of frictional resistance as confining stresses increase.

The economic component of the risk-cost-benefit analysis for the base case scenario revealed that mining activity in design sector R3 should be profitable, resulting in an estimated cumulative net income of $183 million over the life of the mine. It was predicted that a possible failure of the ultimate pit wall will pose the greatest monetary risk, estimated at $46.2 million.

Because the base case design for the ultimate pit wall appeared to be unstable, three alternative design strategies were proposed and evaluated with the risk-cost-benefit framework to determine which strategy would lead to maximum expected profitability for HVC. The design alternatives that were considered included:

(1) Dewatering the toe area with horizontal drains while maintaining the current pit profile.
(2) Reducing the overall slope angle to 26° without additional drainage provisions.
(3) Implementing both a reduction in slope angle and additional dewatering measures.

It was determined that dewatering would reduce the probability of failure to 67%, flattening of the slope would reduce the probability of failure to 30% and adopting both stabilizing measures would result in an approximate 0% probability of failure. The economic suitability of the alternate designs was evaluated by comparing the corresponding expected net income projections. The RCB analysis showed that of the three design strategies considered, flattening of the pit wall to 26°, in combination with a horizontal drain drilling program in the toe area of the slope will result in the most profitable mining approach, provide that the drains will be capable of effectively depressurizing the lower sequence in advance of mine development. More detailed hydrologic investigations will be required to confirm that the proposed drainage strategy is technically feasible.

In summary, the findings of this case history study suggest that there is potential for improving slope stability and increasing profitability in design sector R3 through flattening of the slope and increased groundwater control efforts. Based on the results of this RCB analysis a number of specific actions were recommended. They included a re-evaluation of geologic data, additional shear strength testing, more detailed investigation of the horizontal drainage concept and expansion of the RCB framework to other designs sectors. Details were provided in *Section 8.10* of this dissertation.

9.2 SUMMARY OF PRINCIPAL ASSUMPTIONS

Although the risk-cost-benefit framework that is documented in this dissertation is believed to be applicable to a wide variety of groundwater control problems in open pit mines, the specific conclusions and results that are reported in the sensitivity and case history chapters are based on several assumptions that influenced the outcome of the groundwater flow, slope stability and economic analyses. The more important of these assumptions are summarized below:

- The hydraulic conductivity field is assumed to be log-normally distributed and spatially autocorrelated.
- The variability in pore pressures in the pit wall is due only to uncertainty in the hydraulic conductivity field. Boundary conditions are assumed to be known exactly.
- The three dimensional groundwater flow problem is assumed to be accurately represented by an equivalent two dimensional vertical cross section model.
- In the model, dewatering wells are represented as vertical columns of nodes for which a constant discharge flux is specified, horizontal drains are represented as horizontal rows of finite elements with increased hydraulic conductivity.
- Steady state pore pressure distributions for each pumping configuration predicted by the model are assumed to be representative of long term pore pressure conditions in the pit wall.
- Any potential slope failures are assumed to develop along a critical failure surface. The critical failure surface is identified as the surface that yields the lowest factor of safety in a deterministic stability analysis using mean values of all shear strength and hydrologic parameters.
- The critical acceleration coefficient K_c determined by Sarma's two dimensional limit equilibrium method of slices is used as an indicator of stability for each realization.
- Shear strength parameters are assumed to be normally distributed, spatially uncorrelated, and monotonic for each slice boundary.
- Long term, strength parameters, reported in terms of effective stress, are utilized in the stability analyses for the case history study. Short term undrained strength parameters that exhibit a significant cohesive component due to the dilatant nature of the soils at HVC are not used in the analyses because they are not considered representative of long term stability.
- An expected value approach is adopted in selecting the most appropriate design.
- Because the rate of inflation has been set equal to the interest rate in both the sensitivity and case history studies, future net earnings have not been discounted. However, the framework is general in that it can analyze any combination of inflation and interest rates and these rates can change during each design period.
- External constraints and penalties, e.g. regulations concerning maximum water level drawdowns, maximum slope angles in the pit, contractual obligations regarding production, etc. have not been considered.

- The economic consequences of a slope failure have been limited solely to the costs of removing the failed material from the pit. Other costs, that may include penalties for lost production, costs of re-establishing haul roads and other infrastructure, and additional interest on loans, have not been considered.

- Loss of human life, and the impact that this risk would have on decision making has not been incorporated in the framework because it is believed that modern slope monitoring methods should provide sufficient warning for mine operators to clear the pit prior to a large failure occurring.

In summary, some of the assumptions will lead to underestimates of the monetary risk associated with a slope failure, others will lead to overestimates. The assumptions have been made to limit the complexity of the analysis and to focus on the key issue at hand, determining the worth of groundwater control in open pit mines. However, it is important to emphasize that the framework presented in this dissertation is general, each of the above assumptions can be removed or improved upon within the framework as required for each site specific study.

LIST OF SELECTED REFERENCES

Alabert, F., *The Practice of Fast Conditional Simulations Through the LU Decomposition of the Covariance Matrix*, Mathematical Geology, Vol. 19, No. 5, 1987, pp. 369-387.

ASCE Task Committee on Geostatistical Techniques in Geohydrology of the Groundwater Hyrology Committee of the ASCE Hydraulics Division, *Review of Geostatistics in Geohydrology, 1: Basic Concepts*, Journal of Hydraulic Engineering, Volume 116, No. 5, May 1990, pp. 612-631.

ASCE Task Committee on Geostatistical Techniques in Geohydrology of the Groundwater Hydrology Committee of the ASCE Hydraulics Division, *Review of Geostatistics in Geohydrology, II: Applications*, Journal of Hydraulic Engineering, Volume 116, No. 5, May 1990, pp. 632-658.

Baecher, G.B.M.E. Pate and R. de Neufville, *Risk of Dam Failure in Benefit-Cost Analysis* Water Resources Research, Vol. 16, No. 3, 1980, pp. 449-456

Bakr, A.A., L.W. Gelhar, A.L. Gutjahr and J.R. MacMillan, *Stochastic Analysis of Spatial Variability in Subsurface Flows: 1, Comparison of One and Three Dimensional Flows*, Water Resources Research, Vol. 14, No. 2, 1978, pp. 263-271.

Barnsley, M.F. et al. *The Science of Fractal Images*, H.O. Peitgen and D. Saupe, Editors, Springer-Verlag, New York, 1988

Bishop, A.W., *The Use of the Slip Circle in the Stability Analysis of Slopes,* Geotechnique, Vol. 5, 1955, pp. 7-17

Bishop, A.W. and N.R. Morgenstern, *Stability Coefficients for Earth Slopes*, Geotechnique, Vol. 10, 1960, pp. 129-147

Brawner, C.O. *Stabilization of Rock Slopes*, Proceedings of the Third International Conference on Stability in Surface Mining Vancouver, 1981, pp. 289-310

Cavers, D.S., *Simple Methods to Analyze Buckling of Rock Slopes*, Rock Mechanics, Vol. 14, 1981, pp. 87-104

Clifton, P. M. and S.P. Neuman, *Effects of Kriging and Inverse Modelling on Conditional Simulation of the Avra Valley Aquifer in Southern Arizona*, Water Resources Research, Vol. 18, No. 4, 1982, pp. 1215-1234.

Dagan, G. *Stochastic Modelling of Groundwater Flow by Unconditional and Conditional Probabilities, 1, Conditional Simulation and the Direct Problem*, Water Resources Research, Vol. 18, No. 4, 1982, pp. 813-833.

Dagan, G. *Stochastic Modelling of Groundwater Flow by Unconditional and Conditional Probabilities, 2, The Inverse Problem*, Water Resources Research, Vol. 21, No. 1, 1985, pp. 65-72.

Davis, M.W. *Production of Conditional Simulations via the LU Triangular Decomposition of the Covariance Matrix*, Mathematical Geology, Vol. 19, No. 2, 1987, pp. 90-99.

De Marsily, G. *Spatial Variability of Properties in Porous Media: A Stochastic Approach*, in Fundamentals of Transport Phenomena in Porous Media, NATO ASI Series, J. Bear & M.Y. Corapcioglu, Editors, Martinus Nijhoff, Boston, 1984, pp. 719-769.

De Marsily, G. *Quantitative Hydrogeology - Groundwater Hydrogeology for Engineers*, Academic Press Inc., Toronto, 1986, pp. 284-337.

Delhomme, J.P. *Kriging in the Hydrosciences*, in Flow Through Porous Media - Recent Developments, G.F. Pinder, Editor, C.M.L. Publications, London, 1983.

Delhomme, J.P. *Spatial Variability and Uncertainty in Groundwater Flow Parameters, A Geostatistical Approach*, Water Resources Research, Vol. 15, No. 2, 1979, pp. 269-280.

Dettinger, M.D. and J.L. Wilson, *First Order Analysis of Uncertainty in Numerical Models of Groundwater Flow, 1, Mathematical Development*, Water Resources Research, Vol. 17, No. 1, 1981, pp 149-161.

Feinerman, E., G. Dagan and E. Bresler *Statistical Inference of Spatial Random Functions*, Water Resources Research, Vol. 22, No. 6, 1986, pp. 935-942.

Fellenius, W., *Calculation of the Stability of Earth Dams*, Transceedings of the 2nd Congress on Large Dams, Vol. 4, 1936, pp. 445

Finn, W.D.L., *Finite-Element Analysis of Seepage through Earth Dams*, Journal of the Soil Mechanics and Foundations Division, ASCE Vol 96, No. SM6, 1967, pp. 41-62

Fournier, A., D. Fussel and L. Capenter *Computer Rendering of Stochastic Models*, in Graphics and Image Processing, James Foley, Editor, Association for Computing Machinery, 1982, pp. 371-

Fredlund, D.G., *Slope Stability Usage In Canada, Proceedings of Specialty Session 12, Computer Analysis of Soil Mechanics, Present and Future*, International Conference on Soil Mechanics and Foundation Engineering, Tokyo, Japan, July 1977.

Fredlund, D.G. and Krahn, J., *Comparisons of Slope Stabilty Methods of Analysis,* Canadian Geotechnical Journal, Volume 14, No. 3, pp. 429-439, 1977.

Fredlund, D.G., *Usage Requirements and Features of Slope Stability Computer Software,* Canadian Geotechnical Journal , Volume 15, No. 1, pp. 83-95, 1978.

Fredlund, D.G., Krahn, J. and Pufahl, D.E., *The Relationship Between Limit Equilibrium Slope Stability Methods*, International Conference on Soil Mechanics and Foundation Engineering , Volume 3, Stockholm, Sweden, June 1981. pp. 409-416.

Fredlund, D.G., *Slope II Slope Stability User's Manual, S-20,* Geo-Slope Programming Limited, Calgary, Alberta, 1983. 840 pp.

Freeze, R.A., *A Stochastic Conceptual Analysis of One-Dimensional Groundwater Flow in Nonuniform Homogenous Media*, Water Resources Research, Vol. 11, No.5, 1975, pp. 725-741.

Freeze, R.A., J. Massmann, L. Smith, T. Sperling and B. James, *Hydrogeological Decision Analysis, 1. A Framework*, Groundwater, Vol. 28, 1990, pp. 738-766.

Gelhar, L.W., *Effects of Hydraulic Conductivity Variations on Groundwater Flows*. Paper presented at the 2nd International Symposium on Stochastic Hydraulics, International Association of Hydraulic Research, Lund, Sweden, 1976.

Gelhar, L.W., A.L. Gutjahr and R.L. Naff, *Stochastic Analysis of Macrodispersion in a Stratified Aquifer*, Water Resources Research, Vol. 15, No. 6, 1979, pp. 1387-1397.

Gelhar, L.W. *Stochastic Analysis of Flow in Heterogeneous Porous Media,* in Fundamentals of Transport Phenomena in Porous Media, NATO ASI Series, J. Bear & M.Y. Corapcioglu, Editors, Martinus Nijhoff, Boston, 1984, pp. 675-717

Golub G.H. and C.F. Van Loan *Matrix Computations*, John Hopkins University Press, Baltimore, 1984, pp. 87-93

Gutjahr, A.L., L.W. Gelhar, Bakr, A.A., J.R. MacMillan, *Stochastic Analysis of Spatial Variability in Subsurface Flows: 2, Evaluation and Applications*, Water Resources Research, Vol. 14, No. 5, 1978, pp. 953-959.

Hoek, E. and J.W. Bray, *Rock Slope Engineering*, The Institution of Mining and Metallurgy, London, 1981.

Hoek, E., *General Two-Dimensional Slope Stability Analysis*, Analytical and Numerical Methods in Rock Engineering E.T. Brown, Ed. George Allen and Unwin, London, 1986

Janbu, N., *Earth Pressures and Bearing Capacity Calculations by Generalized Procedures of Slices*, Proceedings of the Fourth International Conference on Soil Mechanics and Foundation Engineering, Vol. 2, 1957, pp. 207-212

Journel, A.G. and CH. J. Huijbregts, *Mining Geostatistics*, Academic Press, San Francisco, Ca., 1978.

Journel, A.G., *Geostatistics for Conditional Simulations of Ore Bodies*, Economic Geology, Vol. 69, No. 5, 1974, pp. 673-687.

Kitanidis, P.K. and Lane, R.W., *Maximum Likelihood Parameter Estimation of Hydrologic Spatial Processes by the Gauss-Newton Method*, Journal of Hydrology, Volume 79, 1985, pp. 53-71.

Kitanidis, P.K., *Statistical Estimation of Polynomial Generalized Covariance Functions and Hydrologic Applications*, Water Resources Research, Volume 19, No. 4, 1983, pp. 909-921.

Krahn, J., Fredlund, D.G. and Klassen, M.J., *Effect of Soil Suction on Slope Stability at Notch Hill*, Canadian Geotechnical Journal, Volume 26, January 3, 1989, pp. 269-278.

Krahn, J, D.G. Fredlund, L. Lam, and S.L. Barbour, *PC-Seep: A Finite Element Program for Modelling Seepage*, 1st Canadian Symposium on Microcomputer Applications in Geotechnique, Regina, Sask., 1987, pp. 243-251.

Lewis, J.P. *Generalized Stochastic Subdivision*, Association for Computing Machinery Transactions on Graphics, Vol. 6, 1987, pp. 167-190

Mantoglou, A. and J.L. Wilson, *The Turning Bands Method for Simulation of Random Fields Using Line Generation by a Spectral Method*, Water Resources Research, Vol. 18, No. 5, 1982, pp. 1379-1384.

Massman, J. and R.A. Freeze, *Groundwater Contamination from Waste Management Sites: The Interaction Between Risk-Based Engineering Design and Regulatory Policy*, Water Resources Research, Vol. 23, No. 2, 1987, pp. 351-367

Massmann, J. and R.A. Freeze, *Groundwater Contamination from Waste Management Sites: The Interaction Between Risk-Based Engineering Design and Regulatory Policy, 2. Results,* Water Resources Research, Vol. 23, 1987, pp. 368-380

Massman, J. R.A. Freeze, L. Smith, T. Sperling and B. James, *Hydrogeological Decision Analysis, 2. Applications to Groundwater Contamination*, Ground Water, in press.

Matheron, G., *The Theory of Regionalized Variables and its Applications*, Ecole des Mines, Fontainebleu, France, 1971.

Matheron, G., *The Intrinsic Random Functions and their Applications*, Advanced Applied Probability, Vol. 5, 1973, 438-468.

Matheron, G. & G. de Marsily, *Is Transport in Porous Media Always Diffusive? A Counterexample,* Water Resources Research, Vol. 16, No. 5, 1980, pp. 901-917.

Matheron, G., *Eléments pour une Théorie des Millieux Poreux,* Masson et Cie, Paris, 1967.

Miller, V.J., *The Northeast Tripp Slide - A 11.7 Million Cubic Meter Wedge Failure at Kennecott's Nevada Mining Division*, Proceedings of the Third International Conference on Stability in Surface Mining Vancouver, 1981, pp. 725-743

Morgenstern, N.R. and V.E. Price, *The Analysis of the Stability of General Slip Surfaces*, Geotechnique, Vol. 15, No. 1, 1965, pp. 79-93

Neuman, S.P., *Saturated-Unsaturated Seepage by Finite Elements*, Journal of the Hydraulics Division, ASCE Vol. 99, No. HY12, 1973, pp. 2233-2250

Neuman, S.P. and S. Yakowitz, *A Statistical Approach to the Inverse Problem of Aquifer Hydrology, 1, Theory*, Water Resources Research, Vol. 15, No. 4, 1979, pp. 845-860

Neuman, S.P. and P.A. Witherspoon, *Finite Element Method of Analyzing Steady State Seepage with a Free Surface,* Water Resources Research, Vol. 6, No. 3, June 1970, pp. 889-897

Neuman, S.P., G.E. Fogg and E.A. Jacobson, *A Statistical Approach to the Inverse Problem of Aquifer Hydrology, 2, Case Study*, Water Resources Research, Vol. 16, No. 1, 1980, pp. 32-58

Neuman, S.P. *Statistical Characterization of Aquifer Heterogeneity, An Overview*, in Recent Trends in Hydrogeology, Geological Society of Amperica Special Paper No. 184, 1982, pp. 81-102.

Neuman, S.P. *A Statistical Approach to the Inverse Problem of Aquifer Hydrology, 3, Improved Solution Method and Added Perspective*, Water Resources Research, Vol. 16, No. 2, 1980, pp. 331-346.

Press, W.H. et. al. *Numerical Recipes, the Art of Scientific Computing*, Cambridge University Press, New York, 1986

Sarma, S.A., *Stability Analysis of Embankments and Slopes*, Journal of the Geotechnical Engineering Division, ASCE 105, No. GT12, 1979, pp. 1511-1524

Russo, D. and Jury, W.A., *A Theoretical Study of the Estimation of the Correlation Scale in Spatially Variable Fields, 1: Stationary Fields*, Water Resources Research, Volume 23, No. 7, July 1987, pp. 1257-1268.

Russo, D. and Jury, W.A., *A Theoretical Study of the Estimation of the Correlation Scale in Spatially Variable Fields, 2: Nonstationary Fields*, Water Resources Research, Volume 23, No. 7, July 1987, pp. 1269-1279.

Savely, J.P. and V.L. Kastner, *Slope Instability at Inspiration's Mines*, Proceedings of the Third International Conference on Stability in Surface Mining, Vancouver, 1981, pp. 609-634

Schwartz, F.W. *Macroscopic Dispersion Dispersion in Porous Media: The Controlling Factors*, Water Resources Research, Vol. 13, No. 4, 1977, pp. 743-752.

Schwydler, M.I., *Flow in Heterogeneous Media* (in Russian) Izv. Akad. Nauk SSSR. Mekh., Vol. 3, No. 185, 1962

Smith, L. and R.A. Freeze, *Stochastic Analysis of Steady State Groundwater Flow in a Bounded Domain, 1, One Dimensional Simulations*, Water Resources Research, Vol. 15, No. 3, 1979, pp. 521-528.

Smith L. F.W. Schwartz, *Mass Transport, 3 Role of Hydraulic Conductivity Data in Prediction*, Water Resources Research, Vol. 17, No. 5, 1981b, pp. 1463-1479.

Smith, L. and R.A. Freeze, *Stochastic Analysis of Steady State Groundwater Flow in a Bounded Domain, 2, Two Dimensional Simulations*, Water Resources Research, Vol. 15, No. 6, 1979, pp. 1543-1559.

Smith L. F.W. Schwartz, *Mass Transport, 2 Analysis of Uncertainty in Prediction*, Water Resources Research, Vol. 17, No. 2, 1981a, pp. 351-369.

Smith, L., *Stochastic Models of Fluid Flow in Heterogeneous Media*, in I.S.S.S. Workshop on Spatial Variability, Las Vegas, 1984.

Spencer, E., *A Method of Analysis of the Stability of Embankments Assuming Parallel Interslice Forces*, Geotechnique, Vol. 17, 1967, pp. 11-26

Sperling T., W.K. Munro and R.A. Freeze, *Dewatering the Overburden at Highland Valley Copper*, 41st Canadian Geotechnical Conference, Kitchener, Ont. 1988, pp. 272-280

Sperling, T. and R.A. Freeze, *A Risk-Cost-Benefit Framework for the Design of Dewatering Systems in Open Pit Mines*, 28th US Symposium on Rock Mechanics, Tucson, Az., 1987, pp. 999-1007

Sperling, T., *Using Risk-Cost-Benefit Analysis to Design a Dewatering System at Highland Valley Copper*, 43rd Canadian Geotechnical Conference, Quebec City, 1990

Sperling, T. and S. Brennan, *Overburden Dewatering Strategy for the Valley Pit, 1988 to 1994*, Highland Valley Copper Internal Report HV88-R2, 1988

Stewart, R.M. and B.A. Kennedy, *The Role of Slope Stability in the Economics, Design and Operation of Open Pit Mines*, Proceedings of the First International Conference on Stability in Open Pit Mining Vancouver, 1970, pp. 5-21

Strang, G., *Linear Algebra and its Applications*, Academic Press, New York, 1980, pp. 249-253

Terzaghi, K., *Mechanism of Landslides Engineering Geology*, (Berkey) Volume - The Geological Society of America, 1950, pp. 83-123

Wagner, B.J. and Gorelick, S.M., *Reliable Aquifer Remediation in the Presence of Spatially Variable Hydraulic Conductivity*: From Data to Design, Water Resources Research, Volume 25, No. 10, October 1989, pp. 2211-2225.

Wagner, B.J. and Gorelick, S.M., *Optimal Groundwater Quality Management Under Parameter Uncertainty*, Water Resources Research, Volume 23, No. 7, July 1987, pp. 1162-1174.

Warren, J.E. and F.F. Skiba, *Macroscopic Dispersion*, Transactions of the Society of Petroleum Engineers, AIME., Vol. 231, 1964, pp. 215-230.

Warren, J.E. and H.S. Price, *Flow in Heterogeneous Porous Media,* Society of Petroleum Engineering Journal Vol. 1, No. 3, 1961, pp. 153-169

Whitman, R.V., *Evaluating Calculated Risk in Geotechnical Engineering,* Journal of the Geotechnical Engineering Division, ASCE 110, No. 2, 1984, pp. 145-189

Wright, S.G., Kulhawy, F.H. and Duncan, J.M., *Accuracy of Equilibrium Slope Stabilty Analysis*, Journal of the Soil Mechanics and Foundation Division, ASCE, Volume 99, No. SM10, October 1973, pp. 783-790.

APPENDIX A KRIGING EQUATIONS

This appendix presents a derivation of the kriging equations, a system of linear equations that is used to assign optimal kriging weights λ_i to each measured hydraulic conductivity value z_i that will result in the best linear unbiased estimate *(BLUE)* of the true hydraulic conductivity $Z(X_m)$ over a chosen estimation volume V_m. The kriging estimator $Z^*(X_m)$ is expressed as a weighted sumation of nearby measurements:

$$Z^*(X_m) = \sum_{i=1}^{imax} \lambda_i \cdot z(x_i) \qquad \textit{Equation A.1}$$

Equation A.1 clearly satisfies the *linearity* condition in that $Z^*(X_m)$ is a linear combination of measured values. The remainder of this appendix will examine the mathematical relations that ensure that $Z^*(X_m)$ is also *unbiased* and *best* (in terms of minimum estimation variance). Prior to developing the kriging equations it is necessary to establish some of the fundamental underlying assumptions on which the theory of kriging has been established.

A.1 UNDERLYING ASSUMPTIONS

Before kriging can be applied to the prediction of population characteristics from a limited sample it is necessary to make some assumptions about the statistical properties that describe the variability of the population. Several kriging techniques have evolved in the mining industry, each technique adopting a different set of statistical assumptions. Possible assumptions include:

Stationarity: assumes that all statistical properties, including mean, variance, covariance, and higher order moments are stationary in space.

Weak Stationarity: assumes that only the first two moments are stationary; that the mean of the hydraulic conductivity field is constant and independent of location $\boldsymbol{x}$:

$$E[Z(x)]=m \qquad \textit{Equation A.2}$$

and that the covariance of points $\boldsymbol{x}$ and $\boldsymbol{x+h}$ is dependent only on the separation vector $\boldsymbol{h}$ (both distance and direction), not on the location $\boldsymbol{x}$.

$$C(h)=E[Z(x)\cdot Z(x+h)]-m^2 \qquad \textit{Equation A.3}$$

Weak stationarity is also refered to as *second order stationarity.*

Intrinsic Hypothesis: is a set of assumptions that is less stringent than weak stationarity. As illustrated in *Figure A.1*, the hypothesis was developed to analyze field problems where variability continues to increase with increasing size of the sampling domain and a finite variance $C[0]$ (or *sill*) cannot be defined over the maximum size of the domain sampled. Under the intrinsic hypothesis it is assumed that the variance of first order increments (the differences $[Z(x+h)-Z(x)]$) is finite and the increments themselves are second order stationary, with mean and variance being functions of $\boldsymbol{h}$ only:

$$E[Z(x+\boldsymbol{h})-Z(x)]=m(\boldsymbol{h}) \qquad \textit{Equation A.4}$$

$$VAR[Z(x+\boldsymbol{h})-Z(x)]=2\gamma(\boldsymbol{h}) \qquad \textit{Equation A.5}$$

Equation A.5 indicates that kriging equations based on the intrinsic hypothesis have the advantage that they can be applied to field problems where the covariance does not exist at the size of the sampling domain, but the variorgram can still be evaluated at any lag $\boldsymbol{h}$ even if $C[0]$ cannot be defined. This advantage of the intrinsic hypothesis is illustrated in *Figure A.2*.

Figure A.1 Increasing Variogram

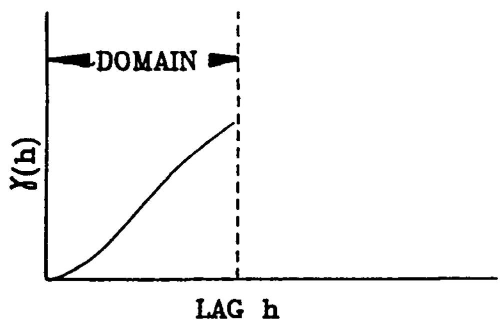

Figure A.2 Scale Dependent Covariance Function

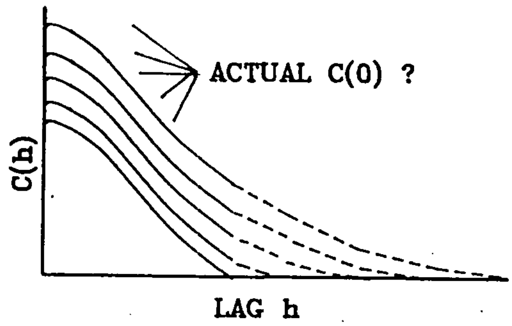

A.2 POSITIVE DEFINITE CONDITIONS

In *Section 5.4* it was shown that kriging estimates of the true value of log hydraulic conductivity are based on a weighted linear combination of supporting measurements. To be physically acceptable, the estimates must have an estimation variance that is greater than or equal to *0*. In this section it will be shown that estimation variances that are ≥ 0 can be achieved only if the covariance function, $C[h]$, is positive definite. In the case that the log hydraulic conductivity field is intrinsic only and $C[0]$ cannot be defined, then the negative variogram function, $-\gamma[h]$, must be conditionally positive definite.

Given that $Z(x)$ is a *2nd order stationary* log hydraulic conductivity field to be estimated, and the estimator $Y(x)$ consists of a weighted linear combination of available data $z(x_i)$:

$$Y(x) = \sum_{i=1}^{I} \lambda_i \bullet z(x_i) \qquad \textit{Equation A.6}$$

If $Y(x)$ is to be physically acceptable:

$$VAR[Y(x)] = E[\{Y - m_y\} \bullet \{Y - m_y\}] \geq 0 \qquad \textit{Equation A.7}$$

Since $Z(x)$ is stationary, the expectation m_y is given by:

$$m_y = E[Y(x)] = E[\sum_{i=1}^{I} \lambda_i \bullet z(x_i)] = \sum_{i=1}^{I} \lambda_i \bullet m \qquad \textit{Equation A.8}$$

Substituting *Equation A.6* for $Y(x)$ and *Equation A.8* for m_y yields:

$$VAR[Y(x)] = E[\{\sum_{i=1}^{I} \lambda_i \bullet z(x_i) - \sum_{i=1}^{I} \lambda_i \bullet m\} \bullet \{\sum_{i=1}^{I} \lambda_i \bullet z(x_i) - \sum_{i=1}^{I} \lambda_i \bullet m\}] \qquad \textit{Equation A.9}$$

On evaluating the product of the two braces and simplifying:

$$VAR[Y(x)] = E[\sum_{i=1}^{I}\sum_{j=1}^{I} \lambda_i \lambda_j \cdot \{z(x_i) \cdot z(x_j) - z(x_i) \cdot m - z(x_j) \cdot m + m^2\}] \qquad \textit{Equation A.10}$$

Since $Z(x)$ is second order stationary, the expectation $E[z(x_i)]$ is equal to m.

$$VAR[Y(x)] = \sum_{i=1}^{I}\sum_{j=1}^{I} \lambda_i \lambda_j \cdot E[z(x_i) \cdot z(x_j) - m^2] \qquad \textit{Equation A.11}$$

Upon recognizing that the expectation in *Equation 5.11* is the definition of the covariance $C[x_i, x_j]$ the definition of a *positive definite* covariance function is obtained:

$$VAR[Y(x)] = \sum_{i=1}^{I}\sum_{j=1}^{I} \lambda_i \lambda_j \cdot C[x_i, x_j] \geq 0 \qquad \textit{Equation A.12}$$

In the case that the log hydraulic conductivity field is intrinsic only and the covariance function $C[h]$ cannot be defined, *Equation 5.12* must be expressed in terms of the variogram:

$$VAR[Y(x)] = \sum_{i=1}^{I}\sum_{j=1}^{I} \lambda_i \lambda_j \cdot C[0] - \sum_{i=1}^{I}\sum_{j=1}^{I} \lambda_i \lambda_j \cdot \gamma[x_i, x_j]) \geq 0 \qquad \textit{Equation A.13}$$

Since $C[0]$ does not exist, it must be eliminated from *Equation A.13* by imposing the condition that the sum of all weights λ_i be equal to *0*: *Equation 5.14* & *5.15* provide the final mathematical expression for a *conditionally positive definite* variogram function.

$$VAR[Y(x)] = \sum_{i=1}^{I}\sum_{j=1}^{I} \lambda_i \lambda_j \cdot (-\gamma[x_i, x_j]) \geq 0 \qquad \textit{Equation 5.14}$$

$$\sum_{i=1}^{I} \lambda_i = 0 \qquad \textit{Equation 5.15}$$

Upon recongnizing that $-\gamma(h)$ is conditionally positive definite, it can be shown (Journel, 1978) that the variogram has to increase more slowly than h^2 at very large lags.

$$\lim_{|h| \to \infty} \frac{\gamma(h)}{h^2} = 0 \qquad \textit{Equation 5.16}$$

An experimental variogram that increases more rapidly than h^2 for large lags indicates that the underlying correlation structure does not satisfy the intrinsic hypothesis. A large increase in the variogram generally indicates the presence of a trend in the log hydraulic conductivity field.

A.3 KRIGING METHODS

Adoption of the different assumptions listed in *Appendix A.1* has lead to the evolution of several kriging methods:

Simple Kriging: is based on the assumption of second order stationarity. The method further requires that the population mean m is known prior to starting the analysis.

Ordinary Kriging: is based on the intrinsic hypothesis. The population mean m need not be known, but it is assumed to be constant (no trend present).

Universal Kriging: Also based on the intrinsic hypothesis, this method is used when a trend is suspected in the hydraulic conductivity field. The system of kriging equations based on this method is solved simultaneously for the unknown functional coefficients that describe the trend as well as the optimal kriging weights that give the *BLU* estimate.

Ordinary kriging has been adopted in this framework for the following practical reasons:

- It is the simplest geostatistical tool that is capable of analyzing geologic environments where the mean hydraulic conductivity is not known with certainty, a case commonly encountered on hydrogeologic investigations where the data set is relatively sparse.
- By adopting the variogram or *pseudo covariance* (Journel, 1978) it is possible to apply ordinary kriging to geologic environments where $C(0)$ cannot be defined over the size of domain being investigated.
- Geologic environments with a recognized trend in hydraulic conductivity can still be analyzed by removing the trend prior to analyzing the spatial variability, thus reducing the complexity of the method relative to universal kriging.

A.4 UNBIASED CONDITION

If the kriging estimator $Z^*(X_m)$ is to be unbiased, the mean error of predicting $Z(X_m)$ by $Z^*(X_m)$ should be equal to 0; the estimator must satisfy:

$$E[Z^*(X_m)-Z(X_m)] = 0 \qquad \text{Equation A.17}$$

$$E[\sum_{i=1}^{imax} \lambda_i \cdot z(x_i)] - E[Z(X_m)] = 0$$

$$m \sum_{i=1}^{imax} \lambda_i - m = 0$$

$$\sum_{i=1}^{imax} \lambda_i = 1 \qquad \text{Equation A.18}$$

Equation A.18 presents the non-bias condition as it appears in the kriging system. The equation states that if Z^*_m is to be unbiased, the sum of all kriging weights λ_i must be equal to unity. It is also intuitively clear that each weight should be greater than or equal to zero.

A.5 EQUATION FOR ESTIMATION VARIANCE

In *Section A.5* it will be shown that best linear estimator is the estimator that results in a minimum variance of estimation errors. Before the combination of λ_i that result in the minimum variance can be identified it is necessary to develop the equation for the variance of estimation errors σ_m^2. The development begins with the definition of variance:

$$VAR\{Z(X_m) - Z^*(X_m)\} = \sigma_m^2 = E[\{Z(X_m) - Z^*(X_m)\}^2 - m_e^2] \qquad \textit{Equation A.19}$$

Because $Z^*(X_m)$ is unbiased, m_e, the mean estimation error, is equal to zero. Therefore:

$$\sigma_m^2 = E[Z(X_m)^2] - 2 \cdot E[Z(X_m) \cdot Z^*(X_m)] + E[Z^*(X_m^2] \qquad \textit{Equation A.20}$$

Each of the three terms on the right hand side of *Equation A.20* can be expressed in terms of the covariance function $C[V_1,V_2]$, where V_1,V_2 represent the support or prediction volumes at the end points between which the covariance function is being evaluated.

To develop the expression for $E[Z(X_m)^2]$ it is necessary to recall that $Z(X_m)$ is stationary; therefore, the expected value over the entire prediction volume V_m will be equal to the expected value of A point values within V_m:

$$E[Z(X_m)] = E\left[\frac{1}{A} \cdot \sum_{a=1}^{A} Z(x_{ma})\right] \qquad \textit{Equation A.21}$$

Recognizing that $E[Z(X_m)^2] = E[Z(X_m)] \cdot E[Z(X_m)]$, substituting *Equation A.21* for each term in the product, and introducing a dummy variable b to avoid doubling of indices:

$$E[Z(X_m)^2] = E\left[\frac{1}{A} \sum_{a=1}^{A} Z(x_{ma}) \cdot \frac{1}{A} \sum_{b=1}^{A} Z(x_{mb})\right] \qquad \textit{Equation A.22}$$

Upon moving all constants and summaptions outside the expectation:

$$E[Z(X_m)^2] = \frac{1}{A^2} \sum_{a=1}^{A} \sum_{b=1}^{A} E\,[Z(x_{ma}) \cdot Z(x_{mb})] \qquad \textit{Equation A.23}$$

The covariance between two points x_{ma},x_{mb} in the prediction volume V_m is:

$$C[x_{ma},x_{mb}] = E[\{Z(x_{ma})-m\} \cdot \{Z(x_{mb})-m\}]$$

$$C[x_{ma},x_{mb}] = E[Z(x_{ma}) \cdot Z(x_{mb})] - E[Z(x_{ma}) \cdot m] - E[Z(x_{mb}) \cdot m] + m^2$$

$$C[x_{ma},x_{mb}] = E[Z(x_{ma}) \cdot Z(x_{mb})] - m^2 - m^2 + m^2$$

$$C[x_{ma},x_{mb}] = E[Z(x_{ma}) \cdot Z(x_{mb})] - m^2 \qquad \textit{Equation A.24}$$

On substituting *Equation A.24* into *A.23* the desired expression for $E[Z(X_m)^2]$ is obtained:

$$E[Z(X_m)^2] = \frac{1}{A^2} \sum_{a=1}^{A} \sum_{b=1}^{A} C[x_{ma},x_{mb}] + m^2 \qquad \textit{Equation A.25}$$

The double summation of the covariance represents the average value of the covariance function between all point values within V_m. The value is designated $C_{av}[X_m,X_m]$. In practice, $C_{av}[X_m,X_m]$ is calculated by defining a grid of A point values (e.g. *6* by *6*), evaluating the covariance between each pair of point values, and taking the average. *Equation A.25* then simplifies to:

$$E[Z(X_m)^2] = C_{av}[X_m, X_m] + m^2 \qquad \textit{Equation A.26}$$

The logic followed to develop *Equation A.26* (described by *Equations A.22* to *A.25*) can also be used in developing expressions for $E[Z(X_m)\cdot Z^*(X_m)]$ and $E[Z^*(X_m)^2]$. The only difference is that instead of being a single value, $Z^*(x_m)$ is a weighted linear combination of I measurements given by *Equation A.1*. Since each measurement is taken over a support volume v_i, the measured value z_i can be expressed as an average of B point values within the support volume v_i.

$$E[Z(X_m) \bullet Z^*(X_m)] = E\left[\frac{1}{A}\sum_{a=1}^{A} Z(x_{ma}) \bullet \sum_{i=1}^{I} \lambda_i \bullet \frac{1}{B}\sum_{b=1}^{B} \bullet z(x_{mib})\right] \qquad \textit{Equation A.27}$$

On taking the summations and constants outside the expectation:

$$E[Z(X_m) \bullet Z^*(X_m)] = \sum_{i=1}^{I} \lambda_i \bullet \frac{1}{A\bullet B}\sum_{a=1}^{A}\sum_{b=1}^{B} E[Z(x_{ma}) \bullet z(x_{mib})] \qquad \textit{Equation A.28}$$

Upon replacing the expectation by the covariance:

$$E[Z(X_m) \bullet Z^*(X_m)] = \sum_{i=1}^{I} \lambda_i \bullet \frac{1}{A\bullet B}\sum_{a=1}^{A}\sum_{b=1}^{B} C[x_{ma}, x_{mib}] + m^2 \qquad \textit{Equation A.29}$$

Once again, the summation of the covariance terms can be expressed as an average covariance between all point values in prediction volume V_m and each support volume v_i, thereby obtaining the desired expression.

$$E[Z(X_m) \bullet Z^*(X_m)] = \sum_{i=1}^{I} \lambda_i \bullet C_{av}[x_m, x_{mi}] + m^2 \qquad \textit{Equation A.30}$$

Following the procedures described above, the averaged expression obtained for $E[Z^*(X_m)^2]$ is:

$$E[Z^*(X_m)^2] = \sum_{i=1}^{I}\sum_{j=1}^{I} \lambda_i \, \lambda_j \bullet C_{av}[x_{mi}, x_{mj}] + m^2 \qquad \textit{Equation A.31}$$

On substituting *Equations A.26, A.30*, and *A.31* into estimation variance expression given by *Equation A.9* and cancelling the m^2 terms, the desired working equation is obtained:

$$\sigma_m^2 = C_{av}[X_m, X_m] - 2\{\sum_{i=1}^{I} \lambda_i \bullet C_{av}[x_m, x_{mi}]\} + \sum_{i=1}^{I}\sum_{j=1}^{J} \lambda_i \, \lambda_j \bullet C_{av}[x_{mi}, x_{mj}] \qquad \textit{Equation A.32}$$

Equation A.32 was developed on the premise that all measured hydraulic conductivities z_i were exact. In the case that measurement errors are anticipated at any or all of the I sampling locations, and the distribution of the measurement error at each sample point x_i is approximated by a normal distribution $N[0,\sigma_i]$ then *Equation A.32* must be modified to account for the extra variability.

$$\sigma_m^2 = C_{av}[X_m, X_m] - 2\{\sum_{i=1}^{I} \lambda_i \bullet C_{av}[x_m, x_{mi}]\} + \sum_{i=1}^{I}\sum_{j=1}^{J} \lambda_i \, \lambda_j \bullet \{C_{av}[x_{mi}, x_{mj}] + \delta_{ij} \bullet \sigma_i \bullet \sigma_j \qquad \textit{Equation A.33}$$

A.6 MINIMIZING ESTIMATION VARIANCE - THE KRIGING SYSTEM

The final requirement to be satisfied if $Z^*(X_m)$ is to be the best linear unbiased estimator is that a set of weights λ_i is selected such that the variance of the estimation error as given by *Equation A.33* results in a global minimum. The method of *Lagrange Multipliers* is invoked to solve the minimization problem subject to the non-bias constraint *(Equation A.7)*.

In the Lagrange multiplier method all terms in the non-bias constraint are brought to one side of the equation (so they equal zero), multiplied by the Lagrange multiplier 2μ, and introduced directly into *Equation A.33*:

Equation A.34

$$\sigma_m^2 = C_{av}[X_m,X_m]-2\{\sum_{i=1}^{I}\lambda_i \cdot C_{av}[X_m,x_{mi}]\} + \sum_{i=1}^{I}\sum_{j=1}^{J}\lambda_i\,\lambda_j \cdot \{C_{av}[x_{mi},x_{mj}] + \delta_{ij}\cdot\sigma_i\cdot\sigma_j\} + 2\,\mu\cdot\{\sum_{i=1}^{I}\lambda_i - 1\}$$

To find the set of λ_i that result in a global minimum of *Equation A.34*, the equation is differentiated with respect to each λ_i and μ and each partial derivative is set equal to 0. This procedure results in $I+1$ equations in $I+1$ unknowns. Taking I partial derivatives $\delta/\delta\lambda_i(\sigma_m^2)$ yields I linear equations of the form given by *Equation A.35:*

i=constant $$\sum_{j=1}^{J}\lambda_j \cdot C_{av}[x_{mi},x_{mj}] + \lambda_i\cdot\sigma_i^2 + \mu = C_{av}[X_m,x_{mi}]$$ *Equation A.35*

Differentiating *Equation A.34* with respect to μ and setting the derivative equal to zero, $\delta/\delta\mu(\sigma_m^2)=0$, recovers the original non-bias constraint:

$$\sum_{i=1}^{imax}\lambda_i = 1$$ *Equation A.7*

Together, the I equations of form *A.35* and *Equation A.7* comprise the kriging system of simultaneous linear equations. The system of equations can be expressed in matrix form as shown in *Equation A.36* (for the case with three support points), and then solved for the unknown λ_i and μ with a linear equation solver subroutine such as *LU Decomposition.* The kriging weights λ_i obtained from the solution of *Equation A.36* are introduced into *Equation A.1*. Together with the corresponding hydraulic conductivity measurements z_i, they yield a value of $Z^*(X_m)$ that is the best linear unbiased estimate of $Z(X_m)$, the actual hydraulic conductivity value over the estimation volume V_m.

$$\begin{bmatrix} C(x_1,x_1)+\sigma_1^2 & C(x_1,x_2) & C(x_1,x_3) & 1 \\ C(x_2,x_1) & C(x_2,x_2)+\sigma_2^2 & C(x_2,x_3) & 1 \\ C(x_3,x_1) & C(x_3,x_2) & C(x_3,x_3)+\sigma_3^2 & 1 \\ 1 & 1 & 1 & 0 \end{bmatrix} \cdot \begin{bmatrix} \lambda_1 \\ \lambda_2 \\ \lambda_3 \\ \mu \end{bmatrix} = \begin{bmatrix} C(X_m,x_1) \\ C(X_m,x_2) \\ C(X_m,x_3) \\ 1 \end{bmatrix}$$ *Equation A.36*

More advanced and considerably more complex geostatistical methods have been developed to yield estimates of $Z(X_m)$ that are not restricted to simple linear combinations of available data. However, these methods cannot be applied to most practical problems for lack of information, since they require assumptions about higher order moments of the probability density function, assumptions that cannot be validated with the sparse data sets available on most hydrogeologic projects.

APPENDIX B LU DECOMPOSITION EQUATIONS

This appendix describes the methodology used in SG-STAT to generate an ensemble of log hydraulic conductivity field realizations that are isomorphic with statistics obtained from available field data, i.e. having same mean, variance, and correlation structure. Equations are presented for generating both unconditional and conditional realizations. Both sets of equations are based on the fast and robust LU decomposition of the covariance matrix (Clifton & Neuman, 1982, Davis, 1984).

B.1 UNCONDITIONAL SIMULATION

The objective of unconditional simulation is to generate an ensemble of realizations that are *isomorphic* with the correlation structure observed in the field, i.e. that statistics of each realization reproduce the statistical properties of the actual log hydraulic conductivity field. Unlike conditional realizations, unconditional realizations need not duplicate measured values at sample locations. Realizations satisfying these criteria can be generated by first assigning the mean log hydraulic conductivity, $Z^*_u(X_m)=m$, at each estimation point and then adding a vector of estimation errors, $e_u(X_m)$, that have a mean equal to 0 and possess the desired correlation structure to the unconditional estimates.

$$\{Z\} = \{Z^*_u\} + \{e_u\} \qquad \textit{Equation B.1}$$

If each realization vector is to be isomorphic with the correlation structure observed in the field, the expected value of the covariance function $C[h]$, calculated over the realization must reproduce the covariance model selected to match the experimental covariance structure of the original field data.

$$C[h]_{model} = E[e_u(X_m)\cdot e_u(X_m+h)] \qquad \textit{Equation B.2}$$

The condition given by *Equation B.2* will be satisfied if the expected value of the point covariance between each pair of estimation blocks (m,n) will be equal to the model covariance for the lag separating the two blocks. If each point covariance C_{mn} is placed in a global covariance matrix $[C]_u$ then the isomorphic condition can be expressed as a global matrix equation.

$$E(\{e_u\}\{e_u\}^T) = [C]_u \qquad \textit{Equation B.3}$$

Each term C_{mn} in the unconditional covariance matrix can be calculated if the location, size and shape of the estimation blocks is known and a valid covariance model is selected. If log hydraulic conductivities are being simulated as point values, then C_{mn} is simply equal to the value of the covariance function for the lag separating points X_m & X_n; each diagonal entry, C_{mm}, is equal to the sill, $C[0]$. If the simulated values are to apply over areas of finite dimensions then the array averaging procedure described in *Section 5.4.5* must be utilized when calculating $C_{av}[X_m,X_n]$ to account for volume effects.

Cholesky decomposition of $[C]_u$ yields two triangular matrices, a lower triangular matrix $[L]$ and an upper triangular matrix $[U]$.

$$[C]_u = [L][U] \qquad \textit{Equation B.4}$$

A unique feature of the Cholesky LU scheme is that the $[L]$ matrix is equal to the transpose of $[U]$.

$$[L] = [U]^T \qquad \textit{Equation B.5}$$

This property of Cholesky decomposition guarantees that *Equation B.3* will be satisfied when $\{e_u\}$ is set equal to $[U]\{N\}$, where $\{N\}$ is a vector of M independent random numbers generated from $N(0,1)$, i.e. a Gaussian normal population with mean 0 and variance 1.

$$\{e_u\} = [U]\{N\} \qquad \text{Equation B.6}$$

$$\{e_u\}^T = \{N\}^T[U]^T = \{N\}^T[L] \qquad \text{Equation B.7}$$

$$E(\{e_u\}\{e_u\}^T) = E([U]\{N\}\{N\}^T[L]) = [U]\cdot E(\{N\}\{N\}^T)\cdot[L] \qquad \text{Equation B.8}$$

Since $[U]$ and $[L]$ are not random variables, the expectation operator can be brought inside the expression. Expansion of the product $\{N\}\{N\}^T$ shows that it is a compact expression for the covariance matrix of $N(0,1)$. Because all terms in $\{N\}$ are independent the expected value of all off-diagonal covariance terms is 0 and the expected value of the diagonal entries is equal to the population variance, 1.

$$E(\{N\}\{N\}^T) = [I] \qquad \text{Equation B.9}$$

On substituting *Equation B.9* into *B.8* the proof is completed.

$$E(\{e_u\}\{e_u\}^T) = E([U][I][L]) = [U][L] = [C]_u \qquad \text{Equation B.10}$$

Because the procedure requires that $[C]_u$ be decomposed only once to obtain $[U]_u$ the generator is very efficient. Any desired number of realizations can be generated very quickly by substituting a new random vector $\{N\}$ into *Equation B.11*.

$$\{Z_u\} = m + [U]_u\{N\} \qquad \text{Equation B.11}$$

The only drawback of the LU decomposition method is imposed by computer memory requirements needed to store the full covariance matrix. Davis (1987) indicates that only medium size realizations not exceeding *700* blocks can be handled in a single step by most modern computers. This restriction does not present a major hurdle for two dimensional design studies such as the dewatering analysis presented in this thesis; however, it would preclude the method from use on detailed two dimensional analyses with a very fine mesh and all three dimensional analyses. Fortunately, techniques are being developed that permit the creation of very large realizations by dividing the domain into smaller zones and then sequentially generating realizations for each sub-domain in much the same manner as kriging with a moving neighbourhood (Alabert, 1987).

B.2 CONDITIONAL SIMULATION

Besides reproducing the desired correlation structure, a conditional realization must also reproduce observed data values at measurement locations. Any realization that is isomorphic with the true log hydraulic conductivity field, $Z(X_m)$, will satisfy this requirement. *Equation B.12* shows that by itself the kriging estimate $Z^*_k(X_m)$ is not isomorphic with the actual hydraulic conductivity field.

$$\{Z\} = \{Z^*_k\} + \{e_k\} \qquad \text{Equation B.12}$$

Kriging is an exact interpolator, so the kriging estimate will honour measurements; however, since kriging is a smoothing function the correlation structure of the kriging estimate will not exhibit the desired degree of variability. The variability can be introduced by adding a set of correlated kriging errors, $e_k(X_m)$, to the vector of kriging estimates. If the realization statistics are to match statistics of the actual log hydraulic conductivity field, the vector of kriging errors, $\{e_k\}$, must be drawn from a population with mean 0, a variance equal to σ_m^2 at each prediction point X_m, and covariances given by *Equation B.13*. Furthermore, the set of kriging errors must be chosen such that the correlation structure specified by these statistics is maintained.

The Cholesky decomposition method described in *Appendix B.1* will generate the desired correlation structure. The proof is not given here as it follows exactly the same lines as the derivation presented in *Appendix B.1*. The only changes that must be made to the derivation presented in that section include substitution of $\{e_k\}$ at each occurrence of $\{e_u\}$ and the replacement of the unconditional covariance matrix $[C]_u$ by the better constrained covariance matrix of kriging errors $[C]_k$.

Each entry in $[C]_k$ is given by:

Equation B.13

$$C_{mn} = C_{av}[X_m,X_n] - \sum_{i=1}^{I} \lambda_i \cdot C_{av}[x_m,x_{mi}] - \sum_{j=1}^{J} \lambda_j \cdot C_{av}[x_n,x_{nj}] + \sum_{i=1}^{I} \sum_{j=1}^{J} \lambda_i \lambda_j \cdot \{C_{av}[x_{mi},x_{nj}] + \delta_{ni,mj} \cdot \sigma_i \cdot \sigma_j$$

In the special case when $m=n$ C_{mn} will simplify to expression for the kriging variance of estimation errors, σ_m^2, given by *Equation A.33* and reproduced below.

$$\sigma_m^2 = C_{av}[X_m,X_m] - 2\{ \sum_{i=1}^{I} \lambda_{mi} \cdot C_{av}[X_m,x_{mi}]\} + \sum_{i=1}^{I} \sum_{j=1}^{J} \lambda_{mi} \lambda_{mj} \cdot \{C_{av}[x_{mi},x_{mj}] + \delta_{mi,mj} \cdot \sigma_i \cdot \sigma_j \qquad \text{Equation A.33}$$

The process of computing the diagonal entries σ_m^2 can be made much more efficient by recognizing that the Lagrange multiplier term for each prediction volume, μ_m, is equal to the most complex summation terms in *Equation A.33*. Recall from *Appendix A* that the kriging system consists of I equations of the form:

$$i=constant \qquad \sum_{j=1}^{J} \lambda_{mj} \cdot C_{av}[x_{mi},x_{mj}] + \lambda_{mi} \cdot \sigma_{mi}^2 + \mu_m = C_{av}[X_m,x_{mi}] \qquad \text{Equation B.14}$$

Multiplying each of the I equations of form *B.14* by λ_i, summing them together, and recognizing that the sum of kriging weights λ_i is equal to 1 yields:

$$\mu_m = - \sum_{j=1}^{J} \lambda_{mj} \cdot C_{av}[X_m,x_{mj}]\} + \sum_{i=1}^{I} \sum_{j=1}^{J} \lambda_{mi} \lambda_{mj} \cdot \{C_{av}[x_{mi},x_{mj}] + \sum_{i=1}^{I} \lambda_{mi} \cdot \lambda_{mi} \cdot \sigma_{mi}^2 \qquad \text{Equation B.15}$$

Substitution of μ_m for the terms on the right side of *Equation B.14* in *Equation A.33* results in the final simplified expression:

$$\sigma_m^2 = C_{av}[X_m,X_m] - \sum_{i=1}^{I} \lambda_i \cdot C_{av}[X_m,x_{mi}] + \mu_m \qquad \text{Equation B.16}$$

Since the Lagrange multipliers μ_m are determined during the kriging estimation phase of the analysis, it is a simple programming task to store these parameters and then re-introduce them into *Equation B.16* during the simulation phase.

Once the matrix $[C]_k$ is constructed and decomposed by the Cholesky scheme any number of conditional realizations can be obtained very quickly by generating the appropriate number of $N(0,1)$ random vectors $\{N\}$ and evaluating *Equation B.17* for each vector.

$$\{Z_k\} = \{Z^*_k\} + [U]_k\{N\} \qquad \text{Equation B.17}$$

Each realization generated by this process will be conditioned such that simulated values will duplicate measurements at all observation points[1] and the correlation structure will be isomorphic with the correlation structure of the selected covariance model.

[1] Provided measurements are error free and estimation volume is a point.

B.3 IMPLEMENTATION DIFFICULTIES

A Cholesky decomposition of *[C]* is possible only if the covariance matrix is symmetric and positive definite. In theory, the matrix construction procedure described above guarantees that the resulting matrix will be symmetric and positive definite provided a valid, positive definite covariance or semi-variogram model is used to construct the matrix.

In practice, round-off errors in the calculation of kriging weights and evaluation of the numerous summations in *Equation B.13* can destroy the positive definite character of the covariance matrix. Before explaining how this happens, it is necessary to review the characteristics of positive definite matrices.

By definition, a square matrix *[C]* is positive definite if the inequality:

$$\{X\}^T[C]\{X\} > 0$$

holds for any non-zero vector *{X}*. However, this definition is not useful for checking whether a matrix is positive definite since *Equation B.18* would have to be verified for an infinite number of vectors *{X}*. Positive definite matrices have three additional characteristics (Straug, 1980):

- All eigen values of *[C]* are greater than 0.
- *[C]* and all sub-matrices of *[C]* have positive determinants
- All pivots (without row exchanges) are greater than *0*, i.e. diagonal entries *Cmm* are greater than *0*.

From a computational perspective, the last test is the most useful. It states that the Cholesky decomposition will fail if any diagonal entries in *[C]* (variances of estimation errors) are negative or equal to zero. The first two tests are computationally more demanding then the actual Cholesky decomposition.

The variance of estimation errors will be equal to *0* if hydraulic conductivity is already known exactly at the estimation point. This will result in a divide by *0* error in the Cholesky decomposition. The problem is easily remedied by partitioning the covariance matrix to remove all simulation points that are known exactly.

In *Appendix A.2* it was stated that a negative variance of estimation errors is physically unacceptable and will never occur in theory if a valid covariance model is used. However, when the variance of estimation errors is calculated for a prediction volume with lots of support, the resulting σ_m^2 will be very close to *0*. Although encountered only infrequently, the situation can arise where σ_m^2 is actually smaller than the round-off error and the computer assigns a negative value to the diagonal entry. To correct this numerical problem SG-STAT increases the diagonal entry to an arbitrary variance equal to *2%* of the sill whenever negative variances are encountered.

In the early stages of program development problems with non-positive definite matrices were also encountered when semi-variogram models that continue to increase to infinity (e.g. exponetial model) were truncated at large distances. The truncation was performed to reduce computation time since such semi-variogram models approach the sill value quickly and then continue to increase ever so slightly at larger lags. It was felt that the speed of computing the semi-variogram could be dramatically increased if the sill value was simply assigned at large lags instead of computed by the full semi-variogram model. Unfortunately, the small errors introduced by this approximation were sufficient to destroy the positive definite nature of the covariance system. Therefore, SG-STAT now evaluates the full semi-variogram equation for all lag distances.

APPENDIX C FFT TECHNIQUE

In *Chapter 4* it was stated that the FFT stochastic method provides an attractive tool for generating large realizations of unconditional autocorrelated hydraulic conductivity fields. This appendix first reviews key concepts of spectral analysis on which the FFT generator is based, followed by a description of how the generator has been implemented in *SG-STAT* to produce realizations in two dimensions. The closing paragraphs demonstrate how FFT analysis can be used to establish a covariance model of regularly gridded data and to confirm that realizations generated by any type of simulation model do indeed possess the desired covariance structure.

BASICS OF SPECTRAL METHODS: Spectral techniques are most commonly applied in the analysis of one dimensional time series. A time series is a one dimensional digital signal that fluctuates as a function of time *(Figure C.1A)*. Using spectral analysis, the same signal can also be examined in the frequency domain *(Figure C.1B)*. Spectral methods are based on the fact that any time series $s(t)$ can be broken down into a finite set of periodic sinusoidal functions of progressively decreasing frequencies. In general, the spectral method associates two sinusoidal functions with each frequency f_j, (also known as a *harmonic*), a cosine function for even contributions and a sine function to duplicate the odd component of the source signal.

$$s(t) = \Sigma A_j \cdot cos(2\pi f_j + \phi_j) + i \cdot A_j \cdot sin(2\pi f_j + \phi_j) \qquad \textit{Equation 5.26}$$

To fully describe a time series $S(f)$ in the frequency domain, it is necessary to specify the amplitude, A_j, and phase delay, ϕ_j, for each pair of sinusoidal harmonics. It is more convenient to represent amplitude/phase information as distinct amplitude coefficients for the real and imaginary portions of the signal.

$$a_j = A_j cos(\phi_j) \quad b_j = A_j sin(\phi_j) \qquad \textit{Equation 5.27}$$

Figure C.1 Digital Signal in Time and Frequency Domain

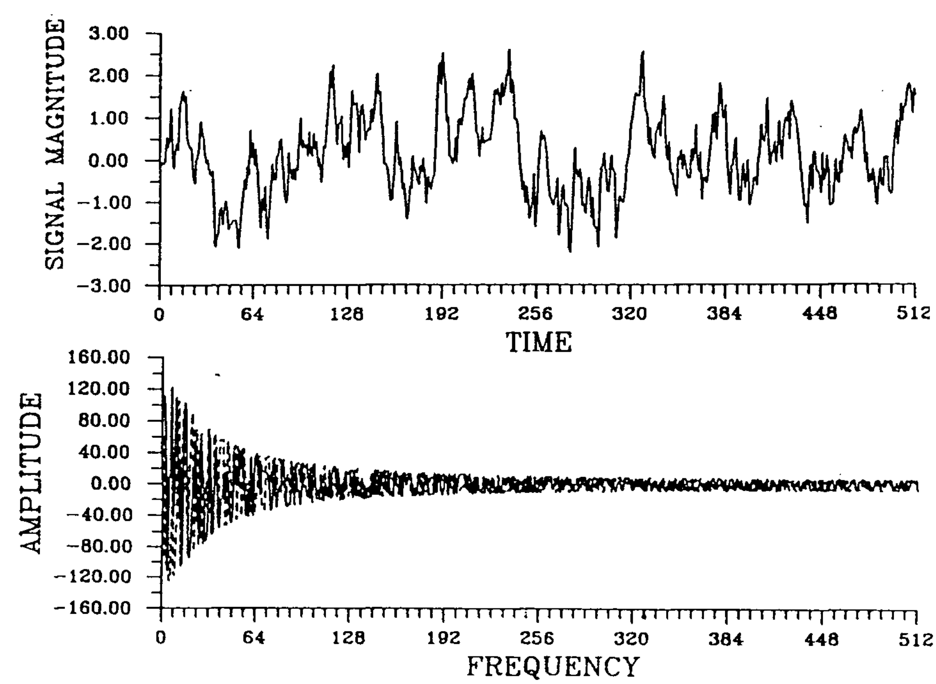

Figure C.2 Phase Circle Relationship

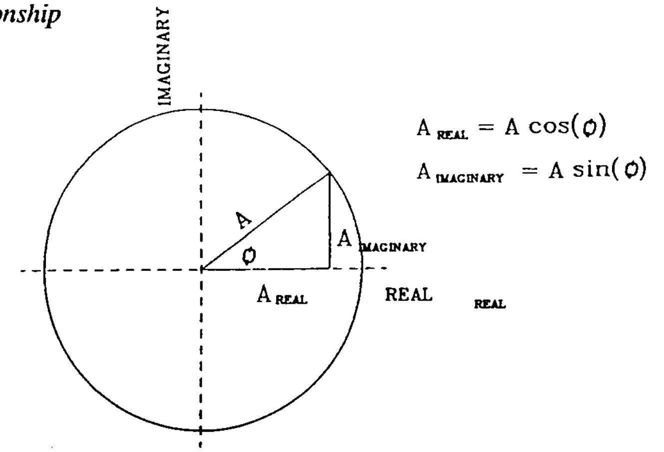

Figure C.2 illustrates how the two representations are related on the phase circle.

FAST FOURIER TRANSFORM: Given a time series $s(t_k)$, the amplitude coefficients of the spectral representation can be determined via a discrete Fourier transform. The *Fast Fourier Transform*, developed in the mid 1960's, provides a very efficient algorithm for evaluating the Fourier Transform. Standard *FFT* algorithms and public domain software are available for evaluating the FFT in one, two and three dimensions (Press et al., 1986, pp.381-453). The FFT can be applied in both directions, a forward transform converts the signal to a frequency domain representation, an inverse transform converts the frequency representation back to time series. In equations that follow, the FFT operation will be designated by $\rightarrow$.

AMPLITUDE SPECTRUM: Defined as the square of amplitude coefficient A_j, the amplitude spectrum is indicative of the relative energy carried by waves of each harmonic frequency f_j.

$$H(f_j) = A_j^2 \qquad \textit{Equation 5.28}$$

If $S(f)$ is represented by the real and imaginary amplitude coefficients, the amplitude spectrum can be obtained from:

$$H(f_j) = a_j^2 + b_j^2 \qquad \textit{Equation 5.29}$$

The amplitude spectrum is related to the autocorrelation function. To demonstrate this point conceptually, consider the time series, covariance function, and amplitude spectra illustrated in *Figure 3*.

Figure 3A illustrates a perfectly correlated signal. The covariance function appears as a constant value with infinite range. The amplitude spectrum indicates that all of the energy is carried by waves of 0 frequency, i.e. infinite wave length.

Figure 3B shows a signal that is strongly correlated. The covariance function decreases as the separation lag increases, and vanishes to 0 at a large but finite range, indicating that beyond that point, the signal is no longer correlated. The amplitude spectrum indicates that most of the energy is carried by low frequency waves, i.e. waves with long wave lengths.

Figure 3C shows a weakly correlated signal. The covariance function decreases rapidly. The amplitude spectrum decreases slowly, indicating the presence of high frequency waves in the signal. This means that the time series fluctuates over short distances.

Figure C.3 Covariance, Amplitude Spectra and Realizations for Time Series of Varying Correlation

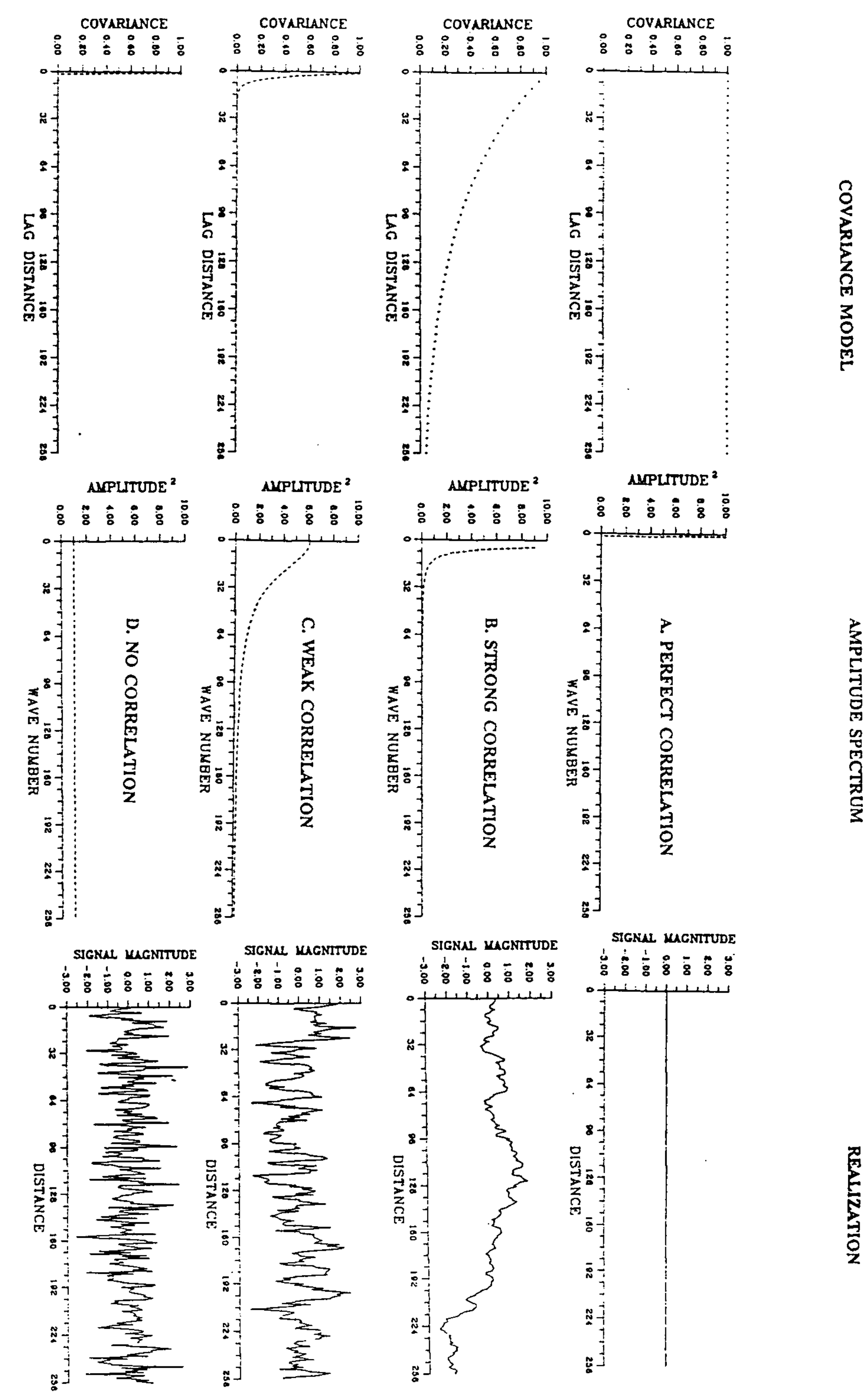

Finally, *Figure 3D* illustrates a perfectly random signal (also known as pure nugget effect or white noise). The covariance function is a spike at the origin, indicating that the signal is not autocorrelated. The amplitude spectrum is a constant horizontal line, indicating that the signal is comprised from the full spectrum of harmonics, all with equal weighting..

The preceding discussion indicates that the amplitude spectrum behaves in an opposite sense to the covariance function. If one indicator of autocorrelation decreases rapidly, the other will decrease gradually. The Wiener-Khintchine theorem confirms this casual observation. This classic theorem states that the autocorrelation function $a(t)$ and the amplitude spectrum are a Fourier transform pair:

$$a(t) \leftrightarrow A(f) \qquad \textit{Equation 5.30}$$

Either functional form can be obtained if the other is known.

GENERATING REALIZATIONS: The Wiener-Khintchine theorem dictates that all autocorrelated fields that are described by an autocorrelation function $a(t)$ will have the same amplitude spectrum, $A(f)$, given by *Equation 5.30*. This relationship is exploited when generating realizations. An infinite number of realizations $S(f)$ can be obtained in the spectral domain by selecting a random phase delay, ϕ_j, for each harmonic. An inverse FFT then converts each realization $S(f)$ back into the spatial domain. Although each realization $s(t)$ will appear unique because of the random phase shift associated with each sinusoidal harmonic, all realizations will have exactly the same autocorrelation structure, since they originated from a single amplitude spectrum.
Figure 4 illustrates the simulation process in one dimension.

- The first step is to select a valid covariance model that will closely approximate the expected correlation structure of the hydraulic conductivity field to be simulated. *Figure 4A* illustrates the exponential covariance model selected for this example.

- Next, a decision is made on the density of the spatial discretization (i.e. number of nodes in FFT). The sampling interval must be selected carefully to ensure that a sufficiently large number of nodes is utilized so that information will not be lost during the FFT.

- A forward FFT is applied to the covariance model to obtain the amplitude spectrum representation in the wave number domain, shown in *Figure 4B*. Note that the amplitude spectrum decays faster than the covariance function.

- The maximum amplitude of each harmonic, $A(f_j)$, is calculated by taking the square root of each amplitude spectrum term; $A(f_j)$ then remains constant for each harmonic frequency throughout the simulation.

- Autocorrelated realizations are generated by associating a random phase delay for each harmonic from a uniform distribution between 0 and 2π. The phase circle relationship is then used to compute the real and imaginary amplitude coefficients, a_j, b_j. These coefficients, shown in *Figure 4C* provide a complete description of each realization in the spectral domain.

- In the final step of the simulation, each spectral realization is transformed back into the spatial domain with an inverse FFT. *Figure 4D* provides the spatial domain representation of the spectral realization illustrated in *Figure 4C*.

Generation of two dimensional hydraulic conductivity fields follows exactly the same lines as described above for one dimensional simulations. The only difference is that the covariance function must be represented as a two dimensional form.

Figure C.4 Generating Realizations via FFT Method in One Dimension

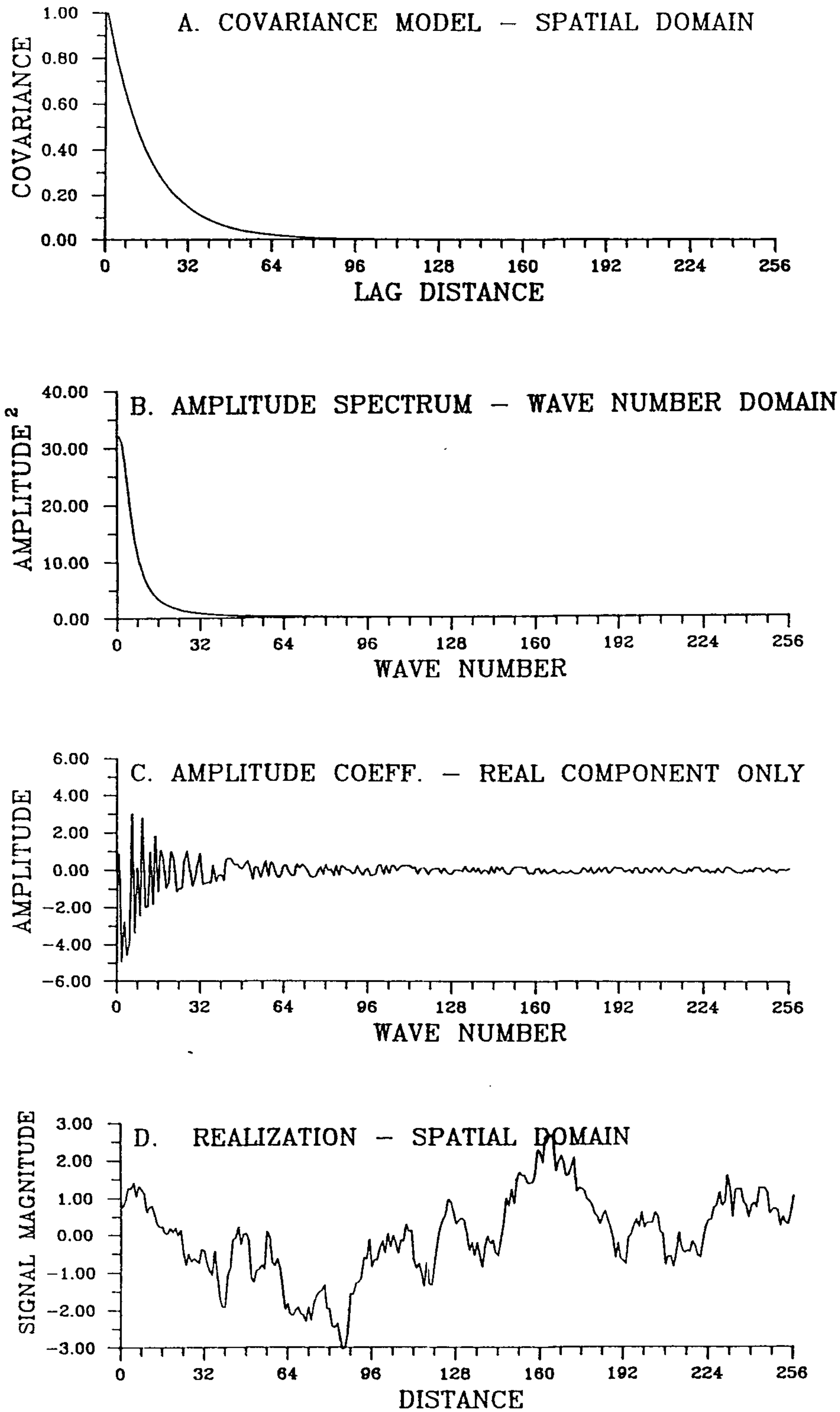

Figure C.5 Anisotropic Covariance Models in Two Dimensions

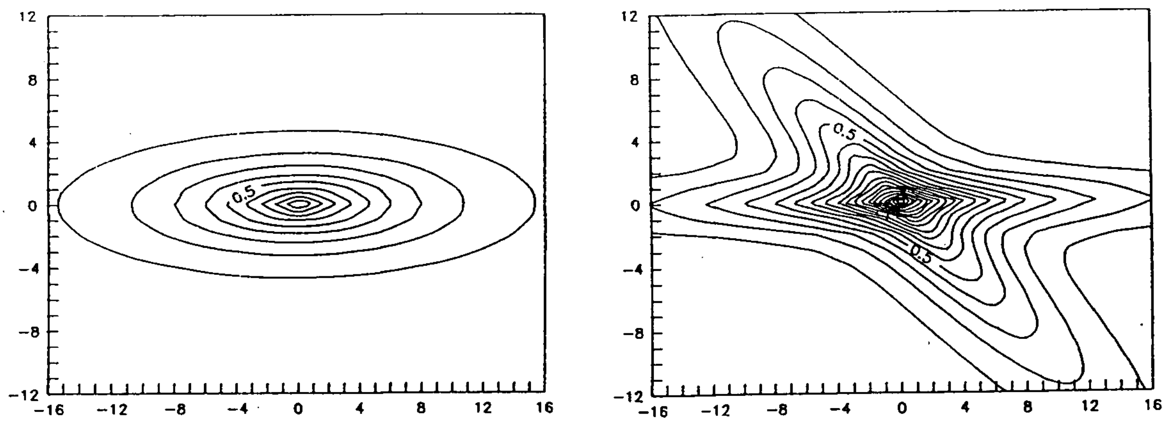

ANISOTROPY: Isotropic, two dimensional, covariance models are generated by rotating the desired one dimensional covariance model about the *Z* axis. In order to preserve the one dimensional correlation structure it is essential that the rotation be performed in the spatial domain, prior to taking the two dimensional FFT; rotation of a one dimensional amplitude spectrum in the wave number domain produces erroneous results.

Geologic materials frequently exhibit anisotropic autocorrelation structures. Material properties of sedimentary deposits, for example, are likely to be correlated over much larger distances in the plane of stratification than in the direction normal to stratification. Two basic types of anisotropy structures have been recognized (Journel & Huijgbrets, 1978). Anisotropies that exhibit an elliptical profile in the X-Y plane (e.g. *Figure 5A)* are classified as *geometric anisotropies.* Other, more complex anisotropy structures that may exhibit very strong correlation in one or more narrow bands of preferred directions (e.g. fractures), have been designated *zonal anisotropies* in geostatistical nomenclature. A typical example is illustrated in *Figure 5B.*

Covariance models that exhibit geometric anisotropy can be generated by: 1) deforming the cartesian coordinate system such that an ellipse having the desired aspect ratio is mapped as a circle in the new coordinate system, 2) generating an isotropic covariance model in the deformed coordinate system, and 3) mapping the covariance model values back to the original cartesian system, effectively stretching the conical model as required. Zonal anisotropy models are constructed by superimposing any number of valid one or two dimensional covariance models, taking advantage of the linearity of geostatistical operators.

Figure 6A & B illustrate two anisotropic realizations in the spatial domain. The realizations correspond to the covariance models illustrated in *Figure 5.* The hydraulic conductivity field depicted in *Figure 6A* in plan view would be typical of a stratified sedimentary deposit in cross section. For example, all geologic cross-sections in the glaciofluvial overburden at Highland Valley Copper exhibit similar anisotropic correlation patterns. Although the preferred correlation directions are difficult to see, the hydraulic conductivity field illustrated in *Figure 6B* may be representative of a highly fractured rock mass, where high permeability zones are controlled by fracture density and orientation.

Figure C.6 Hydraulic Conductivity Realizations - Anisotropic Correlation Structures

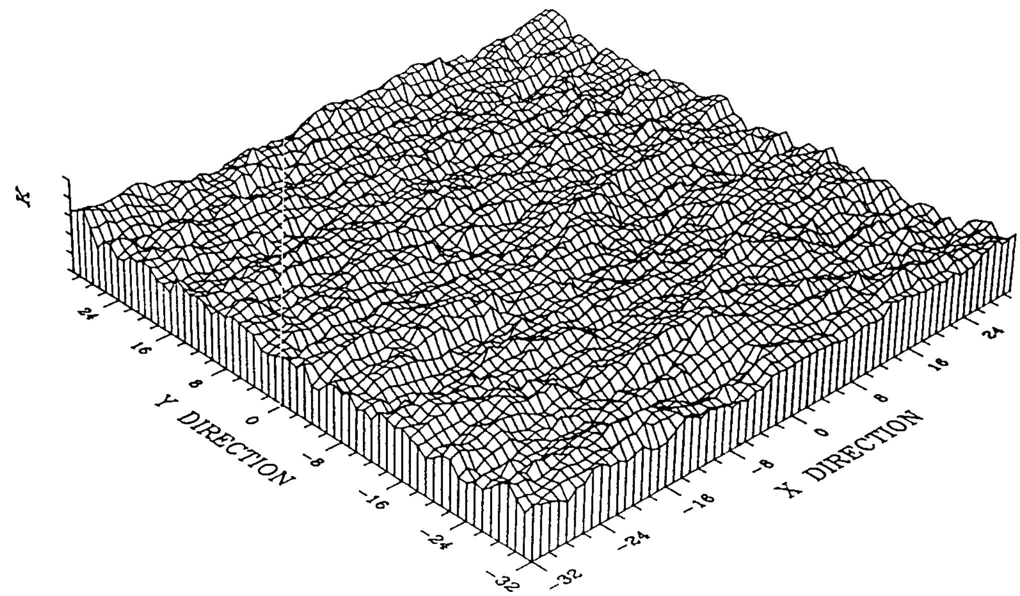

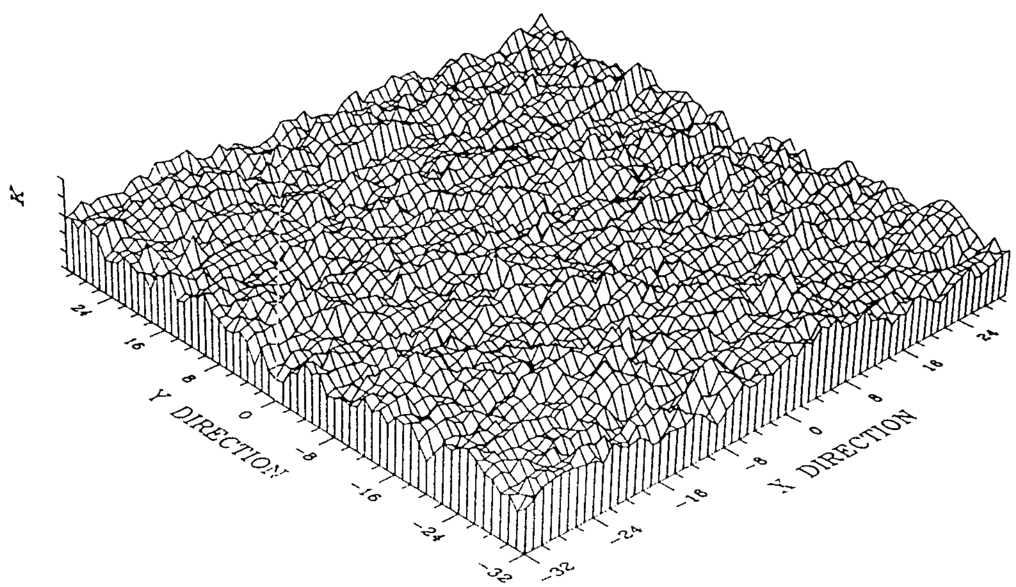

CONDITIONING: Realizations generated by the FFT technique can be conditioned on data only after the unconditional realizations are generated. The most popular conditioning approach utilizes kriging estimation to remove random low frequency oscillations observed in the unconditional simulation by equivalent oscillations that pass through the data points (Journel & Huijgbrets, 1978, pp. 492-496, Delhomme, 1979, Neuman, 1982, Smith & Schwartz, 1981b).

The conditioning proceeds as follows:

- The FFT method is utilized to generate simulated log hydraulic conductivity values, $Z_u(x_m)$ at each prediction point x_m that are not conditioned on available data.

- The unconditional realization is sampled at existing measurement points, x_i. Kriging is utilized to compute a smooth surface, $Z_{uk}(x_m)$, that passes through the FFT generated values at each point x_i. Since the FFT realization is based on the same covariance model as is exhibited by field data the unconditional kriged surface will possess essentially the same statistics as those obtained from kriging of actual data.[1]

- The kriged surface is subtracted from the unconditional realization, the remaining component of the unconditional realization is random, high frequency noise. Furthermore, the high frequency noise function will have a value of 0 at all measurement points since kriging is an exact interpolator, i.e. $Z_u(x_i)-Z_{uk}(x_i)=0$.

- Next, the original data set is kriged to obtain a smooth surface that duplicates observed values at measurement points, i.e. $Z_k(x_i)=Z(x_i)$. This surface is added to the noise component to obtain the conditioned realization.

$$Z_c(x_m) = Z_u(x_m) - Z_{uk}(x_m) + Z_k(x_m) \qquad \textit{Equation 5.31}$$

This section has demonstrated that the FFT simulation method is a very practical stochastic tool. Ease of implementation, ability to simulate the most complex covariance models, and minimum memory overhead make the FFT method very attractive for generating detailed unconditional realizations in two dimensions. Conditional realizations can be generated at a speed comparable to that achieved with LU decomposition, but with much less memory overhead. This makes the FFT ideal for implementation on personal computers where memory may be limited to 640Kb by the operating system.

---

1 Journel and Huijgbrets (1978, pp. 495) provide a detailed proof of this relationship.

APPENDIX D SENSITIVITY SIMULATION RESULTS

APPENDIX D.1 SENSITIVITY TO MEAN HYDRAULIC CONDUCTIVITY (SEN1)

CONDITIONS:
RANGE K: 1E-10 TO 1E-2 M/S
SDEV K = 0.25
RANGE = 200 M
PHI MEAN = 30 DEG
PHI SDEV = 1.0 DEG
C MEAN = 50 KN/M^2
C SDEV = 10 KN/M^2

RUN NO.	K MEAN	KC MEAN	Kc SDEV	FOS MEAN	FOS SDEV	POF
1	-10.0	-0.0476	0.0444	0.84	0.15	0.86
2	-9.0	-0.0471	0.0422	0.84	0.14	0.85
3	-8.0	0.0265	0.0488	1.09	0.16	0.33
4	-7.0	0.0422	0.0380	1.14	0.13	0.13
5	-6.0	0.0687	0.0354	1.23	0.12	0.03
6	-5.0	-0.0256	0.0523	0.91	0.17	0.74
7	-4.0	-0.0458	0.0448	0.85	0.15	0.80
8	-3.0	-0.0467	0.0436	0.84	0.15	0.84
9	-2.0	-0.0472	0.0429	0.84	0.14	0.85

APPENDIX D.2 SENSITIVITY TO SDEV IN HYDRAULIC CONDUCTIVITY (SEN2)

CONDITIONS:
KMEAN 1E-6 M/S
RANGE SDEV K: 0.1 TO 1.41
RANGE = 200 M
PHI MEAN = 30 DEG
PHI SDEV = 1.0 DEG
C MEAN = 50 KN/M^2
C SDEV = 10 KN/M^2

RUN NO.	SDEV K	KC MEAN	Kc SDEV	FOS MEAN	FOS SDEV	POF
1	0.1	0.0296	0.0181	1.10	0.06	0.03
2	0.2	0.0314	0.0308	1.10	0.10	0.19
3	0.3	0.0375	0.0348	1.13	0.12	0.14
4	0.5	0.0377	0.0447	1.13	0.15	0.21
5	0.7	0.0336	0.0527	1.11	0.18	0.31
6	1.0	0.0262	0.0607	1.09	0.20	0.29
7	1.4	0.0179	0.0689	1.06	0.23	0.41

APPENDIX D.3 SENSITIVITY TO RANGE IN CORRELATION OF K (SEN3)

CONDITIONS:
KMEAN 1E-6 M/S
SDEV K = 0.25
RANGE IN RANGE: 25 TO 1000 M
PHI MEAN = 30 DEG
PHI SDEV = 1.0 DEG
C MEAN = 50 KN/M^2
C SDEV = 10 KN/M^2

RUN NO.	RANGE K	KC MEAN	Kc SDEV	FOS MEAN	FOS SDEV	POF
1	25.0	0.0330	0.0260	1.11	0.09	0.07
2	50.0	0.0330	0.0315	1.11	0.11	0.14
3	100.0	0.0308	0.0307	1.10	0.10	0.17
4	200.0	0.0394	0.0439	1.13	0.15	0.22
5	400.0	0.0401	0.0511	1.13	0.17	0.23
6	500.0	0.0393	0.0525	1.13	0.17	0.24
7	750.0	0.0369	0.0492	1.12	0.16	0.24
8	1000.0	0.0348	0.0490	1.12	0.16	0.24

APPENDIX D.4 SENSITIVITY TO MEAN FRICTION ANGLE (SEN4)

CONDITIONS:
KMEAN 1E-6 M/S
SDEV K = 0.00
RANGE: UNDEFINED
RANGE IN PHI MEAN = 25 TO 35 DEG
PHI SDEV = 1.0 DEG
C MEAN = 50 KN/M^2
C SDEV = 10 KN/M^2

RUN NO.	PHI MEAN	KC MEAN	Kc SDEV	FOS MEAN	FOS SDEV	POF
1	25.0	-0.0537	0.0089	0.82	0.03	1.00
2	26.0	-0.0417	0.0080	0.86	0.03	1.00
3	27.0	-0.0275	0.0095	0.91	0.03	1.00
4	28.0	-0.0134	0.0085	0.96	0.03	0.97
5	29.0	0.0000	0.0089	1.00	0.03	0.50
6	30.0	0.0127	0.0089	1.04	0.03	0.12
7	31.0	0.0288	0.0088	1.10	0.03	0.00
8	32.0	0.0449	0.0089	1.15	0.03	0.00
9	33.0	0.0575	0.0091	1.19	0.03	0.00
10	34.0	0.0744	0.0094	1.25	0.03	0.00
11	35.0	0.0875	0.0096	1.29	0.03	0.00

APPENDIX D.5 SENSITIVITY TO MEAN COHESION (SEN5)						
CONDITIONS:	KMEAN = 1E-6 M/S SDEV K = 0.00 RANGE = UNDEFINED PHI MEAN = 30 DEG PHI SDEV = 1.0 DEG RANGE C MEAN 0 TO 200 KN/M^2 C SDEV = 10 KN/M^2					
RUN NO.	C MEAN	KC MEAN	Kc SDEV	FOS MEAN	FOS SDEV	POF
1	0.0	-0.2400	0.0088	0.92	0.03	1.00
2	20.0	-0.0087	0.0085	0.97	0.03	0.86
3	40.0	0.0073	0.0090	1.02	0.03	0.21
4	60.0	0.0218	0.0086	1.07	0.03	0.01
5	80.0	0.0390	0.0088	1.13	0.03	0.00
6	100.0	0.0557	0.0089	1.19	0.03	0.00
7	120.0	0.0715	0.0083	1.24	0.03	0.00
8	140.0	0.0860	0.0089	1.29	0.03	0.00
9	160.0	0.1011	0.0086	1.34	0.03	0.00
10	180.0	0.1183	0.0082	1.39	0.03	0.00
11	200.0	0.1341	0.0083	1.45	0.03	0.00

APPENDIX D.6 SENSITIVITY TO SDEV FRICTION ANGLE (SEN 6)						
CONDITIONS:	KMEAN = 1E-6 M/S SDEV K = 0.00 RANGE = UNDEFINED PHI MEAN = 30 DEG RANGE PHI SDEV: 0 TO 3.0 DEG C MEAN = 50 KN/M^2 C SDEV = 10 KN/M^2					
RUN NO.	PHI SDEV	KC MEAN	Kc SDEV	FOS MEAN	FOS SDEV	POF
1	0.0	0.0157	0.0038	1.05	0.01	0.00
2	0.5	0.0157	0.0057	1.05	0.02	0.00
3	1.0	0.0162	0.0092	1.05	0.03	0.02
4	1.5	0.0158	0.0134	1.05	0.04	0.11
5	2.0	0.0171	0.0156	1.06	0.05	0.11
6	2.5	0.0182	0.0218	1.06	0.07	0.22
7	3.0	0.0152	0.0246	1.05	0.08	0.29

APPENDIX D.7 SENSITIVITY TO SDEV COHESION (SEN7)

CONDITIONS:
KMEAN = 1E-6 M/S
SDEV K = 0.00
RANGE = UNDEFINED
PHI MEAN = 30 DEG
PHI SDEV = 1.0 DEG
C MEAN = 50 KN/M^2
RANGE C SDEV: 0 TO 25 KN/M^2

RUN NO.	C SDEV	KC MEAN	Kc SDEV	FOS MEAN	FOS SDEV	POF
1	0.0	0.0158	0.0083	1.05	0.03	0.00
2	2.5	0.0152	0.0080	1.05	0.03	0.02
3	5.0	0.0141	0.0084	1.05	0.03	0.05
4	7.5	0.0158	0.0081	1.05	0.03	0.01
5	10.0	0.0144	0.0093	1.05	0.03	0.06
6	15.0	0.0145	0.0089	1.05	0.03	0.06
7	20.0	0.0155	0.0108	1.05	0.04	0.07
8	25.0	0.0164	0.0149	1.05	0.05	0.11

APPENDIX D.8 SENSITIVITY TO COMBINED SDEV ALL PARAMETERS (SEN 8)

CONDITIONS:
KMEAN = 1E-6 M/S
RANGE SDEV K: 0.1 TO 1.41
RANGE = UNDEFINED
PHI MEAN = 30 DEG
RANGE PHI SDEV: 0 TO 3.0 DEG
C MEAN = 50 KN/M^2
RANGE C SDEV: 0 TO 20 KN/M^2

RUN NO.	ANGE SDEV	KC MEAN	Kc SDEV	FOS MEAN	FOS SDEV	POF
1	NONE	0.0194	0.0135	1.06	0.04	0.05
2	VERY LOW	0.0198	0.0146	1.07	0.05	0.09
3	LOW	0.0365	0.0349	1.12	0.12	0.17
4	MEDIUM	0.0388	0.0432	1.13	0.14	0.22
5	HIGH	0.0376	0.0521	1.13	0.17	0.22
6	VERY HIGH	0.0237	0.0655	1.08	0.22	0.35
7	EXTREME	0.0172	0.0696	1.06	0.23	0.38

APPENDIX D.9 SENSITIVITY TO SDEV COHESION ONLY (SEN9)

CONDITIONS:

K = 1E-6 M/S
SDEV K = 0.00
RANGE = 200 M
PHI MEAN = 30 DEG
PHI SDEV = 0.0 DEG
C MEAN = 50 KN/M^2
RANGE C SDEV: 5 TO 50 KN/M^2

RUN NO.	SDEV C	KC MEAN	Kc SDEV	FOS MEAN	FOS SDEV	POF
1	5.0	0.0151	0.0018	1.05	0.01	0.00
2	10.0	0.0155	0.0038	1.05	0.01	0.00
3	15.0	0.0152	0.0060	1.05	0.02	0.01
4	20.0	0.0148	0.0072	1.05	0.02	0.02
5	30.0	0.0148	0.0114	1.05	0.04	0.08
6	40.0	0.0137	0.0147	1.05	0.05	0.15
7	50.0	0.0110	0.0192	1.04	0.06	0.29

APPENDIX D.10 SENSITIVITY TO SDEV. IN FRICTION ANGLE ONLY (SEN10)

CONDITIONS:

K = 1E-6 M/S
SDEV K = 0.00
RANGE = 200 M
PHI MEAN = 30 DEG
RANGE PHI SDEV: 0 TO 3.0 DEG
C MEAN = 50 KN/M^2
C SDEV = 0.0 KN/M^2

RUN NO.	PHI SDEV	KC MEAN	Kc SDEV	FOS MEAN	FOS SDEV	POF
1	0.5	0.0147	0.0046	1.05	0.02	0.00
2	1.0	0.0147	0.0090	1.05	0.03	0.04
3	1.5	0.0166	0.0141	1.06	0.05	0.09
4	2.0	0.0155	0.0169	1.05	0.06	0.17
5	2.5	0.0128	0.0215	1.04	0.07	0.25
6	3.0	0.0119	0.0251	1.04	0.08	0.33
7	3.5	0.0171	0.0268	1.06	0.09	0.29

APPENDIX D.11 SENSITIVITY TO SDEV. IN HYDRAULIC COND. ONLY (SEN11)

CONDITIONS:

K = 1E-6 M/S
RANGE SDEV K: 0.1 TO 1.41
RANGE = 200 M
PHI MEAN = 30 DEG
PHI SDEV = 0.0 DEG
C MEAN = 50 KN/M^2
C SDEV = 0.0 KN/M^2

RUN NO.	K SDEV	KC MEAN	Kc SDEV	FOS MEAN	FOS SDEV	POF
1	0.1	0.0882	0.0083	1.29	0.03	0.00
2	0.2	0.0882	0.0083	1.29	0.03	0.00
3	0.3	0.0811	0.0230	1.27	0.08	0.00
4	0.5	0.0739	0.0334	1.24	0.11	0.04
5	0.7	0.0629	0.0450	1.20	0.15	0.07
6	1.0	0.0481	0.0558	1.16	0.19	0.17
7	1.4	0.0332	0.0641	1.11	0.21	0.29

APPENDIX E CASE HISTORY DATA

E.1 OVERVIEW

This appendix contains background data about geologic, hydrologic and economic conditions at Highland Valley Copper. The information was collected and analyzed as part of this thesis research while the author was on site at Highland Valley Copper during the summers of 1987 and 1988.

E.2 GEOLOGIC DATA

This section first describes the systematic geologic logging procedures that have been used to construct the geologic model at Highland Valley Copper. The geologic data is then presented, starting with the geologic logs for each of the six drill holes located on section R3, followed by graphic Strip Logs, and ultimately by the geologic cross-section. The geologic cross-section is very important, it is used extensively in many parts of the case history study to predict:

- The range of correlation of the hydraulic conductivity field.
- The anisotropy ratio.
- The distribution of shear strength zones for the slope stability analysis.

E.2.1 DATA COLLECTION PROCEDURES

The overburden geologic interpretation that is presented in *Chapter 8* is based primarily on information collected during well and piezometer drilling programs completed over the past four years. Logs from 21 wells and 19 piezometer holes comprise this data base. Additional information is derived from surface mapping of pit faces. The mapping information will become increasingly important as the pit progresses to depth.

Most piezometer holes and small diameter wells are drilled with air-rotary rigs while large diameter wells are completed with a cable-tool rig. Geologic data collection begins with the drillers, who maintain a geologic log, noting each change in lithology and drilling conditions. Grab samples (approximately 15 kg) are also collected at 2 m intervals for future analysis. Later, a representative sample is split from each bag and stored in a small plastic sample cup.

The "cup" samples are logged in detail. Information that is collected includes: 1) geologic description of material, 2) "primary-secondary-tertiary" ranking, 3) visual estimate of the percentage of each grainsize and 4) estimate of the water bearing potential of the soil mass. Complete geologic logs for each of the six drill holes on Geotechnical Section R3 are presented on the following pages.

In the "primary-secondary-tertiary" assessment the three most common grainsizes or material types (listed in *Table E.1*) are identified in each sample interval. The most common grainsize is recorded in the primary column, the intermediate grainsize is noted in the secondary column, and the third most common grainsize is noted in the tertiary column. For example, "Gravel, sandy, with minor clay seams" would be coded as "1 2 4". The numeric and colour coding scheme has proven extremely valuable as a correlation tool when constructing geologic cross-sections.

Water bearing potential is indicated on a scale from 0 to 5. 0 indicates very impermeable materials such as clay or dense till, 5 indicates highly permeable material such as coarse, clean sand and gravel.

Table E.1 Soil Type Composition Codes

Material	Code	Colour
Gravel	1	Orange
Sand	2	Yellow
Silt	3	Brown
Clay	4	Green
Till	5	Blue
Organics	6	Black
Bedrock - Weathered	7	Pink
Bedrock - Fresh	8	Red

The descriptive and quantitative observations are entered into SG-CoreLog, a PC based data base and graphics program developed by this author. The software is then used to process the data and generate "Strip Logs" (also presented on following pages) and cross sections. Both types of graphic output are used to update the geologic model as additional drilling information becomes available.

E.2.2 GEOLOGIC LOGS

The following pages contain descriptive geologic logs for each of the six holes on geologic section R3. *Figure E.1* shows the location of *Section R3* as well as the other six geotechnical sections in relation to the ultimate pit wall. The location of existing wells and piezometers are also indicated in the figure.

Figure E.1 Plan Showing Location of Geotechnical Sections

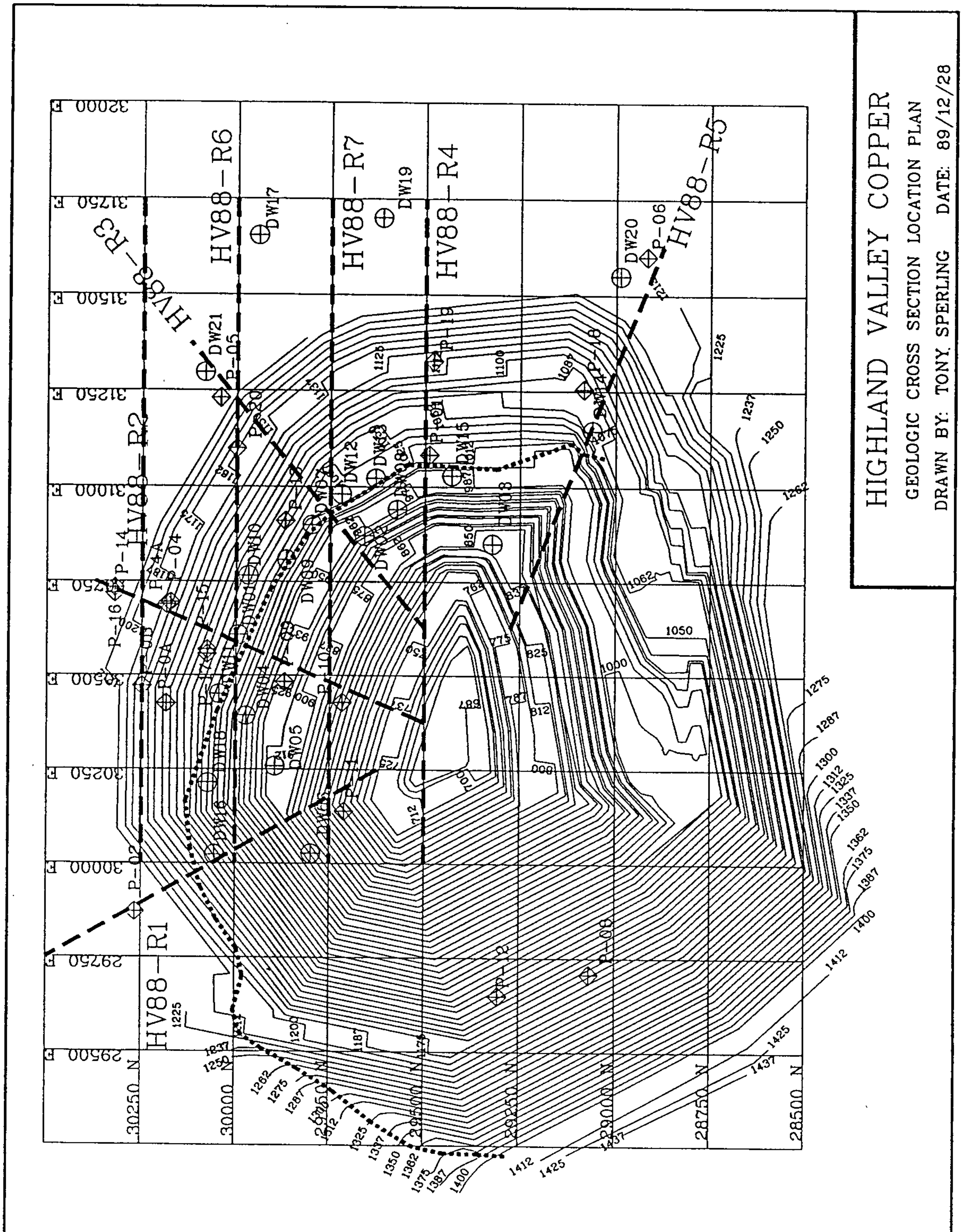

DH83P005	HIGHLAND VALLEY COPPER - VALLEY PIT GROUNDWATER	Page 1 of 2

LOCATION INFORMATION	PURPOSE
Permit/Claim: VALLEY PIT Location: OVERBURDEN Grid Northing: 30044.17 metres Grid Easting: 31231.12 metres Ground Elevation: 1209.69 metres Collar Height: 0.50 metres Hole - Azimuth: 000 deg. - Inclination: 090 deg. - Length: 138.32 metres	To monitor pore pressures in the vicinity of the pit crest in the north-east pit-wall.

GENERAL INFORMATION	REMARKS
Date Started: 830616 Date Completed: 830620 Logged by: UNKNOWN Core Size: 16" CABLE TOOL Contractor: DRILL WELL ENT. Core Storage: OLD LORNEX MILL Boxes of Core: SAMPLE BAGS Pages in Log: 2	

SG-CoreLog Version 5.2

A software system for the collection and analysis of geologic data obtained from diamond drill core.

Developed and supported by:
Sperling GeoComp Incorporated
Suite 101 - 3663 West 16th Ave.
Vancouver, B.C., V6R 3C3

SAMPLE INFORMATION		ORIENTATION TESTS			
LAB REPORT #	SAMPLE NUMBERS COLLECTED	METHOD	DEPTH	AZIM	INCLN

SEMIQUANTITATIVE COLUMN DEFINITIONS

COL#	NAME	DEFINITION
1	PRIM	primary grain size
2	SEC	secondary grain size
3	TERT	tertiary grain size
4	WTR	water bearing potential

ASSAY COLUMN DEFINITIONS

COL#	NAME	DEFINITION

288

DH83P005			HIGHLAND VALLEY COPPER - VALLEY PIT GROUNDWATER				Page 2	
metres		ID	DESCRIPTION	SEMIQUANT. DATA				ASSAYS
FROM	TO	CD		PRIM	SEC	TERT	WTR	SAMPLE #
0.00	2.44	1g	Coarse gravel and boulders.	1	0	0	0	
0.00	0.00	1c	Collar: 1209.69					
2.44	8.53	1g	Sand and gravel, silty, water-bearing.	2	1	3	2	
8.53	17.37	1g	Clay.	4	0	0	0	
8.53	8.53	1c	Piezo: 4					
17.37	18.29	1g	Gravel, coarse.	1	0	0	2	
18.29	18.75	1g	Boulders.	1	0	0	0	
18.75	37.19	1g	Gravel, water-bearing, some silt.	1	3	0	3	
37.19	40.84	1g	Gravel, silty, some water.	1	3	0	2	
40.84	60.35	1g	Gravel, water-bearing.	1	0	0	3	
48.77	48.77	1c	Piezo: 3					
60.35	64.01	1g	Gravel, silty, water-bearing.	1	2	0	3	
64.01	88.39	1g	Gravel, water-bearing.	1	0	0	3	
88.39	96.93	1g	Gravel, silty, water-bearing.	1	3	0	3	
88.39	88.39	1c	Piezo: 2					
96.93	98.15	1g	Silt, black.	3	0	0	0	
98.15	103.33	1g	Sand, silty, water-bearing.	2	3	0	2	
103.33	103.94	1g	Silt.	3	0	0	0	
103.94	108.45	1g	Sand, very silty, water-bearing.	2	3	0	2	
108.45	116.98	1g	Silt with sand stringers.	3	2	0	0	
116.98	117.90	1g	Sand and gravel, silty.	2	1	3	0	
117.90	118.81	1g	Silt.	3	0	0	0	
118.81	123.38	1g	Sand and gravel with silt layers.	2	1	3	0	
123.38	126.13	1g	Sand and gravel, some silt, water-bearing.	2	1	3	3	
126.13	135.88	1g	Silt with water-bearing sand and gravel.	3	2	1	2	
135.88	136.80	1g	Sand and gravel.	2	1	0	1	
136.55	136.55	1c	Piezo: 1					
136.80	138.32	1g	Silt.	3	0	0	0	

289

DH83P013	HIGHLAND VALLEY COPPER - VALLEY PIT GROUNDWATER	Page 1 of 4

LOCATION INFORMATION

Permit/Claim: VALLEY PIT
Location: OVERBURDEN
Grid Northing: 29870.52 metres
Grid Easting: 30909.18 metres
Ground Elevation: 1210.80 metres
Collar Height: 0.50 metres
Hole - Azimuth: 000 deg.
- Inclination: 090 deg.
- Length: 249.90 metres

PURPOSE

To establish a permanent monitoring point in the vicinity of R1 interior wells. This piezometer extends to bedrock.

GENERAL INFORMATION

Date Started: 860720
Date Completed: 860730
Logged by: UNKNOWN
Core Size: 16" CABLE TOOL
Contractor: DRILL WELL ENT.
Core Storage: OLD LORNEX MILL
Boxes of Core: SAMPLE BAGS
Pages in Log: 4

REMARKS

SG-CoreLog Version 5.2

A software system for the collection and analysis of geologic data obtained from diamond drill core.

Developed and supported by:
Sperling GeoComp Incorporated
Suite 101 - 3663 West 16th Ave.
Vancouver, B.C., V6R 3C3

SAMPLE INFORMATION

LAB REPORT #	SAMPLE NUMBERS COLLECTED

ORIENTATION TESTS

METHOD	DEPTH	AZIM	INCLN

SEMIQUANTITATIVE COLUMN DEFINITIONS

COL#	NAME	DEFINITION
1	PRIM	primary grain size
2	SEC	secondary grain size
3	TERT	tertiary grain size
4	WTR	water bearing potential

ASSAY COLUMN DEFINITIONS

COL#	NAME	DEFINITION

DH83P013	HIGHLAND VALLEY COPPER - VALLEY PIT GROUNDWATER	Page 2

metres		ID	DESCRIPTION	SEMIQUANT. DATA				ASSAYS
FROM	TO	CD		PRIM	SEC	TERT	WTR	SAMPLE #
0.00	5.79	1g	Sand and gravel, very silty, brown.	2	1	3	0	
0.00	0.00	1c	Collar: 1210.80					
5.79	10.06	1g	Sand and gravel, very silty, grey.	2	1	3	0	
10.06	10.97	1g	Coarse gravel.	3	0	0	2	
10.97	11.58	1g	Sand and gravel, very silty, grey.	2	1	3	0	
11.58	14.33	1g	Sand and gravel, grey.	2	1	0	2	
14.33	18.59	1g	Sand and gravel, coarse, brown, trace water.	2	1	0	1	
18.59	20.73	1g	Sand and gravel, very silty, brown.	2	1	3	0	
20.73	21.34	1g	Gravel, coarse, water bearing.	1	0	0	3	
21.34	24.38	1g	Sand, coarse, brown.	2	0	0	1	
24.38	26.52	1g	Sand, silty, fine, brown.	2	3	0	0	
26.52	29.87	1g	Sand, very silty, fine, grey.	2	3	0	0	
29.87	30.48	1g	Sand, silty, grey.	2	3	0	0	
30.48	32.31	1g	Sand and gravel, silty, brown.	2	1	3	0	
32.31	40.23	1g	Gravel, very coarse, with boulders.	1	0	0	1	
39.32	39.32	1c	Piezo: 3					
40.23	54.25	1g	Till, gravelly, with boulders, brown.	5	1	0	0	
54.25	60.66	1g	Till, gravelly, with boulders, brown.	5	1	0	0	
60.66	65.23	1g	Till, gravelly, grey.	5	1	0	0	
65.23	73.76	1g	Sand, very coarse, water bearing, lots of water.	2	0	0	4	
73.76	78.64	1g	Sand, silty, grey, water bearing, lots of water.	2	3	0	4	
78.64	79.86	1g	Sand, silty, grey, water bearing.	2	3	0	3	
79.86	81.69	1g	Sand, coarse, clean, water bearing, fair amount water.	2	0	0	4	
80.16	80.16	1c	Piezo: 2					
81.69	86.56	1g	Sand, very silty, grey, not as much water in zone.	2	3	0	1	
86.56	94.79	1g	Dark grey clay and black clay.	4	0	0	0	
94.79	97.54	1g	Greenish clay.	4	0	0	0	
97.54	103.94	1g	Clay, grey.	4	0	0	0	
103.94	116.13	1g	Clay with sandy layers and tight silt, grey.	4	2	3	0	
116.13	117.96	1g	Clay, dark grey.	4	0	0	0	
117.96	121.31	1g	Clay, black.	4	0	0	0	
121.31	124.66	1g	Clay, black.	4	0	0	0	
124.66	128.32	1g	Silt with clay, tight, grey.	3	4	0	0	
128.32	131.06	1g	Silt layers, grey, water bearing.	3	0	0	2	
131.06	131.98	1g	Clay, grey.	4	0	0	0	

DH83P013			HIGHLAND VALLEY COPPER - VALLEY PIT GROUNDWATER					Page 3
metres		ID	DESCRIPTION	SEMIQUANT. DATA				ASSAYS
FROM	TO	CD		PRIM	SEC	TERT	WTR	SAMPLE #
131.98	134.11	1g	Sand, silty, grey, with a little water.	2	3	0	1	
134.11	140.51	1g	Silt, with sandy layers, grey.	3	2	0	0	
140.51	143.26	1g	Black clay.	4	0	0	0	
143.26	145.69	1g	Clay, greenish.	4	0	0	0	
145.69	152.40	1g	Clay, greenish.	4	0	0	0	
152.40	156.06	1g	Silt, grey.	3	0	0	0	
156.06	157.28	1g	Sand, silty, water bearing.	2	3	0	3	
157.28	160.93	1g	Clay, grey.	4	0	0	0	
160.93	163.07	1g	Black clay.	4	0	0	0	
163.07	165.20	1g	Sand, silty, grey, with clay layers.	2	3	4	0	
165.20	166.12	1g	Sand, very silty, water bearing.	2	3	0	2	
166.12	167.94	1g	Clay, black.	4	0	0	0	
167.94	173.13	1g	Silt, dark grey.	3	0	0	0	
173.13	174.65	1g	Sand, very silty, grey, with water.	2	3	0	1	
174.65	175.26	1g	Sand, very silty, with clay, grey.	2	3	4	0	
175.26	179.83	1g	Sand, very silty, grey, water bearing.	2	3	0	2	
179.83	181.66	1g	Sand, black.	2	0	0	0	
181.66	182.27	1g	Clay, black.	4	0	0	0	
182.27	184.71	1g	Clay, black.	4	0	0	0	
184.71	185.62	1g	Silt, grey.	3	0	0	0	
185.62	187.76	1g	Sand, silty, grey, water bearing.	2	3	0	3	
187.76	188.37	1g	Clay, grey.	4	0	0	0	
188.37	190.20	1g	Sand, silty, grey, water bearing.	2	3	0	3	
190.20	192.02	1g	Clay, greenish.	4	0	0	0	
192.02	192.63	1g	Sand, greenish grey, water bearing.	2	0	0	3	
192.63	193.24	1g	Clay, greenish.	4	0	0	0	
193.24	199.03	1g	Clay, greenish.	4	0	0	0	
199.03	219.46	1g	Till, small layers of w.b. sand and gravel, grey.	5	2	1	1	
219.46	222.20	1g	Gravel and sand, silty, grey, makes fair amount water.	1	2	3	3	
222.20	226.47	1g	Sand and gravel, finer, silty, grey, fair amount water.	2	1	3	3	
226.47	228.60	1g	Sand, clean, brown, makes water, lots of heave.	2	0	0	3	
228.60	230.73	1g	Sand, silty, grey.	2	3	0	0	
230.73	235.61	1g	Sand, clean, brown, water bearing.	2	0	0	3	
235.61	239.27	1g	Bedrock, oxide zone, brownish, soft.	7	0	0	0	
239.27	240.79	1g	Bedrock, granite.	7	0	0	0	

290

DH83P013			HIGHLAND VALLEY COPPER - VALLEY PIT GROUNDWATER					Page 4
metres		ID	DESCRIPTION	SEMIQUANT. DATA				ASSAYS
FROM	TO	CD		PRIM	SEC	TERT	WTR	SAMPLE #
240.79	242.93	1g	Oxide zone bedrock, very broken, makes lots of water.	7	0	0	3	
242.93	249.94	1g	Open hole in bedrock, broken, soft, water bearing.	7	0	0	3	
245.97	245.97	1c	Piezo: 1					

DH84W002	HIGHLAND VALLEY COPPER - VALLEY PIT GROUNDWATER	Page 1 of 2

LOCATION INFORMATION	PURPOSE
Permit/Claim VALLEY PIT Location: OVERBURDEN Grid Northing: 29660.59 metres Grid Easting: 30869.82 metres Ground Elevation: 1214.58 metres Collar Height: 0.50 metres Hole - Azimuth: 000 deg. - Inclination: 90 deg. - Length: 97.20 metres	To dewater interior of Valley Pit before Pit-5 and Pit-6 excavation begins.

GENERAL INFORMATION	REMARKS
Date Started: 860626 Date Completed: 860626 Logged by: UNKNOWN Core Size: 16" CABLE TOOL Contractor: DRILL WELL ENT. Core Storage: OLD LORNEX MILL Boxes of Core: SAMPLE BAGS Pages in Log: 2	

SG-CoreLog Version 5.2	SAMPLE INFORMATION		ORIENTATION TESTS			
	LAB REPORT #	SAMPLE NUMBERS COLLECTED	METHOD	DEPTH	AZIN	INCLN
A software system for the collection and analysis of geologic data obtained from diamond drill core. Developed and supported by: Sperling GeoComp Incorporated Suite 101 - 3663 West 16th Ave. Vancouver, B.C., V6R 3C3						

162

SEMIQUANTITATIVE COLUMN DEFINITIONS			ASSAY COLUMN DEFINITIONS		
COL#	NAME	DEFINITION	COL#	NAME	DEFINITION
1	PRIM	primary grain size			
2	SEC	secondary grain size			
3	TERT	tertiary grain size			
4	WTR	water bearing potential			

DH84W002			HIGHLAND VALLEY COPPER - VALLEY PIT GROUNDWATER					Page 2
metres		ID	DESCRIPTION	SEMIQUANT. DATA				ASSAYS
FROM	TO	CD		PRIM	SEC	TERT	WTR	SAMPLE #
0.00	21.03	1g	Silty sand and gravel with cobbles and boulders.	2	1	3	0	
0.00	0.00	1c	Collar: 1214.58					
21.03	32.31	1g	Silty clay, brown, some fine gravel.	4	3	1	0	
32.31	42.06	1g	Sand and gravel, silty, loose, water bearing.	2	1	3	3	
35.66	66.14	1c	Screen:30/1000					
42.06	48.46	1g	Sand and gravel with cobbles, very silty, and tight.	2	1	3	0	
48.46	52.42	1g	Sand, medium to coarse with gravel, water bearing.	2	1	0	3	
52.42	55.17	1g	Gravel, coarse, clean, water bearing.	2	0	0	3	
55.17	57.00	1g	Gravel, medium with silt.	1	3	0	1	
57.00	58.83	1g	Sand and gravel, silty, tight.	2	1	3	0	
58.83	62.18	1g	Sand, coarse, gravel.	2	1	0	2	
62.18	64.62	1g	Sand, fine to coarse, silt.	2	3	0	1	
64.62	66.14	1g	Sand, fine to coarse, loose heaving.	2	0	0	0	
66.14	67.97	1g	Sand fine to coarse, silty, tight.	2	3	0	0	
67.97	69.80	1g	Sand, fine to coarse, loose, water bearing.	2	0	0	3	
69.80	70.71	1g	Till, grey.	5	0	0	0	
70.10	70.10	1c	Pump: 40					
70.71	81.99	1g	Gravel, very coarse, clean, water bearing.	1	0	0	3	
72.24	84.43	1c	Screen:30/1000					
81.99	84.43	1g	Sand and gravel, black.	2	1	0	1	
84.43	85.04	1g	Sand and gravel, black, very silty.	2	1	3	0	
85.04	96.62	1g	Clay, black.	4	0	0	0	
96.62	97.23	1g	Clay, sandy, brown.	4	0	0	0	
97.23	97.23	1c	End of hole.					

DH85W007	HIGHLAND VALLEY COPPER - VALLEY PIT GROUNDWATER	Page 1 of 3

LOCATION INFORMATION

Permit/Claim: VALLEY PIT
Location: OVERBURDEN
Grid Northing: 29798.75 metres
Grid Easting: 30899.23 metres
Ground Elevation: 1210.48 metres
Collar Height: 0.50 metres
Hole - Azimuth: 000 deg.
- Inclination: 90 deg.
- Length: 193.80 metres

PURPOSE

To dewater interior of pit prior to Pit-5 and Pit-6 excavation.

GENERAL INFORMATION

Date Started: 851108
Date Completed: 851108
Logged by: UNKNOWN
Core Size: 16" CABLE TOOL
Contractor: DRILL WELL ENT.
Core Storage: OLD LORNEX MILL
Boxes of Core: SAMPLE BAGS
Pages in Log: 3

REMARKS

SG-CoreLog Version 5.2

A software system for the collection and analysis of geologic data obtained from diamond drill core.

Developed and supported by:
Sperling GeoComp Incorporated
Suite 101 - 3663 West 16th Ave.
Vancouver, B.C., V6R 3C3

SAMPLE INFORMATION

LAB REPORT #	SAMPLE NUMBERS COLLECTED

ORIENTATION TESTS

METHOD	DEPTH	AZIM	INCLN

SEMIQUANTITATIVE COLUMN DEFINITIONS

COL#	NAME	DEFINITION
1	PRIM	primary grain size
2	SEC	secondary grain size
3	TERT	tertiary grain size
4	WTR	water bearing potential

ASSAY COLUMN DEFINITIONS

COL#	NAME	DEFINITION

292

DH85W007	HIGHLAND VALLEY COPPER - VALLEY PIT GROUNDWATER	Page 2

metres		ID	DESCRIPTION	SEMIQUANT. DATA				ASSAYS
FROM	TO	CD		PRIM	SEC	TERT	WTR	SAMPLE #
0.00	4.57	1g	Till, brown, back hoe dug.	5	0	0	0	
0.00	0.00	1c	Collar: 1210.48					
4.57	6.40	1g	Sand and gravel, tight, silty.	2	1	3	0	
6.40	7.92	1g	Till, grey, silty.	5	3	0	0	
7.92	10.06	1g	Sand and gravel, tight, silty, water-bearing lenses.	2	1	3	1	
10.06	11.89	1g	Till, grey.	5	0	0	0	
11.89	15.24	1g	Sand and gravel, coarse, water-bearing.	2	1	0	3	
15.24	19.51	1g	Sand and gravel, tight, silty.	2	1	3	0	
19.51	28.65	1c	Screen: 20/1000					
19.51	26.21	1g	Clay, silty, sandy.	4	3	2	0	
26.21	28.65	1g	Silt, tight and silty sand.	3	2	0	0	
28.65	43.89	1c	Screen: 20/1000					
28.65	36.27	1g	Sand and gravel, very tight, silty.	2	1	3	0	
36.27	37.18	1g	Silt and cobbles.	3	1	0	0	
37.18	39.62	1g	Sand and gravel, silty, water-bearing.	2	1	3	3	
39.62	41.15	1g	Sand and gravel, tight, silty.	2	1	3	0	
41.15	42.37	1g	Sand and gravel, boulders, water-bearing.	2	1	0	3	
42.37	43.59	1g	Till, silty brown.	5	3	0	0	
43.59	45.72	1g	Sand and gravel, tight, silty.	2	1	3	1	
45.72	58.83	1g	Till, clayey, grey.	5	4	0	0	
58.83	65.23	1g	Till, sandy and silty.	5	2	3	0	
59.13	65.23	1c	Screen: 20/1000					
65.23	65.53	1g	Clay, black.	4	0	0	0	
65.53	66.14	1g	Gravel, silty, tight, black.	1	3	0	0	
66.14	70.10	1g	Gravel, silty, tight, with layers of tight silt.	1	3	0	0	
67.36	73.46	1c	Screen: 20/1000					
70.10	73.46	1g	Sand and gravel, silty, water-bearing.	2	1	3	2	
73.46	74.68	1g	Silt, tight, green.	3	0	0	0	
74.68	75.89	1g	Clay, silty, black.	4	3	0	0	
75.89	77.11	1g	Gravel, silty, tight, black.	1	3	0	1	
77.11	78.33	1g	Till, silty.	5	3	0	0	
77.72	83.82	1c	Screen: 20/1000					
78.33	83.82	1g	Sand and gravel, silty with water-bearing strings blk.	2	1	3	2	
83.82	85.65	1g	Silt and silty clay, tight, dark grey to black.	3	4	0	0	
85.65	89.91	1g	Clay with silt layer, sticky dark grey.	4	3	0	0	

DH85W007 — HIGHLAND VALLEY COPPER - VALLEY PIT GROUNDWATER — Page 3

metres FROM	metres TO	ID CD	DESCRIPTION	SEMIQUANT. DATA PRIM	SEC	TERT	WTR	ASSAYS SAMPLE #
89.91	93.57	1g	Clay, black, sticky.	4	0	0	0	
93.86	128.93	1g	Clay, black with seams of silty clay, green.	4	3	0	0	
128.93	152.40	1g	Clay, black with layers of tight silt.	4	3	0	0	
152.40	161.54	1g	Clay, black with silty sand.	4	3	0	0	
161.54	169.16	1g	Silt, tight, very stiff.	3	0	0	0	
169.16	175.26	1g	Clay, black and silt.	4	3	0	0	
175.26	179.83	1g	Clay, silty, black with layers of silty sand.	4	3	2	0	
178.61	190.80	1c	Screen: 20/1000					
179.83	190.80	1g	Sand, silty, with layers of silt and silty sand. w-b.	2	3	0	1	
190.80	193.80	1g	Bedrock, granitic.					

DH87V021 — HIGHLAND VALLEY COPPER - VALLEY PIT GROUNDWATER — Page 1 of 3

LOCATION INFORMATION

Permit/Claim: VALLEY PIT
Location: OVERBURDEN
Grid Northing: 30085.74 metres
Grid Easting: 31297.08 metres
Ground Elevation: 1209.60 metres
Collar Height: 0.50 metres
Hole - Azimuth: 000 deg.
- Inclination: 090 deg.
- Length: 152.40 metres

PURPOSE

GENERAL INFORMATION

Date Started: 870624
Date Completed: 870814
Logged by: K. NEWMAN
Core Size: 16" CABLE TOOL
Contractor: DRILL WELL ENT.
Core Storage: OLD LORNEX MILL
Boxes of Core: SAMPLE BAGS
Pages in Log: 3

REMARKS

SG-CoreLog Version 5.2

A software system for the collection and analysis of geologic data obtained from diamond drill core.

Developed and supported by:
Sperling GeoComp Incorporated
Suite 101 - 3663 West 16th Ave.
Vancouver, B.C., V6R 3C3

SAMPLE INFORMATION

LAB REPORT #	SAMPLE NUMBERS COLLECTED

ORIENTATION TESTS

METHOD	DEPTH	AZIM	INCLN

SEMIQUANTITATIVE COLUMN DEFINITIONS

COL#	NAME	DEFINITION
1	PRIM	primary grain size
2	SEC	secondary grain size
3	TERT	tertiary grain size
4	WTR	water bearing potential

ASSAY COLUMN DEFINITIONS

COL#	NAME	DEFINITION

293

OH87V021			HIGHLAND VALLEY COPPER - VALLEY PIT GROUNDWATER	Page 2				
metres		ID	DESCRIPTION	SEMIQUANT. DATA				ASSAYS
FROM	TO	CD		PRIM	SEC	TERT	WTR	SAMPLE #
0.00	4.27	1n	UPPER AQUIFER (unit 1)					
0.00	4.27	1g	Gravel, some cobbles, silty. Brown.	1	3	0	3	
		2g	Gravel, silty brown, with large cobbles.	1	3	0	0	
0.00	0.00	1c	Dug in. (June 23)					
4.27	19.20	1n 1g	TILL-0 (unit 2) Till, silty and sandy with cobbles. Some silt layers. Brown.	5	3	2	0	
4.27	4.88	2g	Gravel, silty, brown.	1	3	0	0	
4.88	5.79	2g	Till, brown, dark with some cobbles.	5	1	0	0	
5.79	9.75	2g	Till, brown.	5	0	0	0	
9.75	14.33	2g	Till, with silt layers. Grey.	5	3	0	0	
14.33	19.20	2g	Till, brown.	5	0	0	0	
19.20	28.04	1n 1g	ON-ONE DIVIDER (unit 3) Gravel, coarse, mostly boulders, cemented with silt. Layers of till and coarse water bearing gravel. Boulders are granitic. Colour is brown.	1	2	0	4	
19.20	21.34	2g	Gravel. Grey, water bearing.	1	2	0	3	
21.34	22.56	2g	Gravel, mostly granitic boulder. Gravel grey, cemented.	1	3	0	2	
22.56	24.99	2g	Gravel, coarse, with layers of till. Water bearing.	1	2	0	4	
24.99	25.91	2g	Gravel, very coarse. Water bearing.	1	0	0	5	
25.91	27.13	2g	Gravel, coarse. Brown, water bearing.	1	2	0	4	
27.13	28.04	2g	Gravel, mostly boulders.	1	2	3	3	
28.04	60.96	1g	Numerous layers of cemented brown gravel. Some gravel layers are water bearing.	5	3	1	1	
28.04	42.06	1n 1g	TILL-1 (unit 4) Till, silty and sandy with cobbles. Sand is graded. Colour is brown.					
28.04	31.09	2q		1	2	3	4	
28.04	28.96	2g	Till, brown.	5	0	0	0	
28.96	31.09	2g	Gravel. Brown, water bearing.					
31.09	31.70	2g	Till, brown.	5	0	0	0	
31.70	34.44	2g	Gravel, some silt. Mostly cemented gravel, some water bearing layers, brown.	1	3	0	3	
34.44	36.58	2g	Till, brown.	5	0	0	0	
36.58	42.06	2g	Till, with cobbles. Brown.	5	1	0	0	
42.06	48.16	2g	Gravel, some silt. Gravel mostly cemented some water bearing layers. Brown. One layer of grey clay.	1	3	4	1	
48.16	50.60	2g	Clay. Grey.	4	0	0	0	
50.60	52.43	2g	Till, some layers of water bearing material. Brown.	5	0	0	0	
52.43	55.47	2g	Dark grey till with layers of silt and clay.	5	2	4	0	
55.47	56.39	2g	Gravel, coarse, silty. Brown, water bearing.	1	3	0	2	
56.39	57.91	2g	Till, with layers of water bearing gravel and silt lenses. Very coarse	5	1	3		

294

OH87V021			HIGHLAND VALLEY COPPER - VALLEY PIT GROUNDWATER	Page 3				
metres		ID	DESCRIPTION	SEMIQUANT. DATA				ASSAYS
FROM	TO	CD		PRIM	SEC	TERT	WTR	SAMPLE #
			gravel, water bearing, silty, brown.					
57.91	60.96	2g	Till, with layers of water bearing gravel. Brown.	5	3	1	1	
60.96	73.15	1n 1g	UPPER SILTY AQUIFER (unit 4) Gravel, coarse, silty, some sand. Sand is graded. Brown, mostly water bearing, becoming cleaner with depth.	1	2	3	3	
60.96	66.14	2g	Coarse gravel, silty. Brown, water bearing.	1	3	0	3	
66.14	68.58	2g	Gravel with layers of silt. Coarse, water bearing, brown.	1	3	0	3	
68.58	70.10	2g	Gravel, coarse, silty. Brown, water bearing.	1	3	0	3	
70.10	73.15	2g	Gravel, coarse, brown. Silty, getting cleaner.	1	2	3	4	
73.15	86.87	1n 1g	LOWER SILTY AQUIFER (unit 4) Sand, medium to fine, silty layers, some fine gravel. Dark grey, water bearing.	2	3	1	2	
73.15	77.72	2g	Sand, some coarse gravel, one layer of silt. Brown, water bearing.	2	1	3	3	
77.72	80.77	1c 2g	Casing becoming tight. Sand, with a few layers of silt. Getting a lot more fines, water bearing.	2	3	0	2	
80.77	82.30	2g	Sand, silty. Brown, tight.	2	3	0	1	
82.30	83.82	2g	Silt, with layers of till. Dark grey, water bearing.	3	2	1	2	
83.82	85.34	2g	Gravel, medium with sand and layers of silt. Dark grey, water bearing.	1	2	3	3	
85.34	86.87	2g	Sand, with fine gravel, silty. Dark grey.	2	1	3	3	
86.87	92.96	2g	Gravel, silty. Water bearing with layers of till.	1	3	5	1	
86.87	108.20	1n 1g	TILL-2 (unit 5) Till, clayey, some sand and cobbles. Dark grey.	5	4	2	0	
92.96	99.06	2g	Silt turning to till. Grey.	3	5	0	1	
99.06	103.63	2g	Gravel, some cobbles. Grey.	5	1	3	0	
103.63	108.20	2g	Gravel, turning to dark grey clay with some sand.	5	4	2	0	
108.20	152.40	1n 1g	BLACK CLAY (unit 7) Silt with layers of cobbly till and clay. Dark grey. Transition layer between till and black clay unit.	3	4	1	0	
108.20	118.87	2g	Clay, silty. Dark grey. Occassional layers of grey till.	4	3	5	0	
118.87	121.01	2g	Till, layers of silt. Dark grey.	5	3	0	0	
121.01	129.24	2g	Silt, dark grey with layers of dark grey till.	3	5	0	0	
129.24	134.72	2g	Silt with layers of cobbly till. Dark grey.	3	1	5	0	
134.72	142.65	2g	Silt, with few cobbles. Turning to dark grey clay.	3	4	1	0	
142.65	148.74	2g	Silt, with layers of clay. Dark grey.	3	4	0	0	
148.74	152.40	2g	Silt, turning to grey till. Dark grey.	3	4	5	0	

DH88P020	HIGHLAND VALLEY COPPER - VALLEY PIT GROUNDWATER	Page 1 of 7

LOCATION INFORMATION	PURPOSE
Permit/Claim VALLEY PIT Location: OVERBURDEN Grid Northing: 29963.45 metres Grid Easting: 31131.93 metres Ground Elevation: 1204.27 metres Collar Height: 0.50 metres Hole - Azimuth: 360 deg. - Inclination: -90 deg. - Length: 228.60 metres	To complete central piezometer on geotechnical section R-3. This piezometer will provide pore pressure information in center portion of final pit wall as well as in crest area of initial push backs. Information about the nature of the the fine sediments at depth (black clay) was also desired from this drill hole.

GENERAL INFORMATION	REMARKS
Date Started: 880410 Date Completed: 880623 Logged by: TONY SPERLING Core Size: 8 INCH ROTARY Contractor: DRILL WELL ENT. Core Storage: OLD LORNEX MILL Boxes of Core: SAMPLE BAGS Pages in Log: 7	The hole was completed at 750 ft. It did not encounter bedrock. It did encounter a massive silt an clay unit at the bottom of the hole. The hole was completed at 750' because this is the approximate depth of the bedrock overburden contact in the ultimate pit wall. Any overburden material below this depth would not daillight.

SG-CoreLog Version 5.2	SAMPLE INFORMATION		ORIENTATION TESTS			
	LAB REPORT #	SAMPLE NUMBERS COLLECTED	METHOD	DEPTH	AZIM	INCLN
A software system for the collection and analysis of geologic data obtained from diamond drill core. Developed and supported by: Sperling GeoComp Incorporated Suite 101 - 3663 West 16th Ave. Vancouver, B.C., V6R 3C3						

SEMIQUANTITATIVE COLUMN DEFINITIONS			ASSAY COLUMN DEFINITIONS		
COL#	NAME	DEFINITION	COL#	NAME	DEFINITION
1	PRIM	primary grain size			
2	SEC	secondary grain size			
3	TERT	tertiary grain size			
4	WTR	water bearing potential			

DH88P020			HIGHLAND VALLEY COPPER - VALLEY PIT GROUNDWATER					Page 2
metres		ID	DESCRIPTION	SEMIQUANT. DATA				ASSAYS
FROM	TO	CD		PRIM	SEC	TERT	WTR	SAMPLE #
0.00	0.00	1c	Collar: 1204.00					
71.01	71.01	1c	Piezo: 5					
99.06	99.06	1c	Piezo: 4					
134.72	134.72	1c	Piezo: 3					
165.81	165.81	1c	Piezo: 2					
220.98	220.98	1c	Piezo: 1					
0.00	1.82	1c	Rock fill.					
1.82	5.18	1g	Sand and gravel. Grey.	2	1	0	4	
5.18	9.44	1g	Till, silt and gravel.	5	3	4	0	
7.62	9.44	2g	Silt and clay, tan grey. Soupy when wet. No coarse fraction noted by driller observed in sample. Possible till, but appears fluvial.	3	4	0	0	
9.44	22.86	1g	Till, some boulders. Dark grey.	5	3	1	0	
9.44	10.66	2g	Till, silt and clay, some graded gravel. Gravel is subrounded, mostly volcanics, red, brown, etc. Till colour is brown grey.	5	4	1	0	
10.66	12.19	2g	Till, silt and clay, trace gravel. Brown, moist.	5	3	4	0	
12.19	15.24	2g	Till, silt and clay, trace gravel. Brown grey, dry, dense.	5	3	4	0	
15.24	16.76	2g	Till, silt and clay, trace fine sand. Tan grey, wet.	5	3	4	0	
16.76	18.28	2g	Till, coarse gravel, silty, clayey. Grey tan.	5	1	4	0	
18.28	19.81	2g	Till, medium to fine sand, clayey, silty. Tan grey.	5	2	4	0	
19.81	21.33	2g	Till, silt and graded gravel. Grey brown.	5	3	1	0	
21.33	22.86	2g	Till, sandy. Some graded gravel. Grey green. Gravel is rounded.	5	2	1	0	
22.86	27.43	1g	Graded fluvial, including gravelly silt and sandy gravel. Dark grey green. Transition unit between overlying till, and underlying sand and gravel.	2	3	1	2	
22.86	24.38	2g	Sand, medium to coarse, silty. Dark grey green.	2	3	0	2	
24.38	25.90	2g	Till, sandy, some graded gravel. Grey green.	5	2	1	0	
25.90	27.43	2g	Gravel, graded, sandy, some silt. Tan grey. Gravel is sub-angular, mostly dark volcanics.	1	2	3	2	
27.43	36.27	1g	Medium to coarse sand, silty, lenses of water bearing sand and gravel and till. Driller reports unit as till, most appears fluvial.	2	1	0	2	
27.43	28.95	2g	Medium to coarse sand and fine gravel, silty. Tan grey.	2	1	3	2	
28.95	30.48	2g	Gravel, coarse, silty, some sand. Tan grey, possible till, but unlikely??	1	2	3	2	
30.48	32.00	2g	Graded sand and gravel, silty. Grey, salt and pepper, granitic source.	2	1	3	2	
32.00	33.52	2g	Medium to coarse sand, gravelly, some silt.	2	1	3	3	
33.52	35.05	2g	Medium to coarse sand, silty. Tan grey.	2	3	0	3	
35.05	36.27	2g	Medium to coarse sand, silty, trace fine gravel. Tan grey.	2	3	1	2	
36.27	41.75	1g	Sand and gravel, silty. Brown, water bearing, gravel mostly coarse.	2	1	0	4	
36.27	38.10	2g	Gravel, graded, sandy, some silt. Tan grey, gravel is rounded.	1	2	0	4	

296

DH88P020			HIGHLAND VALLEY COPPER - VALLEY PIT GROUNDWATER					Page 3
metres		ID	DESCRIPTION	SEMIQUANT. DATA				ASSAYS
FROM	TO	CD		PRIM	SEC	TERT	WTR	SAMPLE #
38.10	39.62	2g	Graded sand and gravel. Grey tan, clean. Gravel is rounded.	2	1	0	5	
39.62	41.75	2g	Medium to coarse sand, gravelly, grey green. Clean.	2	1	0	4	
41.75	47.24	1g	Fine gravel and sand, very silty. Brown.	2	1	3	4	
41.75	42.67	2g	Coarse sand, gravelly, some silt. Tan grey.	2	1	3	4	
42.67	44.19	2g	Silt, some clay and fine sand. Dark grey when wet, grey tan when dry.	3	2	4	0	
44.19	45.72	2g	Silt and very fine sand, some clay. Tan grey, soupy.	3	2	4	0	
45.72	47.24	2g	Graded sand and gravel, silty. Grey tan.	2	1	3	0	
47.24	50.29	1g	Dense brown silt, layers of water bearing silty sand and gravel.	2	3	4	1	
47.24	48.76	2g	Silt and very fine sand, some clay. Medium grey tan.	3	2	4	0	
48.76	50.29	2g	Very fine sand, silty. Grey tan.	2	3	0	1	
50.29	55.77	1g	Graded sand, silty, some fine gravel. Grey, dense, some water bearing layers of silty sand. Driller reports lithology as till. Appears to be fluvial unit when cup sample examined.	5	2	3	0	
50.29	51.81	2g	Sandy till, some silt. Possibly fluvial.	5	2	3	0	
51.81	54.86	2g	Till. Graded sand, some fine gravel, silty.	5	2	1	1	
54.86	55.77	2g	Fine gravel, some sand, silty. Medium grey green.	1	2	3	1	
55.77	74.06	1g	Grey silt and grey silty sand and gravel, interbedded. Water bearing.	3	4	0	0	
55.77	57.91	2g	Silt, clayey. Dark grey, grey tan when oxidized.	3	4	0	0	
57.91	59.43	2g	Graded sand, very silty. Dark grey.	2	3	0	1	
59.43	60.96	2g	Graded sand, silty, some clay layers. Dark grey.	2	3	4	1	
60.96	62.48	2g	Medium to fine sand, silty. Dark grey.	2	3	0	2	
62.48	64.00	2g	Medium to fine sand, silty. Dark grey.	2	3	0	2	
64.00	65.53	2g	Medium to fine sand, silty. Dark grey.	2	3	0	2	
65.53	67.05	2g	Graded sand, trace silt. Medium grey.	2	3	0	3	
67.05	68.58	2g	Graded sand, trace gravel. Clean, medium grey.	2	1	3	3	
68.58	70.10	2g	Fine sand, silty. Medium grey.	2	3	0	2	
70.10	71.62	2g	Graded sand, some silt. Medium grey.	2	3	0	3	
71.62	73.15	2g	Medium to coarse sand, trace silt.	2	1	3	3	
73.15	74.06	2g	Medium to fine sand, some silt, medium grey.	2	3	0	2	
74.06	82.29	1g	Clay, dark grey to black, with silt layers.	4	3	0	0	
74.06	76.20	2g	Fine sand and silt, clayey. Dark grey.	2	3	4	0	
76.20	77.72	2g	Clay, silty. Dark grey. Grey green when oxidized.	4	3	0	0	
77.72	79.24	2g	Clay, silty. Dark grey, medium grey green when oxidized.	4	3	0	0	
79.24	83.82	2c	Missing samples 260 ft to 275 ft.					
79.24	82.29	1c	Ran core 260 ft to 270 ft. 100% recovery in clay and silt.					
82.29	89.91	1g	Clay and silt. Dark green, black and grey. Dense.	4	3	0	0	

DH88P020			HIGHLAND VALLEY COPPER - VALLEY PIT GROUNDWATER					Page 4
metres		ID	DESCRIPTION	SEMIQUANT. DATA				ASSAYS
FROM	TO	CD		PRIM	SEC	TERT	WTR	SAMPLE #
83.82	85.34	2g	Silt and clay, black. Oxidized to medium grey green. Organics.	3	4	0	0	
85.34	86.86	2g	Clay and silt. Dark green grey to black.	4	3	0	0	
86.86	88.39	2g	Clay and silt, dark grey to black.	4	3	0	0	
88.39	89.91	2g	Clay, silty. Dark grey, oxidized to medium grey green.	4	3	0	0	
89.91	93.26	1g	Fine gravel and sand, dark grey, silty, water bearing.	2	3	0	2	
89.91	91.44	2g	Medium to fine sand, silty. Dark grey.	2	3	0	2	
91.44	93.26	2c	Missing sample 300 to 305 ft.					
93.26	94.48	2g	Silt and clay. Dark grey, very soupy.	3	4	0	0	
93.26	106.68	1g	Dark grey to black silt and clay, some thin layers of silty sand and gravel. Water bearing.	3	4	0	0	
94.48	96.01	2g	Silt and clay. Dark grey, soupy, oxidized to medium grey green.	3	4	0	0	
96.01	97.53	2g	Silt and clay. Dark grey, soupy, oxidized to medium grey green.	3	4	0	0	
97.53	99.06	2g	Very fine sand and silt, some clay. Medium grey green.	2	3	4	0	
99.06	100.58	2g	Silt and clay. Dark grey to medium grey green.	3	4	0	0	
100.58	102.10	2g	Silt and clay. Dark grey to medium grey green.	3	4	0	0	
102.10	103.63	2g	Clay and silt. Dark grey to medium grey green.	4	3	0	0	
103.63	105.15	2g	Clay and silt, dark grey to medium grey green.	4	3	0	0	
105.15	106.68	2g	Silt and clay, medium grey.	3	4	0	0	
106.68	108.20	1g	Fine sand, silty. Dark grey. Driller reports sand and gravel, water bearing?	2	3	0	2	
		2g	Fine sand, silty. Dark grey.	2	3	0	2	
108.20	120.09	1g	Silt and clay. Dark grey to medium grey green or black. Dense.	3	4	0	0	
108.20	109.72	2g	Silt and clay, dark grey to medium grey green.	3	4	0	0	
109.72	111.25	2g	Clay and silt. Dark grey to medium grey green. Swelling.	4	3	0	0	
111.25	112.77	2g	Clay, some silt. Dark grey. Very soupy in vial.	4	3	0	0	
112.77	114.30	2g	Clay, some silt. Dark grey. Very soupy.	4	3	0	0	
114.30	115.82	2g	Clay, silty. Medium grey green. Very soupy.	4	3	0	0	
115.82	118.87	2c	Cored 300 ft to 390 ft in dense silt. 6.5 ft recovery.					
115.82	117.34	2g	Clay, silty. Medium grey green. Very soupy.	4	3	0	0	
117.34	118.87	2c	Missing sample 385-390 ft.					
118.87	120.39	2g	Clay, some silt. Medium grey, bright grey green when oxidized. Possibly swelling.	4	3	0	0	
		2c	** Take sample for test @ 390 to 395 ft. **					
120.09	123.44	1g	Silty sand. Dark grey. Water bearing.	2	3	0	2	
120.09	121.92	2g	Fine sand, silty. Dark grey.	2	3	0	2	
121.92	123.44	2g	Fine sand, silty. Dark grey.	2	3	0	2	
123.44	139.29	1g	Silt and clay. Dark grey, becoming grey green with depth. Oxidized to	3	4	0	0	

297

DH88P020			HIGHLAND VALLEY COPPER - VALLEY PIT GROUNDWATER	Page 5				
metres		ID	DESCRIPTION	SEMIQUANT. DATA				ASSAYS
FROM	TO	CD		PRIM	SEC	TERT	WTR	SAMPLE #
			medium grey green colour. Cuttings soupy, but fragments indicate original material dense.					
123.44	124.96	2g	Silt and clay, dark grey. Soupy.	3	4	0	0	
124.96	126.49	2g	Silt and clay. Dark grey oxidized to medium grey green.	3	4	0	0	
126.49	128.01	2g	Silt, clayey, some sand. Dark grey.	3	4	2	0	
128.01	129.54	2g	Silt and clay. Trace fine sand. Dark grey. Oxidized to medium grey green.	3	4	2	0	
129.54	131.06	2g	Clay, silty, dark grey green, oxidized to medium grey grden.	4	3	0	0	
131.06	132.58	2g	Clay, silty. Dark grey to black. Oxidized to medium grey green, chunks of plastic clay in cuttings.	4	3	0	0	
132.58	134.11	2g	Silt and clay, trace fine sand. Dark grey, oxidized to medium grey green.	3	4	2	0	
134.11	135.63	2g	Clay, silty, trace sand. Dark grey green.	4	3	0	0	
135.63	137.16	2c	No sample 445-450 ft.					
137.16	138.68	2g	Silt, sandy, some clay. Medium grey to medium grey green.	3	2	4	0	
138.68	140.20	2g	Clay and silt. Dark grey green to black. Very dense cuttings in soupy vial.	4	3	0	0	
139.29	141.73	1g	Sand and gravel, dark grey to blackish, water bearing.	2	1	0	4	
		2g	Sand, medium to coarse, some gravel. Dark grey, gravel is rounded, clean.	2	1	0	4	
141.73	164.28	1g	Dark grey to black silt and clay, dense to very dense.	3	4	0	0	
141.73	143.25	2g	Silt, clayey, trace fine sand. Dark grey, oxidized to medium grey green. Cuttings occasionally as dense chunks.	3	4	2	0	
143.25	144.78	2g	Silt and clay, medium grey. Oxidized to medium grey green.	3	4	0	0	
144.78	146.30	2g	Clay and silt, dark grey. Oxidized to medium grey green.	4	3	0	0	
146.30	149.35	2c	Ran core 480-490 ft, recovery 9.5 ft in silt.					
146.30	147.82	2g	Clay and silt. Dark grey.	4	3	0	0	
147.82	149.35	2g	Silt and clay, dark grey. Oxidized to medium grey green.	3	4	0	0	
149.35	150.87	2c	Missing sample 490-495 ft.					
150.87	152.40	2g	Silt and clay. Medium grey green.	3	4	0	0	
152.40	153.92	2g	Very fine sand, silty. Dark grey green.	2	3	4	1	
153.92	155.44	2g	Clay, silty. Dark green grey to black. Soupy.	4	3	0	0	
155.44	156.97	2g	Silt and clay, trace fine sand. Dark grey.	3	4	2	0	
156.97	158.49	2g	Silt, sandy and some clay. Dark grey, oxidized to medium grey green.	3	2	4	0	
158.49	160.02	2g	Silt, clayey, medium grey green.	3	4	0	0	
160.02	161.54	2g	Silt and clay, dark grey. Soupy.	3	4	0	0	
161.54	164.28	2c	No sample taken.					
164.28	167.33	1g	Dark grey to black silty gravel and sand, water bearing.	2	3	0	2	
164.28	164.59	2g	Sand, very fine, silty. Dark grey.	2	3	0	2	

DH88P020			HIGHLAND VALLEY COPPER - VALLEY PIT GROUNDWATER	Page 6				
metres		ID	DESCRIPTION	SEMIQUANT. DATA				ASSAYS
FROM	TO	CD		PRIM	SEC	TERT	WTR	SAMPLE #
164.59	166.11	2g	Sand, very fine, silty. Dark grey.	2	3	0	2	
166.11	167.33	2g	Sand, fine, silty, dark grey, trace medium sand size rock chips, red and green.	2	3	0	2	
167.33	178.30	1g	Interbedded very fine silty sand and silt. Dark grey green. Water bearing.	2	3	0	2	
167.33	169.16	2g	Fine to medium sand, some silt. Dark grey green.	2	3	0	2	
169.16	170.68	2g	Very fine sand, silty. Dark grey green.	2	3	0	2	
170.68	172.21	2g	Very fine sand, silty, dark grey.	2	3	0	2	
172.21	173.73	2g	Fine to medium sand, some silt. Dark grey, oxidized to medium grey green.	2	3	0	3	
173.73	175.26	2g	Fine sand, some silt. Dark grey, oxidized to medium grey green.	2	3	0	2	
175.26	176.78	2g	Sand, very fine, some silt. Dark grey green.	2	3	0	2	
176.78	178.30	2g	Sand, very fine, silty. Dark grey green to black.	2	3	4	1	
178.30	182.88	1g	Clay and silt. Dark grey green. Oxidized to medium grey green.	4	3	0	0	
178.30	179.83	2g	Clay, silty. Dark grey, oxidized to medium grey green, soupy, possibly swelling.	4	3	0	0	
179.83	181.35	2g	Silt and clay. Dark grey, oxidized to medium grey green, soupy.	3	4	0	0	
181.35	182.88	2g	Silt and clay, sandy, medium grey, oxidized to medium grey green.	3	4	2	0	
182.88	184.40	2g	Silt and clay, some sand, very fine, medium grey, oxidized to medium grey green.	3	4	2	0	
182.88	228.60	1g	Silt and clay. Medium grey, dense, oxidized to medium grey green. Colour is lighter than previous unit. Some sandy layers.	3	4	0	0	
184.40	185.92	2g	Clay, silty. Medium grey tan, possibly swelling.	4	3	0	0	
185.92	187.45	2g	Clay, some silt. Light grey tan, swelling.	4	3	0	0	
187.45	190.50	2g	Clay, trace silt, light grey tan. Cored as dense cuttings.	4	3	0	0	
190.50	192.02	2g	Clay, trace silt, light grey tan. Cored as cuttings, some cuttings dark brown in colour.	4	3	0	0	
192.02	193.54	2g	Sand, very fine, some silt. Dark grey to black.	2	3	0	1	
193.54	195.07	2g	Clay, some silt. Light grey tan. Dense cuttings.	4	3	0	0	
195.07	196.59	2g	Clay, trace silt. Light grey tan.	4	3	0	0	
196.59	198.12	2g	Clay, trace silt. Light grey tan, dense chips.	4	3	0	0	
198.12	199.64	2g	Clay, silty. Medium grey. Dense chips.	4	3	0	0	
199.64	201.16	2g	Clay, some silt. Tan grey, dense, chips are tan coloured.	4	3	0	0	
201.16	202.69	2g	Clay, some silt. Dense chips. Grey tan, lots of tan coloured cuttings. Approaching lithified claystone.	4	3	0	0	
202.69	204.21	2g	Clay, trace silt. Medium grey tan. Some dense chips.					
204.21	205.74	2g	Clay, some silt. Light grey green. Soupy.	4	3	0	0	
205.74	207.26	2g	Clay, some silt. Medium grey. Soupy.	4	3	0	0	
207.26	208.78	2g	Clay, some silt. Medium grey. Soupy.	4	3	0	0	

DH88P020			HIGHLAND VALLEY COPPER - VALLEY PIT GROUNDWATER					Page 7
metres		ID	DESCRIPTION	SEMIQUANT. DATA				ASSAYS
FROM	TO	CD		PRIM	SEC	TERT	WTR	SAMPLE #
208.78	210.31	2g	Clay, trace silt. Medium grey tan. Dense chips.	4	3	0	0	
210.31	211.83	2g	Clay, some silt. Medium grey tan, some chips.	4	3	0	0	
211.83	213.36	2g	Clay, some silt. Medium grey tan, soupy.	4	3	0	0	
213.36	214.88	2g	Clay, some silt. Medium grey tan. Lots of dense chips, tan.	4	3	0	0	
214.88	216.40	2c	Missing sample 705-710 ft, cored 700-710 ft.					
216.40	217.93	2g	Clay, trace silt. Tan, lots of very fine tan brown chips.	4	3	0	0	
217.93	219.45	2g	Clay, some silt. Medium grey tan. Very fine. Clay, some silt. Medium grey tan. Very fine, chips almost appear as fine sand grains.	4	3	0	0	
219.45	220.98	2g	Clay, some silt. Medium grey tan. Fine chips.	4	3	0	0	
220.98	222.50	2g	Clay, some silt. Medium grey tan. Few black specs, appear to be mica?? Lots of fine tan colour chips.	4	3	0	0	
222.50	224.02	2g	Clay, some silt. Medium tan grey, chips present.	4	3	0	0	
224.02	225.55	2g	Clay, some silt. Medium tan grey. Fine chips.	4	3	0	0	
225.55	227.07	2g	Clay, silty. Medium grey tan to green. Fine chips.	4	3	0	0	
227.07	228.00	2g	Clay, some silt. Medium grey tan. Fine tan chips.	4	3	0	0	
228.00	228.60	2g	Clay, some silt. Medium grey tan. Fine chips.	4	3	0	0	
228.60	228.60	1c	End of hole at 750 ft.					

298

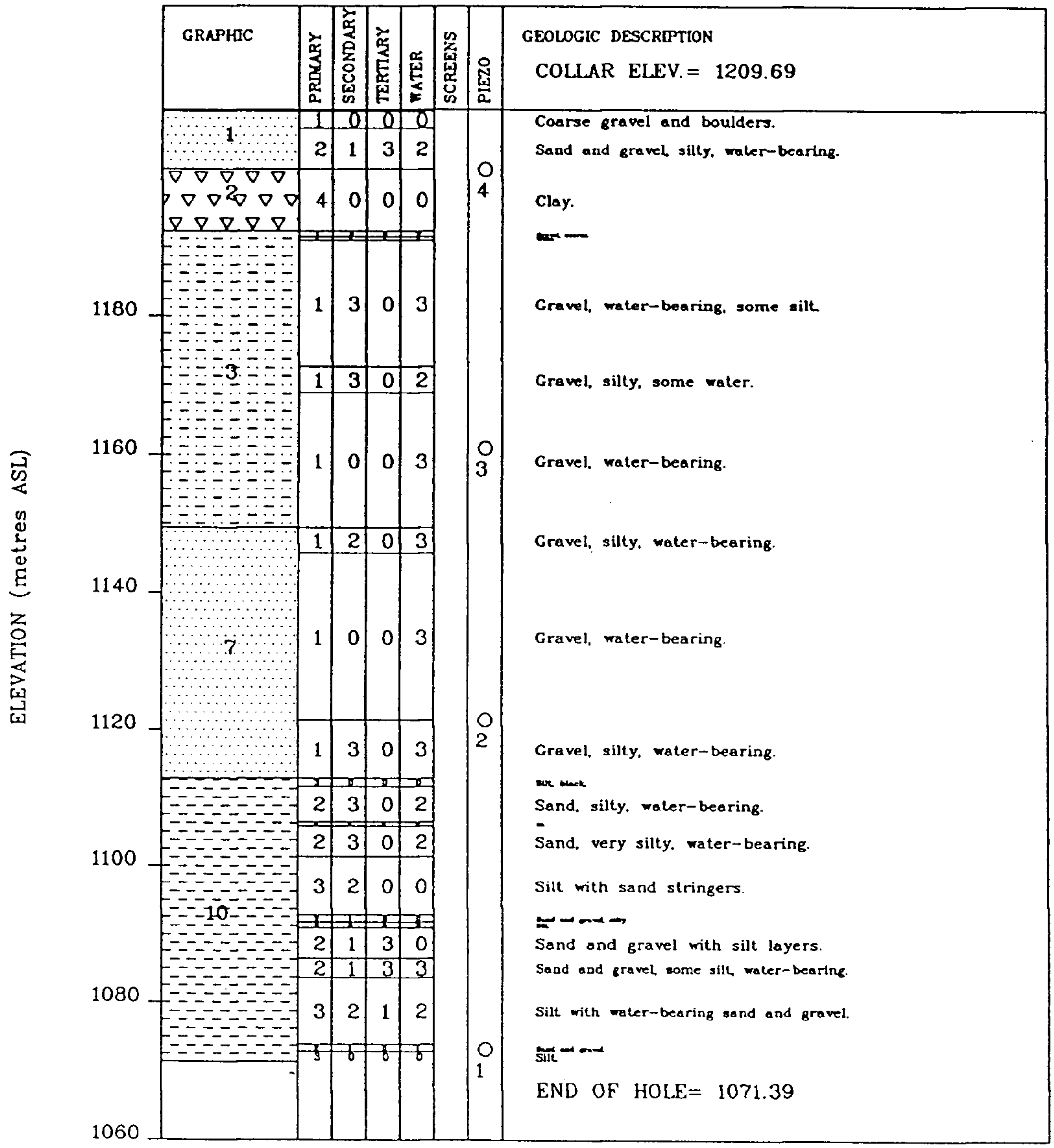

GL-STRIPLOG by: Gartner Lee Limited	HIGHLAND VALLEY COPPER OVERBURDEN GEOLOGY LOGS	Project: 89-001 Borehole: 88P020 File: FL83P005.DXF 01-28-1990 18:55:56

ELEVATION (metres ASL)

COLLAR ELEV.= 1210.8

ELEVATION	PRIMARY	SECONDARY	TERTIARY	WATER	PIEZO	GEOLOGIC DESCRIPTION
	2	1	3	0		Sand and gravel, very silty, brown.
1200	2	1	3	0		Sand and gravel, very silty, grey.
	[illegible]	[illegible]	[illegible]	[illegible]		[illegible]
	2	1	0	2		Sand and gravel, grey.
	2	1	0	1		Sand and gravel, coarse, brown, trace water.
	2	1	3	0		Sand and gravel, very silty, brown.
	2	0	0	1		Sand, coarse, brown.
	2	3	0	0		Sand, silty, fine, brown.
1180	2	3	0	0		Sand, very silty, fine, grey.
	2	1	3	0		Sand and gravel, silty, brown.
	1	0	0	1	O 3	Gravel, very coarse, with boulders.
1160	5	1	0	0		Till, gravelly, with boulders, brown.
	5	1	0	0		Till, gravelly, with boulders, brown.
	5	1	0	0		Till, gravelly, grey.
1140	2	0	0	4		Sand, very coarse, water bearing, lots of water.
	2	3	0	4		Sand, silty, grey, water bearing, lots of water.
	[illegible]	[illegible]	[illegible]	[illegible]		Sand, silty, grey, water bearing.
	[illegible]	[illegible]	[illegible]	[illegible]	O	Sand, coarse, clean, water bearing, fair amount water.
	2	3	0	1	2	Sand, very silty, grey, not as much water in zone.
1120	4	0	0	0		Dark grey clay and black clay.
	4	0	0	0		Greenish clay.
	4	0	0	0		Clay, grey.
1100	4	2	3	0		Clay with sandy layers and tight silt, grey.
	4	0	0	0		Clay, dark grey.
	4	0	0	0		Clay, black.
	4	0	0	0		Clay, black.
	3	4	0	0		Silt with clay, tight, grey.
1080	3	0	0	2		Silt layers, grey, water bearing.
	2	3	0	1		Sand, silty, grey, with a little water.
	3	2	0	0		Silt, with sandy layers, grey.
	4	0	0	0		Black clay.
	4	0	0	0		Clay, greenish.
1060	4	0	0	0		Clay, greenish.
	3	0	0	0		Silt, grey.
	[illegible]	[illegible]	[illegible]	[illegible]		Sand, silty, water bearing.
	4	0	0	0		Clay, grey.
	4	0	0	0		Black clay.
	2	3	4	0		Sand, silty, grey, with clay layers.
	4	0	0	0		Clay, black.
1040	3	0	0	0		Silt, dark grey.
	[illegible]	[illegible]	[illegible]	[illegible]		Sand, very silty, grey, with water.
	2	3	0	2		Sand, very silty, grey, water bearing.
	2	0	0	0		Sand, black.
	4	0	0	0		Clay, black.
	2	3	0	3		Sand, silty, grey, water bearing.
1020	2	3	0	3		Sand, silty, grey, water bearing.
	4	0	0	0		Clay, greenish.
	4	0	0	0		Clay, greenish.
1000	5	2	1	1		Till, small layers of w.b. sand and gravel, grey.
	1	2	3	3		Gravel and sand, silty, grey, makes fair amount water.
	2	1	3	3		Sand and gravel, finer, silty, grey, fair amount water.
	2	0	0	3		Sand, clean, brown, makes water, lots of heave.
980	2	3	0	0		Sand, silty, grey.
	2	0	0	3		Sand, clean, brown, water bearing.
	7	0	0	0		Bedrock, oxide zone, brownish, soft.
	7	0	0	0		Bedrock, granite.
	7	0	0	3		Oxide zone bedrock, very broken, makes lots of water.
960	7	0	0	3	O 1	Open hole in bedrock, broken, soft, water bearing.

END OF HOLE= 960.9

GL–STRIPLOG
by: Gartner Lee Limited

HIGHLAND VALLEY COPPER
OVERBURDEN GEOLOGY LOGS

Project: 89-001
Borehole: 83P013
File: FL83P013.DXF
01-28-1990 17:54:34

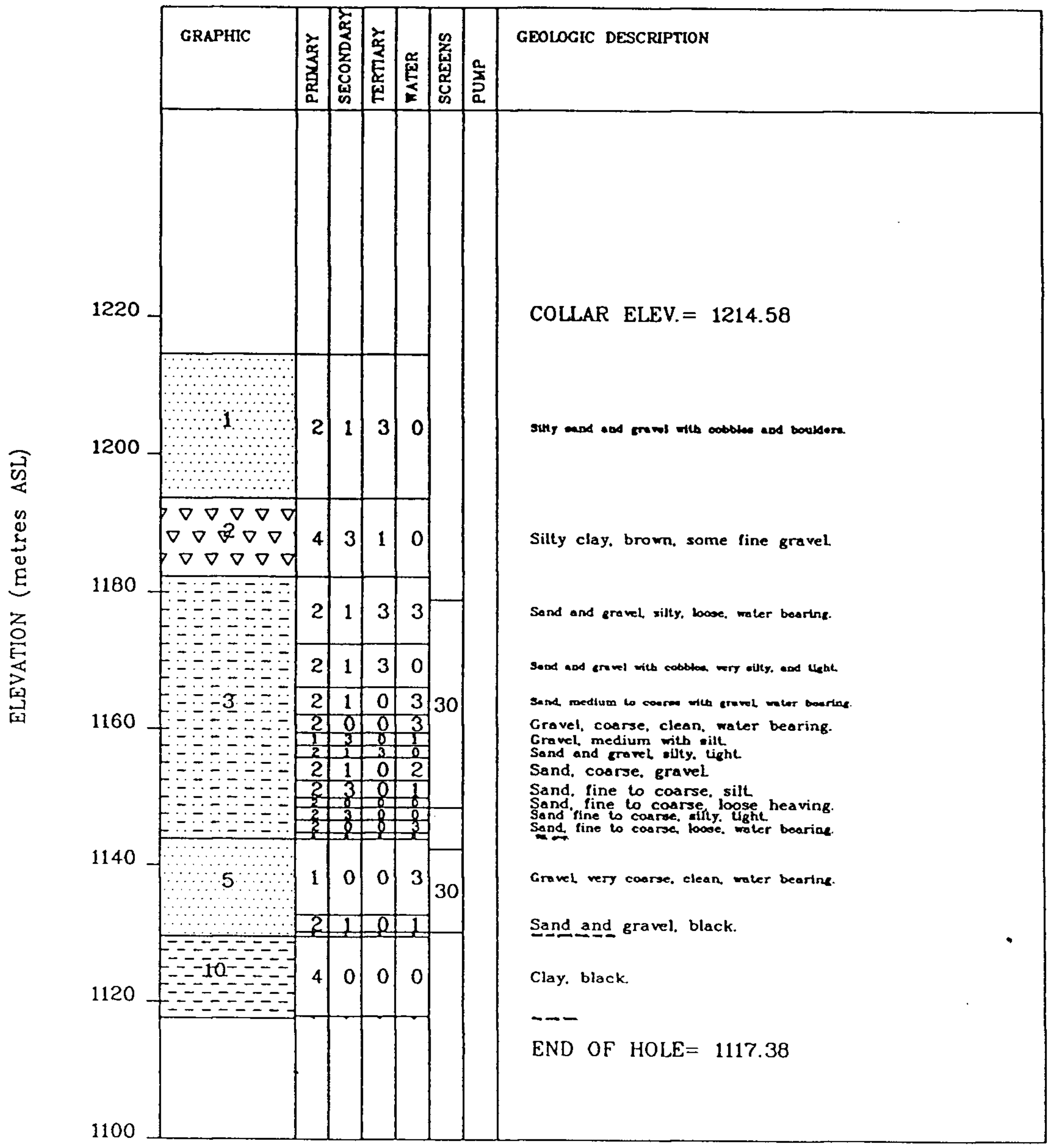

GL-STRIPLOG

by: Gartner Lee Limited

HIGHLAND VALLEY COPPER

OVERBURDEN GEOLOGY LOGS

Project: 89-001
Borehole: 84W002
File: FL84W002.DXF
01-28-1990 16:06:07

ELEVATION (metres ASL): 1190, 1170, 1150, 1130, 1110, 1090, 1070, 1050, 1030, 1010

COLLAR ELEV.= 1210.48

GRAPHIC	PRIMARY	SECONDARY	TERTIARY	WATER	SCREENS	PUMP	GEOLOGIC DESCRIPTION
	5	0	0	0		O	Till, brown, back hoe dug.
2	2	1	3	0			Sand and gravel, tight, silty.
	[illegible]	[illegible]	[illegible]	0			Till, grey, silty.
	2	1	3	1			Sand and gravel, tight, silty, water-bearing lenses.
	5	0	0	0			Till, grey.
	2	1	0	3			Sand and gravel, coarse, water-bearing.
	2	1	3	0			Sand and gravel, tight, silty.
	4	3	2	0	20		Clay, silty, sandy.
3	3	2	0	0			Silt, tight and silty sand.
	2	1	3	0			Sand and gravel, very tight, silty.
	[illegible]	[illegible]	[illegible]	[illegible]			[illegible]
	2	1	3	3	20		Sand and gravel, silty, water-bearing.
	[illegible]	[illegible]	[illegible]	[illegible]			Sand and gravel, tight, silty.
	[illegible]	[illegible]	[illegible]	[illegible]			Sand and gravel, boulders, water-bearing.
	[illegible]	[illegible]	[illegible]	[illegible]			Till, silty, brown.
	2	1	3	1			Sand and gravel, tight, silty.
4	5	4	0	0			Till, clayey, grey.
	5	2	3	0	20		Till, sandy and silty.
	[illegible]	[illegible]	[illegible]	[illegible]			[illegible]
5	1	3	0	0			Gravel, silty, tight, with layers of tight silt.
	2	1	3	2	20		Sand and gravel, silty, water-bearing.
	[illegible]	[illegible]	[illegible]	[illegible]			Silt, tight, green.
	[illegible]	[illegible]	[illegible]	[illegible]			Clay, silty, black.
	[illegible]	[illegible]	[illegible]	[illegible]			Gravel, silty, tight, black.
	[illegible]	[illegible]	[illegible]	[illegible]			Till, silty.
	2	1	3	2	20		Sand and gravel, silty with water-bearing stringe blk.
	3	4	0	0			Silt and silty clay, tight, dark grey to black.
	4	3	0	0			Clay with silt layer, sticky dark grey.
	4	0	0	0			Clay, black, sticky.
10	4	3	0	0			Clay, black with seams of silty clay, green.
	4	3	0	0			Clay, black with layers of tight silt.
	4	3	0	0			Clay, black with silty sand.
	3	0	0	0			Silt, tight, very stiff.
	4	3	0	0			Clay, black and silt.
	4	3	2	0			Clay, silty, black with layers of silty sand.
12	2	3	0	1	20		Sand, silty, with layers of silt and silty sand. w-b.
21							Bedrock, granitic.

END OF HOLE= 1016.68

GL-STRIPLOG

by: Gartner Lee Limited

HIGHLAND VALLEY COPPER

OVERBURDEN GEOLOGY LOGS

Project: 89-001
Borehole: 85W007
File: FL85W007.DXF
01-28-1990 17:34:22

ELEVATION (metres ASL): 1190, 1170, 1150, 1130, 1110, 1090, 1070, 1050

GRAPHIC	PRIMARY	SECONDARY	TERTIARY	WATER	SCREENS	PUMP	GEOLOGIC DESCRIPTION
							COLLAR ELEV.= 1211.6
1	1	3	0	3		O	Gravel, some cobbles, silty. Brown.
2	5	3	2	0			Till, silty and sandy with cobbles. Some silt layers. Brown.
3	1	2	0	4			Gravel, coarse, mostly boulders, cemented with silt. Layers of till and coarse water bearing gravel. Boulders are granitic. Colour is brown.
4	5	3	1	1			Till, silty and sandy with cobbles. Sand is graded. Colour is brown. Numerous layers of cemented brown gravel. Some gravel layers are water bearing.
5	1	2	3	3			Gravel, coarse, silty, some sand. Sand is graded. Brown, mostly water bearing, becoming cleaner with depth.
	2	3	1	2			Sand, medium to fine, silty layers, some fine gravel. Dark grey, water bearing.
6	5	4	2	0			Till, clayey, some sand and cobbles. Dark grey.
7	3	4	1	0			Silt with layers of cobbly till and clay. Dark grey. Transition layer between till and black clay unit.
							END OF HOLE= 1059.2

GL-STRIPLOG

by: Gartner Lee Limited

HIGHLAND VALLEY COPPER

OVERBURDEN GEOLOGY LOGS

Project: 89-001
Borehole: 87W021
File: FL87W021.DXF
01-28-1990 19:40:10

GRAPHIC	PRIMARY	SECONDARY	TERTIARY	WATER	SCREENS	PIEZO	GEOLOGIC DESCRIPTION
							COLLAR ELEV.= 1204
1	2	1	0	4			Sand and gravel. Grey.
2	5	3	4	0			Till, silt and gravel.
	5	3	1	0			Till, some boulders. Dark grey.
3	2	3	1	2			Graded fluvial, including gravelly silt and sandy gravel. Dark grey green. Transition unit between overlying till and underlying sand and gravel.
	2	1	0	2			Medium to coarse sand, silty, lenses of water bearing sand and gravel and till. Driller reports unit as till, most appears fluvial.
	2	1	0	4			Sand and gravel, silty. Brown, water bearing, gravel mostly coarse.
	2	1	3	4			Fine gravel and sand, very silty. Brown.
	2	3	4	1			Dense brown silt, layers of water bearing silty sand and gravel.
4	5	2	3	0			Graded sand, silty, some fine gravel. Grey, dense, some water bearing layers of silty sand. Driller reports lithology as till. Appears to be fluvial unit when cup sample examined.
5	3	4	0	0		O 5	Grey silt and grey silty sand and gravel, interbedded. Water bearing.
10.1	4	3	0	0			Clay, dark grey to black, with silt layers.
	4	3	0	0			Clay and silt. Dark green, black and grey. Dense.
	2	3	0	2			Fine gravel and sand, dark grey, silty, water bearing.
	3	4	0	0		O 4	Dark grey to black silt and clay, some thin layers of silty sand and gravel. Water bearing.
	[illegible]	[illegible]	[illegible]	[illegible]			Fine sand, silty. Dark grey. Driller reports sand and gravel, water bearing?
	3	4	0	0			Silt and clay. Dark grey to medium grey green or black. Dense.
	2	3	0	2			Silty sand. Dark grey. Water bearing.
	3	4	0	0		O 3	Silt and clay. Dark grey, becoming grey green with depth. Oxidized to medium grey green colour. Cuttings soupy, but fragments indicate original material dense.
	2	1	0	4			Sand and gravel, dark grey to blackish, water bearing.
	3	4	0	0			Dark grey to black silt and clay, dense to very dense.
	2	3	0	2		O 2	Dark grey to black silty gravel and sand, water bearing.
	2	3	0	2			Interbedded very fine silty sand and silt. Dark grey green. Water bearing.
	4	3	0	0			Clay and silt. Dark grey green. Oxidized to medium grey green.
10.2	3	4	0	0		O 1	Silt and clay. Medium grey, dense, oxidized to medium grey green. Colour is lighter than previous unit. Some sandy layers.

ELEVATION (metres ASL): 1175, 1155, 1135, 1115, 1095, 1075, 1055, 1035, 1015, 995, 975

END OF HOLE= 975.4

GL–STRIPLOG by: Gartner Lee Limited	HIGHLAND VALLEY COPPER OVERBURDEN GEOLOGY LOGS	Project: 89-001 Borehole: 88P020 File: FL88P020.DXF 02-03-1990 18:08:03

E.3 HYDROLOGIC DATA

Estimates of hydraulic conductivity in the overburden have been obtained from five different methods, including:

1. Pump Tests
2. Long Term Well Response
3. Laboratory Triaxial Tests - C_v
4. Grain Size Analyses
5. Correlation to Logged Geologic Descriptions

This appendix presents several figures that portray the types of hydrologic data that are routinely analyzed at HVC. Because the hydrologic data base is extensive and details of the various analyses have been compiled previously in a number of technical reports prepared by Brown-Erdman, by Golder Associates and by this author, only a small number of selected figures are portrayed in this appendix. The objective is to provide the reader some background as to the types of information that have been utilized in obtaining the hydraulic conductivity values presented in *Section 8.4.*

E.3.1 PUMP TESTS

Figures E.9 to *E.11* present the results of Jacob-Cooper semi-log pump test analyses for wells DW-12, DW-14 and DW-19. In the semi-log evaluation, drawdown is first plotted against the logarithm of elapsed time (as depicted in upper left windows in figures). Any interval for which pumping continued at a constant rate can then be analyzed (upper right window zooms in on specified interval). The best straight line segment is then identified. The slope and Y-intercept of the line segment are used to calculate transmissivity and storativity.

All pump tests were evaluated with computer program SG-PUMP. The user friendly, graphic intensive program was developed by the author in 1987-1988 as part of this thesis research to analyze the stepped pump test data at Highland Valley Copper. The program is now fully tested and documented. In addition, it has been incorporated in the UBC geological engineering curriculum as a laboratory exercise.

Figure E.9 SG-PUMP Results for DW-12

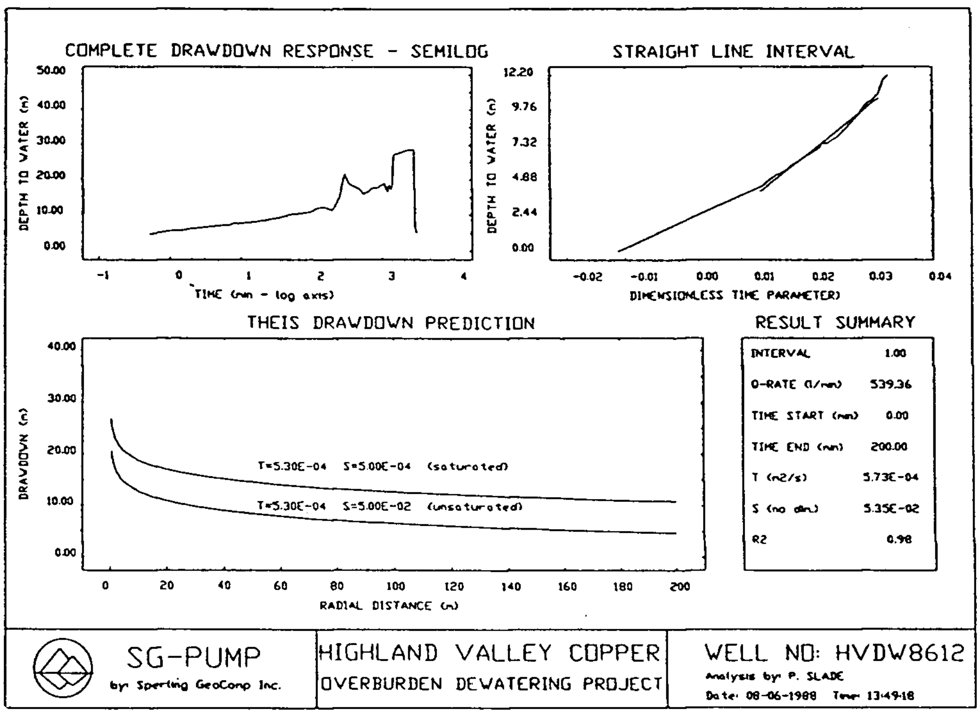

Figure E.10 SG-PUMP Results for DW-14

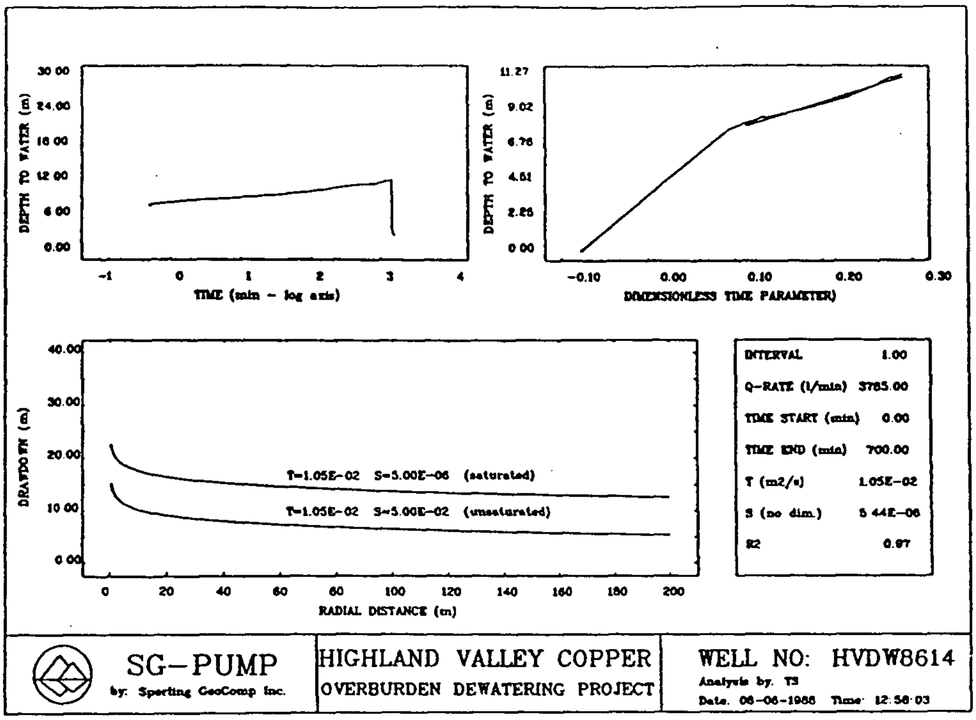

Figure E.11 SG-PUMP Results for DW-19

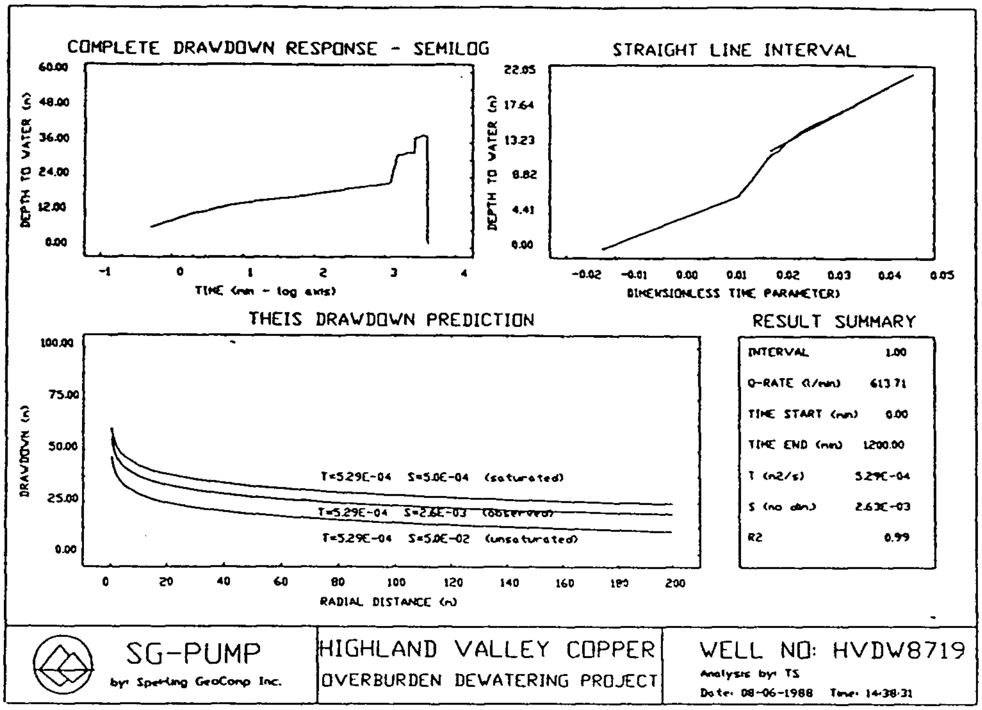

E.3.2 LONG TERM WELL RESPONSE

The long term piezometric response in a well bore can be used to back-calculate aquifer transmissivity via the Theis equation provided that an accurate record of water levels and pumping rates in the well bore is maintained. At Highland Valley Copper, water levels, flow rates and a number of other parameters are monitored on a routine basis at each well location. All groundwater monitoring data is routinely entered into the SG-WELL computer data base that was developed for HVC by the author in 1987. SG-WELL is used to store the large quantities of information in a compact and easily retrievable format and to generate a variety of graphs to assist in interpretation. *Figure 8.12* shows a typical SG-WELL time graph of the long term drawdown response at DW-01. The figure indicates that a steady state drawdown of approximately 24 m was attained in mid-1986 after two years of pumping. A transmissivity estimate is obtained from this data by substituting the observed drawdown, the average pumping rate and an assumed confined aquifer storativity into the Theis equation and solving for T. In this example, upon substituting the values listed in *Figure 8.12*, the calculation yielded $T = 5\text{x}10^{-4}$ m^2/s. The same approach was used to calculate each of the long term hydraulic conductivity estimates reported in *Section 8.4.4.*

Figure E.12 Long Term Drawdown Response at DW-01

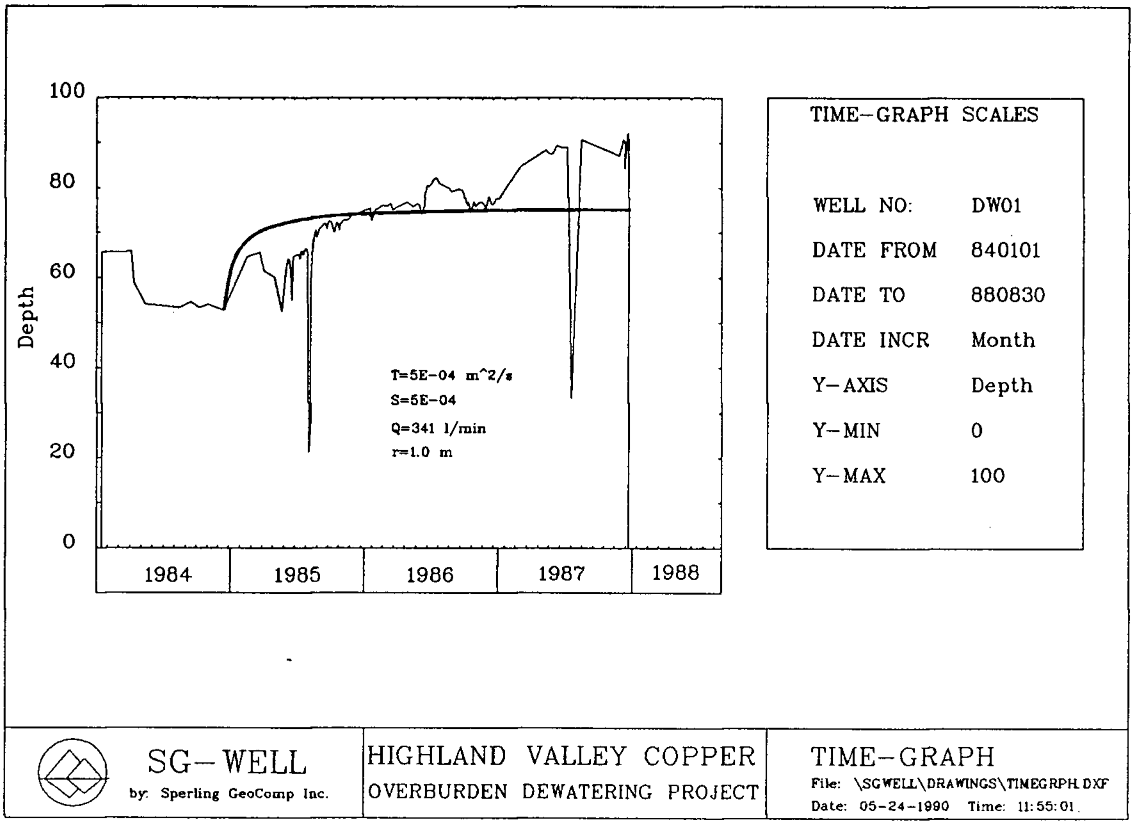

E.3.3 GRAIN SIZE CURVES

The methodology for estimating K from grain size distributions is documented in *Section 8.4.6*. This appendix presents a number of figures that depict representative grain size distributions for most of the overburden horizons at Highland Valley Copper. The complete set of grain size distribution data from which the following figures were reproduced can be found in Appendix A of Golder Associates Technical Report 872-1416.

Figure E.13 Grain Size Distribution - Unit 3, OH-ONE DIVIDER

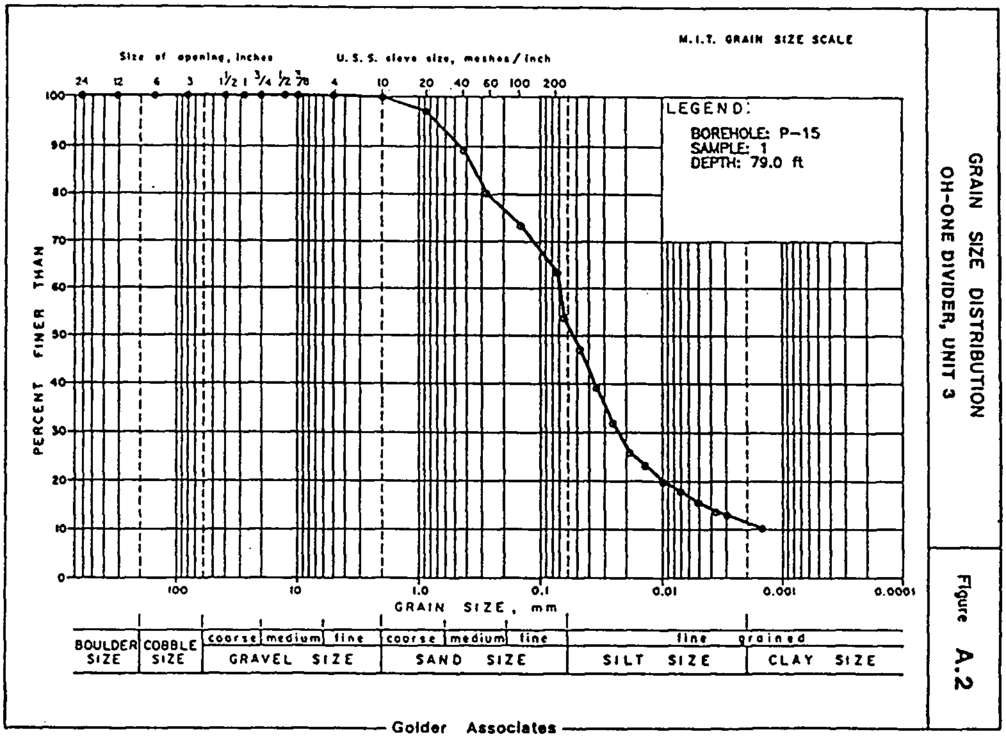

Figure E.14 Grain Size Distribution - Unit 4, TILL-1

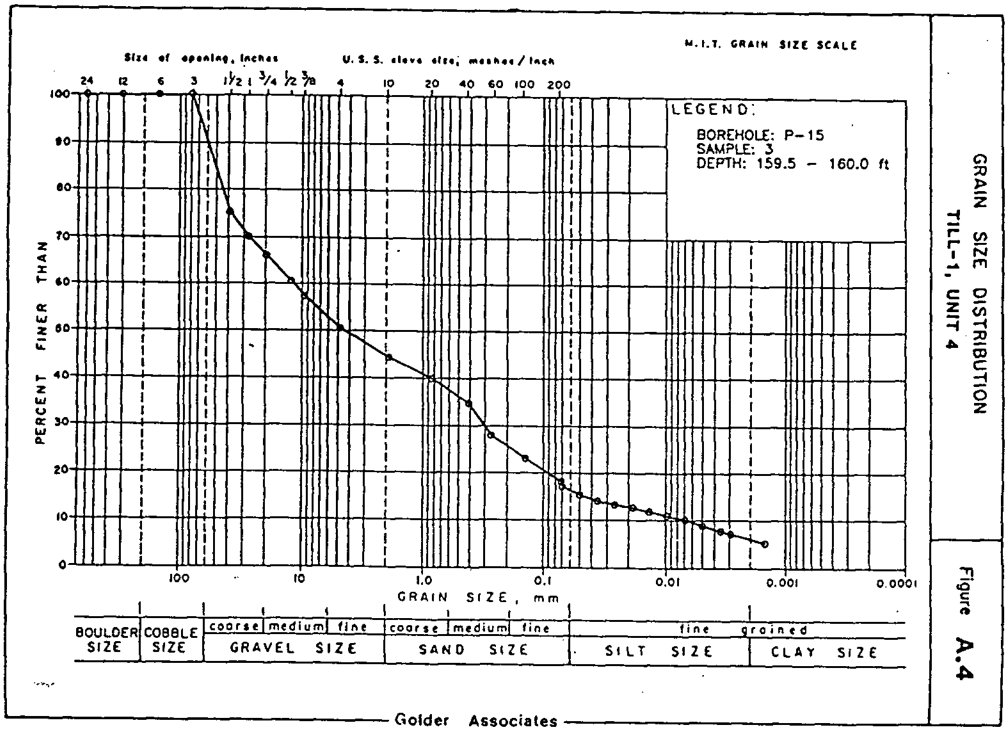

Figure E.15 Grain Size Distribution - Unit 5, SILTY AQUIFER

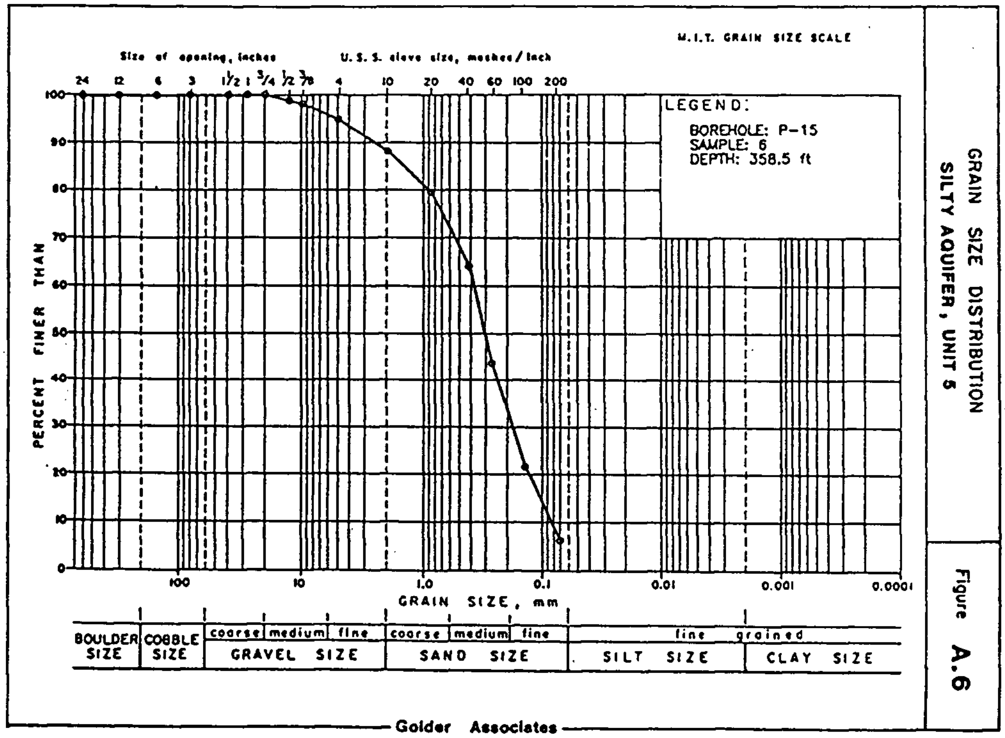

Figure E.16 Grain Size Distribution - Unit 7, MAIN AQUIFER

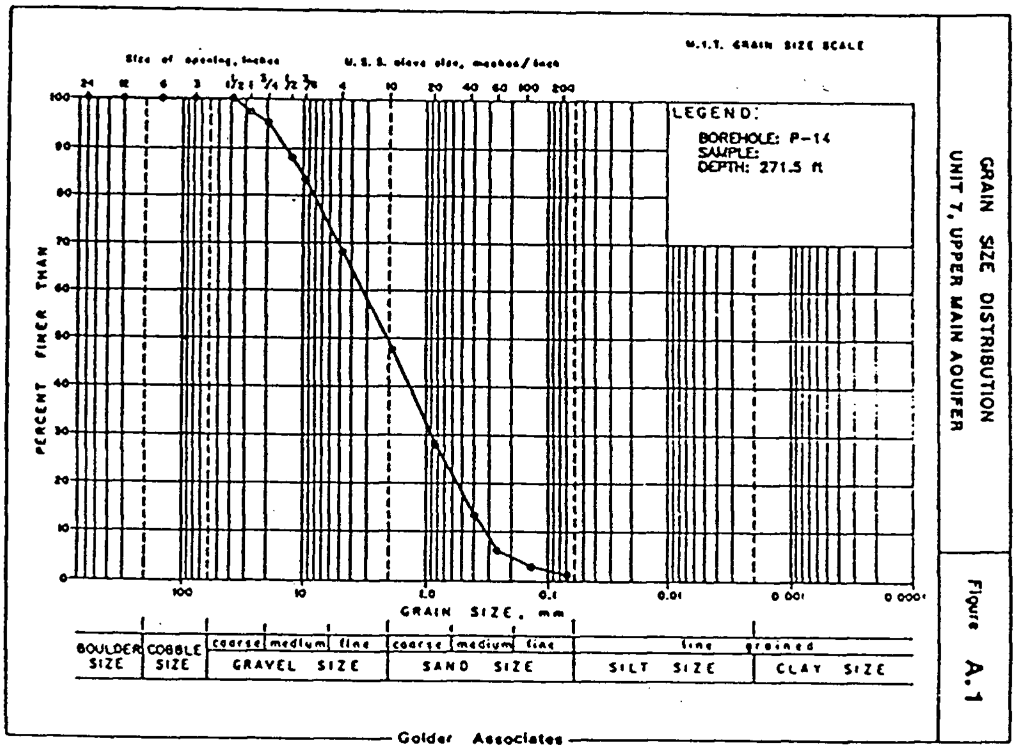

Figure E.17 Grain Size Distribution - Unit 10A, OLIVE GREEN SILT

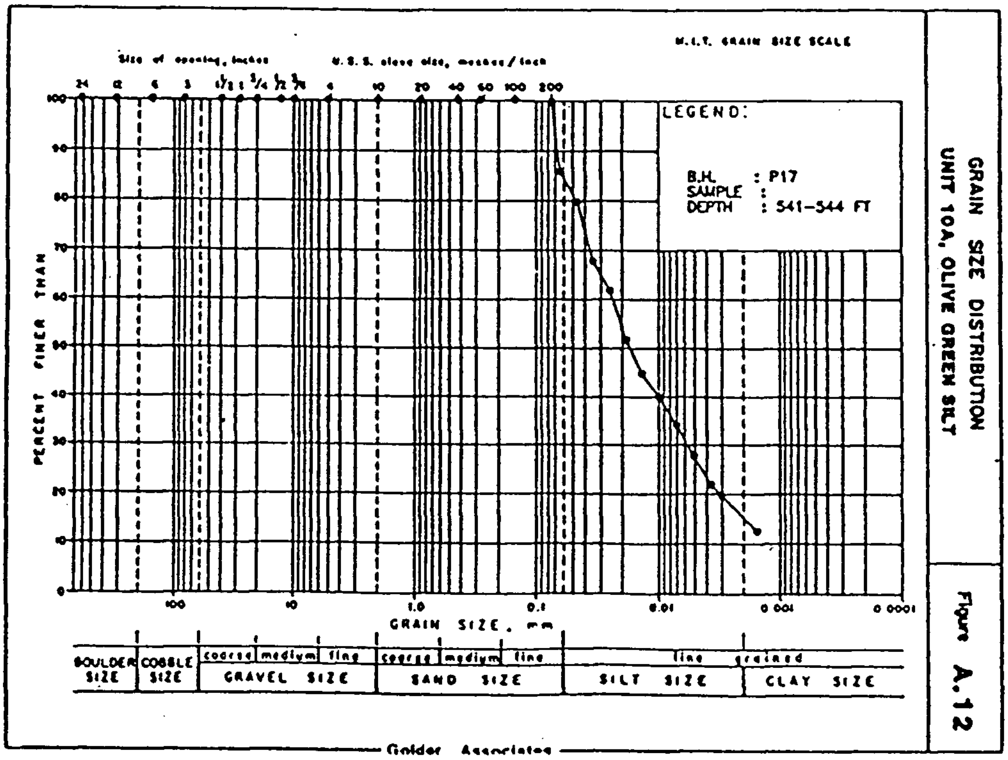

Figure E.18 Grain Size Distribution - Unit 10B, TAN GREY CLAYEY SILT

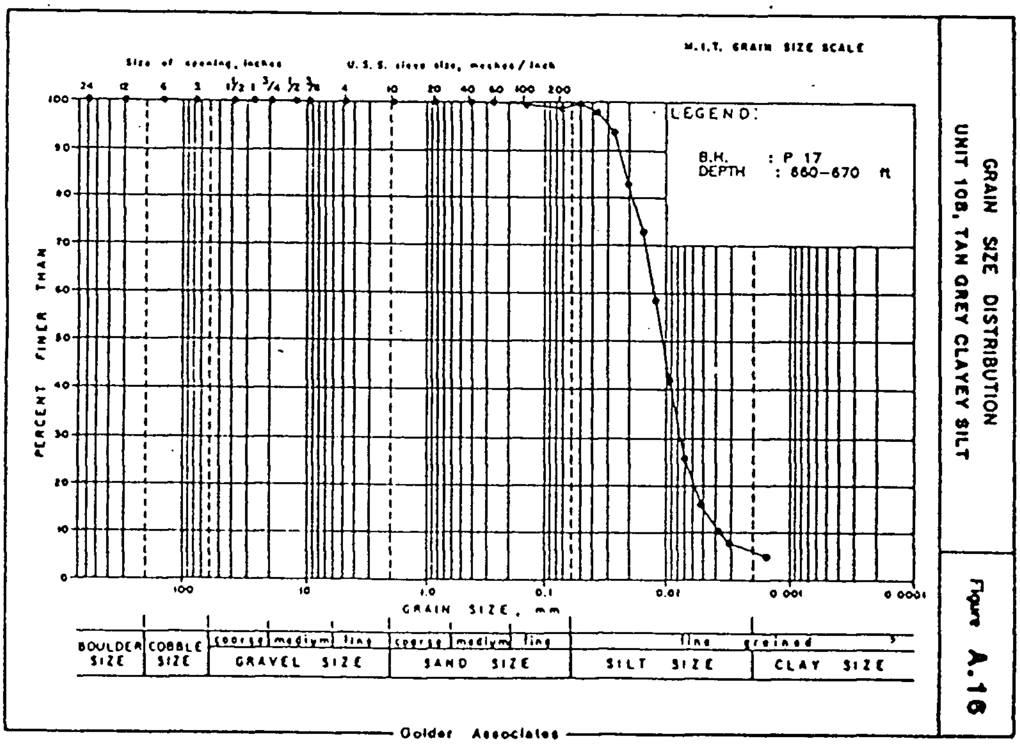

E.4 ECONOMIC DATA

At Highland Valley Copper, as at other open pit mines, annual operating costs will depend on the following factors: mining rate (tonnes/year), unit costs of mining and milling, costs of groundwater control, and possibly, costs associated with slope failure. This section documents the various production statistics and cost coefficients that were required in order to complete the risk-cost-benefit analysis in design sector R-3. The intent is to provide a useful reference for future design studies at HVC and an example of the types of information required to conduct an economic assessment of groundwater control options at other open pit mines.

Appendix E.4.1 illustrates the latest mine plan for the design sector. *Figure E.19* defines the extent of the various expansion pits on section, while *Figures E.20* to *E.23* illustrate the development of the pit in plan view at five year intervals. The location of active dewatering wells and the anticipated pumping rates (in USGPM) are also illustrated in the figures.

Appendix E.4.2 documents production statistics and cost coefficients for the analysis. *Table E.2* provides a summary of the important aspects of the risk-cost-benefit model for the design sector, including geologic conditions, slope stability parameters, hydrogeologic parameters, economic coefficients, production statistics, and information on the frequency of subsurface measurements. The information summarized in this table provides a useful reference for direct comparison studies of the dewatering program at HVC to those at other operating mines. The expected costs of the groundwater control program in sector R-3 are summarized in *Tables E.3* to *E.5*. *Table E.3* presents a break-down of expenditures for each aspect of the groundwater control program, including well development, operating costs, and a water supply bonus. *Table E.4* identifies unit costs associated with well development for well diameter independent items, while *Table E.5* provides a list of unit costs for diameter dependent items.

***Figure E.19** Cross-Section Illustrating Development of Pit.*

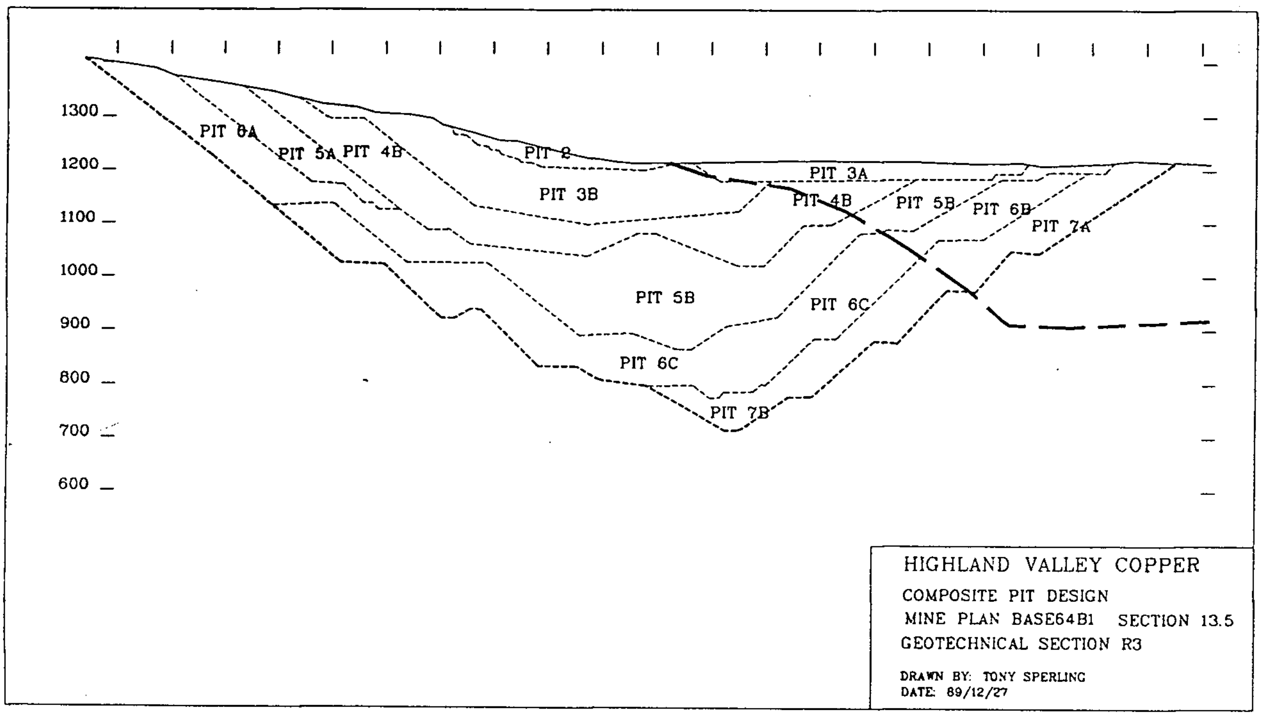

Figure E.20 Plan Showing 1987 Pit Configuration and Active Dewatering Wells

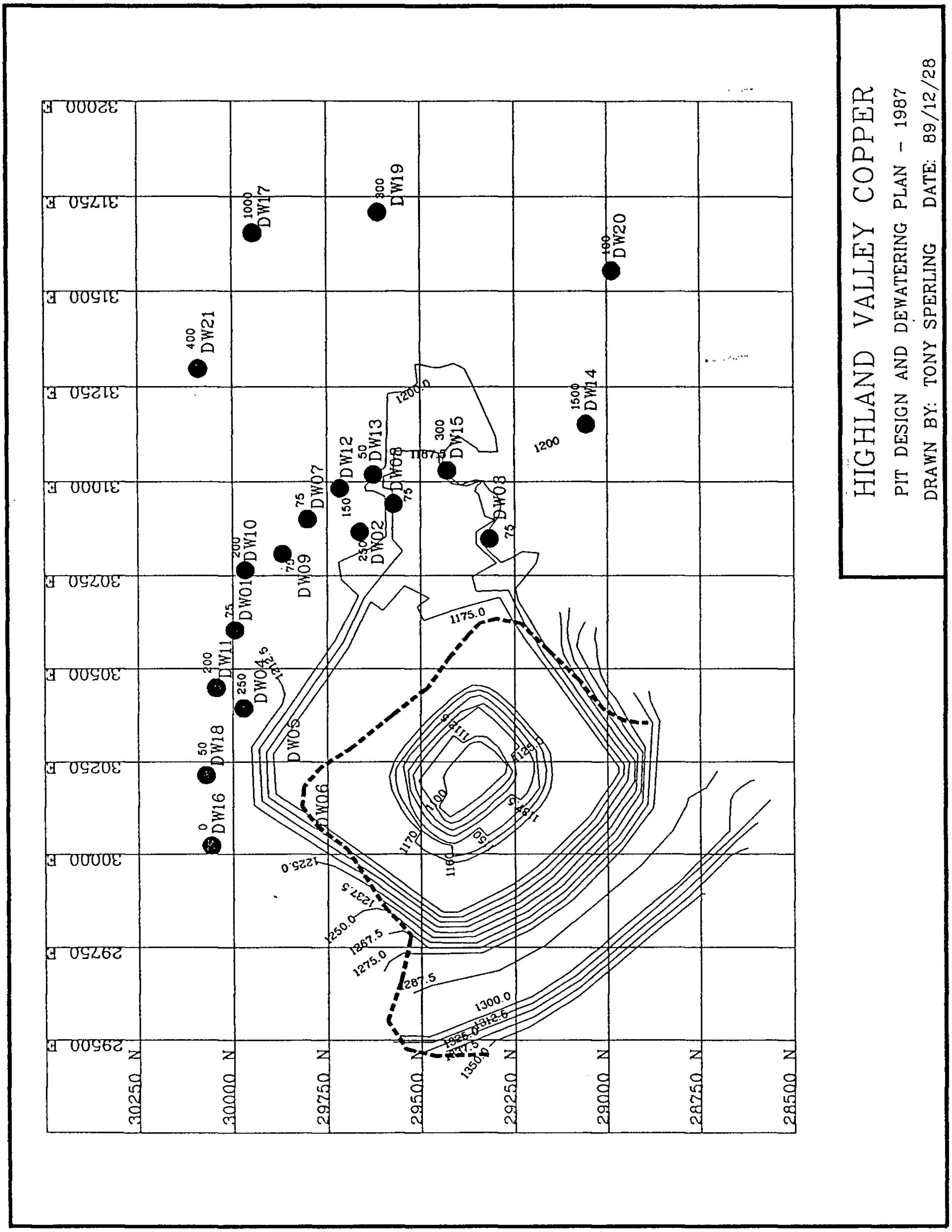

Figure E.21 Plan Showing 1992 Pit Configuration and Active Dewatering Wells

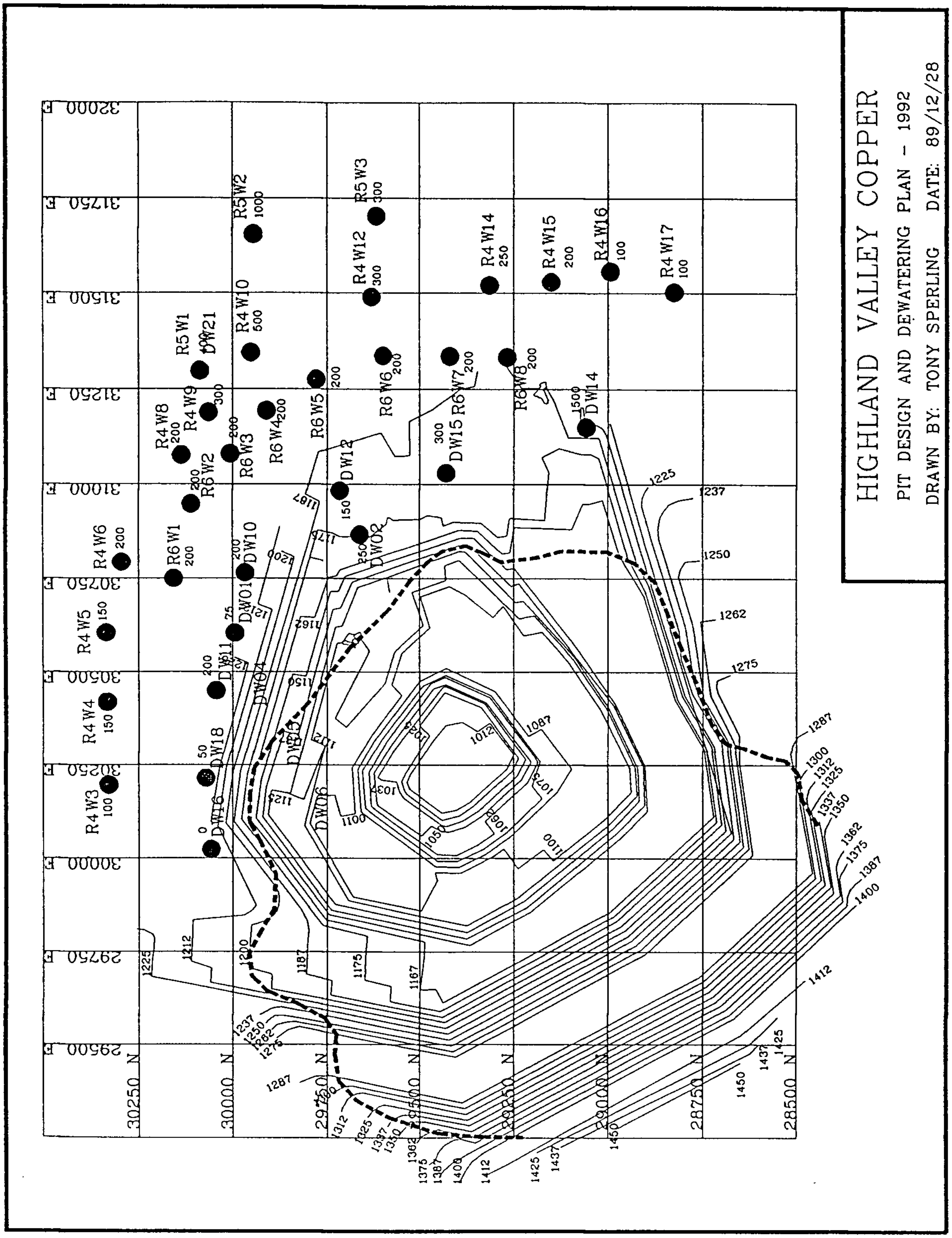

Figure E.22 Plan Showing 1997 Pit Configuration and Active Dewatering Wells

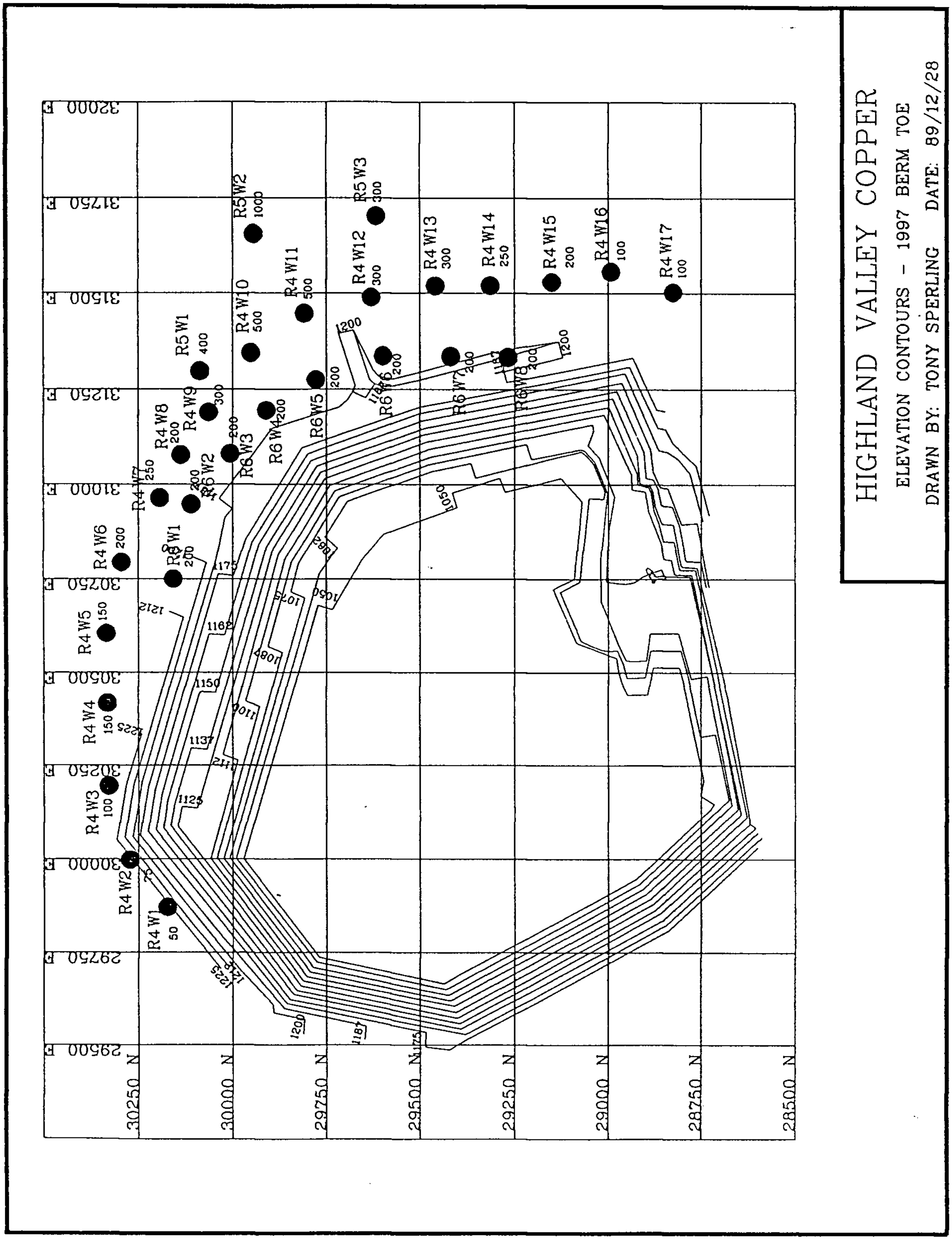

Figure E.23 Plan Showing Ultimate Pit Configuration and Active Dewatering Wells

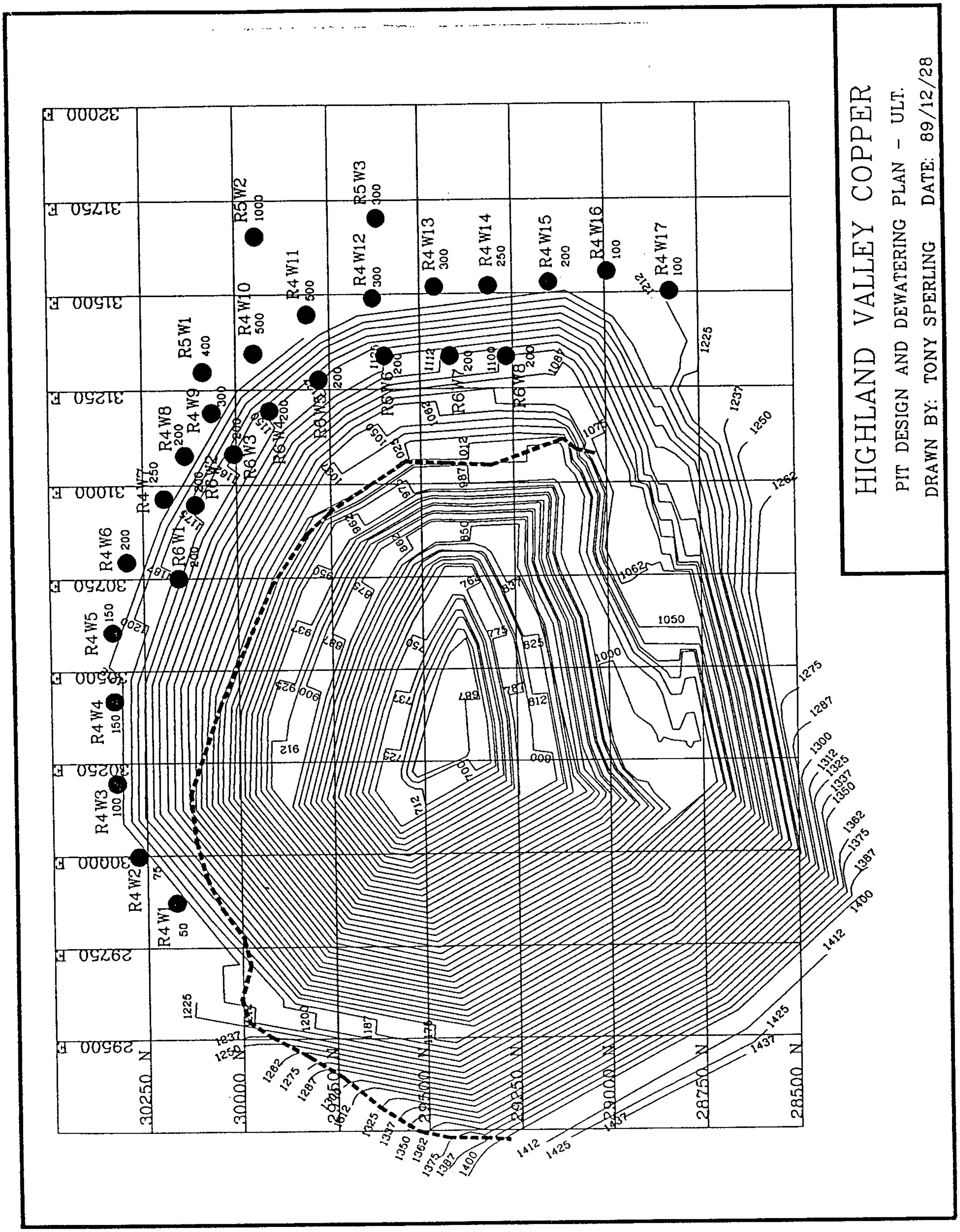

Table E.2 Overview of Risk-Cost-Benefit Model Parameters

PARAMETER	LOWER LIMIT	UPPER LIMIT	BASE CASE
1. GEOLOGY - ORE GRADE			
Size of ore body (billion tonnes)	2.1		
Shape of ore body	disseminated copper porphyry		
massive			
planar vein			
zoned			
disseminated			
Orientation of ore body	Fault controlled. High grade zones have have near vertical boundaries relative to pit wall.		
horizontal			
vertical			
inclined parallel to pit wall			
inclined orthogonal to pit wall			
Average grade (%Cu equivalent)	0.35 (approximate)		
Grade Intervals (%Cu equivalent)			
waste	0.00	0.15	0.075
low grade	0.15	0.35	0.25
medium grade	0.35	0.55	0.45
high grade	>0.55		0.65
Nature of ore/waste transition	gradational boundary		
sharp boundary			
local pockets			
gradational boundary			
2. GEOLOGY - ROCK/OVERBURDEN TYPE			
Location ovb. bedrock contact	inclined orthogonal		
horizontal			
inclined parallel			
inclined orthogonal			
Angle ovb. bedrock contact (degrees)	20 degrees		
Height ovb. slope (meters)	220 m		
Type of overburden deposit	stratified, sands, silts, gravels, tills		
Digability characteristics rock (%)			
hard	60		
medium	15		
soft	25		
problem	0		
Digability characteristics ovb. (%)			
hard	10		
medium	30		
soft	55		
problem	5		
Dry Unit weight rock (tonnes/m^3)	2.55		
Dry Unit weight ovb. (tonnes/m^3)	1.50		

Table E.2 cont. Overview of Risk-Cost-Benefit Model Parameters

PARAMETER	LOWER LIMIT	UPPER LIMIT	BASE CASE
3. SLOPE STABILITY			
Anticipated failure mechanism	composite, predominantly circular with		
circular	preferential shear through unit 10B		
planar			
block			
toppling			
composite			
Critical failure surface	deep		
shallow seated			
medium seated			
deep seated			
Mean friction angle (degrees)	17	36	depends on
Stnd. dev. friction angle (degrees)	1	2	geologic
Mean cohesion (kN/m^2)	0	121.5	horizon
Stnd. dev. cohesion	0	60	10
4. HYDROGEOLOGY			
Type of flow system	layered aquifer/aquitard		homogeneous
aquifer / aquitard			
homogeneous			
Mean hydraulic conductivity (m/s)	1E-11	1E-4	1E-6
Stnd. dev. log hydraulic cond.	0.75		
Correlation Range (metres)	20 vertical, 1000 horizontal		
Anisotropy ratio range (vert./hor.)	0.05		
Semi-variogram model	spherical		
nugget			
exponential			
spherical			
Gaussian	specified flux in lower sequence		
Boundary condition inflow face	specified head in upper sequence		
specified head (metres)	1170	1200	
specified flux (m^3/s/m^2)	8.0E-11	8.0E-7	
Recharge rate on slope (cm/yr)	30		
Recharge rate in uplands (cm/yr)	6.9		
Initial water table position (metres)	1200		
5. ECONOMIC PARAMETERS			
Cut of grade (%Cu equivalent)	0.15		
Inflation rate each period (%)	10.0		
Interest rate each period (%)	10.0		
Price received for Cu concentrate ($/kg)	1.40		

Table E.2 cont. Overview of Risk-Cost-Benefit Model Parameters

PARAMETER	LOWER LIMIT	UPPER LIMIT	BASE CASE
6. PRODUCTION COSTS			
Mining hard rock ($/tonne)	1.00		
Mining medium rock ($/tonne)	0.97		
Mining soft rock ($/tonne)	0.95		
Mining failed rock ($/tonne)	0.90		
Mining hard ovb. ($/tonne)	1.25		
Mining medium ovb. ($/tonne)	1.17		
Mining soft ovb. ($/tonne)	1.10		
Mining failed ovb. ($/tonne)	1.00		
Milling ore ($/tonne)	2.00		
Mill recovery (%)	89		
7. PIT DESIGN			
Size ultimate pit (billion tonnes)	2.1		
Radius ultimate pit (metres)	1000		
Depth ultimate pit (metres)	700		
Production rate (million tonnes/yr)	20		
Frequency pit designs (yrs.)	5		
Expected life of mine (years)	20		
Pit angle bedrock	45		
Pit angle overburden	26		
Height design sector (metres)	220		
Width design sector (metres)	500		
8. DEWATERING SYSTEM DESIGN	(see Section 8.5.2 and Appendix E.4)		
Type of dewatering system	vertical wells		
Number of wells per pushback (avg.)	5		
Depth of each well (metres)	120		
Spacing of each well (metres)	100	200	
Number of drains per pushback	0	0	
Spacing of drains (metres)	NA		
Length drainage adit (metres)	0		
Cost installing well ($/metre)	1250		
Cost operating well ($/year)	20000		
Pumping rate each well (m^3/day)	50	1500	
Discharge rate each drain (m^3/day)	NA		
Production water requirements (m^3/day)	290,000		
Cost alternate water supply ($/m^3)	0.10		
9. SUBSURFACE MEASUREMENTS			
Type of measurement			
Geotechnical logging	all holes		
Shear strength tests	22 (avg. 3 per hole)		
Sieve analyses	34		
Slug tests in piezo	none		
Pump tests in well	21		
Geophysical logging	none		

Table E.3 Break-down of Dewatering Costs per Push-back.

YEAR FROM	YEAR TO	WELLS DRILLED	TOTAL METRES	DEVELOP COST	OPERATING WELLS	PUMP RATE (m^3/day)	OPERATING COST	SUPPLY BONUS	TOTAL COST
1984	1987	9	1428	$1,710,126	9	1375	$1,002,692	$968,548	$1,744,270
1987	1992	3	341	$518,213	7	3000	$2,112,875	$2,279,813	$351,277
1992	1997	7	985	$1,276,532	11	4150	$3,149,729	$3,476,841	$949,421
1997	2002	0	0	$0	11	4150	$3,810,040	$4,072,870	($262,830)

Table E.4 *List of Unit Costs for Well Diameter Independent Items*

ITEM	UNIT	UNIT COST
Pump Test	$/unit	9900
Lower Pump	$/unit	1650
Lift Pump	$/unit	2475
Rig Time	$/hour	165
Well Head Labour	$/unit	3960
Pump <750 gpm	$/unit	12000
Pump >750 gpm	$/unit	18000
Starter <750 gpm	$/unit	2000
Starter >750 gpm	$/unit	8000
Cable	$/m	20
Electric Power	$/m^3/day/yr	27.5
Maintenance	$/well/yr	10000
Monitoring	$/well/yr	2500
Water Supply Bonu	$/m^3/day/yr	40.37

Table E.5 List of Unit Costs for Well Diameter Dependent Items.

ITEM		16 INCH	12 INCH	10 INCH	08 INCH	06 INCH
Drill and Case	$/m	187	144	127	116	94
Cut Shoe	$/u	2640	2640	2640	2200	2200
String Casing	$/m	0	121	100	88	73
Casing Left	$/m	132	90	61	51	33
Screens	$/m	0	307	220	187	165
Blanks	$/m	0	77	55	43	30
Drop Pipe	$/u	0	0	0	209	44
Discharge Head	$/u	0	0	0	1346	1038
Gate Valve	$/u	0	0	0	932	560
Check Valve	$/u	0	0	0	1209	620